Ejection de matière dans les objets protostellaires et les étoiles jeunes de faible masse

Sylvie Cabrit

THESE de DOCTORAT

de l'UNIVERSITE PIERRE ET MARIE CURIE

PARIS 6

Spécialité: Physique Quantique

présentée par

Sylvie CABRIT

pour obtenir le titre de

Docteur de l'Université Paris 6

EJECTION DE MATIERE DANS LES OBJETS PROTOSTELLAIRES ET LES ETOILES JEUNES DE FAIBLE MASSE

Soutenue le 5 Janvier 1989, devant le jury composé de:

M. Jean AUDOUZE	Président
M. Thierry MONTMERLE	Rapporteurs
M. Jean-Loup PUGET	
Mme. Monique AUBIER	Examinateurs
Mme. Suzan EDWARDS	
M. Claude BERTOUT	
M. Alain OMONT	
M. Steve STROM	

THESE de DOCTORAT

de l'UNIVERSITE PIERRE ET MARIE CURIE

PARIS 6

Spécialité: Physique Quantique

présentée par

Sylvie CABRIT

pour obtenir le titre de

Docteur de l'Université Paris 6

EJECTION DE MATIERE DANS LES OBJETS PROTOSTELLAIRES ET LES ETOILES JEUNES DE FAIBLE MASSE

Soutenue le 5 Janvier 1989, devant le jury composé de:

M. Jean AUDOUZE	Président
M. Thierry MONTMERLE	Rapporteurs
M. Jean-Loup PUGET	
Mme. Monique AUBIER	Examinateurs
Mme. Suzan EDWARDS	
M. Claude BERTOUT	
M. Alain OMONT	
M. Steve STROM	

REMERCIEMENTS

Je tiens tout d'abord à exprimer ma gratitude à Claude Bertout, qui a proposé et encadré cette thèse. Il m'a guidée avec un talent, un enthousiasme, et une patience que je ne cesse d'admirer. Les 5000 km de continent américain qui nous ont souvent séparés pendant mes deux dernières années de thèse ne l'ont pas empêché de suivre avec attention mon travail (*thank you* AT& T !). Son soutien amical et son humour m'ont été également très précieux, et ont contribué au plaisir que j'ai eu à travailler avec lui.

Je suis reconnaissante à Jean Audouze d'avoir bien voulu m'accueillir à l'Institut d'Astrophysique de Paris, où j'ai trouvé d'excellentes conditions de travail et une ambiance très chaleureuse. Je le remercie pour les moyens qu'il a mis à ma disposition et pour avoir accepté d'assumer la présidence de ce jury de thèse.

Mon séjour à l'Université du Massachusetts à Amherst n'aurait pas été aussi fructueux sans l'accueil chaleureux et les conseils de Suzan Edwards. Avec intelligence et imagination, elle m'a guidée dans la poursuite de mon travail tout en m'ouvrant de nouveaux horizons grâce à l'étude des raies interdites. Son dynamisme et sa grande gentillesse m'ont aidée à m'installer et à me sentir rapidement à mon aise dans ma nouvelle vie américaine.

Grâce à Steve Strom, j'ai pu prolonger d'un an mon séjour à Amherst et approfondir l'étude des raies interdites qui constitue le deuxième volet de mon travail de thèse. Sa vivacité d'esprit, son amour de l' échange d' idées, et l'étendue de sa culture astrophysique, ont fait que j'ai énormément appris à son contact. Steve a su me communiquer son enthousiasme non seulement pour les étoiles T Tauri mais aussi pour le Sud-Ouest américain et la cuisine mexicaine. C'est avec plaisir que je le remercie pour tout cela.

Thierry Montmerle a depuis le début suivi de près mes travaux. Je le remercie pour les nombreuses discussions que nous avons eues, au cours desquelles il m'a prodigué conseils et suggestions et m'a fait profiter de son expérience des étoiles jeunes. J'ai eu aussi grand plaisir à discuter avec Jean-Loup Puget des différents aspects et implications de mes recherches, à la lumière de sa connaissance des nuages moléculaires. Je suis reconnaissante à Thierry et à Jean-Loup de l'intérêt qu'ils ont manifesté pour mon travail et de l' efficacité avec laquelle ils se sont acquittés de leur tâche de rapporteurs.

Je remercie également les autres membres du jury, Monique Aubier, professeur à Paris 6, et Alain Omont, professeur à l'Université de Grenoble, pour avoir gentiment accepté de juger ce travail.

Je suis aussi vivement reconnaissante aux membres de l' American Women's Group pour la bourse importante qu'elles m'ont attribuée en 1986, grâce à laquelle j'ai pu effectuer ma première année de recherche aux Etats-Unis. Les collaborations et les contacts que j'ai établis lors de ce séjour ont considérablement enrichi mon travail et élargi mes horizons (ainsi que mon cercle d'amis).

Beaucoup d'autres personnes ont contribué à la réalisation de ce travail de thèse par leur aide scientifique ou pratique. Merci en particulier à Philippe André, François Boulanger, Jérôme Bouvier, Fabienne Casoli, Christophe Dupraz, Thierry Forveille, Paul Goldsmith, Russ Levreault, Christian Magnan, Mike Margulis, Jean-Claude Pecker, Michel Perault, Ron Snell, et Karen Strom. Ma gratitude va aussi aux informaticiens auxquels j'ai si souvent fait appel dans les moments critiques: Diégo Césarsky, George Debève, Michèle Péron, et Brigitte Zanda à l'IAP, Jim Morgan, Lowell Tacconi-Garman, et Allan Welty à Umass. Merci également aux nombreuses autres personnes qui contribuent à la bonne marche et à l'atmosphère agréable de l'IAP et du Five College Astronomy Departement, en particulier les amateurs de la pause thé (aussi indispensable que l'ordinateur à ma productivité): Pierre, Antonella, Khalil, Eduardo, Jean, Monique, Brigitte, Mark, John, Pat, Lori ... (join the club!).

Enfin, c'est un grand plaisir de pouvoir remercier ici ma famille et mes amis pour l'affection et le soutien moral qu'ils m'ont apportés au cours de ces années de thèse: Annie, Bertrand, Billy, Eric, François, François, et François, Marine, Mark, Mathilde, Mike, Nick, Pat, Philippe, Russ, Steve, Sue, Valérie, Virginia, et tant d'autres encore. Un coup de chapeau spécial à Bertrand pour son aide décisive à l'instant le plus critique; la virtuosité dont il a fait preuve aux commandes de la photocopieuse de l'IAP représente un veritable tour de force!

TABLE DES MATIERES

Annexe 3: *CO Line Formation in Bipolar Flows. II. Decelerated Outflow Case and Summary of Results*, Sylvie Cabrit et Claude Bertout, soumis à *Ap. J.*

Annexe 4: *The Large-Scale Structure of Bipolar Flows: Hollow Shells versus Filled Cones*, Sylvie Cabrit, *Bull. Am. Astr. Soc.* 1986, **18**, 1027. Résumé et figures d'un poster présenté au 169ème meeting de l' American Astronomical Society, 4-8 Janvier 1987, Pasadena, California.

Annexe 5: *Identification of RNO 43 and B335 as two highly collimated bipolar flows oriented nearly in the plane of the sky*, Sylvie Cabrit, Paul Goldsmith, et Ronald Snell 1988, *Ap. J.*, **334**, 196.

Annexe 6: *CO Line Formation in Bipolar Flows. III. The Energetics of Molecular Flows revisited*, Sylvie Cabrit et Claude Bertout, à soumettre à *Ap. J.*

Annexe 7: *Forbidden Line and Hα Profiles in T Tauri Star Spectra: A Probe of Anisotropic Mass Outflows and Circumstellar Disks*, Suzan Edwards, Sylvie Cabrit, Stephen Strom, Ingeborg Heyer, Karen Strom, et E. Anderson 1987, *Ap. J.*,**321**, 473.

Annexe 8: *Forbidden Line Emission and Infrared Excesses in T Tauri stars: Evidence for Accretion-driven Mass-loss ?*, Sylvie Cabrit, Suzan Edwards, Steve Strom, et Karen Strom, à soumettre à *A. J.*

Annexe 9: *Circumstellar material associated with solar-type pre main-sequence stars: A possible constraint on the timescale for planet-building*, Karen Strom, Steve Strom, Suzan Edwards, Sylvie Cabrit, et Michael Skrutskie, *A. J.*, **97**, 1451.

INTRODUCTION

Au cours des 20 dernières années, notre compréhension de la formation stellaire et de l'évolution des objets jeunes s'est profondément modifiée et enrichie grâce à l' accès aux domaines de longueur d'onde X, ultraviolet, infrarouge, millimétrique, et centimétrique. Ces progrès ont été permis en particulier par le lancement des satellites Einstein, IUE, et *IRAS*, et la construction des grands radiotélescopes millimétriques et de l' interféromètre radio du VLA. On distingue à présent trois grandes classes d'objets stellaires jeunes, qui diffèrent notamment par les propriétés de leur milieu circumstellaire:

• *Les sources enfouies*: De luminosité $\sim$ 1 à 10^5 $L_\odot$, elles ont été découvertes par cartographie infrarouge des nuages moléculaires (Wynn-Williams 1982; Beichman *et al.* 1986; Myers *et al.* 1987; Wilking, Lada, et Young 1989) et sont trop obscurcies par la poussière environnante pour être détectées dans le domaine optique ($A_V \geq 10$ mag). Leur distribution d' énergie augmente vers les grandes longueurs d'onde et culmine vers 100 μm. Leur association fréquente avec des "coeurs moléculaires denses" détectés dans la molécule NH_3 (Myers 1985) suggère qu'il s'agit d' objets stellaires très jeunes ($t \leq 10^5$ ans) encore enfouis dans le cocon où ils se sont formés. Leur stade d'évolution exact reste peu clair car ils ne peuvent être situés dans le diagramme de Hertzprung-Russell. Il est possible que certains de ces objets soient en fait des "proto-étoiles" en train de se former par effondrement gravitationnel (Beichman *et al.* 1986), mais cette hypothèse est difficile à tester avec les moyens d'observation actuels. De récentes études dans le domaine radio millimétrique montrent au contraire que beaucoup de ces sources sont dans une phase d'intense éjection de matière (*e. g.* Bally et Lada 1983; voir section 1.2), un phénomène non prédit par les scenario classiques de formation stellaire. L'effondrement n'est donc probablement pas sphérique à ce stade d'évolution.

Les observations à haute résolution dans les raies rotationnelles de molécules sensibles aux hautes densités telles que CS, $C^{18}O$, et ^{13}CO, et dans l'infrarouge proche suggèrent aussi une symétrie non-sphérique dans l'environnement des sources enfouies, sous la forme de structures aplaties de taille $\sim$ 500 AU-0.1 pc et de masse $\sim$ 0.1-100 $M_\odot$, dont la géométrie et la distribution en vitesse sont compatibles avec des disques inclinés, en rotation autour de l'objet central (cf. la revue de Rodriguez 1988). De tels disques apparaîssent spontanément dans les simulations numériques de l'effondrement gravitationnel

d'une sphère gazeuse en rotation (Boss 1987), et pourraient être une conséquence directe du processus de formation stellaire. La distribution d'énergie des sources infrarouges semble bien reproduite par un modèle où la luminosité provient de l'effondrement d'une enveloppe résiduelle sur le disque et la condensation protostellaire centrale, ainsi que de l'accrétion du disque vers son centre (Adams, Lada, et Shu 1988).

• *Les étoiles T Tauri "classiques"*: ces étoiles visibles de faible luminosité ($\leq 30\ L_\odot$) et de type spectral F à M sont observées à proximité de régions de formation stellaire et sont caractérisées par la présence d'émission dans les raies de Hα et de CaII H et K, avec une largeur équivalente W_λ(Hα) supérieure à 5 Å. Leur jeunesse est indiquée par leur association cinématique avec le nuage moléculaire ambiant, leur forte absorption dans la raie du Lithium (un élément léger qui est rapidement brûlé sur la séquence principale), et une position au-dessus de la séquence principale dans le diagramme de Hertzprung-Russel qui suggère un âge $\sim 3 \times 10^5 - 10^7$ ans (Herbig 1962; Herbig 1977; Cohen et Kuhi 1979). Plusieurs caractéristiques spectroscopiques de ces objets suggèrent une forte perte de masse (voir chapitre 1).

En plus de leur spectre d'émission, ces étoiles sont caractérisées par la présence d'un important excès de luminosité infrarouge de 2μm à 100 μm provenant de poussière circumstellaire (Cohen et Kuhi 1979; Rucinski 1985), et d'un excès ultraviolet (UV), parfois accompagné d'une diminution de contraste des raies photosphériques ("optical veiling"), suggérant une zone chromosphérique dense (Calvet, Basri, et Kuhi 1984). Ces propriétés sont actuellement le mieux expliquées dans le cadre d'un modèle où l'étoile est encore entourée d'un disque circumstellaire de gaz et de poussière, probablement en accrétion. L'excès infrarouge provient alors de la surface du disque, chauffée par absorption de photons stellaires (Adams, Lada et Shu 1987; Kenyon et Hartmann 1987) et par dissipation d'énergie gravitationnelle (Bertout, Basri, et Bouvier 1988, Basri et Bertout 1988). L'excès UV et le "veiling" sont attribués à l'émission de la couche limite entre le disque et l'étoile, de température $\sim$ 8000 K, où la matière en accrétion, initialement en rotation képlérienne ($V \sim 300$ km s^{-1}), est brutalement freinée et ramenée aux vitesses de rotation caractéristiques de la photosphère ($V \sim 25$ km s^{-1}).

• *Les T Tauri de faible émission*: Récemment découvertes par des études dans le domaine X (Walter et Kuhi 1981; Feigelson et Kriss 1981; Montmerle *et al.* 1983) et dans les raies de CaII H et K (Herbig, Vrba, et Rydgren 1986), il s'agit d'étoiles pré-séquence

principale de faible luminosité qui avaient échappé aux premières recherches d' étoiles T Tauri à cause de leur faible largeur équivalente Hα ($<$ 5 Å). Certaines de ces étoiles apparaissent très près de la séquence principale (il s'agit alors plutôt d'étoiles "post-T Tauri" d'âges $\geq 10^7$ ans; *e. g.* Lada et Wilking 1984) mais la plupart sont globalement similaires aux T Tauri classiques décrites plus haut (où W_λ(Hα) $>$ 5 Å) en termes de position dans le diagramme H-R, périodes de rotation, et émission X (Walter *et al.* 1988).

Par contre, les T Tauri de faible émission montrent des excès infrarouges et ultraviolets plus faibles que les T Tauri classiques, suggérant qu'elles ne possèdent pas les disques circumstellaires opaques caractéristiques de cette autre classe d'objets. Leur luminosité provient alors uniquement de leur contraction quasi-statique vers la séquence principale et des réactions nucléaires amorcées en leur intérieur. Leur distribution d'énergie est en fait proche de celle d'une photosphère normale (voir annexe 9). Elles ne semblent pas non plus subir de perte de masse importante, et leur spectre d'émission peut être expliqué par une activité chromosphérique d'origine magnétique (Walter *et al.* 1988).

Le déclin progressif de l'excès infrarouge illustré par ces trois classes d'objets s'accompagne d'une diminution de la pente $\alpha = \mathrm{dlog}\lambda F_\lambda / \mathrm{dlog}\lambda$ de leur distribution d'énergie infrarouge, des objets enfouis où $\alpha > 0$ aux étoiles T Tauri de faible émission où $\alpha \sim -3$ (*e. g.* Lada 1987; Cohen *et al.* 1989). Les étoiles T Tauri classiques constituent une classe intermédiaire: elles ont en moyenne une pente $\alpha \sim$ -0.8, mais des variations importantes peuvent être observées d'une étoile à l'autre. En particulier, les étoiles les plus obscurcies ($A_V \sim 5-10$ mag) montrent des distributions d'énergie infrarouge comparables à celles de sources enfouies de faible luminosité (Myers *et al.* 1987). Le fait que les étoiles T Tauri classiques et à faible émission apparaissent dans la même région du diagramme H-R implique que ces trois classes ne constituent pas une séquence temporelle stricte, et que d'autres facteurs (rotation, champ magnétique ?) influencent le temps passé dans chacune de ces phases avant l'arrivée sur la séquence principale.

L'éjection de matière, qui apparaît comme un phénomène courant dans les objets jeunes encore entourés d'un milieu circumstellaire dense, pourrait jouer un rôle crucial dans cette évolution en (1) s'opposant à l'accrétion de matériau ambiant, limitant ainsi la masse finale de l'objet et celle de son disque circumstellaire (Shu, Adams, et Lizano 1987), (2) évacuant le moment angulaire initialement présent dans la matière circumstellaire, qui dépasse par 3 ordres de grandeur celui présent dans les étoiles de la séquence principale,

(3) dissipant le cocon de poussière qui empêchait l'apparition de la source dans le domaine optique. Ce phénomène pourrait aussi avoir une influence importante sur l'équilibre dynamique du nuage ambiant, en entretenant la turbulence nécessaire à sa stabilité gravitationnelle (Norman and Silk 1980; Franco et Cox 1983). L'étude de ces différents problèmes passe par l'identification du mécanisme d'éjection, qui pourrait être intimement lié au processus de formation stellaire, lui-même encore mal compris. Il faut pour cela pouvoir exploiter et interpréter au mieux les informations apportées par les observations. C'est cet aspect qui constitue la motivation principale de ma thèse.

Je commence par rappeler dans le chapitre 1 les diverses signatures de perte de masse observées, de l'échelle spatiale la plus petite ($\leq$ 200 AU) à la plus grande ($\sim$ 0.1-1 pc), en précisant dans quelle classe d'objets chaque diagnostic est rencontré, le degré de collimation qu'il indique, et les taux de perte de masse qui en sont deduits. Cette vue d'ensemble nous permettra dans le chapitre 2 d' expliciter les problèmes posés par l'éjection et la collimation de la perte de masse dans les objets stellaires jeunes, et de discuter les différents mécanismes proposés pour expliquer les observations. Je présenterai ensuite les résultats de deux approches complémentaires de ce problème: l'étude de l'émission CO dans les flots moléculaires bipolaires autour des sources infrarouges (chapitre 3) et l'étude des raies interdites dans les étoiles T Tauri (chapitre 4). Je terminerai en résumant les conséquences de ces résultats pour notre compréhension du phénomène de perte de masse, ainsi que les questions restant à élucider et les nouvelles directions de recherche qu'elles suggèrent (chapitre 5).

CHAPITRE 1

DIAGNOSTICS DE PERTE DE MASSE DANS LES OBJETS STELLAIRES JEUNES

1.1 Manifestations à petite échelle

Cette première catégorie comprend les diagnostics observés dans le spectre d'émission de l'objet ou dans sa distribution d'énergie, et caractérisent la perte de masse sur une échelle inférieure à quelques centaines d' unités astronomiques.

1.1.1: *Profils P Cygni des raies de Hα , NaI D, et CaII H et K*

Les profils d'émission Hα caractéristiques du spectre optique des étoiles T Tauri classiques sont dans 70 % des cas coupés par des absorptions décalées vers le bleu (profils de type P Cygni) dont la vitesse radiale par rapport à l'étoile est en moyenne $\sim$ - 80 km s^{-1}, et atteint - 300 km s^{-1}dans certains objets (Herbig 1977; Kuhi 1978; voir par exemple la figure 4 de l'Annexe 7). Un phénomène similaire est observé dans les raies de NaI D et de CaII H et K (Mundt 1984). Ces absorptions suggèrent la présence d'une couche de gaz froid en expansion entre l'observateur et l'étoile, et ont été très tôt interprétées comme une signature de perte de masse (Herbig 1962).

Depuis Kuhi (1964), de nombreux auteurs ont tenté d'estimer le taux de perte de masse $\dot{M}_*$ à partir des profils d'emission de la raie Hα , supposée entièrement formée dans une enveloppe en expansion (voir *e. g.* la revue de Bertout 1984*a*). Cependant, ce diagnostic s'est avéré très difficile à interpréter; Le champ de vitesse et la géométrie dans les parties internes de l'enveloppe sont probablement complexes, car plusieurs objets présentent aussi des absorptions décalées vers le rouge dans les raies de Na I (Ulrich and Knapp 1979) ou dans les membres supérieurs de la série de Balmer (Walker 1972), suggérant qu'une partie du gaz est en train de tomber sur l'étoile. La présence même de perte de masse n'est vraîment sans ambiguité que dans les cas, peu nombreux, où la composante d'absorption descend en dessous du continu et se trouve à l'extrémité bleue de la raie (*e. g.* Wagenblast, Bertout, et Bastian 1982). De plus, la structure en temperature et l'importance de la turbulence dans l'élargissement des profils d'emission Hα observés (où $\Delta V \sim 400$ km s^{-1}) sont mal connues. Il en résulte une ambiguite sur la valeur de $\dot{M}_w$ qui peut atteindre trois ordres de grandeur (De Campli 1981, Hartmann 1986). Les modèles les plus récents, qui

calculent la température et le champ de vitesse du vent de facon cohérente et incluent un traitement détaillé du transfert radiatif, suggèrent des taux de perte de masse de l'ordre de 2×10^{-9} à 10^{-8} $M_\odot$ yr^{-1} (Hartmann, Edwards, and Avrett 1982). Les absorptions observées dans les raies de CaII H et K posent une limite inférieure sur le taux de perte de masse d'environ 10^{-9} $M_\odot$ yr^{-1} (Hartmann 1986).

1.1.2: *Raies interdites*

La preuve la plus solide de l'existence de perte de masse dans les étoiles T Tauri classiques est obtenue à partir des raies interdites métalliques à basse excitation, telles que [OI]λ6300 et [SII]λ6731, souvent présentes dans leur spectre optique (Herbig 1962). Ces raies ont l'avantage sur Hα d'etre optiquement minces, et donc de refléter exactement la géométrie et le champ de vitesse dans la region émettrice. De récentes études ont montré que la majorité de l'émission est décalée vers le bleu par rapport à l'étoile (Janckovics, Appenzeller, et Krautter 1983), impliquant que les raies sont formées dans une enveloppe en expansion dont la partie qui s'eloigne de nous est cachee par un *écran opaque* (Appenzeller, Janckovics, et Ostreicher 1984). De plus, la faible extension en vitesse du côté rouge de la raie, et le fait que les profils présentent souvent deux pics, impliquent que la perte de masse est nécessairement *anisotrope* (voir section 4.1).

Les raies interdites sont assez fréquentes dans les etoiles T Tauri: environ 40 % des T Tauri classiques possèdent une raie de [OI]λ6300 avec une largeur équivalente de plus de 0.5 Å(Cohen et Kuhi 1979). Ce diagnostic de perte de masse est relié aux profils P Cygni décrits plus haut: (1) les raies interdites ont souvent le même décalage en vitesse que l'absorption observée dans le profil Hα (voir Annexe 7), suggérant qu' elles sont toutes deux formées dans une même enveloppe, (2) les etoiles T Tauri présentant des profils P Cygni dans les raies de Na I D et CaII H et K ont des raies interdites plus intenses que les autres T Tauri (Mundt 1984), (3) le flux dans la raie de [OI] λ6300 est corrélé avec le flux Hα (Cohen et Kuhi 1979).

Des raies interdites intenses ont également été observées dans des étoiles T Tauri très obscurcies (Cohen et Fuller 1985, Reipurth *et al.* 1986, Levreault *et al.* 1987), et dans la source infrarouge L1551-IRS 5, dont un spectre optique a pu être obtenu par réflection (Mundt *et al.* 1985). Ce résultat suggère que la perte de masse pourrait avoir des caractéristiques communes dans les objets jeunes visibles et enfouis.

L'étude détaillée des raies interdites dans les étoiles T Tauri ne datant que de quelques années, leur processus d'excitation n'est pas encore établi avec certitude. On ignore encore dans quelle mesure l'emission vient d'un vent ionisé en équilibre thermique ou d'un choc entre le vent et le milieu ambiant, par exemple au niveau du disque circumstellaire. Les valeurs actuellement éstimées dans ces deux hypothèses sont relativement similaires et varient de $\sim 10^{-8}$ à 10^{-6} $M_\odot$ yr^{-1}suivant les étoiles si une vitesse du vent de 200 km s^{-1} est adoptée (Annexe 7 et 8; Hartmann et Raymond 1988).

1.1.3: *Emission dans le continu radio et les raies IR de l'hydrogène*

Plusieurs objets stellaires jeunes possédant de forts excès infrarouges ont été détectés dans le continu radio (Bieging, Cohen, et Schwartz 1982, Pravdo *et al.* 1985, Snell et Bally 1986). Cette émission est interprêtée comme le rayonnement de freinage (bremsstrahlung) d' électrons en équilibre thermique dans une enveloppe ionisée. Les objets très brillants ($L_* > 10^3$ $L_\odot$) présentent en général des spectres radio $S_\nu \propto \nu^\alpha$ avec $\alpha \sim 0.6$ compatibles avec l'emission free-free d'un vent ionisé sphérique à vitesse constante (Panagia et Felli 1975). Les sources infrarouges peu lumineuses ont tendance à montrer des spectres plus plats ($0.5 > \alpha > -0.1$) suggérant une émission optiquement mince ou une loi de densité décroissant moins rapidement que r^{-2}, par exemple dans une enveloppe en effondrement ou à symétrie non-sphérique (André 1987). En direction de la source infrarouge L1551-IRS5, l'emission radio à 5 GHz apporte une preuve directe de perte de masse collimatée sous la forme d'un jet de gaz ionisé d'environ 500 AU de long et de moins de 50 AU de diamètre (Bieging et Cohen 1985).

Mises à part les sources d'émission radio non-thermiques telles que V410 Tau et HP Tau/G2, seules les étoiles T Tauri possédant les excès infrarouges et les caractéristiques d'émission les plus extrêmes (en particulier de fortes raies interdites) ont été détectées dans le continu radio (Bertout et Thum 1982; Cohen et Bieging 1986; Brown, Drake, et Mundt 1985; Evans *et al.* 1987). Leur indice spectral est proche de 0.6, mais elles sont souvent entourées d'un halo d'émission marginalement résolu, peut-être dû à des chocs, ce qui complique l'interprétation du flux observé (l'émission à 5 GHz d'un vent à vitesse constante provient d'une région de diamètre angulaire $\theta = 0.07''(F_\nu/\mathrm{mJy})^{1/2}$ qui ne pourrait être résolue par le VLA).

Si le vent est sphérique et complètement ionisé, et si sa vitesse V_w est connue, le taux de perte de masse peut être directement déduit du flux radio en utilisant (Panagia et Felli 1975):

$$(\frac{\dot{M}_w}{10^{-8}\mathrm{M}_\odot \mathrm{yr}^{-1}}) = 2.1(\frac{V_w}{200\ \mathrm{km\ s}^{-1}})(\frac{F_\nu}{0.3\ \mathrm{mJy}})^{3/4}(\frac{\nu}{5\ \mathrm{GHz}})^{-0.45}(\frac{T_e}{10^4\mathrm{K}})^{-0.08}(\frac{D}{160\ \mathrm{pc}})^{3/2}.$$

Les valeurs ainsi estimées varient de quelques 10^{-6} $\mathrm{M}_\odot$ yr^{-1} dans les sources brillantes (Snell et Bally 1986) à $10^{-8} - 10^{-7}$ $\mathrm{M}_\odot$ yr^{-1} dans les quatre T Tauri extrêmes détectées (Brown, Drake, et Mundt 1986; Cohen et Bieging 1986). Le fait que les autres étoiles T Tauri observées dans les nuages de Taurus-Auriga et ρ Ophiuchi ne soient pas détectées à 5 GHz (Bieging, Cohen, et Schwartz 1984; André, Montmerle, et Feigelson 1987) suggère que leurs taux de perte de masse sont inférieurs à 2×10^{-8} et 7×10^{-8} $\mathrm{M}_\odot$ yr^{-1} respectivement si le vent est ionisé jusqu'à l' infini.

Dans les objets dont les indices spectraux $\alpha < 0.5$ ne sont pas compatibles avec le modèle de vent standard, une limite inférieure de la mesure d'émission $EM = \int n_e^2\ dV$ dans l' enveloppe peut être obtenue en supposant que l'émission est optiquement mince:

$$EM_{min} = 2.6 \times 10^{54}\ \mathrm{cm}^{-3}(\frac{F_\nu}{0.3\ \mathrm{mJy}})(\frac{\nu}{5\ \mathrm{GHz}})^{0.1}(\frac{T_e}{10^4\mathrm{K}})^{0.35}(\frac{D}{160\ \mathrm{pc}})^2.$$

Mais la valeur du taux de perte de masse (ou plus exactement de $\dot{M}_w / V_w$) ne peut être déduite que moyennant une hypothèse sur la loi de densité et le rayon de l'enveloppe. Les taux de perte de masse ainsi estimés par Snell et Bally (1986) pour plusieurs sources infrarouges à spectre plat, en supposant une densité constante et un rayon égal à la taille observée de la région d'émission, vont de 2×10^{-7} a 2×10^{-6} $\mathrm{M}_\odot$ yr^{-1}(avec $V_w = 200$ km s^{-1}).

Notons que plusieurs incertitudes sont présentes dans ces estimations: (1) la vitesse terminale du vent: la quantité déduite des observations est en fait $\dot{M}_w / V_w$, et la vitesse est au moins incertaine par un facteur 2; (2) la géométrie de l'enveloppe: les mêmes flux radio pourraient être obtenus avec des taux de perte de masse plus faibles si le vent est très anisotrope ou inhomogène (Reynolds 1986); (3) l'ionisation de l'enveloppe: Comme un vent avec $\dot{M}_* \geq 10^{-11}$ $\mathrm{M}_\odot$ yr^{-1} est optiquement épais dans le continu radio, le flux radio pourrait être diminué de façon importante si l'enveloppe devient neutre avant d'atteindre le rayon effectif d'émission R_{eff} (tel que $F_\nu = \pi B_\nu R_{eff}^2/D^2$ si l' enveloppe était ionisée

jusqu' à l'infini). Par exemple, le flux radio à 5 GHz d'un vent avec avec $\dot{M}_w = 10^{-7}$ $M_\odot$ yr^{-1}et $V_w = 100$ km s^{-1} sera divisé par 6 si le vent n'est pas ionisé au delà de quelques unités astronomiques (Simon *et al.* 1983). Le flux radio sera également plus faible si le vent n'est que partiellement ionisé, ce qui pourrait être le cas dans les objets peu lumineux (Natta *et al.* 1988).

Les propriétés de l'enveloppe ionisée sont aussi étudiées par le biais des raies infrarouges de l'hydrogène, en particulier Brα (4.05 μm), Brγ (2.17 μm), et Pfγ (3.74 μm). L'élargissement et l'intensité des raies permettent d'estimer la vitesse du vent près de l'étoile et le taux de perte de masse. De telles études ont été faites en direction de nombreux objets jeunes de luminosité 5 à 10^5 $L_\odot$ (voir Panagia 1988). Les vitesses obtenues, $\sim$ 100-400 km s^{-1}, sont souvent inférieures à la vitesse d'échappement à la surface de l'étoile, et semblent indépendantes de la luminosité de l'objet L_{bol}. Les taux de perte de masse $\dot{M}_w$, $\sim 10^{-8} - 10^{-5}$ $M_\odot$ yr^{-1}, sont par contre corrélés avec L_{bol}. Ces taux de perte de masse pourraient être sous-estimés par un facteur $\sim 1/$(fraction d'ionisation) si le vent n'est que partiellement ionisé.

1.2 Manifestations à l'échelle circumstellaire

1.2.1: *objets de Herbig-Haro, jets optiques, et masers H_2O*

Les objets de Herbig-Haro sont des nébuleuses d'émission compactes (en général < 2") dont le spectre, composé en majorité de raies interdites à basse excitation et des raies Balmer de l'hydrogène, est caractéristique d'un choc radiatif de vitesse $\sim$ 100 km s^{-1} (Schwartz 1975). Ces objets sont toujours observés à proximité d'objets stellaires jeunes, et apparaissent dans 70% des cas décalés vers le bleu par rapport au nuage moléculaire (Strom, Grasdalen, et Strom 1974), souvent par plus de 150 km s^{-1}. Ils sont interprétés comme une zone de choc résultant de l'interaction entre le milieu ambiant et la matière supersonique éjectée par l'étoile (Schwartz 1983; Hartigan, Raymond, et Hartmann 1987).

Les mesures de mouvements propres de ces objets (*e. g.* Cudworth et Herbig 1979; Herbig et Jones 1981; Herbig et Jones 1983) confirment cette hypothèse. En effet, les vecteurs vitesse observés pointent toujours dans la direction opposée à l'étoile jeune, et atteignent 200 à 350 km s^{-1}. De plus, les objets de Herbig-Haro sont souvent situés le

long d'un même axe par rapport à la source, ce qui suggère que l'éjection de matière est fortement *anisotrope* à une distance de $\sim 10^{17}$ cm de l'objet central.

Une preuve encore plus spectaculaire d'éjection anisotrope a été obtenue dans plusieurs objets stellaires jeunes par la découverte, sur des images CCD optiques de grande sensibilité, d'un étroit jet de gaz ionisé émanant directement de l' objet central, de largeur $\leq 10^{15}$ cm, et s'étendant sur des distances de $10^{16} - 10^{17}$ cm (*e. g.* Dopita, Schwartz, et Evans 1982; Mundt, Stocke, et Stockman 1983; Reipurth *et al.* 1986). Comme les objets de Herbig-Haro, les jets optiques possèdent de grandes vitesses radiales $\sim 100 - 400$ km s^{-1}et un spectre d'émission caractéristique de chocs à basse excitation ($v_s \sim 40 - 100$ km s^{-1}, Mundt, Brugel, et Bührke 1987), attribué à des chocs obliques entre la matiere éjectée et le milieu environnant.

Les objets de Herbig-Haro et les jets optiques sont le plus souvent observés autour d'objets peu lumineux ($L_{bol} < 100$ L$_\odot$), en majorité des sources infrarouges. Ils ont été observés dans moins de 10% des T Tauri connues, toutes des etoiles très actives et obscurcies (Cohen et Schwartz 1983; Mundt, Brugel, et Bührke 1987). Les sources infrarouges plus brillantes que 100 L$_\odot$ sont plus souvent entourées de masers H_2O et OH compacts ($< 10 - 100$ AU), probablement aussi produits par interaction entre milieu ambiant et matière éjectée (Rodriguez *et al.* 1980), et dont les vitesses radiales et les mouvements propres suggèrent une expansion à partir de l'objet central (Genzel *et al.* 1981). Cependant, les conditions physiques dans les masers H_2O et OH sont encore trop mal connues pour permettre une estimation du taux de perte de masse.

Les observations de jets optiques permettent par contre d'estimer la vitesse V_w et la densité n_w du gaz avant le choc, ainsi que l'angle solide dans lequel la matiere est éjectée, et donc d'en deduire le taux de perte de masse de l'objet central. Les jets optiques ont typiquement $V_w \sim 300$ km s^{-1} et $n_w \sim 50$ cm^{-3}, pour un rayon $r \sim 5 \times 10^{15}$ cm; on en déduit un taux de perte de masse $\dot{M}_w = \pi r^2 V_w n_w m_H \sim 3 \times 10^{-9}$ M$_\odot$ yr^{-1}, pouvant atteindre 3×10^{-8} M$_\odot$ yr^{-1} dans le cas du jet associe au systeme de HH1-2 (Mundt, Brugel, et Bührke 1987). Cependant, aucun de ces parametres n'est connu très précisement et les taux estimés sont probablement incertains par un ordre de grandeur.

Schwartz (1978) a appliqué une méthode similaire aux objets de Herbig-Haro HH1-2. Il estime $V_w \sim 100$ km s^{-1} et $n_w \sim 300$ cm^{-3} à une distance $d \sim 10^{17}$ cm de l'étoile, et obtient un taux de perte de masse $\dot{M}_* = 4\pi d^2 V_w n_w m_H \sim 10^{-5}$ M$_\odot$ yr^{-1} en supposant

que l'ejection est isotrope. Si l'on ne tient compte que de l'angle solide couvert par HH1 et HH2 à partir de l'étoile, $\sim 2\pi(5"/60")^2 = 0.05$ steradian, $\dot{M}_*$ est ramene a $\sim 3 \times 10^{-8}$ $M_\odot$ yr^{-1}. Notons que cette démarche suppose que c'est le vent qui est choqué contre un milieu ambiant plus dense et non le contraire. Cette hypothèse pourrait ne pas être justifiée pour les objets de Herbig-Haro (en particulier pour HH1-2), dont les spectres et la forme en arc incurvé vers l'étoile sont mieux reproduits par un modèle où c'est *le milieu ambiant* qui est choqué par une condensation ejectée a une vitesse $V_w \sim 200$ km s^{-1}(Hartigan, Raymond, et Hartmann 1987).

En fait, la luminosite totale L_{HH} de l'objet de Herbig-Haro observé (en général $\sim$ 0.1-1 $L_\odot$; Bohm 1983) représente la contrainte la plus sévère puisqu'elle implique que le taux de perte de masse doit etre superieur a $2\,L_{HH}{V_w}^{-2}$, c'est a dire $\sim 10^{-7} - 10^{-6}$ $M_\odot$ yr^{-1} si $V_w \sim 100$ km s^{-1}. Ces dernières valeurs sont similaires à celles estimées par Cohen *et al.* (1988) à partir de l'intensité de la raie de [OI] a 63 μm dans plusieurs objets de Herbig-Haro autour d'étoiles T Tauri enfouies.

1.2.2: *Flots moléculaires bipolaires à grande vitesse*

Un des progrès majeurs dans l'étude de la perte de masse des objets stellaires jeunes a été la découverte, grâce à l'étude des raies rotationnelles de la molécule de CO, de gaz moléculaire froid supersonique (T $\sim$ 10-20 K, $V \geq 10$ km s^{-1}) dans l'environnement de nombreuses sources infrarouges (Zuckerman, Kuiper, et Rodriguez-Kuiper 1976; Kwan et Scoville 1976; Snell, Loren, et Plambeck 1980; Bally et Lada 1983). L'émission du gaz à grande vitesse, qui apparait à une vitesse radiale distincte de celle du nuage ambiant dans les profils des raies de CO, peut être mesurée et cartographiée. Les lobes de ces "flots moléculaires" s'étendent jusqu'à des distances de l'ordre de 0.1 à 2 pc de la source infrarouge centrale (voir par exemple les figures 2 à 4 de l'annexe 5).

Plusieurs arguments indiquent qu'il s'agit de mouvements *d'expansion anisotrope* à partir de l'objet stellaire: (1) les vitesses observées sont trop grandes par rapport à la masse centrale pour être dues à des mouvements de rotation ou d'effondrement gravitationnel; (2) le champ de vitesse est organisé et la plupart du temps anisotrope, le gaz situé d'un côté de l'étoile étant decalé vers le bleu alors que celui situé de l'autre côté est decalé vers le rouge; le flot est alors qualifié de *bipolaire*; (3) les lobes de gaz acceleré sont souvent associés à d'autres signatures de perte de masse, telles que des objets de Herbig-Haro ou des

masers H_2O dont les mouvements propres indiquent l'éjection à partir de la source centrale (Edwards et Snell 1984; Genzel *et al.* 1981), et des jets optiques ou radio alignés avec l'axe du flot (Mundt and Fried 1983, Bieging et Cohen 1985). Mais les flots moléculaires n'apparaissent pas aussi collimatés que les jets optiques; leur rapport longueur/largeur apparaît inférieur à 5, et leur angle d'ouverture est typiquement $\sim 30^o$ (voir annexe 5), similaire à celui des nébuleuses de réflection coniques avec lesquelles ils sont parfois associés (Levreault 1985; Bachiller, Cernicharo, et Martin-Pintado 1988).

Plus de 80 flots moléculaires ont été cartographiés autour d' objets stellaires jeunes de luminosités comprises entre 5 et 10^5 $L_\odot$ (Lada 1985; Fischer *et al.* 1985; Fukui *et al.* 1986; Heyer *et al.* 1987; Myers *et al.* 1988; Snell *et al.* 1988; Margulis et Lada 1988). Plusieurs ont aussi été observés dans les raies d'autres molécules moins abondantes, telles que HCO^+ (Loren *et al.* 1984, Wootten *et al.* 1984) ou OH (Mirabel *et al.* 1987). Mais à cause de leur intensité ($T_A \sim 0.1$ a 10 K), et de la résolution spatiale ($\sim$ 15" à 1' dans la raie $J = 1 \rightarrow 0$, suivant le téléscope) et spectrale (~ 0.2 km s^{-1}) qu'elles permettent, les raies rotationnelles de CO restent l'outil privilegié pour étudier en détail la structure à grande échelle et les propriétés cinématiques des flots bipolaires. Moyennant certaines hypothèses (voir section 3.4) il est possible d' estimer à partir de ces observations divers paramètres physiques du flot, tels que sa masse, son étendue spatiale, sa vitesse, et son échelle de temps dynamique.

La masse du flot ainsi obtenue est en moyenne ~ 3 $M_\odot$, indiquant que le gaz moléculaire à grande vitesse ne provient pas directement de l'étoile et qu'il s'agit plutôt de matière ambiante accélérée par le vent stellaire proprement dit, ou de matière éjectée à partir d'un disque circumstellaire. La quantité de mouvement et l'énergie cinétique contenus dans les flots sont très importantes, ~ 10 $M_\odot$ km s^{-1} et 10^{45} ergs respectivement, ce qui est souvent comparable ou supérieur à la quantité de mouvement et à l'énergie gravitationnelle du nuage (Snell 1987).

Les tailles et les vitesses typiquement observées sont ~ 0.3 pc et ~ 12 km s^{-1}, indiquant des échelles de temps $\sim 2 \times 10^4$ yr. Le nombre de flots observés à moins d' 1 kpc du soleil (au moins 60), combiné à leur duree estimée ($\sim 2 \times 10^4$ yr), suggère que tous les objets de plus d'une masse solaire pourraient passer par une phase de flot moléculaire au cours de leur évolution vers la séquence principale (Snell 1987). Les recherches systématiques de Levreault (1985), Myers *et al.* (1988), et Terebey, Vogel, et Myers (1988) montrent qu'il pourrait en être de même pour les objets de plus faible masse. Cependant, des flots

moléculaires n'ont été detectés que dans 10% des étoiles T Tauri — à nouveau uniquement dans les plus enfouies et actives — (Edwards et Snell 1982; Calvet, Canto, et Rodriguez 1983; Levreault 1985), suggérant que cette phase est en general achevée (ou devenue non détectable) lorsque l'objet devient entièrement visible.

En divisant la quantité de mouvement et l'énergie cinétique du flot par son échelle de temps dynamique, on peut estimer la force et la luminosite mécanique du gaz moléculaire à grande vitesse. Les paramètres ainsi déduits sont corrélés avec la luminosité totale L_{bol} de la source (Lada 1985), et valent en moyenne $\sim 10^{-4}$ $M_\odot$ km $s^{-1}yr^{-1}$ et 10^{-1} $L_\odot$ pour une source de 100 $L_\odot$. Le taux de perte de masse de l'objet central est généralement estimé à partir du taux de quantité de mouvement dans le flot en supposant que le gaz moléculaire est poussé par la force du vent de l'étoile. Pour une vitesse du vent $V_w \sim 200$ km s^{-1}, $\dot{M}_w$varie de 10^{-8} $M_\odot$ yr^{-1} dans les objets de faible luminosité et les T Tauri extrêmes à 10^{-3} $M_\odot$ yr^{-1} dans les objets les plus brillants (Levreault 1988).

Citons également d'autres observations, plus fragmentaires que les observations CO mais qui apportent des informations indépendantes sur les propriétés du flot:

(1) Dans plusieurs flots, l'observation d'émission étendue dans les raies vibrationnelles de l'hydrogène moléculaire (Fischer *et al.* 1985; Lane et Bally 1986) indique la présence de gaz dense ($n \gg 10^5$ cm^{-3}) soumis à des chocs à faible vitesse ($v_s \sim 7 - 30$ km s^{-1}). L'émission H_2 est plus localisée et indique une température plus grande ($T_{vib} \sim 3000$ K) que le CO. La luminosité émise dans les raies de H_2 représente jusqu'a 10% de la luminosité mécanique du flot déduite des observations CO; L'émission provient probablement de l'interface où l'énergie cinétique du vent est convertie en rayonnement.

(2) Dans le flot de L1551-IRS5, les lobes de gaz moléculaire à grande vitesse sont entourés d'un halo d'émission dans l'infrarouge lointain ($\lambda \geq 60\mu$m) trop intense et étendu pour être dû au champ de radiation de la source centrale. L'émission peut être expliquée en supposant que la poussière à proximité des lobes est chauffée par absorption des photons optiques et UV émis dans le choc entre le flot et le nuage statique ambiant (Edwards *et al.* 1986, Clark *et al.* 1986). La luminosité émise dans l'infrarouge lointain (> 7 $L_\odot$) excède la luminosité mécanique du flot par un facteur > 10, ce qui suggère que la luminosité mécanique du vent pourrait être sous-estimée par les observations en CO.

(3) Dans les flots autour de NGC 2071 et SVS13, des observations dans la raie hyperfine de l'atome d'hydrogène à 21 cm (Bally et Stark 1983, Lizano *et al.* 1988) montrent la

présence près de la source centrale de gaz atomique à grande vitesse ($V \sim 40$ à 170 km s^{-1}) s'éloignant dans la même direction que les lobes du flot CO. Ce "vent neutre" ne représente que $\sim$ 0.5 % de la masse du flot moléculaire, mais semble posséder une force suffisante pour pousser le flot observé en CO (Snell *et al.* 1984; Lizano *et al.* 1988). Une autre interprétation possible est que le gaz atomique n'est pas éjecté par l'objet mais résulte de la dissociation d'une partie des molécules H_2 dans le choc entre le flot et le milieu ambiant (Bally et Stark 1983).

CHAPITRE 2
ORIGINE DE L'EJECTION DE MATIERE ANISOTROPE DANS LES OBJETS JEUNES

Dans les sections suivantes, nous résumons les contraintes globales posées jusqu'ici par les observations, et discutons les caractéristiques des différents mécanismes d'éjection et de collimation proposés.

2.1 Contraintes dynamiques

Les flots moléculaires présentent l'avantage sur d'autres diagnostics de perte de masse de refléter l'impact total du vent sur le milieu ambiant, et non les propriétes du seul vent ionisé, comme l'émission radio, ou ses effets localisés, comme les objets de Herbig-Haro. De plus, leur apparence n'est pas affectée par l'extinction. Ils représentent donc le diagnostic de perte de masse le plus utile pour les sources infrarouges. Un des résultats les plus importants de l'étude des flots moléculaires (*e. g.* Lada 1985, Levreault 1985, Snell 1987) est que la force F_{CO} et la luminosité mécanique L_{CO} du flot déduits des observations CO restent corrélés avec la luminosité bolométrique L_{bol} de l'objet sur 5 ordres de grandeur ($F_{CO} \sim 10^{-6} - 10^{-1}$ $M_\odot$ km s^{-1} yr^{-1}; $L_{CO} \sim$ 0.001-100 $L_\odot$; $L_{bol} \sim 1 - 10^5$ $L_\odot$). Ce résultat suggère la présence d'un mécanisme d'éjection universel dans les jeunes objets stellaires, dont la source d'énergie serait liée à la source de luminosité de l'objet central. En moyenne, la luminosité mécanique du flot moléculaire represente $\sim 0.1\%$ de L_{bol}, et la force du flot excède par un facteur ~ 100 la pression L_{bol}/c dans le champ de radiation de l'objet. La dispersion totale autour de ces relations moyennes atteint cependant 3 à 4 ordres de grandeur ($F_{CO} \sim 1 - 1000\ L_{bol}/c$, $L_{CO} \sim 10^{-5} - 10^{-1}\ L_{bol}$) (cf. Figures 1*a* et 1*b* de l'annexe 6).

Si les flots moléculaires résultent en majorité de l'interaction d'un vent stellaire avec le nuage environnant (*i. e.* si la contribution du gaz moléculaire éventuellement éjecté à partir d'un disque circumstellaire est négligeable par rapport à celle du gaz ambiant entraîné) on peut déduire des contraintes ci-dessus les relations entre L_{bol} et la force F_w et la luminosité mécanique L_w du vent. Deux régimes limite peuvent être distingués, suivant la vitesse du vent et la densité du milieu ambiant qu'il rencontre (voir *e. g.* Dyson 1984; Kwok et Volk 1985): Si le vent choqué se refroidit en un temps plus court que

l'echelle de temps dynamique du flot moléculaire, celui-ci sera poussé par l'impulsion du vent (cas "momentum-driven"). On a alors $F_w \sim F_{CO}$ et $L_w \sim (V_w/V_{CO})L_{CO}$. Si par contre les pertes radiatives du vent sont faibles, le gaz moléculaire sera poussé par la pression thermique du vent choqué (cas "energy-driven"), et on aura $F_w \sim (V_{CO}/V_w)F_{CO}$ et $L_w \sim L_{CO}$.

Le vent sera dans le second régime si sa vitesse dépasse une certaine vitesse critique V_c qui dépend du taux de perte de masse et de la distribution de densité dans le milieu ambiant (Dyson 1984; voir figure 2 de l'annexe 6). Pour une densité $\sim 10^4$ cm^{-3} et un taux de perte de masse $\dot{M}_w \leq 10^{-6}$ M$_\odot$ yr^{-1}, $V_c \sim 200 - 300$ km s^{-1}. Cette valeur est comparable ou légèrement inférieure aux valeurs estimées dans les étoiles T Tauri et les sources infrarouges à partir des profils de la raie Hα , des raies interdites, des raies infrarouges de l'hydrogène, et des vitesses radiales et tangentielles des jets optiques et objets de Herbig-Haro. L'hypothèse la plus courante que le vent est "momentum-driven" n'est donc pas forcément justifiée, et le régime qui s'applique reste difficile à établir. Comme la vitesse du vent est de l'ordre de 10 fois la vitesse V_{CO} du flot moléculaire, il en résulte une ambiguité supplémentaire d'un facteur 10 sur les paramètres dynamiques du *vent* estimés à partir des observations de flots bipolaires. Les contraintes "moyennes" suggérées par les observations de flots bipolaires sont donc

$$F_w \sim 10 - 100\ L_{bol}/c$$
$$L_w \sim 0.1\% - 1\%\ L_{bol},$$

la valeur exacte de ces rapports restant très incertaine.

Il est intéressant de noter que les étoiles jeunes visibles de type T Tauri, où l'on estime à partir de la raie Hα et des raies interdites des taux de perte de masse $\dot{M}_* \sim 10^{-9} - 10^{-7}$ M$_\odot$ yr^{-1} et des vitesses du vent $V_w \sim 200$ km s^{-1} pour des valeurs de $L_{bol} \sim 1$ L$_\odot$, obéissent à des relations à peu près similaires. En effet, on a

$$F_w = \dot{M}_w V_w \sim 10 - 1000\ L_{bol}/c$$
$$\text{et } L_w = \frac{1}{2}\dot{M}_w {V^2}_w \sim 0.3\% - 30\%\ L_{bol}.$$

Les contraintes dynamiques posées par ces corrélations pourraient permettre de choisir entre les différents mécanismes d'éjection de masse possibles dans les objets stellaires jeunes. Nous faisons le point sur ce problème dans la section suivante.

2.2 Mécanismes d'éjection proposés

L' objet stellaire est susceptible de contenir de l'énergie sous trois formes: photons, énergie de rotation, et champ magnétique. Différents mécanismes d'éjection utilisant ces ingrédients ont été considérés. Il s'agit de : la pression de radiation (qui utilise uniquement les photons de l'étoile), l'expansion thermique et la propagation d'ondes d'Alfvén (où l'énergie provient de l'amplification du champ magnétique stellaire par effet dynamo dans une zone convective en rotation), et l'éjection centrifuge et l'éjection magnétodynamique (qui sont basées sur un couplage entre la rotation très rapide de l'objet et le champ magnétique).

Avant d'examiner en détail chacun de ces mécanismes, il est important de noter que les formes d'énergie qu'ils utilisent sont probablement aussi présentes dans les disques circumstellaires des objets jeunes possédant de la perte de masse. En effet, le disque constitue un énorme réservoir de moment angulaire et d'énergie de rotation. Il pourrait aussi posséder un champ magnétique résiduel, parallèle à son axe principal, si son évolution dynamique a été contrôlée par les forces magnétiques (Mouschovias 1976) ou par les forces centrifuges dans une condensation en rotation le long d'un axe parallèle au champ magnétique ambiant (Boss 1987). De plus, si la viscosité intrinsèque du disque entraîne un flux d'accrétion $\dot{M}_{acc}$ vers le noyau central, l'énergie gravitationnelle ainsi libérée va provoquer une émission de photons, de luminosité $L_{acc} \sim G\dot{M}_{acc}M_*/R_*$. L_{acc} pourrait représenter une fraction importante de L_{bol} si le taux d'accrétion est élevé, et la corrélation observée entre L_{bol} et les paramètres dynamiques du vent pourrait être due principalement à cette contribution.

Ces propriétés des disques circumstellaires, alliées à leur faible gravité de surface (et donc leur faible vitesse d'échappement) ont motivé le développement d'une seconde classe de modèles, basés sur les mêmes mécanismes physiques, mais où l'éjection de matière a lieu à partir de la surface du disque lui-même, et non à partir de l'étoile.

Les paragraphes qui suivent discutent successivement chaque mécanisme physique et son application à l'éjection de matière à partir de l'objet stellaire et à partir du disque circumstellaire. Chaque fois que possible, nous tenterons de voir si le mécanisme proposé est capable d'expliquer les corrélations observées entre paramètres du vent et luminosité de la source centrale.

• *Pression de radiation:* La corrélation observée entre les paramètres dynamiques du vent et la luminosité de l'objet central (étoile et disque confondus) suggère que la perte

de masse pourrait être provoquée par la pression de radiation de l' objet, comme c'est le cas dans les étoiles O. Pour que cela soit possible, deux conditions doivent être remplies (voir *e. g.* Königl 1986): (1) L_{bol} doit excéder la luminosité critique $L_{crit} = 4\pi GM_* c/\kappa$, où κ est l'opacité effective dans le continu. (2) Le vent doit avoir une profondeur optique $\tau \sim cF_w/L_{bol}$. Comme ce rapport est en moyenne $\sim 10-100$ dans les objets jeunes, le vent doit être très optiquement épais, ce qui pose une limite inférieure sur la colonne densité de matériau absorbant dans la zone d'accélération.

Si les grains de graphite constituent la principale source d'opacité, on a $\kappa \sim 100(T_c/3300\mathrm{K})^{1.93}$ cm^{2}g^{-1} (où T_c est la température de couleur du rayonnement; Königl 1986). Les objets plus lumineux que 10^3 L$_\odot$ sont donc énergétiquement capables d' engendrer un vent par pression de radiation sur les grains. Un exemple possible est l'étoile V645 Cyg ($L_{bol} = 3 \times 10^4$ L$_\odot$; $L_{crit} \sim 3 \times 10^3$ L$_\odot$), où les paramètres du flot CO (Levreault 1985) sont compatibles avec un vent optiquement mince poussé par pression de radiation ($F_{CO} = 9 \times 10^{-4}$ M$_\odot$ km s^{-1} yr^{-1}, $\tau = cF_w/L_{bol} \leq cF_{CO}/L_{bol} \sim 1.4$).

Cependant, ce mécanisme semble difficilement applicable aux sources de flots brillantes où $\tau \gg 1$. En effet, lorsque le vent devient optiquement épais, la poussière moins chaude va absorber le rayonnement visible et le ré-émettre dans l'infrarouge ($\lambda > 1\mu$m) où il n' est plus diffusé efficacement par les grains. Une source d'opacité possible à ces longueurs d'onde vient des bandes d'aborption de molécules telles que H_2O, qui contiennent de nombreuses raies dans le domaine de 1 μm à 1 mm. Si l'abondance de ces molécules est $\sim 10^{-3} - 10^{-4}$, la superposition de leurs raies, élargies par la rotation de l'enveloppe, pourrait produire une opacité effective dans le continu infrarouge $\kappa \sim 200 - 1000$ cm^{2}g^{-1} (Bally 1986). La luminosité critique correspondante serait alors ≥ 100 L$_\odot$.

La pression de radiation ne peut donc être un mécanisme d'éjection efficace que dans les objets très brillants. Le fait qu'il existe une correlation générale entre les paramètres des flots moléculaires (qui sont moyennés sur $10^4 - 10^5$ ans) et la luminosité actuelle de l'objet central suggère que L_{bol} n'a pas dramatiquement décru depuis que l'éjection de matière a eu lieu. Un second mécanisme doit donc être présent afin d'expliquer l'éjection de masse dans les objets moins lumineux que $10^2 - 10^3$ L$_\odot$.

• *Expansion thermique:* Lorsque la vitesse thermique dans l'enveloppe devient comparable à la vitesse d'échappement, un vent peut être engendré par expansion thermique de type Parker. DeCampli (1981) et Hartmann (1986) ont discuté l'application de ce

mécanisme à la perte de masse des étoiles T Tauri, et ont montré qu'il ne pouvait expliquer les taux de perte de masse $> 10^{-9}$ $M_\odot$ yr^{-1} observés car les pertes radiatives du gaz chaud, qu'il soit accéléré dans une "couronne" de température 10^6 K ou dans une enveloppe étendue à 10^4 K, excèderaient la luminosité de l'objet par 1 ou 2 ordres de grandeur. Comme les pertes radiatives sont proportionnelles à $\dot{M}_*^2$ et que les taux de perte de masse déduits des observations CO semblent augmenter rapidement avec la luminosité de l'objet ($\dot{M}_* \propto L_{bol}^{0.7}$; Levreault 1985), le même problème devrait être rencontré pour l'éjection thermique à partir des sources plus lumineuses que les T Tauri.

Plusieurs modèles d'éjection thermique à partir d'un *disque circumstellaire* ont été proposés. Dans le modèle de Torbett (1984), l'éjection a lieu dans la couche limite où la matière du disque en rotation képlérienne est brutalement freinée en tombant à la surface de l'étoile. Si le temps de diffusion radiative dans cette couche devient supérieur au temps dynamique d'accrétion, de forts gradients de pression thermique apparaîssent, et une partie du gaz est éjectée loin de l'étoile. Mais des modèles numériques à une dimension montrent que l'efficacité du mécanisme β $(= \dot{M}_w / \dot{M}_{acc})$ est inférieure à 10^{-3}. Comme la vitesse du vent est comparable à la vitesse d'échappement à la surface de l'étoile ($\sim 200 - 300$ km s^{-1}), et que la luminosité totale de l'objet L_{bol} est probablement au moins égale à la luminosité d'accrétion $L_{acc} = G\dot{M}_{acc}M_*/R_*$, on a alors $F_w c/L_{bol} \leq \beta c/V_w \leq 1$ et $L_w/L_{bol} \leq \beta/2 \leq 5 \times 10^{-4}$. L'efficacité de ce mécanisme semble donc trop faible par au moins un ordre de grandeur pour expliquer la perte de masse dans les objets jeunes.

Une autre possibilité est que la surface du disque est chauffée par absorption des photons ionisants émis dans la région centrale, où la dissipation d'énergie gravitationnelle est la plus forte (Pudritz 1985). Une enveloppe ionisée est alors créée dans les parties internes du disque ($R \leq 10^{15}$ cm), dont la pression thermique provoque l'expansion le long des lignes de champ magnétique poloïdales. Cependant, le taux de perte de masse $\dot{M}_{ion}$ dans ce vent ionisé n'est que de $\sim 10^{-6}$ $M_\odot$ yr^{-1} pour un taux d'accrétion de 10^{-3} $M_\odot$ yr^{-1}, ce qui donne une efficacité comparable au modèle de Torbett (1984).

Il apparaît donc peu probable que l'éjection de matière dans les objets stellaires jeunes soit dûe à un mécanisme d'expansion thermique.

• *Propagation d'ondes d'Alfvèn:* DeCampli (1981), Hartmann, Edwards, et Avrett (1982), et Lago (1979,1984) ont proposé un modèle où les vents des T Tauri sont accélérés par la pression magnétique résultant de la propagation d'ondes d'Alfvèn dans l' enveloppe

de l'étoile. Ces modèles supposent que les ondes hydromagnétiques sont engendrées par perturbation du champ magnétique stellaire dans les mouvements turbulents des couches convectives. Comme les ondes ne doivent pas être amorties avant que le gaz ait atteint le rayon d'Alfvén, l'efficacité du mécanisme dépend fortement de l'intensité du champ magnétique à la surface de l'étoile; des taux de perte de masse $\sim 10^{-8}$ $M_\odot$ yr^{-1} nécessitent un champ magnétique d'au moins une centaine de gauss (DeCampli 1981).

Les modèles indiquent que seulement $\sim 10\%$ de la luminosité L_A disponible sous forme d'ondes d'Alfvén est convertie en luminosité mécanique du vent. La relation observée dans les étoiles T Tauri, $L_w \sim 0.1 - 10\%\ L_{bol}$, nécessite que plus de 1% de la luminosité de l'objet soit convertie en ondes d'Alfvén.

La généralisation de ce mécanisme à l'ensemble des objets jeunes possédant de la perte de masse est délicate, car on s'attend à ce que le rapport L_A/L_{bol} dépende fortement de l'intensité du champ magnétique stellaire et de la taille de la zone convective, qui devrait diminuer lorsque la masse de l'objet augmente. La pente de la corrélation entre L_w et L_{bol} devrait alors être inférieure à 1.

Une deuxième possibilité est que les ondes ne prennent pas naissance dans l'étoile elle-même mais dans la couche limite turbulente d'un disque d'accrétion. Les propriétés du vent resteraient alors naturellement indépendantes de la structure interne de l'étoile. Un modèle physique réaliste de la couche limite serait nécessaire pour évaluer précisément les caractéristiques du vent dans ce cas. Si l'efficacité du mécanisme reste globalement la même que dans le cas d'une éjection à la surface de l'étoile, les taux de perte de masse observés devront nécessiter une conversion très efficace d'énergie d'accrétion en ondes d' Alfvén.

• *Ejection centrifuge*: Lorsque l'objet central tourne sur lui même à une vitesse proche de sa vitesse de rupture $\sqrt{GM_*/R_*}$ et possède un champ magnétique suffisant pour mettre l'enveloppe en corotation, l'énergie de rotation peut être transférée à l'enveloppe et accélérer un vent par force centrifuge (*e. g.* Mestel 1968).

Ce mécanisme n'est pas applicable aux T Tauri, où les vitesses de rotation sont en général inférieures ou égales à 25 km s^{-1}(Vogel et Kuhi 1981, Bouvier, Bertout, Benz, et Mayor 1986) pour une vitesse de rupture ~ 300 km s^{-1}. Par contre, il est concevable que les objets stellaires récemment formés possèdent des vitesses de rotation beaucoup plus élevées. En effet, la matière des coeurs moléculaires denses dont ils sont issus possède

un moment angulaire spécifique $J/M \sim 10^{21}$ cm^2 s^{-1} (Arquilla et Goldsmith 1985) qui excède par un facteur 10^3 les valeurs de $J/M \sim 10^{17} - 10^{18}$ cm^2 s^{-1} observées dans les T Tauri.

Hartmann et MacGregor (1982) ont appliqué le mécanisme d'éjection centrifuge au cas d'une proto-étoile massive (M_*= 10 M$_\odot$, $R_* = 10^{14}$ cm, $L_{bol} = 5 \times 10^4$ L$_\odot$), et obtiennent des taux de perte de masse $\sim 10^{-4} - 10^{-3}$ M$_\odot$ yr^{-1}, des vitesses du vent $\sim$ 50-100 km s^{-1}, et un rapport $F_w c/L_{bol} \sim 10 - 50$, à condition que l'objet tourne à plus de 90% de la vitesse de rupture et que le champ magnétique radial excède 10 gauss. L'éjection de matière s'accompagne d'une forte perte de moment angulaire, qui ralentit l'objet central sur une échelle de temps $\sim 10^3 - 10^4$ ans, comparable à la durée estimée des flots bipolaires, au bout de laquelle la rotation de l'objet est trop lente pour que le mécanisme soit opérant. L'éjection centrifuge en présence d'un champ magnétique permet donc d' expliquer naturellement les faibles vitesses de rotation observées dans les étoiles jeunes visibles, et constituerait alors une étape nécessaire dans le processus de formation stellaire.

Une variante de ce modèle a été récemment proposée par Shu *et al.* (1988), où l'étoile en rotation à la vitesse de rupture reçoit en permanence de la matière et du moment angulaire par l'intermédiaire d'un disque d'accrétion. Pour que l'étoile puisse incorporer cette matière, la majorité du moment angulaire apporté doit être évacué dans un vent. L'éjection a lieu au voisinage de l'équateur de l'étoile (où la gravité effective est la plus faible), dans une étroite bande de largeur ϵR_* où ϵ est le rapport de la vitesse thermique et de la vitesse de rotation equatoriale $V_{equ} = \Omega R_* = \sqrt{GM_*/R_*}$. Le gaz est initialement poussé par la pression thermique locale, puis maintenu en corotation avec l'étoile par le champ magnétique et accéléré jusqu'à la surface d' Alfvén (située à quelques rayons stellaires). Une analyse dimensionnelle des paramètres pour une étoile ayant $R_* \sim 5$ R$_\odot$, $M_* \sim 0.5$ M$_\odot$, et $\epsilon \sim 0.04$, suggère qu'un taux de perte de masse $\sim 3 \times 10^{-6}$ M$_\odot$ yr^{-1} peut être atteint avec un champ magnétique de $\sim$ 150 G. Shu *et al.* (1988) proposent que les champs magnétiques requis apparaissent par effet dynamo lorsque l'étoile en rotation (de masse $\leq$ 2 M$_\odot$) est rendue convective après l'allumage du deutérium en son centre. Pour ces paramètres, la densité du gaz au point sonique est $\sim 6 \times 10^9$ cm^{-3}, et le vent devrait être en majorité *atomique*. Ce modèle pourrait expliquer la récente détection de gaz atomique à grande vitesse dans plusieurs flots bipolaires (Bally et Stark 1983; Lizano *et al.* 1988)

En régime stationnaire, le taux de perte de masse $\dot{M}_w$ sera régulé par le moment angulaire apporté par le disque, et relié au taux d'accrétion $\dot{M}_{acc}$ par $\dot{M}_w = f\ \dot{M}_{acc}$, où $1/f$ est approximativement égal au rapport $J = l_w/l_{equ}$ du moment angulaire spécifique dans le gaz éjecté à celui du gaz en orbite à l'équateur ($l_{equ} = \Omega R_e^2$)[1] . Pour que l'étoile gagne de la matière il faut que $f < 1$, donc que $J > 1$ (*i. e.* que le rayon d' Alfvén soit supérieur au rayon de l'étoile).

Dans la limite où l'effet du champ magnétique devient négligeable loin de l'étoile, J est relié à la vitesse terminale moyenne du vent par $J = 1/2(V_w/V_{equ})^2 + 3/2$. Les paramètres du vent sont alors reliés aux paramètres d'accrétion par:

$$\frac{\dot{M}_w}{\dot{M}_{acc}} = f = \frac{2-4b}{(V_w/V_{equ})^2 + 3 - 2b} \sim 0.3$$

$$\frac{L_w}{L_{acc}} = f \times \frac{1}{2}(\frac{V_w}{V_{equ}})^2 \sim 0.3$$

$$\frac{F_w c}{L_{acc}} = 10^3 \times f\ (\frac{300\ \mathrm{km\ s^{-1}}}{V_w})(\frac{V_w}{V_{equ}})^2 \sim 900$$

où les valeurs numériques indiquées correspondent à un objet situé sur la séquence de combustion du deutérium ($V_{equ} \sim 140$ km s^{-1}, $b = 0.14$) avec $V_w = 200$ km s^{-1}. Contrairement aux autres modèles, ce mécanisme prédit des valeurs de L_w/L_{bol} et de $F_w c/L_{bol}$ plutôt supérieures à celles typiquement observées dans les objets jeunes, et comparables aux valeurs maximales obtenues à partir du CO.

Comme l'équateur de l'étoile tourne à la vitesse képlérienne, ce modèle prédit que le disque d'accrétion ne devrait pas posséder de couche limite, et donc pas d'excès ultraviolet important.

D'un autre côté, à la fin du processus de fragmentation et de contraction, le moment angulaire résiduel ne se retrouve pas nécessairement dans l'objet central. De récentes simulations numériques de l'effondrement gravitationnel d'une sphère de gaz en rotation (Boss 1987) suggèrent que la plupart du gaz à fort moment angulaire se condense dans le disque, alors que la structure centrale se forme initialement à partir de matière à faible moment angulaire située près de l'axe de rotation.

---

[1] Si l'étoile continue à tourner à la vitesse critique, on a plus précisément $f = (1-2b)/(J-2b)$, où b est égal au moment angulaire spécifique de l'étoile, normalisé à l_{equ}, et vaut 0.14 pour une étoile complètement convective en rotation uniforme (Shu *et al.* 1988)

Mais le mécanisme d'éjection centrifuge peut être appliqué au disque circumstellaire lui-même, qui devrait contenir un énorme quantité de moment angulaire et d'énergie de rotation. Pudritz et Norman (1983, 1986) ont développé un modèle analytique simplifié de l'éjection centrifuge à partir d'un disque d'accrétion magnétisé. Le modèle suppose que les lignes de champ magnétique sont globalement parallèles à l'axe de rotation du système (champ poloïdal) mais qu'elles sont resserrées dans le plan du disque par les mouvements d'accrétion vers le noyau central, ce qui leur donne une géométrie "en sablier". Si l'angle entre les lignes de champ et l'axe de rotation est supérieur à $\sim 30^{o}$ (Blandford et Payne 1982), l'enveloppe du disque, chauffée par le rayonnement émis dans la zone d'accrétion, est accélérée le long des lignes de champ magnétique par la force centrifuge (comme des perles le long d'une tige en rotation) jusqu'au rayon d'Alfvén r_A, où les composantes poloïdales de l'énergie cinétique et magnétique sont égales. Le gaz éjecté atteint ensuite une vitesse asymptotique $V_w \sim \Omega r_A \sim (r_A/r_d)V_d$, où V_d est la vitesse de rotation dans le disque au point d' origine r_d, et où $\Omega = V_d/r_d$.

Le bras de levier (r_A/r_d) étant ~ 10 dans ce modèle, la matière éjectée le long d'un tube de champ emporte un moment angulaire spécifique $l_w = \Omega r_A^2$ bien supérieur à celui qu'elle possédait dans le disque, $l_d = \Omega r_d^2$. Cette perte de moment angulaire permet à la matière du disque de spiraler vers le centre, et entraîne un flux d'accrétion $\dot{M}_{acc}$. En régime stationnaire, $\dot{M}_{acc}$est relié au taux de perte de masse à partir du disque $\dot{M}_w$ par $\dot{M}_{acc} l_d = \dot{M}_w l_w$, soit $(\dot{M}_{acc}/\dot{M}_w) \sim (r_d/r_A)^2 \sim 100$.

Comme la vitesse de rotation et la température dans le disque devraient décroître avec la distance à l'objet central, ce modèle prédit l'existence de plusieurs composantes de vent aux propriétés différentes: Les parties extérieures du disque ($r_d \sim 10^{15} - 10^{16}$ cm), où $V_d \sim$ 1-5 km s^{-1}, produisent un vent froid moléculaire qui est accéléré jusqu'à une vitesse finale $V_w \sim$ 10-50 km s^{-1}sur des distances $r_A \leq 0.1$ pc. Cette composante représente la majorité de la perte de masse $\dot{M}_w$. Elle pourrait constituer une partie de la matière moléculaire observée dans les flots bipolaires.

Les parties les plus internes du disque, ionisées par le rayonnement UV émis dans la zone d'accrétion, produisent une composante de vent ionisé à grande vitesse ($V_{ion} \sim 200 - 600$ km s^{-1}), qui contient un taux de perte de masse plus faible $\dot{M}_{ion} \sim 2 \times 10^{-2}\ \dot{M}_w$. Pudritz et Norman (1986) suggèrent que les jets optiques émanant des sources infrarouges correspondent à cette composante, ce qui expliquerait à la fois leur haute collimation et

leurs faibles taux de perte de masse ($\sim 10^{-9}$ $M_\odot$ yr^{-1}, voir section 1.2.1) par rapport aux flots moléculaires avec lesquels ils sont associés.

Entre ces deux zones, le matière du disque sera sous forme atomique et produira un vent accéléré jusqu'à des vitesses $\sim$ 100-200 km s^{-1}, qui pourrait correspondre au gaz atomique à grande vitesse détecté en direction de plusieurs flots moléculaires (voir 1.2.2).

De plus, la relation précédente entre $\dot{M}_{acc}$ et $\dot{M}_w$ avec $r_A/r_d \sim 10$ implique que

$$\frac{L_w}{L_{acc}} \sim \frac{1}{2}(\frac{r_d}{r_A})^2 V_w^2 (\frac{R_*}{GM_*}) = \frac{1}{2}(\frac{V_d}{V_{esc}})^2 \sim 0.1\% \ (\frac{V_w}{V_{esc}})^2$$

$$\frac{F_w c}{L_{acc}} \sim (\frac{r_d}{r_A})(\frac{V_d}{V_{esc}})(\frac{c}{V_{esc}}) \sim 10 \ (\frac{300 \text{ km s}^{-1}}{V_w})(\frac{V_w}{V_{esc}})^2.$$

Ce scénario peut donc expliquer les corrélations moyennes observées entre L_{bol} et les paramètres du vent si la majorité de la luminosité bolométrique de l'objet dérive de l'accrétion ($L_{bol} \sim L_{acc}$), et si la vitesse moyenne du vent V_w est de l'ordre de 1-5 fois la vitesse d' échappement $V_{esc} = \sqrt{(GM_*/R_*)}$ de l'objet central, c'est à dire si la vitesse de rotation dans le disque $V_d = (r_d/r_A)V_w$ est $\sim$ 2-10 fois plus faible que la vitesse képlérienne V_{esc} à l'équateur de l'objet. Un exemple possible est le cas étudié par Pudritz et Norman (1986) d'un disque auto-gravitant en rotation à $V_d \sim 5$ km s^{-1}autour d'un objet proto-stellaire avec $R_* = 45$ $R_\odot$, $M_* = 1$ $M_\odot$. On a alors $V_w = 50$ km $s^{-1} \sim V_{esc} = 60$ km s^{-1}, $L_w/L_{acc} \sim 0.5\%$ et $F_w c/L_{acc} \sim 60$. Dans le cas des étoiles T Tauri, où $R_* \sim 2$ $R_\odot$, $M_* \sim 1$ $M_\odot$, et $V_{esc} \sim 300$ km s^{-1}, les valeurs observées de V_w sont également proches de V_{esc}. Comme les disques autour de ces étoiles sont probablement képlériens (Adams, Lada, and Shu 1988), avec $V_d \propto 1/\sqrt{r}$, l'application de ce modèle d'éjection aux T Tauri nécessite que la force et la luminosité mécanique du vent soient dominées par les parties internes du disque où $r_d \sim 4 - 100$ R_*.

• *Ejection magnétodynamique*: Un mécanisme différent utilisant les mêmes ingrédients que le précédent — rotation à la vitesse de rupture d'un objet magnétisé — a été proposé par Draine (1983). A la différence de Hartmann et MacGregor (1982), Draine suppose que le champ magnétique ne diffuse pas entièrement hors de l'étoile au cours de la contraction du nuage, et la connecte encore au milieu ambiant dans lequel il est gelé. La torsion des lignes de champ magnétique sous l'effet de la rotation de l'étoile conduit à une accumulation rapide d'énergie magnétique. Cette perturbation se propage vers l'extérieur à une vitesse supérieure à la vitesse d'Alfvén et il se crée un choc, qui accélère le milieu environnant

dans une couche dense à la surface d'une "bulle magnétique". Ce mécanisme est un phénomène transitoire au cours duquel le moment angulaire de l'étoile est efficacement converti en énergie magnétique, puis en énergie cinétique d'expansion. Il nécessite un champ magnétique stellaire intense ($\sim 10^3$ G) mais un flux magnétique plus faible que le modèle de Hartmann et MacGregor (1982). Cependant, ce modèle néglige toutes les pertes de champ magnétique par reconnection des lignes de champ. Les caractéristiques de la bulle magnétique prédites par les calculs analytiques reproduisent assez bien les densités et tailles observées des flots moléculaires autour des sources de luminosité $L_{bol} > 50\ L_{\odot}$.

Un principe très similaire a été utilisé par Uchida et Shibata (1985) pour un modèle d'éjection transitoire à partir d'un disque circumstellaire hors d'équilibre en rotation sub-képlérienne autour d'une proto-étoile. Le champ magnétique est initialement parallèle à l'axe de rotation du système, et la torsion des lignes de champ a lieu dans les parties internes du disque, en chute libre vers l'étoile. La composante toroïdale ainsi accumulée crée une force de Lorentz $\mathbf{j} \times \mathbf{B}$ qui éjecte vers les directions polaires l'enveloppe du disque, les parties les plus denses continuant leur mouvement de contraction vers l'étoile. La matière éjectée est ensuite progressivement accélérée sur une trajectoire hélicoïdale le long des lignes de champ, au fur et à mesure que la perturbation se propage dans le milieu ambiant. Une différence marquante avec le modèle de Pudritz et Norman (1986) est que le vent moléculaire est confiné sur les parois d'un cylindre, au lieu d' être éjecté à partir de toute la surface du disque. Les flots moléculaires devraient donc avoir une structure creuse dans ce modèle, contrairement à celui de Pudritz et Norman (1986).

Un point commun à ces deux mécanismes est cependant que l'éjection de masse entraîne une forte perte de moment angulaire, qui tend à provoquer l'accrétion du disque sur l'étoile. Uchida et Shibata (1985) proposent que les jets optiques souvent associés aux sources de flots moléculaires sont produits lorsque la matière du disque pénètre dans le champ magnétique de l'étoile par reconnection de lignes de champ dipolaires fermées avec les lignes de champ poloïdales du disque. Le gaz est ensuite redirigé vers les pôles magnétiques de l'étoile; Lorsqu'il tombe à sa surface, il se produit une onde de choc qui est renvoyée dans la matière en accrétion et provoque une éjection de gaz ionisé le long des lignes de champ poloïdales ouvertes. La taille transversale du jet ionisé est alors de 10 à 100 rayons stellaires. La rotation a peu d'importance dans ce modèle car l'énergie est principalement d'origine gravitationnelle et l'éjection est produite par la pression thermique

résultant des températures coronales atteintes dans le choc d'accrétion. Mais les les flux X observés dans les étoiles T Tauri ($\leq 10^{31}$ erg s^{-1}; Feigelson et DeCampli 1981; Montmerle *et al.* 1983) posent des limites sur l' importance de ce mécanisme dans la production de jets optiques (les luminosités X attendues sont $\sim 10^{33}$ erg s^{-1} pour un taux de perte de masse $\sim 2 \times 10^{-8}$ $M_\odot$ yr^{-1}).

2.3 Mécanismes de collimation

Une autre caractéristique de la perte de masse dans les objets stellaires jeunes est sa collimation apparente à toutes les échelles où elle est observée: $10^{15} - 10^{16}$ cm (jets radio et optiques), $10^{16} - 10^{17}$ cm (alignement des objets de Herbig-Haro), $10^{17} - 10^{18}$ cm (nébuleuses cométaires coniques, flots moléculaires bipolaires). Les axes définis par ces divers diagnostics restent en général alignés. Un très bon exemple est celui de la source infrarouge IRS5 dans le nuage L1551. De cet objet émane un jet radio, de longueur $\sim 7 \times 10^{15}$ cm et de diamètre $< 2 \times 10^{15}$ cm (Bieging et Cohen 1985), qui est détecté optiquement sur une longueur $\sim 10^{16}$ cm (Mundt et Fried 1983). Le jet est aligné avec l'axe d'une nébuleuse de réflection cométaire de taille $\sim 10^{17}$ cm et de forme conique, dont les parois coïncident avec l'origine du lobe bleu d'un flot moléculaire bipolaire (Moriarty-Schieven *et al.* 1987). Les lobes du flot gardent ensuite une largeur à peu près constante ~ 0.2 pc et s'étendent jusqu'à une distance ~ 0.5 pc de l'étoile, dans la même direction générale que les jets optiques et radio observés à petite échelle.

L'éjection de matière apparaît donc déjà anisotrope à moins de 10^{15} cm de l'objet, et cette anisotropie est en grande partie conservée lors de l'interaction du vent avec le milieu ambiant. Plusieurs mécanismes ont été proposés pour expliquer la collimation observée sur ces différentes échelles:

• *Collimation magnétique*: Des mesures de polarisation dans les régions de formation d'étoiles montrent que les flots moléculaires et les jets optiques ont tendance à être alignés avec le champ magnétique à grande échelle (Vrba, Strom, et Strom 1976). Un tel alignement est prédit par les modèles d'éjection à partir d'une étoile ou d'un disque magnétisés lorsque l'axe de rotation du système coincide avec celui du champ magnétique (Hartmann et MacGregor 1982, Draine 1983, Pudritz et Norman 1986, Uchida et Shibata 1985). En effet, la composante toroïdale du champ engendrée par la rotation est plus grande à l'équateur que près de l'axe. Le gradient de pression magnétique force alors les lignes de champ (et la matière éjectée qui les suit) à dévier vers les pôles: c'est le phénomène

de "magnetic-pinching". Une élégante démonstration numérique de ce mécanisme a été présentée par Sakurai (1985,1987) pour l'éjection centrifugo-magnétique à partir d'une étoile ou d'un disque, dans le cas où le champ magnétique initial est radial.

• *Collimation par pression ambiante*: Une autre possibilité est que l'éjection est à l'origine isotrope, et que la collimation observée résulte d'un gradient de densité fortement anisotrope dans le milieu environnant. Une telle distribution de matière autour de l'objet pourrait résulter de l' aplatissement de la condensation protostellaire le long de son axe de rotation (Boss 1987) ou le long des lignes de champ magnétique ambiant (Mouschovias 1976). Comme le freinage magnétique est plus rapide pour la rotation perpendiculaire aux lignes de champ, ces deux axes ont tendance à être parallèles lorsque le champ magnétique est important à l'echelle interstellaire, et les deux mécanismes peuvent expliquer l'alignement préférentiel des flots bipolaires et des jets optiques avec le champ magnétique global du nuage.

La structure et l'évolution de la cavité créée par l'interaction d'un vent initialement sphérique avec le milieu ambiant dépendent fortement des pertes radiatives du vent choqué (*e. g.* Königl 1982, Dyson 1984, Kwok et Volk 1985), et ont été étudiées dans deux cas limite: (1) le régime "energy-driven" où le vent choqué a peu de pertes radiatives et où la cavité est remplie de gaz chaud qui pousse le milieu ambiant par simple expansion thermique; (2) le régime "momentum-driven" où le vent choqué se refroidit immédiatement dans une couche mince, et où le milieu ambiant est soumis à l'impulsion du vent non choqué qui se propage librement à l'intérieur de la cavité.

Königl (1982) a montré que la bulle de gaz chaud créée par un vent "energy-driven" en expansion dans un milieu extérieur anisotrope avec une loi de densité $\rho \propto r^{-m}$ où $m \sim 2$, pouvait devenir instable dans la direction de plus fort gradient de pression et former des tuyères de De Laval qui accélèrent le gaz en deux jets supersoniques diamétralement opposés.

Barral et Cantó (1981) se sont intéressés à la collimation d'un vent initialement isotrope dans le régime "momentum-driven" par un disque circumstellaire isotherme en équilibre hydrostatique. Ils ont montré qu'il existe une configuration stationnaire de la cavité où la pression dynamique du vent est exactement compensée par la pression extérieure. La cavité se présente sous la forme de deux lobes bipolaires très alongés, où le vent choqué obliquement s'écoule tangentiellement aux parois. Si la densité dans le milieu

environnant (supposée constante) est non nulle, le vent est ensuite refocalisé vers l'axe du système, car la pression ambiante finit par dominer la pression dans le vent, qui décroît comme $1/r^2$. Il se forme un second choc oblique au point de convergence, à la suite duquel le vent est accéléré dans un jet collimaté le long de l'axe. Pour un taux de perte de masse $\dot{M}_w \sim 10^{-8} - 10^{-7}$ $M_\odot$ yr^{-1} et une vitesse du vent $V_w \sim 100 - 400$ km s^{-1}, les propriétés de ce second choc sont proches de celles des jets optiques observés autour des étoiles jeunes de faible masse (Cantó, Tenorio-Tagle, et Rózyczka 1988). L'interaction de ce jet avec le milieu ambiant donnerait ensuite naissance au flot moléculaire. Pour ces paramètres du vent, la distance R_c entre l'étoile et le point de convergence est de l'ordre de 10 fois le rayon R_o atteint par la cavité dans le plan du disque. Celui-ci est déterminé par l'équilibre de pression entre le disque et le vent et vérifie:

$$(\frac{R_o}{10^{15}\mathrm{cm}})^2 \sim 7 \times (\frac{\dot{M}_w}{10^{-8} M_\odot yr^{-1}}) \times (\frac{V_w}{200\mathrm{km\ s}^{-1}}) \times (\frac{10^8 \mathrm{cm}^{-3}}{n_o}) \times (\frac{10\mathrm{K}}{T_o}).$$

Un tel jet ne pourra donc se former à moins de 10^{15} cm de l'étoile que si la densité dans le plan du disque excède 10^{10} cm^{-3} à une distance de 10^{14} cm. Une autre possibilité est que la cavité focalisante a une dimension interstellaire $\sim 0.1 - 1$ pc, et que les flots moléculaires représentent en fait une couche de gaz ambiant entraîné par viscosité le long des parois de la cavité. Le point de convergence du flot pourrait alors être indentifié aux objets de Herbig-Haro, les jets optiques étant formés par un autre mécanisme (Cantó *et al.* 1981). Une limitation de ce modèle est cependant son hypothèse qu'une configuration stationnaire de la cavité a pu être établie.

Sakashita et Hanami (1986) ont présenté un traîtement plus complet du problème qui utilise la même loi de densité que Barral et Cantó (1981) mais calcule numériquement l'évolution des lobes en fonction du temps dans les deux cas limites "energy-conserving" et "momentum-conserving". Dans les deux régimes, la cavité s' alonge perpendiculairement au plan du disque et prend une forme bipolaire. Cependant, la configuration stationnaire calculée par Barral et Cantó (1981) n'est pas atteinte, car l'expansion est ici supposée localement radiale en tous points de la cavité. Le flot moléculaire est confiné à la surface des lobes, dans une couche en expansion dont l'épaisseur dépend du temps et de la distribution de densité ambiante. La collimation et l'accélération sont plus efficaces dans le régime "energy-driven". Les vitesses obtenues dans ce cas semblent également plus compatibles avec les valeurs observées dans les flots bipolaires.

Il existe de nombreuses indications de la présence de structures aplaties perpendiculaires à l'axe des flots: observations des vecteurs de polarisation IR en direction des sources de flots bipolaires (Sato *et al.* 1985); observations de disques moléculaires à différentes résolutions en CS, $C^{18}O$, et ^{13}CO (voir la revue de Rodriguez 1988); dans la source infrarouge L1551-IRS5, observation à 2 μm d'un halo allongé perpendiculairement au flot, probablement dû à la diffusion de la lumière stellaire par un disque incliné de taille $\sim$ 1000 AU et de densité $\sim 2 \times 10^6$ cm^{-3} (Strom *et al.* 1985). Les structures observées ont une densité $\sim 10^4 - 10^8$ cm^{-3} qui augmente rapidement vers l'étoile avec une loi $n \propto r^{-2}$, et une pression thermique souvent comparable à la pression dynamique du vent (Rodriguez 1988). Aux échelles $\sim$ 0.1 pc, la quantité de mouvement de ces structures denses indiquée par leur dispersion de vitesse est corrélée avec la quantité de mouvement dans le flot (Myers *et al.* 1988), mais elle reste souvent trop faible pour traduire un réel effet de collimation (*e. g.* Takano *et al.* 1984; annexe 5). Il est cependant possible que la focalisation ait lieu dans les parties plus internes du disque circumstellaire, à moins de quelques 10^{15} cm de l'étoile. Une fois collimaté, le vent peut rester confiné à grande échelle si la pression ambiante excède sa pression interne (ce qui est par exemple le cas si la loi de densité dans le nuage décroît moins vite que $1/r^2$).

Il semble donc que tous les mécanismes d'éjection considérés en section 3.2 puissent donner lieu à une perte de masse collimatée. D'un autre côté, les contraintes énergétiques obtenues jusqu'ici, décrites en section 2.1, ne permettent pas non plus de choisir entre les mécanismes d'éjection car la plupart (exceptés l'expansion thermique, et la pression de radiation pour les sources peu lumineuses) semblent compatibles avec les corrélations observées. Il y a deux raisons à cette ambiguité : (1) la dispersion des corrélations observées entre les paramètres dynamiques du flot et la luminosité de la source est trop grande, $\sim$ 3 ordres de grandeur (voir figure 1*a* et 1*b* de l'annexe 6); (2) la luminosité totale L_{bol} contient probablement une contribution purement stellaire et une contribution due à l'accrétion, a priori indépendante de la première. La source d'énergie responsable de l'éjection pourrait être différente suivant que la corrélation de L_{bol} avec les paramètres du vent est due à l'une ou l'autre de ces contributions. Une nouvelle étape dans cette approche est donc nécessaire, qui consiste à (1) évaluer quantitativement les incertitudes présentes dans les estimations des paramètres du vent à partir des observations, (2) établir laquelle de ces contributions (stellaire ou d'accrétion) détermine les caractéristiques de l'éjection de matière.

Un deuxième moyen de distinguer entre les différents mécanismes d'éjection et de collimation envisagés consiste à déterminer la géométrie et le champ de vitesse du vent stellaire ou du flot moléculaire qui lui est associé. Par exemple, le flot devrait remplir la plupart du volume des lobes CO s'il est entraîné par un jet stellaire très collimaté (*e. g.* par le mécanisme de Königl 1982), ou s'il résulte d'un vent moléculaire éjecté de la surface du disque (Pudritz et Norman 1983,1986). Par contre, il devrait rester confiné dans une couche mince à la surface des lobes s' il est poussé par le vent stellaire en expansion dans une cavité bipolaire (Draine 1983; Barral et Cantó 1981; Sakashita et Hanami 1986), ou si le gaz moléculaire est éjecté à partir du disque le long d'un cylindre magnétique (Uchida et Shibata 1985). De même, le champ de vitesse dans le flot donne des informations sur l'échelle sur laquelle le gaz est accéléré, et sur la façon dont le vent interagit avec le milieu ambiant. Pour pouvoir déduire l'information voulue des données d' observation, un travail détaillé de modélisation est nécessaire qui n'avait jusqu'ici pas été entrepris.

Mon travail de thèse représente l'application de ces deux nouvelles approches à deux diagnostics complémentaires: l'émission CO des flots moléculaires bipolaires autour des sources infrarouges, et l'émission des raies interdites dans les étoiles T Tauri. Les principaux résultats sont présentés dans les chapitres suivants, et ont donné lieu à des publications jointes en annexe, auxquelles il sera fait largement référence.

CHAPITRE 3
EMISSION CO DANS LES FLOTS MOLECULAIRES BIPOLAIRES

Afin de poser des contraintes sur la géométrie et le champ de vitesse dans les flots moléculaires bipolaires, j'ai développé en collaboration avec Claude Bertout un code numérique calculant l' excitation et la formation des raies rotationnelles de CO en symétrie axiale en présence de champs de vitesse supersoniques. Cette étude théorique est décrite plus en détail dans les publications qui constituent les annexes 1 à 4. Les sections suivantes en résument les principaux résultats ainsi que les derniers développements, en particulier l' application à l'étude de flots observés, qui fait le sujet des annexes 5 et 6.

Notre modèle est brièvement présenté dans la section 3.1, et les résultats obtenus sont décrits en section 3.2. Nous discuterons en section 3.3 les contraintes posées par cette étude sur la géométrie et le champ de vitesse dans les flots observés. Nous verrons ensuite en section 3.4 comment notre modèle nous permet d'évaluer *quantitativement* les incertitudes entrant dans la détermination des paramètres physiques et dynamiques des flots moléculaires à partir des observations CO.

3.1 Modèle et Méthode

• *Modèle:* Le fait que les profils CO observés en direction des flots moléculaires possèdent une importante dispersion en vitesse et que les lobes montrent une forme évasée à partir de la source centrale (voir par exemple les figures 4 et 6 de l'annexe 5) nous a amenés à considérer un modèle où le gaz moléculaire à grande vitesse est en expansion dans deux lobes de forme conique. Cette géométrie est illustrée dans la figure 1 de l'annexe 1. L'absence des profils à double pics attendus si le gaz moléculaire était confiné dans une coquille mince nous a tout d'abord conduit à nous intéresser au cas où le flot remplit tout le volume des cones (flot "plein"; annexes 1, 2, 3). Cependant, de récentes observations à haute résolution des flots moléculaires autour de la source infra-rouge L1551-IRS5 (Uchida *et al.* 1987; Moriarty-Schieven *et al.* 1987) et de l' étoile jeune R Mon (Bachiller, Cernicharo, et Martin-Pintado 1988) montrent que l'émission projetée à faible vitesse est concentrée au bord des lobes, comme on s'y attendrait si le flot était creux. Nous avons donc ensuite étudié un modèle où le gaz moléculaire s'écoule dans une couche mince à la surface des cones (annexe 4).

Afin de minimiser le nombre de paramètres libres du modèle, nous nous sommes limités au cas d'un flot radial où le champ de vitesse et la distribution de densité ne dépendent que de la distance à l'étoile suivant des lois de puissance. Sans prétendre être une représentation exacte des conditions réelles dans les flots observés, ce modèle simple nous permettra d'étudier comment les caractéristiques de l'émission CO dépendent de la structure à grande échelle et des propriétés cinématiques du flot moléculaire.

• *Transfert radiatif:* Comme la vitesse thermique dans le flot ($v_{th} \sim 0.2$ km s^{-1}) est négligeable par rapport aux vitesses d'expansion $V_{CO} \geq 10$ km s^{-1}, le transfert radiatif des raies de CO peut être considéré comme local. En effet, tout photons émis et non-réabsorbé localement s'échappe du flot à cause de son décalage doppler (cette approximation est connue sous le nom d' "approximation de Sobolev" ou de "Large Velocity Gradient approximation"). Les conditions d'excitation des raies rotationnelles de CO peuvent alors être calculées indépendamment en tout point du flot en résolvant localement les équations de l'équilibre statistique suivant une méthode itérative (voir annexe 1). L'emission de la source centrale, de la poussière, et du nuage ambiant, ne devraient pas avoir d'effet important sur l'excitation du CO à grande vitesse et ne sont pas prises en compte dans nos calculs. Les profils d'émission sont ensuite calculés le long de plusieurs lignes de visée en utilisant une modification de l'algorithme développé par Bertout (1984*b*), qui prend en compte la largeur thermique non-nulle du profil local et la forme exacte des surfaces de vitesse radiale constante. Ce traitement hybride du transfert radiatif permet d'obtenir des résultats très satisfaisants, même pour un flot décéléré, où la fonction source n'est plus rigoureusement locale. Ces diverses approximations sont discutées plus en détail dans les annexes 1,2, et 3.

3.2 Description des résultats

Les spectres synthétiques obtenus sont utilisés pour construire deux sortes de cartes de l'émission CO à grande vitesse, similaires à celles employées par les observateurs: (1) des cartes d'intensité intégrée, où des contours en traits pleins et pointillés indiquent la distribution dans le plan du ciel de l'émission décalée vers le bleu et le rouge par rapport au nuage; (2) des diagrammes vitesse-position, qui présentent des contours d'égale intensité en fonction de la vitesse radiale par rapport au nuage et de la position le long de l'axe du flot. Des exemples de profils et de cartes sont présentés dans les figures 3-6 de l'annexe 1. Nous avons ainsi étudié l'influence des divers paramètres physiques (champ de vitesse,

loi de densité) et géométriques (inclinaison du flot par rapport à la ligne de visée, angle d'ouverture et épaisseur des lobes) sur les caractéristiques de l'émission CO à grande vitesse. Ces résultats sont résumés dans les paragraphes qui suivent.

• *Inclinaison et angle d'ouverture des lobes:* Nous avons montré que le flot pouvait apparaître dans quatre configurations spatiales différentes suivant l'inclinaison i de l'axe du flot par rapport à la ligne de visée, et l'angle d'ouverture du cône θ_{max}. Ces configurations sont représentées en perspective dans la figure 3 de l'annexe 2, et quatre cartes d'intensité intégrée illustrant ces différents cas sont présentées dans la figure 1 de cette thèse.

Le cas 1, où $i < \theta_{max}$ et $i \leq 90^o - \theta_{max}$, correspond au cas où le flot est presque vu de face. Le lobe avant est entièrement décalé vers le bleu, le lobe arrière entièrement décalé vers le rouge; les deux lobes sont circulaires et se recouvrent en grande partie.

Lorsque i devient plus grand que θ_{max} mais reste inférieur à $90^o - \theta_{max}$, nous sommes dans le cas 2: le flot est vu de côté; le lobe bleu et le lobe rouge sont allongés et apparaissent séparés dans le ciel, de part et d'autre de la source centrale. Ce cas ne se produit que si $\theta_{max} \leq 45^o$.

Dans le cas 3, où $i \geq \theta_{max}$ et $i > 90^o - \theta_{max}$, le flot est presque dans le plan du ciel. La face avant du lobe rouge s'approche alors de l'observateur alors que la face arrière du lobe bleu s'en éloigne. Chaque lobe présente donc à la fois de l'émission décalée vers le rouge et de l'émission décalée vers le bleu.

Le cas 4, où $i < \theta_{max}$ et $i > 90^o - \theta_{max}$, remplace le cas 2 comme intermédiaire entre les cas 1 et 3 lorsque $\theta_{max} > 45^o$. Il présente en même temps les caractéristiques de ces deux configurations, c'est à dire des lobes circulaires qui se recouvrent vers le centre, tout en étant en partie décalés vers le rouge et en partie décalés vers le bleu le long de l'axe du flot.

La probabilité d'observer chacune de ces configurations est indiquée en fonction de θ_{max} dans la figure 4 de l'annexe 2. Notons que ces catégories restent valides même si la vitesse dans le flot n'est pas radiale, pourvu que l'angle maximum $\theta_{max}(v)$ entre les vecteurs vitesse et l'axe du flot reste constant en fonction de la distance à l'étoile. Il suffit alors de remplacer $90^o - \theta_{max}$ par $90^o - \theta_{max}(v)$ dans les définitions de chaque configuration.

• *Champ de vitesse et distribution de densité :* Nous avons considéré trois classes de champs de vitesse: constant, accéléré (avec $v(r) \propto r$), et décéléré (avec $v(r) \propto 1/r$).

Les figures 3 à 6 de l'annexe 1 montrent les profils, cartes d'intensité intégrée, et diagrammes vitesse-position obtenus dans les deux premiers cas pour diverses valeurs de l'angle d'inclinaison, et les figures 1 à 4 de l'annexe 3 montrent les résultats obtenus dans le cas décéléré. Dans tous ces modèles, la distribution de densité a été fixée en supposant que la masse est conservée dans le flot (*i. e.* $r^2 n(r) v(r) = \text{cste}$).

Les cartes d'intensité intégrée obtenues pour ces différents modèles ne diffèrent clairement que par la rapidité avec laquelle l'intensité décroît à partir de la source. Des calculs effectués avec d'autres distributions de densité montrent que les différences observées sont principalement dues à la loi de densité adoptée et non au champ de vitesse. En particulier, l'émission CO n'est détectable que dans les régions du flot où $n_{H_2} \geq 100$ cm^{-3}.

L'influence du champ de vitesse sur l'émission CO devient bien sûr plus évidente sur les diagrammes vitesse-position. Les profils obtenus dans des flots à vitesse constante ont une étendue en vitesse indépendante de la position le long de l'axe. Les flots accélérés sont caractérisés par des vitesses plus élevées dans les zones externes des lobes, et les flots décélérés par des vitesses plus élevées près du centre, devenant progressivement plus faibles lorsqu'on s'éloigne le long de l'axe. Rappelons que ces différences sont indirectement dépendantes de la géométrie biconique adoptée (par exemple, si le flot était sphérique, les diagrammes vitesse-position montreraient tous des vitesses décroissant vers zéro lorsqu'on s'éloigne du centre, et ce quel que soit le champ de vitesse, parce que l'émission à la périphérie des lobes proviendrait de gaz se propageant de plus en plus perpendiculairement à la ligne de visée).

• *Lobes creux et pleins:* L' annexe 4 montre une série de cartes d'intensité intégrée (figures 1*a-f*) et de diagrammes vitesse-position (figures 2*a-f*) calculés pour un flot hybride possédant un lobe bleu *creux* (avec $\theta_{max} = 25^o$ et $\theta_{min} = 15^o$) et un lobe rouge *plein* ($\theta_{max} = 25^o$ et $\theta_{min} = 0^o$), les autres paramètres étant les mêmes dans les deux lobes. Les figures 1*a,b,c* et 2*a,b,c* correspondent à un flot accéléré vu à des angles d'inclinaison $i = 10^o, 40^o$, et 75^o (c'est à dire dans les cas 1, 2, et 3). Les figures 1*d,e,f* et 2*d,e,f* qui leur font face montrent les mêmes résultats pour un champ de vitesse constant.

Comme on s'y attend, les lobes creux vus de côté ($i > 25^o$) se distinguent facilement des lobes pleins par un effet centre-bord ("limb-brightnening") dans les cartes d'intensité

intégrée, ainsi que par la présence de profils CO doubles sur les diagrammes vitesse-position, correspondant à la projection de la face avant et de la face arrière des lobes. Ces conclusions ne dépendent pas du champ de vitesse adopté.

Par contre, la différence est beaucoup moins visible lorsque le flot est vu de face: les profils présentent le même nombre de pics dans les deux géométries, et les cartes d'intensité intégrée du lobe creux ne diffèrent de celles du lobe plein que par la présence d'une faible dépression au centre du flot.

Notons aussi que l'émission optiquement épaisse du nuage ambiant, qui s'étend en général de 1 à 2 km s^{-1} de part et d'autre de la vitesse centrale, devrait en pratique rendre plus difficile la distinction entre lobes creux et pleins dans le cas 3 ($i > 90^o - \theta_{max}$). Dans l'exemple présenté en figure 2*c* et 2*f* de l'annexe 4, la composante des profils CO correspondant à la face arrière du lobe bleu creux a une vitesse projetée pratiquement nulle et ne serait pas discernable du nuage ambiant. Le flot serait alors classé comme cas 2, et seule sa carte d'intensité intégrée indiquerait qu'il possède en fait un lobe creux. Dans un flot encore plus incliné sur la ligne de visée ($i \geq 85^o$), la face avant et la face arrière des lobes seraient clairement détectables de part et d'autre de l'émission du nuage, mais l'émission correspondant à l'intérieur des lobes serait projetée à très faible vitesse et ne pourrait être cartographiée. Il serait dans ce cas impossible de savoir si les lobes sont pleins ou creux.

3.3 Contraintes sur la structure des flots observés

• *Angle d'ouverture:* On retrouve parmi les flots observés trois des quatre configurations prédites par notre modèle. La plupart des flots se trouvent dans le cas 1, où le lobe bleu et le lobe rouge se recouvrent en grande partie (voir par exemple la carte du flot de Haro 4-255 en figure 3 de l'annexe 2). Les cas 2 et 3 sont beaucoup moins fréquents, et aucun exemple de cas 4 n'a été reporté. Alors que l'absence de cas 4 peut naturellement s'expliquer si $\theta_{max} < 45^o$, la prédominance de cas 1 est en contradiction avec les prédictions statistiques de notre modèle (voir figure 4 de l'annexe 2). Cependant, il pourrait exister dans les observations un effet de sélection en faveur du cas 1; la vitesse projetée le long de la ligne de visée et la colonne densité de gaz à grande vitesse sont en effet maximales dans cette configuration, ce qui la rend plus facile à détecter.

Dans le cas 2, où les lobes sont plus inclinés par rapport à la ligne de visée, le gaz a des vitesses projetées plus faibles et donc plus difficiles à distinguer du nuage ambiant. L'emission CO est également moins intense car l'épaisseur de flot traversée est plus faible. Finalement, une trop faible résolution spatiale pourrait rendre les lobes plus circulaires et similaires à ceux d'un cas 1. Un excellent exemple de cet effet est le flot NGC 2071, qui paraissait être dans le cas 1 sur une carte obtenue avec une résolution de 90", mais s'est révélé être dans le cas 2 une fois observé à plus haute résolution (Snell 1987).

Les problèmes de détection pour le cas 2 sont encore aggravés dans le cas 3, où l'inclinaison est plus grande et les lobes sont plus éloignés de la source centrale. De plus, l'émission du nuage ambiant fera qu'un cas 3 où i excède à peine $90^o - \theta_{max}$ apparaîtra en fait comme un cas 2. Enfin, la structure complexe des cartes d'intensité intégrée pour le cas 3, où chaque lobe contient à la fois de l'émission décalée vers le bleu et de l'émission décalée vers le rouge, pourrait être par erreur attribuée à deux flots séparés. C'est en fait notre approche théorique de l'émission CO dans les flots bipolaires qui, après avoir établi l'existence probable de cette troisième configuration, a permis d'en identifier les deux premiers exemples, B335 et RNO 43, parmi des objets auparavant considérés comme des flots doubles. Je rappelle ici les circonstances de cette découverte :

• Une première carte de B335 (Goldsmith *et al.* 1984), reproduite en figure 6b de l'annexe 2, suggérait que ce flot était dans le cas 2, mais montrait une détection marginale d'émission décalée vers le rouge dans le lobe bleu. Plus tard, des observations à plus haute sensibilité et à plus grande étendue spatiale (Langer, Frerking et Wilson 1986) confirmèrent cette détection, mais montrèrent également la présence d'un autre lobe bleu, séparé du premier par une "cavité" dans le nuage moléculaire. Ce deuxième lobe, ainsi que l'émission décalée vers le rouge présente dans le premier, furent alors interprétés comme un second flot bipolaire (dans le cas 2) dont le lobe rouge coïnciderait par hasard avec le lobe bleu du flot principal.

En collaboration avec Paul Goldsmith et Ronald Snell, de l'Université du Massachusetts à Amherst, j'ai réobservé cette région à plus haute résolution avec le radiotéléscope de 14 m du Five College Radio Astronomy Observatory et montré que B335 est en fait un exemple de cas 3: Le deuxième lobe bleu est en effet connecté au premier par un pont d'émission à grande vitesse suivant le bord de la cavité, et présente lui aussi de l'émission décalée vers le rouge, alors que le lobe rouge contient de son côté une quantité

comparable d'émission décalée vers le bleu (déjà marginalement détectée par Langer, Frerking, et Wilson 1986). Les diagrammes vitesse-position confirment cette symétrie entre les deux lobes.

• La première carte de l'émission CO à grande vitesse dans la région de RNO 43 (Edwards et Snell 1984), qui est reproduite dans la figure 7b de l'annexe 4, avait été interprétée comme deux flots vus de face, côte à côte le long d'un axe Nord-Sud. Cependant, aucune source d'éjection possible n'avait pu être identifiée au centre de ces composantes. Les mesures de mouvements propres des objets de Herbig-Haro associés à chacune de ces régions d'émission suggéraient plutôt que l'objet responsable du flot était une source infrarouge située au sud de la région cartographiée (Jones *et al.*1984). Il apparaissait donc probable (voir annexe 2) que l'émission observée représentait en fait un seul lobe d'un flot dans le cas 3. Cette hypothèse a été confirmée par une autre série d'observations qui nous ont permis de découvrir un deuxième lobe symmétrique du premier de l'autre côté de la source infrarouge. Les résultats de cette étude observationnelle de B335 et RNO 43 sont présentés plus en détail dans l'annexe 5.

Les problèmes de détection et d'identification des différentes configurations font qu'il est impossible pour l'instant de déduire une valeur statistique de θ_{max} à partir du nombre de flots observés dans chaque cas. Une estimation indépendante de θ_{max} peut être obtenue à partir des cartes de flots observés dans les cas 2 et 3. Celles-ci indiquent toutes un haut degré de collimation, et leur comparaison avec nos modèles suggère un angle d'ouverture $\theta_{max} \leq 30^o$. Notons cependant que les lobes bleus et rouges des flots observés dans le cas 2 ou 3 se recouvrent toujours quelque peu en direction du centre, contrairement à nos modèles, ce qui suggère soit que la résolution spatiale utilisée est insuffisante, soit que l' angle d'ouverture du flot est initialement plus grand à proximité de l'étoile, ou que le flot provient d'une surface déjà étendue (peut-être d'un disque circumstellaire). Des observations à plus haute résolution sont nécessaires pour distinguer entre ces possibilités.

• *Champ de vitesse:* Le fait que la configuration 3 soit effectivement rencontrée est important car il implique que les vecteurs vitesse dans le flot ne sont pas tous parallèles à l'axe du système (*i. e.* que $\theta_{max}(v) > 0^o$). Il n'est donc pas possible que l'écoulement se fasse le long d'un cylindre. D'un autre côté, le fait que tous les flots ne soient pas dans le cas 3 montre que les vecteurs vitesse ne peuvent pas non plus être perpendiculaires à l'axe du flot ($\theta_{max}(v) = 90^o$). Les mouvements dans le flot moléculaire sont donc une combinaison

d'expansion et de translation, et notre hypothèse d'un flot radial s'avère a posteriori une approximation raisonnable. La comparaison des diagrammes vitesse-position observés avec ceux calculés pour nos différents modèles pourrait alors nous permettre d'identifier le champ de vitesse dans le flot.

Des diagrammes vitesse-position de flots observés dans le cas 1 (AFGL 490, MWC 1080, LkH$_\alpha$198; R. Levreault, communication personnelle) montrent que la vitesse maximale dans le profil CO décroît progressivement lorsqu'on s'éloigne du centre du flot, en accord avec nos résultats pour un flot décéléré. Cependant, les flots observés avec suffisamment de résolution dans les cas 2 et 3, qui sont L1551-IRS5 (Moriarty-Schieven *et al.* 1987), Orion B (Sanders et Wilner 1985), R Mon (Bachiller, Cernicharo, et Martin-Pintado 1988), et B335 (annexe 5, Moriarty-Schieven, 1988), montrent des vitesses plus grandes lorsqu'on s'éloigne du centre, et apparaîssent donc accélérés. Ce résultat est surprenant puisque les flots dans le cas 1 ne diffèrent a priori des flots dans les cas 2 et 3 que par leur inclinaison sur la ligne de visée. Plusieurs explications peuvent être envisagées:

(1) Lorsque le flot est observé de face (cas 1) la dépendence en r de la vitesse n'affecte le diagramme vitesse-position qu'indirectement par le biais de la géométrie biconique, du fait que l'émission observée à la périphérie des lobes provient de points situés plus loin de l'étoile (ceci ne serait pas le cas dans une géométrie sphérique). La forme du diagramme dans cette configuration est en fait beaucoup plus sensible à d'éventuelles variations de la vitesse en fonction de la latitude. Par contre, les diagrammes vitesse-position obtenus dans les cas 2 et 3 sont eux vraiment sensibles aux variations de la vitesse en fonction de la distance à l'étoile. Il se pourrait alors que les flots bipolaires soient réellement accélérés, et que la décélération observée dans le cas 1 soit dûe à une diminution de la vitesse lorsqu'on s'écarte de l'axe du flot. Cette hypothèse est appuyée par des calculs préliminaires, présentés en figure 2*a-d*, qui montrent qu'un flot avec une loi de vitesse de la forme $v(r,\theta) \propto r\ (1 - \beta\ \theta)$ peut reproduire les caractéristiques générales des diagrammes vitesse-position observés dans toutes les configurations.

(2) Une deuxième possibilité, proposée par Moriarty-Schieven et Snell (1988) pour expliquer les propriétés du flot de L1551-IRS5, est que le flot est confiné dans une coquille mince à la surface de deux lobes de forme paraboïdale, et qu'il est poussé par un vent dont la vitesse est indépendante de la distance à l'étoile mais possède une variation en latitude similaire à celle invoquée plus haut. Les parties du flot situées plus loin de l'étoile

interceptent le vent émis plus près de l'axe et possèdent donc une plus grande vitesse d'expansion, ce qui explique l'accélération apparente observée dans les cas 2 et 3. Par contre, si la coquille se referme sur elle-même plus loin de l'étoile, le même flot vu de face serait apparemment décéléré à cause de la décroissance de la vitesse en fonction de la latitude.

(3) Finalement, il est possible que nous ne regardions pas une population homogène de flots bipolaires, mais plutôt deux groupes: (a) des flots très collimatés, avec $\theta_{max} \leq 30°$, qui seraient principalement observés dans les cas 2 et 3 (comme prédit par notre modèle) et qui seraient accélérés. (b) des flots quasi-sphériques avec $\theta_{max} \geq 60°$, qui constitueraient la majorité des cas 1 observés. Tous les champs de vitesse seraient alors compatibles avec leurs diagrammes vitesse-position. Le fait que ces flots ne soient pas observés dans le cas 4 pourrait être dû au fait que l'émission à faible vitesse est difficile à distinguer du nuage ambiant.

• *Structure des lobes CO: sont ils pleins ou creux ?* Comme nous l'avons vu dans la section 3.2, le Cas 2 semble le plus favorable pour distinguer entre ces deux options. L' exemple de cette configuration le mieux étudié est sans conteste le flot moléculaire autour de la source infrarouge L1551-IRS5 (Snell and Schloerb 1985; Moriarty-Schieven *et al.* 1987; Uchida *et al.* 1987; Rainey *et al.* 1987; Fridlund *et al.* 1988), qui représente l'archétype du flot bipolaire. Mais de récentes observations à haute résolution avec le radiotélescope de l'IRAM ont révélé un autre exemple de Cas 2 tout aussi intéressant: le flot moléculaire autour de l'étoile jeune R Mon (Bachiller, Cernicharo, et Martin-Pintado 1988), qui comme le flot de L1551-IRS5 a une nébuleuse de réflection cométaire associée à son lobe bleu.

Ces deux flots possèdent une structure remarquablement similaire de l'émission CO, où l'émission à faible vitesse (à moins de quelques km s^{-1} du nuage ambiant) est confinée au bord des lobes, alors que l'émission à grande vitesse est concentrée vers l' axe du flot.

Ces résultats sont interprétés par les observateurs en terme de lobes creux: l'émission à faible vitesse correspond alors au gaz se déplaçant presque perpendiculairement à la ligne de visée, alors que l'émission à grande vitesse correspond à la face avant du lobe bleu (ou à la face arrière du lobe rouge). Dans cette géométrie, l'autre face du lobe devrait produire une deuxième composante d'émission le long de l'axe du flot, d'intensité comparable à la première (voir annexe 4). Cette composante n'étant pas observée, il est supposé qu'elle est en fait projetée à la même vitesse que l'émission optiquement épaisse du nuage ambiant

(*e. g.* Moriarty-Schieven et Snell 1988, Fridlund *et al.* 1988). Il faut alors que l'angle d' inclinaison i soit très proche de $90^\circ - \theta_{max}$ (voir figures 2*d* et 2*f* de l'annexe 4).

Mais cette explication, bien qu'envisageable dans le cas de L1551-IRS5, doit être exclue pour R Mon: En effet, l'émission du nuage ambiant n'est *pas détectable* à l'intérieur des lobes de ce flot.

Nous en concluons que les lobes du flot de R Mon doivent être pleins. La structure centre-bord de l'émission CO peut alors être expliquée par une variation en latitude de la vitesse où le flot est intrinsèquement plus rapide le long de l'axe que vers les bords, similaire à celle proposée plus haut pour expliquer les variations apparentes du champ de vitesse avec l'inclinaison du flot. Le fait que le gaz à faible vitesse ne soit pas également observé en projection le long de l'axe du flot nécessite qu'il ait une faible opacité afin de n'être détecté qu'au bord des lobes, là où la colonne densité est maximale (notons que cette condition n'est pas remplie dans le modèle montré en figure 2).

Un tel modèle de lobe plein avait déjà été suggéré pour L1551-IRS5 par Levreault (1985) à partir d' observations dans la raie $J = 2 \rightarrow 1$ de CO. Dans cette raie, qui est plus optiquement épaisse que la raie $J = 1 \rightarrow 0$, le contraste centre-bord de l'émission à faible vitesse est beaucoup moins visible, suggérant que l'aspect creux des lobes est principalement dû à un effet de profondeur optique.

Les observations de L1551-IRS 5 et de R Mon semblent donc favoriser un même modèle où les lobes du flot moléculaire sont pleins et présentent une dépendence en latitude de la vitesse, le gaz moléculaire le plus rapide étant situé le long de l'axe et le gaz le plus lent vers les parois des lobes. Ce résultat semble difficile à réconcilier avec les modèles où le vent stellaire remplit l'intérieur des lobes bipolaires (Sakashita et Hanami 1986), ainsi qu'avec le modèle de Uchida et Shibata (1985) où le flot devrait être confiné sur les parois d'un cylindre, ou avec celui de Draine (1983) où il devrait être accumulé à la surface d'une "bulle magnétique".

Les modèles décrits en section 2.2 dont la structure semble plus compatible avec ces contraintes sont : un vent stellaire isotrope collimaté en deux jets par le mécanisme proposé par Königl (1982) ou Barral et Cantó (1981), ou un vent magnéto-centrifuge (Hartmann et MacGregor 1982; Shu *et al.* 1988; Pudritz et Norman 1986) intrinsèquement collimaté par "magnetic-pinching" (Sakurai 1985,1987), qui entraineraient par viscosité la matière moléculaire environnante.

3.4 Incertitudes sur les paramètres du flot

• *Nature et estimation des incertitudes:*

Bien que les paramètres dynamiques du flot puissent théoriquement poser des contraintes énergétiques sur le mécanisme d'éjection, l'utilité de cette démarche est limitée en pratique par l'impossibilité de connaître précisément les incertitudes entrant dans l'estimation de ces paramètres à partir des observations CO. De nombreuses sources d'erreur sont présentes (Lada 1985, Levreault 1985): (1) la profondeur optique et les conditions d'excitation dans la raie de CO utilisée, (2) la quantité de gaz projeté à la vitesse radiale du nuage ambiant, (3) le champ de vitesse dans le flot, (4) l'inclinaison du flot sur la ligne de visée (qui affecte à la fois la vitesse radiale et la taille apparente des lobes).

Notre modèle permet pour la première fois d'évaluer *quantitativement* ces incertitudes. Pour cela, nous avons appliqué les différentes méthodes utilisées par les observateurs à nos cartes et profils calculés, et comparé les paramètres obtenus (masse, quantité de mouvement, énergie cinétique, force, et luminosité mécanique) avec leur véritable valeur dans les modèles. Cette étude est décrite en détail dans la dernière section de l'annexe 3.

Nous avons trouvé que la meilleure méthode à ce jour pour estimer la masse du flot consiste à ce jour à cartographier toute l'étendue du flot en ^{12}CO et à estimer la profondeur optique de la raie grâce à un rapport ^{13}CO sur ^{12}CO au pic d'intensité (*e. g.* Snell *et al.* 1984). La précision sur la masse du flot est alors de l'ordre de 50% pour nos modèles.

Nous avons ensuite testé l'hypothèse proposée par Margulis et Lada (1985) que les autres paramètres du flot pouvaient être encadrés entre les valeurs obtenues avec deux méthodes différentes: l'une qui ne prend en compte que la vitesse projetée à laquelle chaque parcelle de gaz est détectée, l'autre qui suppose que tout le flot est en mouvement à la vitesse maximale observée.

Nous avons confirmé que la première méthode donnait toujours une limite inférieure des paramètres, et trouvé que la deuxième en donnait une limite supérieure, sauf dans le cas 3 où la vitesse maximale observée doit en plus être corrigée des effets de projection. Nous avons montré que le facteur de correction nécessaire peut être estimé à partir du rapport des vitesses projetées de la face avant et de la face arrière des lobes. L' annexe 5 contient une description détaillée de cette procédure et de son application à des cas 3

observés. L' utilisation de ces deux méthodes permet alors de déterminer la quantité de mouvement dans le flot à un facteur ≤ 6 près, la force et l'énergie cinétique à un facteur ≤ 30 près, et la luminosité mécanique à un facteur ≤ 100 près (voir figures 5-7 de l'annexe 3).

Dans les flots observés, une incertitude supplémentaire vient de la contribution du gaz projeté à très faible vitesse, qui est difficile à estimer à cause de l'émission optiquement épaisse du nuage. Pour la géométrie qui semble favorisée par les observations, où le flot est bien collimaté et remplit les lobes CO (voir section 3.3), cette contribution devrait rester négligeable tant que le flot est observé dans les configurations 1 et 2. Elle pourrait par contre représenter jusqu'à 50% de la masse du flot dans le cas 3, si les lobes sont uniformément pleins. Cependant, nous avons vu que cette configuration est très rarement observée (2 exemples à ce jour!). La meilleure attitude consiste donc à négliger l'émission à très faible vitesse, ce qui donne une limite inférieure aux paramètres du flot et devrait constituer une très bonne approximation pour la majorité des flots observés.

Il apparaît de cette étude que la force et la luminosité mécanique du flot peuvent être estimés à un facteur 10 à 100 près *à condition* que la masse ait été calculée en utilisant la meilleure méthode décrite plus haut. Ces incertitudes pourraient être ramenées à un facteur 10 si l'inclinaison du flot ou son champ de vitesse sont connus (mais s'y ajoutent en pratique les incertitudes inhérentes aux données et celles dues au choix, forcément arbitraire, des intervalles d'intégration pour l'émission à grande vitesse).

Cependant, notre étude montre également que les paramètres obtenus à partir des mêmes profils CO avec des méthodes différentes peuvent différer par *2 à 3 ordres de grandeur*. En particulier, la méthode employée par Bally et Lada (1983) dans leur étude de flots moléculaires autour de sources infrarouges très lumineuses devrait surestimer systématiquement les paramètres du flot, parce qu'elle suppose qu'une fraction importante du gaz moléculaire est projetée à faible vitesse, et que la colonne densité est partout égale à celle observée au centre du flot. Le choix d'une abondance de CO par rapport à H_2 introduit une source supplémentaire de divergence entre les différents observateurs.

Il serait donc possible qu'une grande partie de la dispersion $\sim$ 3 ordres de grandeur présente dans les corrélations publiées jusqu'ici (Bally et Lada 1983; Lada 1985; Snell 1987) soit due aux différentes méthodes employées par les observateurs plutôt qu'à une dispersion intrinsèque. Plus grave, la *pente* de ces corrélations, qui est un paramètre crucial

pour la comparaison avec des modèles d'éjection proposés, pourrait se trouver faussée par la surestimation systématique des paramètres du flot dans les sources très brillantes observées par Bally et Lada (1983).

• *Application à des flots observés:*

Afin de réexaminer ce problème plus en détail, nous avons entrepris d'homogénéiser les données CO rassemblées par Lada (1985), et d'estimer quantitativement les incertitudes sur les valeurs obtenues. Nous n'avons sélectionné que les 10 flots entièrement cartographiés en ^{12}CO pour lesquels des profils ^{13}CO étaient disponibles et où l'inclinaison du flot pouvait être raisonnablement estimée à partir des cartes d'intensité intégrée. La masse de chaque flot a alors été recalculée en utilisant la "meilleure" méthode décrite plus haut, ainsi qu'un même rapport d'abondance H_2 $/^{13}CO = 5 \times 10^5$ (Dickman 1978). Les paramètres dynamiques du flot ont ensuite été estimés en supposant que la vitesse moyenne du flot est égale à la vitesse maximale observée, la deuxième méthode possible (qui suppose que chaque parcelle de gaz est en mouvement à la vitesse à laquelle elle est détectée) ne pouvant être appliquée sans avoir accès aux profils CO eux-mêmes. Afin d'estimer les "barres d'erreur" sur la force et la luminosité mécanique résultant de l'usage de cette méthode, nous avons divisé les flots en quatre catégories suivant leur angle d'inclinaison apparent: moins de 20^o, de 20^o à 40^o, de 40^o à 60^o, et plus de 60^o, et avons adopté pour chaque inclinaison les erreurs maximales indiquées par nos modèles, tous champs de vitesse confondus. Finalement, nous avons également adopté de nouvelles estimations de la luminosité totale des sources de flot, qui prennent en compte la fraction émise dans l'infrarouge lointain (Mozurkewich *et al.* 1986).

Alors que les corrélations obtenues avec les paramètres initiaux reportés par Lada (1985), présentées dans les figures $1a$ et $1b$ de l'annexe 6, possédaient une dispersion verticale de 3 ordres de grandeur, les corrélations que nous obtenons après homogénéisation des données (figures $3a$ et $3b$ de cette thèse) montrent une dispersion nettement plus faible, de l'ordre d'un facteur 10. Il semble donc que la majorité de la dispersion observée était due aux différentes hypothèses faites dans l'estimation de la masse des flots. De plus, alors que la pente des corrélations initiales était proche de 1, les nouvelles corrélations obtenues suggèrent une pente inférieure, ~ 0.7. Ce résultat est proche des résultats de Levreault (1988) pour un échantillon restreint de flots autour d' étoiles jeunes visibles, qui suggèrent une pente de 0.6 seulement pour la corrélation de $\log(F_w)$ et $\log(L_w)$ avec $\log(L_{bol})$. Cette

valeur est également en accord avec la pente ~ 0.7 trouvée par Panagia (1988) à partir d'observations des raies infrarouges de l'hydrogène dans les étoiles jeunes. Les contraintes énergétiques sur le mécanisme d'éjection pourraient alors différer suivant la luminosité de l'objet.

• *Nouvelles contraintes énergétiques:*

Comme nous l'avons vu en section 2.2, ces contraintes dépendent du régime qui prévaut dans l'interaction entre le vent et le flot moléculaire. La force dans le vent peut être un facteur $\sim (V_{CO}/V_w)$ plus faible que celle du flot si le vent est dans le régime "energy-conserving"; réciproquement, la luminosité mécanique du vent peut être un facteur $\sim (V_w/V_{CO})$ plus grande que celle du flot si le vent est dans le régime "momentum-conserving", les facteurs numériques exacts dépendant de la loi de densité dans le milieu ambiant (*e. g.* Dyson 1984). Le critère déterminant est le temps de refroidissement du vent choqué, qui dépend de la vitesse du vent, de son taux de perte de masse, et de la densité du milieu ambiant rencontré. Bien qu'il soit généralement supposé que l'interaction est dans le régime "momentum-driven", la majorité des flots observés pourraient en fait être dans le régime "energy-driven" si la vitesse du vent est supérieure à 300 km s^{-1}(voir figure 2 de l'annexe 6). Les figures 4*a* et 4*b* de l'annexe 6 montrent les corrélations entre les paramètres du *vent* et la luminosité bolométrique de l'objet obtenues dans ce dernier cas, pour une loi de densité en $1/r^2$ dans le milieu ambiant et pour un rapport V_w/V_{CO} "typique" de 20.

Les sources à haute luminosité $L_{bol} \geq 10^3$ $L_\odot$ ont des rapports $cF_w/L_{bol} \sim 1 - 10$, et $L_w/L_{bol} \sim 0.01\% - 0.1\%$. Il est donc concevable que le vent dans ces étoiles puisse être poussé par la pression de radiation dans une enveloppe optiquement épaisse avec $\tau \sim 1 - 10$, bien que la source d'opacité reste problématique. Il est intéressant de noter que des efficacités similaires sont rencontrées dans les étoiles Wolf-Rayet (*e. g.* Barlow *et al.* 1981).

Par contre, les sources moins lumineuses que 10^3 $L_\odot$ ont des rapports $F_w c/L_{bol} \sim 10 - 100$ et $L_w/L_{bol} \sim 0.1\% - 1\%$ bien supérieurs à ceux observés dans les autres objets. La situation serait encore plus critique si nous adoptions un gradient de densité moins fort dans le milieu ambiant ou si le vent était supposé dans le régime "momentum-driven" (voir figures 3*a* et 3*b* de l'annexe 6). La pression de radiation doit donc être définitivement exclue pour les objets de faible luminosité, et le problème énergétique posé

par l'éjection de matière dans les objets de faible luminosité est bien réel. Les autres mécanismes envisageables (propagation d'ondes d'Alfvén, éjection centrifugo- magnétique, éjection magnétodynamique) peuvent avoir des efficacités comparables à celles que nous obtenons (voir section 2.2).

Un test décisif des modèles d'éjection centrifuge à partir de l'étoile (Hartmann et Mac Gregor 1982; Shu *et al.* 1988) consisterait à vérifier que l'étoile tourne à une vitesse proche de la vitesse critique, mais les sources infrarouges sont trop obscurcies pour que l'on puisse mesurer leur vitesse de rotation. Le fait que leur photosphère ne soit pas visible empêche également d'évaluer la contribution de la luminosité d'accrétion à la luminosité totale, et ainsi d'établir clairement le rôle du disque circumstellaire dans le processus d'éjection. Il est donc difficile pour l'instant de choisir entre les différentes possibilités à partir de simples considérations énergétiques, bien que la *pente* $\sim$ 0.6-0.7 des corrélations constitue une contrainte supplémentaire qui devra être prise en compte lorsque des modèles d'éjection plus détaillés seront développés.

CHAPITRE 4
RAIES INTERDITES DANS LES ETOILES T TAURI

Une autre façon de remonter à la source du flot est d'étudier le vent à son origine, au voisinage immédiat de l'étoile. Parmi les diagnostics qui permettent d' étudier les propriétés de la matière ionisée à moins de 100 AU de la source (émission Hα , raies interdites, émission free-free dans le continu radio; voir section 1.1) les raies interdites sont particulièrement intéressantes car elles sont optiquement minces et apportent une information sur le champ de vitesse dans l'enveloppe. Elles sont observées dans le spectre de nombreux objets stellaires jeunes, mais les objets les mieux étudiés sont les sources peu éteintes (les étoiles T Tauri et leurs équivalentes de plus forte masse les étoiles Ae-Be de Herbig), où le spectre optique et en particulier les raies de [OI]$\lambda\lambda$6300,6364, [SII]$\lambda\lambda$6731,6716, et [NII]$\lambda\lambda$6548,6584 sont directement observables avec une résolution satisfaisante. Il s'agit en majorité d'objets de faible luminosité ($L_{bol} \leq 30$ L$_\odot$).

Bien que ces étoiles ne montrent que rarement (10% des cas) les diagnostics d'éjection à grande échelle caractéristiques des sources infrarouges (jets optiques, objets de Herbig-Haro, flots moléculaires), les taux de perte de masse déduits de l'analyse des raies Hα et des raies interdites sont globalement similaires à ceux déduits des flots CO autour de sources infrarouges de luminosité comparable (Strom, Strom, et Edwards 1988). Par ailleurs, au moins 70% des objets enfouis pour lesquels un spectre optique a pu être obtenu (Mundt *et al.* 1985; Levreault *et al.* 1987) possèdent des raies interdites d'intensité comparable ou supérieure à celles observées dans les T Tauri. Ces ressemblances suggèrent que la perte de masse pourrait avoir des caractéristiques communes dans les deux classes d'objets.

Un autre avantage des T Tauri par rapport aux sources infrarouges, en plus du fait que leurs raies interdites soient facilement mesurables, est que leurs propriétés photosphériques sont la plupart du temps connues. Il est donc théoriquement possible de séparer la luminosité due à un disque circumstellaire de celle due à l'étoile, et ainsi d'étudier individuellement l'influence de chacun de ces éléments sur les propriétés du vent. L'étude des T Tauri pourrait alors nous éclairer sur l'origine de la perte de masse dans tous les objets jeunes de faible masse.

Dans ce but, j'ai profité de mon séjour à l'université du Massachusetts à Amherst pour commencer en collaboration avec Suzan Edwards et Steve Strom une étude observationnelle

et théorique des raies interdites dans les T Tauri, dont les principaux résultats sont résumés dans les sections suivantes.

La section 4.1 présente les caractéristiques des profils de raies interdites dans les T Tauri telles qu'elles sont indiquées par une étude à haute résolution ($\Delta\lambda \sim 0.3$Å). Nous résumerons les contraintes qualitatives que ces observations posent sur la géométrie et le champ de vitesse du vent, et présenterons les différents modèles proposés pour reproduire les profils observés. Ces résultats ont fait l'objet d'une publication, qui constitue l' annexe 7. La section 4.2 présentera les résultats d'une étude statistique à moyenne résolution ($\Delta\lambda \sim 1.8$Å) des raies interdites de [OI]λ6300, [SII]$\lambda\lambda$6731,6716, et [NII]λ6548 dans un échantillon représentatif d'étoiles T Tauri, où nous discuterons leurs propriétés quantitatives (flux, rapports de raies) et les contraintes qu'elles entrainent sur l' origine de l'émission. Nous étudierons ensuite dans la section 4.3 l'influence de la luminosité de l'étoile et celle du disque circumstellaire sur l'intensité des raies interdites, et nous discuterons les implications de ces résultats sur le rôle de l'accrétion dans la perte de masse des étoiles T Tauri. Les résultats des sections 4.2 et 4.3 sont décrits plus en détail dans un article sur le point d'être soumis, joint en annexe 8.

4.1 Profils des raies interdites dans les étoiles T Tauri

Les profils des raies interdites apportent des informations sur la vitesse et la géométrie de l'enveloppe ionisée autour de l'étoile. Une étude à haute résolution ($\sim$ 0.3 Å) a été conduite par S. Edwards et S. Strom sur un échantillon de 12 étoiles T Tauri et Ae-Be de Herbig possédant une raie de [OI]λ6300 avec une largeur équivalente de plus de 0.5 Å. Les profils observés dans les raies de [OI]λ6300, [SII]$\lambda\lambda$6731,6716 et Hα sont présentés dans les figures 1 à 4 de l'annexe 7. Ces profils sont caractérisés par plusieurs propriétés: (1) La majorité de l'émission est décalée vers le bleu par rapport à l'étoile, (2) la forme des profils varie suivant les étoiles. Elle passe progressivement d'un profil à un seul pic centré près de la vitesse de l'étoile, avec une aile du coté bleu s'étendant jusqu'à $\sim$ - 150 km s^{-1}, à un profil à deux pics où le pic décalé vers le bleu est déplacé jusqu'à 200 km s^{-1} par rapport au second pic, centré vers la vitesse de l'étoile; dans tous les cas, l'extension en vitesse est nettement plus faible du coté rouge que du coté bleu de la raie (en moyenne par un facteur $\sim 1/3$). (3) le rapport d'intensité entre les deux pics varie suivant les étoiles et peut-être inférieur ou supérieur à 1.

Indépendamment de tout modèle, ces caractéristiques posent des contraintes sur la géométrie de la région d'émission: (1) la prédominance d'émission décalée vers le bleu nécessite que la partie de l'enveloppe qui s'éloigne de nous soit *fortement éteinte* (avec $A_v \geq$ 6 mag). Deux sources d'extinction sont a priori envisageables: la présence de poussière dans le vent lui même (Mundt 1983), ou la présence d'un disque circumstellaire opaque autour de l'étoile (Appenzeller 1983). (2) La structure des profils implique que *l'éjection n'est pas sphérique.* En effet, des calculs analytiques en symmétrie sphérique qui envisagent les deux sources d'extinction possibles (Appenzeller, Janckovics, et Ostreicher 1984) montrent que les profils devraient être plats, ou avoir un maximum d'intensité à l'extrémité bleue du profil et décroître vers les vitesses positives. Ces résultats sont clairement incompatibles avec les observations.

Pour explorer plus précisément les contraintes posées par les observations sur la géométrie du vent, j'ai développé en collaboration avec Suzan Edwards un code numérique qui calcule les profils des raies interdites dans une géométrie biconique, similaire à celle employée dans le chapitre 3 pour la modélisation des flots moléculaires bipolaires. Comme le vent n'occupe pas uniformément tout le volume de l'enveloppe, nous devons supposer que l' extinction systématique de l'émission décalée vers le rouge est dûe à un *disque circumstellaire opaque.* Seule la moitié avant de l' enveloppe est alors visible. Cette géométrie est illustrée dans la figure 5 de l'annexe 7. Les conditions d'excitation des raies interdites sont calculées en supposant que le vent est entièrement ionisé et isotherme à T $\sim 10^4$ K.

Nous avons tout d'abord exploré en détail les géométries simples étudiées analytiquement dans quelques cas particuliers par Appenzeller, Janckovics, et Ostreicher (1984): un cône plein (avec $\theta_{min} = 0^o$ et $\theta_{max} = 45^o$), correspondant à un vent collimaté; et le volume extérieur à ce cône ($\theta_{min} = 45^o$ et $\theta_{max} = 90^o$) représentant l'interface entre le vent et le milieu circumstellaire ("cône creux").

Aucun des deux modèles n'apparaît complètement satisfaisant: Le modèle de cône plein reproduit de façon satisfaisante la faible extension en vitesse du coté rouge de la raie, mais le profil ne possède qu'un seul pic, à l'extrémité bleue du profil (figure 7*b* de l' annexe 7). Le modèle de cône creux produit un profil à un seul pic lorsque le système est vu presque de face, et un profil à deux pics à plus grande inclinaison, correspondant aux vitesses de la face avant et de la face arrière des cônes (cf. les modèles de lobes creux pour les flots bipolaires décrits en section 3.2, et présentés en annexe 4). Cependant, les pics

sont situés aux deux extrémités des profils, et la grande divergence des vecteurs vitesse dans cette géométrie entraîne trop d' émission décalée vers le rouge, avec une extension en vitesse comparable à l'extension du coté bleu de la raie (figure 7*c* de l'annexe 7). De plus le pic bleu est toujours plus intense, contrairement à ce qui est observé.

Pour diminuer la quantité l'émission décalée vers le rouge tout en conservant la structure en double pics des profils, nous avons proposé un modèle où la densité et la vitesse du vent dépendent de la latitude, la densité diminuant et la vitesse augmentant vers l'axe du système. La majorité du gaz est alors comprise dans un cône creux dense à faible vitesse qui lorsqu'il est vu de face produit un seul pic centré près de zéro, et lorsqu'il est vu de côté deux pics peu séparés, l'un déplacé vers le bleu l'autre centré près de la vitesse zéro ou légèrement décalé vers le rouge. Les parties du vent situées près de l'axe, plus rapides mais moins denses, produisent une aile bleue étendue dans les profils. Les différents rapports d'intensité entre les deux pics peuvent être reproduits en changeant la pente de la dépendence en latitude de la vitesse. Ce modèle reproduit assez bien les caractéristiques des profils observés pour des angles d'ouverture du cône $\theta_{max} \sim 60^o - 90^o$ (voir figures 10*a-c* de l'annexe 7). Notons que la loi de vitesse adoptée est similaire à celle suggérée par les observations CO du flot bipolaire de R Mon (voir section 3.3), et par le comportement des composantes d'absorption dans les raies de Balmer observées par réflection le long de l'axe de la nébuleuse cométaire de ce même objet (Jones et Herbig 1982).

Cependant, une telle explication n'est pas unique et d'autres modèles ont été récemment proposés qui pourraient produire des profils compatibles avec les observations:

(1) Hartmann et Raymond (1988) proposent que les raies interdites sont formées dans des chocs obliques entre le vent et la surface incurvée d'un disque circumstellaire. La géométrie de la région d'émission (et donc l'allure générale des profils) est similaire à celle du cône creux considéré plus haut, mais la collimation supplémentaire due au disque permet de réduire la quantité d'émission décalée vers le rouge et de rendre les profils plus proches de ceux qui sont observés. Bien que le pic bleu soit en théorie plus intense dans ce modèle, des asymétries dans la structure du disque pourraient expliquer les rapports variables observés dans les T Tauri.

(2) Un problème commun à notre modèle et à celui de Hartmann et Raymond (1988) est qú'il est difficile de garder un pic centré sur la vitesse de l'étoile quelle que soit l'inclinaison du système. Pour expliquer cette caractéristique, Kwan et Tademaru (1988)

ont proposé que l'émission provient en fait de deux composantes indépendantes: un vent à faible vitesse ($\sim$ 10 km s^{-1}) éjecté du disque circumstellaire, qui produit le pic centré près de la vitesse de l'étoile, et un jet ionisé à grande vitesse ($\sim$ 200 km s^{-1}) d'origine stellaire, très collimaté ($\theta_{max} \leq 10^o$), qui produit une composante d'émission décalée vers le bleu. La vitesse projetée et l'intensité de cette deuxième composante décroîssent lorsque l'inclinaison du système augmente. Les profils devraient donc montrer deux pics lorsque l'axe du jet est peu incliné sur la ligne de visée, et un seul pic lorsqu' il est suffisamment incliné pour que la vitesse projetée du jet devienne comparable à celle du vent. L'intensité relative des deux pics reflète ici l'importance relative de l'émission du jet stellaire et du vent éjecté du disque, et peut donc aisément varier d'une étoile à l'autre.

(3) Les objets de Herbig-Haro observés à proximité des objets jeunes montrent aussi des raies interdites de [OI], [SII], et [NII] de largeur $\sim$ 200 km s^{-1}, la plupart du temps décalées vers le bleu. Leurs spectres d'émission sont bien reproduits par des modèles de chocs courbes ("bow-shocks") entre une condensation sphérique et le milieu moins dense dans lequel elle se propage (Raga et Böhm 1986; Hartigan, Raymond, et Hartmann 1987). Bien que la géométrie de la zone d'émission soit ici encore proche d'un cône creux collimaté, les profils ne sont pas les mêmes que dans le modèle de Hartmann et Raymond (1988) parce que le gaz situé à l'origine du cône (où le choc est le plus fort) a une vitesse différente de celui situé dans les parties plus extérieures (les "ailes" du choc), où le choc est plus oblique. A faible inclinaison, ces deux parties du choc apparaîssent comme deux pics séparés, l'un décalé vers le bleu, l'autre centré à la vitesse du milieu ambiant. Lorsque l'inclinaison augmente, le pic décalé vers le bleu se rapproche de la vitesse centrale et le profil finit par n'avoir plus qu'un seul pic centré sur la vitesse du nuage. La largeur des profils reste égale à la vitesse du choc quelle que soit l'angle entre l'axe du choc et la ligne de visée.

Notons que la variation des profils en fonction de l'inclinaison prédite par les modèles (2) et (3) va en sens contraire de celle trouvée dans les deux modèles précédents. Il serait donc en principe possible d'éliminer la moitié des possibilités si l'angle de visée en direction de l'étoile est connu. Cet angle i peut être estimé si l'on connait à la fois la période de rotation de l'étoile (à partir des variations périodiques de sa courbe de lumière), l'élargissement rotationnel des raies photosphériques $v \sin i$, et le rayon de la photosphère. Mais de telles données ne sont pour l'instant disponibles que pour les étoiles les moins actives (*e. g.* Bouvier et Bertout 1988), qui en général ne possèdent pas de raies interdites mesurables. Une exception est l'étoile DF Tau, où W_λ ([OI]λ6300) = 1.6 Å,

et où Bouvier et Bertout (1988) estiment $i = 65^o \pm 25^o$. Cependant, pour ces valeurs intermédiaires de i, tous les modèles considérés donnent des profils compatibles avec les profils [OI]λ6300 observés ! Dans le cas de HL Tau et R Mon, des arguments indirects (absorption des silicates, géométrie du disque circumstellaire observé en ^{13}CO et dans l'infrarouge proche, degré de polarisation, et mouvements propres d' objets de Herbig-Haro) suggèrent que l'étoile est vue par l'équateur. La présence de deux pics dans leurs profils de raies interdites est donc a priori plus compatible avec les deux premiers modèles proposés. Cependant, ces objets sont tous deux entourés d'une nébuleuse de réflection brillante, et il est également concevable que les profils observés nous parviennent après avoir été réfléchis par de la poussière située vers les pôles de l'étoile. Des mesures de polarisation dans les raies interdites seraient nécessaires pour distinguer entre ces deux possibilités.

Une autre différence entre ces quatre modèles est le mécanisme d'excitation des raies interdites qu'ils supposent: dans le premier modèle, les raies sont excitées de façon stationnaire dans une enveloppe ionisée thermalisée, alors que dans les trois autres elles sont formées dans la zone de recombinaison d'un choc. Des calculs numériques de la structure en température du vent (Hartmann et Raymond 1988) suggèrent que dans le premier cas les raies ne pourraient être excitées que dans une région très dense proche de l' étoile ($r \leq 100R_*$, $n_e \geq 10^7$ cm^{-3}). Par contre, dans le deuxième cas, la densité serait plus faible car le choc se produit dans les régions externes du vent. La vitesse du choc varie également suivant les modèles: les chocs sont très obliques entre le vent et le disque ($V_{choc} \leq 40$ km s^{-1}; Hartmann et Raymond 1988), modérément obliques dans les jets optiques ($V_{choc} \sim 60 - 90$ km s^{-1}; Mundt, Brugel, et Bührke 1987), et plus forts dans les objets de Herbig-Haro ($V_{choc} \sim 100 - 200$ km s^{-1}à l'apex du bow-shock; Hartigan, Raymond, et Hartmann 1987). On s'attend alors à des degrés d'excitation différents dans la région d'émission. Un moyen de distinguer entre ces diverses possibilités consiste donc à étudier plus précisément les conditions physiques (densité et degré d'ionisation) dans la région d'émission des étoiles T Tauri.

4.2 Propriétés statistiques et origine de l'émission

Dans ce but, nous avons entrepris une étude statistique des raies de [OI]$\lambda\lambda$6300,6364, [SII]$\lambda\lambda$6716,6731, et [NII]$\lambda\lambda$6548,6584 dans les étoiles T Tauri. Le rapport d'intensité dans le doublet [SII]$\lambda\lambda$6731 donne une estimation de la densité électronique dans la région où

les raies de [SII] sont formées (*e. g.* Czyzak, Keyes, et Aller 1986). Les rapports [SII]/[OI] et [NII]/[OI] sont également sensibles à la densité, car les raies de [SII]λ6731 et [NII]λ6584 ont des coefficients d'excitation collisionnelle q_{12} plus grands, mais des coefficients de désexcitation spontanée A_{21} plus faibles, que la raie de [OI]λ6300 (Mendoza 1983). Ces raies sont favorisées par rapport à [OI]λ6300 à faible densité ($n_e < n_c = A_{21}/q_{21} \sim 10^4$ cm^{-3}), où l'émission est contrôlée par le nombre d'excitations collisionnelles ($I_{21} = h\nu_{21} q_{12} n_1 n_e$), mais elles sont défavorisées à haute densité, où les raies sont en équilibre thermodynamique et où l'émission est contrôlée par le taux de désexcitation spontanée ($I_{21} = h\nu_{21} A_{21} n_2$). Le rapport [NII]/[OI] est aussi très sensible au degré d'ionisation dans la région d'émission; en particulier il augmente très vite avec la vitesse du choc (Hartmann et Raymond 1988). Les intensités relatives et absolues de ces raies dans les T Tauri devraient donc poser des contraintes sur les conditions physiques dans leur région d'émission.

Cette étude est basée sur une nouvelle série de spectres d'étoiles T Tauri obtenus en Novembre 1987 au téléscope de 2.1 m de Kitt Peak par Steve et Karen Strom. Ces spectres couvrent le domaine de longueur d'onde de 6240 à 6760 Å, et offrent une meilleure sensibilité ($\sim$ 0.1 Å dans la raie de [OI]λ6300) et une meilleure résolution spectrale ($\Delta\lambda \sim$ 1.8 Å) que la précédente base de donnée de Cohen et Kuhi (1979) où la raie de [OI]λ6300 était mesurée avec une résolution de 7 Å et une sensibilité $\sim$ 0.5 Å. Des exemples de spectres sont présentés en figure 1 de l'annexe 8.

Nous nous sommes plus particulièrement intéressés à 36 étoiles T Tauri situées dans le nuage moléculaire de Taurus-Auriga, pour lesquelles des données photométriques complètes sont disponibles (voir annexe 9). Notre échantillon couvre un vaste domaine de largeur équivalente Hα (2 à 140 Å) représentatif de la population des étoiles jeunes de faible masse (Herbig et Bell 1988). En particulier, il comprend 25 étoiles avec une largeur équivalente Hα publiée de plus de 5 Å ("classical T Tauri stars", ou CTTS), et 11 étoiles avec une largeur équivalente Hα publiée de moins de 5 Å ("weak-line T Tauri stars", ou WTTS). Une interprétation statistique de nos résultats est donc possible.

Comme Cohen et Kuhi (1979) nous trouvons que l'émission [OI]λ6300 est corrélée avec l'émission dans la raie Hα . En particulier, 80% (9/11) des WTTS de notre échantillon ne montrent pas d'émission [OI]λ6300 détectable, alors que 84% (21/25) des T Tauri classiques possèdent une raie [OI]λ6300 de largeur équivalente supérieure à 0.1 Å.

Les étoiles où les raies interdites sont détectées possèdent des propriétés d'émission différentes suivant leur flux intrinsèque dans la raie de [OI]λ6300. Deux groupes peuvent être distingués:

(1) Les étoiles avec un flux dans la raie [OI]λ6300 supérieur à 10^{-13} erg cm^{-2} s^{-1} ont une vitesse centroïde de l'émission [OI]λ6300 décalée vers le bleu de -80 km s^{-1} en moyenne par rapport à la vitesse de l'étoile (et jusqu'à -170 km s^{-1}dans HL Tau). Toutes ces étoiles sauf 2 possèdent une raie de [SII]λ6731 détectable, avec un rapport [SII]λ6731/[OI]λ6300 $\sim$ 0.3. Ce groupe contient les trois étoiles de notre échantillon où les raies de [NII]$\lambda\lambda$6548,6584 sont détectées (DG Tau, HL Tau, et T Tau).

(2) les étoiles avec un flux dans la raie [OI]λ6300 inférieur à 10^{-13} erg cm^{-2} s^{-1} ont une vitesse centroïde de l'émission [OI]λ6300 plus faible : -23 km s^{-1} en moyenne, et au maximum -70 km s^{-1} par rapport à l'étoile. La raie de [SII]λ6731 n'est détectée que dans trois de ces objets, avec un rapport [SII]/[OI] $\sim$ 0.3 similaire à celui observé dans le premier groupe. Les limites supérieures sur le rapport [SII]/[OI] pour les autres objets varient entre 0.3 et 0.04. Cela suggère une plus grande variété de conditions physiques parmi les étoiles de cette catégorie que parmi les étoiles à plus forte émission [OI]λ6300.

Ces propriétés peuvent être comparées aux prédictions des quatre modèles envisagés en section 4.1: Hartmann et Raymond (1988) ont calculé les flux de raie attendus dans les deux premiers modèles (vent photo-ionisé en expansion radiale, et interaction entre le vent et le disque circumstellaire) pour différentes valeurs du taux de perte de masse. Ils trouvent en particulier qu'un vent photo-ionisé devrait produire très peu d'émission [SII] et [NII] car les températures nécessaires pour exciter les raies ne sont atteintes que dans une région dense à moins de 100 rayons stellaires où l'émission [OI]λ6300 domine. Les flux attendus pour les jets ionisés et les objets de Herbig-Haro peuvent être directement estimés à partir d'études observationnelles (Cohen et Jones 1987; Von Hippel, Burnel, et Williams 1988) [1] .

Nous trouvons que les modèles capables de reproduire à la fois les flux absolus et les rapports de raies observés diffèrent suivant le groupe d'objets considéré. Dans les étoiles avec un flux [OI]λ6300 inférieur à 10^{-13} erg s^{-1} cm^{-2}, les flux de [SII] observés peuvent être

[1] il faut toutefois noter que ces observations se rapportent à des chocs situés à plusieurs centaines d'AUs de la source, et que les conditions physiques pourraient différer si le choc se produit plus près de l'étoile.

reproduits soit par des jets ou des objets de Herbig-Haro denses ($n_e \geq 10^4$ cm^{-3}), soit par des chocs obliques simples entre le vent et le disque tels que ceux modélisés par Hartmann et Raymond (1988). Les fortes raies interdites de [SII] (et parfois [NII]) observées dans les autres objets nécessitent soit des jets ou des objets de Herbig-Haro plus brillants, soit des interactions multiples entre le vent et le disque (mais cette dernière suggestion demande à être testée quantitativement).

Dans tous les cas, les rapports de raies [SII]/[OI] et [NII]/[OI] observés dans les T Tauri sont deux à trois fois plus faibles que dans les objets de Herbig-Haro et les jets optiques, indiquant une plus grande densité et un plus faible degré d'excitation dans la région d'émission [OI]λ6300 des étoiles T Tauri. Ces rapports peuvent être reproduits si la majorité de l'émission [OI]λ6300 est formée dans les parties denses d'un vent ionisé (l'émission de [SII] et [NII] venant elle d'un objet de Herbig-Haro ou d'un jet), ou si toute l'émission provient de chocs obliques entre le vent et le disque.

Malgré cette ambiguité sur l'origine de l'émission [OI]λ6300 dans les T Tauri, les modèles de Hartmann et Raymond (1988) suggèrent que les taux de perte de masse nécessaires pour reproduire les observations de [OI]λ6300 sont comparables dans les deux modèles ($\sim 10^{-8}$ à 10^{-6} M$_\odot$ yr^{-1} suivant l'étoile si $V_w \sim 200$ km s^{-1}), et que le flux dans la raie [OI]λ6300 devrait augmenter avec le taux de perte de masse, toutes choses (géométrie de l'interface entre le vent et le milieu circumstellaire, vitesse du vent) étant égales par ailleurs. Si l'intensité de la raie [OI]λ6300 peut-être considérée comme une mesure de la force du vent, l'étude de sa corrélation avec les paramètres de l'objet devrait permettre de poser des contraintes énergétiques sur le mécanisme d'éjection. Nous examinons ce problème en détail dans la section qui suit.

4.3 Corrélation avec les propriétés photosphériques et infrarouges de l'objet

Les résultats obtenus par Cohen et Kuhi (1979) sur un large échantillon d'étoiles T Tauri ont montré que le flux [OI]λ6300 et la luminosité bolométrique de l'objet sont corrélés. Cela suggère que la corrélation à grande échelle trouvée entre les paramètres du vent déduits des flots CO et la luminosité de la source infrarouge pourrait avoir son équivalent à l'intérieur de la classe des objets visibles de faible luminosité. Cependant, comme nous l'avons dit en section 2.3, cette corrélation ne permet pas à elle seule de choisir de façon définitive entre les différents mécanismes d'éjection parce que la luminosité bolométrique

de l'objet contient à la fois une contribution purement stellaire et une contribution du disque circumstellaire. L' étude des étoiles T Tauri nous permet ici d'aller plus loin et *pour la première fois* d'étudier séparément l'influence de chacune de ces contributions sur les caractéristiques du vent.

Afin d'estimer ces contributions à la luminosité totale, nous avons rassemblé les données photosphériques les plus récentes obtenues sur les étoiles T Tauri de notre échantillon et y avons ajouté des mesures dans l'infrarouge lointain obtenues à partir de données du satellite IRAS. Notre base de donnée complète, qui inclut toutes les étoiles T Tauri classiques et de faible émission dans le complexe Taurus-Auriga cataloguées par Herbig et Bell (1988) et possédant une luminosité de moins de 30 $L_\odot$, est présentée dans l'annexe 9.

Nous avons approximé la contribution photosphérique dans chaque objet par la distribution d'énergie d'une étoile standard de même type spectral dont le flux à 0.64μm serait le même que le flux observé. Cette longueur d'onde a été choisie parce qu'elle minimise la contamination possible du flux observé par l'émission du disque circumstellaire. En effet, les modèles de disques d'accrétion développés pour les T Tauri (Bertout, Basri, Bouvier 1988) montrent que la surface du disque émet principalement dans l'infrarouge et domine la photosphère au delà de 1 μm, alors que la couche limite entre le disque et la surface de l'étoile est très chaude ($T \sim 8000$ K) et rayonne principalement dans l' ultraviolet et le visible, où elle pourrait dans certains cas représenter plus de la moitié du continu observé. La luminosité photosphérique est alors calculée en intégrant la distribution d'énergie de cette étoile standard, et l'excès infrarouge L_{IR} est calculé en soustrayant point par point la contribution photosphérique de la distribution d'énergie totale observée au delà de 0.64 μm. Précisons que cet excès, qui mesure l'émission thermique de la poussière dans l'environnement circumstellaire immédiat de l'étoile, peut provenir non seulement de la dissipation d'énergie gravitationnelle qui accompagne l'accrétion du disque sur l'étoile, mais aussi du chauffage de la poussière par absorption des photons stellaires. Alors que la première contribution devrait refléter la luminosité d'accrétion $L_{acc} = GM_* \dot{M}_{acc}/R_*$, la seconde dépend de L_* et de la fraction des photons stellaires interceptée, c'est à dire de la géométrie du disque (Adams, Lada, et Shu 1987; Kenyon et Hartmann 1987).

Nous avons tout d'abord étudié la relation entre le flux dans la raie [OI]λ6300 et la luminosité photosphérique de l'étoile L_* (figure 6*a* de l'annexe 8). Comme la plupart des

étoiles de notre échantillon ont des types spectraux similaires (entre K7 et M0), L_* devrait décroître au fur et à mesure que l'étoile se contracte vers la séquence principale, en même temps que la profondeur de sa zone convective diminue. Nous trouvons que les valeurs de L_* sont pour la majorité comprises entre 0.3 et 3 $L_\odot$, et que ces valeurs sont les mêmes parmi les étoiles où [OI]λ6300 est détectée (en majorité des T Tauri "classiques" avec $W_\lambda(H\alpha) > 5$ Å) que parmi les étoiles où elle ne l'est pas (en majorité des WTTS avec $W_\lambda(H\alpha) \leq 5$ Å). Les propriétés de l'émission [OI]λ6300 apparaissent donc indépendantes de la structure interne de l'étoile. De plus, les WTTS ont également les mêmes périodes de rotation et les mêmes flux X que les T Tauri classiques (Walter *et al.* 1988), indiquant un même niveau d'activité magnétique. Il semble donc que les caractéristiques de la perte de masse dans les étoiles T Tauri ne soient pas principalement déterminées par les propriétés énergétiques intrinsèques de l'étoile, comme on s'y attendrait si l'éjection était d'origine purement stellaire.

Une autre source d'énergie possible pour l'éjection de matière est l' accrétion du disque circumstellaire sur l'étoile, qui a été envisagée dans plusieurs modèles (Shu *et al.* 1988; Pudritz et Norman 1986; Ushida et Shibata 1985; voir section 2.2). On s'attendrait alors à ce que le flux [OI]λ6300 dans les T Tauri soit corrélé avec l' excès infrarouge L_{IR}.

La figure 6*b* de l'annexe 8 montre que c'est bien le cas: Les WTTS ont en majorité un excès infrarouge $L_{IR} \leq 0.5$ $L_\odot$, alors que les étoiles où la raie [OI]λ6300 est détectée ont pour la plupart un excès $L_{IR} \geq 0.5$ $L_\odot$. Dans les étoiles où la raie de [OI]λ6300 est détectée, le flux [OI]λ6300 et l'excès infrarouge sont corrélés sur plus de deux ordres de grandeur.

Cette corrélation reste apparente lorsqu'on soustrait de L_{IR} la contribution statistique $L_{rep} = 1/3\ L_*$ attendue de la réemission des photons stellaires par un disque plat incliné de façon aléatoire par rapport à l'observateur (dans cette géométrie, 1/4 des photons stellaires est absorbé et réémis, mais L_* ne vaut que 3/4 de la luminosité photosphérique réelle car une partie de la surface de l'étoile nous est cachée par le disque). Il est intéressant de noter que la plupart des étoiles où la raie [OI]λ6300 est détectée ont $L_{IR} > L_{rep}$ (voir figure 6*c* et figure 7 de l'annexe 8), comme on s'y attendrait si le taux d'accrétion dans le disque n'est pas négligeable.

Si le flux dans la raie [OI]λ6300 est bien une mesure de la perte de masse, et si la fraction de l'excès infrarouge qui ne provient pas de L_{rep} est bien une mesure de la luminosité d'accrétion, la corrélation de pente $\sim$ 1 que nous trouvons entre ces deux quantités suggère que la luminosité mécanique du vent et la luminosité d'accrétion sont proportionnelles dans les T Tauri, et ce sur plus de deux ordres de grandeur. Un rapport $\dot{M}_w$sur $\dot{M}_{acc}\sim$ 0.5 est obtenu si l'on adopte les valeurs de $\dot{M}_w\sim 10^{-8} - 10^{-6}$ $M_\odot$ yr^{-1} suggérées par les modèles actuels de l'émission [OI]λ6300 (Hartmann et Raymond 1988), et si l'on calcule $\dot{M}_{acc}$en supposant que $L_{IR} - L_{rep}$ représente la moitié de la luminosité d'accrétion (l'autre moitié étant rayonnée dans l'UV par la couche limite).

Une autre explication de cette corrélation pourrait être envisagée, où c'est *l'angle solide* soutenu par le disque circumstellaire à partir de l'étoile qui varie d'un objet à l'autre, le taux de perte de masse et le taux d'accrétion restant à peu près constants. Une augmentation de cet angle solide augmenterait à la fois la fraction de photons stellaires réémis dans l'infrarouge (donc L_{IR}) et la surface d'interaction entre le vent et le disque (donc l'émission [OI]λ6300 formée dans ce choc).

Cependant, un fait indique que le taux d'accrétion ne peut être le même dans toutes les T Tauri, et que les variations de L_{IR} observées ne peuvent être entièrement due à des effets géométriques: Il s'agit de la corrélation entre le flux Hα et L_{IR}, qui est représentée en figure 8 de l'annexe 8. Cette corrélation n'est pas surprenante en tant que telle, car les flux Hα et [OI]λ6300 sont corrélés dans les T Tauri. Mais l'intensité de l'émission Hα dans les T Tauri (Hα /[OI] $\sim$ 100), et le fait que les profils s'étendent symmétriquement de part et d'autre de la vitesse de l'étoile, impliquent que la raie Hα ne peut être formée dans un choc avec le milieu circumstellaire à plusieurs unités astronomiques de l'étoile, comme c'est possible pour la raie [OI]λ6300. Les modèles empiriques de l'émission Hα (*e. g.* Hartmann, Edwards, et Avrett 1982) suggèrent plutôt qu'elle provient d'une enveloppe à haute température située à quelques rayons stellaires. La corrélation de Hα avec L_{IR} et [OI] ne peut donc être expliquée que si Hα est formée dans l'atmosphère de la couche limite du disque d'accrétion, ou bien à la base du vent (les deux pouvant en fait être une seule et même région). Le fait que le flux Hα puisse varier par plus de 2 ordres de grandeur d'une étoile à l'autre implique alors que le taux d'accrétion et/ou le taux de perte de masse varie de façon similaire à l'intérieur de la classe des T Tauri. D'autre part, le fait que les étoiles à plus fort flux [OI]λ6300 aient tendance à montrer des vitesses centroides de la raie [OI]λ6300 plus grandes suggère également que le taux de perte de masse n'est pas constant

dans les étoiles T Tauri. La corrélation observée entre le flux [OI]λ6300 et L_{IR} ne peut donc être entièrement due à des effets géométriques, et apparait mieux expliquée par une corrélation entre le taux de perte de masse et le taux d'accrétion.

Les conditions précises de cette corrélation, en particulier le rapport $\dot{M}_w$ sur $\dot{M}_{acc}$ restent cependant incertaines. En effet, le processus d'émission des raies interdites dans les étoiles T Tauri n'est pas encore clairement établi (voir section 4.2). De plus, les modèles standards de disques circumstellaires prédisent une pente de la distribution d'énergie infrarouge α = d LogλF_λ / d Logλ = -4/3, alors que beaucoup d' étoiles T Tauri classiques ont des valeurs de $\alpha \geq$ -0.8 (Rucinski 1985; Adams, Lada, et Shu 1987). L' étude des raies interdites à plus haute résolution, ainsi que la détermination indépendante du taux d'accrétion à partir d'observations dans le domaine UV, devraient bientôt permettre d'éclaircir ce point.

CHAPITRE 5
CONCLUSIONS ET PERSPECTIVES

5.1 Nature et origine des flots moléculaires

5.1.1 *Contraintes énergétiques sur le mécanisme d'éjection*:

Notre étude de la formation des raies de CO dans les flots bipolaires a permis de montrer que les incertitudes entrant dans la détermination des paramètres dynamiques du flot varient de plusieurs ordres de grandeur suivant la procédure adoptée, mais peuvent être ramenées à un facteur $\sim$ 30 si les hypothèses utilisées sont judicieusement choisies[1] . Il serait souhaitable que les observateurs adoptent le plus souvent possible cette approche, ainsi qu'une même valeur de l'abondance H_2 /^{13}CO , afin d'assurer une plus grande précision dans la définition des corrélations entre paramètres du flot et luminosité totale de l'objet.

Mais même lorsque cette procédure est adoptée, une dispersion intrinsèque d'un ordre de grandeur subsiste dans les corrélations, qui ne semble pas due aux erreurs de calcul des paramètres CO Un exemple particulièrement frappant est celui de B335 et RNO 43; ces deux flots sont dans la même configuration spatiale (Cas 3 avec $i \geq 80°$) et leurs sources ont des luminosités comparables (3 $L_\odot$ et 12.4 $L_\odot$), mais leurs rapports c F_{CO}/L_{bol} et L_{CO}/L_{bol} diffèrent d'un facteur 10. Ce résultat pourrait refléter soit une variation intrinsèque de l' efficacité de l'éjection, due à des facteurs propres à l'objet (*e. g.* rotation, champ magnétique, rapport L_{acc}/L_{bol}), soit une variation de l'efficacité avec laquelle la quantité de mouvement et l'énergie cinétique sont transférés au flot, due à des facteurs "extérieurs": gradients de densité et champs magnétiques différents dans le milieu ambiant, régime "energy-driven" ou "momentum-driven". Nous avons vu que le dernier facteur entraîne à lui seul une incertitude d' un ordre de grandeur dans les propriétés du vent déduites des observations CO, ce qui rend pour l'instant impossible la distinction entre les

[1] *i. e.* si la masse du flot est calculée en intégrant l'intensité ^{12}CO sur toutes les lignes de visée — toute émission à la vitesse du nuage étant exclue — puis corrigée de la profondeur optique à l'aide du rapport ^{13}CO /^{12}CO au pic d'intensité, et si les paramètres cinématiques et dynamiques sont encadrés entre les valeurs inférieures et supérieures obtenues en supposant soit que le gaz se déplace le long de la ligne de visée soit qu'il va à la vitesse maximale observée

divers mécanismes d'éjection proposés (mis à part l'expansion thermique, et la pression de radiation dans les sources de faible luminosité).

Les contraintes énergétiques ne pourront donc être précisées que si l'on peut clairement identifier le régime qui régit l'interaction entre le vent et le milieu moléculaire, ainsi que les facteurs susceptibles d'influer sur son efficacité. Outre la modélisation détaillée des flots moléculaires, dont nous parlons plus en détail dans le paragraphe suivant, certaines observations pourraient permettre de progresser dans cette direction:

• L' étude du gradient de densité dans le nuage ambiant, par cartographie dans des espèces moléculaires telles que ^{13}CO et $C^{18}O$ (*e. g.* Davidson 1987).

• La détermination de la vitesse du vent (ou d'une limite inférieure) à partir d' observations de jets optiques, d'objets de Herbig-Haro, et de gaz moléculaire ou atomique à très grande vitesse ($\geq$ 200 km s^{-1}) près de la source (cf. les observations de HH7-11 par Lizano *et al.* 1988). Cette valeur peut ensuite être comparée à la vitesse critique au-delà de laquelle le flot est dans le régime "energy-driven".

• La mesure de l'intensité du champ magnétique interstellaire par effet Zeeman dans les raies de la molécule OH (*e. g.* Kazès et Crutcher 1986; Myers et Goodman 1988). Ce paramètre pourrait affecter à la fois l'efficacité de l'éjection et le transfert de quantité de mouvement au milieu ambiant.

• Et surtout, l'étude de l' émission étendue dans l'infrarouge lointain (60 à 100 μm) associée aux flots bipolaires. Cette émission n'a été détectée dans les données du satellite IRAS qu'en direction du flot de L1551-IRS5 (Edwards *et al.* 1986; Clark *et al.* 1986), qui a le diamètre angulaire le plus grand ($\sim$ 30') des flots connus. Les autres flots observés pourraient en fait posséder une émission similaire sous le seuil de détectabilité d'IRAS. Le satellite infrarouge ISO, dont la sensibilité et la résolution à 100 μm seront respectivement 100 fois et 3 fois meilleures que celles d'IRAS, permettra dans quelques années de voir si ce phénomène est courant dans les flots bipolaires, et si la luminosité mécanique du vent qu'il indique reste compatible avec la luminosité déduite du CO dans l'hypothèse d'un régime "energy-driven" (comme c'est le cas dans L1551-IRS5; cf. annexe 6), ou bien implique un régime "momentum-driven".

Ces études devraient également aider à mieux comprendre l'impact des flots moléculaires sur la structure et la dynamique du nuage ambiant.

5.1.2 *Structure des flots moléculaires bipolaires*

Comme ce travail de thèse l'a montré, le meilleur moyen de mieux comprendre les caractéristiques des flots moléculaires et de les confronter aux prédictions des différents modèles d'éjection et de collimation proposés reste l'étude de leur structure et de leur champ de vitesse par le biais de la modélisation des profils CO. Cette approche du problème nous a permis de mieux comprendre ce que l'on peut attendre, et déduire, des observations CO. Nous avons ainsi pu identifier les premiers exemples de flots bipolaires orientés dans le plan du ciel. De plus, l' application de nos résultats aux cas les mieux étudiés suggère que les lobes des flots moléculaires sont pleins et que le gaz est accéléré le long de l'axe du flot, tout en présentant une diminution de vitesse de l'axe vers les bords. Mais de nombreuses questions se posent encore:

• *La structure proposée peut-elle vraiment expliquer les observations ?*: Il est nécessaire de confirmer notre suggestion par des calculs détaillés de la formation des raies de CO pour ce champ de vitesse. Les résultats préliminaires montrés en figure 2, où nous avons supposé (1) un flux de masse indépendant de la latitude et (2) une température cinétique constante, produisent encore trop d'émission à faible vitesse en direction de l'axe du flot. Cela suggère que l'émissivité du gaz est en fait une fonction très dépendante de sa vitesse, et que l'une de nos deux hypothèses simplificatrices doit probablement être abandonnée. Nous travaillons actuellement à l'exploration de ces différentes possibilités. Parallèlement, des observations de R Mon dans la raie $J = 2 \rightarrow 1$ de CO devraient poser plus de contraintes sur la profondeur optique et la loi de température dans le flot, qui permettront de mieux déterminer les paramètres libres du modèle.

• *Quelle est la fraction du flot ejectée à partir du disque ?*: La structure du flot et le champ de vitesse que cette étude suggère sont très proches de ceux attendus dans le modèle d'éjection de Pudritz et Norman (1986; voir section 2.2). Il n'est cependant pas possible que tout le gaz moléculaire à grande vitesse ait été éjecté d'un disque circumstellaire. En effet, la relation $\dot{M}_{acc} \sim 100\ \dot{M}_w$ prédite par Pudritz et Norman implique que l'objet central aurait accumulé environ 100 fois la masse éjectée dans le flot, ce qui est incompatible avec les observations (voir *e. g.* les masses des flots moléculaires observés par Levreault [1988] autour de sources visibles de masses connues). Par contre, il est concevable que la composante accélérée à grande vitesse observée dans R Mon et L1551-IRS5 représente effectivement de la matière directement éjectée du disque, alors que le gaz à faible vitesse,

qui contient la majorité de la masse dans le flot L1551-IRS5 (Moriarty-Schieven *et al.* 1988), représente la matière ambiante entraînée.

Pour tester cette hypothèse, il serait nécessaire d'obtenir des cartes à très haute résolution de la composante à grande vitesse dans R Mon et L1551-IRS5, afin de voir si elle provient effectivement d'une structure circumstellaire de taille $\leq$ 1000 AU. L'interféromètre millimétrique de l'IRAM en cours d'achèvement sur le plateau de Bures près de Grenoble devrait bientôt permettre d'effectuer de telles observations. L'observation éventuelle d' hydrogène atomique à grande vitesse dans la raie à 21 cm grâce à l'interféromètre radio du VLA (*e. g.* Bally et Stark 1983) permettrait d'établir plus précisément la nature moléculaire ou atomique de la matière éjectée.

• *Les flots bipolaires ont-ils tous la même structure ?*: Pour l'instant, seuls L1551-IRS5 et R Mon ont été observés avec suffisamment de résolution pour permettre une comparaison détaillée avec nos modèles de l'émission CO. Il est donc important de voir si la structure que nous avons déduite s'applique à d'autres flots. Une étude détaillée du flot bipolaire autour de l'étoile de Herbig LkHα 234 dans la région NGC 7129, effectuée au téléscope de 30 m de l'IRAM (Bertout 1987; Bertout, Cabrit, Thum, et Forveille, en préparation; voir figure 4), montre que le lobe bleu et l'étoile sont séparés par une cavité conique probablement évacuée par un vent non moléculaire en provenance de LkHα 234. Dans ce cas, il semblerait que le lobe bleu soit creux. Mais la région est complexe, et le lobe rouge ne montre pas cette structure. Nos observations de B335 (annexe 5) semblent aussi plutôt favoriser un vent non moléculaire, puisque le lobe bleu du flot est interrompu par une région où aucune émission CO n'est détectée, mais il n'est pas possible d'établir si les lobes sont creux ou pleins car le flot est trop incliné sur la ligne de visée. Un candidat intéressant pour une étude à haute résolution de la structure des flots bipolaires avec l'antenne de l'IRAM est le flot d' Orion B (Sanders et Willner 1985), qui possède un diamètre angulaire relativement grand (6'), et a une géométrie bipolaire clairement définie (Cas 2) similaire à celle de L1551-IRS5.

Un autre problème à élucider est celui de la prédominance de flots vus de face (Cas 1), surtout parmi les sources les plus lumineuses (Lada 1984; Levreault 1988). Nous avons mentionné la possibilité qu'il existe deux familles de flots bipolaires, les uns bien collimatés, les autres presque sphériques. La clef de ce problème réside dans l'étude à plus haute résolution des flots dans le Cas 1, dont la plupart n'ont été cartographiés qu'avec

une résolution de 1' (Bally et Lada 1983; Levreault 1985) ou 45" (Snell *et al.* 1984). Le téléscope de l'IRAM pourrait à nouveau être utilisé pour une telle étude.

• *Les flots sont-ils réellement homogènes* (comme nous l'avons supposé dans nos modèles) *ou "clumpy"?* (littéralement: "avec des grumeaux"), c'est à dire formés d'un grand nombre de petites condensations non résolues ne remplissant au total qu'une fraction $f < 1$ du lobe de l'antenne. Cette question se pose pour la raison suivante: Lorsqu'on suppose que la température d'excitation est constante dans le flot, les rapports de raie ^{12}CO / ^{13}CO et $(J = 2 \rightarrow 1)/(J = 1 \rightarrow 0)$ typiquement observés dans les flots bipolaires impliquent une émission optiquement épaisse et une température similaire à celle du nuage ambiant, $\sim$ 10 K (*e. g.* Snell *et al.* 1984; Margulis et Lada 1985). Pour expliquer les faibles intensités observées dans le gaz à grande vitesse (en général $\leq$ 5 K), il faut alors invoquer un facteur de remplissage $f < 1$, c'est à dire supposer que le flot est "clumpy". Cependant, les rapports de raie peuvent donner des informations erronées si un gradient de température est présent dans le flot (Cantó, Rodriguez, et Anglada 1987). Notre modèle d'émission CO dans les flots bipolaires nous permet de voir dans quelle mesure les rapports de raie observés peuvent être reproduits par un flot homogène avec un gradient d'excitation. Cette étude est en cours. Parallèlement, j'ai commencé à développer sur le CRAY-1 du Centre de Calcul Vectoriel pour la Recherche un code numérique calculant l'excitation des raies de CO par une méthode Monte-Carlo. Ce nouvel outil devrait bientôt nous permettre d'étudier des géométries et des champs de vitesse plus complexes, ainsi que des milieux "clumpy".

5.2 Rôle de l'accrétion dans la perte de masse des étoiles T Tauri

Notre étude statistique, qui représente un gain d'un facteur 4-5 en sensibilité et résolution par rapport à celle de Cohen et Kuhi (1979), a montré qu' au moins 80% des étoiles T Tauri "classiques" (*i. e.* avec $W_\lambda(\mathrm{H}\alpha) > 5$Å) possèdent une raie [OI]λ6300 décalée vers le bleu, indiquant à la fois une perte de masse et la présence d'un disque circumstellaire opaque. Par une analyse détaillée de leur distribution d'énergie, nous avons pu calculer la contribution photosphérique et la contribution de l'excès infrarouge à la luminosité totale de l'objet, et étudier séparément leur influence sur les propriétés de l'étoile. Nous avons démontré que les flux émis dans la raie [OI]λ6300 et la raie Hα varient par plus de 2 ordres de grandeur à l'intérieur de la classe des T Tauri, indépendamment de la luminosité photosphérique, mais qu'ils sont corrélés avec l'excès infrarouge de l'objet. L'interprétation

la plus satisfaisante est que ces trois caractéristiques du phénomène T Tauri (émission [OI]λ6300, Hα , et excès infrarouge) ne sont pas principalement déterminées par l'âge de l'étoile, comme cela avait été suggéré à l'origine (Cohen et Kuhi 1979), mais par le taux d'accrétion dans le disque circumstellaire. En particulier, ces résultats sont compatibles avec l'hypothèse que l' accrétion représente l'ultime source d'énergie pour la perte de masse dans les étoiles T Tauri.

Cependant, le rapport $\dot{M}_w / \dot{M}_{acc} \sim 0.5$ que nous obtenons en adoptant des modèles simples de l'émission [OI]λ6300 et de l'excès infrarouge est difficile à expliquer par les modèles théoriques d'éjection décrits en section 2.2: Le modèle centrifugo-magnétique de Shu *et al.* (1988) prédit bien un rapport comparable, mais ne s'applique pas aux T Tauri qui tournent à une vitesse bien plus faible que leur vitesse critique ($V_{rot} \sim 25$ km s^{-1} au lieu de $V_{esc} \sim 300$ km s^{-1}); celui de Pudritz et Norman (1986) prédit un rapport $\sim$ 0.01 seulement; la propagation d'ondes d'Alfvén à partir du disque ne suffirait que si la luminosité sous forme d'ondes d'Alfvén est supérieure à la luminosité d'accrétion, ou si l'efficacité du transfert d'énergie à l'enveloppe est plus grande que les 10% prédits dans le cas où les ondes sont émises à partir de l'étoile (DeCampli 1981; Hartmann, Edwards, et Avrett 1982)[2] .

Il est peu probable que nous ayons beaucoup sous-estimé la luminosité d'accrétion dans les étoiles T Tauri, car des taux d'accrétion très supérieurs entraîneraient des températures de la couche limite et des excès ultraviolets incompatibles avec ceux qui sont observés (Basri et Bertout 1988). Le calcul du degré de "veiling" de plusieurs étoiles ainsi que la modélisation plus raffinée de leur distribution d'énergie ultraviolette et infrarouge, tous deux actuellement en cours (P. Hartigan, et Claude Bertout, communications personnelles), devraient bientôt permettre de connaître ce paramètre avec encore plus de précision.

D'un autre coté, les taux de perte de masse actuellement déduits des raies interdites sont encore assez incertains et pourraient être systématiquement trop grands, par exemple

---

[2] Une situation comparable est rencontrée dans les variables de type FU Orionis: ces étoiles T Tauri dont la luminosité a soudainement augmenté par un facteur $\sim$ 100 présentent les caractéristiques d'un disque d'accrétion avec $\dot{M}_{acc} \sim 10^{-4}$ M$_\odot$ yr^{-1}, et montrent des profils P Cygni prononcés dans les raies Hα et NaI D qui suggèrent une perte de masse $\dot{M}_w \geq 10^{-5}$ M$_\odot$ yr^{-1}, peut-être directement à partir du disque (Kenyon et Hartmann 1988). Là encore, $\dot{M}_w / \dot{M}_{acc} \geq 0.1$, et le mécanisme d'éjection n'a pas encore été identifié.

si l'émission a une origine hybride (*e. g.* un vent dense mais lent, et un jet rapide mais peu dense). L'identification du mécanisme d'éjection dans les T Tauri nécessite donc une estimation plus précise de leur taux de perte de masse. Plusieurs études devraient bientôt nous faire progresser sur ce plan:

• La mesure des rapports de raies [SII] 6716/6731, [SII]/[OI], et [NII]/[OI] en fonction de la vitesse sur des spectres à haute résolution ($\Delta\lambda \sim 0.3$ Å) devrait permettre d'estimer la densité et le degré d'excitation dans les diverses composantes en vitesse du profil, et ainsi d'identifier leur origine respective (vent dense, interaction vent/disque, jet ionisé, ou objet de Herbig-Haro). Les données nécessaires à cette étude ont été récemment obtenues par Suzan Edwards et Steve et Karen Strom, et leur interprétation, à laquelle je compte collaborer, est en cours.

• Des observations dans les raies infrarouges de l'hydrogène poseraient des contraintes indépendantes sur le taux de perte de masse et le degré d'ionisation dans les parties internes de l'enveloppe. Ces raies n'ont pour l'instant été détectées que dans les étoiles les plus actives (Evans *et al.* 1987) et indiquent un taux de perte de masse inférieur aux 10^{-6} $M_\odot$ yr^{-1} suggérés par leurs raies interdites (annexe 7; figure 3 de l'annexe 8), impliquant que le vent est soit moins fort, soit partiellement ionisé.

• De même, une étude détaillée de l'émission dans le continu radio à plusieurs fréquences pourrait poser des contraintes sur la densité et l'ionisation du vent (en particulier la présence de chocs forts) à quelques unités astronomiques de l'étoile, là où a probablement lieu la majorité de l'émission [SII] dans les étoiles T Tauri (Hartmann et Raymond 1988).

• Finalement, des progrès décisifs seront bientôt accomplis grâce au Hubble Space Telescope et au Very Large Telescope, dont la haute résolution angulaire ($< 0.04''$) permettra de déterminer directement si les raies interdites proviennent de jets collimatés, de condensations de Herbig-Haro, d'enveloppes étendues, ou d'une zone de choc à la surface du disque circumstellaire.

5.3 Comparaison entre objets visibles et enfouis

Un autre problème crucial pour notre compréhension de l'évolution stellaire est de savoir si le mécanisme de perte de masse est le même dans les étoiles T Tauri et dans les sources enfouies, ou bien s'il s'agit de deux phénomènes distincts marquant des phases

d'évolution successives. Jusqu'à présent, les manifestations de perte de masse à grande échelle caractéristiques des sources infrarouges (flots moléculaires, jets optiques et radio, objets de Herbig-Haro) n'ont été observées qu'autour d' étoiles T Tauri actives avec $L_{bol} \geq 5\ L_{\odot}$ (*e. g.* HL Tau, DG Tau, T Tau, AS 353 A, RNO 91; Levreault 1985; Mundt, Brugel, et Bührke 1987). Ce fait semble a priori favoriser la deuxième interprétation, si l'on adopte l'hypothèse traditionnelle que la luminosité *totale* est un indicateur de l'âge de l'objet (les T Tauri les plus brillantes étant alors les plus jeunes). D'un autre côté, notre étude statistique montre clairement que cette hypothèse n'est pas justifiée dans le cas des T Tauri classiques. En effet, l' excès infrarouge varie sur deux ordres de grandeur ($\sim$ 0.1 à 10 $L_{\odot}$) indépendamment de la luminosité photosphérique, et représente plus de la moitié de la luminosité totale dans 50% des cas (voir figure 7 de l'annexe 8). Il en résulte que (1) l'excès infrarouge et les propriétés du milieu circumstellaire ne dépendent pas que du stade évolutif de l'étoile elle-même[3] , et (2) la luminosité totale n'est pas toujours un bon indicateur de l'âge dans les étoiles T Tauri.

Lorsque l'on reconsidère le problème en termes d'excès infrarouge plutôt que d'âge, il apparaît que les étoiles T Tauri montrant des manifestations de perte de masse à grande échelle sont aussi parmi celles qui possèdent les luminosités infrarouges et les raies interdites les plus fortes. De plus, les flots bipolaires et l'émission dans le continu radio associés à ces étoiles extrêmes sont en fait proches de la limite de détectabilité des recherches systématiques effectuées jusqu'ici (Levreault 1988; Bieging et Cohen 1984). La non-détection de ces caractéristiques dans les étoiles T Tauri aux excès infrarouges plus modérés n'est donc finalement pas surprenante si la force de l'éjection est effectivement corrélée avec le taux d'accrétion. De plus, les étoiles T Tauri modérées ont tendance à être dans des parties du nuage moins denses que les T Tauri extrêmes, qui apparaîssent souvent au centre d'une condensation moléculaire. Cette situation pourrait aussi empêcher la formation de flots moléculaires détectables.

La situation est remarquablement similaire pour les sources enfouies de faible luminosité: Myers *et al.* (1988) ont étudié 16 "coeurs denses" cartographiés en NH_3, et ne

[3] Ce point est également indiqué par l'existence d' étoiles T Tauri à faible émission dans la même partie du diagramme H-R que les T Tauri classiques (Walter *et al.* 1988), et par la découverte récente au coeur du nuage ρ Ophiuchi de sources radio probablement très jeunes, mais apparemment dépourvue de tout milieu circumstellaire (André, Montmerle, et Feigelson 1987).

détectent de flots moléculaires que lorsqu' une source infrarouge est présente à l'intérieur de la condensation. Aucun flot n'est détecté lorsque la source infrarouge est plus éloignée du coeur dense, ou lorsque aucune source n'est présente. Les sources qui possèdent un flot moléculaire ou un autre signe de perte de masse intense ont tendance à être plus lumineuses que les sources où ces diagnostics ne sont pas vus. Là encore, il est possible que l' environnement circumstellaire joue un rôle crucial dans l'intensité et la détectabilité du phénomène. De plus, les paramètres CO des flots détectés par Myers *et al.* (1988) sont très proches de ceux obtenus pour les flots détectés autour des étoiles T Tauri.

Les observations sont donc pour l'instant compatibles avec deux interprétations:

(1) Un même mécanisme d'éjection dans les étoiles T Tauri et les sources enfouies, qui serait contrôlé par le taux d'accrétion et non par l'âge de l'objet. La courte échelle de temps des flots observés, $\sim 2 \times 10^4$ ans, suggèrerait alors un phénomène transitoire, peut-être relié au phénomène FU Orionis (voir section 5.2).

(2) Deux mécanismes différents, celui responsable des flots moléculaires étant plus efficace mais ne s'appliquant plus dès que la source a perdu son enveloppe circumstellaire opaque. Par exemple, Shu *et al.* (1988) proposent que les flots moléculaires sont dûs à l'accrétion du disque circumstellaire sur un objet protostellaire magnétisé en rotation à la vitesse critique (voir section 2.2), alors que le mécanisme responsable de la perte de masse dans les étoiles T Tauri, déjà présent dans les sources enfouies, est intrinsèque à l'objet (*e. g.* propagation d'ondes d'Alfvén engendrées dans la zone convective). Lorsque l'enveloppe circumstellaire commence à se dissiper, le taux d'accrétion chute et le freinage magnétique entraîné par la perte de masse d'origine stellaire ralentit l'étoile en dessous de sa vitesse critique. Cet évènement rend le premier mécanisme définitivement inopérant, et marque la fin de la phase de flot moléculaire, en même temps que l'apparition de la source dans le domaine optique.

Plusieurs études sont nécessaires afin de distinguer entre ces deux possibilités:

• La résolution spatiale est particulièrement importante pour une étude détaillée des flots moléculaires autour des étoiles T Tauri, où la taille de la région d'émission est en général ≤ 0.2 pc (Levreault 1985). Le flot autour de l'étoile T Tauri RNO 91 en est une excellente illustration: alors qu'il était tout juste décelable dans la carte de Levreault, effectuée avec un lobe d'antenne de 1.3 arcminutes, il apparaît clairement et avec une intensité plus forte dans la carte obtenue par Myers *et al.* (1988) avec le lobe de 45" du

Five College Radio Astronomy Observatory. Il parait donc urgent d'effectuer une recherche plus approfondie et à plus haute résolution de flots moléculaires autour des étoiles T Tauri, par exemple avec l'antenne de 30 m de l'IRAM (lobe d'antenne de 20" en CO $J = 1 \rightarrow 0$). Cette étude permettrait de voir (1) si les flots déjà détectés sont bien dus aux étoiles visibles et non à des sources enfouies situées à proximité (on sait par exemple à présent que la région de HL Tau contient au moins 5 objets stellaires jeunes; Mundt, Ray, et Bührke 1988), (2) si les étoiles T Tauri ayant des excès infrarouges importants possèdent toutes un flot détectable ou si l'excès infrarouge n'est pas le seul facteur déterminant (l'absence apparente de flot moléculaire autour de DG Tau est particulièrement intrigante, car cette étoile possède un jet optique et est détectée dans le continu radio). Il serait également intéressant d'observer ces étoiles avec une meilleure sensibilité dans le continu radio, et d'obtenir des images dans les raies Hα ou [SII]$\lambda\lambda$6716,6731 afin de rechercher d'éventuels jets optiques.

• D'un autre côté, il serait particulièrement utile d' obtenir les types spectraux, vitesses de rotation, et excès infrarouges de sources de flots moléculaires connues visibles dans le domaine optique. Il serait alors possible de voir si (1) elles possèdent toutes des fortes vitesses de rotation, (2) les paramètres dynamiques du flot moléculaires sont, comme l'émission [OI]λ6300 dans les étoiles T Tauri, corrélés avec la luminosité infrarouge plutôt qu'avec la luminosité photosphérique de l'objet.

Comme on le voit, le problème de la perte de masse dans les objets stellaires jeunes a considérablement évolué au cours des dernières années et représente un domaine de recherche en pleine expansion. Ce travail de thèse a apporté plusieurs éléments de réponse, mais soulève encore plus de questions ! Y répondre nécessitera un important travail de modélisation et une exploitation optimale des nouveaux outils à notre disposition, tels que le télescope de 30 m et l'interféromètre millimétrique de l'IRAM, le futur satellite ISO, le Space Telescope, et le V.L.T. Grâce à eux, il est probable que les années à venir verront des progrès décisifs dans la compréhension de ce phénomène complexe, où se trouve peut-être la clef de l'origine des étoiles.

REFERENCES BIBLIOGRAPHIQUES

Adams, F.C., Lada, C.J., et Shu, F.H. 1987, *Ap. J.* , **312**, 788.

Adams, F.C., Lada, C.J., et Shu, F.H. 1988, *Ap. J.* , **326**, 865.

André, P., 1987, *Protostars and Molecular Clouds*, Eds. T. Montmerle et C. Bertout (Saclay: CEA/Doc), p. 143.

André, P., Montmerle, T., et Feigelson, E.D. 1987, *A. J.* , **93**, 1182.

Appenzeller, I. 1983, *Rev. Mexicana Astron. Astrof.* , **7**, 151.

Appenzeller, I, Jankovics, I., et Ostreicher, R. 1984, *Astron. Astrophys.* , **141**, 108.

Arquilla, R. et Goldsmith, P.F. 1985, *Protostars and Planets II*, Eds. D.C. Black et M.S. Matthews (Tucson: Univ. Ariz. Press)

Bachiller, R., Cernicharo, J., et Martin-Pintado, J. 1988, preprint

Bally, J. 1986, *The Irish Astronomical Journal*, **17**, 270.

Bally, J. et Lada, C.J. 1983 *Ap. J.* , **265**, 824..

Bally, J. et Stark, A.A. 1983 *Ap. J.* , **266**, L61..

Barral, J.F. et Cantó, J. 1981, *Rev. Mexicana Astron. Astrof.* , **5**, 101.

Basri, G. et Bertout, C. 1988, *Ap. J.*, soumis

Beichman, C., Myers, P.C., Emerson, J.P., Harris, S., Mathieu, R., Benson, P.J., et Jennings, R.E. 1986, *Ap. J.* , **307**, 337.

Bertout, C. 1984*a*, *Rep. Prog. Phys.*,**47**, 111

Bertout, C. 1984*b*, *Ap. J.* , **285**, 269.

Bertout, C. 1987, dans *Circumstellar Matter*, Eds. I. Appenzeller et C. Jordan (Dordrecht: Reidel)

Bertout, C. et Thum, C. 1982, *Astron. Astrophys.* , **107**, 368.

Bertout, C., Basri, G., et Bouvier, J. 1988, *Ap. J.* , **330**, 350.

Bieging, J.H., et Cohen, M. 1985, *Ap. J.* , **289**, L5.

Bieging, J.H., Cohen, M., et Schwartz, P.R. 1984, *Ap. J.* , **282**, 699.

Blandford, R.D., et Payne, D.G. 1982, *Mon. Not. Roy. Astron. Soc.* , **199**, 883.

Bohm, K.H. 1983, *Rev. Mexicana Astron. Astrof.* , **7**, 55.

Boss, A.P. 1987, *Ap. J.* , **316**, 721.

Bouvier,J. et Bertout, C. 1988, *Astron. Astrophys.* , sous presse

Bouvier, J., Bertout, C., Benz, W., et Mayor, M. 1986, *Astron. Astrophys.* , **165**, 110.

Brown, A., Drake, S.A., Mundt, R. 1985. dans *Radio Stars* Eds. R.M. Hellming, D.M. Gibson (Dordrecht: Reidel)

Brown, A., Drake, S.A, et Mundt, R. 1986, in *Cool Stars, Stellar systems, and the Sun*, Eds. M. Zeilik et D.M. Gibson, (Heidelberg: Springer-Verlag) p. 451

Calvet, N., Basri, G., et Kuhi, L.V. 1984, *Ap. J.* , **277**, 725.

Calvet, N., Cantó, J., et Rodriguez, L.F. 1983, *Ap. J.* , **268**, 739.

Cantó, J., Rodriguez, L.F., et Anglada, G. 1987 *Ap. J.* , **321**, 877.

Cantó, J., Tenorio-Tagle, G., et Rozyczka, M. 1988, *Astron. Astrophys.* , **192**, 287.

Cantó, J., Rodriguez, L.F., Barral, J.F., et Carral, P. 1981, *Ap. J.* , **244**, 102.

Carroll, T.J., et Goldsmith, P.F. 1981, *Ap. J.* , **245**, 891.

Clark, F.O., Laureijs, R.J., Chlewicki, G., Zhang, C.Y., van Oosterom, W., et Kester, D. 1986 *Astron. Astrophys.* , **168**, L1..

Cohen, M. et Bieging, J.H. 1986, *A. J.* , **92**, 1396.

Cohen, M. et Fuller, G.A. 1985, *Ap. J.* , **296**, 620.

Cohen, M. et Jones, B.F. 1987, *Ap. J.* , **321**, 846..

Cohen, M. et Kuhi, L.V. 1979, *Ap. J. Suppl.* , **41**, 743.

Cohen, M. et Schwartz, P.R. 1983, *Ap. J.* , **265**, 877.

Cohen, M., Emerson, J.P., et Beichmann, C.A. 1989, *Ap. J.* , sous presse

Cohen, M., Hollenbach, D.J., Haas, M.R., et Erickson, E.F. 1988, *Ap. J.* , **329**, 863.

Cudworth, K.M. et Herbig, G.H. 1979, *A. J.* , **84**, 548.

Czyzak, S., Keyes, C.D., et Aller, L.H. 1986, *Ap. J. Suppl.* , **61**, 159..

Davidson, J.A. 1987 *Ap. J.* , **315**, 602..

DeCampli, W.M. 1981, *Ap. J.* , **244**, 124.

Dickman, R.L. 1978, *Ap. J. Suppl.* , **37**, 407.

Dopita, M.A., Schwartz, R.D., et Evans, I. 1982, *Ap. J.* , **263**, L73.

Draine, B.T. 1983 *Ap. J.* , **270**, 519..

Dyson, J.E., 1984, *Ap. Space Science*, **106**, 181.

Edwards, S. et Snell, R., 1982, *Ap. J.* , **261**, 151.

Edwards, S. et Snell, R., 1984, *Ap. J.* , **281**, 237.

Edwards, S., Strom, S., Snell, R.L., Jarrett, T.H., Beichman, C.A., et Strom, K.M. 1986 *Ap. J.* , **307**, L65..

Evans, N.J., Levreault, R.M., Beckwith, S., et Skrutskie, M, 1987, *Ap. J.* , **320**, 364.

Feigelson, E.D., et DeCampli, W.M. 1981, *Ap. J.* , **243**, L89.

Feigelson, E.D., et Kriss, G.A. 1981, *Ap. J.* , **248**, L35.

Fischer, J., Sanders, D.B., Simon, M., et Solomon, P.M. 1985, *Ap. J.* , **293**, 508.

Franco, J., et Cox, D.P. 1983, *Ap. J.* , **273**, 243.

Fridlund, C.V.M., Sandqvist, A., Nordh, H.L., et Olofsson, G. 1988, preprint

Fukui, Y., Sugitani, K., Takaba, H., Iwata, T., Mizuno, A., Ogawa, H., et Kawabata, K. 1986, *Ap. J.* , **311**, L85.

Genzel, R., Reid, M.J., Moran, J.M., et Downes, D. 1981, *Ap. J.* , **244**, 884.

Goldsmith, P.F., Snell, R.L., Hemeon-Heyer, M., et Langer, W.D. 1984, *Ap. J.* , **286**, 599.

Hartigan, P., Raymond, J., et Hartmann, L. 1987, *Ap. J.* , **316**, 323..

Hartmann, L. 1986. *Fundamentals in Cosmic Physics*,**11**, 279

Hartmann, L., Edwards, S., et Avrett, A. 1982, *Ap. J.* , **261**, 279.

Hartmann, L., et MacGregor, K.B, 1982, *Ap. J.* , **259**, 180.

Hartmann, L. et Raymond, J.C. 1988, *Ap. J.* , soumis

Herbig, G.H. 1962, *Advances Astron. Astrophys.*,**1**, 47

Herbig, G.H. 1977, *Ap. J.* , **214**, 747.

Herbig, G.H., et Bell, K.R. 1988, *Lick Observatory Bulletin No. 1111*

Herbig, G.H., et Jones, B.F. 1981, *A. J.* , **86**, 1232.

Herbig, G.H., et Jones, B.F. 1983, *A. J.* , **88**, 1040.

Herbig, G.H., Vrba, F.J., et Rydgren, A.E. 1986, *A. J.* , **91**, 575.

Heyer, M.H., Snell, R.L., Goldsmith, P.F., et Myers, P.C. 1987, *Ap. J.* , **321**, 370.

Jankovics, I., Appenzeller, I., et Krautter, J. 1983, *Publ. Astron. Soc. Pacific* , **95**, 883.

Jones, B.F., et Herbig, G.H. 1982, *A. J.* , **87**, 1223.

Jones, B.F., Cohen, M., Sirk, M., et Jarrett, R. 1984, *A. J.* , **89**, 1404.

Kazès, I. et Crutcher, R.M. 1985, *Astron. Astrophys.* , **164**, 328.

Kenyon, S.J., et Hartmann, L. 1987, *Ap. J.* , **323**, 714.

Kenyon, S.J., et Hartmann, L. 1988, dans *Formation and Evolution of Low-Mass Stars*, Ed. A.K. Dupree (Dordrecht: Reidel) sous presse

Königl, A, 1982, *Ap. J.* , **261**, 115.

Königl, A, 1986, *Can. J. Phys.*, **64**, 362.

Kuhi, L.V. 1964, *Ap. J.* , **140**, 1409.

Kuhi, L.V. 1978, dans *Protostars and Planets* Ed. T. Gehrels

Kwan, J., et Scoville, N. 1976, *Ap. J.* , **210**, L39.

Kwan, J., et Tademaru, E. 1988, *Ap. J.* , **332**, L41.

Kwok, S., et Volk, K, 1985, *Ap. J.* , **299**, 191.

Lada, C.J. 1984 *Galactic and Extragalactic Infrared Spectroscopy*, Eds. M.F. Kessler et J.P. Phillips (Dordrecht: Reidel), p.251.

Lada, C.J. 1985, *Ann. Rev. Astron. Astrophys.* , **23**, 267.

Lada, C.J. 1987, dans *Star Forming Regions*, Eds. M. Peimbert, J. Jugaku (Dordrecht: Reidel)

Lada, C.J., et Wilking, B.A. 1984, *Ap. J.* , **287**, 610.

Lane, A.P., et Bally, J. 1986, *Ap. J.* , **310**, 820.

Langer, W.D., Frerking, M.A., et Wilson, R.W. 1986, *Ap. J.* , **306**, L29.

Lago, M.T.V.T. 1979, *D.Phil Thesis* University of Sussex

Lago, M.T.V.T. 1984, *Mon. Not. Roy. Astron. Soc.* , **210**, 323.

Levreault, R. M. 1985, Thèse non publiée, Département d'Astronomie, Université du Texas à Austin, *Tech. Rep.* No. 85-1.

Levreault, R.M. 1988, *Ap. J.* , soumis.

Levreault, R.M., Myers, P.C., Schild, R.E., Campbell, B.G., et Mathieu, R.D. 1987 *Bull. Am. Astr. Soc.*, **19**, 1092.

Lizano, S., Heiles, C., Rodriguez, L.F., Koo, B.-C., Shu, F.H., Hasegawa, T., Hayashi, S., et Mirabel, I.F. 1988, *Ap. J.* , **328**, 763.

Loren, R.B., Wootten, A., Sandqvist, A., Friberg, P., et Hjalmarson, A. 1984, *Ap. J.* , **287**, 707.

Margulis, M.S., et Lada, C.J. 1985 *Ap. J.* , **299**, 925..

Margulis, M.S., et Lada, C.J. 1988 *Ap. J.* , sous presse

Mendoza, C. 1983, *Planetary Nebulae*, Ed. D.R. Flower (Dordrecht: Reidel), p.143

Mestel, L. 1968, *Mon. Not. Roy. Astron. Soc.* , **138**, 359.

Mirabel, I.F., Ruiz, A., Rodriguez, L.F., et Cantó, J. 1987, *Ap. J.* , **318**, 729.

Montmerle, T., Koch-Miramond, L., Falgarone, E., et Grindlay, J.E. 1983, *Ap. J.* , **269**, 182.

Moriarty-Schieven, G.H., 1988, Thèse non publiée, Département d' Astronomie, Université du Massachusetts, Amherst.

Moriarty-Schieven, G.H., et Snell, R.L. 1988, *Ap. J.* , **332**, 364.

Mouschovias, T. Ch. 1976, *Ap. J.* , **207**, 141.

Moriarty-Schieven, G.H., Snell, R.L., Strom, S.E., Schloerb, F.P., Strom, K.M., et Grasdalen, G.L. 1987, *Ap. J.* , **319**, 742.

Mundt, R. 1983, *Rev. Mexicana Astron. Astrof.* , **7**, 168.

Mundt, R. 1984, *Ap. J.* , **280**, 749.

Mundt, R. 1985 in *Protostars and Planets II*, Eds. D. Black et M. Matthiews, (Tucson: University of Arizona Press) p.414.

Mundt, R. et Fried, J.W. 1983 *Ap. J.* , **274**, L83..

Mundt, R., Brugel, E.W., et Bührke, T. 1987 *Ap. J.* , **319**, 275.

Mundt, R., Stocke, J., et Stockman, H.S. 1983, *Ap. J.* , **263**, L73.

Mundt, R., Stocke, J., Strom, S.E., Strom, K.M., et Anderson, E.R. 1985, *Ap. J.* , **297**, L41.

Mundt, R., Ray, T., et Bührke, T. 1988, *Ap. J.* , **333**, L69.

Myers, P.C. 1985, *Protostars and Planets II*, Eds. D. Black et M. Matthiews, (Tucson: University of Arizona Press) p.81.

Myers, P.C., et Goodman, A. 1988, *Ap. J.* , **326**, L27..

Myers, P.C., Heyer, M., Snell, R.L., et Goldsmith, P.F. 1988, *Ap. J.* , **324**, 907..

Myers, P.C., Fuller, G.A., Mathieu, R.D., Beichman, C.A., Benson, P.J., Schild, R.E., et Emerson, J.P. 1987, *Ap. J.* , **319**, 340..

Natta, A., Giovanardi, C., Palla, F., et Evans, N.J. 1988, *Ap. J.* sous presse

Norman, C., et Silk, J. 1980, *Ap. J.* , **238**, 158.

Panagia, N., 1988, *Galactic and Extragalactic Star Formation*, Eds. R.E. Pudritz et M. Fich (Dordrecht: Kluwer Academic Publishers), p.25

Panagia, N., et Felli, M. 1975, *Astron. Astrophys.* , **39**, 1.

Pravdo, S.H., Rodriguez, L.F., Curiel, S., Cantó, J., Torrelles, J.M., Becker, R.H., et Sellgren, K. 1985, *Ap. J.* , **293**, L35.

Pudritz, R.E. 1985 *Ap. J.* , **293**, 216..

Pudritz, R.E. 1988, *Galactic and Extragalactic Star Formation*, Eds. R.E. Pudritz et M. Fich (Dordrecht: Kluwer Academic Publishers),p.135

Pudritz, R.E., et Norman, C.A. 1983 *Ap. J.* , **274**, 677..

Pudritz, R.E., et Norman, C.A. 1986 *Ap. J.* , **301**, 571..

Raga, A.C., et Bohm, K. 1986, *Ap. J.* , **308**, 829.

Rainey, R., White, G.J., Richardson, K.J., Griffin, M.J., Gronin, N.J., Monkiro, T.S., et Hilton, J., 1987, *Astron. Astrophys.* , **179**, 237.

Reipurth, B., Bally, J., Graham, J.A., Lane, A.P., et Zealey, W.J. 1986, *Astron. Astrophys.* , **164**, 51.

Reynolds, S.P. 1986, *Ap. J.* , **304**, 713.

Rodriguez, L.F. 1988, *Galactic and Extragalactic Star Formation*, Eds. R.E. Pudritz et M. Fich (Dordrecht: Kluwer Academic Publishers), p.97

Rodriguez, L.F., Moran, J.M., Ho, P.T.P., et Gottlieb, E.W. 1980, *Ap. J.* , **235**, .845

Rucinski, S.M. 1985, *A. J.* , **90**, 2321.

Sakashita, S., et Hanami, H., 1986, *Publ. Astron. Soc. Japan*, **38**, 879.

Sakurai, T. 1985, *Astron. Astrophys.* , **152**, 121.

Sakurai, T. 1987, *Publ. Astron. Soc. Japan*,**39**, 821

Sato, S., Nagata, T., Nakajima, T., Nishida, M., Tanaka, M., et Yamashita, T. 1985, *Ap. J.* , **291**, 708.

Sanders, D.B., et Willner, S.P., 1985 *Ap. J.* , **293**, L39..

Schwartz, R.D. 1975, *Ap. J.* , **195**, 631.

Schwartz, R.D. 1978, *Ap. J.* , **223**, 884.

Schwartz, R.D. 1983, *Ann. Rev. Astron. Astrophys.* , **21**, 209..

Shu, F.H., Adams, F.C., et Lizano, S. 1987, *Ann. Rev. Astron. Astrophys.* , **25**, 23.

Shu, F.H., Lizano, S. Ruden, S.P., et Najita, J. 1988, *Ap. J.* , **328**, L19.

Simon, M., Felli, M., Cassar, L., Fischer, J., et Massi, M. 1983, *Ap. J.* , **266**, 623.

Snell, R.L. 1987, in *Star Forming Regions* Eds. M. Peimbert, J. Jugaku (Dordrecht: Reidel), p. 213.

Snell, R.L. et Bally, J. 1986, *Ap. J.* , **303**, 683.

Snell, R.L. et Schloerb, F.P., 1985, *Ap. J.* , **285**, 490.

Snell, R.L., Loren, R.B., et Plambeck, R.L., 1980, *Ap. J.* , **239**, L17.

Snell, R.L., Scoville, N.Z., Sanders, D.B., et Erickson, N.R. 1984 *Ap. J.* , **284**, 176..

Snell, R.L., Huang, Y.L., Dickman, R.L., Claussen, M.J. 1988, *Ap. J.* , **325**, .853

Strom, S.E., Grasdalen, G.L., et Strom, K.M. 1974, *Ap. J.* , **191**, 111.

Strom, S.E., Strom, K.M., Grasdalen, G.L., Capps, R.W., et Thompson, D. 1985, *A. J.* , **90**, 2575.

Strom, S.E., Strom, K.M., et Edwards, S. 1988, *Galactic and Extragalactic Star Formation*, Eds. R.E. Pudritz et M. Fich (Dordrecht: Kluwer Academic Publishers), p.53

Takano, T., Fukui, Y., Ogawa, H., Takaba, H., Kawabe, R., Fujimoto, Y., Sugitani, K., et Fujimoto, M. 1984, *Ap. J.* , **282**, L69.

Terebey, S., Vogel, S.N., et Myers, P.C. 1988, *Galactic and Extragalactic Star Formation*, Eds. R.E. Pudritz et M. Fich (Dordrecht: Kluwer Academic Publishers), p. 297.

Torbett, M. 1984, *Ap. J.* , **278**, 318.

Uchida, Y., et Shibata, K. 1985. *Pub. Astr. Soc. Japan* **37**: 515

Uchida, Y., Kaifu, N., Shibata, K., Hayashi, S.S., et Hasegava, T. 1987, *Star Forming Regions*, Eds. M. Peimbert et J. Jugaku (Dordrecht:Reidel), p. 287

Ulrich, R.K., et Knapp, G.R. 1979, *Ap. J.* , **230**, L99.

Vogel, S.S. Kuhi, L.V. 1981, *Ap. J.* , **245**, 960.

von Hippel, T., Burnell, S.J., et Williams, P.M., 1988, preprint

Vrba, F.J., Strom, S.E., et Strom, K.M. 1976, *A. J.* , **81**, 958.

Wagenblast, R., Bertout, C., et Bastian, U. 1982, *Astron. Astrophys.* , **120**, 6.

Walker, M.F. 1972, *Ap. J.* , **175**, 89.

Walter F.M., Brown, A., Mathieu, R.D., Myers, P.C., et Vrba, F.J. 1988, *Ap. J.* sous presse

Walter, F.M., et Kuhi, L.V. 1981, *Ap. J.* , **250**, 254.*Ap. J.* , **218**, 377.

Wilking, B.A., Lada, C.J., et Young, E.T. 1989, *Ap. J.* , sous presse

Wootten, A., Loren, R.B., Sandqvist, A., Friberg, P., et Hjalmarson, A. 1984, *Ap. J.* , **279**, 633.

Wynn-Williams, C.G., 1982, *Ann. Rev. Astron. Astrophys.* , **20**, 581.

Zuckerman, B., Kuiper, T.B.H., et Rodriguez-Kuiper, E.N. 1976, *Ap. J.* , **209**, L137.

LEGENDES DES FIGURES

Figure 1: Cartes d'intensité intégrée de l'émission CO à grande vitesse pour un flot radial biconique, illustrant les 4 configurations décrites dans la section 3.2. Les contours en traits pleins et pointillés représentent l'émission décalée vers le bleu et vers le rouge par rapport au nuage. L'angle d'ouverture des cones est de 30° dans les Cas 1, 2, et 3, et de 60° dans le Cas 4. Les angles de visée sont indiqués dans chaque panneau.

Figures 2*a-d*: Diagrammes vitesse-position de l'émission CO $J = 1 \rightarrow 0$ le long de l'axe du flot pour un modèle de flot biconique radial où la vitesse augmente avec la distance à l'origine et avec la latitude suivant une loi $v(r,\theta) \propto r\,(1 - \beta\theta)$. La vitesse au bord des lobes (où $\theta = \theta_{max} = 30°$) est ici égale à 0.2 fois la vitesse le long de l'axe du flot (où $\theta = 0°$). Le flux de masse est supposé indépendant de la position, de sorte que la loi de densité est de la forme $n(r) \propto 1/r^3\,(1 - \beta\theta)^{-1}$. L'angle de visée i vaut 10° en Figure 2*a*, 30° en Figure 2*b*, 50° en Figure 2*c*, et 70° en Figure 2*d*. Le flot parait décéléré lorsque l'angle de visée est inférieur à θ_{max} mais son accélération devient de plus en plus apparente au fur et à mesure que i augmente (voir section 3.3). Les autres paramètres entrant dans les calculs sont: $r_{max} = 5r_{min}$; $n_{H_2}(r_{min}) = 10^4\mathrm{cm}^{-3}$; $T_k = 10$ K;$k(r_{min}) = 8\pi^3/3h\mu^2\ n_{CO}(r_{min})\,r_{min}/v(r_{min}) = 100$.

Figure 3*a*: Corrélation entre la force du flot moléculaire déduite des observations CO et la luminosité bolométrique de l'objet central (Mozurkevich *et al.* 1986), après que les paramètres des différents flots (Lada 1985) aient été recalculés de façon cohérente (voir section 3.4).

Figure 3*b*: Même chose que la Figure 3*a* pour la luminosité mécanique du flot.

Figures 4*a-b*: Cartes préliminaires de l'intensité intégrée de l'émission CO $J = 1 \rightarrow 0$ dans la région NGC 7129, cartographiée avec le téléscope de l'IRAM (Le lobe d'antenne est de 21",et l'espacement entre les différente positions observées est de 30"). La Figure 4*a* montre l'émission statique du nuage ambiant. Une cavité est clairement visible, dont la géométrie suggère qu'elle a été évacuée par un vent stellaire en provenance de LkHα 234. Les triangles indiquent la position de deux masers H_2O, les cercles pleins représentent des objets de Herbig-Haro, et le cercle ouvert la position d'une source infrarouge enfouie dans le nuage. La Figure 4*b* montre l'émission CO $J = 1 \rightarrow 0$ à grande vitesse dans cette région. Dans le flot principal, qui semble associé à LkHα 234, l'émission décalée vers le

bleu (traits tiretés) n'est pas observée à l'intérieur de la cavité. Un second flot bipolaire est associé à la source infrarouge (voir Bertout 1987 pour une description plus complète de cette région).

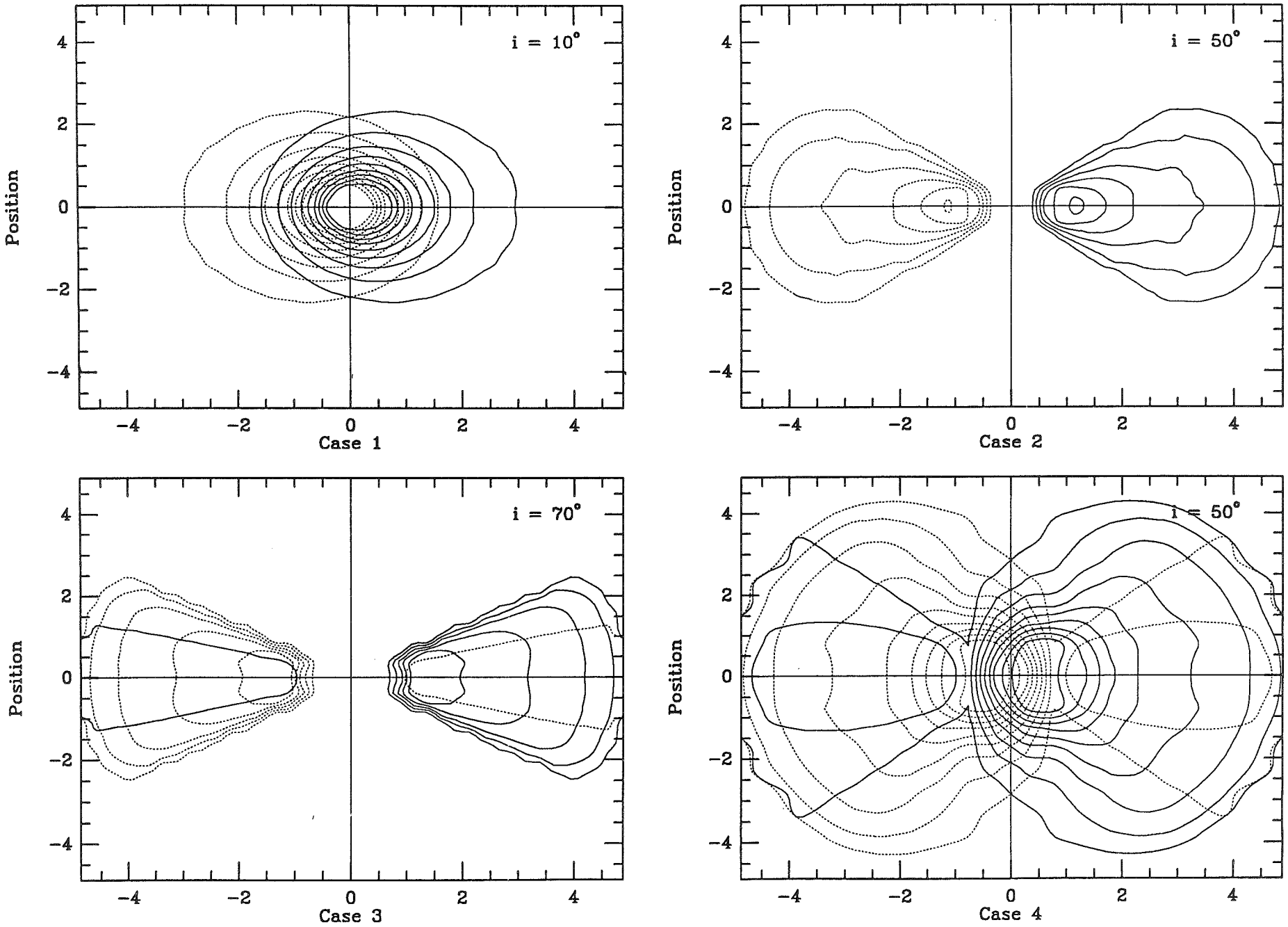

Fig. 1

Fig.2a

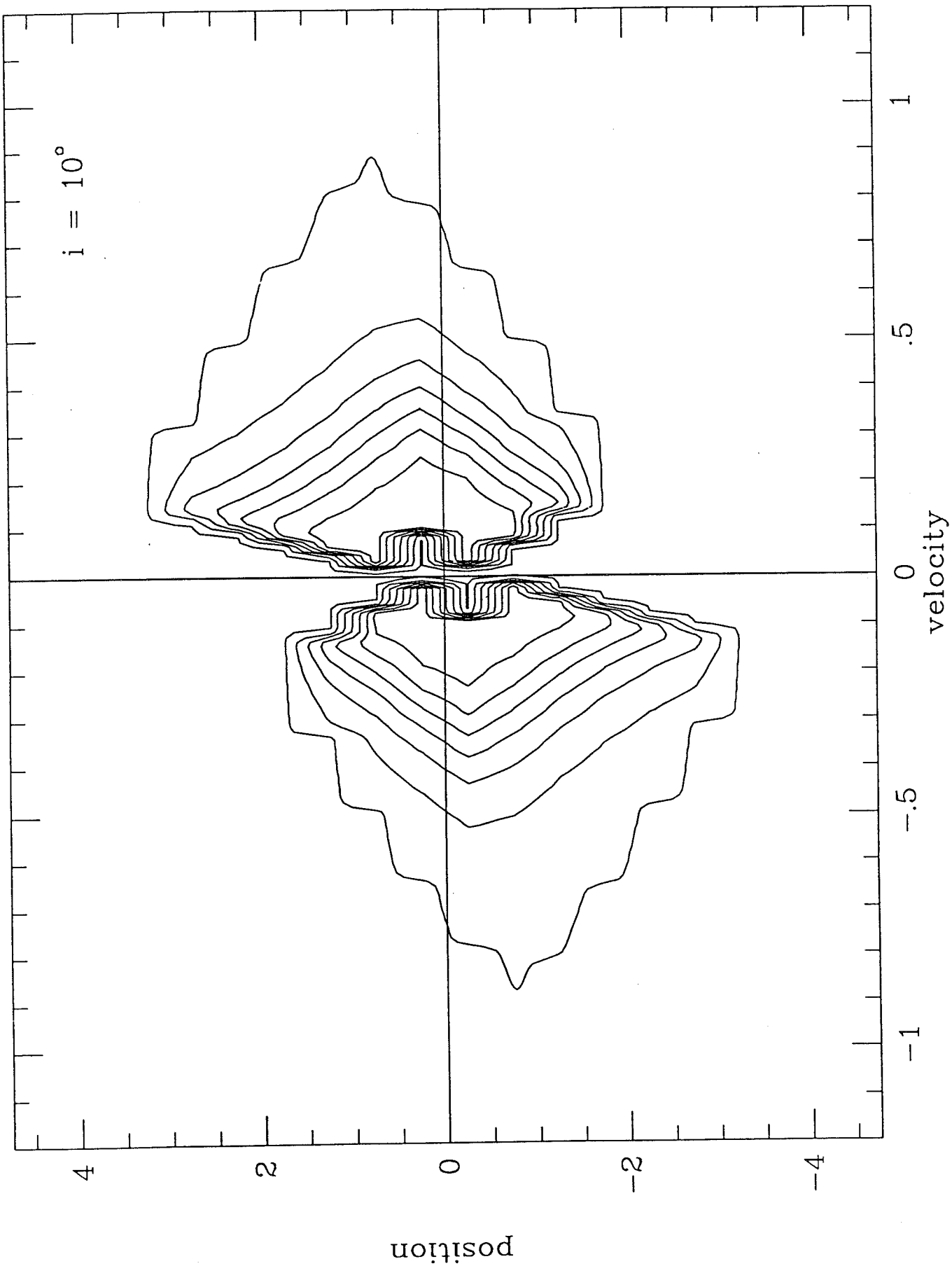

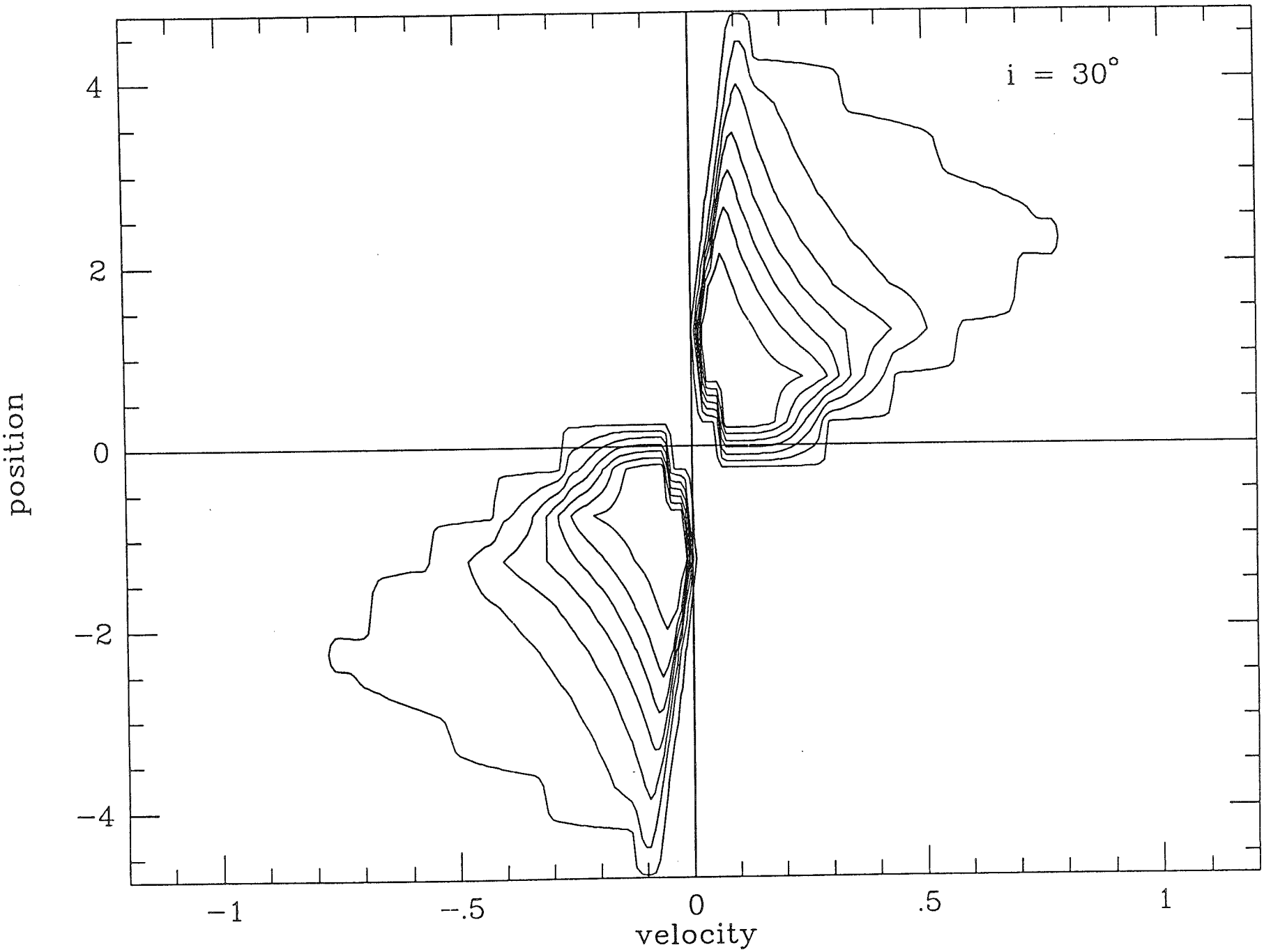

Fig.2b

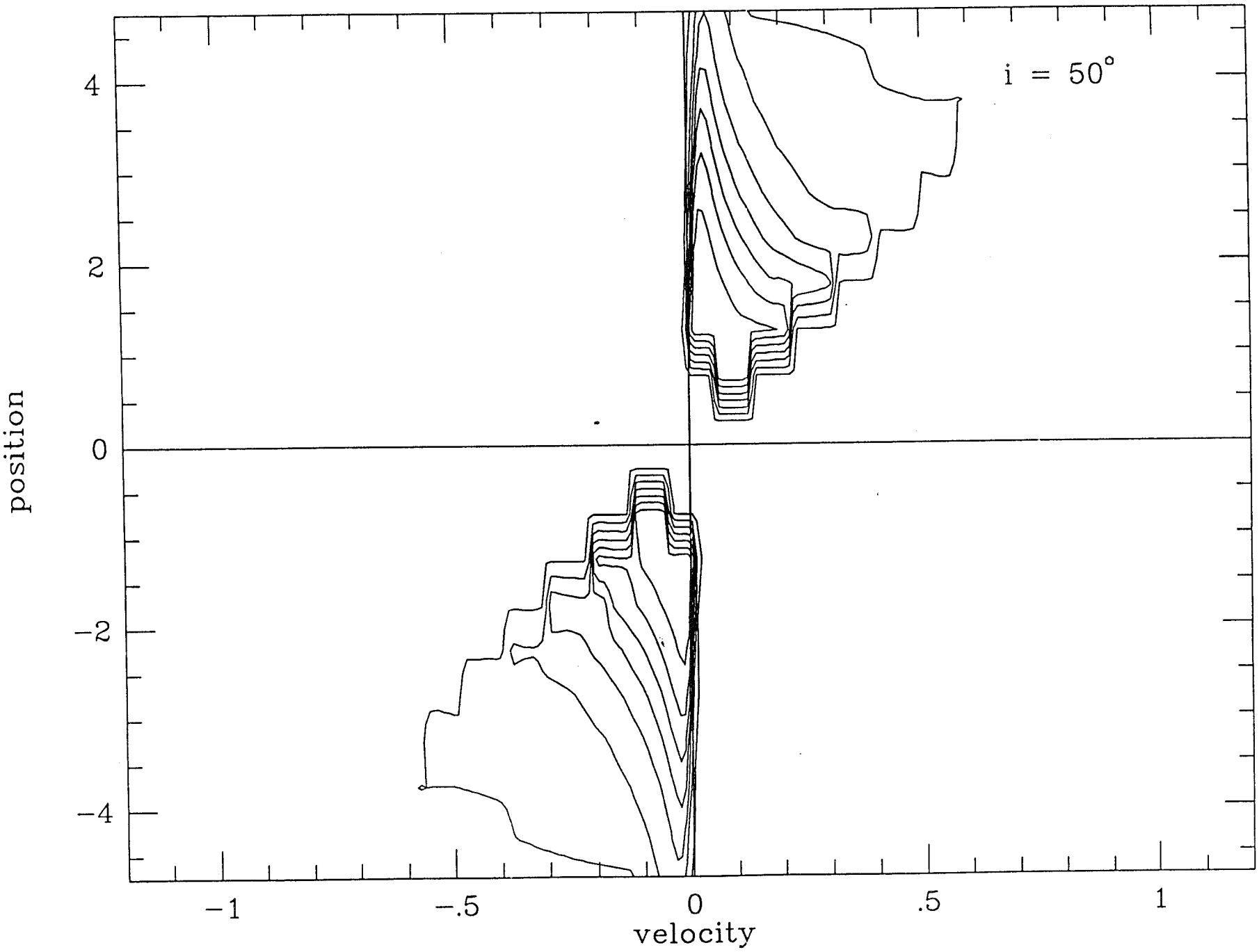

Fig.2c

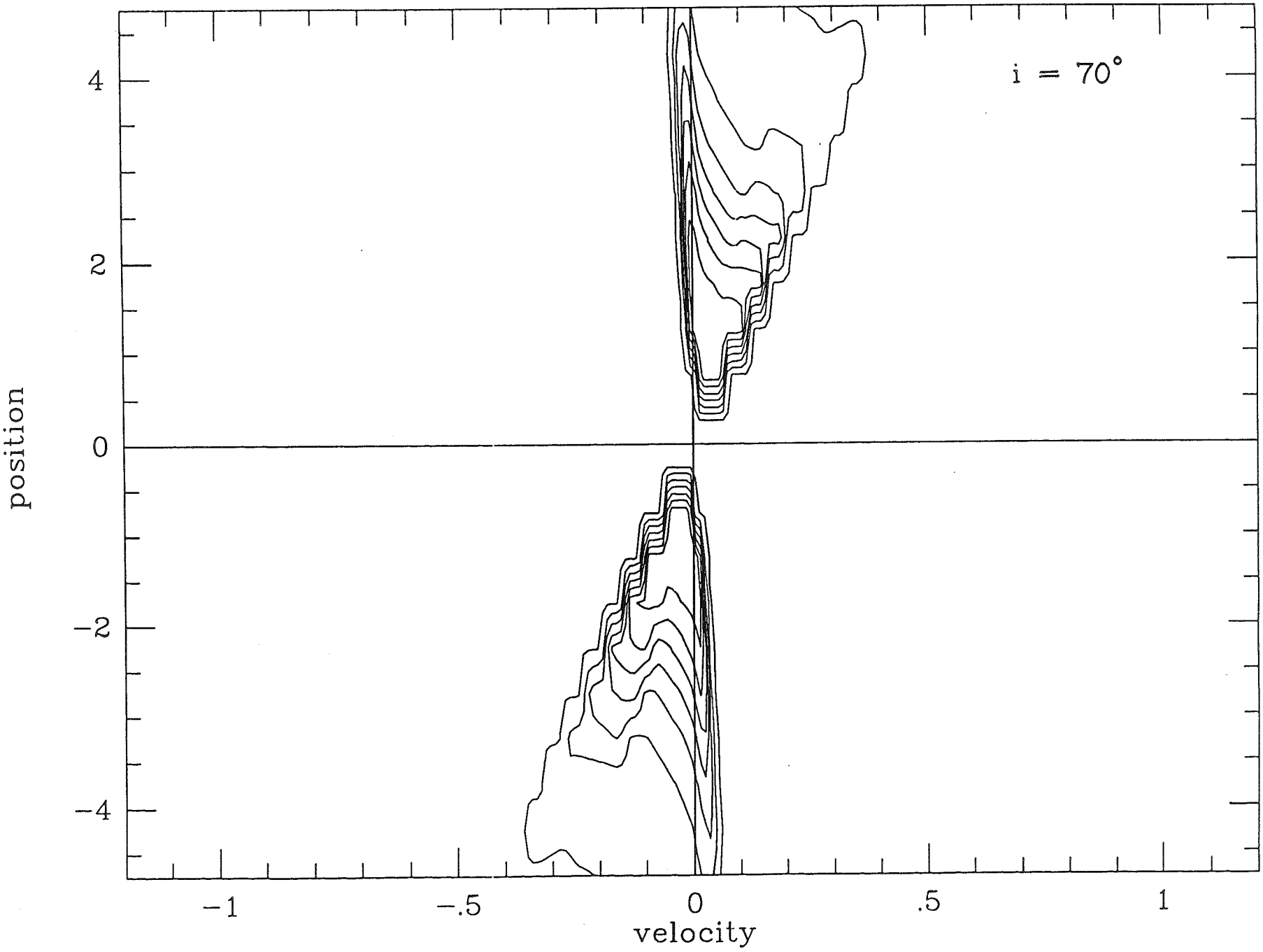

Fig.2d

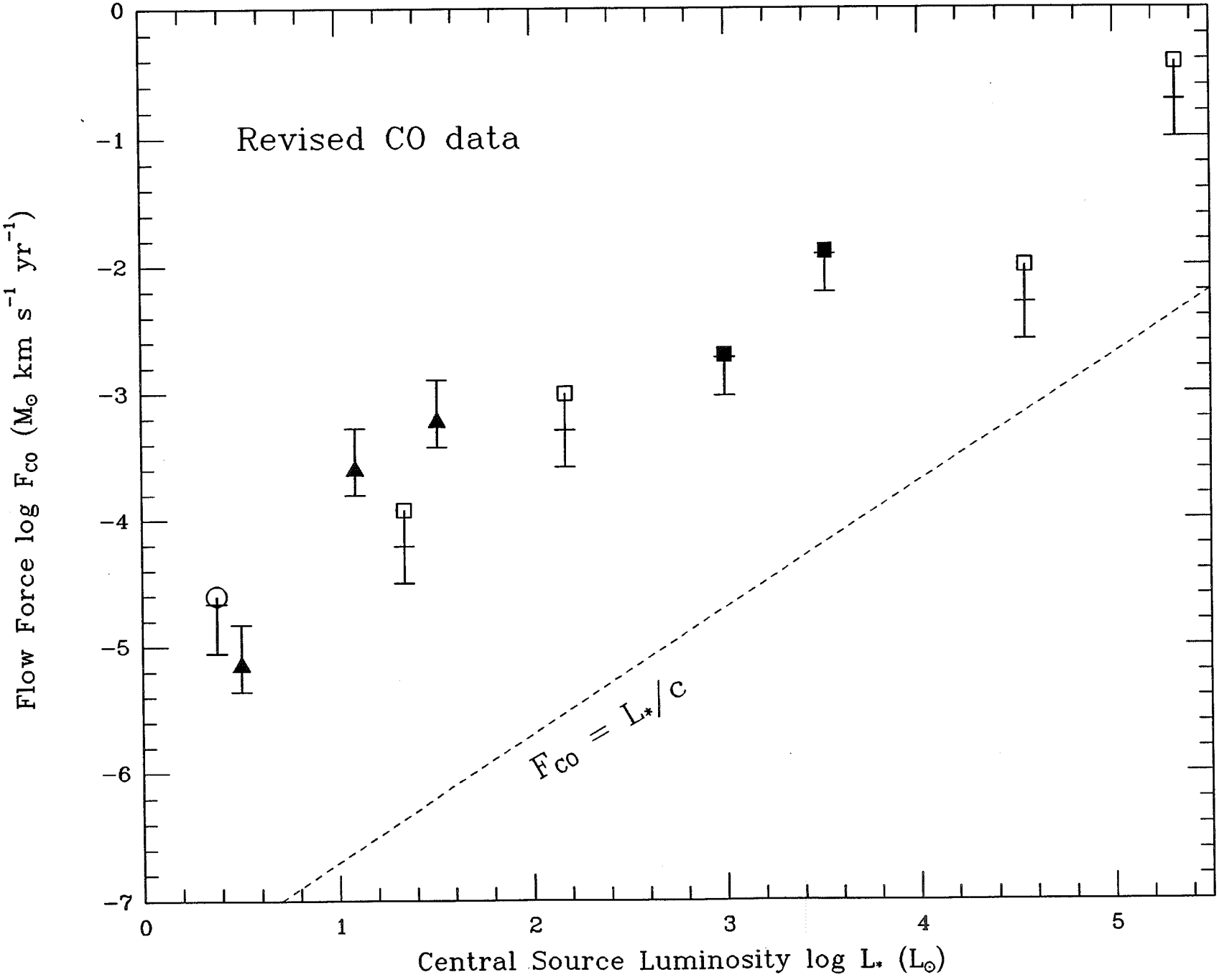
Revised CO data
Flow Force log F_{CO} ($M_\odot$ km s^{-1} yr^{-1})
Central Source Luminosity log L_* ($L_\odot$)
$F_{CO} = L_*/c$
0
-1
-2
-3
-4
-5
-6
-7
0
1
2
3
4
5

Fig. 3a

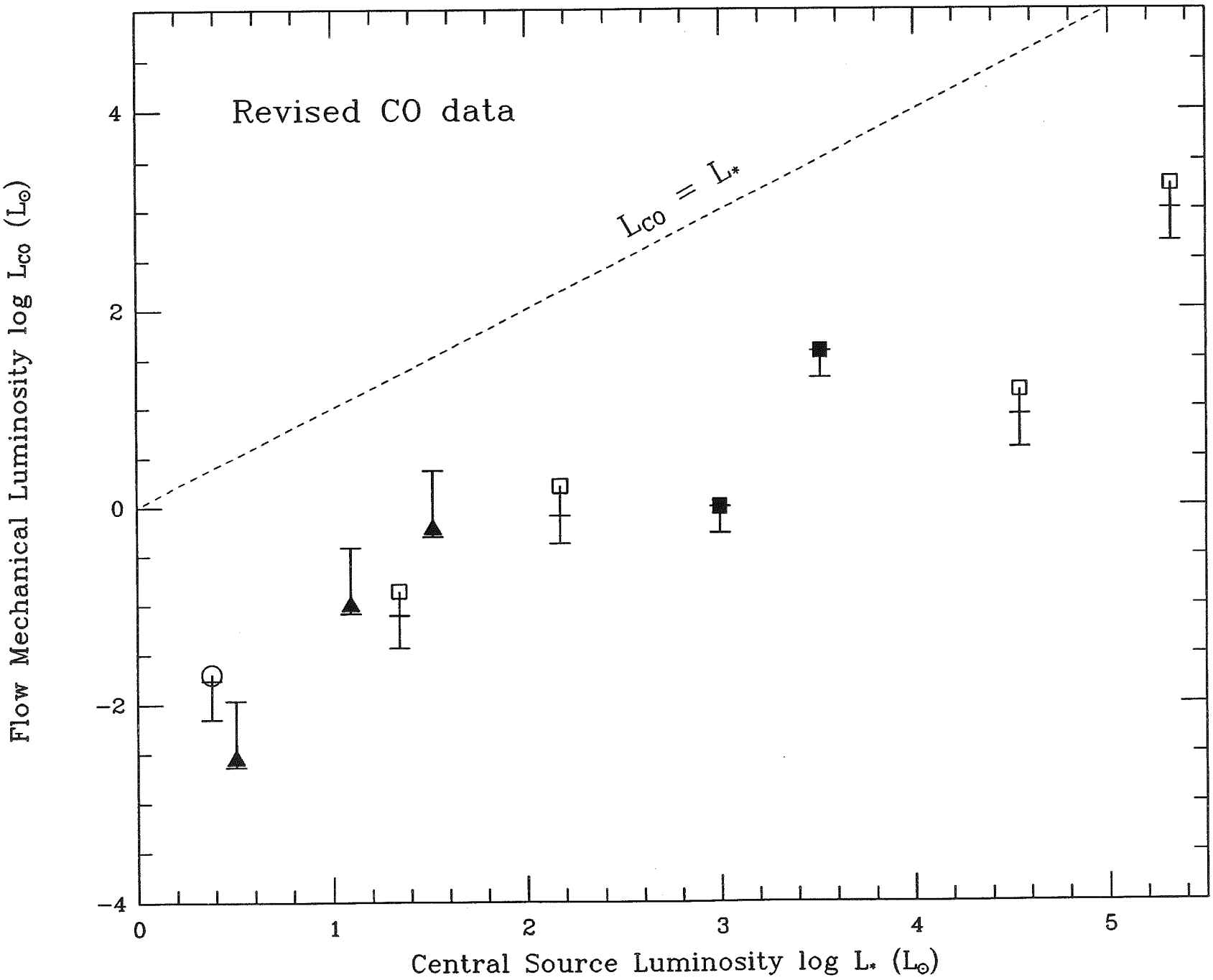
Revised CO data
$L_{CO} = L_*$
Flow Mechanical Luminosity log L_{CO} ($L_\odot$)
Central Source Luminosity log L_* ($L_\odot$)
4
2
0
−2
−4
0
1
2
3
4
5

Fig. 3b

Fig.4a

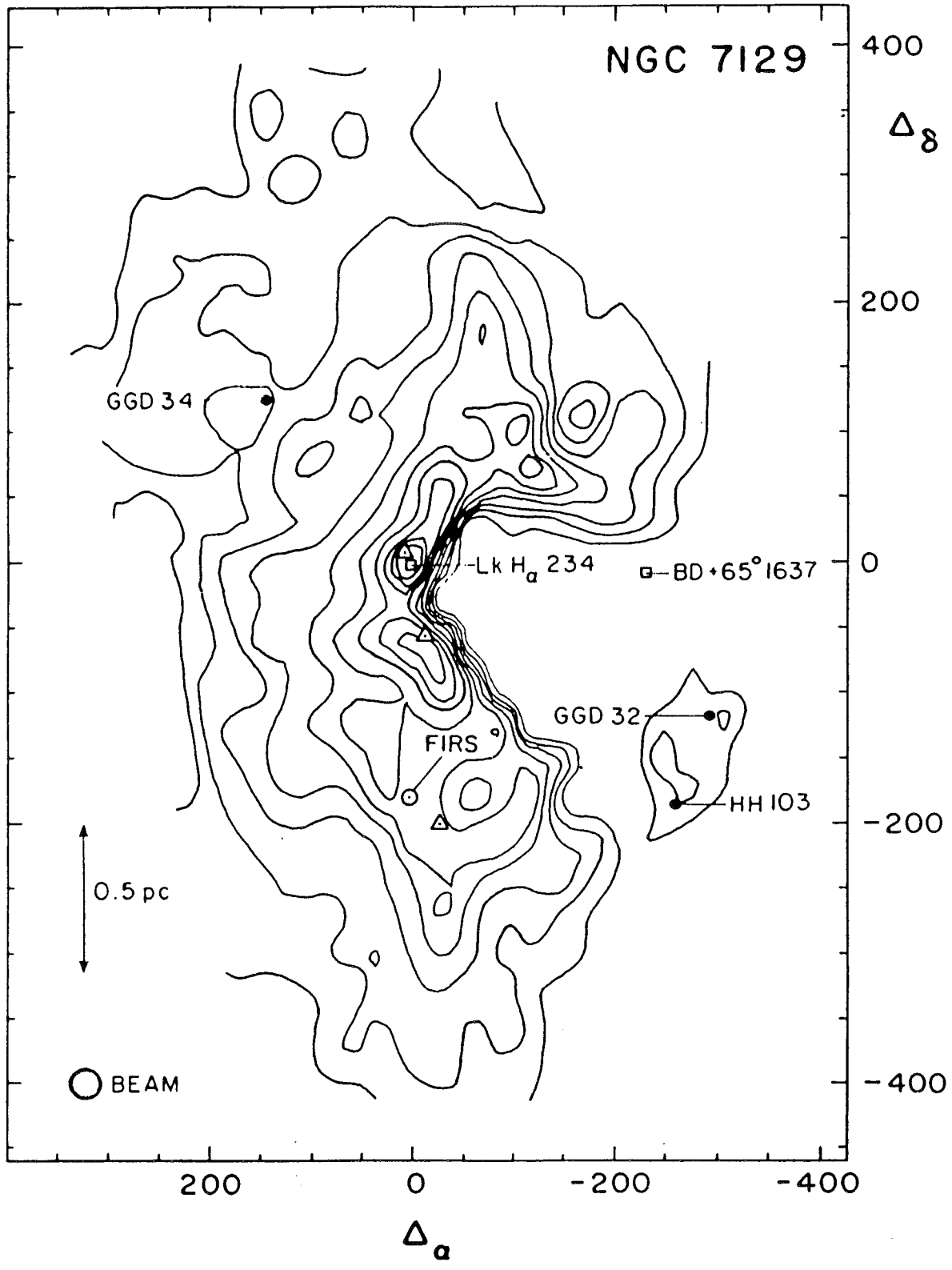
NGC 7129
GGD 34
Lk Hα 234
BD+65°1637
GGD 32
FIRS
HH 103
0.5 pc
BEAM
400
200
0
-200
-400
Δδ
200
0
-200
-400
Δα

Fig.4b

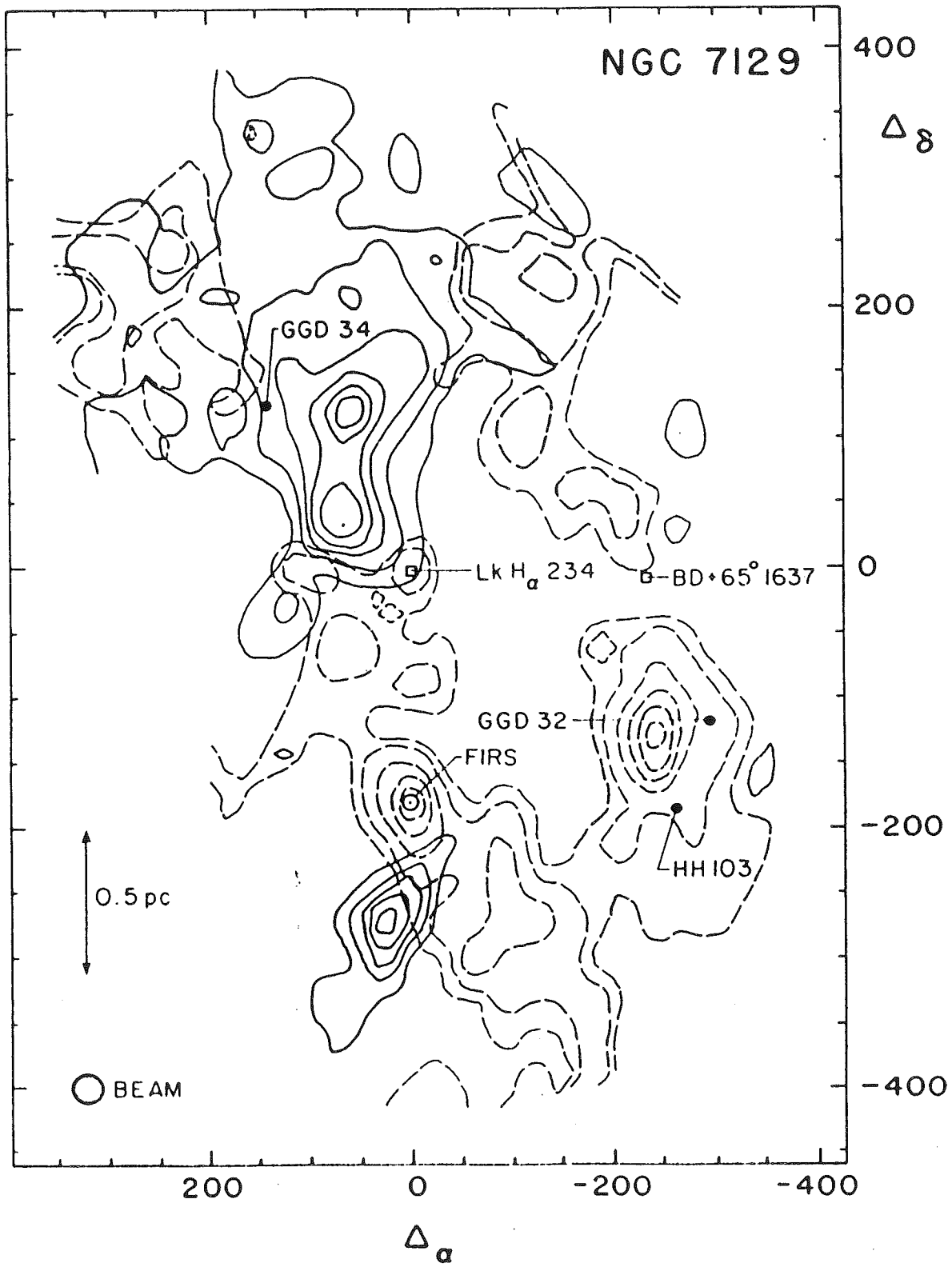
NGC 7129
GGD 34
Lk Hα 234
G-BD+65° 1637
GGD 32
FIRS
HH 103
0.5 pc
BEAM
400
200
0
-200
-400
Δδ
200
0
-200
-400
Δα

ANNEXE 1

THE ASTROPHYSICAL JOURNAL, 307:313–323, 1986 August 1

CO LINE FORMATION IN BIPOLAR FLOWS. I. ACCELERATED OUTFLOWS

SYLVIE CABRIT
Institut d'Astrophysique de Paris; and Ecole Normale Supérieure, Paris
AND
CLAUDE BERTOUT
Institut d'Astrophysique de Paris; and Laboratoire d'Astrophysique Théorique du Collège de France
Received 1985 August 19; accepted 1986 January 14

ABSTRACT

This paper investigates CO line formation in accelerated and constant velocity bipolar outflows. Depending on the view angle and the flow's opening angle, four different classes of characteristic line profiles, velocity versus position maps, and integrated intensity maps can be distinguished. We then use our models to test the most common method for deriving parameters of the flow from observed CO maps and find it to be inaccurate, mainly because in most cases it underestimates both the CO column density and the flow's characteristic time scale. Some suggestions for improved accuracy follow.

Subject headings: interstellar: molecules — line formation — stars: pre-main-sequence — stars: winds

I. INTRODUCTION

The discovery of high-velocity molecular flows in the vicinity of young stellar objects (Snell, Loren, and Plambeck 1980; Edwards and Snell 1982; Bally and Lada 1983; and others) is widely regarded as a major advance in the ongoing research on pre–main-sequence evolution, mainly because bipolar molecular outflows can apparently be driven by embedded pre–main-sequence OB stars as well as by low-luminosity, T Tauri–like objects, which in turn suggests that bipolar mass ejection is a universal phase of pre–main-sequence evolution. And a recent paper by Mundt *et al.* (1985), which reveals that L1551 IRS 5's optical spectrum resembles that of a FU Orionis object, brings together three of the most exciting aspects of stellar formation, namely bipolar CO flows, optical jets, and the FU Orionis phenomenon.

Observations of high-velocity molecular flows (HVMFs) lead one to ask both how they are powered and what the collimation mechanism responsible for the bipolar nature of many HVMFs may be. Snell, Loren, and Plambeck (1980) proposed a qualitative model in which the CO gas is accelerated outward by a collimated stellar wind while remaining confined to a shell surrounding the wind bubble. Pudritz and Norman (1983), Pudritz (1985), and Uchida and Shibata (1984, 1985) suggest instead that the molecular gas is a low-temperature centrifugally driven outflow emerging from an accretion disk; in this picture, outflow occurs along hourglass-shaped surfaces. A third model, in which the molecular material is set in motion by viscous coupling to a gaseous jet, is presently under investigation (R. N. Henriksen, private communication). In the latter, CO emission occurs in most of both lobes' volume. Several wind collimation mechanisms, which differ by the scale on which collimation occurs, have also been discussed. For example, Sakurai (1985) proposes a process intrinsic to the magnetized star, while Königl (1982) advocates collimation on a much larger, interstellar scale.

While the theoretical problems arising from observations of molecular outflows have been so widely addressed, leading to a number of possible models, little has been done so far to exploit the wealth of information contained in the observed CO line profiles, although such analysis could potentially allow one to choose between these various models. This paper, the first in a series exploring velocity fields and CO excitation conditions in bipolar outflows, represents a step in that direction. We developed a computer code which allows for the computation of NLTE CO line formation in bipolar geometry and in the presence of velocity fields. In this paper, we parameterize velocity fields and hydrogen density distributions, and we investigate CO emission originating from two biconical lobes in the presence of accelerating radial outflows. Because observed CO line profiles do not show the double-peak structure which would be expected if the emitting cones were only partially filled up (see also Levreault 1985), we assume in the following that the CO gas fills up the lobes, in contrast to some of the models mentioned above. Our main goal at this stage is not to set constraints on theoretical models, but rather to analyze and quantify uncertainties arising while deriving CO flow parameters from observed maps. Our code can, however, handle arbitrary axially symmetric velocity fields and H_2 densities; and forthcoming papers will be dedicated to the study of proposed models for the CO outflows.

Our computational method is explained in § II, results are presented in § III for two velocity fields, and § IV assesses the validity of the method used by observers to derive, in particular, the momentum rate in the CO flow and the stellar mass loss rate. This study has led us to doubt that accurate stellar mass loss rates can be derived at this point from observations of CO outflow associated with the star; but it did help identify points of uncertainty, so that we can suggest ways to improve the situation.

II. METHOD

The geometry of the model is shown in Figure 1. The molecular gas is confined to a bicone of opening angle θ_{max}, inner radius r_{min}, and outer radius $r_{max} = \sigma r_{min}$. For this exploratory study, we restricted ourselves to power-law velocity fields

$$v(r) = v_{min}(r_{min}/r)^{\alpha} u \ , \qquad (1)$$

where $u = r/r$, and we consider only accelerated and constant velocity outflows with $\alpha \leq 0$ and $v_{min} > 0$. Mass conservation

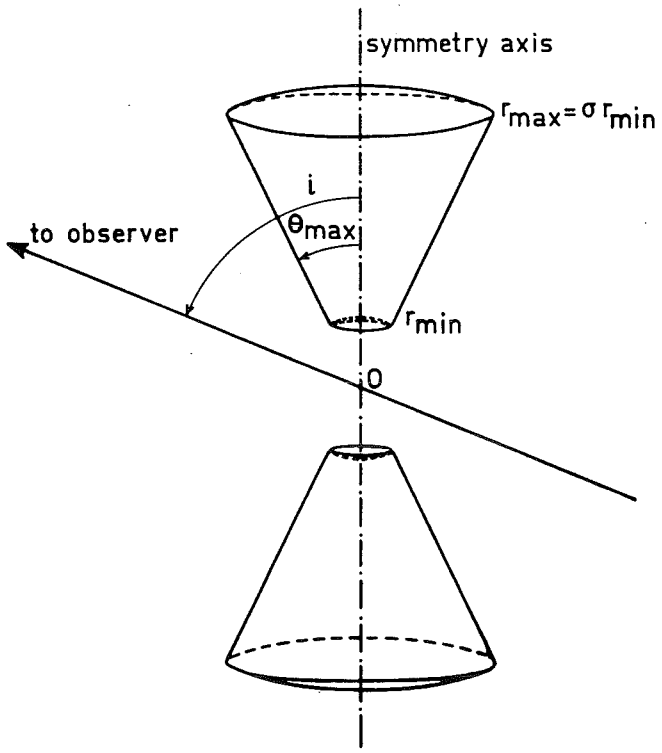

FIG. 1.—Geometry of the model

is assumed within the flow, so that the density $n(r)$ is given by

$$n(r) = n(r_{min})(r_{min}/r)^{\delta}\,, \tag{2}$$

with $\delta = 2 - \alpha$. We further assume that a star of radius r_c located at the symmetry center emits isotropic blackbody radiation at effective temperature T_c.

Bastian *et al.* (1980) and Hamann (1981) have demonstrated that an approach to the line formation problem using the Sobolev (1957) approximation for computing the level populations, but integrating the profiles exactly, gives excellent results for fast flows. We use this approach in the following.

a) CO *Excitation*

In the conditions typical of interstellar clouds, where CO molecules are heated both by the microwave background emission at $T_b = 2.7$ K and by collisions with H_2 molecules at a kinetic temperature T_k of typically 10 K, only the rotational sublevels of the ground electronic and vibrational state of CO are significantly populated. Each rotational level has energy $E_j = hB_0 j(j+1)$, where $B_0 = 57.6$ GHz and where $g_j = 2j + 1$ is the level degeneracy. Neglecting the effects of dust on CO excitation, the two main processes which contribute to populating these levels are radiative transitions and collisions with H_2 molecules.

The rate of change in the statistical population n_j of level j resulting from spontaneous and stimulated radiative transitions is

$$(dn_j/dt)_{rad} = n_{j+1}A_{j+1,j} + (n_{j+1}B_{j+1,j} - n_j B_{j,j+1})\bar{J}_j - n_j A_{j,j-1} - (n_j B_{j,j-1} - n_{j-1}B_{j-1,j})\bar{J}_{j-1}\,, \tag{3}$$

where $\bar{J}_j(r)$ denotes the mean intensity integrated over the local profile for the transition j to $j+1$ at frequency $\nu_j = 2hB_0(j+1)$:

$$\bar{J}_j \equiv \left(\frac{1}{4\pi}\right)\int_0^{\infty} d\nu \int_{4\pi} d\Omega(\boldsymbol{n})\Phi\left[\nu - \nu_j - \nu_j\frac{(\boldsymbol{v}\cdot\boldsymbol{n})}{c}\right] I(\nu, \boldsymbol{n})\,. \tag{4}$$

Since we consider expansion velocities much greater than the CO local velocity dispersion, the radiation field remains essentially local; either each photon is reabsorbed in the immediate vicinity of its emission point, or it escapes from the flow, having been Doppler-shifted in the other molecules' rest frame. This simplifying fact was first used by Sobolev (1957). Extending the same formalism to our case, we find

$$\bar{J}_j = (1 - \beta_j)S_j + \beta_j^c B(\nu_j, T_c) + (\beta_j - \beta_j^c)B(\nu_j, T_b)\,, \tag{5}$$

where S_j, the source function for transition j, is

$$S_j = 2h\nu_j^3/c^2[(2j+3)n_j/(2j+1)n_{j+1} - 1]^{-1}\,. \tag{6}$$

Here, β_j is the total local escape probability, and β_j^c the escape probability reduced to the solid angle Ω_c within which the emitting core is seen from r. Expressions for β_j and β_j^c in axial geometry are found in, e.g., Bertout (1979).

With equations (1) and (2), the line center optical depth for line j in direction $\boldsymbol{n}$ can be written

$$\tau_j = k(r)(j+1)(x_j - x_{j+1})[1 - (1+\alpha)(\boldsymbol{u}\cdot\boldsymbol{n})^2]^{-1}\,, \tag{7}$$

where $k(r)$ is given by

$$k(r) = (8\pi^3\mu^2/3h)n_{CO}(r)r/v(r) = k(r_{min})(r_{min}/r)^{1-2\alpha} \tag{8}$$

and where, following Goldreich and Kwan (1974), we define $x_j(r)$, the normalized level population, as

$$x_j(r) = (1/g_j)n_j(r)/n_{CO}(r)\,. \tag{9}$$

The radiative rate of change for x_j is thus

$$\begin{aligned}(dx_j/dt)_{rad} &= A_{j+1,j}(2j+3/2j+1)[\![\beta_j x_{j+1} + (x_{j+1} - x_j)\\ &\times \{\beta_j^c/[\exp(h\nu_j/kT_c) - 1] + (\beta_j - \beta_j^c)/[\exp(h\nu_j/kT_b) - 1]\}]\!]\\ &- A_{j,j-1}[\![\beta_{j-1}x_j + (x_j - x_{j-1})\{\beta_{j-1}^c/[\exp(h\nu_{j-1}/kT_c) - 1]\\ &+ (\beta_{j-1} - \beta_{j-1}^c)/[\exp(h\nu_{j-1}/kT_b) - 1]\}]\!]\,.\end{aligned} \tag{10}$$

With $C(i\rightarrow j)(r)$ denoting the probability of collisional transition between levels i and j averaged over the relative velocities at point r, we have

$$(2i+1)C(i\rightarrow j) = (2j+1)C(j\rightarrow i)\exp[-(E_j - E_i)/kT_k]\,, \tag{11}$$

and the collisional rate of change for x_j is

$$\left(\frac{dx_j}{dt}\right)_{coll} = \sum_{i\neq j}\left\{x_i \exp\left[-\frac{(E_j - E_i)}{kT_k}\right] - x_j\right\}C(j\rightarrow i)\,. \tag{12}$$

We shall assume that statistical equilibrium has been established in the flow, i.e., that

$$(dx_j/dt)_{rad} + (dx_j/dt)_{coll} = 0\,. \tag{13}$$

For a molecule with N levels, we thus solve $N - 1$ coupled equations (given by eq. [13]) together with a conservation equation for the total number of molecules, using an iterative method; $\beta_j(r)$ and $\beta_j^c(r)$ are computed from starting values of the $x_j(r)$ (for example, the LTE values at $T = T_k$) and the system is then solved, which provides new estimates for the $x_j(r)$. This simple procedure converges because $\bar{J}_j$ is determined locally. Typically, 3–12 iterations are needed to reach a con-

vergence rate of 10^{-4}. The actual computations considered 6–10 rotational levels.

b) *Profiles and Maps*

Computation of the emergent intensity in the observer's direction is performed exactly, using the algorithm proposed by Bertout (1984) after suitable generalization to axial geometry according to the formalism developed in Bertout (1979). Doppler widening at the local kinetic temperature was assumed for computing the absorption profile's width in the comoving frame. Contour maps similar to those presented by observers of high-velocity molecular outflows are drawn once the line profiles have been obtained for all lines of sight. The map of velocity versus position presents line intensity contours as a function of both radial velocity and position along the flow axis projected onto the plane of the sky. The contribution of the static ambient cloud, which appears in the observed maps as vertical contours centered on zero radial velocity, is of course not present in our maps. In the integrated intensity maps, the antenna temperature is integrated separately over the positive and negative radial velocities of each profile, giving levels of constant blue and red integrated intensity. We computed a series of models corresponding to different flow geometries and to various values of the free parameters $k(r_{\rm min})$, the convenient optical depth parameter defined in eq. (8), $n_{\rm H_2}$ at $r_{\rm min}$, T_k, and α, the velocity law exponent.

III. RESULTS

a) CO *Excitation*

We tested our computer code by comparing numerical results to those of Goldreich and Kwan (1974); Goldsmith (1972); and Goldsmith, Young, and Langer (1983) and found in each case excellent agreement. In the actual computations, we used collision rates given by Green and Thaddeus (1976). Although CO excitation conditions are sensitive to the assumed values of the collision rates, Goldsmith, Young, and Langer (1983) have shown, and our tests confirmed, that disagreement between published collision rates was quite small and that resulting differences in CO excitation should not exceed 20%.

Maps of the ambient cloud emission often suggest that a heating source is present near the center of the molecular flows. We thus studied the influence of a central radiating source on excitation in the accelerated gas and, as expected, found that the source function at a point r increases with $\Omega_c I_c$, where Ω_c is the solid angle of the emitting core as seen from r. In the case of intermediate optical thickness [$k(r_{\rm min}) = 200$ and $n_{\rm H_2}(r_{\rm min}) = 10^4$], this term will dominate the source function whenever $(T_c/2.7 \times 10^5\ {\rm K})(r_c/10^4\ R_\odot)^2 \approx (r_{\rm min}/10^{-2}\ {\rm pc})^2$. Since the observed values of $r_{\rm min}$ lie in the range 10^{-2} to 10^{-1} pc (Goldsmith, Snell, and Hemeon-Heyer 1984), we do not expect radiation from a central source to contribute significantly to HVMF excitation, even in the case of a high-luminosity embedded source.

b) *Profiles and Maps*

While line intensities depend mainly on the medium's physical conditions, both profiles and contour maps are affected more by the flow geometry and the view angle i. From Figure 1 we see that if $i \leq \pi/2 - \theta_{\rm max}$, emission from the front cone is entirely blueshifted, while the far cone is entirely redshifted; and if $i \leq \theta_{\rm max}$, both cones are on the line of sight. It therefore becomes convenient to distinguish four cases, shown in Table 1. The probability of observing the flow in a given configuration is shown in Figure 2.

TABLE 1

THE DIFFERENT GEOMETRICAL CASES IN A BICONICAL FLOW

First Cone Blueshifted, Second Cone Redshifted	Each Cone Partly Blue-, Partly Redshifted
Two Cones on the Line of Sight	
Case 1: $i < \theta_{\rm max}$, $i \leq \pi/2 - \theta_{\rm max}$	Case 4: $i < \theta_{\rm max}$, $i > \pi/2 - \theta_{\rm max}$
One Cone on the Line of Sight	
Case 2: $i \geq \theta_{\rm max}$, $i \leq \pi/2 - \theta_{\rm max}$	Case 3: $i \geq \theta_{\rm max}$, $i > \pi/2 - \theta_{\rm max}$

Figures 3–6 correspond to the same flow geometry (with $\theta_{\rm max} = 30°$) and illustrate cases 1, 2, and 3. In each figure, four panels are displayed. The first one shows the line temperature for the sight line which crosses the flow closest to the symmetry center, plotted as a function of the normalized radial velocity $x \equiv v_{\rm rad}/v(r_{\rm max})$, for two velocity fields ($\alpha = -1$ and $\alpha = 0$). The line temperature is defined by

$$T_l(v) \equiv c^2/2kv^2[I(v) - B(v, T_b)] .$$

The second panel then displays maps of velocity versus position for both velocity fields, and the last two panels show the corresponding integrated intensity maps. In all maps, positions in the plane of the sky are given by offsets from the center, in units of $r_{\rm min}/4$. Other parameters entering the computations have the following values, meant to represent a typical molecular outflow: $n_{\rm H_2}(r_{\rm min}) = 10^4\ {\rm cm}^{-3}$, $T_k = 10$ K, $A(^{12}{\rm CO}) = 40A(^{13}{\rm CO}) = 8 \times 10^{-5}$ (where the ^{13}CO abundance is from Dickman 1978), $r_{\rm min} = 0.06$ pc, $\sigma = 10$, and $v(r_{\rm max}) = 10\ {\rm km\ s}^{-1}$.

Figure 3 (with $i = 5°$) corresponds to case 1 above. The profiles have two components, representing the cone emission on each side of zero radial velocity. The influence of the velocity field is better illustrated in the velocity versus position map. Because of the lack of small projected flow velocities when $\alpha = 0$, profiles have narrow components ($\delta x \approx 0.2$) separated by a large gap ($x_{\rm min} \approx 0.8$) in that case, while for $\alpha = -1$ we find broad line wings ($\delta x \approx 0.5$) and a small gap ($x_{\rm min} \approx 0.1$). Since the two cones are seen nearly face-on, the blue and red contours of integrated intensity are circular and overlapping.

One striking feature found in all cases is that emission is always more intense in the red than in the blue, although our model is symmetrical. But this can be understood as the result of absorption in the flow; blue-displaced photons emitted from the innermost, densest layers in the cone closest to the observer can be absorbed by overlying material, while red-displaced photons emitted from the densest layers of the cone farthest from the observer can escape freely in the observer's direction because of their Doppler shift. This property has been observed in most of the high-velocity flows mapped so far and has been used as an argument in favor of outflow by Bally and Lada (1983); our quantitative computations confirm this argument.

Figure 5 ($i = 50°$) illustrates case 2, and Figure 4 corresponds to the limiting case between cases 1 and 2. The line

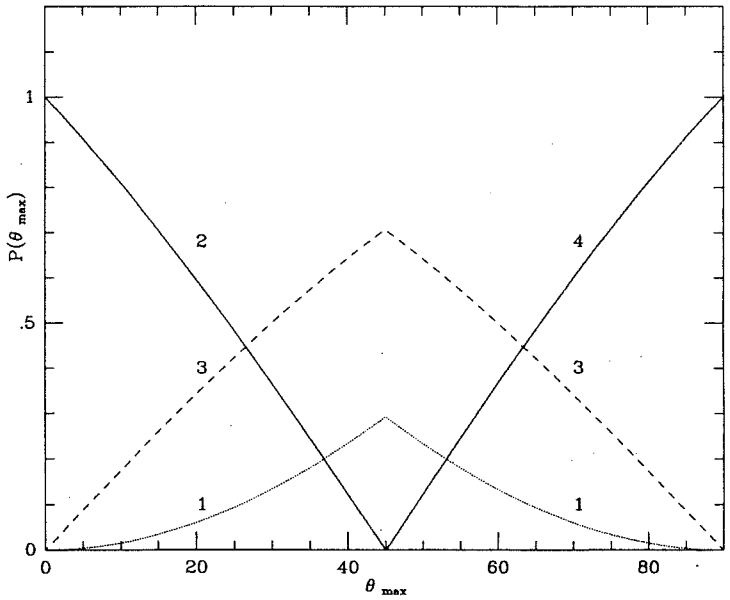

FIG. 2.—Probability $P(\theta_{max})$ of observing a biconical flow in each of the four configurations distinguished in the text as a function of θ_{max}

profiles are now completely asymmetrical. The range of radial velocities seen on the line of sight when $\alpha = 0$ increases with i, and the velocity versus position map for that case shows broad profiles over a velocity range ($\delta x \approx 0.6$) nearly independent of the position and comparable in extent to the central velocity gap ($x_{min} = 0.4$). For $\alpha = -1$, the line profile decreases more steeply and extends only over the lower part of the velocity range ($\delta x \approx 0.3$, $x_{min} = 0$), corresponding to the innermost, densest parts of the flow, where CO emission is sizable (recall that H_2 density varies as r^{-3} when $\alpha = -1$, and as r^{-2} when $\alpha = 0$). The blue and red emissions are formed in distinct regions of the map, thus revealing the bipolar structure of the flow. A central region, extending up to a projected distance $r_g = r_{min} \sin(i - \theta_{max})$ from the center of the flow, shows no emission. Such a gap has been observed in several high-velocity flows, for example in B335 (Goldsmith, Snell and Hemeon-Heyer 1984).

Case 3 is illustrated by Figure 6 (where $i = 80°$). Profiles have a single component extending from negative to positive radial velocities, while the intensity remains fairly constant over this range. The velocity versus position map indicates a maximum velocity extent of $x_{max} = 0.3$ for $\alpha = -1$ and $x_{max} = 0.6$ for $\alpha = 0$ (again with very flat profiles). The integrated intensity map again shows two distinct lobes, but each one now has a blue and a red component.

Although case 3 is the most probable one whenever $\theta_{max} > 30°$ (see Fig. 2), no example of it has been observed as yet. Several reasons could explain the lack of detection. First, emission at low radial velocities is indistinguishable from the ambient cloud contribution, so that case 3 flows might be classified as case 2 after subtraction of the central low-velocity emission. Second, most bipolar flows might have opening angles smaller than 30°. Finally, some observed flows with mixed blue and red emission, which are thought to be two separate outflows, could in fact represent a single case 3 bipolar flow; the CO emission discovered by Edwards and Snell (1984) near RNO 43 is a case in point.

Case 4 is a superposition of cases 1 and 3. We thus show in Figure 7 only an example of the rather complex integrated intensity map corresponding to that case, with $i = 50°$ and $\theta_{max} = 60°$. No flow showing this geometrical aspect has been detected so far, indicating either that the flows are well collimated ($\theta_{max} \leq 45°$) or that the attainable velocity resolution is not high enough.

IV. DISCUSSION

Bally and Lada (1983) emphasized that CO flow momentum rates derived from observations are often much higher than the maximum force supplied by the star to a radiatively driven wind, even for high-luminosity sources. While this result may indicate that other mechanisms, such as rotation, drive the CO flows, its reliability is critically dependent on the validity of the various assumptions (discussed by Lada 1985) underlying the derivation of the flow's momentum rate from observed maps. The same objection applies to computations of stellar mass loss rates based on the assumption that the high-velocity CO gas is accelerated by a stellar wind. In this case, the rate of momentum at the base of the flow $\dot{P}(r_{min})$ is related to the rate of momentum carried in the wind by $\dot{P}(r_{min}) = \epsilon \dot{M} V_{wind}$, where ϵ is the efficiency of the interaction, $\dot{M}$ the stellar mass loss rate, and V_{wind} the wind's end velocity. This assumption has been used by Edwards and Snell (1982) and Calvet, Cantó, and Rodríguez (1983) to derive mass loss rates for low-luminosity, T Tauri–like stars, whose wind-driving mechanisms are still an issue. One would therefore like to assess the usefulness of this method for deriving accurate mass loss rates.

The model presented in this paper is obviously still too crude to offer anything approaching a true and accurate representation of the observed flows. It cannot take the influence of clumps within the flow into account, although the low beam-filling factor noted by Plambeck, Snell, and Loren (1983) may suggest their presence in several molecular outflows. Neither does it consider the possible effect of shocks within the flow on the CO excitation. And as far as the biconical geometry of the flow and the power-law velocity fields are concerned, they are likely to be rather poor representations of the actual flow geometry and velocities. Our model, therefore, can only be a first approximation of the physical situation.

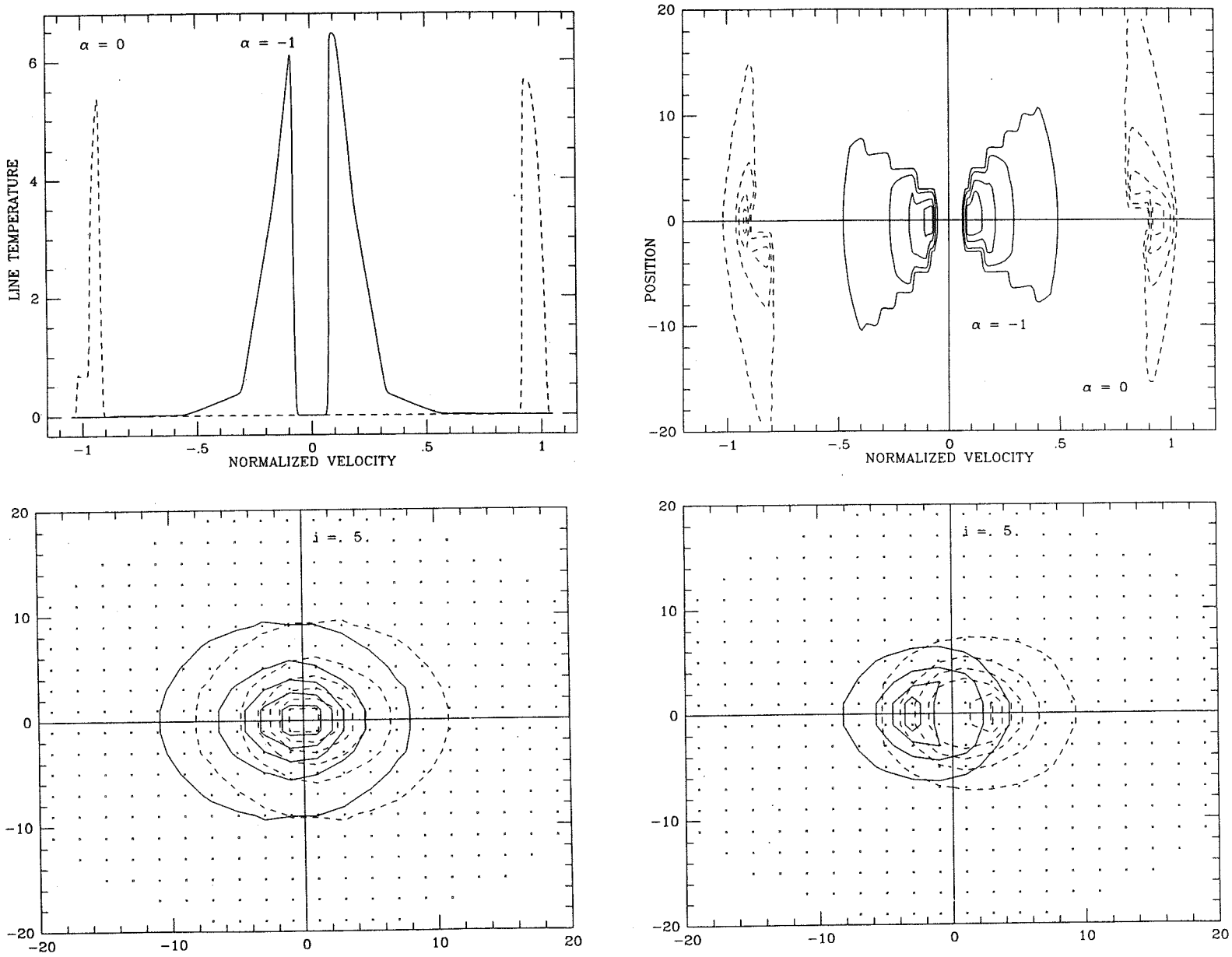

FIG. 3.—Results for a cone opening angle of 30° and an inclination angle $i = 5°$, corresponding to case 1 (see text for details and for the values of other parameters). (*upper left*) Profiles of the ^{12}CO $J = 1 \rightarrow 0$ line for the sight line crossing the molecular flow closest to the stellar core. The solid line is for case $\alpha = -1$, the dashed line for $\alpha = 0$. (*upper right*) Velocity vs. position map, showing contours of constant line temperature for $\alpha = -1$ (*solid lines*) and $\alpha = 0$ (*dashed lines*). Lowest contour level, 0.1 K; second one, 1 K; step between other contours, 2 K. Offsets in units of $r_{min}/4$. (*lower left*) Map of blue (*solid lines*) and red (*dashed lines*) integrated intensity for $\alpha = -1$. Emergent intensities computed at positions indicated by crosses. Contour levels (in K km s^{-1}) and distance scale as in upper right panel. (*lower right*) Same as lower left for $\alpha = 0$. Lowest contour level, 1 K km s^{-1}; second one, 5 K km s^{-1}; step between other contours, 5 K km s^{-1}.

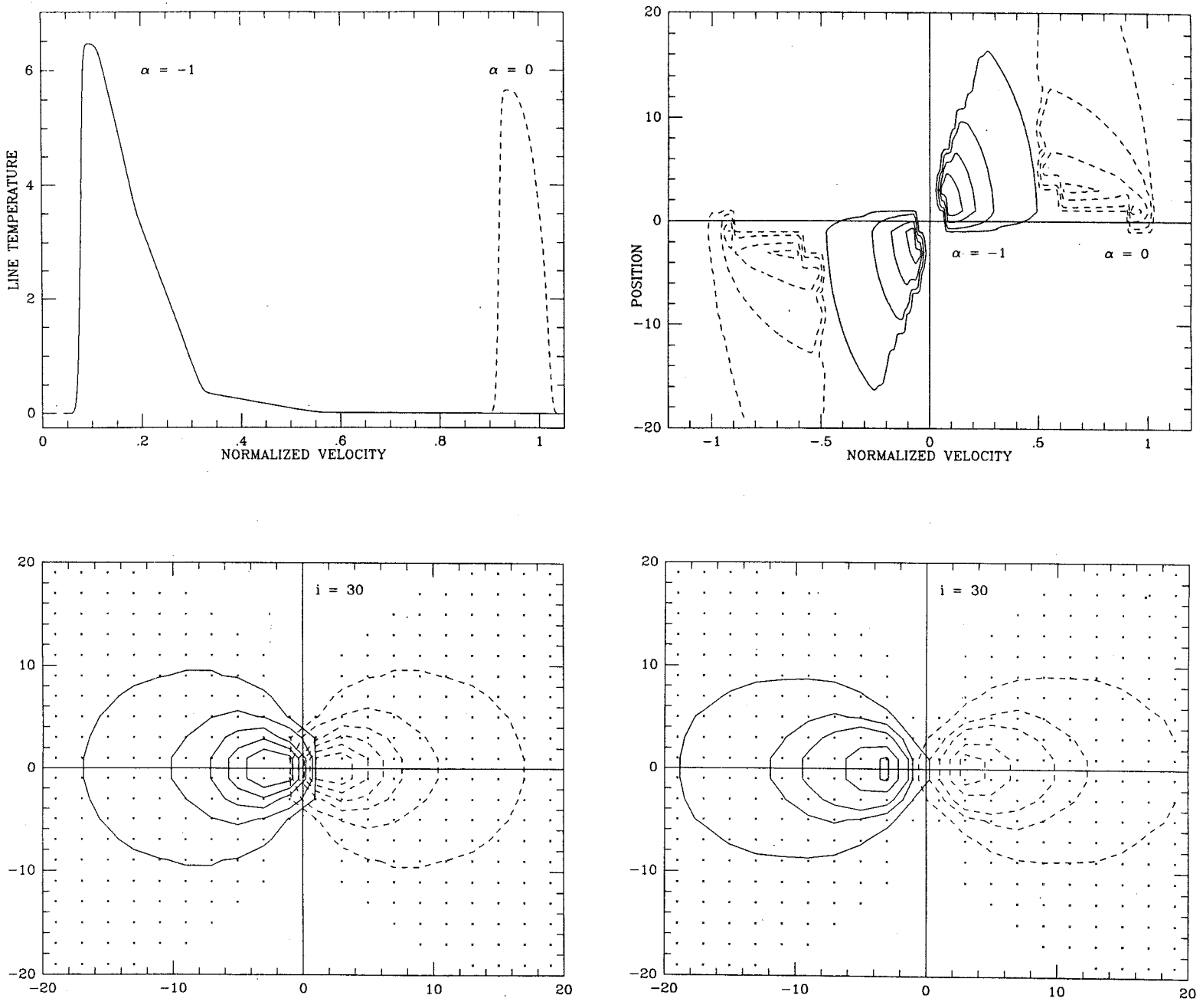

FIG. 4.—Same as Fig. 3, for $i = 30°$

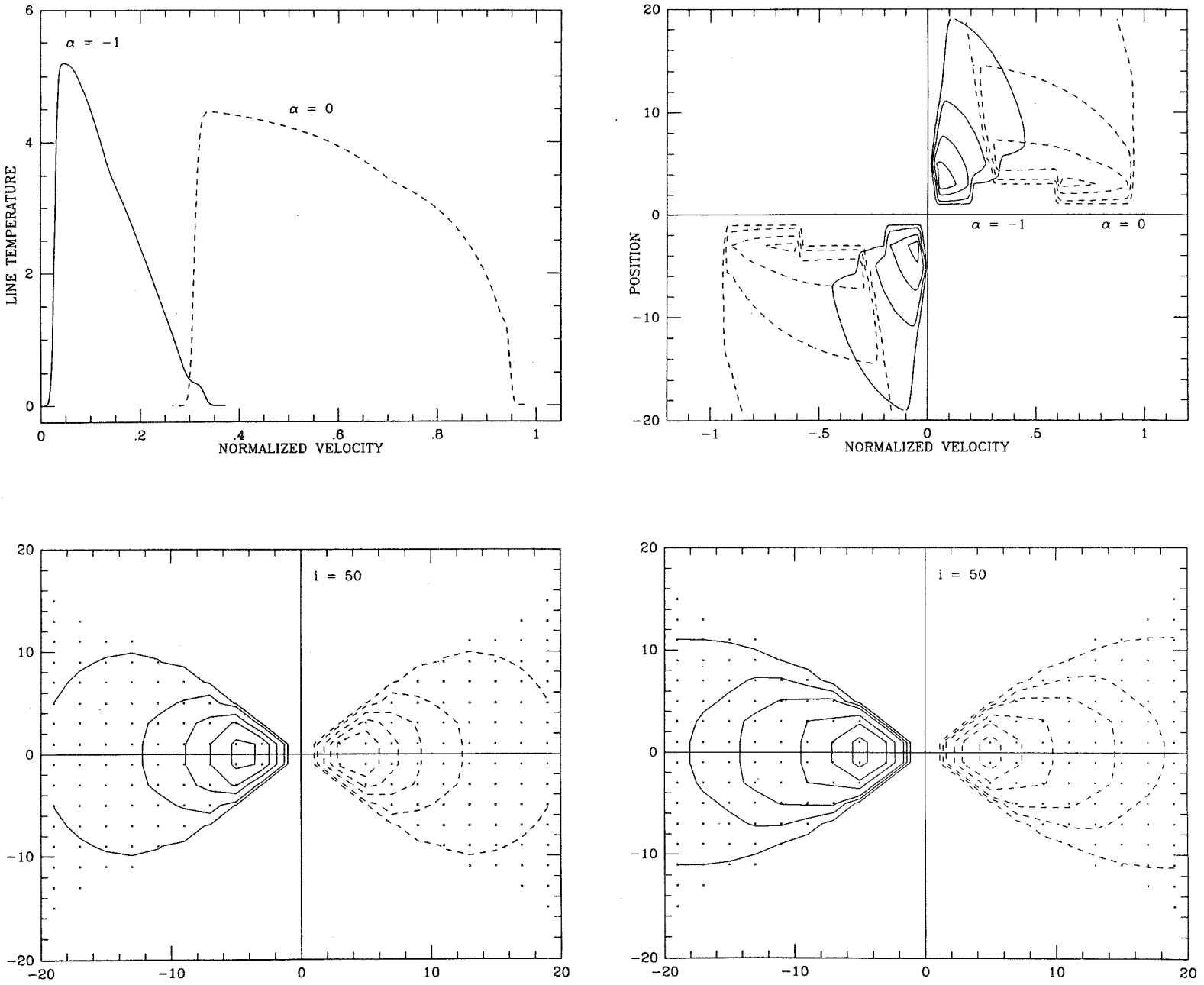

FIG. 5.—Same as Fig. 3, for $i = 50°$ (case 2)

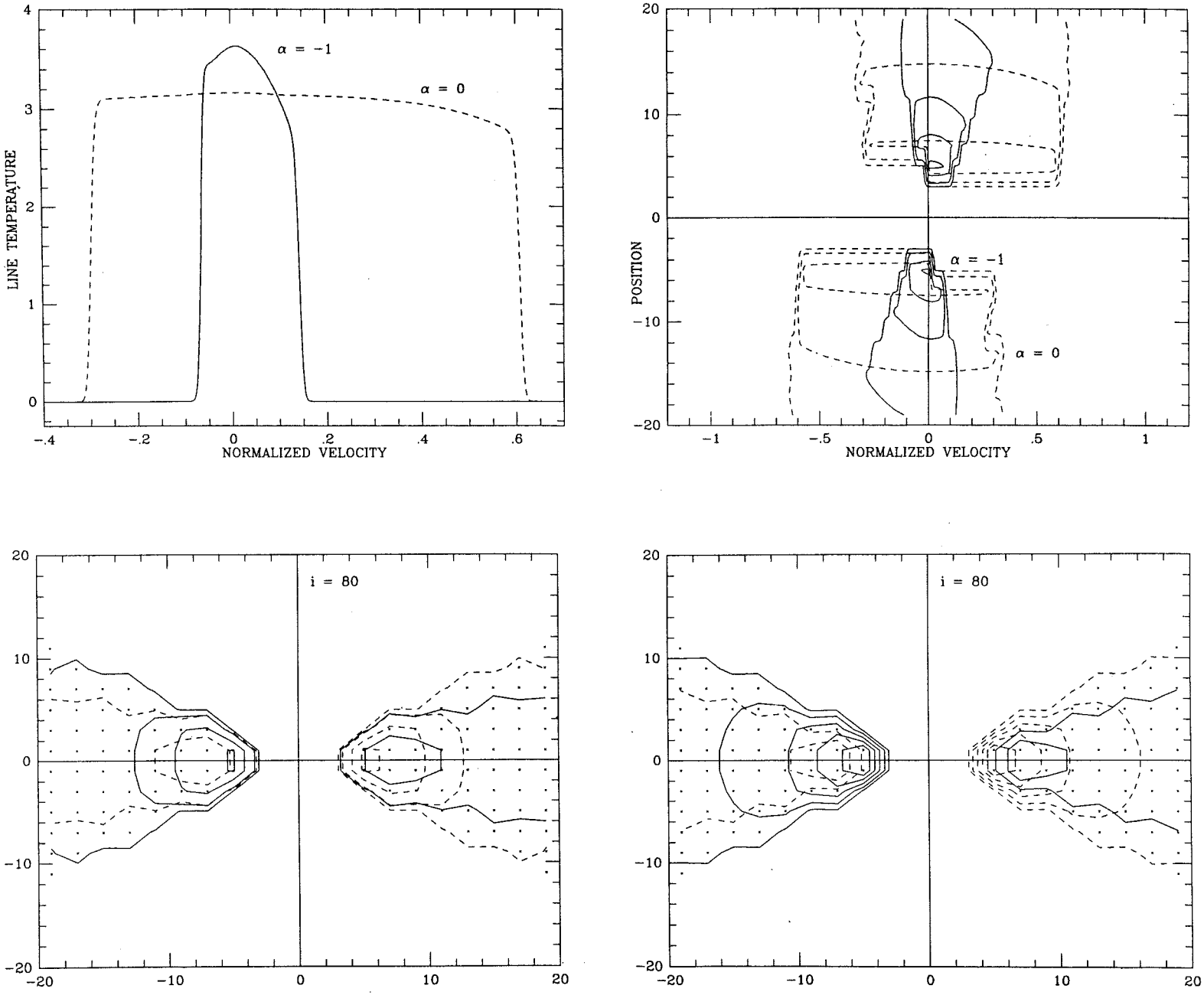

FIG. 6.—Same as Fig. 3, for $i = 80°$ (case 3)

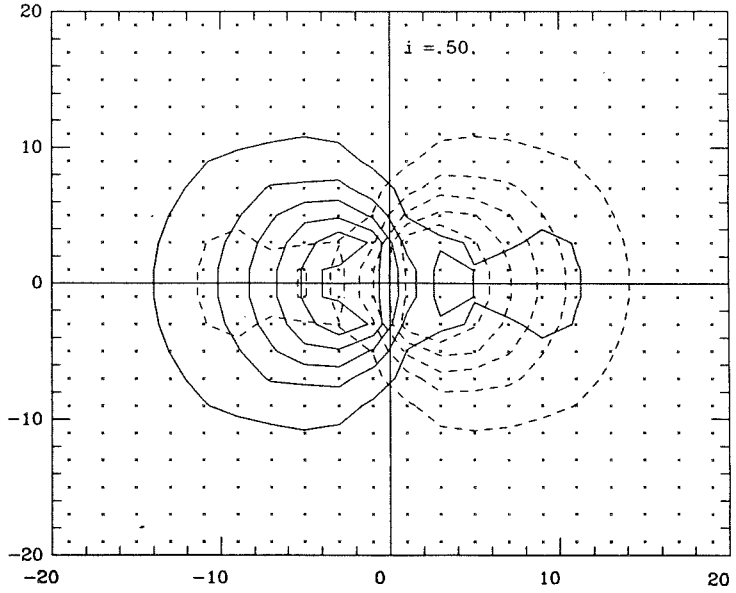

FIG. 7.—Integrated intensity map for $\theta_{max} = 60°$, $i = 50°$, and $\alpha = -1$, corresponding to case 4. Lowest contour level, 0.8 K km s^{-1}; second one, 3 K km s^{-1}; step between other contours, 2 K km s^{-1}.

But no matter how crude, the model investigated here allows one to test the method commonly used by observers, who derive various properties of the flows from the CO maps, against a model flow with known properties, making it possible for the first time to analyze quantitatively the various causes of error in the observers' standard method and their respective importance in the determination of the flow parameters and of the inferred stellar mass loss rate.

In the model discussed above, the actual values of the CO column density $N(\mathrm{CO})_c$ (in cm^{-2}), the flow's mass M_c (in $M_\odot$), the flow's momentum P_c (in $M_\odot$ km s^{-1}), and the flow's momentum rate at $r = r_{min}$ $\dot{P}_c$ (in $M_\odot$ km s^{-1} yr^{-1}) are given by

$$N(\mathrm{CO})_c = \int n_{\mathrm{CO}}(s)ds\,, \tag{14}$$

$$M_c = 0.6157 n_{\mathrm{H_2}}(r_{min}) r_{min}^3 (1 - \cos\theta_{max}) f(\sigma)\,, \tag{15}$$

$$P_c = M_c V_c\,, \tag{16}$$

$$\dot{P}_c(r_{min}) = 1.0374 \times 10^{-6} P_c/T_c\,, \tag{17}$$

where $f(\sigma) = \sigma - 1$ if $\alpha = 0$ or $\ln(\sigma)$ if $\alpha = -1$, $V_c = v_{min}(\sigma - 1)/f(\sigma)$ is the flow's characteristic velocity in km s^{-1}, and $T_c = (\sigma - 1) r_{min}/v_{min}$ is the flow's characteristic time scale in pc km^{-1} s.

The method commonly used by observers to derive the flow's parameters is based on the following expression for the velocity-integrated optical depth in the $J = 1 \rightarrow 0$ transition:

$$\int \tau_o(v)dv = \frac{8\pi^3\mu^2}{3h} \int x_o(1 - e^{-h\nu_o/kT_{ex}}) n_{\mathrm{CO}}(s)ds\,, \tag{18}$$

which can be transformed into the following relationship between integrated line temperature and total CO column density by introducing average values over the line of sight and the velocity profile:

$$\int T_l(v)dv = \left\langle \frac{1 - e^{-\tau_o}}{\tau_o} \right\rangle \langle J(T_{ex}) - J(T_b) \rangle \langle x_o(1 - e^{-h\nu_o/kT_{ex}}) \rangle \times \frac{N(\mathrm{CO}) 8\pi^3\mu^2}{3h}\,. \tag{19}$$

Here, the difficulty lies in evaluating the averaged (bracketed) quantities. The basic assumptions are that the line is optically thin, that LTE holds everywhere, and that the kinetic temperature in the flow is constant. Usually, this procedure is only applied to the line profiles observed at the flow's center, which are considered to be representative of the whole flow region. The resulting CO column density is then used to derive the flow's parameters according to

$$M_o = N_o m_{\mathrm{H_2}} \Sigma_o / A(\mathrm{CO})\,, \tag{20}$$

$$P_o = M_o V_o\,, \tag{21}$$

$$\dot{P}_o = P_o/T_o\,, \tag{22}$$

where Σ_o, the projected surface of the flow; V_o, the maximum radial velocity; and $T_o = R_o/V_o$, the dynamical time scale of the flow, are all measured on the maps.

We thus computed the ratios of these quantities as determined using the standard observers' method (subscript o) to the same quantities computed according to equations (14)–(17) (subscript c). Tables 2 and 3 summarize results for the two velocity fields $\alpha = 0$ and $\alpha = -1$ and for several values of the view angle i. Values of the different computation parameters are given in the tables. Note that results of this comparison depend on $A(\mathrm{CO}) r_{min}/v_{min}$ rather than on the individual values of $A(\mathrm{CO})$, v_{min}, and r_{min}. The various sources of error in the determination of the flow's parameters when applying the standard method to accelerated and constant velocity outflows are discussed below.

Assuming that the transition is optically thin underestimates the ^{12}CO density by a factor of 1/2 to 1/20. Since $T_{ex} < T_k$, the second bracket in equation (19) is always overestimated in the LTE approximation, and the third bracket is underestimated because the levels higher than $j = 2$ are always underpopulated even when the transition is nearly thermalized (see also Dickman 1978). The final result is an underestimate of the central CO *column density* by a factor of 1/30 at worst.

From the computed values of N_c and M_c (cf. eqs. [14] and [15]), we estimate a characteristic projected flow surface Σ_c

TABLE 2

COMPARISON OF THE ACTUAL MODEL PARAMETERS WITH VALUES DERIVED USING THE OBSERVERS' STANDARD METHOD

	$\alpha = 0$				$\alpha = -1$			
RATIO	$i = 5°$	$i = 30°$	$i = 50°$	$i = 80°$	$i = 5°$	$i = 30°$	$i = 50°$	$i = 80°$
N_o/N_c	0.03	0.11	0.16	0.35	0.11	0.11	0.11	0.11
Σ_o/Σ_c	1.53	1.11	0.89	0.74	2.11	3.98	2.10	1.63
M_o/M_c	0.04	0.13	0.15	0.26	0.24	0.46	0.22	0.18
V_o/V_c	1.00	1.00	1.00	0.70	1.28	1.28	1.28	0.77
P_o/P_c	0.04	0.13	0.15	0.18	0.31	0.59	0.29	0.14
T_o/T_c	0.33	0.44	0.55	0.79	0.04	0.08	0.08	0.15
$\dot{P}_o/\dot{P}_c$	0.13	0.29	0.26	0.23	6.98	6.67	3.23	0.95

NOTE.—Input data of computations: $\theta_{max} = 30°$, $\sigma = 10$, $T_k = 10$ K, $n_{H_2}(r_{min}) = 10^4$ cm^{-3}, $k(r_{min}) = 200$ for $\alpha = -1$ and $= 20$ for $\alpha = 0$, corresponding to moderate optical depths.

from

$$M_c = \Sigma_c N_c m_{H_2}/A(\mathrm{CO}); \quad (23)$$

Σ_c can then be compared to Σ_o, the projected area measured on the CO map, which is used in the standard method to compute the CO *mass*. We find that Σ_c is ~ 3 times larger in the case $\alpha = 0$ than in the case $\alpha = -1$, because of the difference in density gradient. In contrast, the apparent surface measured on maps Σ_o is nearly the same in both cases. The quotient Σ_o/Σ_c is around unity for $\alpha = 0$ but can be as large as 3 for $\alpha = -1$. In most cases, the total mass is still underestimated due to the large error in the column density, but it can be overestimated by up to a factor of 2 in flows with small line optical depths. Error in the characteristic flow velocity V_c does not appear critical. Error in the CO *momentum* is thus generally of the same order of magnitude as the error in the CO mass.

Because of the limited sensitivity of available detectors, r_{max} is always underestimated in observations; as a result, high-velocity flows always appear less collimated than in reality. Since v_{min} is always overestimated in the presence of velocity gradients, the *dynamical time scale*, as derived from these quantities, is usually too small by a large factor in accelerated outflows ($\alpha < 0$): more than 20 at small view angles, and typically 2–8 at view angles larger than $\sim 40°$. The *rate of momentum* at the basis of the flow will thus be overestimated by similar factors. The constant velocity case ($\alpha = 0$) may appear more favorable for deriving $\dot{P}$, both because the density falls more slowly outward and because there is no radial velocity gradient in the flow; but one finds that $\dot{P}$ can be underestimated by a factor of up to 10 at small view angles, due mainly to the largely underestimated CO mass in that case.

Several additional uncertainties are introduced when deriving *stellar mass loss rates* from the CO rate of momentum. They stem from: A(CO), the CO abundance relative to H_2; ϵ, the efficiency of the wind to molecular gas momentum exchange; and V_{wind}, the terminal velocity of the wind, which strongly depends on the nature of the central source. That there are so many sources for error, as shown above, convinced us that deriving accurate mass loss rates from observations of high-velocity CO outflows remains impossible at this point. In order to illustrate this conclusion, we now apply the above results to a discussion of T Tauri's mass loss rate. Besides the difficulties discussed above, one has to deal with the multiplicity of T Tauri; the CO outflow could be driven either by the brightest optical component (T Tauri North) or by the radio source (T Tauri South). While previous investigators have attributed the CO flow to T Tauri North, the lack of CO outflows around most T Tauri stars (Levreault 1985) and similarities between the radio source T Tauri South and both IRS 5 in L1551 and the radio source exciting the Herbig-Haro objects HH 1 and HH 2 now suggest that the CO flow is more probably driven by T Tauri South. We briefly consider consequences of both possibilities.

The CO high-velocity flow in the vicinity of T Tauri is peculiar because one sees mainly blue-displaced molecular gas, suggesting that T Tauri is located in front of a dense molecular core (Edwards and Snell 1982). Maps of the CO flow further indicate that we see the outflow almost face-on, a condition hardly favorable to accurate derivation of the flow parameters (cf. Tables 2 and 3). CO line profiles are compatible with those of an accelerated outflow; assuming for the sake of illustration that $\alpha \approx -1$ and $\theta_{max} \approx 30°$, we find $k(r_{min}) > 150$ from the

TABLE 3

COMPARISON OF THE ACTUAL MODEL PARAMETERS WITH VALUES DERIVED USING THE OBSERVER'S STANDARD METHOD

	$\alpha = 0$				$\alpha = -1$			
RATIO	$i = 5°$	$i = 40°$	$i = 60°$	$i = 85°$	$i = 10°$	$i = 40°$	$i = 60°$	$i = 85°$
N_o/N_c	0.11	0.46	0.69	1.01	0.59	0.65	0.67	0.68
Σ_o/Σ_c	1.50	1.20	0.48	0.79	3.29	2.45	1.59	2.30
M_o/M_c	0.16	0.56	0.33	0.79	2.00	1.58	1.07	1.60
V_o/V_c	1.00	1.00	0.85	0.50	0.77	0.77	0.51	0.26
P_o/P_c	0.16	0.56	0.28	0.40	1.50	1.21	0.55	0.40
T_o/T_c	0.22	0.56	0.52	1.11	0.07	0.15	0.22	0.44
$\dot{P}_o/\dot{P}_c$	0.73	1.01	0.54	0.36	20.4	8.20	2.46	0.91

NOTE.—Input data of computations: $\theta_{max} = 30°$, $\sigma = 10$, $T_k = 20$ K, $n_{H_2}(r_{min}) = 5 \times 10^3$ cm^{-3}, $k(r_{min}) = 50$ for $\alpha = -1$ and $= 10$ for $\alpha = 0$, corresponding to low optical depths.

lower limit on the CO central column density derived by Edwards and Snell. We thus conclude that the transition is not optically thin, and Table 2 shows that the CO momentum rate is overestimated by a factor of ~ 7 in the case which comes closest to that of T Tauri's outflow.

We first consider that the CO flow is driven by T Tauri South. Unfortunately, the lack of information about the nature of this source precludes a detailed analysis. Even if its radio spectrum is interpreted as the signature of a hot wind (Schwartz 1984; but see also Bertout 1983 for a different view), we cannot derive a mass loss rate from the CO flow because we do not know the terminal velocity of the wind. If, however, the CO flow emerges directly from the central object, as suggested by Pudritz (1985) and Uchida and Shibata (1985), a mass loss rate of $\sim 2 \times 10^{-6}\ M_\odot\ \mathrm{yr}^{-1}$ is derived from Edwards and Snell's data after correction of the CO momentum rate and the velocity at $r_{\min}$.

If the CO flow is driven by T Tauri North's stellar wind, and if momentum is conserved at the base of the CO flow, then the inferred stellar mass loss rate from our model is $1.4 \times 10^{-8}\ M_\odot\ \mathrm{yr}^{-1}$, while the value of $\dot{M}$ found with the same parameters—in particular, the same CO/H_2 ratio of 5×10^{-5}—but found by using the standard method, is of the order $10^{-7}\ M_\odot\ \mathrm{yr}^{-1}$ (Edwards and Snell 1982; Levreault 1985). Using the probably more realistic value of 10^{-4} for A(CO) (Black and Willner 1984) brings the necessary mass loss rate down to $\dot{M} \approx 7 \times 10^{-9}\ M_\odot\ \mathrm{yr}^{-1}$, a value smaller than the one derived for T Tauri North from VLA data when assuming that its radio emission is thermal ($\dot{M} \approx 4.5 \times 10^{-8}\ M_\odot\ \mathrm{yr}^{-1}$; Schwartz *et al.* 1984). Similar results are found for $\theta_{\max} = 60°$. We thus conclude that the optical star's wind may be massive enough to drive the flow.

V. CONCLUSIONS

The above study suggests that the standard method for deriving flow parameters from observed maps can be improved in several respects. First, we agree with Lada (1985) that observations of ^{13}CO lines should be used whenever possible, both because the transitions are optically thin and because the abundance of ^{13}CO is better known than that of ^{12}CO (Dickman 1978). Second, our results do offer an effective, if approximate, procedure for removing the ambient cloud's contribution to the observed line profiles. One begins by using the maps to determine which of the four cases defined in § III*b* applies to a given observation. If case 1 or 2 applies, then the central range can be entirely excluded; but for cases 3 and 4, taking an average constant value of T_l over the central range gives a better approximation. Finally, we note that considering only the central line of sight leads to overestimating the total mass, while adding up the contribution of each line profile over the flow region would give a true lower limit to the CO mass. We expect these suggestions will remain valid when other velocity fields are investigated.

Section IV demonstrated how difficult it is to predict the HVMF's momentum rate from the observed maps, since the assumption of small optical depth can lead to underestimating the column density, while the underestimation of the flow extent results in characteristic time scales that can be much too small. Extreme caution must therefore be exercised when discussing the possible significance of CO outflow momentum rates and stellar mass loss rates inferred from HVMF observations until the physics of the CO outflows are better understood.

It is a pleasure to thank J. Adams for help in editing the text.

REFERENCES

Bally, J., and Lada, C. J. 1983, *Ap. J.*, **265**, 824.
Bastian, U., Bertout, C., Stenholm, L., and Wehrse, R. 1980, *Astr. Ap.*, **86**, 105.
Bertout, C. 1979, *Astr. Ap.*, **80**, 138.
———. 1983, *Astr. Ap.*, **126**, L1.
———. 1984, *Ap. J.*, **285**, 269.
Black, J. H., and Willner, S. P. 1984, *Ap. J.*, **279**, 673.
Calvet, N., Cantó, J., and Rodríguez, L. F. 1983, *Ap. J.*, **268**, 739.
Dickman, R. L. 1978, *Ap. J. Suppl.*, **37**, 407.
Edwards, S., and Snell, R. L. 1982, *Ap. J.*, **261**, 151.
———. 1984, *Ap. J.*, **281**, 237.
Goldreich, P., and Kwan, J. 1974, *Ap. J.*, **189**, 441.
Goldsmith, P. F. 1972, *Ap. J.*, **176**, 597.
Goldsmith, P. F., Snell, R. L., and Hemeon-Heyer, M. 1984, *Ap. J.*, **286**, 599.
Goldsmith, P. F., Young, J. S., and Langer, W. D. 1983, *Ap. J. Suppl.*, **51**, 203.
Green, S., and Thaddeus, P. 1976, *Ap. J.*, **205**, 766.
Hamann, W. R. 1981, *Astr. Ap.*, **93**, 353.
Königl, A. 1982, *Ap. J.*, **261**, 115.
Lada, C. J. 1985, *Ann. Rev. Astr. Ap.*, **23**, 267.
Levreault, R. M. 1985, Astronomy Dept., University of Texas, Austin, *Tech. Rept.*, No. 85-1.
Mundt, R., Stocke, J., Strom, S. E., Strom, K. M., and Anderson, E. R. 1985, *Ap. J. (Letters)*, **297**, L41.
Plambeck, R. L., Snell, R. L., and Loren, R. B. 1983, *Ap. J.*, **266**, 321.
Pudritz, R. E. 1985, *Ap. J.*, **293**, 216.
Pudritz, R. E., and Norman, C. A. 1983, *Ap. J.*, **274**, 677.
Sakurai, T. 1985, *Astr. Ap.*, submitted.
Schwartz, P. R., Simon, T., Zuckerman, B., and Howell, R. R. 1984, *Ap. J. (Letters)*, **280**, L23.
Snell, R. L., Loren, R. B., and Plambeck, R. L. 1980, *Ap. J. (Letters)*, **239**, L17.
Sobolev, V. V. 1957, *Soviet Astr.—AJ*, **1**, 678.
Uchida, Y., and Shibata, K. 1984, *Pub. Astr. Soc. Japan*, **36**, 105.
———. 1985, *NASA Conf. Pub.*, No. 2358, p. 169.

CLAUDE BERTOUT and SYLVIE CABRIT: Institut d'Astrophysique, 98 bis Bd Arago, F-75014 Paris, France

ANNEXE 2

Protostars and Molecular Clouds, Eds. T.Montmerle and C. Bertout (Saclay: CEA/Doc), 1987, p.42.

A MODEL OF CO EMISSION IN BIPOLAR FLOWS

Sylvie CABRIT

Institut d'Astrophysique de Paris, 98bis Bd Arago,
and Ecole Normale Superieure, 48 Bd Jourdan,
75014 PARIS, FRANCE

and

Claude BERTOUT

Institut d'Astrophysique de Paris, and
Laboratoire d'Astrophysique Theorique du College de France,
98bis Bd Arago, 75014 PARIS, FRANCE

ABSTRACT

We present a model of CO line formation in high-velocity bipolar outflows from young stars. We find that the resulting CO profiles and integrated intensity maps can be divided into four categories, depending on the view angle and the flow opening angle. We then show that the values of the rate of momentum input in the flow derived from the CO J = 1→0 observations must be considered with great caution until the velocity field and the actual geometry of the outflow are better known.

1. INTRODUCTION

Recent millimeter and optical studies of star-forming regions have provided strong evidence that many young stellar objects are undergoing a phase of energetic, collimated outflow activity (see [1] for a review). CO line observations are especially important since they offer a powerful probe of the physical properties, large scale structure, and kinematics of the high-velocity molecular gas. In addition, they potentially allow one to measure the rate of momentum input in the flow, a crucial parameter for the theory of mass-loss in pre-main sequence stars and for the dynamical evolution of star-forming regions.

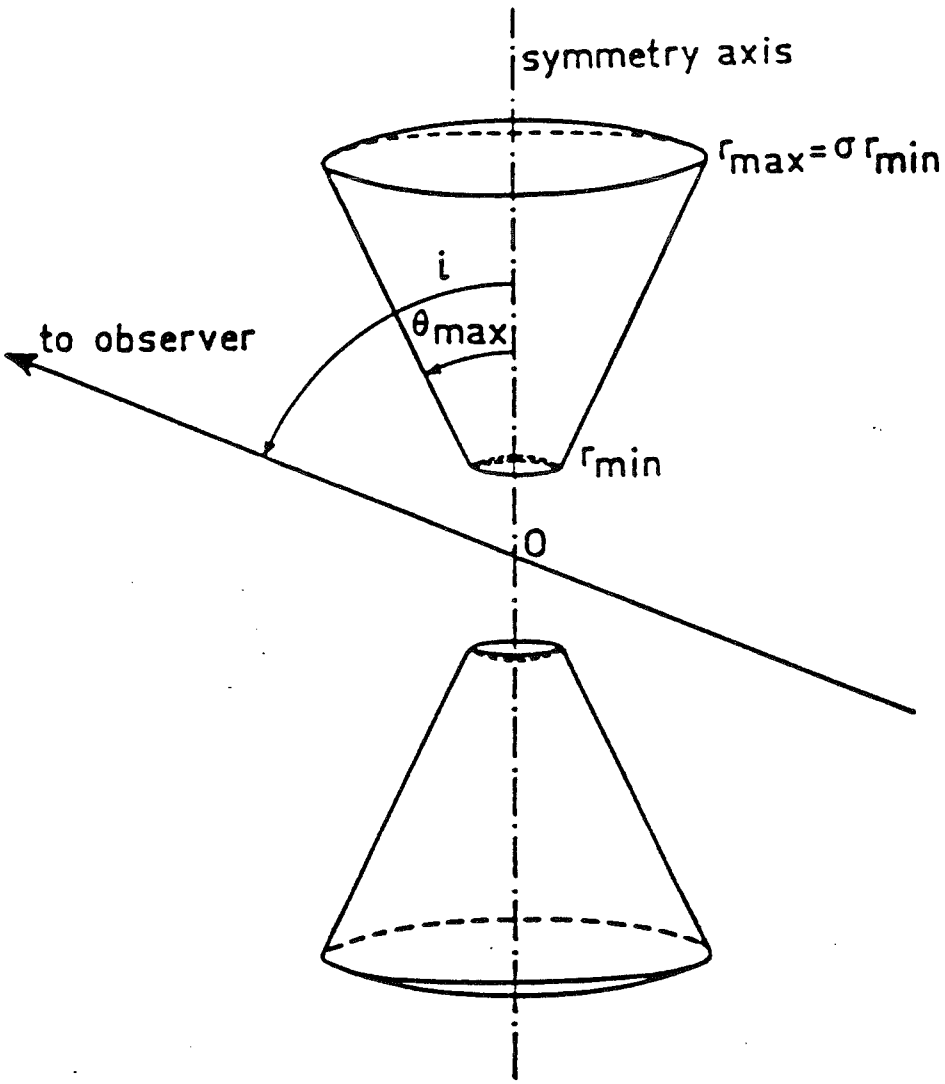

Figure 1: *Geometry of the model.*

In order to exploit the wealth of information contained in CO observations, we have developed a code which computes the excitation and rotational line profiles of CO in axial symmetry in the presence of supersonic accelerated velocity fields. Our first investigation was emission from a steady-state radial outflow expanding in two biconical lobes. In this contribution, we will review our main assumptions and implications for the outflow geometry and the high-velocity CO excitation, and attempt a comparison between our synthetic maps and observed ones. We will then comment on the accuracy of the observers' method for deriving values of the flow parameters, and discuss in detail recent attempts to improve this method. A complete analysis of our results can be found in [2].

2. MAIN ASSUMPTIONS

2.1. Flow geometry

Although many molecular flows have an obvious bipolar geometry, two major uncertainties are whether the high-velocity gas expands radially from the star (conical geometry) or is more tightly collimated into a cylinder, and whether it is filling homogeneously the observed CO lobes or is confined to their surface in a dense shell. In at least one flow, L1551-IRS5, high-resolution CO observations [3] show a bright- rim structure in the innermost high-velocity gas which is suggestive of a conical shell. But in such a geometry, the lines of sight would cross two distinct layers with different radial velocities and the profiles should show two peaks, unless the view angle is such that one of them has a low radial velocity and is "hidden" behind the cloud emission. The fact that such double-peaked profiles have never been observed would be more easily explained by a filled cone model or a cylindrical flow (for example the "flow in a pipe" model described in [4]), which both produce only single-peaked profiles.

CO radiative transfer calculations in these various geometries offer a way of discriminating between the different possibilities. At this time, we present our results for the filled cone model; we assumed that the high-velocity gas was filling a bicone of opening angle 2 θ_{max}, inner radius r_{min} and outer radius r_{max}, (see Fig.1) and that the velocity and density laws were given by

$$v(r) = v(r_{min})\ (r_{min}/r)^{\alpha}$$

$$n_{H_2}(r) = n_{H_2}(r_{min})\ (r_{min}/r)^{\delta}$$

Mass conservation within the flow required that $\delta = 2 - \alpha$. Two cases were investigated: a constant velocity outflow with $\alpha = 0$ and a linearly accelerated outflow with $\alpha = -1$.

2.2. CO excitation

In conditions typical of molecular clouds, the CO rotational lines are excited mainly by radiative transitions and collisions with hydrogen molecules. The sources of radiation external to the high-velocity gas are the line emission of the static ambient cloud, the photospheric emission from the central star, the thermal emission of dust grains, and the cosmic background emission at $T_b = 2.7$ K.

The static cloud line radiation is Doppler-shifted in the high-velocity gas rest frame; therefore, it cannot contribute to the CO excitation in the flow, and did not appear in our computations. For moderate high-velocity CO optical depths, we found that the relative increase in CO excitation temperature due to stellar radiation was, as expected, proportionnal to the surface $\pi\, r_*^2$ and the temperature T_* of the star, but was noticeable only at distances $r < r_*\ (T_*/10{,}000\ K)^{1/2}$. Since the CO observations suggest that $r_{min} > 10^{-2}$ pc [3,5], this may also be neglected.

The ratio of dust grains to molecular gas absorption coefficients in the CO ($J \rightarrow J-1$) line at frequency ν_J can be written as

$$\frac{\kappa_{\nu_J}(dust)}{\kappa_{\nu_J}(gas)} = \frac{n_d \langle Q_{ext}\, \pi a^2 \rangle_{\nu_J}}{n_{H_2}\, A_{CO}\, f_J} \times \left[8\pi^3/3h\, \mu_J^2\ \frac{(e^{-h\nu_J/kT_{ex}} - 1)}{\nu_D} \right]^{-1}$$

We assumed thermodynamic equilibrium at temperature T_{ex} to calculate the fraction f_J of molecules in level J and compute this ratio as a function of T_{ex}. For the other parameters, we adopted the following typical values: $A_{CO} = 10^{-4}$, v_D (the CO Doppler velocity) = 1 km s^{-1}, $n_{H_2}/n_d = 5.10^{10}$, and $\langle Q_{ext}\pi a^2 \rangle_\nu = 2.10^{-14}\ \nu/\nu_1\ cm^{-2}$ (average extinction law for ice-coated grains, from Leung [6]). Our results for the first five transitions of CO are plotted in Fig.2. We find that, although this ratio increases at smaller T_{ex}, it remains small ($\sim 10^{-4}$) unless $J \geq 4$ and $T_{ex} < 5$ K. The effect of dust-to-gas radiative coupling on the transfer of the first two rotational lines of CO is thus always negligible, but it may be important for higher transitions. Computations of dust-to-gas emissivity ratios lead to similar conclusions.

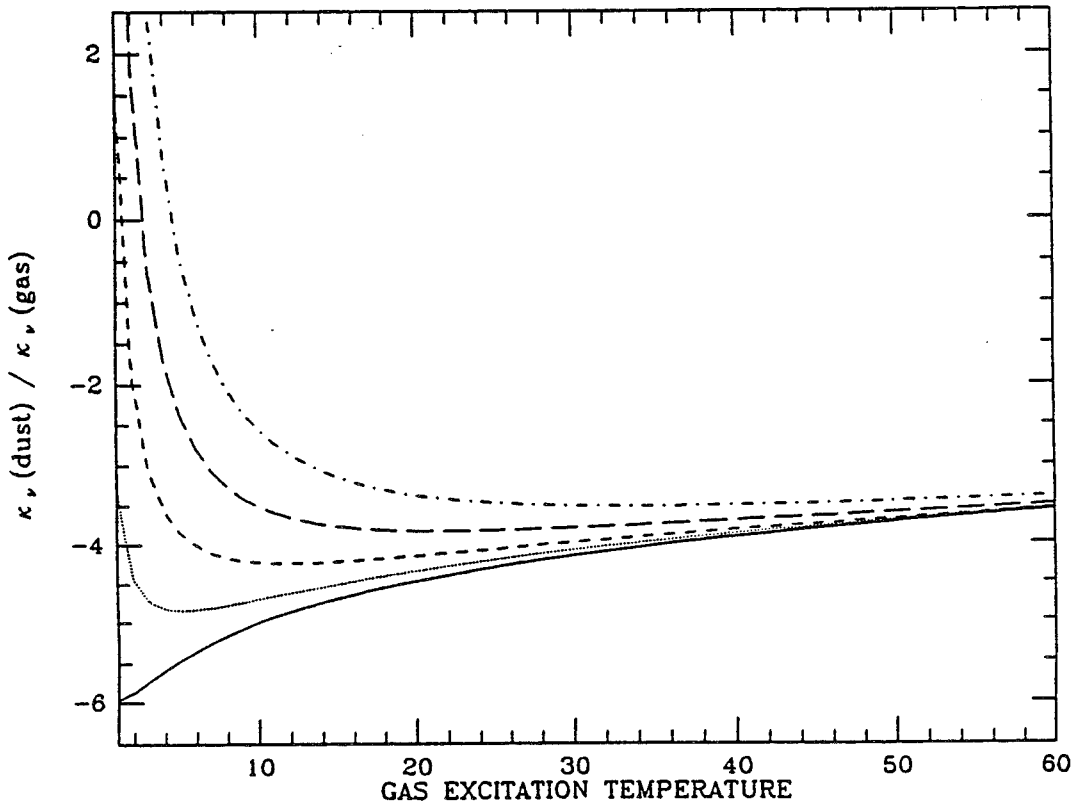

Figure 2: *Ratio of dust grains to molecular gas absorption coefficients in the first five transitions of CO as a function of the gas excitation temperature. J = 1 for the solid curve, and increases from bottom to top.*

The only processes that contribute to the high-velocity CO excitation are thus collisions with molecular hydrogen at a kinetic temperature T_k and absorption of local or cosmic background photons.

Because the outflow velocities inferred from molecular observations ($v \geq 10$ km s^{-1}) are much larger than the CO thermal velocity ($v_{th} = 0.02 \sqrt{T_k}$ km s^{-1}), the radial velocity gradient along most lines of sight is so large that a photon either is reabsorbed very close to its emission point or escapes from the flow with a probability β. This fact was first used by Sobolev [7] to show that, in this limit, the mean radiation intensity over the line profile could be simply expressed in terms of the background intensity and the local values of β and the source function. We adopted this approximation to solve locally the CO statistical equilibrium equations and compute NLTE level populations, but did not use it for the emergent profiles, which were integrated exactly. This hybrid method has been shown to give excellent results for fast flows [8]. The CO excitation conditions at a given point in the flow are therefore uniquely determined by the local values of the following independent parameters: the H_2 kinetic temperature T_k and number density n_{H_2}, the velocity-law exponent α, and the Sobolev optical depth $k(r) = 8\pi^3/3h\ \mu^2\ n_{CO}\ r/v(r)$.

3. PHYSICAL IMPLICATIONS

3.1. CO excitation

In agreement with theoretical expectations, the $J = 1 \rightarrow 0$ transition was thermalized only for:

$$(n_{H_2})^2 > 530\ v(\text{km s}^{-1}) / (\ A_{CO}\ r(\text{pc})\ )\ \text{cm}^{-6}.$$

In a typical molecular flow, where $A_{CO} \sim 10^{-4}$, $r \sim 0.1$ pc, $v \sim 10$ km s^{-1}, this condition becomes :

$$n_{H_2} > 2.5\ 10^4\ \text{cm}^{-3}.$$

NLTE calculations of the CO excitation are thus required if most of the high-velocity emission is formed in an extended region of moderate density. Although observations of widespread HCO^+ emission [9] do suggest that high-density ($\sim 10^5$-10^6 cm^{-3}) gas is present in several outflows, the weakness of this emission also indicates a much higher degree of clumpiness than for the CO gas. Therefore, the dense component probably represents only a small fraction of the total mass of the flow.

3.2. Flow geometry

For a radial biconical outflow, four types of configurations can be distinguished, that depend on the values of θ_{max} and i, the angle between the flow axis and the line of sight. These configurations are represented in 3 dimensions in Fig.3, and the probability of observing each of them is plotted as a function of θ_{max} in Fig.4. These results remain valid for the conical shell geometry. In the following, we briefly describe the characteristics of each case and illustrate them by computed maps of CO $J=1 \rightarrow 0$ integrated intensity (Fig.5a to 8) and, whenever possible,

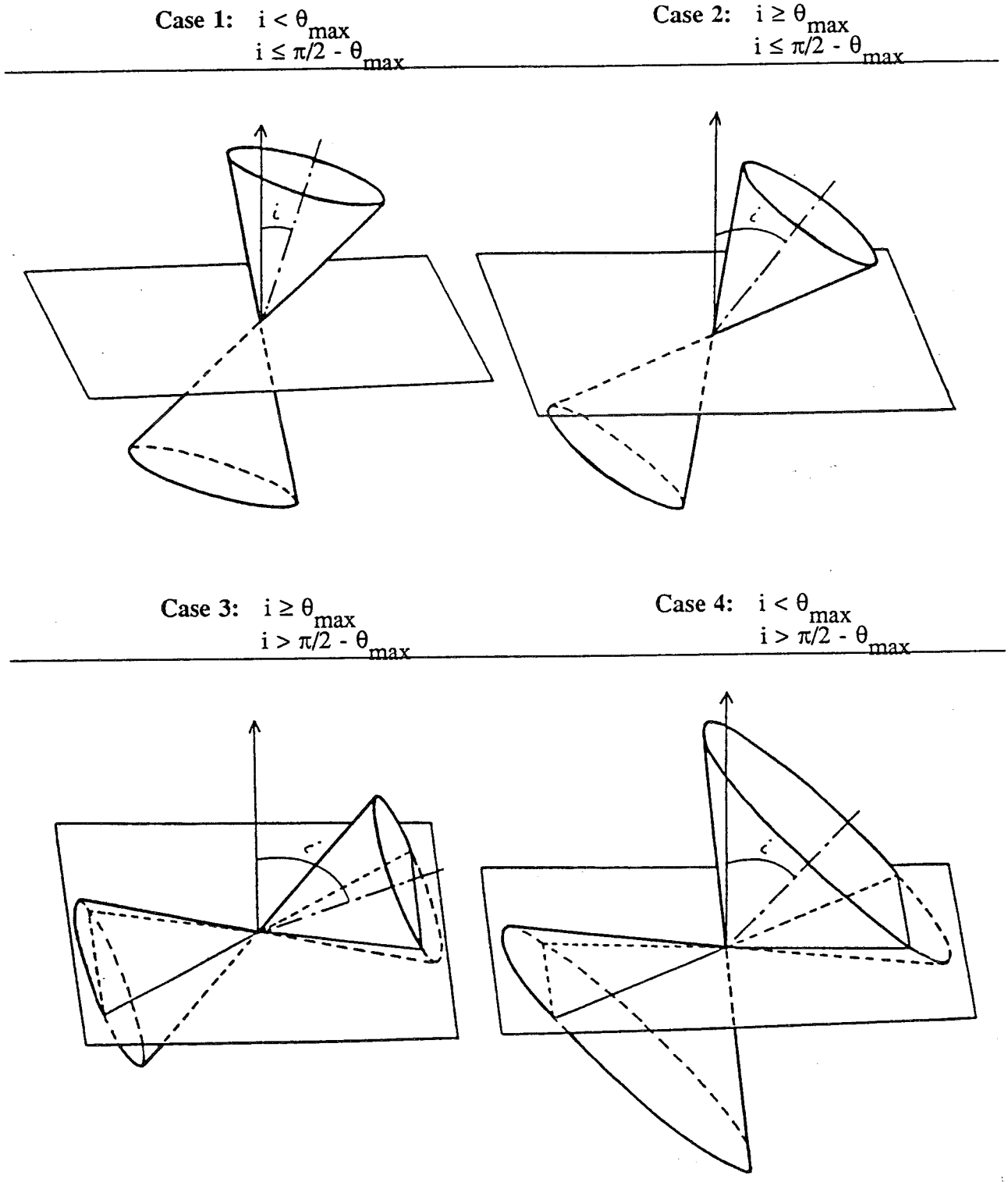

Figure 3: The four configurations of a biconical outflow. *The central line of sight is represented by an arrow. The molecular gas located in front of the plane normal to this direction and containing the flow center approaches the observer and is blue-shifted, while the gas behind this plane moves away and is red-shifted. If* $i < \theta_{max}$, *some lines of sight will cross the two cones, else they will only cross one. If* $i \leq \pi/2 - \theta_{max}$, *each cone will be entirely blue- or red-shifted, else they will be both partly blue-, partly red-shifted.*

by maps of observed flows in a similar configuration (Fig.5b to 7b). For a more detailed study, see [2].

Case 1: $i < \theta_{max}$ and $i < \pi/2 - \theta_{max}$, is illustrated in Fig.5a ($i = 5°$, $\theta_{max} = 30°$) and Fig.5b (Haro-255 outflow, from [4]). The two cones are seen nearly face-on; the contours of blue- and red-shifted integrated intensity are circular and overlapping.

Case 2: $i > \theta_{max}$ and $i < \pi/2 - \theta_{max}$, occurs only if $\theta_{max} < 45°$ and is illustrated in Fig.6a ($i = 50°$, $\theta_{max} = 30°$) and Fig.6b (B335 outflow, from [5]). The blue and red-shifted lobes are now spatially separated by a distance $r_g = 2\ r_{min} \sin(i - \theta_{max})$ and the bipolar structure of the flow is apparent.

Case 3: $i > \theta_{max}$ and $i \geq \pi/2 - \theta_{max}$, is presented in Fig.7a ($i = 80°$, $\theta_{max} = 30°$) and Fig.7b (RNO43 outflow, from [10]). The two cones appear again as two distinct lobes but each one is now partly blue-, partly red-shifted.

Case 4: $i < \theta_{max}$ and $i \geq \pi/2 - \theta_{max}$, occurs only for $\theta_{max} > 45°$ and is illustrated in Fig.8a ($i = 50°$, $\theta_{max} = 60°$). It is basically a Case 3 where the two lobes are still overlapping due to their larger opening angle.

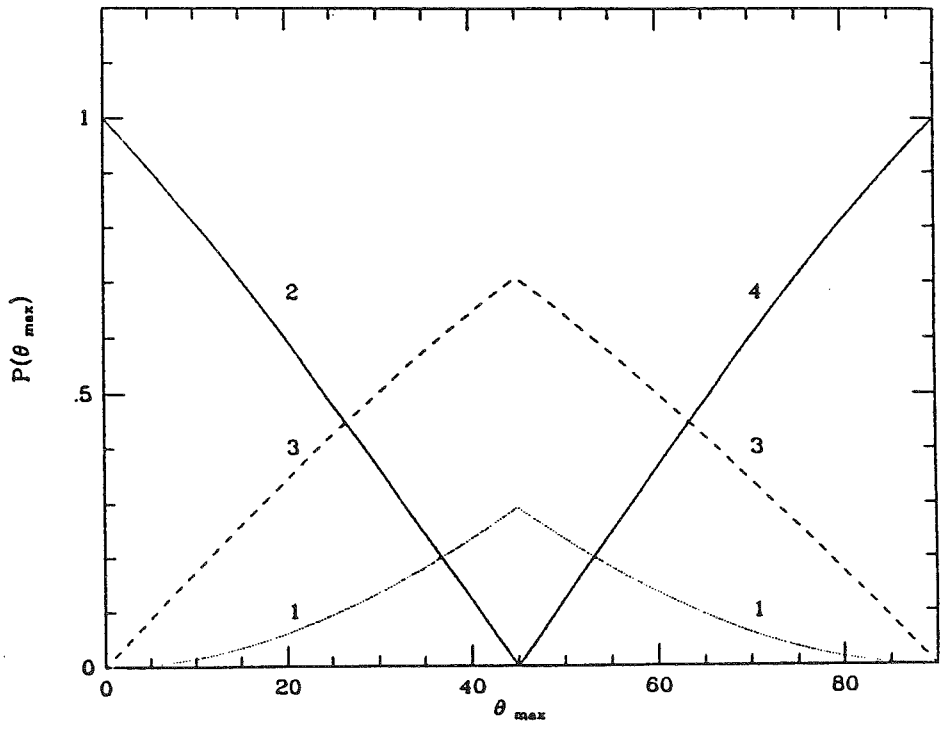

Figure 4: *Probability $P(\theta_{max})$ of observing each of the four configurations distinguished in the text, plotted as a function of θ_{max}.*

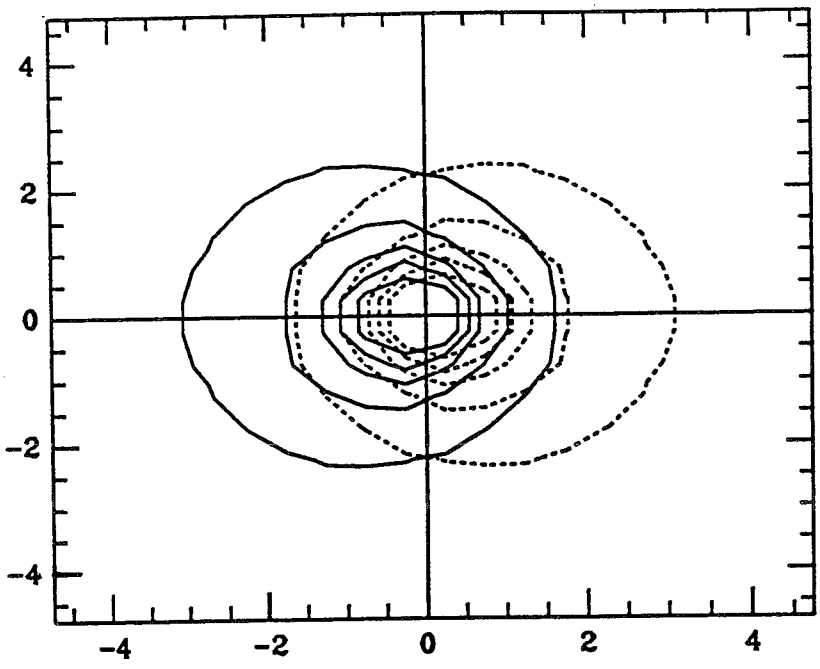

Figure 5a: *Synthetic contour map of blue-shifted (solid lines) and red-shifted (dashed lines) CO $J = 1 \rightarrow 0$ integrated intensity computed for $n_{H_2}(r_{min}) = 10^4\ cm^{-3}$, $T_k = 10$ K, $k(r_{min}) = 100$, $\alpha = -1$, $r_{max} = 10 \times r_{min}$, $i = 5°$ and $\theta_{max} = 30°$, illustrating Case 1.*

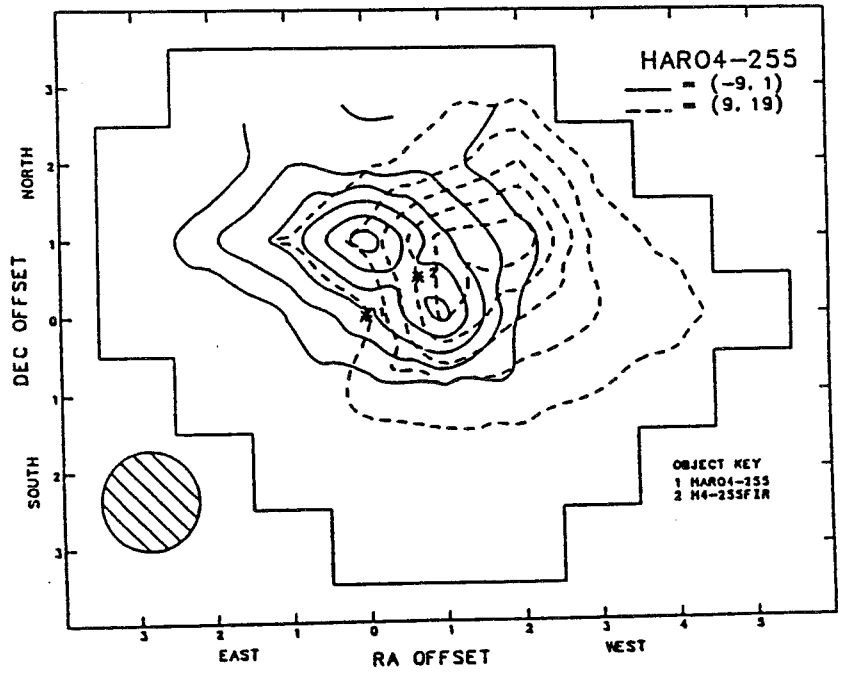

Figure 5b: *Integrated intensity map of the outflow near the Herbig-Haro object HARO-255, from [4]. The *2 sign, close to the center of symmetry, denotes the location of a newly discovered infrared source.*

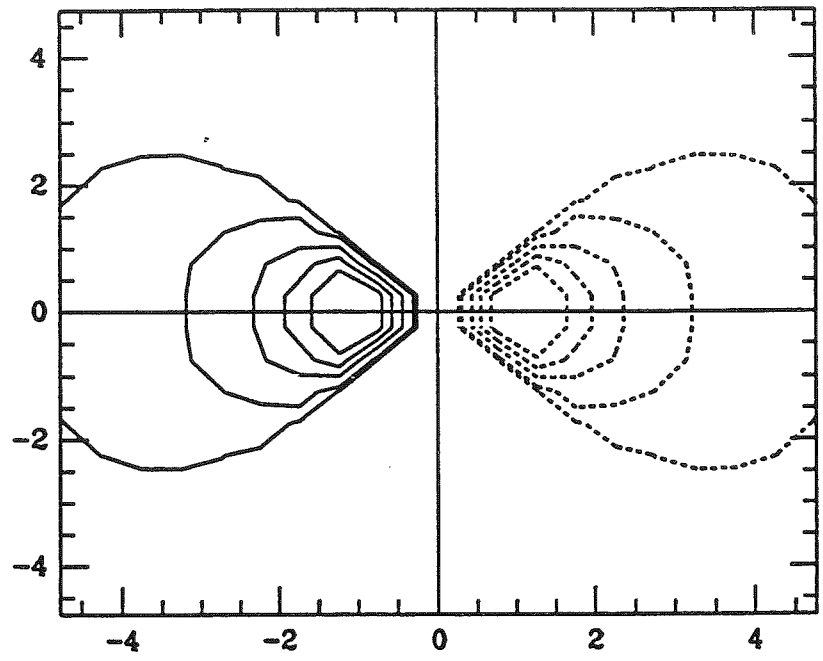

Figure 6a: *Same as Figure 5a with i = 50°, illustrating Case 2.*

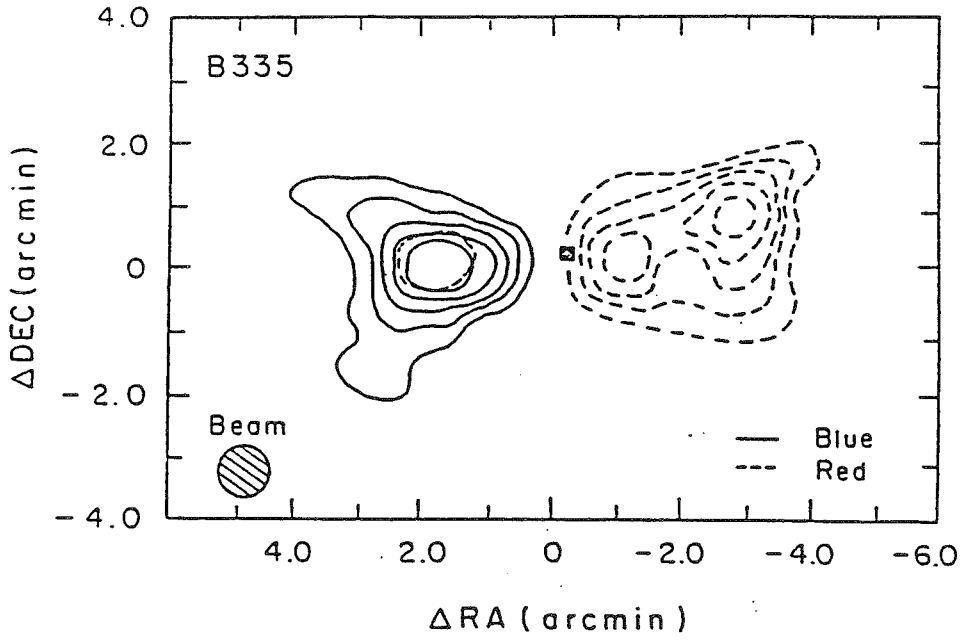

Figure 6b: *Integrated intensity map of the outflow in B335, from [5]. The filled square denotes the location of a far-infrared source.*

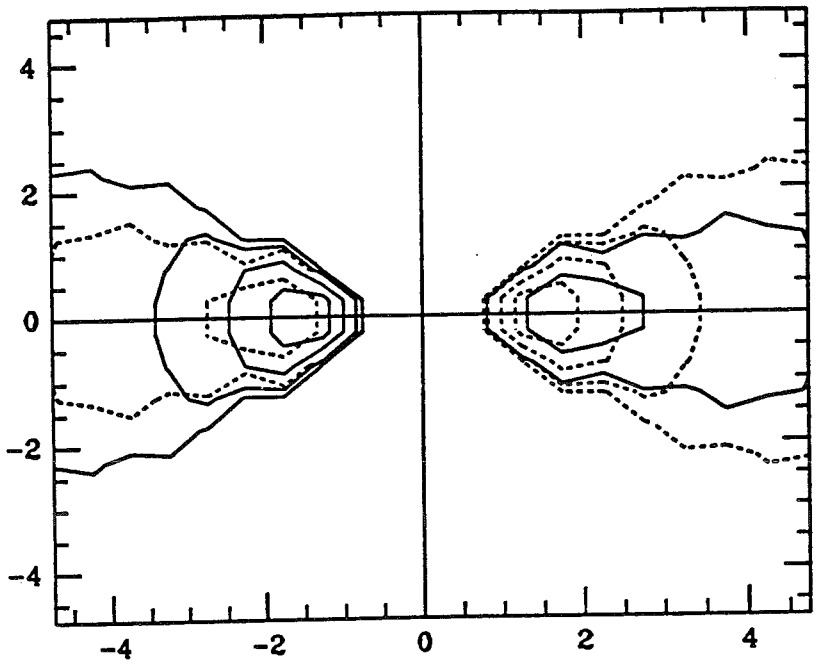

Figure 7a: *Same as Figure 5a with i = 80°, illustrating Case 3.*

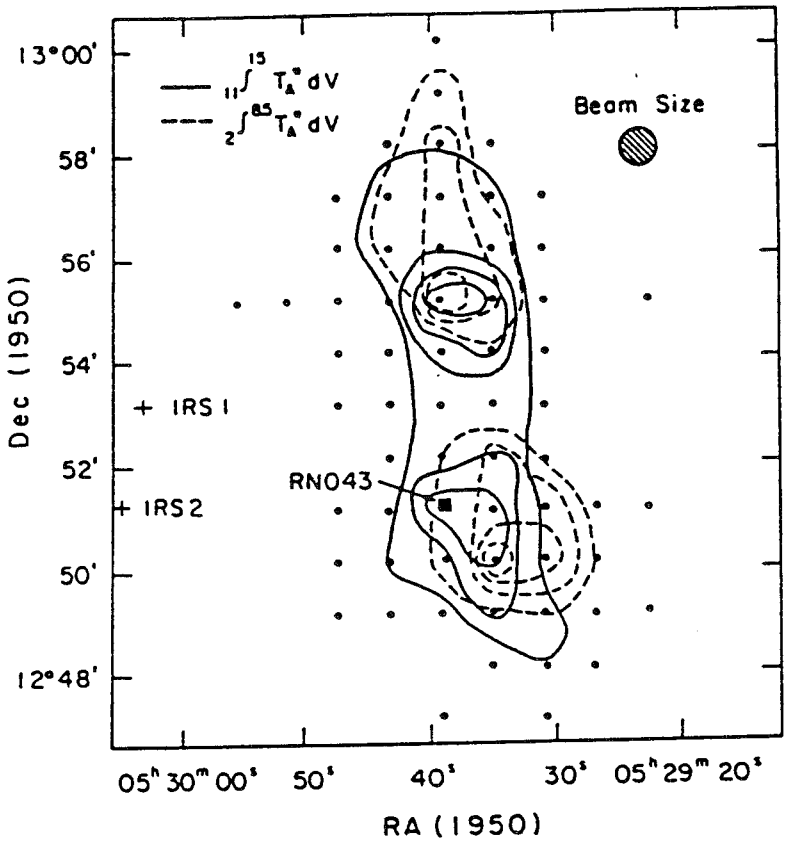

Figure 7b: *Integrated intensity map of the high-velocity CO emission near the Herbig-Haro object RNO43, from [10].*

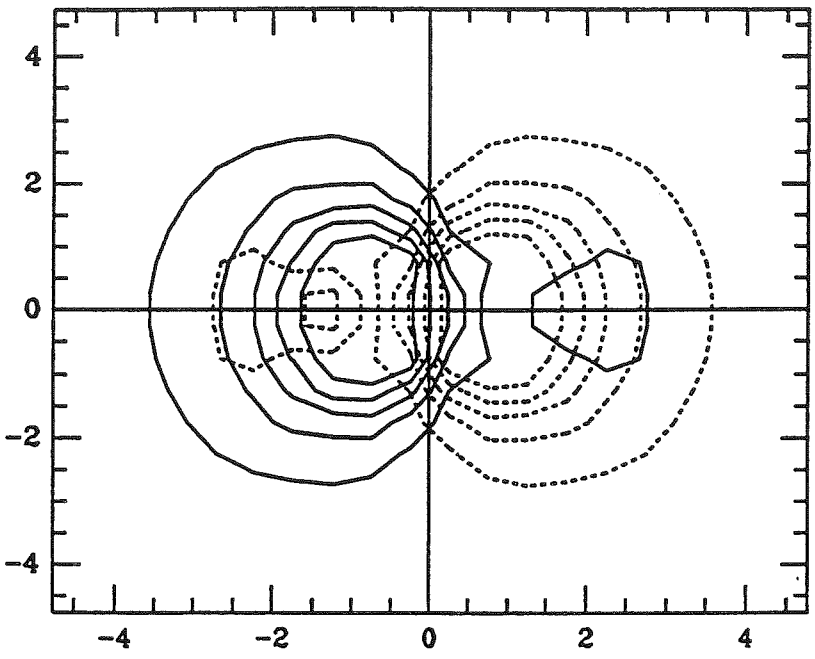

Figure 8: *Same as Figure 5a with i = 50° and θ_{max} = 60 °, illustrating Case 4.*

Although Cases 1 and 2 with $r_{max} \geq 5\ r_{min}$ and $\theta_{max} \sim 30°$ reproduce quite well the main aspects of the observed flows (see [11]), Cases 3 and 4 have never been reported, even though they are expected whenever $\theta_{max} > 30°$ (cf. Fig.4). There are three possible explanations for this lack of detection: First, emission at low radial velocity ($\Delta v \leq 1$ km s^{-1}) is undiscernable from the ambient cloud emission, so that Case 3 (resp. Case 4) flows might be classified as Case 2 (resp. Case 1) flows after subtraction of the central low-velocity emission. Second, observations that are attributed to a pair of outflows seen face-on could in fact represent a single Case 3 outflow. This may be the case for the "double" outflow detected near RNO43 [10] and shown in Fig.7b: The recent finding that the proper motion vectors of the two HH objects associated with each component of this outflow both point away from an infrared source located to the south of these two high-velocity features [12] rather suggests that we are actually looking at a single lobe of a Case 3 outflow emanating from this source. Finally, most bipolar flows might have $\theta_{max} < 30°$, which seems confirmed by all high-resolution CO observations and the fact that the CO lobes always look more elongated than in Fig.8.

3.3. Flow velocity field

As will be shown in section 4.2, determining the actual velocity field in a flow is an important issue if we want to derive accurate values of the flow momentum input rate. Our calculations indeed show that the CO emission profiles are strongly dependent on the velocity law in the cone. At a given view angle, the difference is the most apparent when we compare the series of profiles obtained along the flow axis for both values of α. We find that, for a constant velocity outflow, the range of radial velocities on the line of sight is independent of position along the flow axis, whereas in an accelerated flow the profiles show systematically higher velocities as we look further from the center. The same distinctive behaviors are expected in cylindrical or shell-like geometries.

4. OBSERVATIONAL UNCERTAINTIES IN THE FLOW PARAMETERS

As a test of the method commonly used by observers for deriving flow properties, we applied it to our synthetic profiles and maps and compared the resulting estimates with the actual parameters of our model. This allowed us to identify and quantify the various sources of error present in such a derivation.

4.1. The method.

The "observed" parameters of our models were derived using the following assumptions:
(1) the ^{12}CO J=1→0 line is in thermodynamical equilibrium at the local kinetic temperature and is optically thin, so that on any line of sight the CO column density N_o is given by:

$$N_o = \int T_R^*(v)\, dv \times \left[\left(J_{\nu_1}(T_k) - J_{\nu_1}(T_b) \right) 8\pi^3/3h\, \mu^2\, f_o\, (1-e^{-h\nu_1/kT_k}) \right]^{-1}.$$

(2) N_o does not vary significantly over the flow area Σ_o and is equal to its value on the central line of sight, so that the flow mass is $M_o = N_o\, \Sigma_o\, m_{H_2} / A_{CO}$.
(3) the gas flows at a constant velocity V_o equal to the maximum observed radial velocity; the flow momentum is then given by $P_o = M_o\, V_o$.
(4) there are no projection effects (e.g. the flow is spherical), so that its true length is equal to its dimension R_o in the plane of the sky. The dynamical time scale and the momentum input rate are then $T_o = R_o / V_o$, and $\dot{P}_o = P_o / T_o$.
The actual values of our model's parameters were computed according to the following formula:

Mass	$M_c = \Omega\, n_{H_2}(r_{min})\, r_{min}^3\, m_{H_2} \times f(\sigma) \begin{cases} \ln(\sigma) \text{ if } \alpha = -1 \\ \sigma - 1 \text{ if } \alpha = 0 \end{cases}$
Momentum	$P_c = \Omega\, n_{H_2}(r_{min})\, r_{min}^3\, m_{H_2}\, v(r_{min})\, (\sigma - 1)$ $= M_c\, V_c$ where $V_c = v(r_{min})\, (\sigma - 1) / f(\sigma)$
Time scale	$T_c = r_{min}\, (\sigma - 1) / v(r_{min})$
Momentum input rate	$\dot{P}_c = \Omega\, n_{H_2}(r_{min})\, m_{H_2}\, r_{min}^2\, v(r_{min})^2$

where $\Omega = 4\pi\, (1 - \cos\theta_{max})$ and $\sigma = r_{max}/r_{min}$.

In the following sections, we examine the effect of the various assumptions listed above on the accuracy of the "observed" parameters, and assess the usefulness of current attempts to improve this method.

4.2. Flow mass and momentum

While assumption (1) underestimates the CO column density by a factor $(1-e^{-\tau})/\tau$, where τ is the average line optical depth, (2) tends to overestimate M_c because in our models, as in most of the observed flows, the column density is decreasing outwards. Consequently, M_c is most of the time underestimated (typically by a factor 1/3), except in flows with a high density gradient ($\alpha = -1$) and a small optical depth where, because of (2), it is overestimated by up to a factor 2.

In many cases, however, assuming (2) is not necessary and one rather sums up over the

flow region the ^{12}CO column densities obtained at each point using (1). As the above results show, adopting this procedure indeed removes an important source of error; it also provides a true *lower limit* to the mass in the flow.

In flows where a ^{13}CO profile is available, observers often relax the assumption of small optical depth and rather use the ^{12}CO to ^{13}CO line intensity ratio to derive τ, the ^{12}CO line optical depth, assuming equal excitation conditions for both species and a given abundance ratio (see for example [13]). To compute the total mass, one then generally multiplies the ^{12}CO mass obtained in the optically thin limit by the opacity correction factor $\tau/(1-e^{-\tau})$. Since in most cases ^{13}CO emission is only detected at a few locations in the flow, this procedure uses a value of τ that is probably greater than its mean value across the flow region. Therefore, this last method should be viewed as giving an *upper limit* to the mass in the flow.

We find that (3) gives a fairly good estimate of V_c at moderate view angles ($i < 50°$), but underestimates it at larger i (by up to a factor 1/4 if $\alpha = -1$). This error is due to projection effects and cannot be avoided unless the view angle is known. The error in P_c is thus similar to that in M_c except at large view angles where it is more underestimated.

4.3. Flow time scale and momentum input rate

Because (4) always underestimates the true length of an elongated flow (by a factor $1/\sin\theta_{max}$ at $i = 0°$), it also tends to underestimate T_c, especially at small view angles. The error introduced by (3) in the derivation of T_o and $\dot{P}_o$ is found to be much more critical and strongly dependent on the actual velocity field in the flow:

In *accelerated* outflows, (3) always overestimates the velocity at the base of the flow, by up to a factor 5. This results in dynamical time scales that are too small, and hence in values of the momentum input rate always in excess of their true values, by up to a factor 20 at small view angles.

In *constant* velocity outflows, V_o is never very far from $v(r_{min})$. The dynamical time scale is better determined in this case and the error on the rate of momentum input is the same as that on the total momentum : it is always underestimated, by up to a factor 10 when the optical depth is large.

The error factors given here were obtained for flows with $\sigma = 10$. But the fact that our integrated-intensity maps (see Fig.5a to 7a) only extend up to a distance 5 r_{min} shows that any similar model with $5 \leq \sigma < 10$ would give the same CO emission, and therefore the same *observed* parameters. On the other hand, M_c, P_c and T_c would be smaller, and hence less underestimated (or more overestimated) than previously. However, it is important to note that the final error in $\dot{P}_c$, which is what really matters, would remain *the same*, since this quantity is independent of the assumed value of σ.

According to the above analysis, a true lower limit to the CO mass and momentum in the flow can be derived from the ^{12}CO emission by computing the column densities in the optically thin limit and summing these contributions over the flow region. If a ^{13}CO profile is available, an upper limit to the mass can also be derived by applying an opacity correction to the first value. If we can put an upper limit i_o to the view angle (e.g. from HH objects radial and proper motion measurements), scaling the opacity-corrected value of the flow momentum by $1/\cos i_o$ should

yield an upper limit to this quantity. The actual flow length, and most of all the actual velocity field in the flow, remain critical parameters that should be determined before any reliable values of the time scales and momentum rates can be obtained with this method.

5. CONCLUSION

This model gives a better understanding of what can be expected and deduced from the geometry and emission characteristics of molecular outflows. Our code is now being improved to handle more complex geometries (thin shells) and velocity fields (decelerated flows), which will be investigated in our next papers. We will also attempt detailed comparisons of our computations with recent high-resolution CO observations. Only after such a study will we understand the structure and kinematics of bipolar flows and the constraints they put upon mass-loss mechanisms in pre-main sequence stars.

REFERENCES

[1] Lada, C.J. 1985, Ann. Rev. Astr. Ap. **23**, 267
[2] Cabrit, S., Bertout, C. 1986, Ap.J. **307**, 313
[3] Moriarty-Schieven, G., Snell, R.L., Strom, S.E., Schloerb, F.P., Strom, K.M. 1986, Submitted to Ap.J.
[4] Levreault, R.M. 1985, Tech. Rep. No. 85-1, Astr. Dept., University of Texas, Austin
[5] Goldsmith, P.F., Snell, R.L., Hemeon-Heyer, M., Langer, W.D. 1984, Ap.J. **286**, 599
[6] Leung, C.M. 1975, Ap.J. **199**, 340
[7] Sobolev, V.V. 1957, Soviet. Astr. AJ **1**, 678
[8] Bastian, U., Bertout, C., Stenholm, L., Wehrse, R. 1980, Astr. Ap. **86**, 105
[9] Loren, R.B., Wootten, A., Sandqvist, Aa., Friberg, P., Hjalmarson, A. 1984, Ap.J. **287**, 707
[10] Edwards, S., Snell, R.L. 1984, Ap.J. **281**, 237
[11] Bally, J., Lada, C.J. 1983, Ap.J. **265**, 824
[12] Jones, B.F., Cohen, M., Sirk, M., Jarrett, R. 1984, Astr. J. **89**, 1404
[13] Snell, R.L., Scoville, N.Z., Sanders, D.B., Erickson, N.R. 1984, Ap.J. **284**, 176

ANNEXE 3

CO LINE FORMATION IN BIPOLAR FLOWS.

II. DECELERATED OUTFLOW CASE AND SUMMARY OF RESULTS

Sylvie CABRIT and Claude BERTOUT

Institut d'Astrophysique de Paris

submitted to *Astrophysical Journal*

ABSTRACT

Following our previous study of accelerated and constant velocity fields, we now investigate CO line formation in decelerated bipolar flows. Spatial-velocity diagrams and integrated-intensity maps are presented for four spatial configurations. These results are used together with previous computations to put constraints on the velocity field and the large-scale structure of observed flows. Computed line profiles are also used to estimate the accuracy of various procedures for deriving the flow parameters from CO data. We find that the most accurate method allows us to estimate the flow force within a factor of $\sim$ 20 and the flow mechanical luminosity within a factor of $\sim$ 60. However, different procedures applied to the same set of CO data give parameter values that may differ by up to 3 orders of magnitude.

Subject headings: interstellar: molecules — line formation — stars: pre–main-sequence — stars: winds

I. INTRODUCTION

The presence of bipolar molecular flows around infrared sources of various luminosities (*cf.* Lada 1985 and references therein) shows that young stellar objects often undergo a phase of intense mass-loss during which molecular material is anisotropically accelerated to highly supersonic velocities. This energetic phenomenon, unpredicted by theories of star formation, may play a fundamental role in pre-main sequence evolution by carrying away a large fraction of the angular momentum originally contained in protostellar matter, and by limiting the final mass of the forming star.

Various models of mass ejection and flow collimation from protostellar objects have been proposed to explain the energetics and morphology of bipolar flows (see the reviews of Pudritz [1988] and Boss [1987]). CO line observations offer information about the flow structure and velocity field that should allow one to choose between these models. In order to exploit this information, we have developed a code that computes NLTE CO line formation in bipolar outflows with various velocity fields. In the first paper of this series (Cabrit and Bertout 1986; hereafter Paper I), we investigated CO line emission from biconical lobes with accelerated and constant velocity fields, and made a first study of uncertainties in the kinematic and dynamic flow parameters derived from CO data. The issue of parameter uncertainties is important because flow energetics give an indirect measure of the mass-loss from the underlying protostellar object — averaged over the flow lifetime — and may therefore be used to set constraints on the mechanism driving winds from young stellar objects (e.g. Lada 1985). In Paper I, we found that the simplest procedure used by early observers (from 1980 to about 1983) to derive kinematic and dynamic flow parameters did not give accurate estimates of the model parameters when we applied it to synthetic CO profiles and maps.

In this paper, we extend the analysis of Paper I to decelerated flows and summarize results obtained so far. The computational method is exposed in Section II, and synthetic CO maps for an example of decelerated flow are presented in Section III. These results are used together with those of Paper I to discuss observational constraints on the structure and velocity field of molecular flows (Section IV). The model that seems best able to reproduce the bulk of CO flow observations involves a bright high-velocity accelerated conical lobe surrounded by a slower low-opacity envelope. Section V summarizes various procedures currently used to derive flow parameters from CO observations and discusses

their respective accuracy. We found that the flow mass can now be determined within a factor of two and that results obtained using two of these procedures indeed bracket the correct values of flow kinematic and dynamic parameters.

II. METHOD

The assumed flow model is similar to that used in Paper I for accelerated and constant velocity flows, so that line computations for various velocity fields can be directly compared. We consider a high-velocity molecular flow expanding radially in a bicone of opening angle θ_{max}, inner radius r_{min} and outer radius $r_{max} = \sigma\ r_{min}$ (*cf.* Figure 1 of Paper I). The velocity field $\vec{v}(\vec{r})$ and H_2 density distribution $n_{H_2}(r)$ in the flow are given by

$$\vec{v}(\vec{r}) = v_{max}(r_{min}/r)^{\alpha}\ \vec{u}(\vec{r}), \qquad \text{where } \vec{u}(\vec{r}) = \vec{r}/r,$$

and

$$n_{H_2}(r) = n_{H_2}(r_{min})(r_{min}/r)^{\delta}.$$

Mass conservation within the flow is assumed, requiring that $\delta = 2 - \alpha$.

a) CO excitation:

We assume that CO level populations are in a steady-state. Statistical populations of the various rotational levels are then determined from the balance between collisional and radiative transition rates among these levels. The main colliding agent in interstellar molecular clouds is molecular hydrogen, at a kinetic temperature $T_k \sim$ 10-20 K. Besides cosmic background emission at 2.7 K, sources of radiation external to the high-velocity gas are: (i) black-body radiation from a central star or surrounding warm dust core, (ii) thermal emission from dust grains embedded within the flow, and (iii) CO line emission from the ambient molecular cloud. These three heating sources are nonetheless negligible, as we now show.

(i) The radiation field from a central source of radius r_c and temperature T_c could in principle increase the excitation of surrounding CO molecules by two mechanisms: (a) by directly stimulating radiative transitions among rotational levels of the ground state; and (b) by populating (through absorption of stellar infrared photons) the first excited vibrational state ($\sim$ 3000 K above ground level), from which molecules will spontaneously cascade back to excited rotational levels of the ground v = 0 state. However, because their effect is roughly proportional to the solid angle filled by the source, both mechanisms are inefficient except at short distances from the central object: less than $\sim r_c\sqrt{(T_c/130\,\mathrm{K})}$

for (a) and less than about 0.02 pc for (b) (Paper I; Carroll and Goldsmith 1981). We can therefore ignore them in our computation of the large-scale high-velocity CO excitation.

(ii) Assuming the dust temperature of 10 K typical of dark molecular clouds, as well as standard dust absorption law and dust-to-gas ratio (Leung 1975), one can compare the absorption coefficients and emissivities of dust grains to those of CO molecules at the frequencies of the rotational lines of CO. For the range of CO excitation temperatures expected in high-velocity flows, we find that the role of dust can also be neglected (Cabrit and Bertout 1987).

(iii) CO line photons emitted by the static ambient cloud appear Doppler-shifted in the high-velocity gas rest frame, and can be absorbed only if they propagate at an angle less than $\sin^{-1}(v_{th}/V)$ from the perpendicular to the local flow direction, where V is the outflow velocity and v_{th} the CO thermal line width. Since V ($\geq$ 10 km s^{-1}) is much larger than v_{th} ($\sim$ 0.1 km s^{-1} in our model), the corresponding solid angle $\delta\Omega = 4\pi v_{th}/V$ represents a very small fraction of the total solid angle. The contribution of ambient CO line radiation to high-velocity CO excitation is therefore much smaller than that of the cosmic background and is not included in our computations.

We conclude that high-velocity CO gas is heated mainly by cosmic background radiation at $T_b = 2.7$ K and by collisions with H_2 molecules at a constant kinetic temperature $T_k \sim 10$ K. Because the CO thermal width is much smaller than the flow expansion velocity, we adopt the Sobolev approximation to compute CO excitation in the flow (Sobolev 1957). In this limit, the mean radiation intensity can be expressed as the sum of the background intensity and the local value of the source function, weighted by coefficients that depend on the local photon escape probability (see Eq. 5 in Paper I). Equations of statistical equilibrium can then be solved independently at each point using an iterative method. The resulting non-LTE level populations at distance r from the star are entirely determined by the values of the following four parameters:

$$T_k,\ n_{H_2}(r),\ \alpha, \text{ and } k(r) = (8\pi^3/3h)\,\mu^2\,n_{CO}(r)\,r/v(r) = k(r_{min})\,(r_{min}/r)^{\delta-(\alpha+1)}.$$

One must be cautious, however, in adopting the local Sobolev approximation for a decelerated flow. When $\alpha > 0$, the radial velocity along a given direction $\vec{n}$ is not a monotonical function of position as it is for $\alpha < 0$, because the radial velocity gradient along $\vec{n}$ becomes zero at all positions where $(\vec{u}(\vec{r})\cdot\vec{n})^2 = 1/(1+\alpha)$. Hence, at any position $\vec{r}$ in the flow there exists a particular direction $\vec{n}$ along which the local radial velocity

gradient is zero and the Sobolev approximation does not rigorously hold. This singularity can however be safely ignored in the computation of the mean escape probability without causing major errors in the source function (Bertout 1977). A more profound implication is that two distinct regions of the flow may now have the same radial velocity along $\vec{n}$ and be radiatively coupled (*i. e.,* exchange CO line photons), which introduces a non-local contribution to the CO excitation.

Marti and Noerdlinger (1977) and Rybicki and Hummer (1978) worked out suitable generalisations of the basic Sobolev theory which take this radiative coupling into account. The vector formulation of the solution presented by Rybicki and Hummer makes it particularly useful for multidimensional geometries, and it was implemented in Bertout's (1979) code for solving the two-level atom line formation in axisymmetric envelopes. The role of radiative coupling was studied extensively with that code, and in most cases was found negligible for the source function computation. Radiative coupling becomes important only when the source function stays approximately constant over a large part of the envelope. In all cases where the line local excitation decreases with increasing radius (due *e. g.,* to dilution of the stellar radiation field or to decreasing density) we find that neglecting the radiative coupling generally results in a less than 10% effect on the emergent line flux from a spherically symmetric envelope. Because of the smaller solid angle sustained by the envelope, we expect the error to be even smaller in the biconical geometry considered here. Since computing the non-local coupling requires an integration over the whole envelope, the required computing time is an order of magnitude longer than in the case of a purely local source function (*cf.* Bertout 1979). Considering the many sources of uncertainties in our computations (CO/H_2 abundance ratio and CO to H_2 collision rates), we feel that the local approximation to the source function is sufficient for our purpose.

b) Line Profiles

Although we neglected non-local radiative interactions when determining CO excitation conditions, we did take them into account when computing emergent CO line profiles, the properties of which depend heavily on the detailed shape of constant velocity surfaces (*cf.* Rybicki and Hummer 1978). For that purpose, the algorithm of Paper I was modified to handle non-monotonical variations of the radial velocity along the lines of sight. This generalized algorithm was tested in the case of a spherical envelope with $\alpha = 0.5$ by comparing the total line flux, integrated over all lines of sight, with the flux given by

an independent code that was thoroughly tested beforehand (Bertout 1984). The results presented in this paper were obtained by computing emergent CO line profiles along 1600 lines of sight that mapped the flow area on a square grid of 40 by 40 points.

III. RESULTS

As shown in Paper I, the spatial configurations of a radial biconical outflow relevant to the line formation problem can be divided into four categories, depending on the values of both θ_{max} (the flow opening angle) and i (the angle between the flow axis and the line of sight). Hence, general properties of the CO emission for a given flow model can all be deduced from results obtained in four configurations representative of each of these categories. Figures 1–4 present results for the CO ($J = 1 \rightarrow 0$) emission from a decelerated flow with $v(r) \propto 1/r$ (*i. e.*, where $\alpha = 1$). The other parameters entering the computations have the following values: $\delta = 1$, $n_{H_2}(r_{min}) = 10^4$ cm^{-3}, $T_k = 10$ K, $k(r_{min}) = 2$, $\sigma = 5$, $\theta_{max} = 30^o$ in Figures 1–3, and $\theta_{max} = 60^o$ in Figure 4.

In each of the four figures, the upper panel shows a spatial-velocity diagram where contours of equal line temperature $T_l = c^2/2k\nu^2\left(I_\nu - B_\nu(T_b)\right)$ are plotted as a function of radial velocity and position along the flow axis. The lower panel shows contours of integrated blue-shifted (solid lines) and red-shifted (dashed lines) intensities, which trace the spatial distribution of high-velocity emission. In both maps, radial velocities have been normalized to v_{max}, and position offsets are in units of r_{min}. Note that the velocity and position axes in spatial velocity diagrams have been switched with respect to Paper I, so that the x-axis now corresponds to position offset along the flow axis (as in integrated-intensity maps). CO line emission from the static cloud itself has not been included in the spatial velocity diagrams, where it would appear as a narrow ($\sim$ 0.2 to 2 km/s FWHM width) horizontal band centered on zero velocity. The following paragraphs describe the characteristics of the CO emission for each flow configuration.

i) Case 1 ($i < \theta_{max}$ and $i \leq 90^o - \theta_{max}$)

This case is illustrated in Figure 1, where $i = 10^o$ and $\theta_{max} = 30^o$. Since $i < \theta_{max}$, central lines of sight intersect both cones of the flow, and resulting CO line profiles have a blue-shifted and a red-shifted component. The spatial-velocity diagram shows that the line wings are most prominent toward the central position. The maximum velocity in the profile gradually decreases as we look further away from the flow center, while the minimum velocity, which corresponds to emission from the slower outer layers of the flow, stays roughly constant with position. Since the flow is seen almost pole-on, the integrated-intensity map shows circular and overlapping contours of blue-shifted and red-shifted emission.

ii) Case 2 ($i \geq \theta_{max}$ and $i \leq 90^o - \theta_{max}$)

This case occurs only if $\theta_{max} \leq 45^o$ and is illustrated in Figure 2, where $i = 50^o$ and $\theta_{max} = 30^o$. The two cones now appear spatially separated. Each CO line profile probes only one high-velocity cone and is either blue-shifted or red-shifted, with a maximum radial velocity increasing progressively as one looks closer to the center of the flow. As a consequence and unlike in Case 1, the spatial-velocity diagram shows a sharp discontinuity between blue-shifted and red-shifted profiles on each side of the star. Another difference with Case 1 profiles is that low radial velocity emission is only found far out in the lobes. Profiles emitted close to the flow center only show high radial velocities and might, if actually observed, appear as a distinct high-velocity emission component displaced from the line core emitted by the static cloud. The integrated-intensity map has a clear bipolar structure with a blue and a red lobe of high-velocity emission symmetrically displaced from the central source.

iii) Case 3 ($i \geq \theta_{max}$ and $i > 90^o - \theta_{max}$)

Illustrated in Figure 3, where $i = 70^o$ and $\theta_{max} = 30^o$, this case represents flows oriented almost in the plane of the sky, where the blue-shifted cone (tilted toward us) has its rear side red-shifted, while the red-shifted cone (tilted away from us) has its front blue-shifted. The spatial-velocity diagram differs from Case 2 in that each CO line profile now extends from negative to positive velocities. The profiles are broadest next to the flow

center at the position of highest maximum radial velocity. The integrated intensity map shows two separate lobes, each with superimposed blue and red contours.

iv) Case 4 ($i < \theta_{max}$ and $i > 90^o - \theta_{max}$)

Whenever $\theta_{max} > 45^o$, this case replaces Case 2 as the intermediate configuration between Cases 1 and 3. It is illustrated in Figure 4, where $i = 50^o$ and $\theta_{max} = 60^o$, and can be understood as a flow almost in the plane of the sky where, because of their larger opening angle, the two cones still overlap along the central lines of sight. The spatial velocity map can be considered as the superposition of two maps: that of a Case 1 flow (with $\theta_{max} = 30^o$ and $i = 20^o$) and that of a Case 3 flow (with $\theta_{max} = 30^o$ and $i = 80^o$). The integrated intensity map also combines the characteristics of Cases 1 and 3 shown in Figures 1 and 3, *i. e.*, almost circular lobes overlapping toward the center of the flow and contamination of the blue and red lobes by red and blue emission further out.

IV. COMPARISON WITH OBSERVED FLOWS

a) Accelerated flows vs. decelerated flows

A comparison of the above results with Figures 2–5 of Paper I shows that integrated-intensity maps of a decelerated flow are similar to those of accelerated and constant velocity flows in the same spatial configuration. Integrated-intensity maps in fact only give information about the column density gradient in the flow and about the flow collimation and inclination from the plane of the sky. Spatial-velocity diagrams, on the other hand, differ widely from one flow model to the other, which makes them good indicators of the velocity field. Determining the velocity field of molecular flows would be extremely useful for putting constraints on possible mechanisms of flow ejection and collimation and for understanding the outflow's interaction with its surroundings. We will, therefore, attempt to determine which of the kinematic models investigated so far best reproduces the characteristics of observed flows in each configuration.

Possibly as a result of an observational selection effect, most high-velocity flows are observed almost pole-on (Case 1), where radial velocities and column densities are expected to be highest. Available spatial-velocity diagrams for flows that clearly appear to be in Case 1 (T Tau, LkH$_\alpha$198, AFGL490, MWC1080; R. Levreault, private communication) show a

smooth decline in line-wing maximum velocity as one looks further from the flow center. This corresponds to the behavior of a decelerated Case 1 model and contrasts with the behavior of an accelerated Case 1 outflow, where emission from the faster outer layers of the flow produces narrow high-velocity wings at the periphery of the lobes, or of a constant velocity Case 1 flow, which shows narrow high-velocity profiles almost independent of position (see Paper I).

Only a few well-studied outflows appear at higher inclination to the line of sight (*i. e.*, in Cases 2 and 3). These are L1551-IRS5, Orion B, and R Mon for Case 2 (*e. g.*, Moriarty-Schieven and Snell 1988; Sanders and Willner 1985; Bachiller, Cernicharo, and Martin-Pintado 1988) and B335 and RNO43 for Case 3 (Moriarty-Schieven 1988; Cabrit, Goldsmith, and Snell 1988). In these well-resolved flows, the large scale bipolar lobes appear highly collimated, with $\theta_{max} \leq 30^o$, and (except in RNO43, where the spatial resolution is inadequate for such a study) spatial-velocity diagrams show progressively higher radial velocities as one looks further from the center. These observations appear consistent with CO line computations for an accelerated bipolar flow, but not with a constant velocity or decelerated flow.

None of the simple kinematical models investigated in Paper I and here, therefore, seems able to simultaneously reproduce the observed properties of high-velocity flows in different configurations. There are several possible explanations to this situation:

(i) When the flow is viewed almost pole-on (Case 1), variations in velocity as a function of distance to the source affect spatial-velocity diagrams mostly through the flow's biconical geometry, because emission from the periphery of the lobes comes from points farther from the star. The shape of the diagram in this configuration is in fact much more sensitive to possible variations in velocity as a function of latitude. In contrast, spatial-velocity diagrams of flows that are more inclined to the line of sight (Cases 2 and 3) reflect mainly variations in velocity with distance from the flow source. A possible explanation for the observations is then that molecular flows are actually accelerated and that the apparent deceleration observed in pole-on flows is due to a decrease in flow velocity as one moves farther from the flow axis.

(ii) A variation on this model, recently suggested by Moriarty-Schieven and Snell (1988) for the L1551-IRS5 flow, is that high-velocity CO emission arises from a curved hollow shell of molecular material swept up by a latitude-dependent stellar wind with

velocity decreasing from the pole to the equatorial regions. Such a velocity field has been proposed to explain the forbidden line profile structure in T Tauri stars (Edwards *et al.* 1987) and was also suggested by the radial velocity progression of upper Balmer shell absorption features seen in the conical reflection nebula near the star R Mon (Jones and Herbig 1982). Because of the shell curvature, CO gas farther away from the star is impacted by wind ejected at higher latitudes and hence achieves a higher velocity. Moriarty-Schieven and Snell show that the combined variations in velocity magnitude and projection angle within the high-velocity shell result in an apparent acceleration if the flow is highly inclined to the line of sight. On the other hand, if the shell closes upon itself at some distance from the star (as would be expected if it results from the expansion of a "wind-bubble"; Weaver *et al.* [1977]; Sakashita and Hanami [1986]), the same flow seen pole-on should show lower radial velocities farther away from flow center.

(iii) Alternatively, we might be looking not at a homogeneous population of bipolar flows but rather at two groups with different opening angles: (a) a group of highly collimated flows ($\theta_{max} \leq 30°$) observed mainly in Cases 2 or 3 (as predicted by our model), where high-velocity gas would be accelerated with distance from the source; (b) a group of almost isotropic outflows (with opening angles $\theta_{max} \geq 60°$) which would make up the bulk of known "pole-on" flows. All investigated velocity fields would then be compatible with their observed spatial-velocity diagrams, because gas projected at the periphery of the lobes would be moving in a direction almost perpendicular to the line of sight and always have a small radial velocity. However, higher-resolution observations of pole-on flows are required in order to determine to which extent their poor apparent collimation is not due to a resolution effect[1].

---

[1] An excellent example of this effect is the NGC 2071 outflow, which seemed to be in Case 1 on a 90" resolution map but was later shown to be in Case 2 on maps made with 45" and 23" resolution (Snell 1987).

---

b) Hollow lobes vs. filled lobes

Another important question that has so far remained unsettled is whether the high-velocity CO gas is filling the flow lobes or is confined to their surface in a dense shell (Snell *et al.* 1984; Levreault 1985,1988; Moriarty-Schieven and Snell 1988). Case 2 appears the best choice of flow configuration for investigating this issue, because the front and rear

side of a hollow shell ought to give rise to two distinct velocity components of comparable intensity toward the flow axis, instead of the single high-velocity component of a filled lobe (see *e. g.,* Cabrit 1986). Only two Case 2 flows have been observed at an adequate resolution for such a study: the L1551-IRS5 outflow (Moriarty-Schieven *et al.* 1987; Uchida *et al.* 1987; Rainey *et al.* 1987; Moriarty-Schieven and Snell 1988; Fridlund *et al.* 1988) and the molecular flow around the young Herbig emission star R Mon (Bachiller, Cernicharo, and Martin-Pintado 1988). These two flows show remarkably similar properties: (1) their blue-shifted high-velocity lobe coincides with an optical cometary nebula illuminated by the central object, (2) low velocity CO emission (a few km s^{-1} from cloud velocity) is found mostly near the edges of the lobe, while high velocity emission is concentrated toward the flow axis, (3) high-velocity gas appears to accelerate linearly with distance along the flow axis.

These characteristics have been often interpreted in terms of hollow flow lobes. Low-velocity emission along the lobe edges then corresponds to gas that moves almost perpendicular to the line of sight, while high-velocity emission along the axis traces the front side of the shell in the blue lobe (and the rear side of the shell in the red lobe). However, the lower velocity component expected from the projection of the other side of the shell is not observed in either of the two flows. An explanation commonly invoked for the L1551-IRS5 outflow is that the second velocity component is hidden within low-velocity static ambient cloud emission, *i. e.,* that the inclination angle i is very close to $90^o - \theta_{max}$ (*e. g.,* Moriarty-Schieven and Snell 1988; Fridlund *et al.* 1988). But this explanation must be excluded for the R Mon flow because *no static emission* is detected toward the flow axis (as if most ambient material had been pushed aside or accelerated by the flow).

We therefore conclude that the lobes of the R Mon flow must be filled. The distinct spatial distribution of low and high-velocity CO gas can then be explained if high-velocity CO emission comes from rapidly moving molecular gas accelerated along the flow axis, while low-velocity emission at the edges of the lobes is actually tracing a slower molecular envelope at the flow boundaries. Note that this latitude-dependent velocity law is similar to the one invoked in the previous section to explain apparent variations in flow velocity field with view angle. The absence of detectable low-velocity CO emission toward the R Mon flow axis further requires that the slowly moving flow envelope have a low opacity in order to be seen only toward the cone edges, where its column density and total optical depth are maximum.

A similar filled-lobe model was already suggested by Levreault (1985) based on CO $J = 2 \rightarrow 1$ observations of L1551-IRS5. In this line, where the optical depth is higher than in $J = 1 \rightarrow 0$, limb-brightening of the low-velocity emission is much less apparent, which implies that low-velocity material is actually present toward the flow axis. Latitude-dependent velocity fields thus appear promising to explain both the apparent variation in flow's velocity field with viewing angle and the particular emission properties of two bipolar flows observed at high resolution. This model will be investigated in a forthcoming paper.

V. OBSERVATIONAL UNCERTAINTIES IN FLOW PARAMETERS

Since the discovery of bipolar molecular outflows a decade ago (Zuckerman, Kuiper, and Rodriguez-Kuiper 1976; Kwan and Scoville 1976; Snell, Loren, and Plambeck 1980), a variety of procedures have been developed to derive the flow's global properties (*e. g.*, its mass and momentum) from the high-velocity CO emission. One goal is to obtain the rates at which momentum and kinetic energy are transferred to the flow. This approach may help to constrain possible mass-loss mechanism in young stellar objects. However, it involves several sources of error (Lada 1985; Levreault 1988): (1) optical depth and excitation conditions of the CO transitions, (2) amount of outflowing gas that is projected at cloud velocity, (3) flow's velocity field, (4) flow's inclination to the line of sight (that affects both the radial velocities and the apparent lobe sizes). Whether useful estimates of the flow parameters can still be obtained with simplifying assumptions about geometry and velocity field remains an issue. While an answer may depend on the type of flow that is considered, investigating this problem in detail for a simple flow model helps identify and quantify the sources of error present in the derivation.

In Paper I, we found that the simplest possible method, when applied to our synthetic CO profiles, did not provide accurate estimates of the true parameters of our models. In this paper, we extend our study to seven procedures currently used by various investigators to derive molecular flow properties. We applied all procedures to the same sets of synthetic ^{12}CO and ^{13}CO ($J = 1 \rightarrow 0$) profiles, computed for a series of decelerated, constant, and accelerated flow models ($\alpha = 1, 0, -1$) that spanned a ^{12}CO optical depth range of 1 to 6. ^{13}CO excitation was computed assuming an isotopic ^{12}CO /^{13}CO ratio of 89. Assumptions used in the various methods are summarized below and their accuracy is discussed.

a) Mass determination

The column density N_{obs} of high-velocity H_2 molecules along a particular line of sight can be estimated in two ways.

(i) It can first be evaluated from the integrated intensity in the high-velocity wings of the ^{12}CO ($J = 1 \rightarrow 0$) line by assuming that the line is optically thin and thermalized at the kinetic temperature T_k, using

$$N_{obs} = \left[\frac{H_2}{^{12}CO}\right] \frac{3h}{8\pi^3\mu^2} \frac{1}{\Omega(T_k)} \int T_l^{12}(v)\, dv \tag{3}$$

where $\Omega(T_k) = x_o(T_k)(1 - e^{-h\nu/kT_k})\{J_\nu(T_k) - J_\nu(T_b)\}$, x_o is the fraction of molecules in the $J = 0$ level ($\sim kT_{ex}/h\nu$), $J_\nu(T) = h\nu/k\ (e^{h\nu/kT} - 1)^{-1}$, and μ is the dipole moment of the CO molecule.

(ii) In flows where a ^{13}CO profile is available (generally only at the position of peak integrated ^{12}CO intensity), the ^{12}CO to ^{13}CO intensity ratio in the line wings ($\sim$ 10-20; Levreault 1988) is significantly lower than the terrestrial ^{12}CO to ^{13}CO isotopic ratio of 89, which indicates that high-velocity ^{12}CO emission is saturated. Since ^{13}CO high-velocity emission is probably optically thin anyway, opacity-corrected H_2 column densities can be calculated at all positions from the observed ^{12}CO emission by assuming that the ^{13}CO / ^{12}CO integrated-intensity ratio is independent of position in the flow[2].

---

[2] N_{obs} then depends only on the [H_2 /^{13}CO] abundance ratio, which is the quantity directly inferred from molecular cloud observations.

$$N_{obs} = \left[\frac{H_2}{^{13}CO}\right] \frac{3h}{8\pi^3\mu^2} \frac{1}{\Omega(T_k)} \left(\frac{\int_{peak} T_l^{13}(v)\, dv}{\int_{peak} T_l^{12}(v)\, dv}\right) \int T_l^{12}(v)\, dv. \tag{4}$$

Once H_2 column densities have been obtained, the total H_2 mass in the flow can also be evaluated in two ways: (i) by assuming that the central line of sight is representative of the flow region, *i. e.*,

$$M_{obs} = N_{obs}(\text{center}) \times S_{obs} \times m_{H_2}, \tag{5}$$

where S_{obs} is the observed projected area of the flow, or (ii) by summing up the column densities over all observed positions if the flow has been sufficiently well sampled. We have then

$$M_{obs} = \sum (N_{obs}\ \delta S) \times m_{H_2}. \tag{6}$$

Apart from additional refinements to be discussed later in this section, all procedures used so far to estimate flow mass correspond to one of the four possible combinations of the above assumptions. The errors introduced by the four procedures in determining total flow mass M_c are displayed in the upper panels of Figures 5–7 as a function of the view angle i for a decelerated, accelerated, and constant velocity flow model with $\tau \sim 6$. The error is measured in orders of magnitude by $\log(M_{obs}/M_c)$. Each symbol in the plot corresponds to a different procedure, as summarized in Table 1. The true value of the flow mass was calculated analytically from

$$M_c = \omega\, f(\sigma)\, n_{H_2}(r_{min})\, r_{min}^3\, m_{H_2} \tag{7}$$

where $\omega = 4\pi\,(1-\cos\theta_{max})$, $f(\sigma) = (\sigma^{\alpha+1}-1)/(\alpha+1)$ if $\alpha \neq -1$, $f(\sigma) = \ln(\sigma)$ if $\alpha = -1$, and the other parameters were defined in §II.

We find that the most accurate mass estimates are obtained for the procedure shown as a solid square in Figures 5–7 (*e. g.*, Snell *et al.* 1984), which takes into account both ^{12}CO opacity (Eq. 4) and variations in column density over the flow area (Eq. 6). The mass estimate tends to be slightly too high in constant velocity and accelerated flows, but tends to be slightly too small in decelerated flows. This result is at first surprising: one would intuitively expect the derived mass to be always too high in optically thick flows, because the ^{13}CO /^{12}CO intensity ratio is measured at the position of peak ^{12}CO integrated intensity, where the optical depth should be larger than its actual mean value in the flow. But a detailed study of our complete set of synthetic profiles for the decelerated flow model shows that the ^{13}CO /^{12}CO ratio in fact peaks farther out in the flow, where it can be up to 5 times larger than at the ^{12}CO peak. This is probably because ^{13}CO integrated intensity reflects the true column density on the line of sight, while ^{12}CO integrated intensity reflects the velocity width of the profile when ^{12}CO is optically thick. If the flow is decelerated, the velocity width can decrease more steeply outwards than the column density, and the ^{13}CO/^{12}CO integrated intensity ratio will increase. This interpretation is supported by the reverse tendency observed in accelerated flow models, where the integrated intensity

ratio is maximum at a position closer to the center than that of the ^{12}CO peak. The ^{13}CO $/^{12}$CO ratio that is used is then larger than its mean value in the flow.

The procedure that sums up high-velocity ^{12}CO emission at all positions (Eq. 6) without attempting to correct it for opacity (Eq. 3) always gives a lower limit to the flow mass (*e. g.,* Edwards and Snell 1984). The accuracy of this method, shown as an open square in Figures 5–7, is primarily determined by the optical depth in the flow. The resulting estimate is fairly good in an optically thin flow but is about an order of magnitude too small when $\tau \geq 4$.

In contrast, the method that corrects for ^{12}CO opacity (Eq. 4) but uses only a central line of sight (Eq. 5) always gives an upper limit to the mass (*e. g.,* Bally and Lada 1983). The error in mass for this procedure, shown as a crossed box in Figures 5–7, is strongly dependent on the flow configuration. It increases from a factor 2 to 5 as the view angle i decreases from 70^o to 10^o.

By using only a central column density (Eq. 5) uncorrected for ^{12}CO opacity (Eq. 3) (*e. g.,* Calvet, Canto, and Rodriguez 1983), one combines the uncertainties present in the last two methods. As a result, the magnitude of the error depends both on the view angle and on the opacity in the flow. The derived mass (cross in Figures 5–7) will be either too small (in most cases) due to ^{12}CO optical depth or too large if $\tau \leq 1$ and $i \leq 40^o$. Similar results were found in Paper I for accelerated and constant velocity flows. Since the effect of this procedure is so hard to predict, it should not be used to derive constraints on the flow parameters.

The above analysis does not include recent attempts (*e. g.,* Snell *et al.* 1984; Levreault 1985; Margulis and Lada 1985) to determine the CO excitation temperature T_{ex} from ^{13}CO and ^{12}CO ($J = 2 \rightarrow 1$) to ($J = 1 \rightarrow 0$) line ratios instead of assuming thermalization in Eq. 3. Estimated values of T_{ex} typically range from 8 to 30 K. However, these measurements are still uncertain because ^{12}CO and ^{13}CO may not have identical excitation conditions if the mean H_2 densities in the flows are less than 10^4 cm^{-3}. The presence along the line of sight of regions with differing optical depth or temperature may also seriously affect the line ratios (Canto, Rodriguez, and Anglada 1987; Levreault 1988). As far as the mass estimate is concerned, the choice of a given value of T_{ex} does not appear critical, since the change in $\Omega(T)$ is small (less than a factor of 2 in the 8-30 K temperature range)

with respect to all other uncertainties entering the derivation. And Figures 5–7 show that accurate masses can indeed be found by assuming that $T_{ex} = T_k$.

More difficult when dealing with actual CO observations is to evaluate the amount of high-velocity emission within the ambient cloud line core. While most observers prefer to exclude completely this velocity range from their computations in order to get lower limits to the integrated intensity of high-velocity gas, some authors (*e. g.*, Bally and Lada 1983; Lada 1985; Margulis and Lada 1985) assume that the intensity of high-velocity gas emission is constant over the line core and equal to the average of the line temperature in the wings immediately outside this range. From the spatial velocity maps in Figures 1–4, it appears that this correction overestimates the flow mass in Cases 1 or 2 by at least a factor of 2 if there is no overlap between line core and high-velocity emission. Conversely, not correcting for hidden low radial velocity material in a Case 3 or Case 4 flow might underestimate mass by a similar factor if the high-velocity gas homogeneously fills the observed lobes. To avoid overestimating flow mass, one should first determine which configuration applies. Given our poor knowledge of the actual geometry of most observed flows and the rarity of Case 3 and Case 4 flows it seems quite reasonable at this point to ignore all emission within the line core.

In summary, we find that the true flow mass can be determined within 50% accuracy by summing up the contributions of all observed positions in the flow and then applying a global opacity correction to ^{12}CO column densities. Another possible approach consists in bracketing the actual value of the flow mass between the optically thin value (lower limit) and the opacity-corrected column density at the ^{12}CO peak times the flow area (upper limit). These two values typically differ by a factor of 30 in our models. We find that it is best not to attempt to correct for high-velocity material emitting within the ambient line core, although one might then underestimate the flow mass by a factor $\sim$ 2 if the flow has its axis highly inclined to the line of sight or is poorly collimated (Cases 3 or 4).

b) Kinematic parameters

Once column densities and flow mass have been determined, the total momentum P_{obs} and kinetic energy E_{obs} in the flow can be estimated in two ways:

(i) One can assume that material in the flow is moving at a space velocity similar to the maximum observed radial velocity V_{obs} (*e. g.*, Bally and Lada 1983), *i. e.*,

$$\begin{aligned} P_{obs} &= M_{obs} \times V_{obs} \\ E_{obs} &= \frac{1}{2} M_{obs} \times V_{obs}^2, \end{aligned} \tag{8}$$

(ii) With good signal-to-noise observations, one can use the information contained in each independent velocity channel and assume that material in the flow is moving at a space velocity equal to the radial velocity at which it is detected, as if the gas was flowing along the line of sight (*e. g.*, Margulis and Lada 1985),*i. e.*,

$$\begin{aligned} P_{obs} &= \sum \left(\int m_{obs}(v)\, v\, dv \right) \delta S \\ E_{obs} &= \frac{1}{2} \sum \left(\int m_{obs}(v)\, v^2\, dv \right) \delta S, \end{aligned} \tag{9}$$

$$\text{where } m_{obs}(v) = M_{obs} \times T_l^{12}(v) \times \left[\sum \left(\int T_l^{12}(v)\, dv \right) \delta S \right]^{-1}.$$

Note that the sum over all observed positions is restricted to a single term with $\delta S = S_{obs}$ if only a central line of sight is used (*cf.* Eq. 5).

Out of the eight possible combinations of the above assumptions with the four methods of mass determination presented in the previous section, only six have actually been used in practice, and are summarized in Table 1. Resulting errors in determining the models' momentum and energy are plotted in the second and fourth panels of Figures 5–7. Symbols used in the first panel remain unchanged if the kinematic parameters were derived from flow mass using the maximum observed velocity (Eq. 8), but are rotated by 90° if only radial velocities were used (Eq. 9). The correct values for the flow's momentum P_c and kinetic energy E_c were computed from

$$\begin{aligned} P_c &= \omega\, (\sigma - 1)\, v(r_{min})\, n_{H_2}(r_{min})\, r_{min}^3\, m_{H_2} \\ \text{and } E_c &= \omega\, g(\sigma)\, \frac{1}{2}\, v(r_{min})^2\, n_{H_2}(r_{min})\, r_{min}^3\, m_{H_2}, \end{aligned} \tag{10}$$

where $g(\sigma) = (\sigma^{1-\alpha} - 1)/(1-\alpha)$ if $\alpha \neq 1$ and $g(\sigma) = \ln(\sigma)$ if $\alpha = 1$.

In order to distinguish uncertainties entering the derivation of kinematic parameters from those affecting the mass determination, we will concentrate in the following paragraphs on results obtained with the two methods that most accurately determine flow mass, in conjunction with either Eq. 8 or Eq. 9.

Only taking into account the line-of-sight component of velocity (Eq. 9) always underestimates the true velocity of the emitting material. The error so introduced (solid diamonds in Figures 5–7) is due to projection effects and increases rapidly with the view angle i. The estimated flow momentum and kinetic energy are quite accurate at $i = 10^o$, but they become about one order of magnitude too small at $i = 70^o$.

On the other hand, adopting the maximum observed velocity tends to overestimate the mean velocity in the flow if an intrinsic velocity gradient is present, although this trend is weakened by projection effects. As a result, estimated momentum and energy (solid squares in Figures 5–7) are always too large until $i = 70^o$, where they approach their true values or may even be slightly smaller.

Actual values of the flow kinematic parameters thus almost always fall between estimates given by these two procedures. At small i, they are very close to the value obtained using line of sight velocities, while at large i the maximum observed velocity gives better estimates. Although neither of these procedures is particularly accurate, the use of both allows us to determine the flow's momentum within a factor ~ 5 and the flow's kinetic energy within one order of magnitude, provided mass is computed accurately.

c) Dynamic parameters

One empirical procedure (*e. g.*, Bally and Lada 1983; Snell *et al.* 1984) for estimating the input rate of a given flow parameter consists in dividing the total amount present in the flow by a characteristic flow time scale T_{obs} defined as the time needed to cross a characteristic flow dimension $< R >$ (usually the maximum projected radius of the flow, R_{obs}) at a velocity $< V >= P_{obs}/M_{obs}$. The force F_{obs} and mechanical luminosity L_{obs} in the flow are then determined by

$$\begin{aligned} F_{obs} &= P_{obs}/T_{obs} \\ \text{and } L_{obs} &= E_{obs}/T_{obs}, \\ \text{where } T_{obs} &=< V > / < R > . \end{aligned} \tag{11}$$

Another approach (*e. g.*, Edwards and Snell 1984; Calvet, Canto, and Rodriguez 1983) consists in estimating the mean rate of momentum and energy transfer along the flow by summing up the contributions of elementary momentum fluxes ($\propto T_l(v)\, v^2\, dv$) and kinetic energy fluxes ($\propto \frac{1}{2}\, T_l(v)\, v^3\, dv$) at all positions in the flow, and by dividing them by the observed length of the lobe R_{obs} :

$$\begin{aligned} F_{obs} &= 1/R_{obs}\ \sum\Big(\int m_{obs}(v)\, v^2\, dv\Big)\ \delta S \\ L_{obs} &= 1/R_{obs}\ \sum\Big(\int \frac{1}{2}\, m_{obs}(v)\, v^3\, dv\Big)\ \delta S. \end{aligned} \tag{12}$$

The actual momentum and kinetic energy input rates that are needed to bring outflowing material to its maximum velocity are [3]

---

[3]In Paper I, we considered only the momentum and energy input at the base of the flow ($r = r_{min}$), as would be appropriate if acceleration was due to external forces (*e. g.*, pressure gradients in the surrounding medium). F_c and L_c are then smaller than in Eq. 13 by a factor of σ^{α} and $\sigma^{2\alpha}$ respectively, and errors in F_{obs} and L_{obs} would be correspondingly higher.

$$\begin{aligned} F_c &= \omega\, v_{max}\, v(r_{min})\, n_{H_2}(r_{min})\, r_{min}^2\, m_{H_2} \\ \text{and } L_c &= \omega\, \frac{1}{2}\, v_{max}^2\, v(r_{min})\, n_{H_2}(r_{min})\, r_{min}^2\, m_{H_2}. \end{aligned} \tag{13}$$

From Eq. 10 and 13, we derive the correct time scales for momentum and energy input:

$$\begin{aligned} T_c(P) &= P_c/F_c = (r_{max} - r_{min})/v_{max} \\ \text{and } T_c(E) &= E_c/L_c = g(\sigma) r_{min}/v_{max}. \end{aligned} \tag{14}$$

Note that the formula for $T_c(P)$ is a direct consequence of mass conservation in the flow, while $T_c(E)$ depends on the velocity field in the flow and can be larger or smaller than $T_c(P)$. While the characteristic model input velocity is v_{max} for both time scales, the characteristic model transfer length is $(\sigma - 1)\, r_{min}$ (*i. e.*, the true length of the flow lobe) for momentum, and $g(\sigma) r_{min}$ for energy. The accuracy of the various methods for estimating F_c and L_c then depends on errors in the characteristic transfer length and velocity, combined with previous errors in the derivation of P_{obs} and E_{obs}.

Most investigators adopt the observed length of the flow lobe, R_{obs}, as a characteristic dimension, although Snell *et al.* (1984) use half the distance between the blue and red centroids (usually $\sim R_{obs}/2$). The first choice seems more appropriate to estimate $T_c(P)$, while the second would be more appropriate for $T_c(E)$ if the flow is decelerated. However, in observed flows where the actual velocity field is unknown, using R_{obs} seems more realistic because it gives a true average of the momentum and energy flux along the flow axis. In particular, it would give the correct value of the momentum and energy transfer rates if they were constant along the flow, while the second choice would systematically overestimate them by a factor of 2.

The main difference between the various methods lies in the choice of the characteristic input velocity $< V >$: If kinematic parameters are computed using the maximum observed velocity V_{obs} (Eq. 8), then $< V >= V_{obs}$. But if only line of sight velocities are used to compute the flow parameters (Eq. 12), the characteristic velocities for momentum and energy transfer will be $F_{obs}R_{obs}/P_{obs}$ and $L_{obs}R_{obs}/E_{obs}$ (the former being always smaller than the latter), which are both smaller than V_{obs}[4].

---

[4]Snell *et al.* (1984) use yet another characteristic velocity equal to the mean intensity-weighted line-of-sight velocity P_{obs}/M_{obs}, which is typically a factor of two smaller than $F_{obs}R_{obs}/P_{obs}$. However, this difference is compensated for by their choice of $R_{obs}/2$ as a characteristic dimension. Parameters obtained with this seventh method are therefore similar to those obtained using Eq. 12, and are not plotted in Figures 5–7.

Since R_{obs} increases and $< V >$ decreases as the flow is more inclined to the line of sight, estimated time scales become longer at higher view angles. However, the magnitude of the error is difficult to predict because R_{obs} also depends on the flow's opening angle (especially when the flow is seen pole-on) while $< V >$ also depends on the velocity field. We find that both time scales are always underestimated at small view angles ($i \sim 10^o$), but become overestimated at high view angles. Resulting errors in the dynamic parameters are plotted in the third and last panels of Figures 5–7 for the six methods studied in the previous section. The following paragraphs discuss errors for the two methods using the best mass estimates (filled symbols).

Since momentum and energy calculated from line of sight velocities were already lower limits to their true values, momentum and energy transfer rates obtained with the

same assumption (Eq. 12; solid diamonds in Figures 5–7) are always too small, by as much as a factor of 25 and 100 respectively when $i = 70^o$. At the same time, because kinematic parameters obtained with the maximum observed velocity V_{obs} were sufficiently overestimated, corresponding rates (Eq. 11; solid squares in Figures 5–7) remain too large as long as $i < 60^o$. At higher inclinations, the derived rates come closer to their true values due to projection effects, and even become a factor of 2 to 5 too small in decelerated flows. However, if the flow is in the Case 3 configuration (which is likely at such large view angles) and if θ_{max} can be independently estimated (*e. g.,* from the apparent flow's opening angle on the integrated-intensity map), it becomes possible to estimate the value of i and hence to correct V_{obs} for projection effects.

This procedure, which was recently applied by Cabrit, Goldsmith, and Snell (1988) to observed Case 3 flows, is based on the fact that the maximum blue-shifted and red-shifted velocities observed at a given point along the flow axis correspond to the line-of-sight velocities of the front and rear sides of the high-velocity lobe. If the lobe is assumed to be a cone in radial expansion from the star, the ratio R ≥ 1 of these velocities is equal to $\cos(i - \theta_{max}) \ / \ |\cos(i + \theta_{max})|$, and i can be derived from the ratio R using :

$$\tan i = \frac{R+1}{R-1} \times \frac{1}{\tan \theta_{max}}.$$

One can then correct the observed maximum velocity V_{obs} for inclination by dividing it by $\cos(i - \theta_{max})$. If such a correction is applied to models with $i > 60^o$, dynamical parameters obtained with V_{obs} remain upper limits even at large view angles.

Thus, the true dynamical parameters can also be bracketted between values obtained with these two procedures as long as V_{obs} is corrected for inclination at high view angles. Figures 5–7 show that the range of possible flow parameters between these two limits increases with view angle but remains less than a factor of 30 for F_c and less than a factor of 100 for L_c. Typical errors are of the order of 10 and 30 respectively.

V. SUMMARY

We extend here our earlier study of CO line formation in high-velocity bipolar flows to decelerated velocity fields. These results are used together with previous computations for accelerated and constant velocity fields to discuss observational constraints on the large-scale properties of bipolar flows. We find that the velocity field in observed flows seems to change with view angle : from decelerated in pole-on flows to accelerated in flows that are more inclined to the line of sight. We also discuss recent observations of the R Mon outflow, which suggest that the flow lobes are filled. The most promising model to explain these various aspects involves a bright high-velocity accelerated molecular jet surrounded by a low-opacity slower envelope. Such a latitude-dependent velocity field may naturally arise if high-velocity material along the flow edges is slowed down by friction with the surrounding medium. This model will be investigated in detail in a forthcoming paper.

Our model also allows us to estimate the accuracy of various methods currently used by observers to derive the parameters of bipolar flows from CO data. We find that flow mass can be determined within a factor of 2 by computing H_2 column-densities at all positions in the flow (assuming optically thin ^{12}CO emission in LTE) and by applying a global opacity correction, estimated from the ^{13}CO /^{12}CO intensity ratio at the peak of ^{12}CO integrated intensity. We also confirm within the limits of our model the suggestion by Margulis and Lada (1985) that the kinematic and dynamic parameters of the flow can be bracketted between a lower limit obtained by considering only the line of sight component of the velocities and an upper limit obtained by assuming that the entire flow moves at the maximum observed velocity, although correcting these latter values for inclination may be necessary at large view angles ($i > 70°$). Final uncertainties in model flow parameters are typically a factor of $\sim$ 5 for P_c, 10 for F_c and E_c, and 30 for L_c, provided flow mass is carefully estimated using the procedure outlined above. Actual uncertainties for observed flows are probably twice as large because of uncertainties in the choice of the velocity ranges where high-velocity emission dominates over static cloud emission.

Finally, we find that flow masses estimated with different procedures can differ by a factor $\sim$ 30 when applied to the same set of CO data. The resulting spread in estimated flow parameters then reaches two to three orders of magnitude. In view of this result, it becomes obvious that no clear understanding of the mass-loss mechanism will be gained

from the study of bipolar flow parameters unless one looks at a homogeneous set of data, with flow masses that involve the same assumptions and H_2 /CO abundance ratios.

TABLE 1

Various methods for deriving flow parameters from CO data

	Flow mass		Flow velocity	
Symbol in Fig. 5-7	Corrected for ^{12}CO opacity	Summed on all positions	Maximum velocity (else, intensity-weighted)	Ref.
Crossed square	yes	no	yes	1
Solid square	yes	yes	yes	2
Solid diamond	yes	yes	no	3
Open square	no	yes	yes	4
Open diamond	no	yes	no	5
Cross	no	no	no	6

References : 1: Bally and Lada (1983); 2: Lada (1985); 3: Margulis and Lada (1985); 4: Edwards and Snell (1982); 5: Edwards and Snell (1984); 6: Calvet, Canto, and Rodriguez (1983).

REFERENCES

Bachiller, R., Cernicharo, J., and Martin-Pintado, J. 1988, preprint

Bally, J., and Lada, C.J. 1983, *Ap. J.* , **265**, 824.

Bertout, C. 1977, *Astron. Astrophys.* , **58**, 153

Bertout, C. 1979, *Astron. Astrophys.* , **80**, 138

Bertout, C. 1984, *Ap. J.* , **285**, 269

Boss, A.P. 1987, *Ap. J.* , **316**, 721

Cabrit, S. and Bertout, C. 1986, *Ap. J.* , **307**, 313 (Paper I)

Cabrit, S. 1986, *Bull. Am. Astr. Soc.*, **18**, 1027

Cabrit, S. and Bertout, C. 1987, in *Protostars and Molecular Clouds*, Eds. T. Montmerle, C. Bertout (Saclay: CEA/Doc) p. 42

Cabrit, S., Goldsmith, P.F., and Snell, R.L. 1988, *Ap. J.* , **334**, 196

Calvet, N., Cantó, J., and Rodriguez, L.F. 1983, *Ap. J.* , **268**, 739

Cantó, J., Rodriguez, L.F., and Anglada, G. 1987, *Ap. J.* , **321**, 877

Carroll, T.J., and Goldsmith, P.F. 1981, *Ap. J.* , **245**, 891

Edwards, S., and Snell, R., 1982, *Ap. J.* , **261**, 151

Edwards, S., and Snell, R., 1984, *Ap. J.* , **281**, 237

Edwards, S., Cabrit, S., Strom, S.E., Heyer, I., Strom, K.M., and Anderson, E. 1987, *Ap. J.* , **321**, 473

Fridlund, C.V.M., Sandqvist, A., Nordh, H.L., et Olofsson, G. 1988, preprint

Kwan, J., and Scoville, N. 1976, *Ap. J.* , **210**, L39

Lada, C.J. 1985, *Ann. Rev. Astron. Astrophys.* , **23**, 267

Leung, C.M. 1975, *Ap. J.* , **199**, 340

Levreault, R. M. 1985, Unpublished Ph.D. Thesis, Department of Astronomy, University of Texas at Austin, *Tech. Rep.* No. 85-1.

Levreault, R.M. 1988, *Ap. J.* , submitted

Margulis, M.S., and Lada, C.J. 1985, *Ap. J.* , **299**, 925.

Marti, F., and Noerdlinger, P.D. 1977, *Ap. J.* , **215**, 247

Moriarty-Schieven, G.H., Snell, R.L., Strom, S.E., Schloerb, F.P., Strom, K.M., and Grasdalen, G.L. 1987, *Ap. J.* , **319**, 742

Moriarty-Schieven, G.H., 1988, Unpublished Ph.D. Thesis, Astronomy Department, University of Massachusetts, Amherst.

Moriarty-Schieven, G.H., and Snell, R.L. 1988, *Ap. J.* , **332**, 364

Pudritz, R.E. 1988, *Galactic and Extragalactic Star Formation*, Eds. R.E. Pudritz et M. Fich (Dordrecht: Kluwer Academic Publishers),p.135

Rainey, R., White, G.J., Richardson, K.J., Griffin, M.J., Gronin, N.J., Monkiro, T.S., Hilton, J., 1987, *Astron. Astrophys.* , **179**, 237

Rybicki, G.B., and Hummer, D.G. 1978, *Ap. J.* , **219**, 654

Sakashita, S., and Hanami, H. 1986, *Publ. Astr. Soc. Japan*, **38**, 879

Sanders, D.B., and Willner, S.P. 1985, *Ap. J.* , **293**, L39.

Snell, R.L., Loren, R.B., and Plambeck, R.L. 1980, *Ap. J.* , **239**, L17

Snell, R.L., Scoville, N.Z., Sanders, D.B., and Erickson, N.R. 1984, *Ap. J.* , **284**, 176.

Sobolev, V.V. 1957, *Soviet. Astr.* — *AJ*, **1**, 678

Uchida, Y., Kaifu, N., Shibata, K., Hayashi, S.S., Hasegava, T. 1987, *Star Forming Regions*, Eds. M. Peimbert et J. Jugaku (Dordrecht:Reidel), p. 287

Weaver, R., McCray, R., Castor, J., Shapiro, P., and Moore, R. 1977, *Ap. J.* , **218**, 377

Zuckerman, B., Kuiper, T.B.H., and Rodriguez-Kuiper, E.N. 1976, *Ap. J.* , **209**, L137

FIGURE CAPTIONS:

Fig. 1: Results for a cone opening angle of 30^o and an inclination angle $i = 10^o$, illustrating Case 1 (see text for values of other parameters). (*upper panel*) Spatial-velocity diagram showing contours of constant CO $J = 1 \rightarrow 0$ line temperature along the flow axis. Radial velocities are in units of v_{max} and position offsets in units of r_{min}. Lowest contour level, 0.1 K; second one, 1 K; step between other contours, 1 K. (*lower panel*) Contour map of integrated intensity in the blueshifted (solid lines) and redshifted (dashed lines) CO $J = 1 \rightarrow 0$ emission. Position offsets are in units of r_{min}. Lowest contour level 0.1 K $\times v_{max}$, step between contours, 0.2 K $\times v_{max}$.

Fig. 2: Same as Figure 1 for an inclination angle $i = 50^o$, illustrating Case 2.

Fig. 3: Same as Figure 1 for an inclination angle $i = 70^o$, illustrating Case 3.

Fig. 4: Same as Figure 1 for a cone opening angle of 60^o and an inclination angle $i = 50^o$, illustrating Case 4.

Fig. 5: Errors on flow parameters derived from CO line profiles for an optically thick decelerated flow model with $v(r) \propto 1/r$ ($\alpha = 1$) seen at various view angles (see text for values of other parameters). The error on a given quantity Q is measured by $\log(Q_{obs}/Q_c)$ where Q_{obs} is the value derived from the CO profiles and Q_c the correct value. Each symbol denotes a different procedure, as summarized in Table 1. Filled symbols are procedures that both use the best mass estimate, but assume either that all material is moving at the maximum observed radial velocity (solid square) or that material is flowing along the line of sight (solid diamond).

Fig. 6: Same as Figure 5 for an accelerated model with $v(r) \propto r$ ($\alpha = -1$).

Fig. 7: Same as Figure 5 for a constant velocity model ($\alpha = 0$).

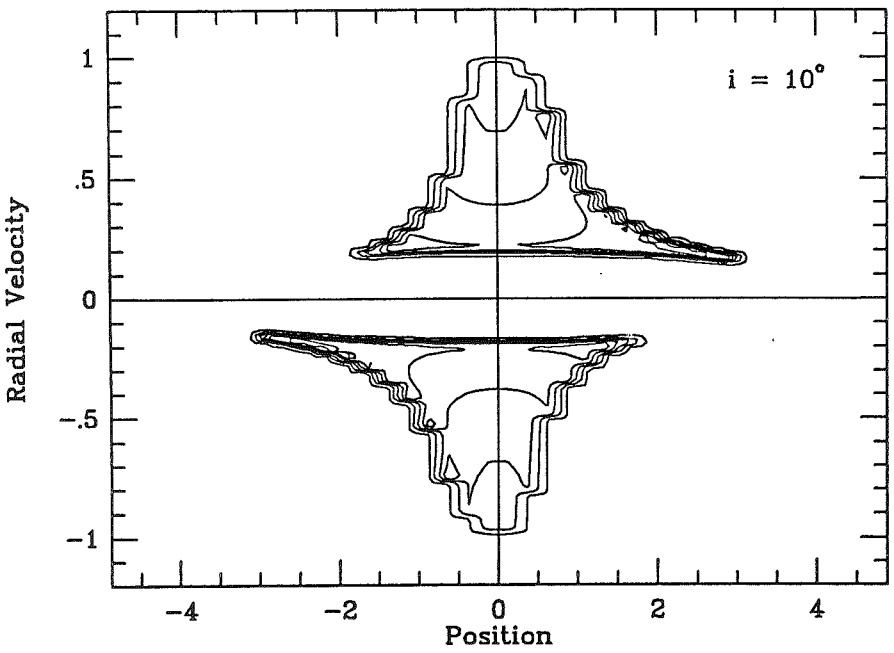
i = 10°
Radial Velocity
Position
1
.5
0
-.5
-1
-4
-2
0
2
4

Fig. 1

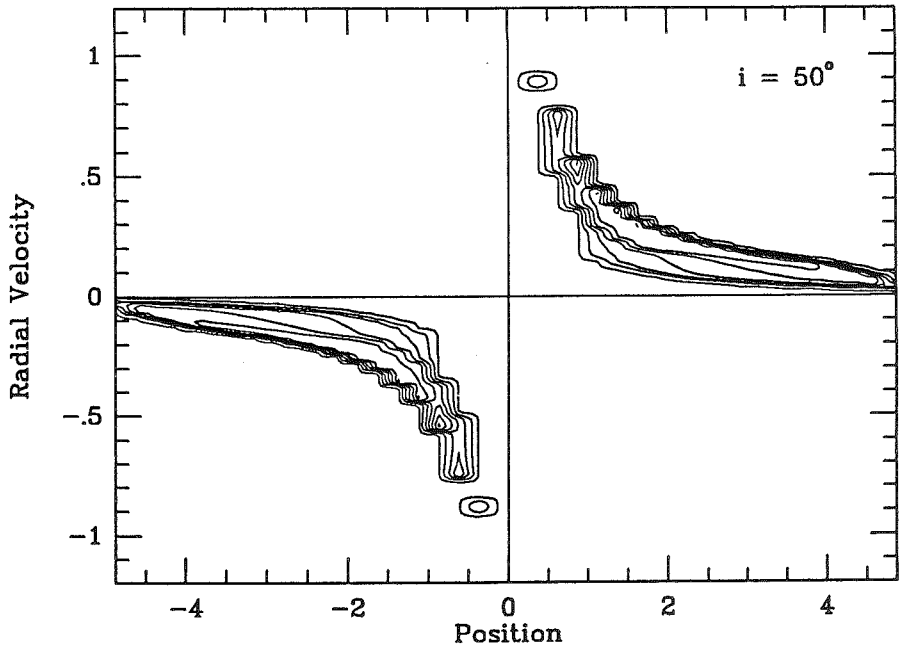
i = 50°
Radial Velocity
Position
1
.5
0
-.5
-1
-4
-2
0
2
4

Fig. 2

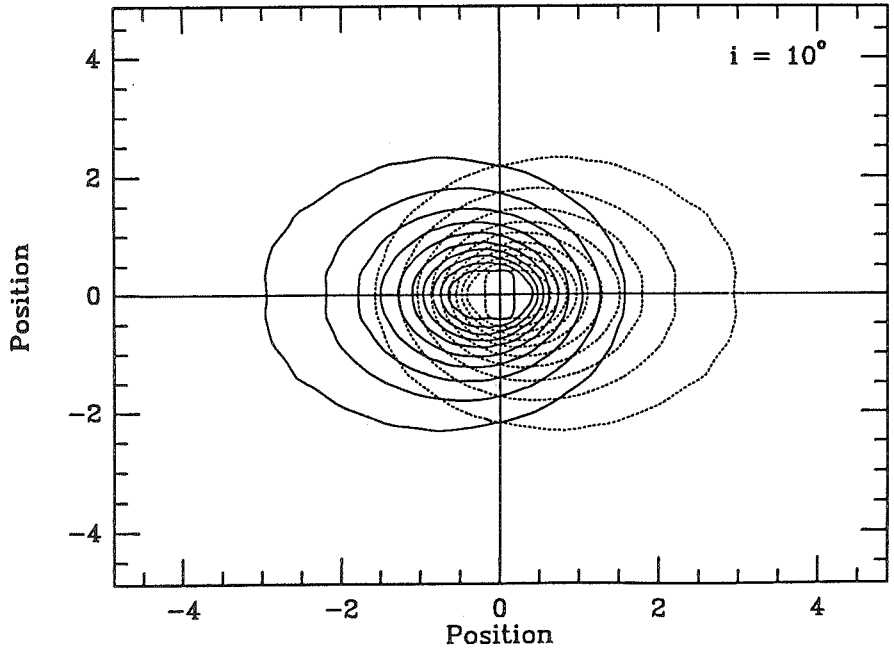
i = 10°
Position
Position
4
2
0
-2
-4
-4
-2
0
2
4

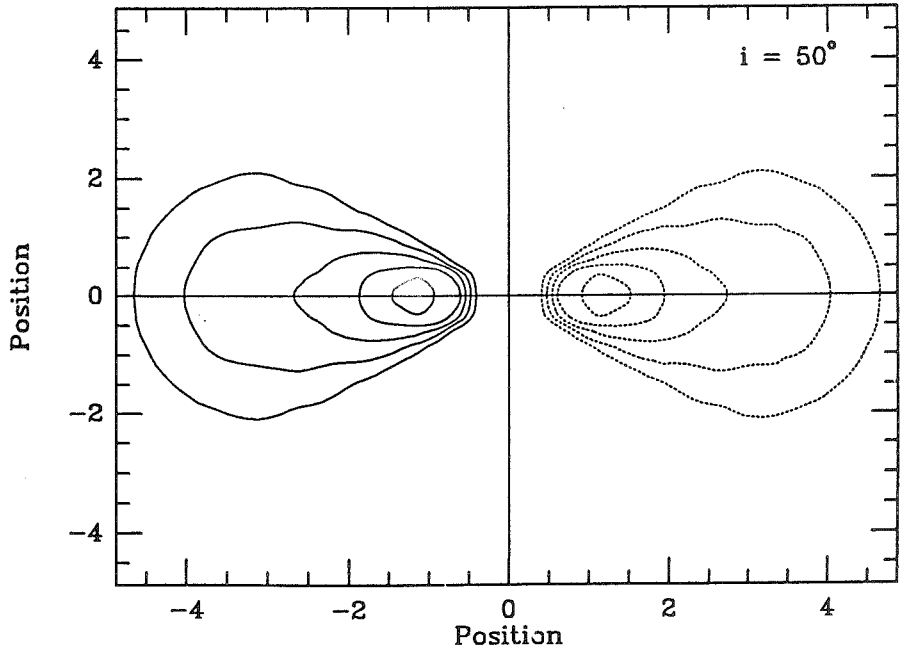
i = 50°
Position
Position
4
2
0
-2
-4
-4
-2
0
2
4

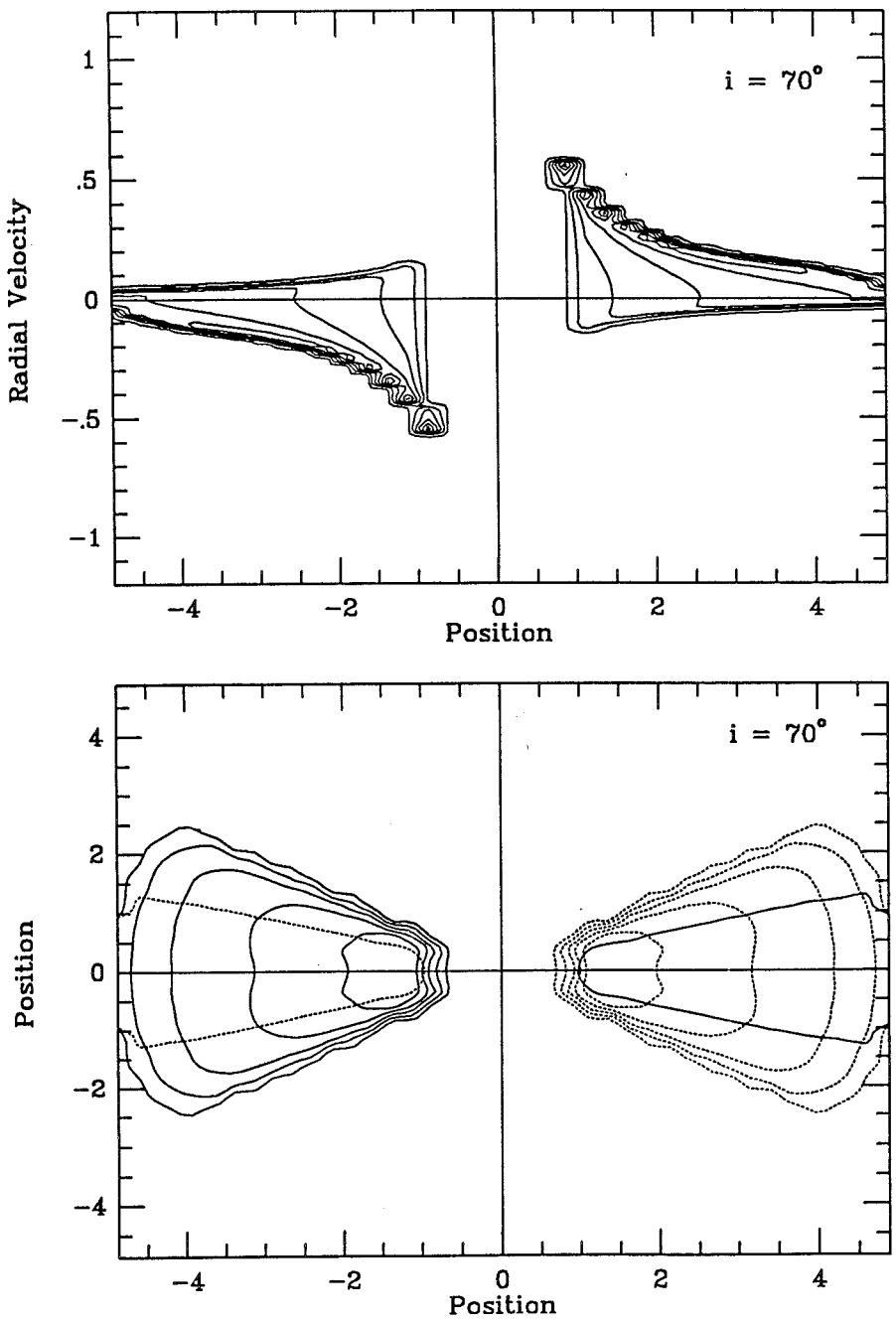
i = 70°
Radial Velocity
Position
1
.5
0
-.5
-1
-4
-2
0
2
4

Fig. 3

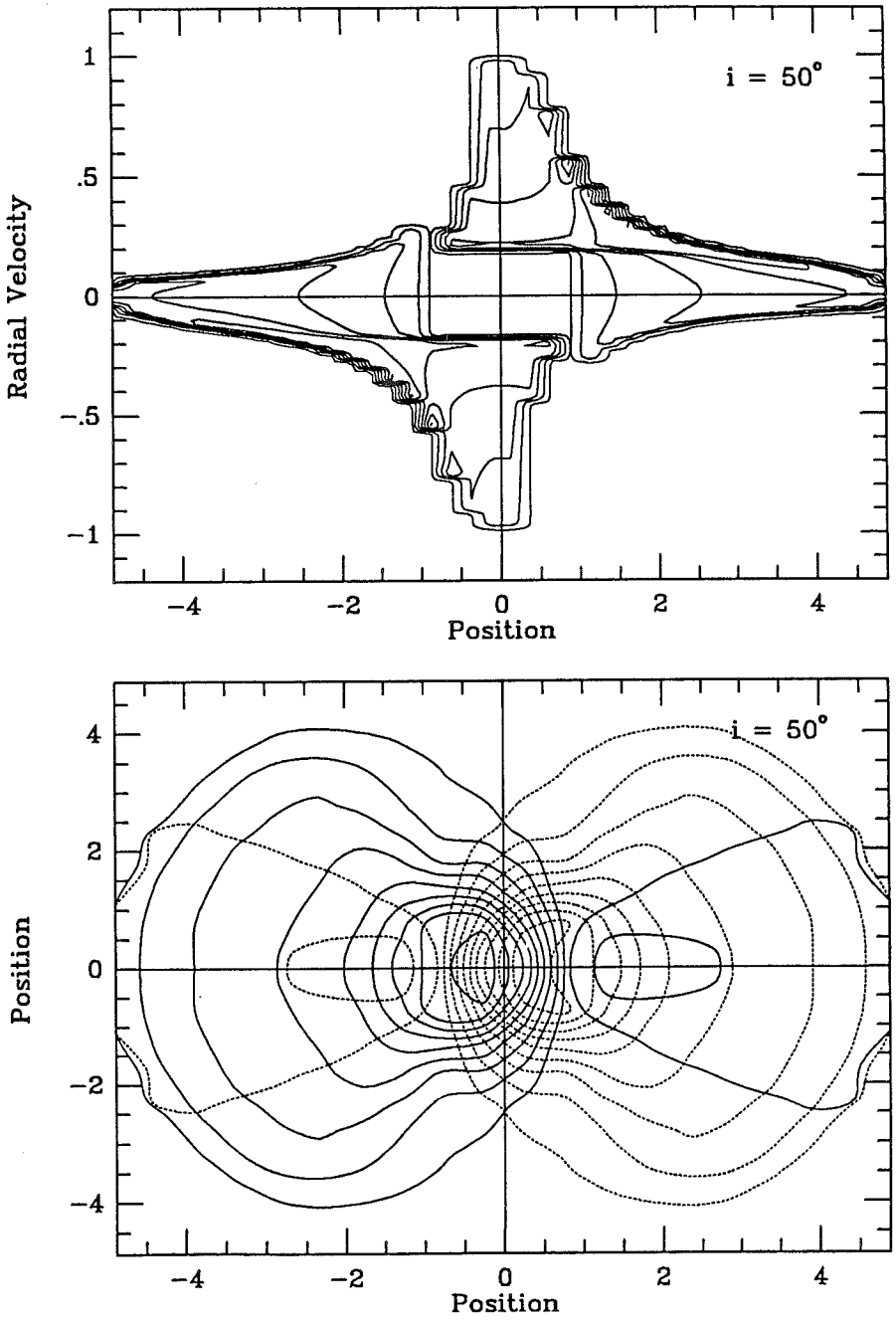
i = 50°
Radial Velocity
Position
1
.5
0
-.5
-1
-4
-2
0
2
4

Fig. 4

Fig.5

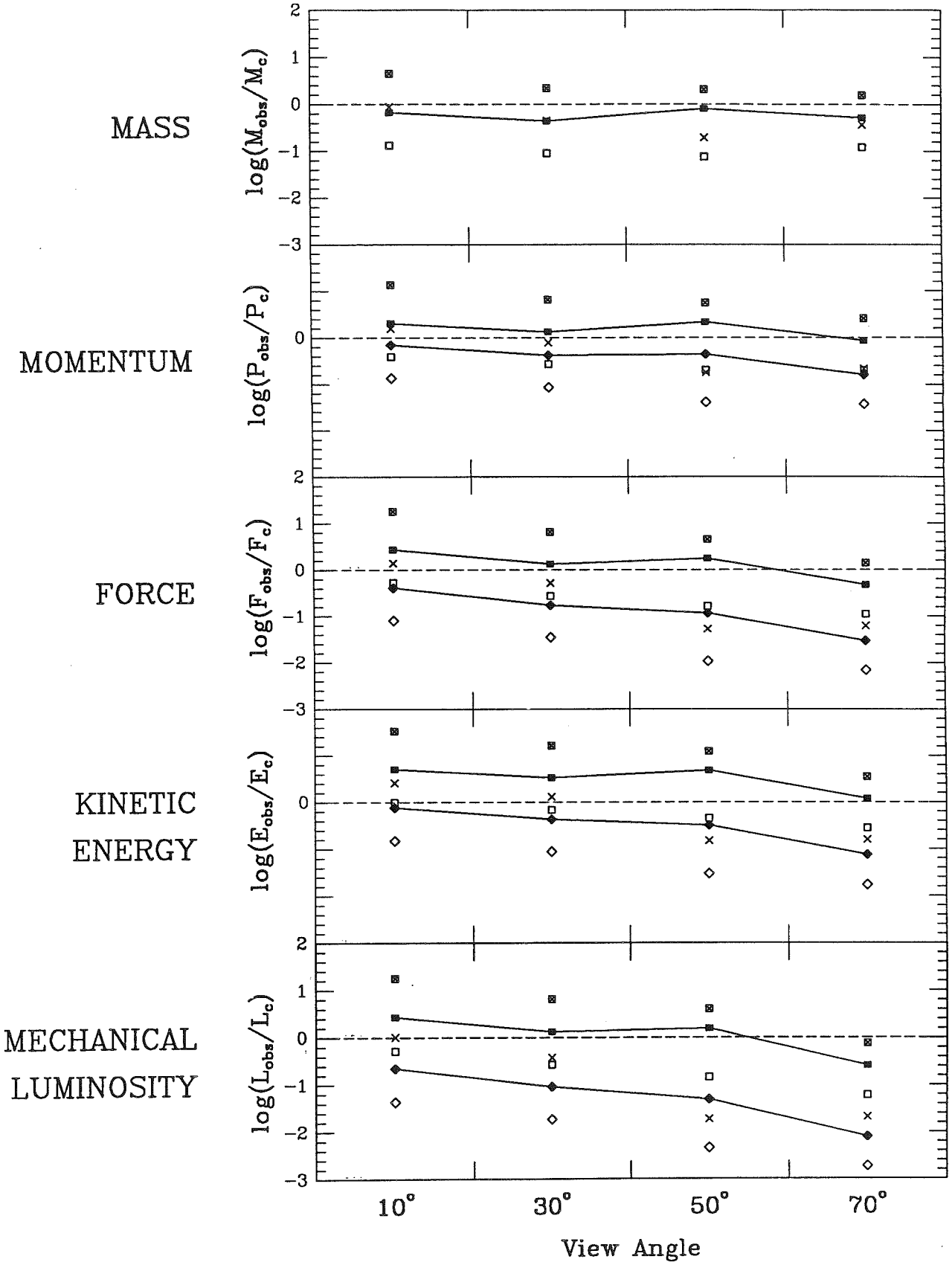
MASS
MOMENTUM
FORCE
KINETIC ENERGY
MECHANICAL LUMINOSITY
log(Mobs/Mc)
log(Pobs/Pc)
log(Fobs/Fc)
log(Eobs/Ec)
log(Lobs/Lc)
2
1
0
−1
−2
−3
10°
30°
50°
70°
View Angle

Fig.6

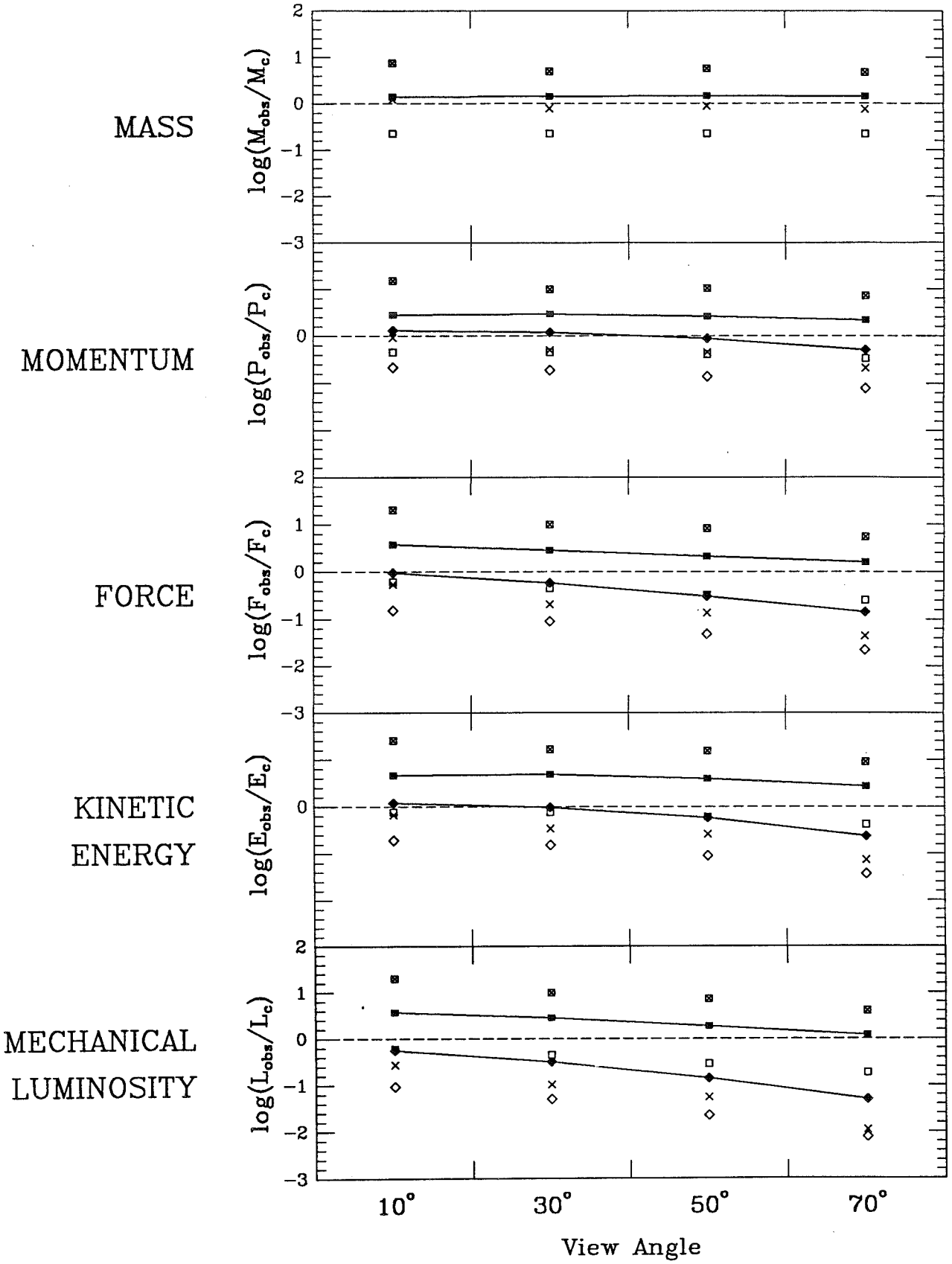
MASS
MOMENTUM
FORCE
KINETIC ENERGY
MECHANICAL LUMINOSITY
log(Mobs/Mc)
log(Pobs/Pc)
log(Fobs/Fc)
log(Eobs/Ec)
log(Lobs/Lc)
2
1
0
−1
−2
−3
10°
30°
50°
70°
View Angle

Fig.7

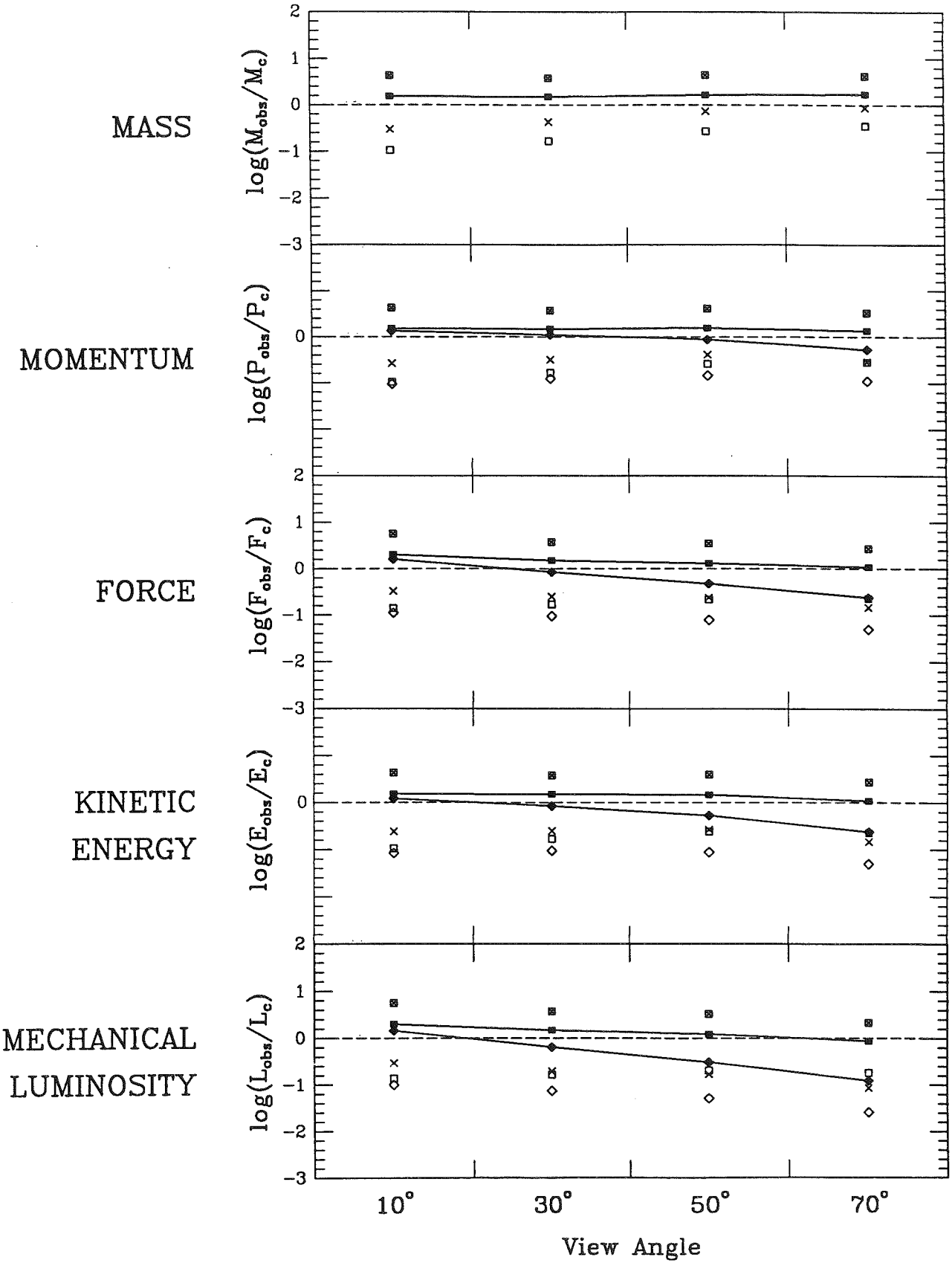
MASS
MOMENTUM
FORCE
KINETIC ENERGY
MECHANICAL LUMINOSITY
log(Mobs/Mc)
log(Pobs/Pc)
log(Fobs/Fc)
log(Eobs/Ec)
log(Lobs/Lc)
2
1
0
−1
−2
−3
10°
30°
50°
70°
View Angle

ANNEXE 4

The Large-Scale Structure of Bipolar Flows: Hollow Shells versus Filled Cones

S. Cabrit (Five College Radio Astronomy Observatory, and Institut d'Astrophysique de Paris)

Although many molecular flows have an obvious bipolar geometry, a major uncertainty is whether the high-velocity molecular gas fills the observed lobes or traces the surface of an expanding hollow shell. In order to discriminate between these two possiblities, we extend our theoretical study of CO line formation in bipolar flows to hollow shell geometries. We compute NLTE populations for the first 10 rotational levels of CO, assuming that statistical equilibrium has been established in the flow and that only collisions and absorption of local or cosmic background photons contribute to the high-velocity CO excitation. Several velocity fields and density distribution are investigated. The resulting profiles and maps of CO emission are presented and contrasted with our previous computations for the filled cone model. Both models are then compared with recent high-resolution observations of the L1551-IRS5 outflow and used to put constraints on the physical properties and large-scale structure of this bipolar flow.

Abstract of a poster paper presented at the 169^{th} meeting of the American Astronomical Society, 4-8 January 1987, Pasadena, California. (cf. Bull. Am. Astr. Soc. 1986, **18**, 1027)

The following figures present computed maps of the CO $J = 1 \rightarrow 0$ emission from a biconical flow where the lobe tilted toward the observer (solid lines) is *hollow* ($\theta_{min} = 15^o$ and $\theta_{max} = 25^o$) while the lobe tilted away from us (dashed lines) is *filled* ($\theta_{min} = 0^o$ and $\theta_{max} = 25^o$). The velocity field and density distribution in the flow are approximated by power laws: $v(r) \propto r^{-\alpha}$ and $n(r) \propto r^{-\delta}$, and mass conservation is assumed so that $\delta = 2 - \alpha$. Results are shown for several view angles and for both accelerated and constant velocity flows.

FIGURE CAPTIONS:

Figure 1*a-c*: Integrated-intensity maps of high-velocity CO $J = 1 \rightarrow 0$ emission for an accelerated flow with $\alpha = -1$ and $\delta = 3$. The view angle i between the line of sight and the flow axis is 10^o in Fig. 1*a*, 40^o in Fig. 1*b*, and 75^o in Fig. 1*c*, which corresponds to three different outflow configurations (Cases 1, 2, and 3). Position offsets are in units of r_{min}. Contour levels start at 0.1 K $\times v_{max}$ and increase by steps of 1 K $\times v_{max}$. Values of the other parameters entering the computations are: $r_{max} = 5\, r_{min}$; $n_{H_2}(r_{min}) = 10^4 \mathrm{cm}^{-3}$; $T_k = 10$ K;$k(r_{min} = 8\pi^3/3h\mu^2\ n_{CO}(r_{min})\, r_{min}/v(r_{min}) = 10^2$.

Figure 1*d-f*: Same as Figure 1*a-c* for a constant velocity flow with $\alpha = 0$, $\delta = 2$, and $k(r_{min}) = 10$.

Figure 2*a-c*: Same as Figure 1*a-c* for spatial-velocity diagrams which plot contours of constant line temperature as a function of radial velocity and position along the flow axis. Position offsets are in units of r_{min} and velocities in units of v_{max}. Contour levels start at 0.1 K and increase by steps of 1 K. Note that hollow lobes produce double- peaked profiles whenever $i > \theta_{max}$.

Figure 2*d-f*: Same as Figure 2*a-c* for a constant velocity flow with $\alpha = 0$, $\delta = 2$, and $k(r_{min}) = 10$.

Fig.1d

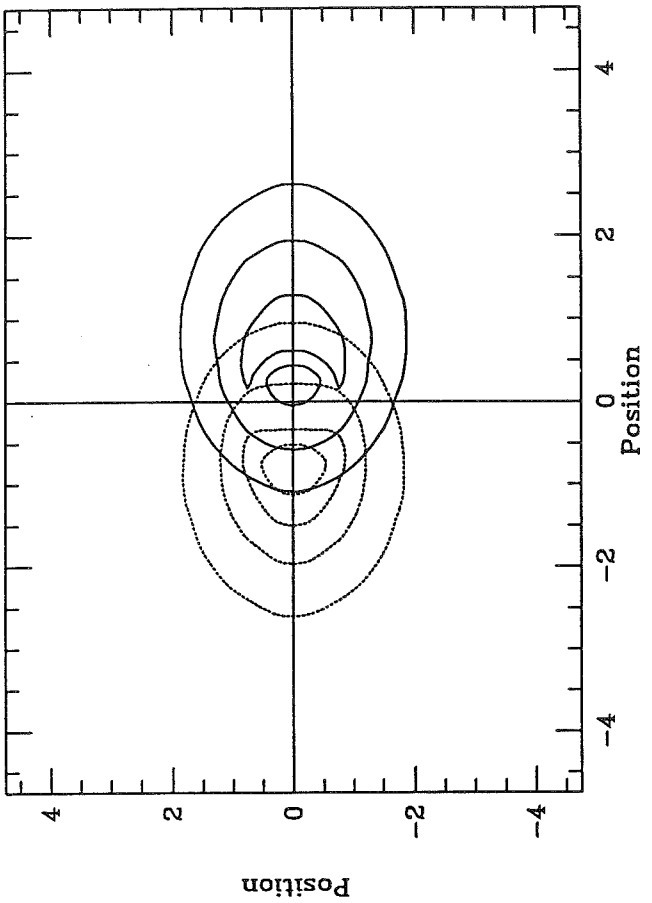

Fig.1e

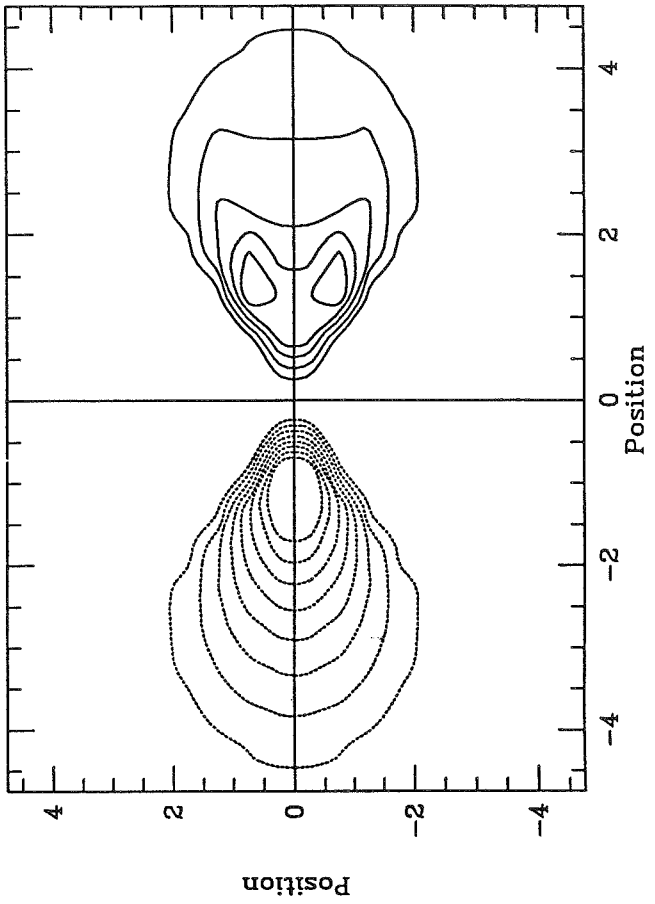

Fig.1a

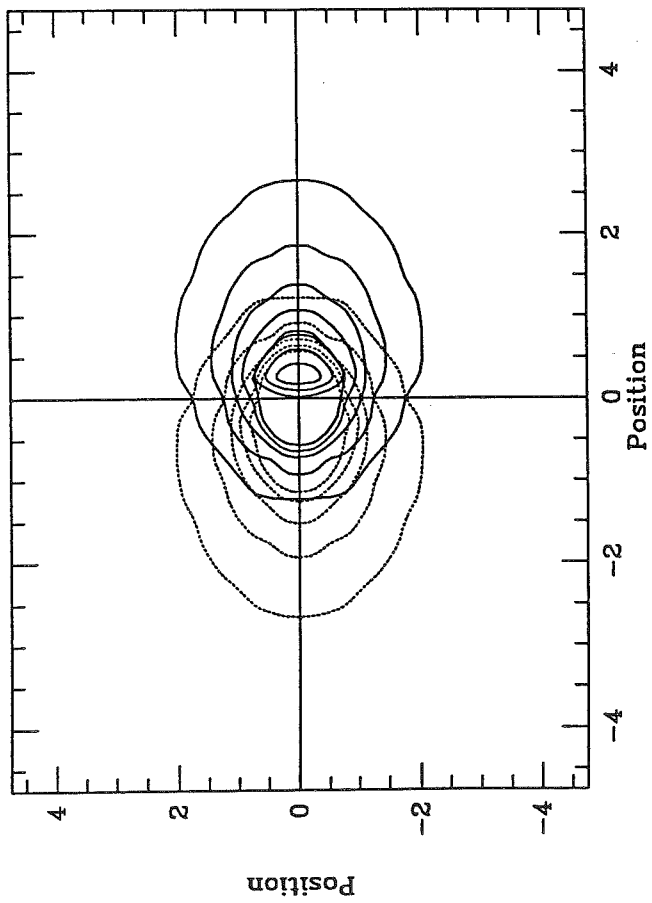

Fig.1b

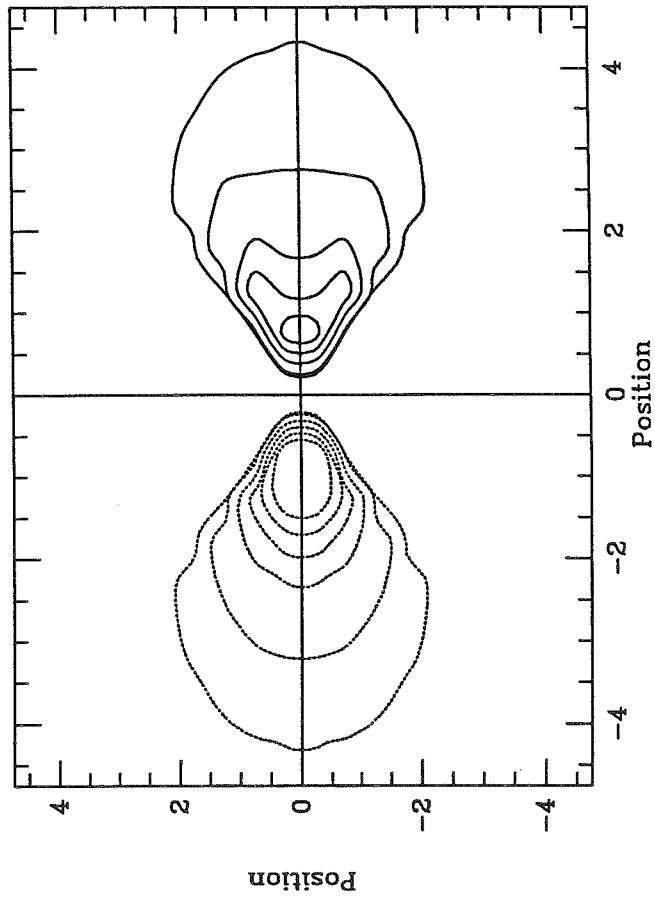

Fig.1f

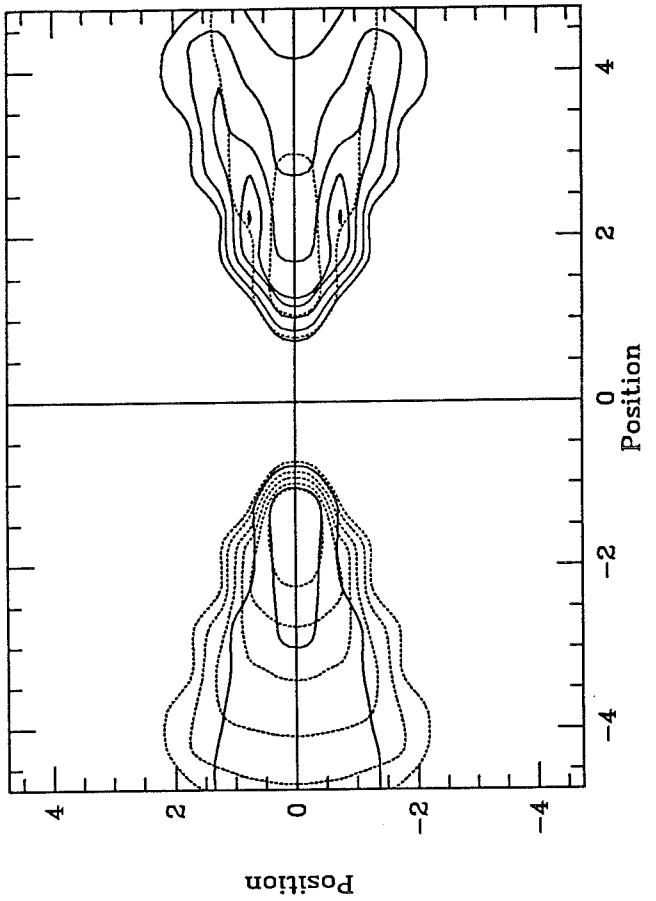
4
2
0
-2
-4
Position
4
2
0
-2
-4
Position

Fig.1c

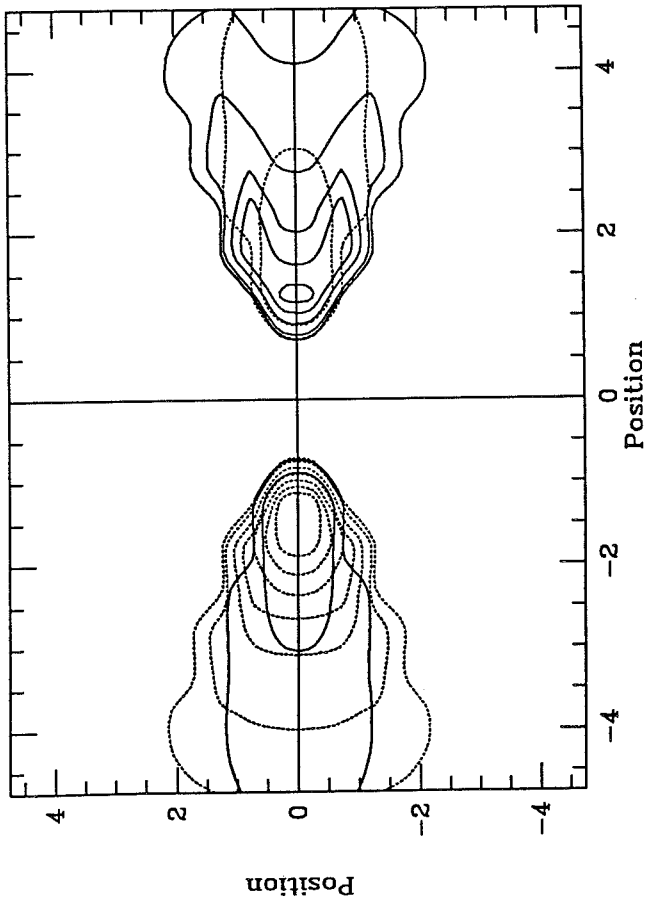
4
2
0
-2
-4
Position
4
2
0
-2
-4
Position

Fig.2d

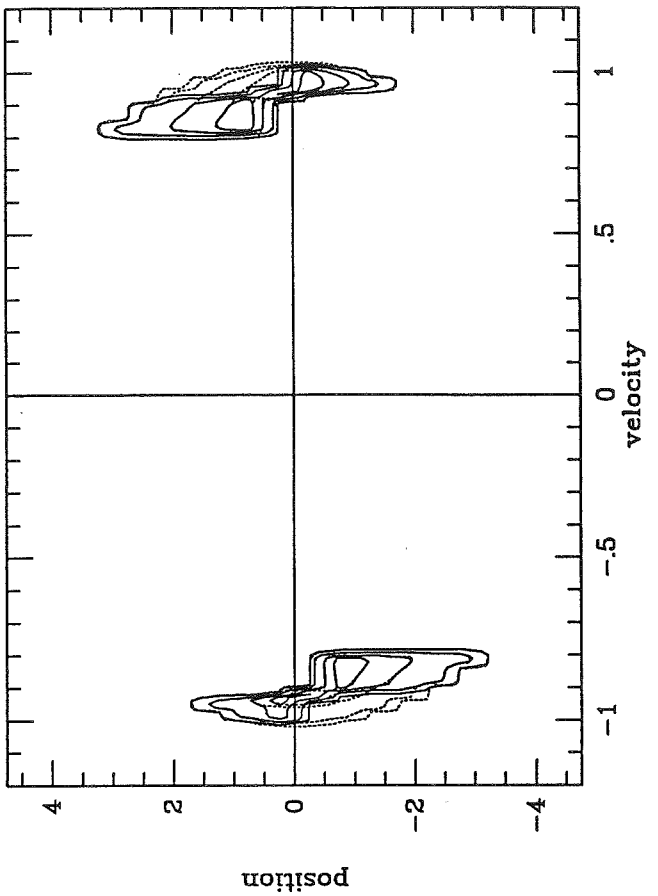

Fig.2e

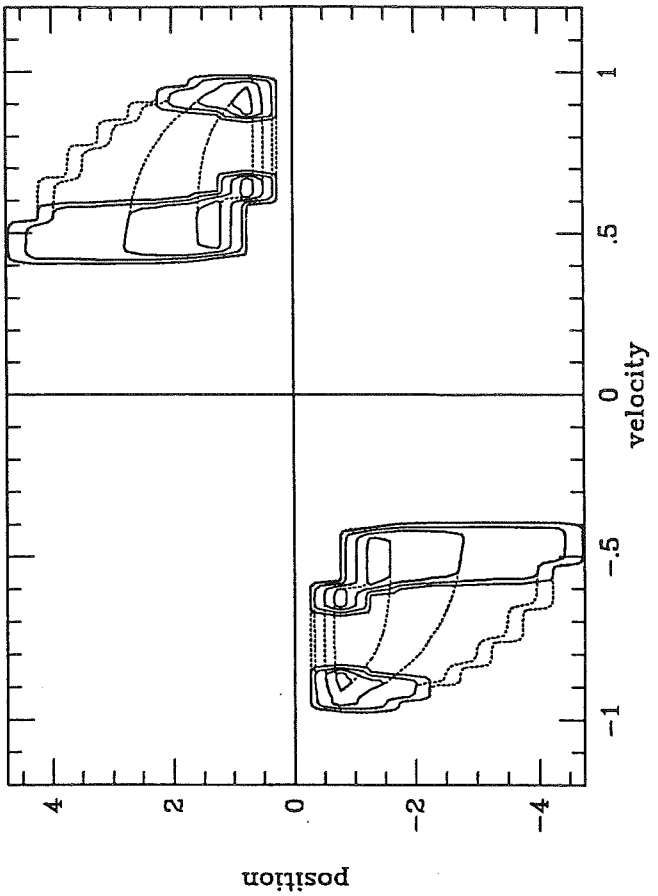

Fig.2a

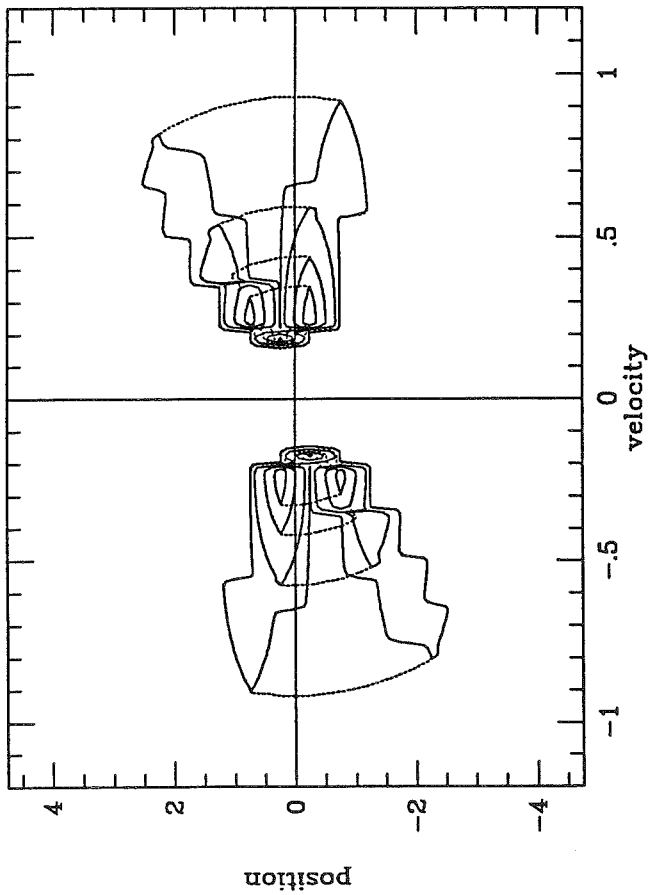

Fig.2b

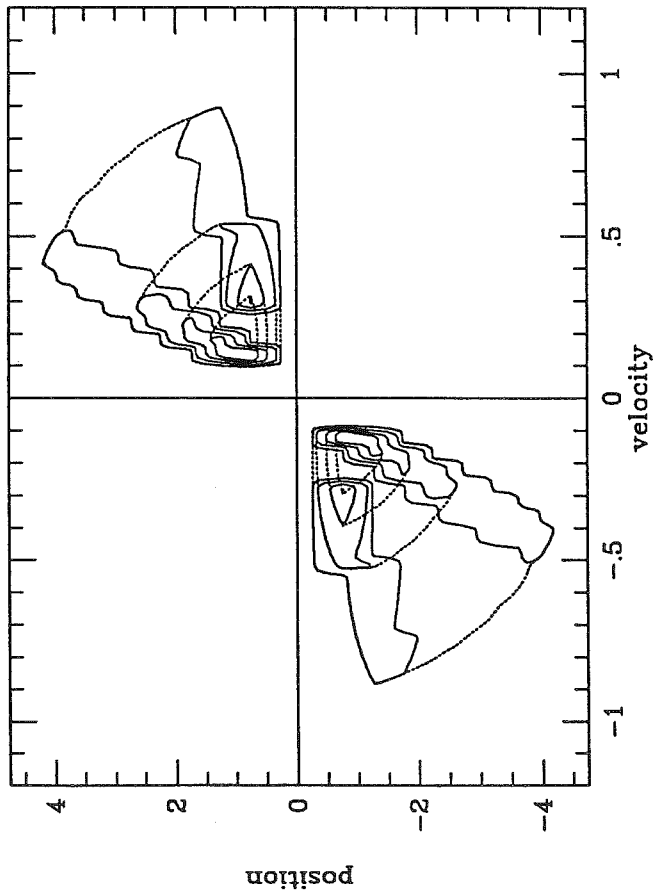

Fig.2f

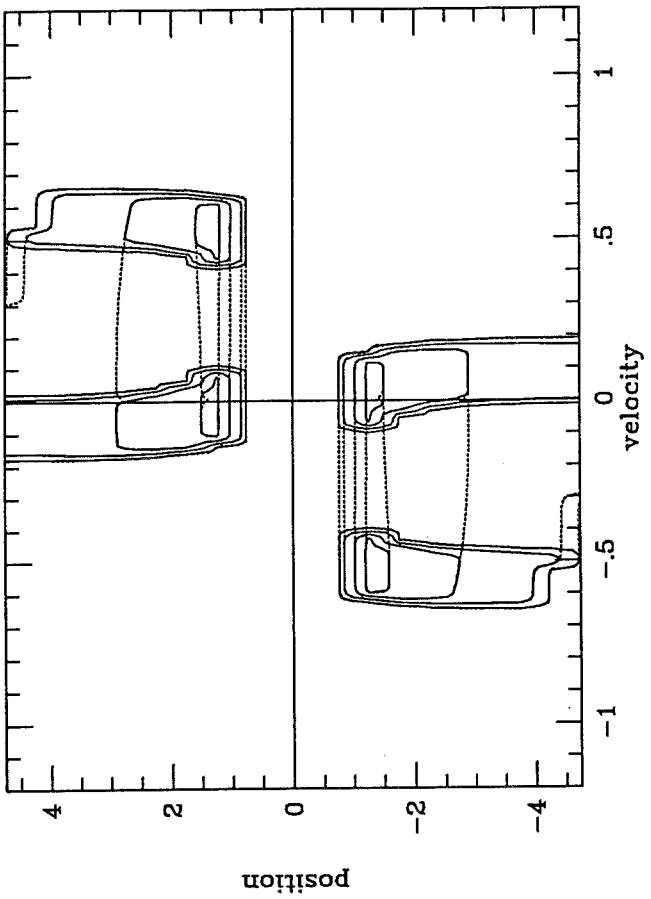
velocity
position
1
.5
0
-.5
-1
4
2
0
-2
-4

Fig.2c

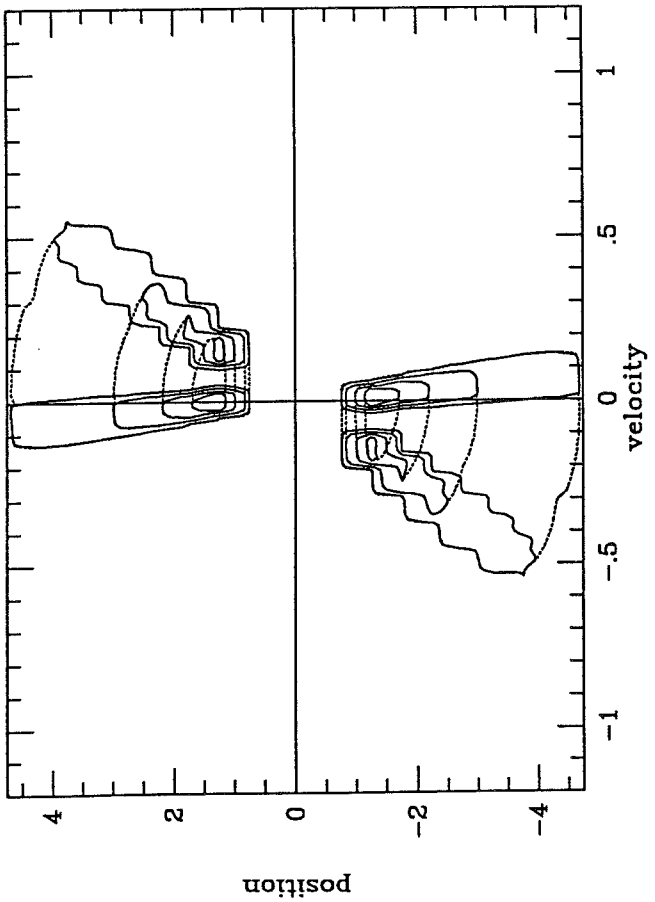
velocity
position
1
.5
0
-.5
-1
4
2
0
-2
-4

ANNEXE 5

THE ASTROPHYSICAL JOURNAL, 334:196–208, 1988 November 1

IDENTIFICATION OF RNO 43 AND B335 AS TWO HIGHLY COLLIMATED BIPOLAR FLOWS ORIENTED NEARLY IN THE PLANE OF THE SKY

SYLVIE CABRIT,[1,2] PAUL F. GOLDSMITH,[1,3] AND RONALD L. SNELL[1,3]

Received 1988 January 25th; accepted 1988 April 12

ABSTRACT

The RNO 43 and B335 molecular outflow regions both show a complex high-velocity emission pattern, previously attributed to several independent outflows. We present new CO and CS line observations which demonstrate that RNO 43 and B335 are in fact single highly collimated bipolar flows oriented nearly in the plane of the sky. We estimate the view angle between the line of sight and the flow axis to be 85° in RNO 43 and 82° in B335. We also study in detail the dynamics, the collimation, and the large-scale structure of the high-velocity lobes. In particular, we find that each of these flows must have a significant expansion velocity perpendicular to its axis, and that the flow in B335 must be driven by a mostly nonmolecular wind component.

Subject headings: interstellar: molecules — nebulae: internal motions — stars: winds

I. INTRODUCTION

Recent millimeter and optical studies of star-forming regions have provided strong evidence that many young stellar objects are undergoing a phase of energetic outflow activity (see, for example, Lada [1985] and Edwards and Strom [1987] for reviews). CO line observations have proved especially useful as a probe of the physical properties, spatial distribution, and kinematics of the expanding molecular gas surrounding young stars. In many cases, these observations reveal an anisotropic distribution of the high-velocity gas, with blueshifted and redshifted emission symmetrically displaced with respect to the star, indicating that the flows have a bipolar geometry. The spatial extent of the CO emission can also be used to estimate the age of the large-scale molecular flow, and thus the average rates at which momentum and energy have been transferred to it. Using these simple estimates, the rate of momentum transfer to the flow appears typically 10–100 times higher than what can be expected from a radiatively driven stellar wind. In fact, the rate of energy input seems comparable to the amount needed to support the ambient cloud against gravitational collapse (Lada 1985; Snell 1987). Obtaining reliable values of these rates for a large sample of objects is therefore crucial if we want to understand the mass-loss mechanism in pre–main-sequence stars and its consequences for the cloud evolution.

It is especially important that the geometry of the flow be well determined: a misinterpretation of the observed structure will lead to erroneous estimates of the flow extent and age, resulting in large errors in the momentum and energy input rates. Computations of CO line formation in biconical flows with radial expansion (Cabrit and Bertout 1986) show that, for a given flow geometry, the appearance of the CO map is critically dependent on the value of the view angle i and of the flow semi-opening angle θ_{max}. Four cases are distinguished by Cabrit and Bertout (1986); in one extreme case, the flow is viewed almost down its axis, or "pole-on," ($i < \theta_{max}$) and the blue and the red lobes are circular and overlapping, whereas in the opposite extreme case the flow is viewed nearly perpendicular to its axis, or "face-on" ($i > 90° - \theta_{max}$) and appears as two spatially distinct high-velocity components with superposed blue and redshifted emission, due to the projection of the front and back sides of the lobes on each side of the star. This second geometry, of particular importance for the present study, is illustrated in Figure 1. The remaining two cases correspond to intermediate view angles, respectively for large ($\geq 45°$) and small ($<45°$) values of θ_{max}. Most observed outflows show a blue and a red lobe, often overlapping near the center but otherwise well separated, and thus are either in the pole-on or the intermediate cases (Cabrit and Bertout 1987). More difficult to interpret are the configurations where the outflow region shows a multiple pattern of superposed blueshifted and redshifted emission, as seen in the RNO 43 and B335 regions (Edwards and Snell 1984; Langer, Frerking, and Wilson 1986). In both regions, the high-velocity emission has been attributed to two independent outflows. However, the locations of the prominent infrared sources in B335 and RNO 43 as well as recent Herbig-Haro object proper motion measurements in RNO 43 (Jones *et al.* 1984) do not support this interpretation (see § III).

Alternatively, the apparent multiplicity of the outflow pattern could be produced by a *single large-scale bipolar outflow* observed in the "face-on" configuration described above. In order to investigate this possibility, we mapped in ^{12}CO the predicted extent of these large-scale flows using the 14 m telescope of the Five College Radio Astronomy Observatory.[4]

Our observing method is presented in § II. Our results, summarized in § III, confirm that B335 and RNO 43 are indeed single bipolar outflows oriented almost perpendicular to the line of sight. The implications of this interpretation for the structure and dynamics of these molecular flows are discussed in § IV.

[1] Five College Astronomy Department, University of Massachusetts.
[2] Institut d'Astrophysique de Paris, and Ecole Normale Supérieure, Paris.
[3] Five College Radio Astronomy Observatory, Department of Physics and Astronomy, University of Massachusetts.

[4] The Five College Radio Astronomy Observatory is supported by the National Science Foundation and the Commonwealth of Massachusetts and is operated by permission of the Metropolitan District Commission.

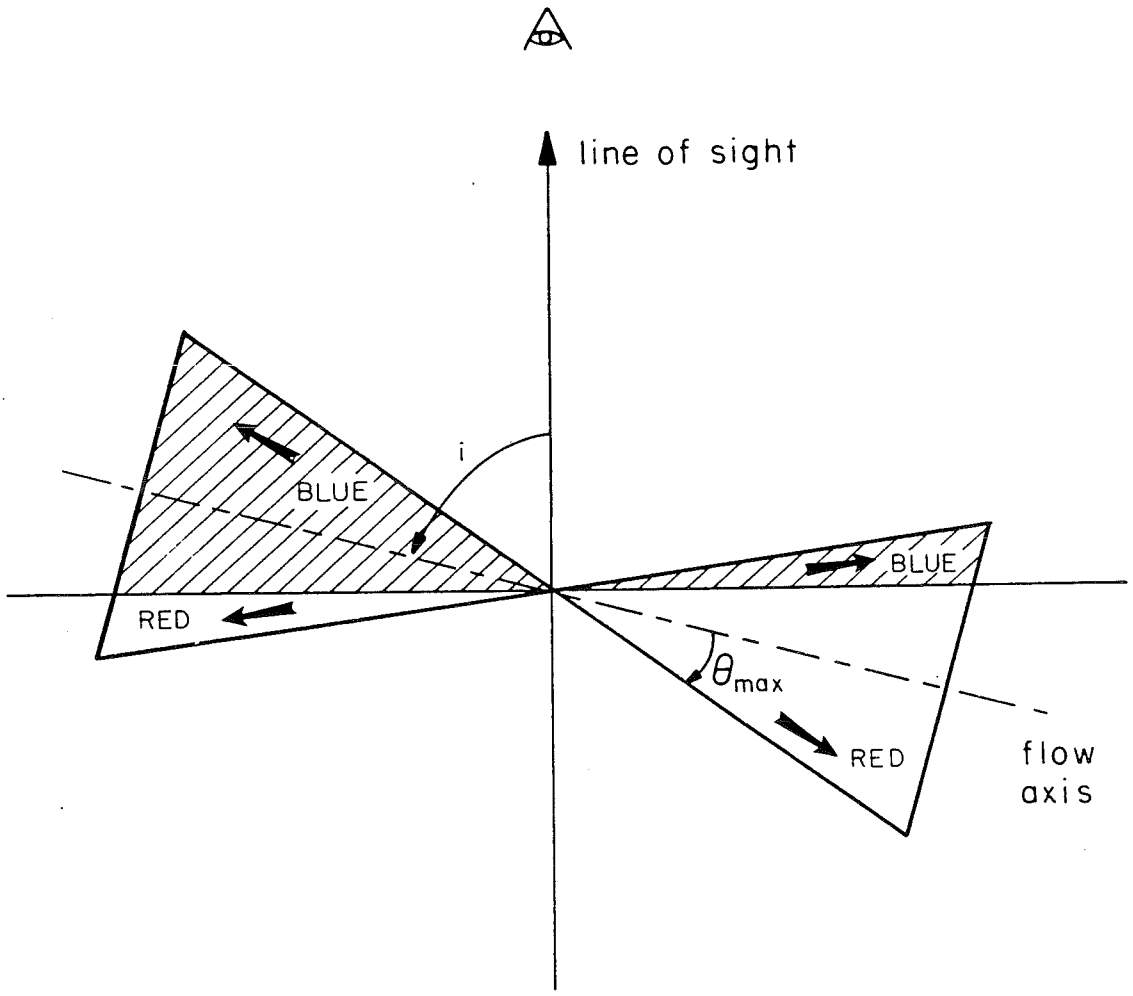

FIG. 1.—This diagram illustrates the geometry of the "face-on" configuration studied in this paper, here for a biconical outflow with radial expansion. The velocity vectors (*arrows*) are making a maximum angle θ_{max} with the flow axis. The view angle i between the line of sight and the flow axis is greater than $90° - \theta_{max}$, so that material in the front part of the lobes (*shaded areas*) is approaching us, while material in the back part of the lobes is receding from us. The observer therefore sees redshifted emission in the blue lobe and blueshifted emission in the red lobe.

II. OBSERVATIONS

Our observations were obtained in 1987 May and October at the FCRAO (Five College Radio Astronomy Observatory) 14 m radio telescope located in New-Salem, Massachusetts. A quasi-optical sideband filter and a 256 channel filterbank with 100 kHz spectral resolution were used together with a cryogenic Schottky-diode mixer receiver. The data were taken in a position-switching mode, utilizing a common reference observation for 4 on-source positions. For B335, we used a reference position located 30′ south of the $(\Delta\alpha, \Delta\delta) = (0, 0)$ position at $\alpha(1950) = 19^h34^m34^s$, $\delta(1950) = 07°27'00''$. For RNO 43, the reference position was 30′ east and south of the (0, 0) position at $\alpha(1950) = 5^h29^m32^s.7$, $\delta(1950) = 12°47'33''$.

Data were calibrated using a chopper wheel that allowed switching between the sky and an ambient load. All line temperatures in this paper (T_A^*) have been corrected only for the ambient temperature losses and for absorption by Earth's atmosphere. The true radiation temperature of the high-velocity gas, used in our column density calculations, is given by (Kutner and Ulich 1981) $T_R = T_A^*/(\eta_{fss}\eta_c)$, where η_{fss} is the forward efficiency on a uniform spatially extended source (typically the angular diameter of the Moon), and η_c the remaining coupling efficiency of the source brightness distribution to the antenna main beam pattern, here taken for a source a few arcminutes in angular size, such as the high-velocity regions studied here.

The B335 outflow and the southern part of the RNO 43 outflow region were mapped at 1′ spacing in the $J = 1 \rightarrow 0$ line of ^{12}CO at 115.2712 GHz, with a velocity resolution of 0.26 km s^{-1}. At this frequency, the antenna half-power beam width θ_{FWHM} is 45″, η_{fss} is 0.70, and η_c is 0.70. The total integration time per point was typically 900 s in B335 and 250 s for RNO 43, resulting in rms temperature uncertainties of 0.1 and 0.2 K respectively. Additional high signal-to-noise spectra of the $J = 1 \rightarrow 0$ line of ^{12}CO and ^{13}CO were taken south of RNO 43 at the position of the broadest line wings to determine the optical depth in the high-velocity CO gas. Also, a central region 5′ by 6′ in extent was mapped at 1′ spacing in the $J = 2 \rightarrow 1$ line of CS at 97.9810 GHz, in order to study the spatial distribution and kinematics of the denser gas surrounding the RNO 43 outflow source. At this frequency, $\theta_{FWHM} = 53''$, $\eta_{fss} = 0.70$ and we adopt $\eta_c = 0.70$. The velocity resolution

of the CS spectra is 0.31 km s^{-1}, and the rms temperature uncertainty is 0.1 K, for a typical integration time of 350 s per point.

III. EVIDENCE FOR SINGLE LARGE-SCALE FLOWS

a) The RNO 43 Outflow

RNO 43 (Cohen 1980) is the brightest of a group of Herbig-Haro objects knots (RNO 43*a* to *d*, Jones *et al.* 1984) located at the edge of a dark filament coincident with a northern fragment of the λ Orionis molecular ring, at an estimated distance of 400 pc (Maddalena and Morris 1987). The high-velocity CO emission present around the Herbig-Haro objects shows a double pattern of overlapping blueshifted and redshifted gas previously attributed to a pair of outflows seen nearly pole-on (RNO 43 N and RNO 43 S, see Edwards and Snell 1984). However, no exciting sources could be found for these flows. Later, Jones *et al.* (1984) found that the proper motion vectors of the Herbig-Haro objects associated with the two outflow components all pointed *away* from a single far-infrared source of luminosity 12.4 $L_\odot$ (Cohen and Schwartz 1987, assuming a distance of 400 pc) located farther south, on the axis defined by the two high-velocity emission regions. This result could be reconciled with the CO observations if the RNO 43 N and RNO 43 S components were in fact both part of the northern lobe of a *single* large-scale outflow emanating from the far-infrared source, and oriented almost perpendicular to the line of sight. If that were actually the case, a second lobe of high-velocity emission should also be present to the south of this source.

In order to test this hypothesis, we have extended the ^{12}CO map of Edwards and Snell (1984) to the region south of the far-infrared source driving the RNO 43 Herbig-Haro objects. Our map extends approximately from $\Delta\delta = +1$ to $\Delta\delta = -12$ and from $\Delta\alpha = +1$ to $\Delta\alpha = -5$ and is sampled every 1′. Over the whole region, the ^{12}CO spectra show relatively narrow ($\Delta V \sim 2$ km s^{-1} at half-intensity) cloud emission centered at 10.2 km s^{-1}. Extended line wings, attributed to high-velocity gas, were detected within the velocity intervals 4–9 km s^{-1} (blue) and 11–16 km s^{-1} (red). A contour map of the integrated high-velocity emission combining our data and those of Edwards and Snell (1984) is presented in Figure 2. All offsets ($\Delta\alpha$, $\Delta\delta$) are given in arcminutes relative to the position of the far-infrared source from the *IRAS* point source catalog: $\alpha(1950) = 5^h29^m32^s.7$, $\delta(1950) = 12°47'33''$. The RNO 43 N and RNO 43 S features have been renamed RNO 43 N2 and RNO 43 N1 respectively, in explicit reference to their position with respect to the far-infrared source. This new nomenclature avoids possible confusion between northern and southern high-velocity components.

A new lobe of superposed blueshifted and redshifted emission (RNO 43 S1) is found centered at (−2, −3). Lines of ^{12}CO and ^{13}CO obtained at this position, where the high-velocity emission is greatest in both wings, are presented in Figure 3. Two arguments indicate that this component is the expected southern counterpart of the RNO 43 N1 lobe: First, it is similar in size to RNO 43 N1 and is symmetrically displaced from it with respect to the far-infrared (FIR) source. Second, instead of monotonically decreasing with increasing radial velocity, its ^{12}CO line profile shows "shoulders" on both sides of the line core, a peculiar property also observed in the line wings of RNO 43 N1 (see Fig. 2 of Edwards and Snell 1984). In addition, we note that the ^{12}CO to ^{13}CO integrated-intensity ratio is ~12.1 in both line wings, very similar to the values found in RNO 43 N1 (11.5 in the blue wing and 14.0 in the red wing). To be unambiguously interpreted as the two lobes of a single bipolar flow, these two components must also show a *velocity* symmetry with respect to the cloud systemic velocity. Such evidence is found in Figure 4 which displays a spatial-velocity diagram obtained along the flow axis: RNO 43 N1 appears more blueshifted, with maximum blueshifted and redshifted velocities from line center (at the 0.5 K level) $V_b = 5.2$ km s^{-1} and $v_r = 3.6$ km s^{-1}, while RNO 43 S1 is more redshifted, with $v_b = 2.8$ km s^{-1} and $V_r = 4.3$ km s^{-1}. We here use a capital letter to denote the larger of the two radial velocities within the same lobe. Indeed, we find that $V_b \sim V_r$ and $v_b \sim v_r$,

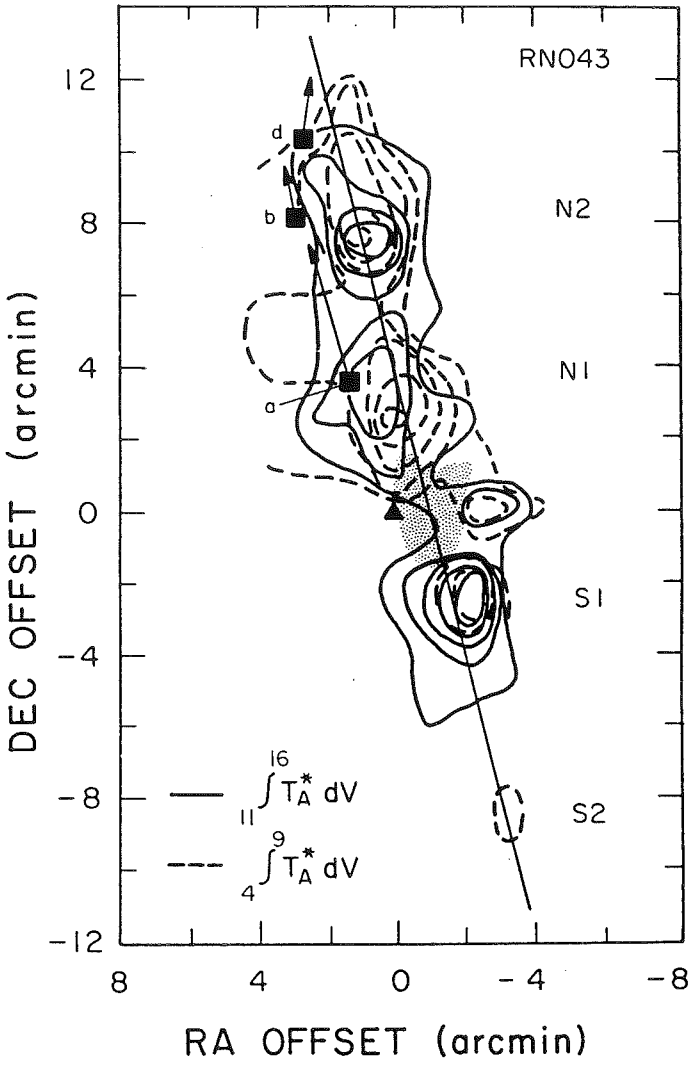

FIG. 2.—Contour map of the ^{12}CO $J = 1 \rightarrow 0$ integrated-intensity of the redshifted (*solid lines*) and blueshifted (*dashed lines*) gas in the RNO 43 outflow region, from Edwards and Snell (1984) and this paper, identifying the various high-velocity components described in the text. The contour levels start at 2 K km s^{-1} and are spaced by 2 K km s^{-1}. The Herbig-Haro objects RNO 43*a*, *b*, and *d* are shown as filled squares and their proper motion vectors, measured by Jones *et al.* (1984), are indicated by arrows. These vectors point away from the position of the far-infrared source, indicated by a filled triangle. The solid line marks the axis along which the spatial-velocity diagram in Fig. 4 was taken, and the dotted region at the center represents the FWHM extent of the CS $J = 2 \rightarrow 1$ emission.

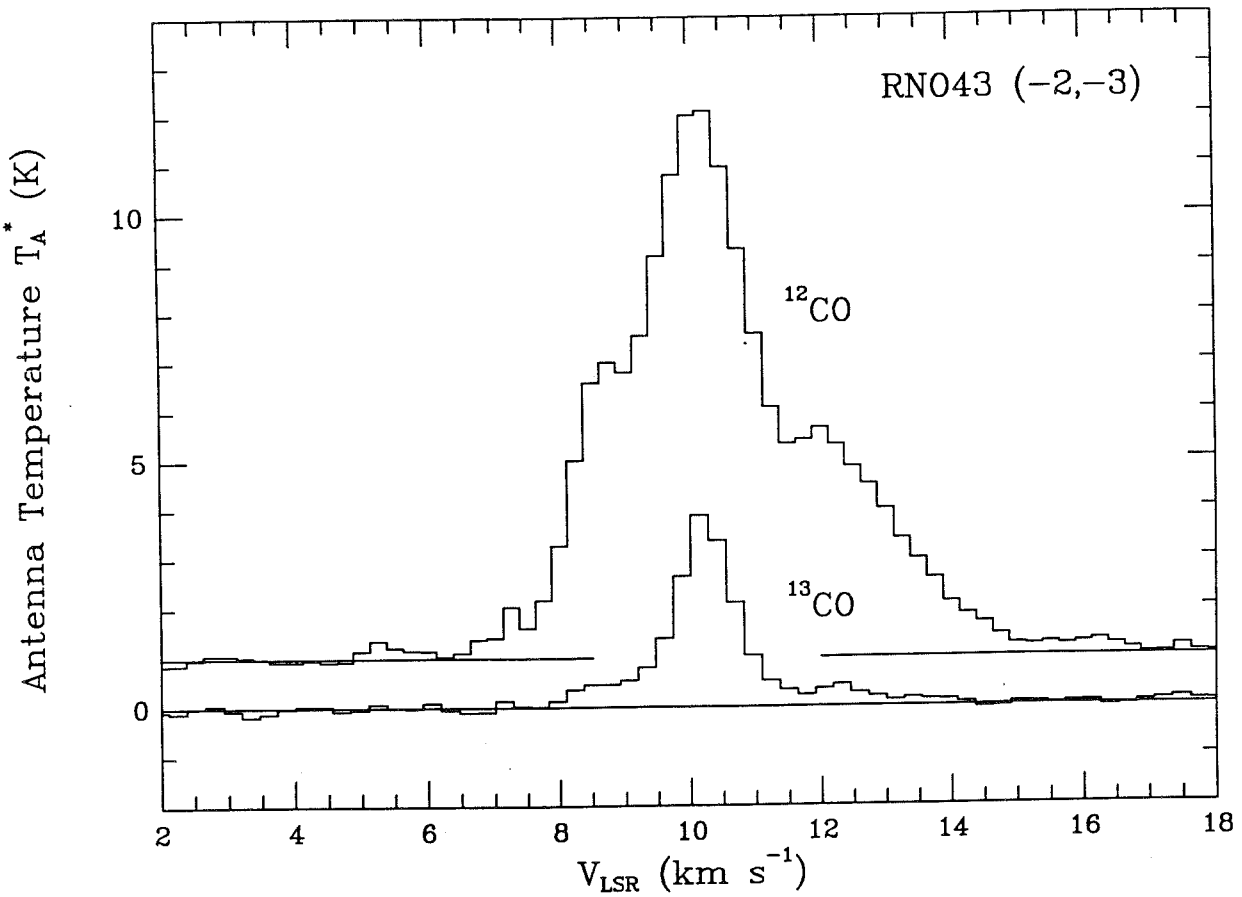

FIG. 3.—^{12}CO and ^{13}CO spectra taken at the position of maximum high-velocity emission in the southern lobe of the RNO 43 outflow. The velocity resolution is 0.26 km s^{-1}. The average ratio of ^{12}CO to ^{13}CO integrated intensity in the line wings is 12.1, indicating a mean ^{12}CO optical depth of 7.4.

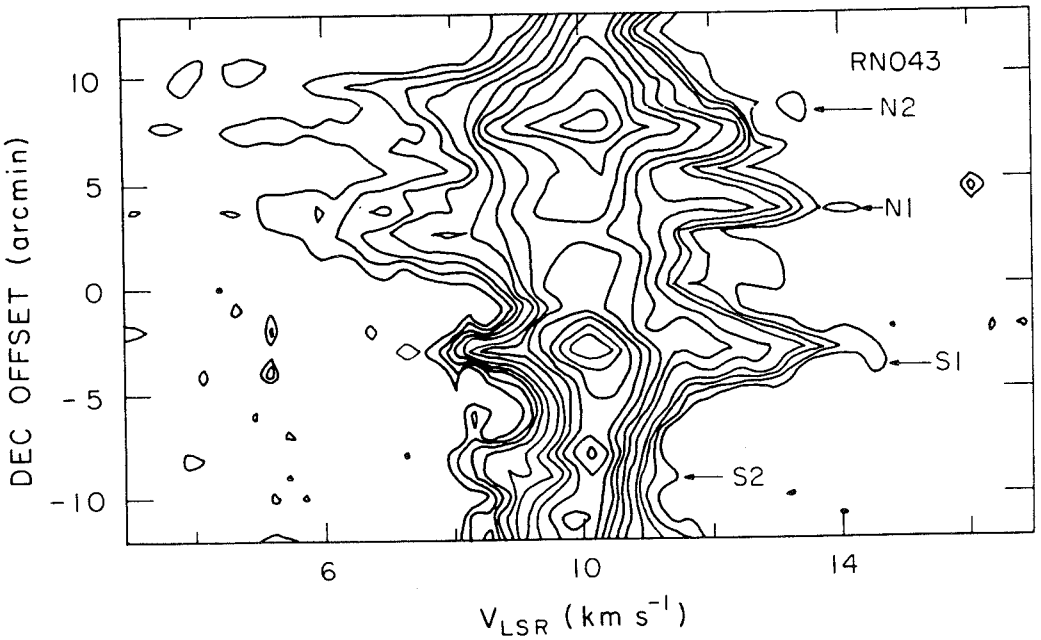

FIG. 4.—Spatial-velocity diagram of the ^{12}CO $J = 1 \rightarrow 0$ emission along the axis of the RNO 43 outflow (shown as a solid line in Fig. 2). Contours of equal antenna temperature are plotted as a function of radial velocity and declination offset from the position of the far-infrared source. The various high-velocity components are identified as in Fig. 2 (see text). The contour levels extend from 0.5 K to 10 K, with a spacing of 0.5 K up to the 2 K level, and a spacing of 1 K above.

confirming the existence of a true symmetry between the two lobes.

Figure 4 further shows that the RNO 43 N1 and RNO 43 N2 components have very similar radial velocities ($V_b = 5.5$ km s^{-1} and $v_r = 3.1$ km s^{-1} in RNO 43 N2). Since these components appear spatially connected in Figure 2, have similar sizes, and are both elongated along the flow axis, we suggest that they belong to a *single* northern high-velocity lobe, of length 12′ (1.4 pc). Recent CCD imaging by Ray (1987) and Mundt, Brugel and Bührke (1987) has revealed that the RNO 43 Herbig-Haro objects are in fact bright spots along two highly collimated optical jets. The northern jet, which contains RNO 43*b* to *d*, is oriented north-south along the eastern edge of RNO 43 N2, while the southern jet, which contains RNO 43*a*, lies within the RNO 43 N1 lobe and is pointing back toward the position of the CS emission peak, 1′ west of the FIR source (see below). We think that these observations provide additional evidence that both RNO 43 N1 and RNO 43 N2 are powered by the observed far-infrared source, although the existence of a connection between the two optical jets has not yet been firmly established (see the discussion of Mundt, Brugel, and Bührke 1987).

The total extent of the flow to the south is not nearly as large as it is to the north; a component of high-velocity emission (RNO 43 S2) is indeed observed at $(-3, -8)$, symmetric in position to the RNO 43 N2 component with respect to the FIR source (see Figs. 2 and 4). However, the observed radial velocities ($v_b = 2.5$ km s^{-1} and $v_r = 1.2$ km s^{-1}) are smaller than expected. A possible explanation is that this lobe is located deeper into the ambient cloud than the rest of the flow. The spatial distribution of the extinction on the Palomar Sky Survey prints and the variations in 60 and 100 μm emission seen in the co-added *IRAS* map (S. Edwards, private communication) indeed suggest that the FIR source is located near the northern edge of the ambient molecular cloud. The flow to the south would then encounter more resistance from the denser surrounding medium and its expansion velocity would be reduced. Such an effect may already be present in the RNO 43 S1 lobe, since the radial velocities there are slightly smaller than those found in RNO 43 N1.

Finally, further evidence that the molecular flow lies almost in the plane of the sky is provided by our CS $J = 2 \rightarrow 1$ observations, which probe the denser ($n_{H_2} \geq 10^4$ cm^{-3}) gas surrounding the infrared source. Contour maps of the total integrated intensity in the line and of the maximum antenna temperature are presented in Figure 5*a* and Figure 5*b*. The CS emission is centered on $(-1, 0)$, and is *elongated along the axis of the CO flow* (see Fig. 2) with a FWHM extent of 4′ by 2.′5, indicating that collimation of the flow is already effective 1′ (0.12 pc) from the central source. Although the peak temperature decreases with distance from the source, the integrated intensity (and hence the line width) increases as one moves farther from the source along the flow axis, suggesting a kinematic interaction between the CS core and the flow. This is illustrated in Figure 5*c*, which plots longer integration CS spectra obtained at three positions along the flow axis. Toward the central position at $(-1, 0)$, the line is narrow ($\Delta V_{FWHM} = 0.6$ km s^{-1}) and shows only modest line wings extending out to ~ 1 km s^{-1} on each side of the line center at the cloud velocity, whereas at positions (0, 2) and $(-2, -2)$, the lines are much broader ($\Delta V_{FWHM} = 2$ km s^{-1}) and have extended blueshifted and redshifted wings with a full width at zero intensity of ~ 6 km s^{-1}. This increase in high-velocity emission as one progresses along the flow axis is comparable to that observed in CO at the same positions (see Fig. 4). It suggests that the high-velocity CS participates in the same expansion as the CO and delineates the denser parts of the molecular outflow.

We conclude that all the high-velocity emission around RNO 43 is due to a single bipolar outflow powered by the FIR source driving the Herbig-Haro objects, and oriented with its axis almost perpendicular to the line of sight. Its northern lobe, composed of RNO 43 N2 and RNO 43 N1, is 12′ (1.4 pc) long, slightly tilted toward us, and contains the visible Herbig-Haro objects and optical jets, while its southern lobe (RNO 43 S1) is only 6′ (0.7 pc) in extent and is slightly tilted away from us. The spatial distribution and kinematics of the dense CS gas support this interpretation. RNO 43 is thus one of the largest and most highly collimated bipolar outflows found to date.

b) The B335 Outflow

The structure of the Bok globule B335 has been recently studied in detail by Frerking, Langer, and Wilson (1987) using extensive molecular line observations. They adopt a distance of 250 pc, based on the spatial and kinematic association of the cloud with the Lindblad ring, and on large-scale extinction measurements. B335 is found to consist of an opaque core of size 2′ × 3′ and mass 11–14 $M_\odot$ surrounded by a more diffuse envelope extending over 34′ × 20′, of mass ~ 25 $M_\odot$. The dense core shows NH_3 (Myers and Benson 1983) and CS (Heyer *et al.* 1986) emission, and contains a cold ($T \sim 15$ K) far-infrared source of luminosity 3 $L_\odot$ (assuming a distance of 250 pc) at position $\alpha(1950) = 19^h34^m34^s.7 \pm 0^s.7$, $\delta(1950) = 07°27'20'' \pm 10''$ (Keene *et al.* 1983). Variations in the ^{12}CO line wings toward the core region, indicating the presence of a bipolar outflow, were first noticed by Frerking and Langer (1982). A ^{12}CO map at 48″ resolution by Goldsmith *et al.* (1984) resolved the high-velocity emission into a blueshifted and a redshifted lobe, respectively east and west of the central FIR source. Later, higher signal-to-noise, but lower resolution (1.′6) observations (Langer, Frerking, and Wilson 1986) revealed the existence of a separate component of blueshifted emission, to the east of the core outflow, and confirmed the presence of redshifted emission in the blue lobe of the main flow. These two features were attributed to a second independent outflow to the east, whose red lobe would overlap with the main flow. However, the geometrical center of this secondary outflow is not associated with any known stellar source, but rather coincides with a local *minimum* in the ^{13}CO column density. Also difficult to explain in this context is the alignment of all high-velocity structures along a common east-west axis, as well as the presence of low-level blueshifted emission in the redshifted lobe of the main flow. These facts suggest that all the high-velocity gas in B335 might be due to a single flow driven by the known infrared source and oriented almost in the plane of the sky.

In order to elucidate the spatial and kinematic relationship between the various high-velocity features, we obtained a series of high signal-to-noise ^{12}CO $J = 1 \rightarrow 0$ spectra ($T_{rms} \leq 0.2$ K) on a 1′ square grid extending from $\Delta\delta = +3$ to $\Delta\delta = -2$, and from $\Delta\alpha = +13$ to $\Delta\alpha = -6$. The resulting map includes both the main flow and the eastern blueshifted component. The ambient ^{12}CO cloud emission is centered on 8.3 km s^{-1}, and has a width of ~ 1.1 km s^{-1} at half-intensity, while the high-velocity emission extends from 4 to 7.5 km s^{-1} (blue) and from 9 to 12.5 km s^{-1} (red). A contour map of integrated-intensity in the blueshifted and redshifted gas is presented in Figure 6,

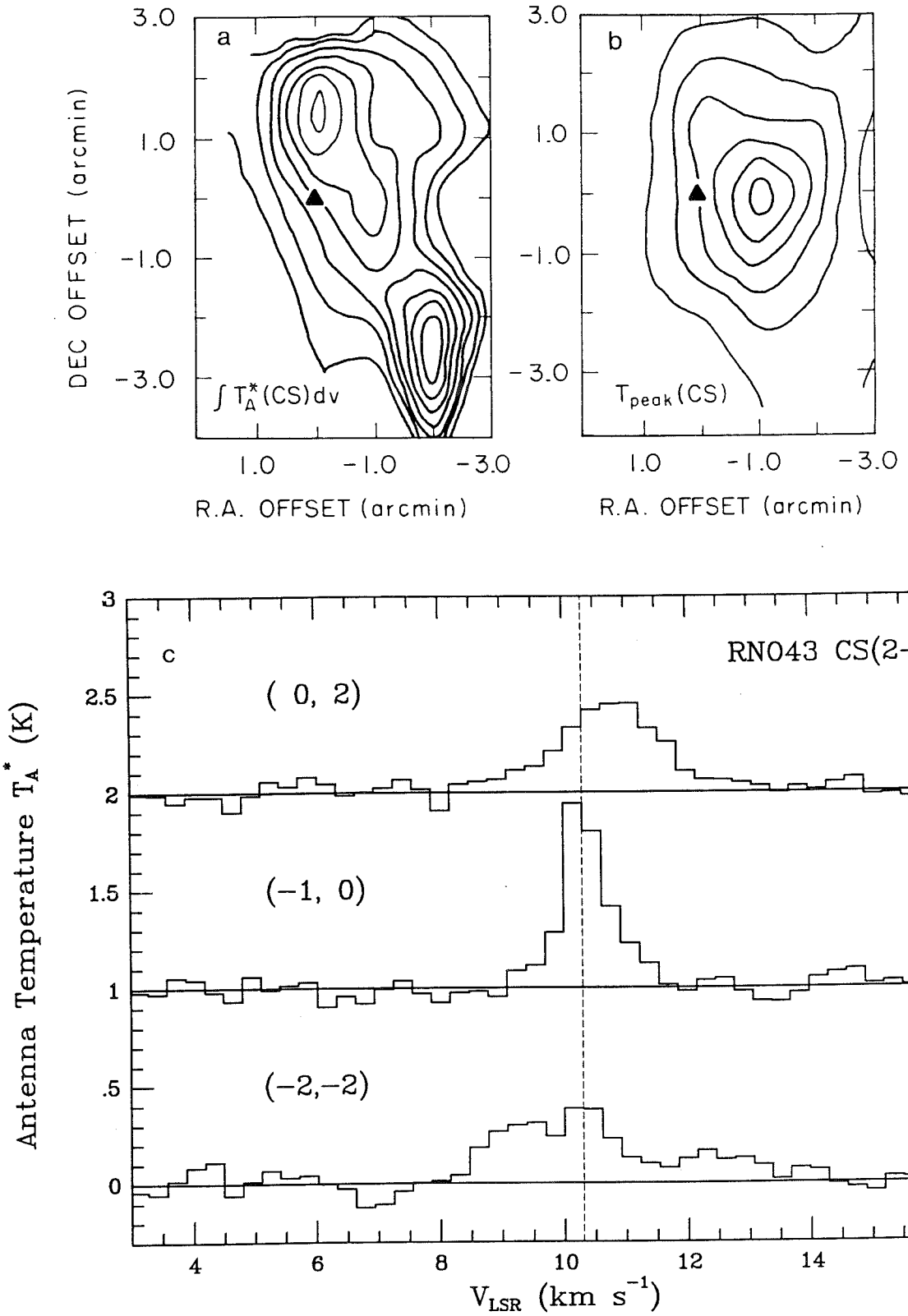

FIG. 5*a–b*.—Maps of the CS $J = 2 \rightarrow 1$ total integrated intensity (*left*) and maximum antenna temperature (*right*) near the far-infrared source driving the RNO 43 outflow. The *IRAS* position of the source is shown as a filled triangle. The contour levels start at 0.3 K km s^{-1} in Fig. 5*a* and 0.2 K in Fig. 5*b* and are spaced by 0.1 K km s^{-1} in Fig. 5*a* and by 0.1 K in Fig. 5*b*. (*c*)—CS $J = 2 \rightarrow 1$ spectra obtained at three different positions along the flow axis: in the blue lobe (*top*), toward the peak of the CS emission (*middle*), and in the red lobe (*bottom*). The velocity resolution is 0.31 km s^{-1}. The dashed line indicates the cloud systemic velocity. Note the extended blueshifted and redshifted wings in the top and bottom spectra.

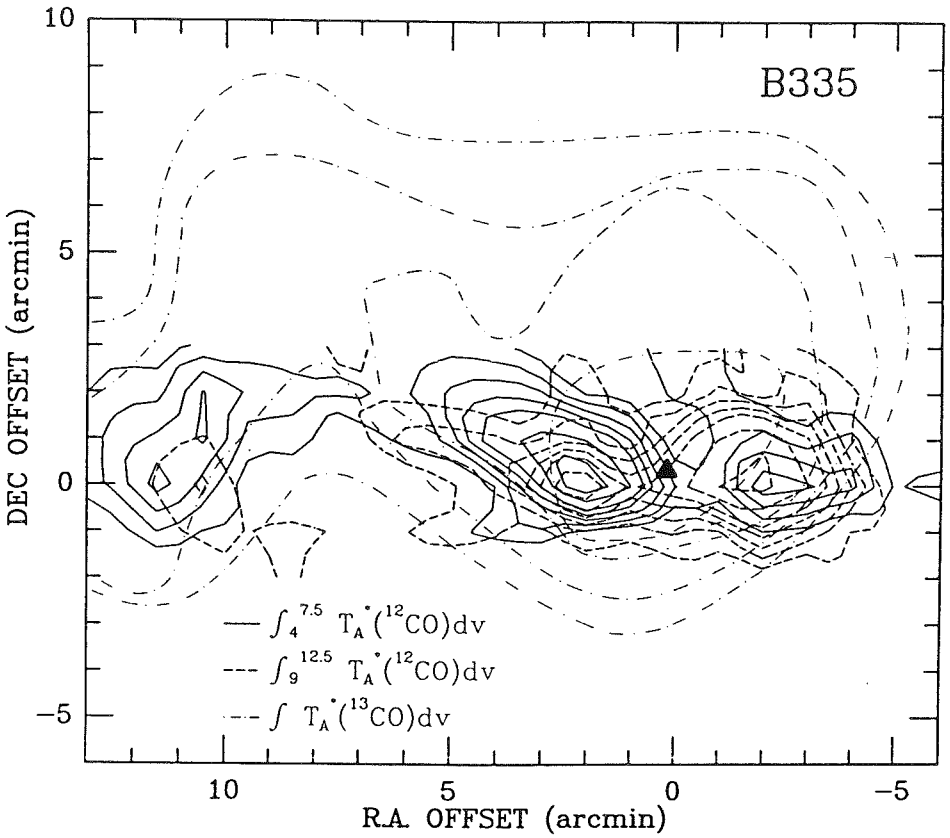

FIG. 6.—Contour map of the ^{12}CO $J = 1 \rightarrow 0$ integrated-intensity of the blueshifted (*solid lines*) and redshifted (*dashed lines*) emission in B335, superposed on a contour map of the ^{13}CO integrated intensity adapted from Langer, Frerking, and Wilson (1986) (*dot-dashed lines*). The filled triangle denotes the location of the far-infrared source powering the flow. The contour levels are 0.3, 0.6, 0.9, 1.2, 1.5, 2, and 2.5 K km s^{-1} for ^{12}CO, and 0.25, 0.5, 1, and 2 K km s^{-1} for ^{13}CO.

superposed on a contour map of the total ^{13}CO integrated-intensity adapted from Langer, Frerking, and Wilson (1986).

Our observations of the main flow are in excellent agreement with theoretical expectations for a flow oriented nearly perpendicular to the line of sight: both high-velocity lobes show superposed blueshifted and redshifted emission. They are symmetric with one another not only in location with respect to the flow center, but also in *velocity* with respect to the cloud systemic velocity. This can be seen in Figure 7*a* to 7*d* which present spatial-velocity diagrams taken along four east-west axes (parallel to the flow axis) at declination offsets $\Delta\delta = +2$, $+1$, 0, and -1. In these diagrams, a blueshifted wing in one lobe always corresponds to a redshifted wing of similar velocity extent from line center in the other lobe, and vice versa. The symmetry between the two lobes is particularly striking at $\Delta\delta = 1$ (Fig. 7*b*). There, the maximum blueshifted and redshifted velocities from line center (at the 0.4 K level) are $V_b = 4.8$ km s^{-1} and $v_r = 2.7$ km s^{-1} in the blue lobe, and $v_b = 2.1$ km s^{-1} and $V_r = 4.2$ km s^{-1} in the red lobe. Indeed $V_b \sim V_r$ and $v_b \sim v_r$.

Our higher resolution data also allow us to clarify the nature of the blueshifted component found by Langer, Frerking, and Wilson (1986) to the east of the main flow. We find that this component also shows redshifted emission, and appears connected to the main flow by a bridge of low-level blueshifted emission, clearly visible in Figure 7*a*. Furthermore, it exhibits at *all* $\Delta\delta$ maximum radial velocities strikingly similar to those found in the main blue lobe (see Fig. 7*a* to 7*d*). These facts strongly suggest that the secondary and main components are *physically associated*, and form a single high-velocity lobe of length 12′ (0.9 pc). A comparison of our CO map with the ^{13}CO data obtained by Freking, Langer, and Wilson (1987) reveals that the gap between these two components coincides with a region of very low ^{13}CO column density, about 4′ by 3′ in extent, in which we did not detect any ambient or high-velocity ^{12}CO gas. Rather, the bridge of blueshifted emission is seen to closely follow the edge of this "cavity." No more ^{13}CO or ^{12}CO emission is found beyond the western high-velocity lobe, indicating that that side of the B335 outflow has reached the edge of the molecular cloud.

We conclude that the high-velocity components in B335 are all part of *one* bipolar flow viewed nearly perpendicular to its axis. The eastern lobe is 12′ (0.9 pc) long, is tilted toward us, and includes the component detected by Langer, Frerking, and Wilson (1986), while the western lobe is only 6′ (0.4 pc) in extent, is tilted away from us, and is apparently breaking out of the cloud.

IV. DISCUSSION

a) Flow Geometry and Velocity Field

In the previous section, we have presented strong evidence that B335 and RNO 43 are single large-scale bipolar outflows oriented nearly in the plane of the sky, and that their high-velocity lobes contain both blueshifted and redshifted gas. If we assume that the flows are axially symmetric, this result has

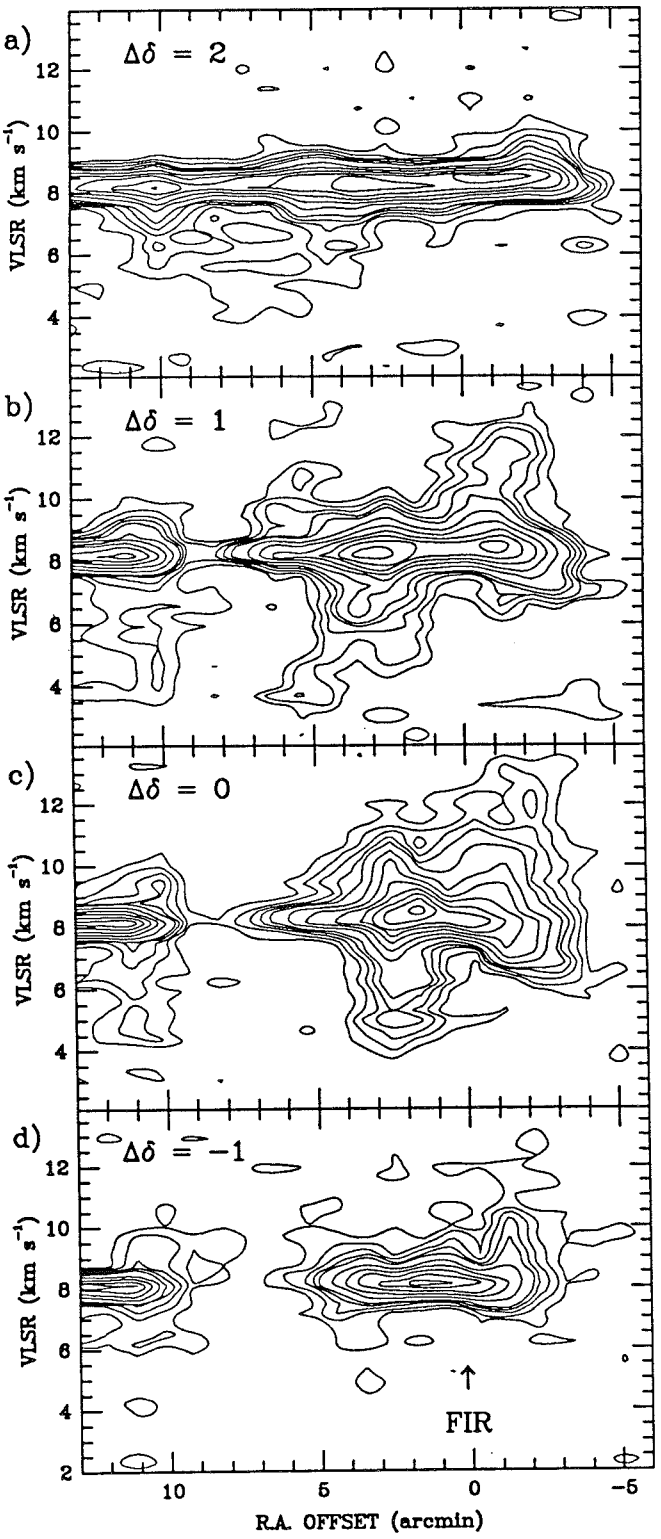

FIG. 7*a–d*.—Spatial-velocity diagrams of the ^{12}CO $J = 1 \rightarrow 0$ intensity in B335 obtained along east-west axes (parallel to the flow axis) at four different declination offsets $\Delta\delta$. Note the velocity symmetry between the two lobes and the similarity in maximum velocity between the high-velocity wings at $\Delta\alpha = +5$ and $\Delta\alpha = +10$. The contour levels extend from 0.2 to 4.5 K km s^{-1}, with a spacing of 0.2 K km s^{-1} up to the 1 K km s^{-1} level, and a spacing of 0.5 K km s^{-1} above.

two implications: (1) the flow must have a *nonzero* expansion velocity perpendicular to its axis; (2) the flow must be viewed at an angle $i > 90° - \theta_{max}$ with respect to its axis, where θ_{max} denotes the maximum angle between the velocity vectors in the lobes and the axis of the flow. Note that both conditions have to be met, otherwise the high-velocity lobes would appear entirely blue or entirely redshifted. This geometry is illustrated in Figure 1 for a biconical flow with radial expansion, in which case θ_{max} is simply equal to the cone semiopening angle. If the flow velocity V_0 depends only on the distance from the star and if i is close to 90°, V_0 can be assumed constant along any given line of sight; then, the maximum blueshifted and redshifted radial velocities in the blue lobe, V_b and v_r, come respectively from the front and back sides of that lobe and are given by $V_0 \cos(i - \theta_{max})$ and $V_0 |\cos(i + \theta_{max})|$. The observed difference between V_b and v_r (noted in § III) hence implies that the flow is inclined from the plane of the sky ($i \neq 90°$), and also requires that $\theta_{max} \neq 0°$ *and* $\theta_{max} \neq 90°$, meaning that *the flow motion is neither pure translation parallel to the flow axis, nor pure expansion perpendicular to it, but a combination of the two.* The values of V_b and v_r can further be used to estimate the flow inclination and velocity: Since projection effects on dimensions are minimized in this particular configuration, we can estimate θ_{max} from the spatial map of the CO emission, assuming that it is indeed equal to the geometrical semiopening angle of the lobe. We can then derive the view angle i from the observed velocity ratio V_b/v_r, and estimate $V_0 = V_b/\cos(i - \theta_{max})$ once i is known. One could equivalently use the maximum redshifted and blueshifted velocities in the red lobe, V_r and v_b, since by symmetry between the two lobes $V_r \sim V_b$ and $v_b \sim v_r$.

In B335, the high-velocity lobes have an almost constant semiopening angle $\theta_{max} \sim 25° \pm 5°$, and an average velocity ratio, V_b/v_r, of 1.9 ± 0.5, which yields $i = 82° \pm 5°$. The maximum radial velocity found along the flow axis is ~ 5 km s^{-1}, from which we estimate a true outflow velocity V_0 of 9.2 km s^{-1}. The RNO 43 flow has a more complex geometry: although the northern lobe appears highly collimated on the large scale, which would imply a small value of θ_{max}, the high-velocity emission appears fragmented into two components, RNO 43 N1 and RNO 43 N2. We therefore choose to adopt for θ_{max} the observed opening angle of RNO 43 N1 and RNO 43 S1 as seen from the infrared source: $\sim 25° \pm 5°$. From an average velocity ratio of 1.5 ± 0.4 and a maximum observed radial velocity ~ 5 km s^{-1} we derive a view angle i of $85° \pm 3°$, and a true flow velocity of 10 km s^{-1}.[5]

In this analysis, we have assumed that there are no velocity gradients in the flow. While our spatial resolution is inadequate to give us any indication about the velocity field in RNO 43, our observations of B335 (see Fig. 7*a* to 7*d*) clearly show a systematic *increase* in radial velocity as one moves away from the infrared source. If this results from true acceleration with distance from the star, then the value of V_0 that we derived using the *maximum* observed V_b and v_r should be an *upper limit* to the mean velocity in the flow. On the other hand, since the flow is almost perpendicular to the line of sight, any high-velocity gas moving along the flow axis would have a very small radial velocity and remain unobservable, because it would emit within the optically thick static line core. There-

[5] If the flows were nonradial, the true θ_{max} could be larger than the observed geometrical opening angle. Since increasing the adopted value of θ_{max} would decrease both i and V_0, the values that we derive assuming radial expansion are probably *upper limits* to the true values.

fore, if the flow velocity depends on the polar angle θ from the flow axis and increases with decreasing θ, our value of V_0 might underestimate the mean flow velocity.

b) Flow Dynamics

Our observations have revealed that the spatial extents of the B335 and RNO 43 outflows are much larger than previously suspected: the western lobe of B335 is now 0.9 pc long (instead of 0.3 pc), and the northern lobe of RNO 43 1.4 pc (instead of 0.4 pc). It is thus necessary to reevaluate the energetics of these flows and compare them with the properties of their now well-identified driving sources.

If we assume LTE conditions at temperature T_{ex}, the column density of H_2 gas in the flow is related to the integrated intensity of the high-velocity ^{12}CO gas by

$$N(H_2) = \left[\frac{H_2}{^{12}CO}\right]\left(\frac{\tau}{1-e^{-\tau}}\right)\frac{4.2\times10^{13}T_{ex}}{\exp(-5.5/T_{ex})} \times \int T_R(^{12}CO)dv \text{ cm}^{-2}, \quad (1)$$

where τ is the average ^{12}CO optical depth in the line wings, T_R the radiation temperature in the $J = 1 \rightarrow 0$ line in kelvins, and v the radial velocity in km s^{-1}. Since ^{13}CO is optically thin ($\tau \ll 1$), we also have

$$N(H_2) = \left[\frac{H_2}{^{13}CO}\right]\frac{4.2\times10^{13}T_{ex}}{\exp(-5.5/T_{ex})}\int T_R(^{13}CO)dv \text{ cm}^{-2}, \quad (2)$$

from which we derive the following relationship between ^{12}CO and ^{13}CO integrated intensity:

$$\left[\frac{H_2}{^{12}CO}\right]\left(\frac{\tau}{1-e^{-\tau}}\right) = \left[\frac{H_2}{^{13}CO}\right]\frac{\int T_R(^{13}CO)dv}{\int T_R(^{12}CO)dv}. \quad (3)$$

We can calculate *lower limits* to the total mass of high-velocity gas by summing over all positions the column densities derived from equation (1), assuming optically thin ^{12}CO emission (i.e., $\tau/(1-e^{-\tau}) = 1$), $T_{ex} = 10$ K in B335 and 15 K in RNO 43, an H_2 to ^{13}CO abundance ratio of 5×10^5 (Dickman 1978), and a terrestrial ^{12}CO to ^{13}CO ratio of 89.

However, the high-velocity ^{12}CO gas is probably not optically thin: At the emission peak in RNO 43 S1, the average ^{12}CO to ^{13}CO integrated-intensity ratio in the line wings is 12.1; applying equation (3) then yields $\tau \sim 7.4$, if a terrestrial isotopic ratio is assumed. Goldsmith *et al.* (1984) similarly find an average optical depth of 4 for the high-velocity gas in B335. Therefore, at the positions where these ^{13}CO spectra were obtained, the optically thin approximation severely underestimates the true H_2 column density.

In order to correct for this effect, we can replace the $[H_2/^{12}CO]\tau/(1-e^{-\tau})$ term in equation (1) by its value estimated from equation (3), assuming a constant ^{12}CO to ^{13}CO integrated-intensity ratio throughout the flow. One advantage of this method is that the resulting value of the mass is *independent of the ^{12}CO to ^{13}CO isotopic ratio* and is only proportional to the abundance of H_2 relative to ^{13}CO, which is the quantity directly derived from molecular cloud observations. Both the uncorrected and the opacity-corrected flow masses are given in Table 1.

Computations of the CO line transfer in several models of high-velocity flows (Cabrit and Bertout 1988) have shown that the corrected value is usually within a factor of 2 of the true mass, even if the ^{12}CO to ^{13}CO integrated-intensity ratio is only estimated at the peak of integrated high-velocity emission. We will thus adopt the opacity-corrected mass to determine the other flow parameters. It should be noted that the true mass of the flow could still be larger if a significant fraction of the high-velocity material is projected at low radial velocities within the line core and therefore does not fall within our integration limits.

We calculate the kinematic and dynamic flow parameters using two different methods: First, we only take into account the radial component of the velocity, assuming that the molecular gas is flowing along the line of sight and that the observed range in radial velocity is due to intrinsic velocity gradients in the flow. The flow momentum, P, and kinetic energy, E, are then proportional to $\sum \int T_R(v)v\,dv$, and $\frac{1}{2}\sum \int T_R(v)v^2\,dv$, where $\sum$ denotes a sum over all observed positions. The rates of momentum and energy transfer, F and L (also referred to as the force and mechanical luminosity of the flow), are pro-

TABLE 1

KINEMATIC AND DYNAMIC PARAMETERS OF THE B335 AND RNO 43 BIPOLAR OUTFLOWS[a]

	B335 (d = 250 pc)		RNO 43 (d = 400 pc)	
QUANTITY	Lower	Upper	Lower	Upper
Mass $M(M_\odot)$	[0.06]	0.24	[1.83]	13.4
Momentum $P(M_\odot$ km s$^{-1})$	0.36	2.20	22.5	134
Energy $E(M_\odot$ km^2 s$^{-2})$	0.36	10.1	24.2	672
Force $F(M_\odot$ km s^{-1} yr$^{-1})$	8.5(−7)	2.4(−5)	3.5(−5)	9.8(−4)
Mechanical luminosity $L(L_\odot)$	1.7(−4)	1.8(−2)	8.0(−3)	7.9(−1)
Characteristic velocity V (km s^{-1})	2.5	9.2	2.8	10.0
Time scale T (yr)	3.5(5)	9.3(4)	4.9(5)	1.4(5)
Momentum transfer efficiency Fc/L_*	15	380	140	3900
Energy transfer efficiency L/L_*	5.6(−5)	5.9(−3)	6.5(−4)	6.4(−2)
Stellar mass-loss rate $\dot{M}_*(M_\odot$ yr$^{-1})$[b]	4.2(−9)	1.2(−7)	1.8(−7)	4.9(−6)
Stellar mass-loss rate $\dot{M}_*(M_\odot$ yr$^{-1})$[c]	1.6(−10)	1.6(−8)	7.4(−9)	7.4(−7)

[a] The lower values for the masses (in brackets) are obtained assuming optically thin ^{12}CO emission, while the upper values have been corrected for the line opacity. Only these last values are used to calculate the other flow quantities. The lower values of the kinematic and dynamic parameters are obtained using radial velocities only, while the upper values include a correction for inclination (see § IVa). The numbers in parentheses indicate powers of 10.

[b] Assuming a momentum-conserving wind-flow interaction.

[c] Assuming an energy-conserving wind-flow interaction with $\epsilon = 3$.

portional to $1/R \sum \int T_R(v)v^2\,dv$ and $1/(2R) \sum \int T_R(v)v^3\,dv$, where R is the observed length of the flow lobe (0.9 pc for B335 and 1.4 pc for RNO 43). Because we do not account for the tranverse component of the velocities, the momentum and energy estimated using this method should represent *absolute lower limits* to their true values in the flow.

Alternatively, we assume that all material in the flow is moving at the velocity V_0 that we derived in the previous section by correcting the maximum observed radial velocity for inclination. Since the flow is nearly in the plane of the sky, we do not need to correct R for projection. The parameters P, E, F, and L are then simply given by MV_0, $\frac{1}{2}MV_0^2$, MV_0^2/R, and $\frac{1}{2}MV_0^3/R$. As discussed earlier, we expect V_0 to be greater than the mean velocity in the flow, if there is no very high-velocity gas flowing perpendicular to the line of sight. Therefore these values probably represent *upper limits* to the flow parameters.

Table 1 lists the values of the kinematic and dynamic parameters obtained using both methods, as well as a characteristic flow velocity $V = 2L/F$, and time scale $T = E/L$. Cabrit and Bertout (1988) applied the same methods to synthetic CO profiles and maps of bipolar flow models with various velocity fields and found that, for flows seen at large view angle, the two estimates indeed bracketed the true values of the flow parameters. In both RNO 43 and B335, the upper and lower limits differ by about a factor of 6 for P, 30 for E and F, and 100 for L. Since the flow extent is well determined in this configuration, these uncertainties are mostly due to our ignorance of the true direction and magnitude of the velocity vectors in the flow, as well as of the details of the momentum and energy transfer in the flow.

Although the B335 and RNO 43 outflows have comparable physical dimensions, and similar radial velocities and inclination from the line of sight, the high-velocity ^{12}CO emission is much stronger and more optically thick in RNO 43; as a result, this flow is about 50 times more massive and energetic than B335. If we compare the mechanical luminosity and force of these flows with the luminosity L_* and radiative momentum output rate L_*/c available from their central infrared sources, we find that the ratios L/L_* and Fc/L_* (given in Table 1) are 10 times higher for RNO 43 than for B335. Because these flows have such a similar geometry and configuration, it seems unlikely that this difference is due to errors on the flow parameters, although variations in the ^{13}CO abundance cannot be excluded. Other possible explanations are a nonlinear dependence of the flow momentum and energy input rates on the stellar luminosity, or the existence of more favorable conditions for efficient momentum and energy transfer (e.g., magnetic fields, density gradients) in the ambient cloud surrounding RNO 43.

Despite this difference, the dynamical properties of RNO 43 and B335 are still globally similar to those of other observed low-luminosity flows (Lada 1985); in particular, the flow mechanical luminosity is less than 5% of the total stellar luminosity, but the flow force is at least 10 times (and more probably 100 times) larger than the force that can be provided by single scattering of the stellar photons. Therefore, the high-velocity molecular gas cannot be accelerated by a radiatively driven stellar wind if momentum is conserved ($F_{\rm wind} \sim F$) in the wind-flow interaction. On the other hand, if the stellar wind cooling rate becomes longer than the dynamical time scale, the molecular gas could be driven by the thermal pressure of the hot wind and gain more momentum than was originally present in the wind. In this case, the kinetic energy would be conserved at the wind-flow interface ($L_{\rm wind} = \epsilon L$), and the force in the wind would be equal to the force in the flow scaled down by $\epsilon V/V_{\rm wind}$, where ϵ is a factor of order 3 to 8 depending on the density distribution in the cloud (Dyson 1984). The momentum requirements derived from the molecular observations would thus become less stringent. However, a radiatively driven wind still seems unlikely for these low-luminosity sources, since it would need to have unrealistic velocities ($V_{\rm wind} \geq 1000$ km s^{-1}) to satisfy $F_{\rm wind} \leq L_*/c$, unless we adopt the lowest limits to the flow force.

If we still assume that the high-velocity gas is ambient material swept up by a (nonradiatively driven) stellar wind, the mass-loss rate $\dot{M}_*$ necessary to drive the high-velocity gas is $\dot{M}_* = F/V_{\rm wind}$ in the momentum-conserving case, and $\dot{M}_* = 2\epsilon L/V_{\rm wind}^2$ in the energy-conserving case. Table 1 gives the estimates obtained assuming a wind velocity $V_{\rm wind}$ of 200 km s^{-1} (typical of optically visible T Tauri stars) and $\epsilon = 3$ at the wind-flow interface (corresponding to an r^{-2} density law in the ambient cloud). Although the uncertainties are quite large, these values are comparable to the mass-loss rates $\sim 10^{-9}$–10^{-7} $M_\odot$ yr^{-1} derived for T Tauri stars, for example from analysis of their forbidden line emission (Edwards *et al.* 1987), suggesting that the winds from embedded and visible young stellar objects might share a common origin.

c) *Flow Collimation*

Our observations reveal that the B335 and RNO 43 outflows are among the most highly collimated of known flows, with a total length-to-width ratio of ~ 5. In RNO 43, the lobes expand with $\theta_{\rm max} \sim 25°$ until approximately 3′ (0.35 pc) from the star, and then keep a roughly constant width of 3.′5 (0.4 pc) over a distance as large as 1 pc. This, together with the progressive change in direction of the HH objects proper motion vectors, from P.A. 15° in RNO 43*a* to 10° and −6° in RNO 43*b* and *d* (Jones *et al.* 1984), suggests that large-scale reconfinement of the flow might be occurring. In B335, the lobes keep an almost constant semiopening angle $\sim 25°$ out to 5′ (0.4 pc) from the star. This was interpreted as free expansion by Goldsmith *et al.* (1984). Reconfinement of the blue lobe, if present, does not occur until 7′ (0.5 pc) along the flow, where the blueshifted emission starts bending back toward the flow axis to form the eastern component.

In both the B335 and the RNO 43 regions, the orientation of the large-scale magnetic field inferred from polarimetric measurements is *parallel* to the direction of the CO lobes (Vrba *et al.* 1986, and S. Strom, private communication). Therefore, magnetic pressure could be responsible for the large-scale confinement of these bipolar flows, by preventing expansion of the high-velocity lobes perpendicular to the field lines. Pudritz and Norman (1986) also predict that the centrifugal wind ejected from a low-gravity rotating magnetized accretion disk should be reconfined along the global direction of the magnetic field by the toroidal component of the field generated by the disk rotation.

Our CO observations show that the high-velocity lobes keep getting narrower and their radial velocities smaller as one looks closer to the star, indicating that the flows are initially collimated on a scale smaller than our spatial resolution of $\sim 1'$. A mechanism often invoked to explain the small-scale collimation of bipolar flows is the presence of a dense circumstellar disk of gas that would focus an initially isotropic stellar wind in the direction of maximum density gradient (Snell, Loren, and Plambeck 1980; Barral and Cantó 1981; Königl

1982). CS emission from dense gas was detected around the sources driving the RNO 43 outflow (see § III of this paper) and the B335 outflow (Heyer *et al.* 1986). In RNO 43, the three-dimensional velocity dispersion σ deduced from the CS line FWHM is 0.54 km s^{-1} and the CS half-power radius R is 1'.5 = 0.17 pc, while in B335, $\sigma = 0.67$ km s^{-1} and $R = 1' = 0.07$ pc. Assuming homogeneous spheres, these values yield virial masses of respectively 19 $M_\odot$ and 13 $M_\odot$ (consistent with the 11–14 $M_\odot$ mass derived by Frerking, Langer, and Wilson (1987) for the B335 dense core using $C^{18}O$ observations), and H_2 densities of respectively 1.7×10^4 and 1.4×10^5 cm^{-3}.

If these structures were collimating the flows, one would expect them to absorb a significant fraction ($\sim \cos \theta_{max}$) of the wind momentum (or energy, if this is the quantity that is conserved in the wind-disk interaction), the remainder of which would be transferred to the high-velocity molecular gas. Defining Ω as the fraction of momentum of energy absorbed by the disk, we should have $P_{disk} = \Omega/(1 - \Omega)P$ (if momentum is conserved), or $E_{disk} = \Omega/(1 - \Omega)E$ (if energy is conserved). Since the CO flow is almost perpendicular to the line of sight, the disk is seen almost edge-on and the observed CS line width should yield a good estimate of its expansion velocity. Therefore, we adopt for V_{disk} the value of σ derived above. In B335, the resulting momentum and kinetic energy of the dense gas are 9 $M_\odot$ km s^{-1} and 3 $M_\odot$ km^2 s^{-2}. By applying the equations above to the range of possible values of P and E given in Table 1, we infer that $0.80 \leq \Omega \leq 0.96$ if momentum is conserved, and $0.23 \leq \Omega \leq 0.89$ if energy is conserved. Therefore, the observed CS condensation could presently be collimating an initially isotropic wind from the B335 outflow source to the observed $\theta_{max} \sim 25°$ ($\Omega \sim 0.91$). In RNO 43, the momentum and kinetic energy in the dense gas are respectively 10 $M_\odot$ km s^{-1} and 3 $M_\odot$ km^2 s^{-2}, implying that $0.07 \leq \Omega \leq 0.31$ if momentum is conserved, and $0.004 \leq \Omega \leq 0.12$ if energy is conserved. Since Ω is here much less than $\cos \theta_{max}$, the observed dense gas cannot be collimating the wind, and it seems more likely that the RNO 43 outflow is being collimated on a different spatial scale, or by another mechanism (for example, the centrifugal hydromagnetic ejection proposed by Pudritz and Norman 1986).

The anisotropic spatial distribution and kinematics of the CS gas around the RNO 43 infrared source are therefore probably due to the interaction of an already collimated wind with the dense core from which the source has formed. The CS line widths $\Delta V_{FWHM} \sim 2$ km s^{-1} observed a few arcminutes away from the core center along the flow axis (see Fig. 5*c*) imply a dispersion velocity along the line of sight $\sigma_x \sim 0.76$ km s^{-1} close to the escape velocity from the CS core ($V_{esc} \sim 0.7$ km s^{-1}), confirming that the core is actually being disrupted by the flow. One intringuing fact is that the centroid of the CS line is shifted by 0.6 km s^{-1} to the *red* in the blue CO lobe, and 0.5 km s^{-1} to the *blue* in the red CO lobe, contrary to what would be expected if the gas were participating in the outflow; it seems that the more quiescent CS gas emitting in the line core reflects a different global motion than the high-velocity gas. A possible explanation is that this more quiescent gas is located in a torus-like structure oriented perpendicular to the outflow and expanding at $\sim$0.5 km s^{-1}: Since the flow is not exactly in the plane of the sky, the expanding torus would be slightly tilted and most of the receding gas would then appear projected onto the blue CO lobe, while most of the gas approaching us would be projected onto the red lobe.

d) Flow Structure

Because the projection effects on distances parallel to the flow axis are minimized when the flow is oriented in the plane of the sky, such a configuration is ideal for studying the large-scale structure of the bipolar flow lobes. One of the most interesting results of this study of the B335 and RNO 43 outflows is the finding that high-velocity lobes can be inhomogeneous or fragmented on a scale comparable to their overall size.

In B335, the blue lobe is interrupted by a region about 4'(0.3 pc) by 3'(0.2 pc) in extent in which we did not detect any high-velocity or static molecular gas. Beyond this cavity, the high-velocity emission reappears with unchanged radial velocities (see Fig. 6 and Figs. 7*a* to 7*d*). In the RNO 43 outflow, the high-velocity emission strongly decreases in the 2'(0.2 pc) region between RNO 43 N1 and RNO 43 N2 (and completely disappears between RNO 43 S1 and RNO 43 S2). Again, the radial velocities in the two high-velocity components are very similar (see Fig. 2 and Fig. 4), but in this case no decrease of the static cloud emission is found.

We consider it unlikely that the inhomogeneity of the B335 and RNO 43 flow lobes reflects two different episodes of mass outflow, since the various high-velocity components still appear connected, by a blueshifted bridge of emission in B335, and by faint extended redshifted emission in the northern lobe of RNO 43. More likely, this apparent fragmentation reflects an intrinsic property of the high-velocity lobes, imposed by the outflow process, or results from the interaction of the flow with an already inhomogeneous ambient medium. In the following, we examine briefly the implications of each possibility.

The first hypothesis is that the cavity observed in B335 has been created by the wind itself as it sweeps up the surrounding molecular material and accumulates it into a dense high-velocity shell. This wind-swept cavity would be visible because its size has become comparable to the cloud thickness along the line of sight. The absence of high-velocity emission toward the cavity would then imply that the swept-up shell has been disrupted and expelled from the B335 cloud. Such a wind-excavated cavity has actually been observed in the ambient material around the infrared outflow source IRS 4 in the dark cloud B5 (Goldsmith, Langer, and Wilson 1986).

A wind-swept cavity might also exist in the RNO 43 lobes, but it could remain undetected since the surrounding cloud is still optically thick in the ^{12}CO $J = 1 \rightarrow 0$ line. The "shoulders" observed in the ^{12}CO profiles toward RNO 43 N1 and RNO 43 S1 might indeed be indicative of a possible hollow structure of the high-velocity lobes. Since there is still ambient material around the RNO 43 lobe, the absence of high-velocity emission between the RNO 43 N1 and RNO 43 N2 components cannot be due to disruption of the swept-up shell. The most natural explanation in this case is that the high-velocity gas is flowing almost perpendicular to the line of sight, and is thus projected at low radial velocities within the line core. Since $i \sim 85°$, this would occur naturally if the flow between RNO 43 N1 and RNO 43 N2 is being reconfined parallel to its axis ($\theta_{max} \sim 0°$), as suggested in § IV*c*. The similarity between the radial velocities of RNO 43 N2 and RNO 43 N1 could then be explained if, after it has been reconfined, the high-velocity gas is diverging again at RNO 43 N2 with the previous value of θ_{max}, or is being forced to converge back toward the flow axis at a similar angle (the blueshifted emission would then come from the back side of RNO 43 N2 and the redshifted emission from its front side).

Alternatively, the observed inhomogeneities might not be intrinsic to the lobe structure but may result from the interaction of the flow with a preexisting cavity in the ambient cloud, visible in B335 but undetected in RNO 43 for the reason mentioned above. In this case, the absence of high-velocity emission reflects the fact that the wind is not encountering any ambient material, and that most of the high-velocity emission in the flow comes from *locally entrained* molecular gas. The wind travels ballistically across the cavity, conserving its original momentum, and then impacts again on the cloud, entraining this new material to the same velocity as the gas it encountered before crossing the cavity.

Regardless of its origin, the presence of a molecular cavity in the blue lobe of B335 implies that energy and momentum are being transported along the flow by a mostly *nonmolecular* component, presumably an ionized or atomic wind from the central star. Assuming a stellar mass-loss rate of $\dot{M}_* = 10^{-8}$ $M_\odot$ yr^{-1} and a flow time scale of 2×10^5 yr, the total mass now present in the wind should be 2×10^{-3} $M_\odot$, half of which would be contained in the blue lobe. If we assume that the wind material is uniformly spread in that lobe over an area 10′ by 2′, we expect a column density of hydrogen atoms $N_H = 1.6 \times 10^{18}$ cm^{-2}. Such an atomic wind has been detected in HH 7–11, a pole-on flow favorably oriented to produce distinctive high-velocity wings in the H I line profiles (Lizano *et al.* 1988). Isolating such a small enhancement from the background H I emission would be much more difficult in B335, where the wind is flowing almost in the plane of the sky and therefore probably emitting at small radial velocities.

V. CONCLUSIONS

Our CO and CS line observations unambiguously show that RNO 43 and B335 are not multiple outflows but single bipolar flows viewed almost perpendicular to their axis, and that each component of superposed blueshifted and redshifted emission is the projection of the front and the back sides of the same high-velocity lobe. This result implies that each of these flows has a *nonzero* expansion velocity perpendicular to its axis, and that the view angle i between the line of sight and the axis of the flow is larger than $90° - \theta_{max}$, where θ_{max} denotes the maximum angle between the velocity vectors in the lobes and the flow axis. This configuration has several interesting aspects.

First, the difference between the radial velocities of the front and back sides of the lobes can be used to derive the view angle i if θ_{max} is known. We estimate $i = 82°$ in B335 and $i = 85°$ in RNO 43, assuming $\theta_{max} = 25°$ in both flows. This allows us to correct the observed flow velocities for inclination and derive upper limits to the flow kinematic and dynamic parameters. The remaining uncertainties on these parameters stem primarily from our ignorance of the true velocity field in the flow.

Second, this configuration appears especially favorable for studying the large-scale collimation and structure of the high-velocity lobes. We find that the RNO 43 and B335 outflows remain aligned with the large-scale magnetic field direction over distances greater than or equal to 1 pc, and that they are among the most highly collimated bipolar flows known to date, with a total length-to-width ratio ~ 5. We also observed strong variations in the column density and radial velocity of the high-velocity gas in both B335 and RNO 43, over a scale ~ 0.2 pc, comparable to the overall lobe size. This result suggests that inhomogeneous high-velocity lobes might be an intrinsic outcome of the outflow process, if not a simple consequence of the clumpy structure of the interstellar medium. In either case, the presence of a cavity in the blue lobe of B335 implies that momentum and kinetic energy are being transported along the flow by a mostly *nonmolecular* wind component.

Although a given outflow should have a fairly high probability ($\sim \sin \theta_{max}$) of being seen nearly in the plane of the sky, RNO 43 and B335 are the only two examples of this configuration found so far, which suggests that the present sample of ~ 50 mapped bipolar flows might be biased toward cases observed at relatively small view angle. This bias could result from two selection effects: First, flows almost in the plane of the sky are harder to detect than pole-on flows, because of their smaller radial velocities and the larger offset of their lobes from the central source. Second, they have a complex outflow pattern which may easily be misinterpreted due to incomplete spatial coverage, low spatial resolution, or insufficient sensitivity. The present study indeed shows that spatial-velocity diagrams are necessary to unambiguously determine the actual geometry of a flow. We conclude that bipolar flows might be intrinsically more collimated than previously suspected, and that their poor apparent degree of collimation (Snell 1987) might result from the fact that they are preferentially observed at small view angles.

We thank R. Levreault, D. Lis, C. Magri, and Y. Minh for assistance with some of the data collection, and W. Langer for discussions and information on the B335 cloud. S. C. gratefully acknowledges support by a scholarship from the American Women's Group in Paris and by grants from NSF and NASA awarded to S. Strom. P. G. and R. S. acknowledge support by NSF grant 85-12903 to the Five College Radio Astronomy Observatory of the University of Massachusetts. This is contribution no. 642 of the Five College Astronomy Department.

REFERENCES

Barral, J. F., and Cantó, J. 1981, *Rev. Mexicana Astr. Ap.*, **5**, 101.
Cabrit, S., and Bertout, C. 1986, *Ap. J.*, **307**, 313.
———. 1987, in *Protostars and Molecular Clouds*, ed. T. Montmerle and C. Bertout (Saclay: CEN/Doc), p. 43.
———. 1988, in preparation.
Cohen, M. 1980, *A.J.*, **85**, 29.
Cohen, M., and Schwartz, R. D. 1987, *Ap. J.*, **316**, 311.
Dickman, R. L. 1978, *Ap. J. Suppl.*, **37**, 407.
Dyson, J. E. 1984, *Ap. Space Sci.*, **106**, 181.
Edwards, S., Cabrit, S., Strom, S. E., Heyer, I., Strom, K. M., and Anderson, E. 1987, *Ap. J.*, **321**, 473.
Edwards, S., and Snell, R. L. 1984, *Ap. J.*, **281**, 237.
Edwards, S., and Strom, S. E. 1987, in *Proc. Fifth Cambridge Cool Stars Workshop*, ed. J. L. Linsky and R. Stencel (NY: Springer-Verlag), in press.
Frerking, M. A., and Langer, W. D. 1982, *Ap. J.*, **256**, 523.
Frerking, M. A., Langer, W. D., and Wilson, R. 1987, *Ap. J.*, **313**, 320.
Goldsmith, P. F., Snell, R. L., Hemeon-Heyer, M., and Langer, W. D. 1984, *Ap. J.*, **286**, 599.
Goldsmith, P. F., Langer, W. D., and Wilson, R. W. 1986, *Ap. J. (Letters)*, **303**, L11.
Heyer, M. H., Snell, R. L., Goldsmith, P. F., Strom, S. E., and Strom, K. M. 1986, *Ap. J.*, **308**, 134.
Jones, B. F., Cohen, M., Sirk, M., and Jarrett, R. 1984, *A.J.*, **89**, 1404.
Keene, J., Davidson, J. A., Harper, D. A., Hildebrand, R. H., Jaffe, D. T., Loewenstein, R. F., Low, F. J., and Pernic, R. 1983, *Ap. J. (Letters)*, **274**, L43.
Königl, A. 1982, *Ap. J.*, **261**, 115.
Kutner, M., and Ulich, B. L. 1981, *Ap. J.*, **250**, 341.
Lada, C. J. 1985, *Ann. Rev. Astr. Ap.*, **23**, 267.
Langer, W. D., Frerking, M. A., and Wilson, R. W. 1986, *Ap. J. (Letters)*, **306**, L29.
Lizano, S., Heiles, C., Rodriguez, L. F., Koo, B.-C., Shu, F. H., Hasegawa, T., Hayashi, S., and Mirabel, I. F. 1988, preprint.

Maddalena, R. J., and Morris, M. 1987, *Ap. J.*, 323, 179.
Mundt, R., Brugel, E. W., and Bührke, T. 1987, *Ap. J.*, 319, 275.
Myers, P. C., and Benson, P. J. 1983, *Ap. J.*, 266, 309.
Pudritz, R. E., and Norman, C. A. 1986, *Ap. J.*, 301, 571.
Ray, T. P. 1987, *Astr. Ap.*, 171, 145.
Snell, R. L. 1987, in *IAU Symposium 115, Star Forming Regions*, ed. M. Peimbert and J. Jugaku (Dordrecht: Reidel), p. 213.
Snell, R. L., Loren, R. B., and Plambeck, R. L., 1980, *Ap. J. (Letters)*, 239, L17.
Vrba, F. J., Luginbuhl, C., Strom, K. M., and Heyer, M. H. 1986, *A.J.*, 92, 633.

SYLVIE CABRIT: Institut d'Astrophysique, 98 bis Bd Arago, 75014 Paris, France

PAUL F. GOLDSMITH and RONALD L. SNELL: Five College Radio Astronomy Observatory, 619 Lederle GRC Tower B, University of Massachusetts, Amherst, MA 01003

ANNEXE 6

CO LINE FORMATION IN BIPOLAR FLOWS.

III. THE ENERGETICS OF MOLECULAR FLOWS REVISITED

Sylvie CABRIT and Claude BERTOUT

Institut d'Astrophysique de Paris

to be submitted to *Astrophysical Journal*

Preliminary draft

ABSTRACT

Results obtained in a previous analysis of the CO line formation problem in bipolar flows are used to investigate the hypothesis that CO flows are pushed by winds emanating from the infrared central sources associated with the molecular outflows. We reach the conclusion that radiation-pressure driven winds from high-luminosity embedded sources (with $L_{bol} \gtrsim 10^3\ L_\odot$) can drive their associated CO flows, and that the molecular flow is more likely to be driven by the thermal pressure of the wind than by its momentum. The ionized winds of these high-luminosity objects appear massive enough to drive the CO flows. The case of low-luminosity embedded sources is more difficult. While there is indication in one case that the CO flow might also be energy-driven by a hot wind, in most cases the winds' momentum rate appears larger than the stellar radiative momentum output rate unless the circumstellar medium is very optically thick. Several differences found between high-luminosity and low-luminosity sources in fact suggest that the physical mechanisms driving their winds might be quite different. We discuss constraints placed on various theoretical mechanisms by our data and conclude that circumstellar disks must play a major role in driving the winds of low-luminosity protostellar objects.

I. INTRODUCTION

Although they were discovered almost a decade ago, high-velocity molecular outflows remain as puzzling as ever. There is no consensus at this point about the physical mechanism(s) responsible for driving and collimating them. The challenges that CO bipolar flows pose to theoretical models have been summarized by Lada (1985), and Figure 1 shows slightly modified versions of two key diagrams from his paper. The mechanical luminosity in the CO flows, L_{CO}, is plotted against the bolometric luminosity of the embedded infrared objects associated with the flows in Fig. 1a. There, symbols for the data points differ according to the flow view angle, estimated by comparing the flow morphology to synthetic maps computed by Cabrit and Bertout (1986; 1988). Open squares denote flows viewed at less than 20^o (i.e., seen almost pole-on); open circles are for view angles in the range 20^o - 40^o; filled squares indicate view angles in the range 40^o - 60^o; and filled triangles are for view angles larger than 60^o. Only those flows in Lada's list whose view angle could be reasonably well estimated have been included in Fig. 1. L_{CO} is defined by

$$L_{CO} = M_{CO} V_{CO}^3 / 2R_{CO}, \tag{1}$$

where M_{CO}, V_{CO}, and R_{CO} are, respectively, mass, velocity, and scalelength of the moving CO gas; these quantities are derived directly from the millimetric observations of CO outflows. Fig. 1a shows that a correlation exists between the flow mechanical energy and the bolometric luminosity of the central source. This suggests that the energy contained in the radiation field of the central source is sufficient to drive the flows provided they have been steady over their dynamical lifetimes.

Figure 1b displays a plot of the CO momentum rate F_{CO} versus the stellar bolometric luminosity L_*, with F_{CO} defined by

$$F_{CO} = M_{CO} V_{CO}^2 / R_{CO}. \tag{2}$$

Again, a correlation between the CO gas momentum rate and the overall radiative momentum rate of the central object is found. But the momentum rate in the molecular gas is usually much larger than L_*/c, which apparently rules out a radiatively driven wind as the powering mechanism. There are, however, several reasons to look more closely at this interpretation of Figure 1.

(a) Dyson (1984) and Kwok and Volk (1985) adapted the theory of wind bubble expansion to physical conditions found in interstellar clouds. They showed that the interaction of the wind with the CO gas can be either energy-conserving or momentum-conserving; and in the former case, the CO momentum rate can be much larger than the wind momentum rate. Their refined theoretical approach must be taken into consideration.

(b) Cabrit and Bertout (1986, 1988) have shown that uncertainties in the CO flow parameters derived from observations can be more than one order of magnitude. Their estimates of the uncertainty can be used to bracket the true value of the flow's mechanical luminosity and and momentum rate.

(c) The bolometric luminosities of the embedded sources associated with CO flows are now more accurately known from the detailed study of IRAS data by Mozurkewich *et al.* (1986). Furthermore, a large number of radio continuum data are available for these sources (e.g. Snell and Bally 1986) which makes it possible to discuss the possible role of the ionized wind component in driving the CO flow.

The picture of a CO outflow tested in this paper was first proposed by Snell *et al.*(1980). It assumes that the central source emits a stellar wind which interacts with the ambient, cold circumstellar material, thereby creating an expanding shell of molecular gas that is identified with the CO flow. Questions to be addressed include (i) What is the nature of the interaction between wind and molecular gas? (ii) Can the wind from the central source be driven radiatively? (iii) Can the ionized wind component (seen in the radio continuum) drive the CO flow?

II. ENERGY DRIVEN VS. MOMENTUM DRIVEN WINDS

Weaver *et al.*(1977) developed the theory of wind bubble expansion. They showed that the shell of swept-up circumstellar material is driven by the pressure of the shocked wind as long as the radiative losses from the shocked wind region are small. This phase is referred to as the energy-driven regime. But when radiative losses become important, the shocked wind region collapses and the stellar wind collides directly with the shell; this is the momentum-driven regime. [1] As Dyson (1984) emphasizes, one must find out

[1] In both cases, the thin shell assumption for the swept-up material implies efficient radiative cooling within the shell. If the circumstellar material is primarily H_2, far-infrared emission from the shell is expected.

which type of flow is originally set up and also whether the driving mechanism will change in time. The wind velocity determines whether the wind is initially driven by energy or momentum. Assuming that thermal conduction is suppressed by the magnetic field present in the molecular swept-up material, the critical velocity (below which the flow is momentum-driven; cf. Eq. 8 in Dyson 1984 and Figure 2) is in the range 200-300 km/s for mass-loss rates up to about 10^{-6} $M_\odot$/yr and for $n_H = 10^4$ cm^{-3}, which is a density typical of molecular cores.

Little is known about the wind velocity of embedded protostellar sources. If high-luminosity infrared sources are similar to optical OB stars – a likely possibility since they have already reached the main-sequence – we expect their winds to have velocities about 1000 km/s or larger, and their CO flows to be energy-driven. IRS5 in Lynds 1551 is representative of low-luminosity sources driving molecular outflows, and its H_α profile has been observed by Mundt *et al.* (1985). It is a typical P Cygni profile, and its blue absorption wing indicates that the maximum velocity in the H_α flow is about 500-600 km/s. If this wind actually pushes the CO bipolar gas in L1551, then the interaction is likely to be pressure-driven rather than momentum-driven. From his study of the flow evolution, Dyson (1984) concludes that all the molecular outflows he investigates are likely to be energy-driven during most of their lifetime. We shall nevertheless consider both types of flows in the following discussion.

An important point stressed by Dyson (1984) and Kwok and Volk (1985) is that the momentum rate and mechanical luminosity of the molecular flow cannot be used directly to find both the wind momentum rate and mechanical luminosity because the conserved quantity depends on the flow type. In a momentum-driven flow, most of the wind kinetic energy is radiated away, while in an energy-driven flow the momentum of the swept-up gas depends both on the pressure inside the bubble and on the wind momentum. Assuming that the stellar wind expands isotropically with a velocity V_w in a medium with density gradient given by

$$\rho(r) = \rho_o r^\beta, \; \beta \leq 0, \tag{3}$$

Dyson (1984) and Kwok and Volk (1985) find that the wind mechanical luminosity L_w and momentum rate F_w are given, respectively, by

$$L_w^m = \frac{4+\beta}{2} \frac{V_w}{V_{CO}} L_{CO} \tag{4a}$$

and

$$F_w^m = \frac{4+\beta}{2} F_{CO} \tag{5a}$$

if the wind is momentum-driven, and by

$$L_w^e = \frac{77 + 29\beta + 2\beta^2}{9} L_{CO} \tag{4b}$$

and

$$F_w^e = \frac{77 + 29\beta + 2\beta^2}{9} \frac{V_{CO}}{V_w} F_{CO} \tag{5b}$$

if the wind is energy-driven. In these equations, V_{CO} is the velocity of the molecular gas, while L_{CO} and F_{CO} are given by Eqs. 1 and 2. Since Eqs. 4 and 5 assume spherical symmetry, we need to assess their usefulness for bipolar, rather than for spherical, winds.

The evolution of a stellar wind bubble in a plane-parallel, stratified cloud was investigated by Sakashita and Hanami (1986), who find that the bubble becomes bipolar and that the flow collimation depends on the type of flow established as well as on the details of the interstellar density distribution. Their work demonstrates that conservation of momentum (viz. energy) occurs globally in the two lobes, so that the spherical case mentioned above is a useful first approximation of the bipolar situation, provided the flow collimation is caused by density gradients in the interstellar medium (see Königl 1982). While other collimation mechanisms have been proposed for which the above picture would certainly fail – in particular, mechanisms in which collimation is intrinsic to the star/disk system – observational evidence (e.g. Bertout 1987) for strong interstellar density gradients in the immediate vicinity of many young stellar objects that show collimated flows justifies our interest in this model.

III. DERIVATION OF FLOW PARAMETERS FROM OBSERVATIONS

Another area of concern is the large uncertainties associated with the physical parameters of molecular flows, i.e., the quantities which enter Eqs. 1 and 2 above. Cabrit and Bertout (1986; 1988) estimated these uncertainties quantitatively by assuming various kinematic models for the CO flows and then solving the CO line formation problem in some detail. Specifically, power-law velocity fields $v(r) \propto r^\alpha$ with $-1 \leq \alpha \leq 1$ were investigated. Synthetic maps obtained for known flow parameters were analyzed in the same way as observed CO maps, and from there the main sources of error in the derived flow parameters were identified.

One disturbing conclusion of these investigations is that the flows most easily detected are those whose physical parameters are most likely to be in error. About one half of the CO flows appearing in Fig. 1 are what the study calls Case I flows, i.e., flows seen at small view angles. This is because the flow radial velocities are largest, and detection of high velocity wings easiest, when the angle between observer and the flow's symmetry axis is small. But the CO flow dynamical time, found from its extent and velocity, is particularly uncertain in this configuration because of projection effects, so that dynamical parameters are not well constrained. More specifically, the momentum rate tends to be overestimated in that case.

Using this study of several CO velocity distributions, we determine a typical uncertainty range on a given physical parameter as a function of the view angle (this is done for each of the methods used to determine that physical parameter). We then define an "error bar" from the minimum and maximum errors found in computations for the different velocity fields. While these error bars, given in Table 1, are in principle valid only for the few simple velocity fields we studied, they do provide a first estimate of the magnitude of possible systematic effects on the determination of the flow's parameters; and they allow us to discuss whether the momentum problem is really as critical as it was assumed to be so far.

IV. RESULTS AND DISCUSSION

We use 10 molecular outflows in Lada's (1985) list, chosen according to two criteria. Their integrated intensity maps present some degree of symmetry, so that we can tentatively derive a view angle based on the flow morphology; and the CO mass in the flow can be determined accurately, i.e., by integrating over all lines of sight and by correcting for optical depth effects when the $^{13}CO/^{12}CO$ line ratio indicates that the $^{12}CO(J = 1 - 0)$ line is optically thick. CO masses were also renormalized to the same CO abundance, using $N(^{13}CO)/N(H_2) = 2.5\ 10^{-6}$. We used CO velocities from Lada (1985) and bolometric luminosities of the central sources from Mozurkewich *et al.* (1986). The list of sources and their properties are given in Table 2.

Figure 3*a* displays the wind momentum rate computed from Eq. 5a and plotted as a function of the central source bolometric luminosity for the 10 CO flows. We assume here that the stellar wind is expanding in a medium with $\beta = -2$, a value expected in the outer, isothermal regions of a collapsed molecular core. If the wind were expanding in a

constant density medium, all data points would be displaced upwards by 0.3 dex. Error bars associated with data points indicate the uncertainty range on the CO momentum rate, as discussed in the preceding section. The two dotted lines which cross the diagram indicate the maximum stellar radiative momentum output rate $\tau L_*/c$ for $\tau = 1$ and $\tau = 10$. This plot shows that the wind momentum rate is almost always greater than the stellar radiative momentum rate, even when the wind optical depth is as large as 10, which indicates that a radiatively-driven wind does not have enough momentum to drive the CO flow if the interaction is momentum-conserving. The two most luminous sources might represent an exception to this statement.

Figure 3*b* shows the wind's mechanical luminosity (Eq. 4a) as a function of the central source bolometric luminosity. Symbols have the same meaning as before, and the dotted line represents $L_* = L_w$. In order to draw this diagram, we must first deal with the ratio of wind to CO velocities, so we adopt a single, representative value of 20 for this insufficiently known parameter. The ratio of L_w to L_* is typically 1 to 10 % for the low-luminosity sources, but it diminishes to about 0.1 % for the high-luminosity sources, which is roughly similar to that inferred for optical OB stars. One might, therefore, conclude with Mozurkewich *et al.* (1986) that CO flows around high-luminosity objects can in principle be driven by the momentum of radiatively driven winds. But if the high-luminosity sources have wind velocities comparable to those of OB stars, their associated CO flows are likely to be energy-driven rather than momentum-driven.

Figure 4*a* displays the wind mechanical luminosity as a function of the bolometric luminosity of the central source for an energy-driven interaction. Here, the mechanical luminosity is found from Eq. 4b, and we assume again that the stellar winds expand in a circumstellar medium with a density distribution proportional to r^{-2}. The high-luminosity sources driving CO flows and optically visible OB stars share the same general region in this diagram. As far as the energy budget is concerned, winds from high-luminosity embedded sources could therefore be driven by radiation-pressure as are winds from OB stars. The force as defined by Eq. 5b is plotted against the central source radiative momentum rate in Figure 4*b*. We assumed as before that the ratio of wind to CO gas velocity is 20 for all sources. Although this last assumption introduces some uncertainty, it does not seem unreasonable to conclude that an optical depth in the range 1-10 would be sufficient for the star's maximum radiative momentum rate $\tau L_*/c$ to account for the wind's momentum rate. When the wind expands in a constant density medium, all points

in Figure 4 go up by 0.46 dex, so that the momentum budget becomes more critical. The wind momentum rate of optical OB stars usually represents a smaller fraction of the total stellar radiative momentum output, even for the favorable case of outwardly decreasing circumstellar density considered above. Protostellar sources appear to be able to transfer their radiative momentum to the wind as efficiently as do Wolf-Rayet stars.

We conclude from this re-examination of the energetics of CO flows that a wind driven by radiation pressure can actually push molecular flows associated with high-luminosity protostellar sources (i.e., $L_{bol} > 10^3$ L_o), provided the density of the interstellar medium decreases away from the star. However, the flow must be driven by the pressure of the shocked wind rather than directly by the stellar wind momentum. If the wind velocities of embedded protostellar sources are comparable to those of OB stars, this is likely. Furthermore, the wind momentum rate represents a significant fraction of the overall stellar radiative momentum output rate, suggesting that the wind is optically thick close to the central source.

CO flows associated with low-luminosity sources might also be energy-driven by stellar winds, although it is unlikely in view of the more stringent momentum rate requirement that these winds are of the same nature as those of high-luminosity sources. The main argument in favor of energy-driven CO flows from low-luminosity sources is the observed high velocity of the L1551/IRS5 wind. Yet, the finding by Edwards *et al.* (1986) and Clark and Laureijis (1986) that extended infrared emission is associated with the L1551/IRS5 outflow might lead to the dismissal of this model. Edwards *et al.*(1986) find that the infrared diffuse luminosity enclosing IRS5 is equal to 7 $L_\odot$, a value ten times greater than the mechanical luminosity in the CO flow. They attribute the extended emission to cooling radiation from the shock between ambient and swept-up material. Using the results of Weaver *et al.*(1977) and Dyson (1984) to derive the luminosity L_{rad} radiated away by the swept-up gas, we find

$$L_{rad} = \left[\frac{6}{11}\left(\frac{77 + 29\beta + 2\beta^2}{9}\right) - 1\right] L_{CO}. \tag{6}$$

Bracketting L_{rad} by using our "error bars" on L_{CO}, we get

$$0.3 \leq L_{rad} \leq 1.53 L_\odot \text{ for } \beta = -2,$$

and

$$1.76 \leq L_{rad} \leq 8.8 L_\odot \text{ for } \beta = 0.$$

Thus, predictions based on the theory of energy-driven flows yield smaller values of L_{rad} than observed for the case $\beta = -2$, but comparable values for the case $\beta = 0$. Whether the extended infrared emission allows one to rule out an energy-driven interaction for L1551/IRS5 is therefore unclear at this point. Further information on far-infrared emission associated with other CO flows would obviously be valuable for understanding the driving mechanism of CO flows.

The physical mechanism responsible for the massive winds from low-luminosity protostellar objects remains elusive. The ratios of both wind mechanical luminosity to stellar luminosity and wind force to stellar radiative momentum output are, on the average, about ten times higher in low-luminosity sources than in sources with $L_{bol} > 10^3$ L_o, which indicates an extremely efficient wind-driving mechanism. The problem of finding such a mechanism for T Tauri winds is well-documented (cf. DeCampli 1981; Hartmann *et al.*1982; Hartmann 1986), and obviously we are confronted with a similar problem in the case of low-luminosity embedded sources driving CO flows. Compared to T Tauri stars, protostellar low-luminosity sources have the main advantage of being potentially fast rotators, and a newly developed wind model takes advantage of this possibility (Shu *et al.*1987).

Another difference between low-luminosity protostellar sources and optical T Tauri stars lies in their radio properties. While optical pre-main-sequence stars are infrequent radio-emitters (cf. Montmerle and André 1988), many embedded sources associated with molecular outflows are radio sources and their emission is apparently thermal. The mass-loss in the ionized component can therefore be derived and compared to the wind mass-loss rate derived from the CO observations.

Snell and Bally (1986) have shown that most high-luminosity infrared sources, as well as several low-luminosity sources, associated with molecular outflows are also radio sources. While this suggests that CO flows and ionized winds are somehow connected, the nature of this connection is unclear because mass-loss rates derived by these authors from the radio data are usually lower than those derived from the CO data. It is therefore believed that the ionized wind component cannot drive the molecular gas, and a neutral wind component has been suggested (cf. Shu *et al.*1987).

Since we have seen above that CO dynamical parameters are often overestimated, a re-examination of the relationship between CO mass-loss and ionized gas mass-loss is in

order. Among the 10 flows investigated in the preceding section, 6 are associated with radio-emitting central objects (T Tau, L1551/IRS5, SVS13, LkH$_\alpha$ 234, NGC 2071, and S140). We derived "radio mass-loss rates" for these objects by assuming that their 5 GHz fluxes originate from a constant-velocity ionized wind. Although this assumption may be incorrect for some low-luminosity objects with relatively flat radio spectra, we ignored the error introduced by possible deviations from a constant velocity wind. An overestimation of our derived radio mass-loss rates is likely to result from this assumption and from the hypothesis of spherical symmetry for the wind. An additional source of uncertainty is the often unknown terminal velocity of the wind. Terminal velocities used here are the same as the wind velocities used in the derivation of wind momentum rates above ($V_w = 20\,V_{CO}$). In optically visible objects, these velocities are usually lower than those estimated from the H$_\alpha$ line, which underestimates the mass-loss rate. We estimate the overall uncertainty to be a factor 2-3.

We can now compare the wind mass-loss rates $\dot{M}_w$ derived directly from the wind momentum rates (as found from the assumption of an energy-driven CO flow) with the mass-loss rates $\dot{M}_{radio}$ in the ionized wind components. The result is shown in Figure 5, where wind mass-loss rates are plotted (with their associated error-bars as defined above) against radio mass-loss rates. The dotted line indicates equal wind and radio mass-loss rates. Again, low-luminosity and high-luminosity sources exhibit qualitatively different behavior.

For high-luminosity sources, the mass-loss in the ionized wind component is higher than the wind mass-loss derived under the assumption that the CO is pressure-driven by the wind. We, therefore, conclude that the ionized wind component is in fact driving the CO flows in these objects.

In low-luminosity sources, the ionized component's mass-loss appears comparable to the wind's mass-loss when the error bars are taken into account. Because of the uncertainties mentioned above, it is difficult at this point to assess the need for an additional, neutral wind. There is however mounting observational evidence for such neutral wind components (cf. Lizano *et al.*1987). If taken at face value, our data suggest that the momentum rate in the neutral wind component might not need to be larger than that in the ionized component.

REFERENCES

André, P., 1987, in *Protostars and Molecular Clouds*, Eds. T. Montmerle and C. Bertout (Saclay: CEA/Doc)

Bertout, C., Cabrit, S., Roland, J., 1988, in preparation

Cabrit, S., Bertout, C., 1986, *Ap. J.*, **307**, 313

Cabrit, S., Bertout, C., 1988, in preparation

Cabrit, S., Goldsmith, P.F., Snell, R.L., 1988, *Ap. J.*, **334**, 196

Clark, F.O., Laureijis, R.J., 1986, *Astron. Ap.*, **154**, L26

Dyson, J.E., 1984, *Ap. Space Science*, **106**, 181

Edwards, S., Snell, R., 1982, *Ap. J.*, **261**, 151

Edwards, S., Snell, R., 1983, *Ap. J.*, **270**, 605

Evans, N.J., Levreault, R.M., Beckwith, S., Skrutskie, M, 1987, *Ap. J.*, **320**, 364

Hartmann, L., 1986, *Fund. Cosmic Phys.*, **11**, 279

Hartmann, L., Edwards, S., Avrett, A., 1982, *Ap.J.*, **261**, 279

Königl, A, 1982, *Ap. J.*, **261**, 115

Kwok, S., Volk, K, 1985, *Ap. J.*, **299**, 191

Lada, C.J., 1985, *Ann. Rev. Astron. Ap.*, **23**, 267

Lizano, S., Heiles, C., Rodriguez, L.F., Koo, B.-C., *et al.*, 1988, *Ap.J.*, **328**, 763

Montmerle, T., and André, P. 1988, in *Formation and Evolution of Low-mass stars* Ed. A.K. Dupree (Dordrecht: Reidel), in press

Mozurkewich, D., Schwartz, P.R., Smith, H.A., 1986, *Ap. J.*, **311**, 371

Myers, P., Heyer, M., Snell, R., Goldsmith, P., 1988, *Ap. J.*, **324**, 907

Natta, A., Giovanardi, C., Palla, F., Evans, N.J., 1988, *Ap. J.*, **327**, 817

Sakashita, S., Hanami, H., 1986, *Publ. Astron. Soc. Japan*, **38**, 879

Shu, F.H., Lizano, S., Ruden, S.P., Najita, J., 1988, *Ap.J.*, **328**, L19

Snell, R.L., Bally, J., 1986, *Ap. J.*, **303**, 683

Snell, R.L., Schloerb, F.P., 1985, *Ap. J.*, **285**, 490

Snell, R.L., Loren, R.B., Plambeck, R.L., 1980, *Ap. J.*, **239**, L17

Weaver, R., McCray, R., Castor, J., Shapiro, P., Moore, R., 1977, *Ap. J.*, **218**, 377

Table 1

Error bars on flow dynamical parameters derived from CO data

i	10^o	30^o	50^o	70^o
$\log_{10}(F_{obs}/F_c)$	0.3 – 0.6	0.06 – 0.5	0.02 – 0.3	-0.3 – 0.2
$\log_{10}(L_{obs}/L_c)$	0.3 – 0.6	0.06 – 0.5	0.00 – 0.3	-0.6 – 0.1

Table 2

Revised CO data

Flow	L_*	M_{CO}	F_{CO}	L_{CO}	V_w	$\dot{M}_{radio}$	$\dot{M}_w$
	$L_\odot$	$M_\odot$	$M_\odot$ km $s^{-1}yr^{-1}$	$L_\odot$	km s^{-1}	$M_\odot$ yr^{-1}	$M_\odot$ yr^{-1}
HH7-11	150	0.95	1.0 (-3)	1.6	400	6.7 (-8)	3.7 (-7)
T Tau	22	0.20	1.2 (-4)	0.14	240	1.6 (-7)	7.5 (-8)
L1551	33	0.85	6.0 (-4)	0.6	300	2.0 (-7)	3.0 (-7)
Orion A	2.1 (5)	3.7	3.8 (-1)	1.8 (3)	1280	—	4.4 (-5)
NGC 2071	3.3 (3)	4.4	1.3 (-2)	38	740	5.0 (-6)	2.6 (-6)
LkHα 234	1.0 (3)	23.6	2.0 (-3)	1.0	140	4.7 (-7)	2.1 (-6)
S 140	3.5 (4)	11.0	1.0 (-2)	15	420	1.7 (-5)	3.6 (-6)
L723	2.4	0.22	2.5 (-5)	0.02	200	—	1.8 (-8)
B335	3.0	0.24	7.0 (-6)	2.8 (-3)	100	—	7.6 (-9)
RNO 43	12.4	13.4	2.5 (-4)	0.1	100	—	3.3 (-7)

Figure Captions

Figure 1: (a) Momentum rate of the CO molecular outflows plotted against the bolometric luminosity of the embedded central objects. (b) Mechanical luminosity of the molecular outflows plotted against the bolometric luminosity of the embedded central objects. The meaning of the various symbols is given in the text.

Figure 2: Critical velocity above which the flow becomes energy-driven, as a function of wind mass-loss rate and ambient density (cf. Eq. 8 in Dyson 1984).

Figure 3: (a) Momentum rate of the stellar winds plotted against the bolometric luminosity of the embedded central objects. It is assumed here that the CO flow is driven by the momentum of the stellar wind. The bars indicate uncertainties on the momentum rate (see text for details). (b) The mechanical luminosity of the stellar wind is plotted against the bolometric luminosity of the embedded central objets, with the same assumption as (a).

Figure 4: (a) The mechanical luminosity of the stellar wind is plotted against the bolometric luminosity of the embedded central objets. It is now assumed that the CO flow is driven by the thermal pressure of the shocked wind. The bars indicate uncertainties on the mechanical luminosity (see text for details). (b) Momentum rate of the stellar winds plotted against the bolometric luminosity of the embedded central objects, with the same assumption as (a).

Figure 5: The mass-loss rate derived from CO data (assuming an energy- driven flow with $\beta = -2$) is plotted against the mass-loss rate derived from radio continuum data. Error bars indicate uncertainties on the CO mass-loss rates.

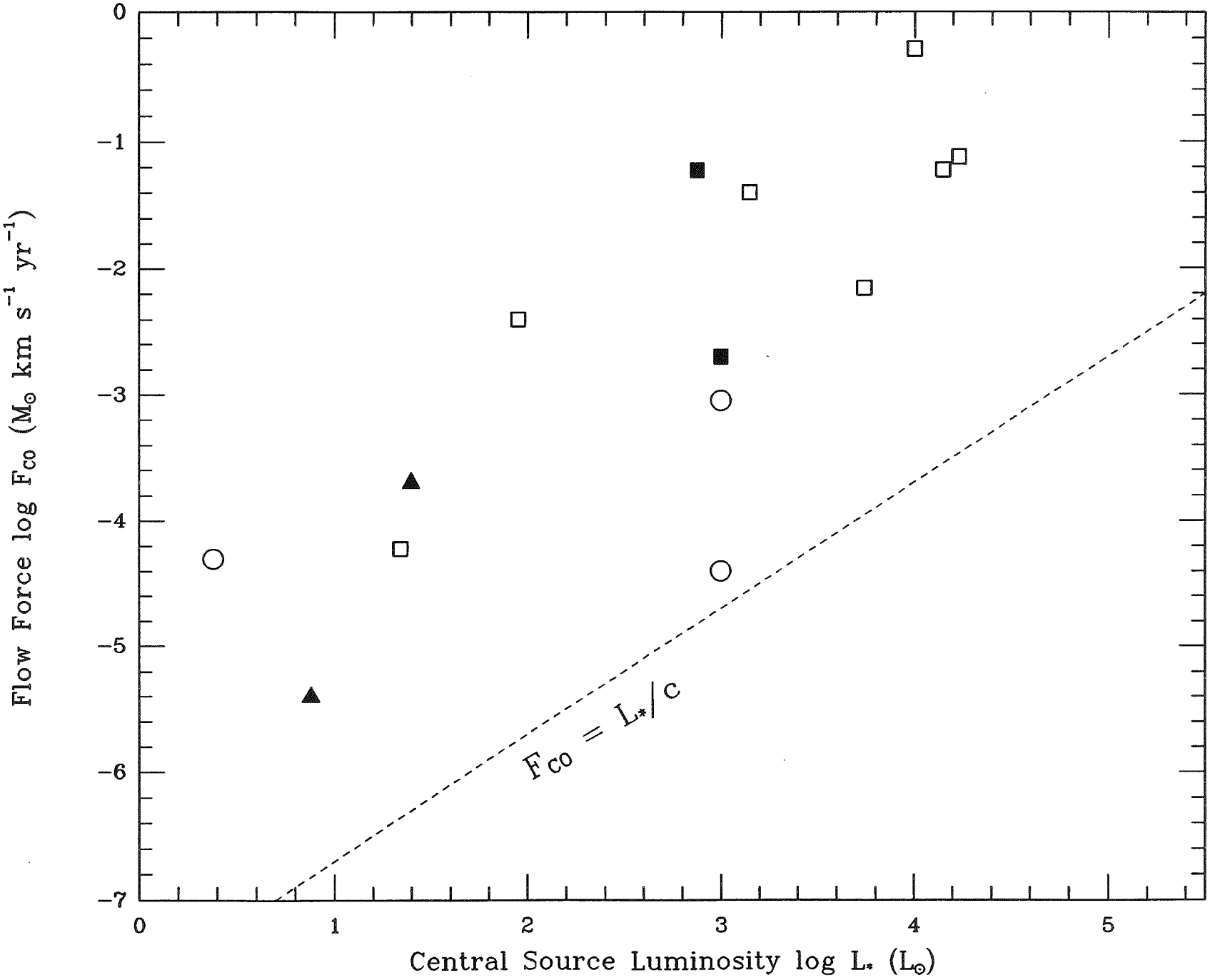
Flow Force log F_{CO} ($M_\odot$ km s^{-1} yr^{-1})
Central Source Luminosity log L_* ($L_\odot$)
$F_{CO} = L_*/c$
0
−1
−2
−3
−4
−5
−6
−7
0
1
2
3
4
5

Fig. 1a

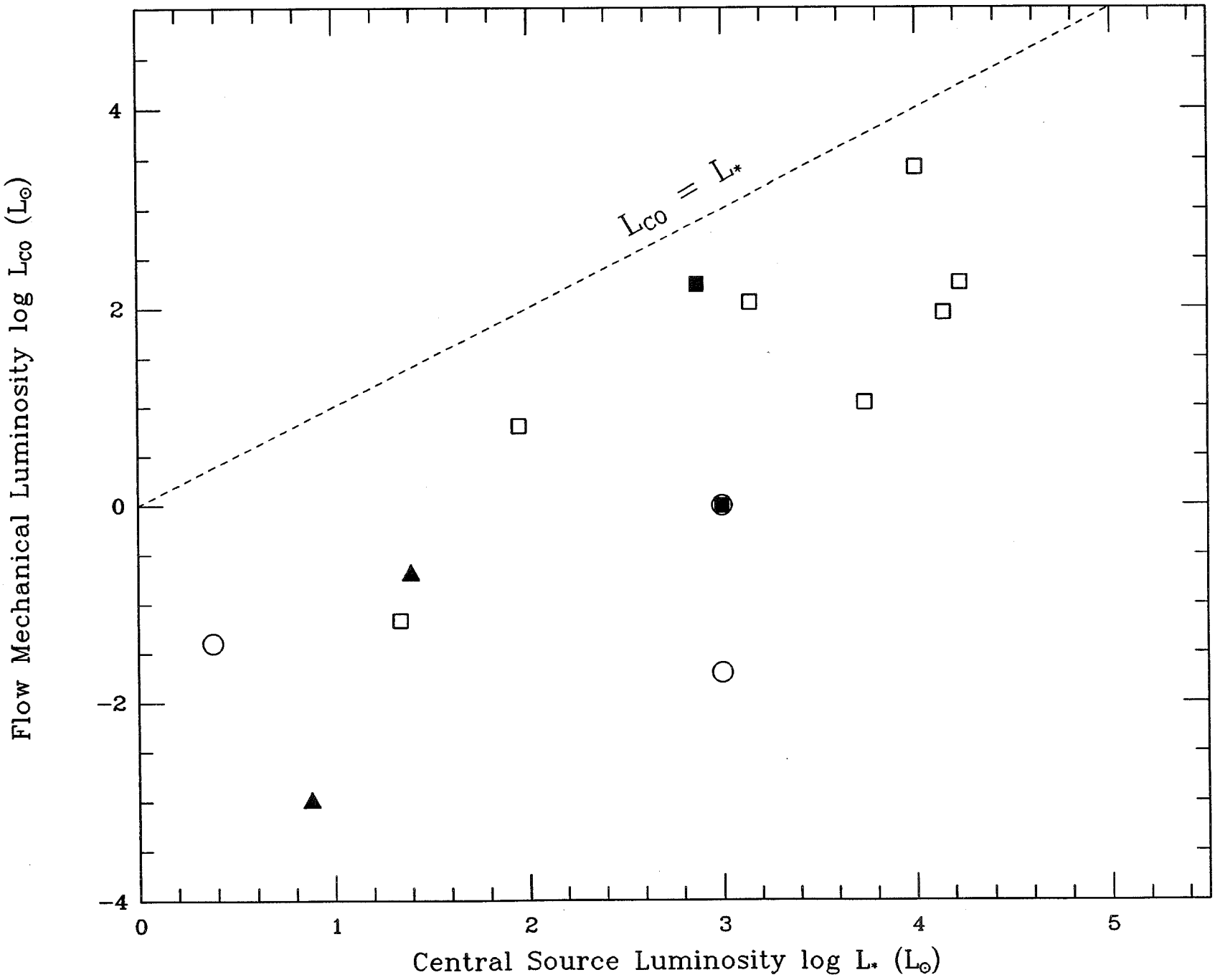
Flow Mechanical Luminosity log L_{CO} ($L_\odot$)
Central Source Luminosity log L_* ($L_\odot$)
$L_{CO} = L_*$
4
2
0
−2
−4
0
1
2
3
4
5

Fig. 1b

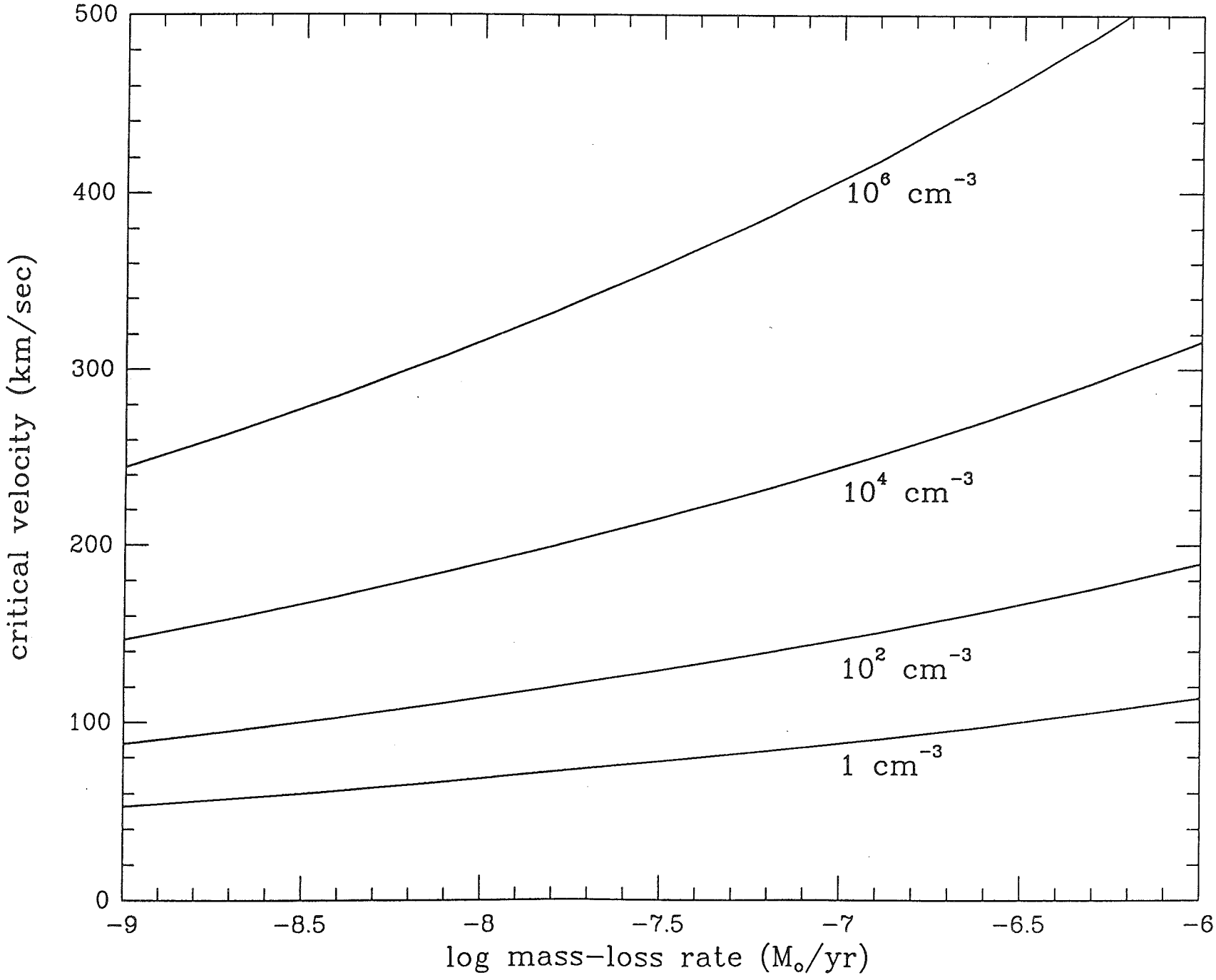
500
400
300
200
100
0
critical velocity (km/sec)
10^6 cm^{-3}
10^4 cm^{-3}
10^2 cm^{-3}
1 cm^{-3}
−9
−8.5
−8
−7.5
−7
−6.5
−6
log mass−loss rate (M_o/yr)

Fig. 2

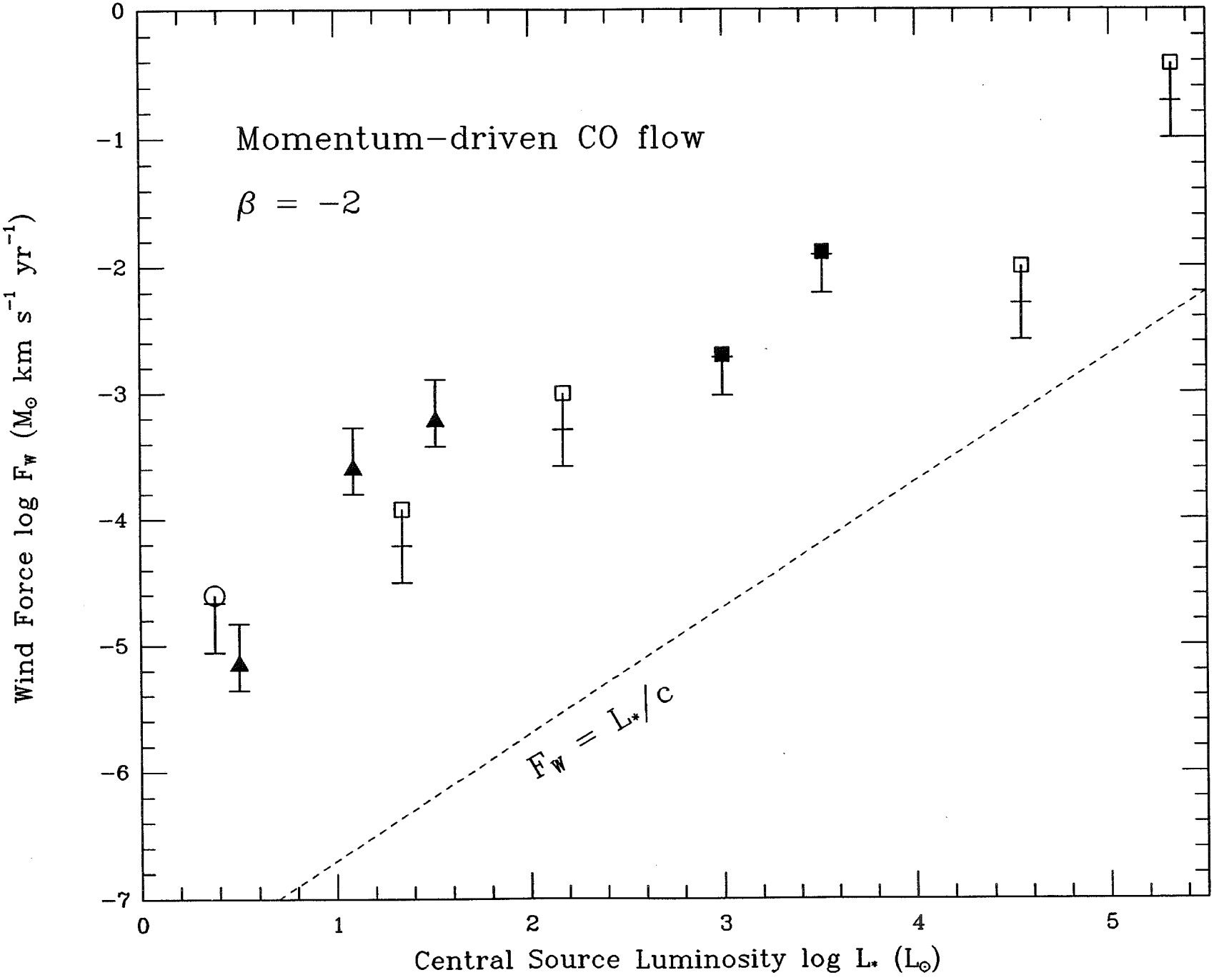
Momentum-driven CO flow
$\beta = -2$
$F_w = L_*/c$
Wind Force log F_w ($M_\odot$ km s^{-1} yr^{-1})
Central Source Luminosity log L_* ($L_\odot$)
0
-1
-2
-3
-4
-5
-6
-7
0
1
2
3
4
5

Fig. 3a

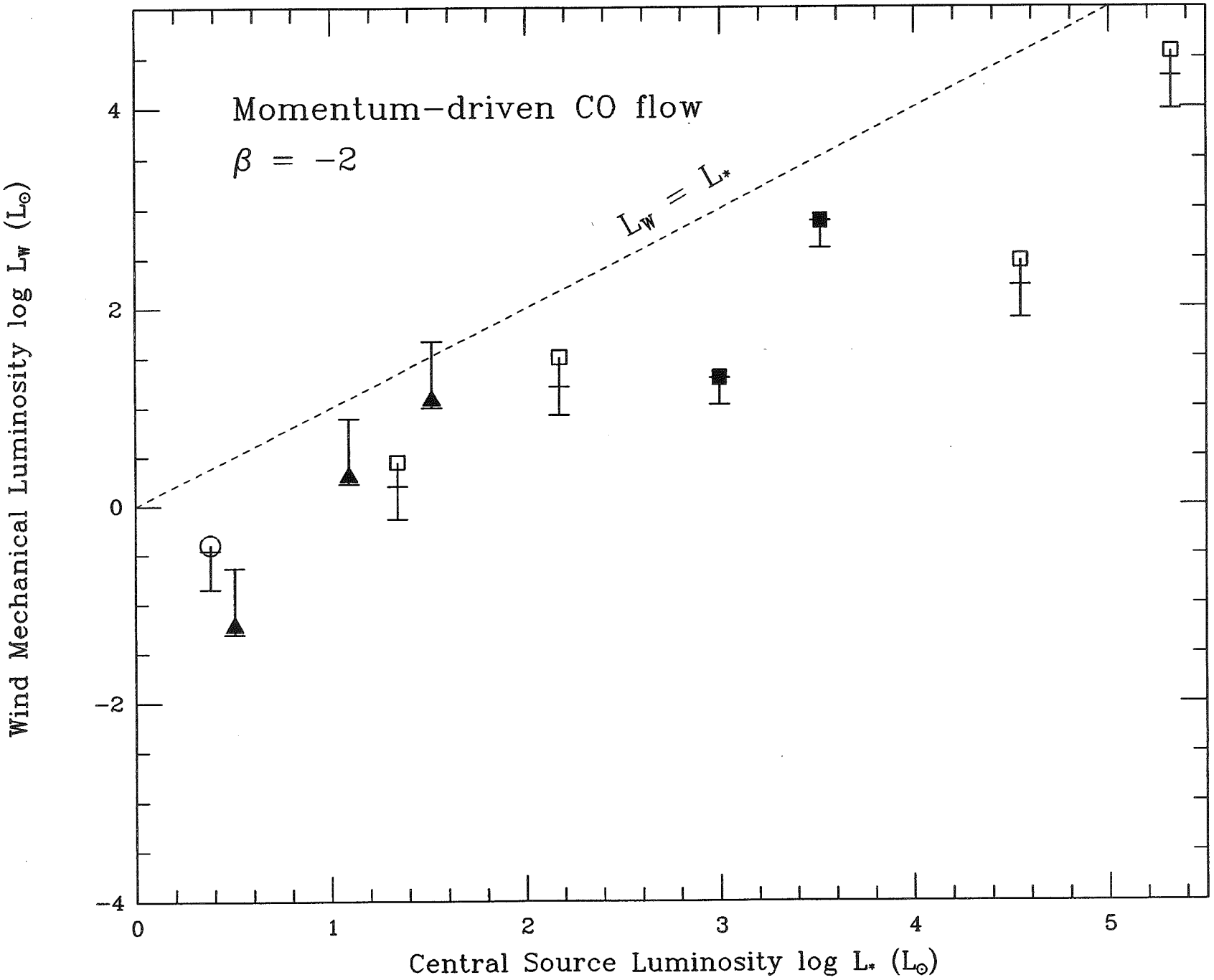
Momentum−driven CO flow
β = −2
$L_w = L_*$
Wind Mechanical Luminosity log L_w ($L_\odot$)
Central Source Luminosity log L_* ($L_\odot$)
4
2
0
−2
−4
0
1
2
3
4
5

Fig. 3b

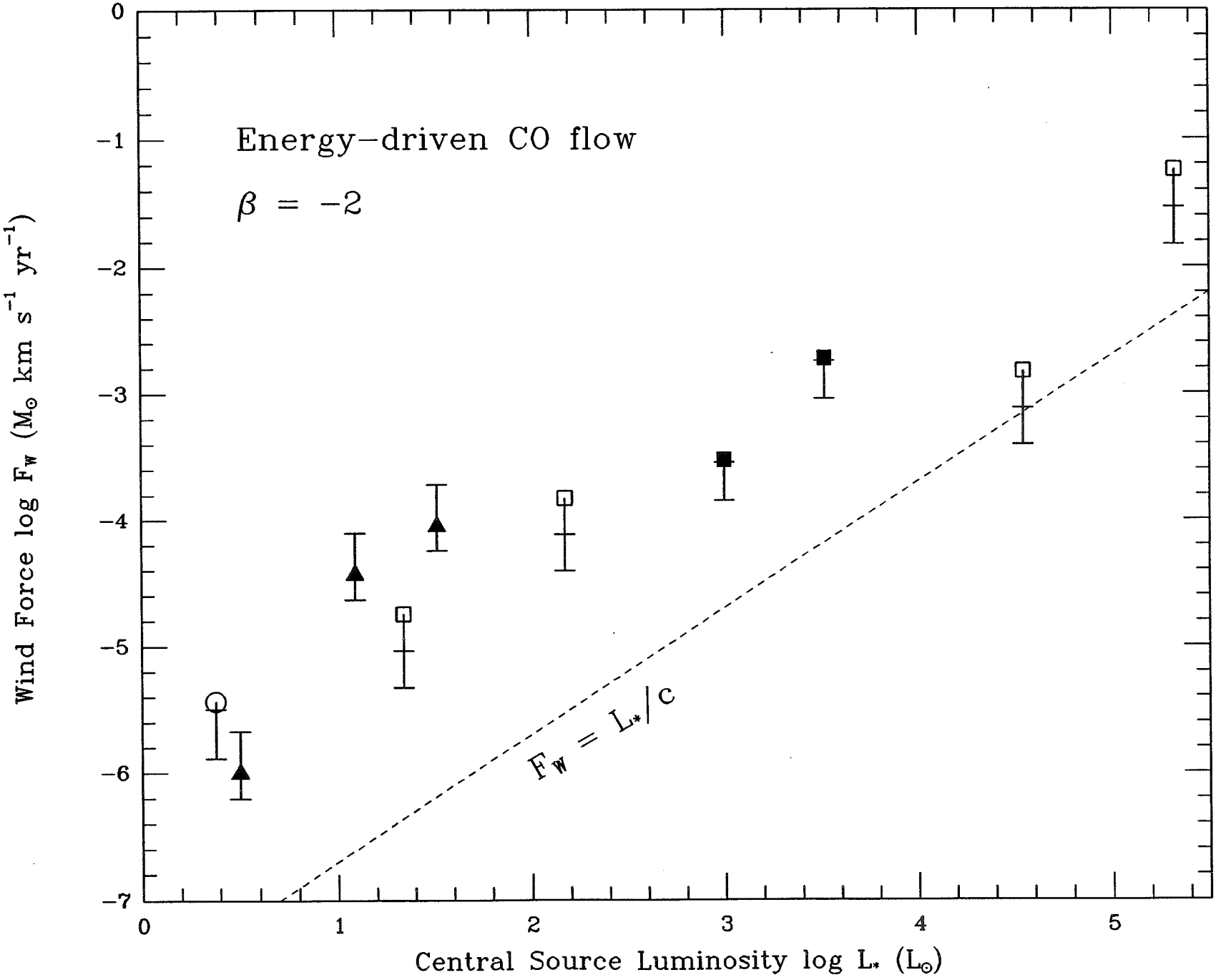
Energy–driven CO flow
$\beta = -2$
$F_w = L_*/c$
Wind Force log F_w ($M_\odot$ km s^{-1} yr^{-1})
Central Source Luminosity log L_* ($L_\odot$)
0
−1
−2
−3
−4
−5
−6
−7
0
1
2
3
4
5

Fig. 4a

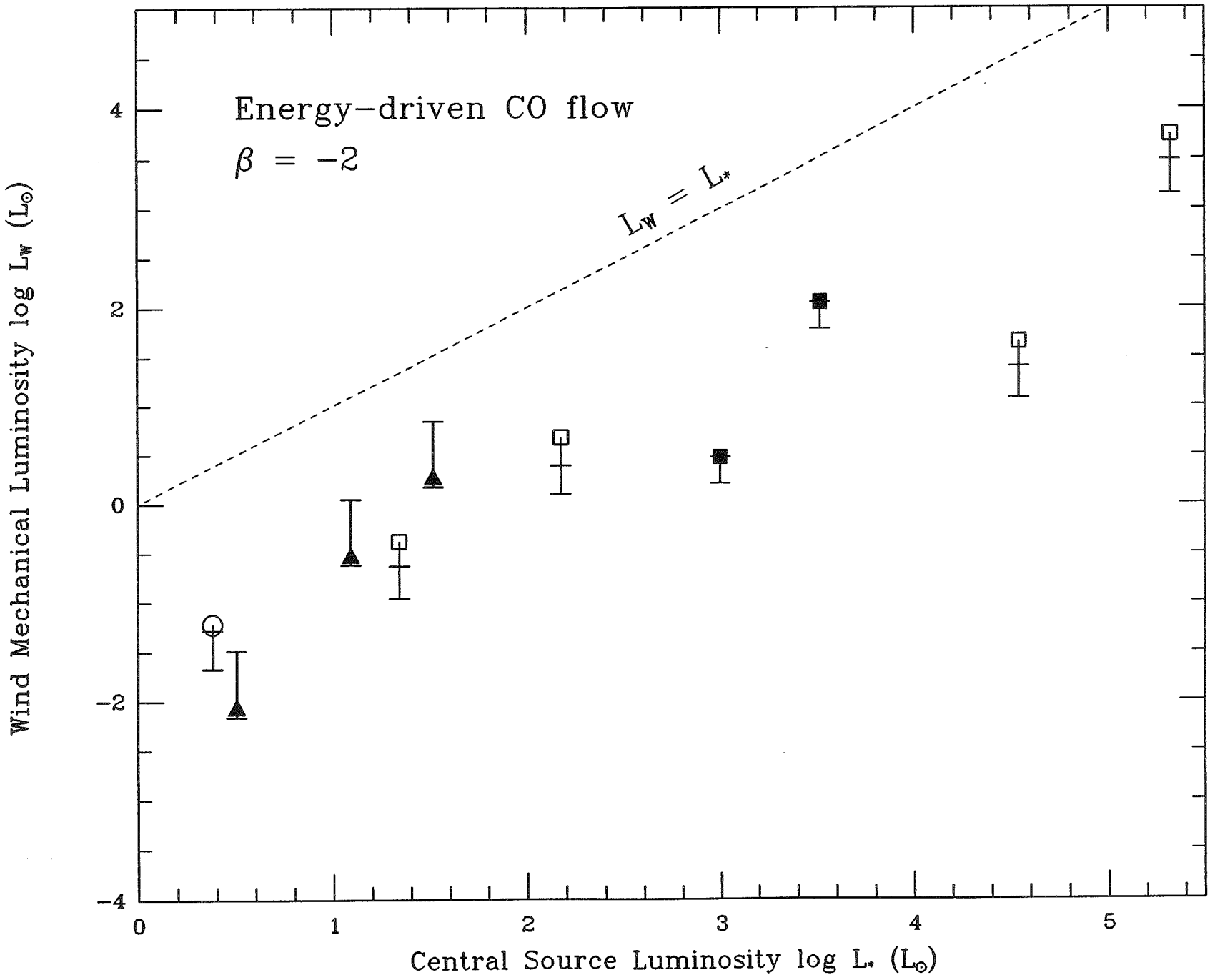
Energy–driven CO flow
$\beta = -2$
$L_w = L_*$
Wind Mechanical Luminosity log L_w ($L_\odot$)
Central Source Luminosity log L_* ($L_\odot$)
4
2
0
−2
−4
0
1
2
3
4
5

Fig. 4b

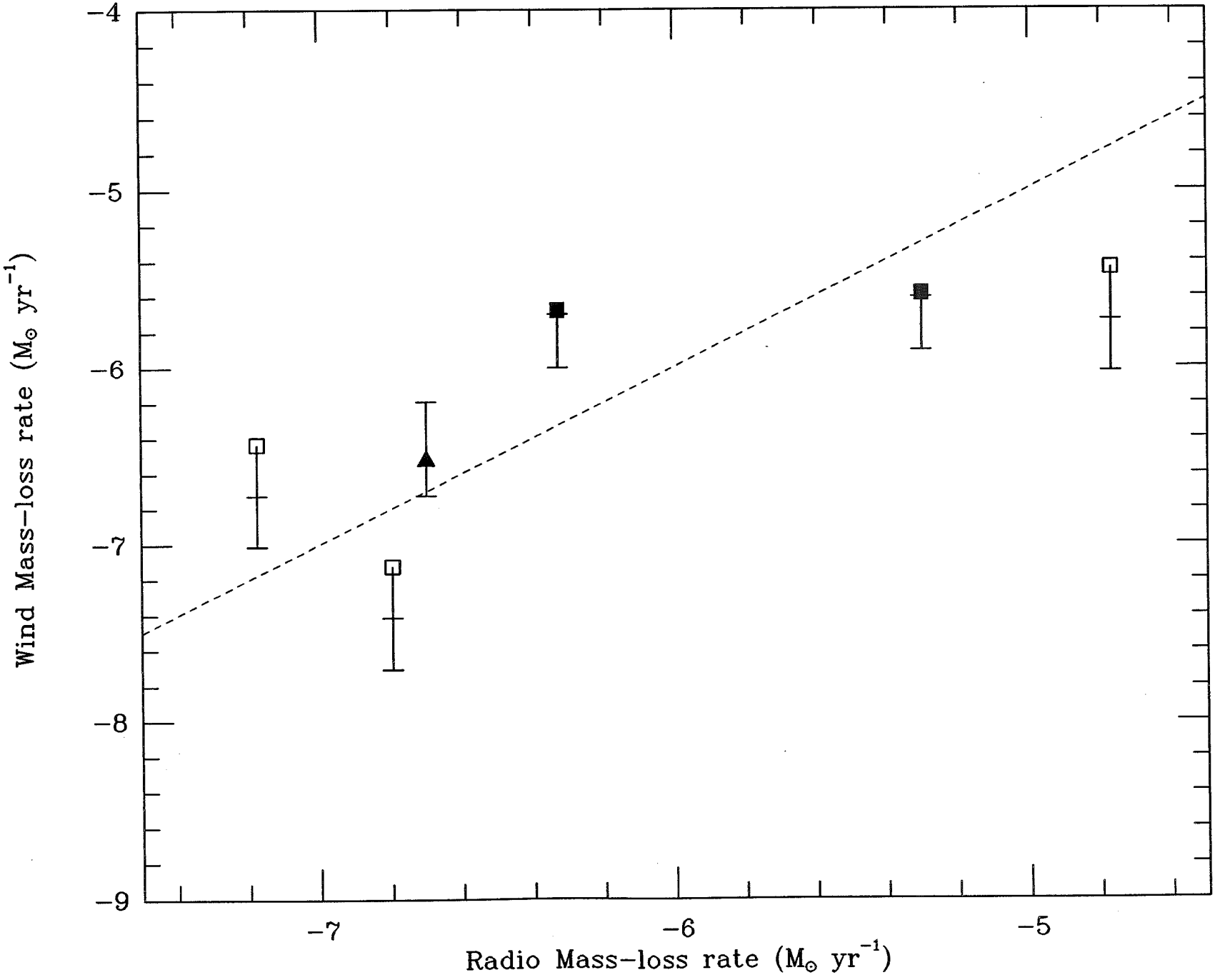
−4
−5
−6
−7
−8
−9
−7
−6
−5
Wind Mass-loss rate ($M_\odot$ yr^{-1})
Radio Mass-loss rate ($M_\odot$ yr^{-1})

Fig. 5

ANNEXE 7

THE ASTROPHYSICAL JOURNAL, 321:473–495, 1987 October 1

FORBIDDEN LINE AND Hα PROFILES IN T TAURI STAR SPECTRA: A PROBE OF ANISOTROPIC MASS OUTFLOWS AND CIRCUMSTELLAR DISKS

SUZAN EDWARDS,[1,2] SYLVIE CABRIT,[3,4] STEPHEN E. STROM,[2,3] INGEBORG HEYER,[1,2]
KAREN M. STROM,[3] AND E. ANDERSON[5]
Received 1987 January 14; accepted 1987 March 17

ABSTRACT

High spectral resolution observations of [S II], [O I], and Hα profiles for a sample of 10 T Tauri stars and two Herbig emission stars provide a probe of the velocity fields, spatial extents and mass-loss rates characterizing the winds from these young stellar objects (YSOs).

The forbidden lines sample the outer, lower density regions of YSO mass outflows. In all cases, only blueshifted forbidden emission is seen. A continuous progression of profile types characterizes the velocity structure of [O I] and [S II]: from single-peaked profiles with maxima near the stellar rest velocity and with broad (150 km s^{-1}) wings extending to the blue, to double-peaked profiles with blueshifted emission maxima displaced by as much as 200 km s^{-1} from the second peak near the stellar rest velocity.

These profile characteristics are not well modeled by a constant velocity spherical or conical outflow. The observed range of profile types is better explained by assuming that one is viewing a wind with a latitude-dependent velocity and density structure from different aspect angles. Such a wind leaves the stellar poles with higher speeds than in the equatorial regions and has a latitude dependent density that varies as $r^{-2}v^{-1}$. The mass-loss rates estimated from this model range from 10^{-7} to 10^{-9} $M_\odot$ yr^{-1}.

Additional support for this wind model is provided by the observed velocity difference between the bluest emission peaks in the forbidden lines and the absorption reversal observed in Hα. This velocity difference will be a function of view angle if the Hα reversal is formed in the wind along the line of sight to the star. The correspondence of the observed forbidden line profile shapes with this velocity difference is as expected from the model for most of our sample objects.

The sizes of the outer wind regions probed by the forbidden lines can be estimated from the emission measure observed for the [S II] lines and the electron densities inferred from the [S II] 6731/6716 line ratios; for most of the YSOs in our sample the wind extents are of the order of tens of AU, but for HL Tau and R Mon, they are on the order of hundreds of AU.

The absence of redshifted forbidden line emission compels us to propose that each of our sample YSOs is surrounded by an opaque circumstellar dust disk of a size adequate to obscure the receding portion of the YSO outflows. Independent estimates of the disk radii can be made from the measured 60 μm flux, an assumed disk dust temperature of 50 K, and an assumed disk optical depth $\tau_{100\mu} > 1$; the computed sizes fall in the range 10–800 AU and are comparable to the sizes estimated for the forbidden line emission regions.

The inferred disk masses range from 0.01 to 0.1 $M_\odot$, comparable to the mass thought to characterize proto-planetary systems. Our observations thus suggest that optically thick disks with sizes of approximately 100 AU and with proto-solar system masses surround a significant number of YSOs of ages $\lesssim 3 \times 10^6$ yr. The persistence of such optically thick disks to ages of up to 10^6 yr challenges current assumptions regarding the dust settling times in the primitive solar nebula.

Subject headings: line profiles — stars: circumstellar shells — stars: mass loss — stars: pre–main-sequence

I. INTRODUCTION

Within 10^5 yr following the onset of protostellar collapse, most or all low-mass young stellar objects (YSOs) appear to develop powerful, often highly collimated winds (Lada 1985). The observable signatures of these winds, emanating from heavily reddened or optically obscured YSOs, include (1) spatially extended and often bipolar streams of supersonically expanding molecular gas; (2) shock-excited Herbig-Haro objects whose motion, determined from both radial and tangential velocities, suggests collimated ejection (Cudworth and Herbig 1979; Schwartz 1983) and shock excited H_2 emission (Fischer, Righini-Cohen, and Simon 1980; Shull and Beckwith 1982) and (3) narrow optical and radio continuum jets of ionized gas (Cohen, Bieging, and Schwartz 1982; Mundt and Fried 1983; K. M. Strom *et al.* 1986). The mass-loss rates inferred for YSOs in these very early evolutionary stages are in the range $10^{-6} \leq \dot{M} \leq 10^{-7}$ $M_\odot$ yr^{-1} (Lada 1985; Snell *et al.* 1985). These energetic winds are probably important in halting the collapse of the dense molecular core, in dissipating remnant protostellar material, and in providing turbulent support for molecular clouds against further collapse (Shu, Adams, and Lizano 1987; Norman and Silk 1980).

Following the dissipation of remnant protostellar material, solar mass YSOs become optically visible as T Tauri stars (TTS) on time scales $< 10^6$ yr. The TTS are believed to possess

[1] Five College Astronomy Department, Smith College.
[2] Visiting Astronomer, Kitt Peak National Observatory, National Optical Astronomy Observatories, operated by the Association of Universities for Research in Astronomy, Inc., under contract with the National Science Foundation.
[3] Five College Astronomy Department, University of Massachusetts, Amherst.
[4] Institut d'Astrophysique, Paris.
[5] Kitt Peak National Observatory.

strong winds, based on the line profile structure at Hα, Na D, and Ca II (Kuhi 1964; Hartmann 1982; Mundt 1984). Mass-loss rates for TTS winds are subject to some uncertainty, but are generally estimated to be $10^{-8} \leq \dot{M} \leq 10^{-9}\ M_\odot\ \mathrm{yr}^{-1}$ for the most active stars (Kuhi 1964; Kuan 1975), in agreement with the maximum energy that should be available to drive winds via MHD energy dissipation in the form of Alfvén waves (DeCampli 1981; Hartmann, Edwards, and Avrett 1982). Most TTS wind models to date have assumed spherical symmetry, although a scenario posed by Bertout (1985) posits a bipolar wind to explain the P Cygni type III Hα profiles common to many TTS.

The relationship between the strong, well-collimated winds observed at the earliest evolutionary stages and the later TTS winds is at present not clear since (1) the mass-loss rates for the winds from the embedded objects are 10–100 times the $\dot{M}$ characterizing the TTS winds and (2) highly anisotropic mass outflows are common among the embedded sources, while H-H objects, optical or radio continuum jets, and molecular outflows are found in less than 10% of the TTS (Edwards and Snell 1982; Calvet, Cantó and Rodríguez 1983; Levreault 1985; Beiging, Cohen, and Schwartz 1984).

In this contribution, we make use of high spectral resolution observations of [O I], [S II], and Hα line profiles to probe the geometry of TTS winds on spatial scales from several stellar radii to tens of astronomical units. Our goal is to determine whether anisotropic mass outflows are restricted to the earliest evolutionary phases of YSOs when they are still embedded in their natal molecular cores or if instead, collimated outflows continue for a significant fraction of a star's pre–main-sequence lifetime.

The utility of optically thin forbidden line emission in probing TTS winds was first suggested by Jankcovics, Appenzeller, and Krautter (1983, hereafter JAK). These lines probe the mass outflows at relatively large distances from the stellar surface, where gas densities are low and terminal flow velocities have been achieved. The line of [O I] λ6300 is detected in about 30% of all TTS spectra studied at moderate ($\Delta\lambda \approx 7$ Å) spectral resolution (Cohen and Kuhi 1979, hereafter CK). The [S II] doublet λλ6731, 6716 is also commonly found (Herbig 1962), although these lines are often weaker than the [O I] λ6300 line by a factor of 5–10.

From an initial survey of forbidden line properties, JAK report that the intensity-weighted systemic velocity of the forbidden lines is blueshifted. A closer look at forbidden line profiles in TTS has been conducted by Appenzeller, Jankovics, and Ostreicher (1984, hereafter AJO), who computed profiles for several simple outflow geometries. They concluded that the observed velocity structure in the forbidden lines was best explained by one of two variations on a bipolar geometry, where the extinction of receding material was provided by an opaque circumstellar disk.

We report here the results of a high-resolution spectroscopic study of 10 TTS and two Herbig emission stars. Red echelle spectra include the lines of [O I] λ6300, [N II] λ6584, [S II] λλ6716, 6731, as well as Hα. Section II describes the selection of sample objects, outlines the observational techniques and reduction procedures, and presents the [O I], [S II], and Hα profiles for each star. The forbidden lines display a continuous progression of profile types, from single-peaked profiles with maxima near the stellar rest velocity and broad (150 km s^{-1}) blue wings, to double-peaked profiles with blueshifted maxima displaced by as much as 200 km s^{-1} from the second peak near the stellar rest velocity.

In § III we critically examine the velocity structure in the forbidden lines and compare them to computed line profiles for a number of different wind models. We find that constant velocity spherical or conical winds fail to reproduce the observed line profiles. Instead, we find that the observed range of profile types is better explained by a wind with a latitude dependent velocity field similar to that posited by Jones and Herbig (1982) for the YSO R Mon, such that the wind velocity is higher at the poles than at the equator. In § IV, we explore a prediction of our wind model correlating the velocity of the reversal at Hα and the forbidden line velocity structure as a function of the view angle to the star. Most of the program stars show the expected relationship between Hα and the forbidden lines and the two stars with known orientation agree well with the predicted orientation, providing additional support for our wind model.

In § V, we present estimates of the average densities (10^4 cm^{-3}), sizes (tens of AU) for the TTS forbidden emission regions, and compute mass-loss rates (10^{-7} to $10^{-9}\ M_\odot\ \mathrm{yr}^{-1}$) based both on our latitude-dependent wind model and on simpler descriptions of TTS winds. As noted by JAK and AJO, the absence of redshifted forbidden line emission demands that the receding part of the mass outflows must be obscured; an optically opaque circumstellar disk seems a logical candidate for such a screen. In § VI, we use *IRAS* far-infrared fluxes to independently estimate the disk sizes on the assumption that they are optically thick at 100 μm. We find that the disk sizes are greater than or about comparable to the wind extensions, as required by the observations. The implied masses of these circumstellar disks range from 0.01 to 0.1 $M_\odot$, which is similar to the mass expected from precursors to solar systems similar to our own. These optically thick disks appear to persist around YSOs with ages as large as 3×10^6 yr. Section VII presents a summary and a discussion of future work.

II. OBSERVATIONS

a) Selection Criteria, Data Collection, and Reduction

Our program stars, listed in Table 1, were selected from the list of CK to cover a wide range in [O I] and Hα equivalent widths (0.5–10 Å for [O I], 10–158 Å for Hα) in order to probe a range of wind strengths. Our observations were made on 1984 December 5–7 on the 4 m Mayall telescope at KPNO with the echelle spectrograph and a thinned Texas Instruments charge-coupled device. The red, long-focus f/2.5 camera with a 58.5 groove mm^{-1} echelle grating in combination with a 226 grove mm^{-1} cross-disperser yields a dispersion of 2.6 Å mm^{-1} at 5000 Å. With our adopted slit width of 1.″3 the effective resolving power is 2.5×10^4. The six observed orders were centered on wavelengths of 6171, 6296, 6452, 6569, 6715, and 6870 Å; each order covers a spectral range of about 40 Å. In order to correct our echelle spectra for small scale variations in chip sensitivity, flat-field exposures were taken using an internal quartz calibration source. To ensure linearity at low light levels, each stellar exposure was subjected to a 40 s preflash from a faint quartz lamp, thus ensuring a background level of at least 100 equivalent electrons per pixel. We selected a preslit decker with a length of 17.″2. The slit was oriented in an east-west direction for all spectra, and except for the close pair UZ Tau E and W, our objects were located at the center of the slit. This procedure provided ample sky for background subtraction, which is essential for interpretation of the [O I] profile, as will be shown later. Our observational technique also permitted us to search for extended emission nebulosity

around the stars, but visual examination of the CCD frames revealed no evidence of extended emission nebulosity in excess of the limitation imposed by the seeing (3″–6″). (Extended reflection nebulosity at Hα was seen around both R Mon and Z CMa.) Hence all further processing proceeded with the stellar, sky, and comparison spectra reduced from a two-dimensional image to intensity, wavelength vectors. The spectral processing was carried out on a Cyber 175 at the University of Massachusetts using software developed by Nicholas Minutillo.

The wavelength calibration provided by the thorium-neon-argon comparison recorded after each stellar exposure was inadequate, because of the dearth of Th lines in this spectral region combined with a technical problem with the Th arc. We therefore relied on multiple exposures of a radial velocity standard, HD 75935 (G8 V; 1957 *Trans. IAU*, 9, 442) to provide the fundamental wavelength calibration for our spectral orders. The dispersion relation was then shifted for each stellar and sky spectrum by an appropriate amount determined by alignment with the comparison and night sky spectral lines. This method, applied to repeated observations of the radial velocity standard, gave a measured heliocentric radial velocity of -18.7 ± 0.3 km s^{-1} compared to the published value of -18.9 ± 0.3 km s^{-1}. Velocity errors for a single measurement are ~ 1 km s^{-1}.

In addition to the echelle spectra, a lower resolution ($\Delta\lambda = 2$ Å) red spectrum of HL Tau was obtained on 1985 January 20 (UT) with the RC spectrograph and intensified CCD (ICCD) detector on the Mayall 4 m telescope at KPNO. Again, sufficient sky was admitted to effect an accurate subtraction of terrestrial airglow and scattered moonlight. Internal precision in the velocity measurements in this case is about ± 10 km s^{-1}.

b) *Determination of Stellar Rest Velocities*

The rest velocities for most stars were determined from the Li I line λ6707.82 Å, the most prominent photospheric feature in the spectral range covered. Exceptions are HL Tau, HN Tau, and R Mon, extreme emission stars exhibiting no photospheric features, and DO Tau, whose spectrum was contaminated by a cosmic ray event superposed on the Li I line. Table 1 lists our Li I velocity and, for comparison, both the stellar velocity measured by Herbig (1977), along with the molecular cloud velocity toward the star (all velocities are heliocentric). For most stars there is agreement to within a few km s^{-1} between these three velocities; the two exceptions are discussed below.

Two stars show a large velocity discrepancy with respect to the ambient molecular cloud, in contrast to most TTS, which typically have a difference of ≤ 1–2 km s^{-1} from the velocity of the molecular cloud (Herbig 1977; Hartmann *et al.* 1986). The TTS CW Tau was previously noted to have a velocity discrepant by $+12$ km s^{-1} from the cloud velocity and was suggested as a possible spectroscopic binary (Herbig 1977). The Li I velocity measured here differs by -17 km s^{-1} from the previous stellar velocity measurement and by -5.3 km s^{-1} from the cloud velocity. The second example of a discrepant stellar and cloud velocity is seen in one member of the close pair UZ Tau E and W, separated by 3″.7. (Spectra of both stars were recorded in the same 17″ E–W slit.) Although UZ Tau W has a Li I velocity close to that of the cloud, UZ Tau E has a

TABLE 1

PROGRAM STARS: LITHIUM AND Hα VELOCITIES

HRC (1)	STAR (2)	JD (2,446,00+) (3)	EXPOSURE (minutes) (4)	V_{Li} (km s^{-1}) (5)	V_* (km s^{-1}) (6)	V_{MC} (km s^{-1}) (7)	Hα VELOCITIES: Emission Peaks (km s^{-1}) (8)	Hα VELOCITIES: Absorption Reversals (km s^{-1}) (9)
25	CW Tau	41.73	101	+10.7	+28	+16	−176, −63, +113	−106, +8
34	RY Tau	41.68	60	+19.3	+21	+18	−145, +161	−8
36	DF Tau	40.95	30	+13.9	+12	+17	−117, +15, +70	−73
49n.....	HL Tau*	85.58	10	*	...	+17	−192, +128	−90
53	UZ Tau W	41.82	65	+13.6	...	+16	−10, +115	+83
53	UZ Tau E	41.82	65	+1.2	...	+16	−122, +65	−42
60	HN Tau	39.84	90	*	...	+21	+65	...
67	DO Tau	40.84	43	*	+20	+17	−152, +1, +112	−66
74	DR Tau	40.93	20	+19.4	...	+22	−185, +111	−297, −165, +60
76	UY Aur	40.89	54	+14.1	+18	+16	−178, +26	−145, −54
207	R Mon	41.99	30	*	...	+25	−94, 120	−2
243	Z CMa	39.99	10	*	...	+32	+29	−467, −210

Col. (1).—The numbers from the Herbig-Rao Catalog 1972.

Col. (3).—The Julian Date when the spectrum was taken.

Col. (4).—The exposure time of the spectrum in minutes. The spectrum of HL Tau, taken with the ICCD, is of lower spectral resolution than the other spectra; see text.

Col. 5.—The (heliocentric) radial velocity in km s^{-1} as measured on the current spectra from the centroid of the Li I λ6707 line. Typical errors are ± 1 km s^{-1}. For HL Tau, HN Tau, and R Mon, no photospheric lines are seen. For DO Tau, a cosmic-ray event prevents the accurate measurement of a Li I velocity. For Z CMa the Li I line is highly asymmetric; see Fig. 2.

Col. (6).—The stellar (heliocentric) radial velocity in km s^{-1} as given by Herbig 1977. Typical errors are ± 2 km s^{-1}.

Col. (7).—The heliocentric radial velocity of the ambient molecular material toward the star, taken from either Herbig 1977 or Edwards and Snell 1982.

Col. (8).—Heliocentric radial velocities of the emission peaks in the Hα line measured on the current spectra.

Col. (9).—Same as Col. (8) for absorption reversals.

velocity discrepant by -14.7 km s^{-1}. L. W. Hartmann (private communication) also finds both CW Tau and UZ Tau E to be radial velocity variables.

c) Line Profiles, Radial Velocities, and Equivalent Widths

The [O I] λ6300 line intensity profiles for our program stars are plotted as a function of radial velocity in Figure 1. Zero radial velocity corresponds to the heliocentric velocity of the star or, if unavailable, to the heliocentric velocity of the ambient molecular cloud in Table 1. The full spectral range of the echelle order that includes the Li I and [S II] $\lambda\lambda$6716, 6731 lines is shown for 11 stars in Figure 2. The ICCD spectrum of HL Tau from 6300 to 6800 Å is shown in Figure 3. The Hα line profiles are shown in Figure 4, with the [O I] profiles from Figure 1 superposed with the same velocity scale but arbitrarily shifted in relative intensity. The line of [N II] λ6583 is

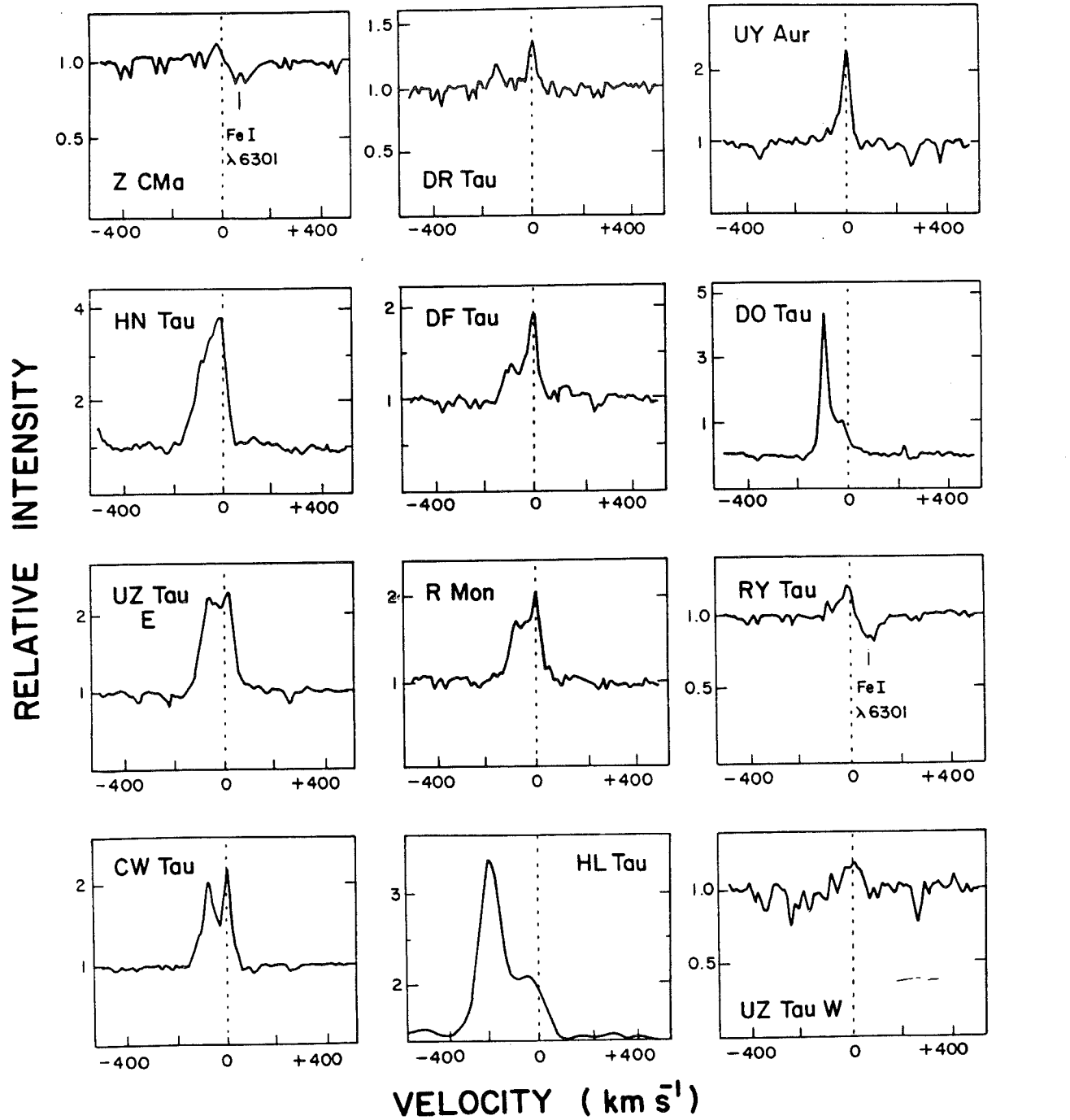

FIG. 1.—The [O I] λ6300 line profiles for the program T Tauri stars are plotted in units of relative intensity against heliocentric radial velocity in km s^{-1}. The continuum slopes have been normalized. Telluric absorption features are present in some spectra. The vertical lines represent the stellar rest velocity from Li I (these spectra), or if this is unavailable, the ambient molecular cloud velocity.

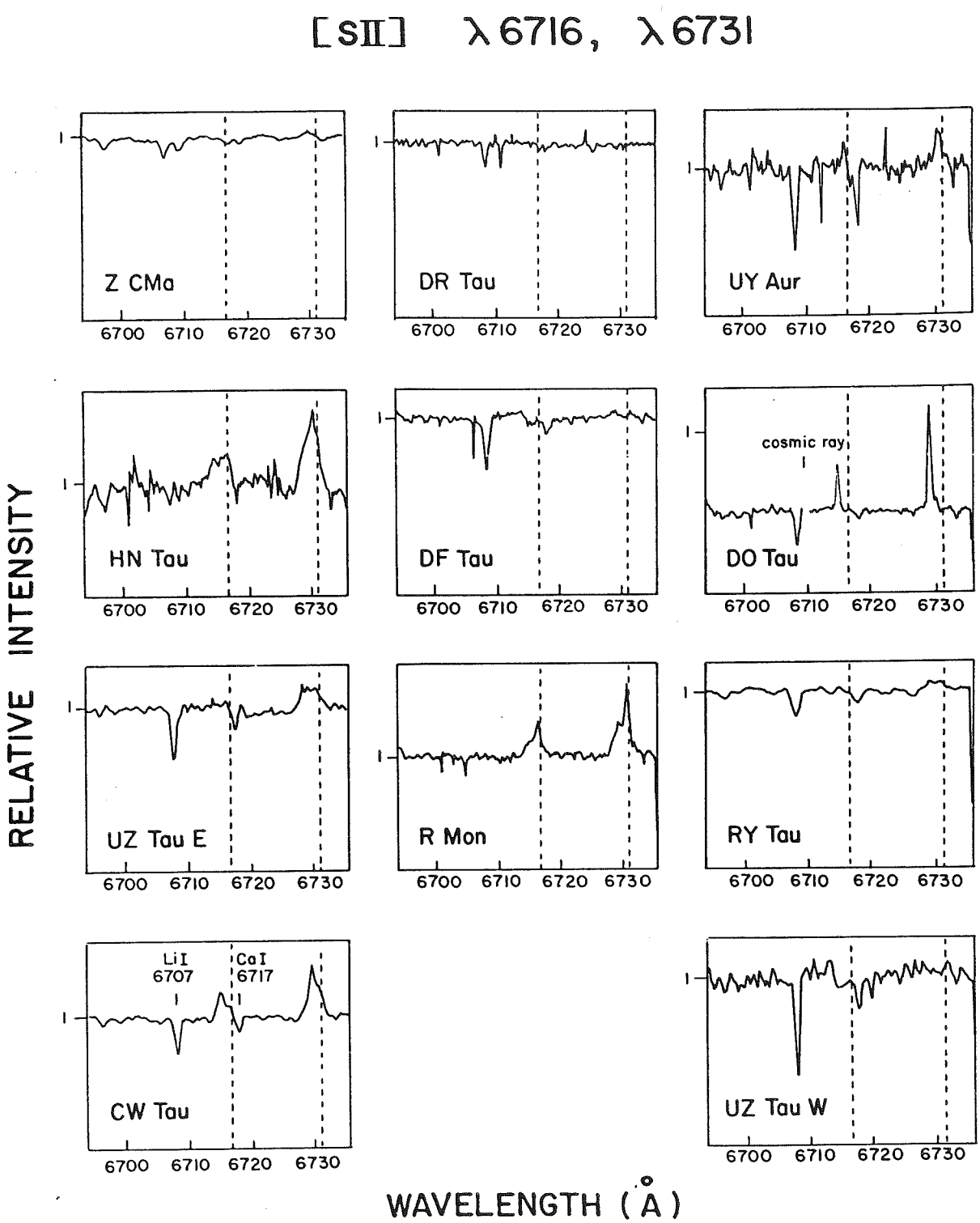

FIG. 2.—Intensity vs. wavelength is plotted for the full echelle orders centered at 6715 Å, including Li I λ6707, Ca I λ6717, and [S II] λ6716, 6734. The vertical lines represent the stellar rest velocity or ambient molecular cloud velocity relative to the lab wavelength of the [S II] lines.

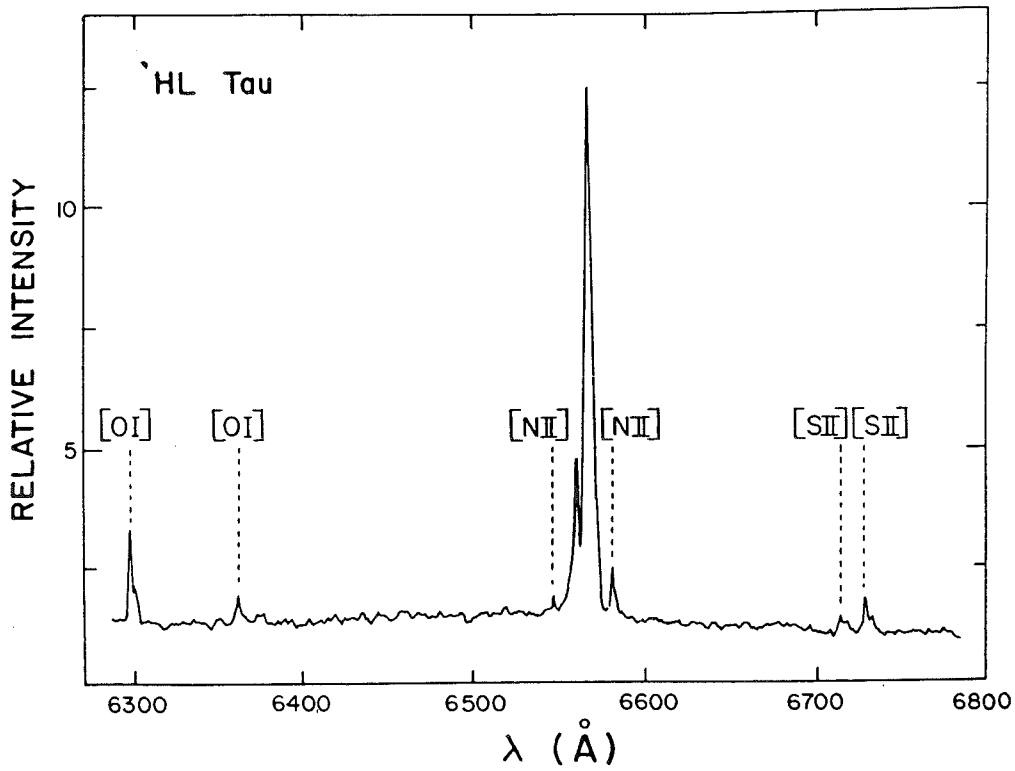

FIG. 3.—The ICCD spectrum of HL Tau showing the forbidden lines of [O I] λ6300, 6364, [N II] λ6548, 6584, and [S II] λ6716, 6731 as well as Hα. Relative intensity is plotted against wavelength.

seen in only three stars, HL Tau, HN Tau, and UZ Tau E (not shown).

Heliocentric radial velocities for forbidden line features are presented in Table 2. These velocities must be shifted by an amount equal to the stellar rest velocity from Table 1 in order to reconcile them with the velocity scale in Figures 1 and 4. The nomenclature used in Table 2 is defined as follows: (1) w_b and w_r are the velocities where the blue or red wing of the profile meets the continuum level; these are difficult to measure with precision and should be regarded as approximate; (2) v_b and v_c are the velocities of the blueward and central emission peaks, if they are resolved. In a few stars the atmospheric O_2 band features are strong enough to be seen near λ6300; its effect on the inferred velocity structure of O I λ6300 is minimal, as judged by a comparison of the O I and S II profiles. In some stars the [S II] λ6716 feature is not easily measured because it is blended with a photospheric Ca I λ6717 absorption line. Heliocentric velocities for Hα emission peaks and absorption reversals are given in Table 1; the full extent of the wing emission at Hα could not be determined reliably from our spectra due to the off-center position of this very broad line in the narrow (40 Å) echelle order.

Equivalent widths for the forbidden lines, Li I, and Hα features are listed in Table 3. The forbidden line and Hα equivalent widths refer to the emission above continuum level.

The Hα line profiles for our program stars are similar to previously published profiles for the same stars, although small differences in velocity structure are seen, which may be due to our higher spectral resolution. An exception is RY Tau, which normally does not show a depressed redward emission peak (Schneebeger, Worden, and Wilkerson 1979; Hartmann 1982; Ulrich and Knapp 1985).

The forbidden line profiles of all stars share some common characteristics:

1. Most of the emission is blueward of the stellar rest velocity.
2. A progression of profile shapes is observed, which ranges from single-peaked profiles with maxima near the stellar rest velocity and showing a blue wing extending 150 km s^{-1} to the blue (e.g., UY Aur) to double-peaked profiles with blueshifted emissson maxima displaced by as much as 200 km s^{-1} from a second peak near the stellar rest velocity (e.g., HL Tau).
3. The intensity ratio between these two peaks may be less than, greater than, or about equal to unity.
4. For each star the [O I], [S II], and [N II] profiles are similar, although in CW Tau the relative intensity of the blueward to central peaks is inverted between [O I] and [S II].

III. FORBIDDEN LINE VELOCITY STRUCTURE AS A PROBE OF THE NEAR ENVIRONS OF T TAURI STARS

a) Circumstellar Obscuration and Wind Anisotropy

The forbidden emission lines probe the extended low-density outer regions of the TTS winds. This, in combination with the observed velocity structure in the forbidden lines, leads to the following twofold conclusion, also reached by AJO;

1. *The receding hemisphere of TTS winds must be heavily obscured:* The lack of any redshifted forbidden emission necessitates that minimum values of A_v in excess of 6 mag are required to occult the receding portions of the winds. The nature of this obscuring material will be discussed in § VI.
2. *TTS winds must be anisotropic:* The necessity for anisotropy is demanded by the velocity structure of the blueshifted forbidden emission. This conclusion was explored analytically

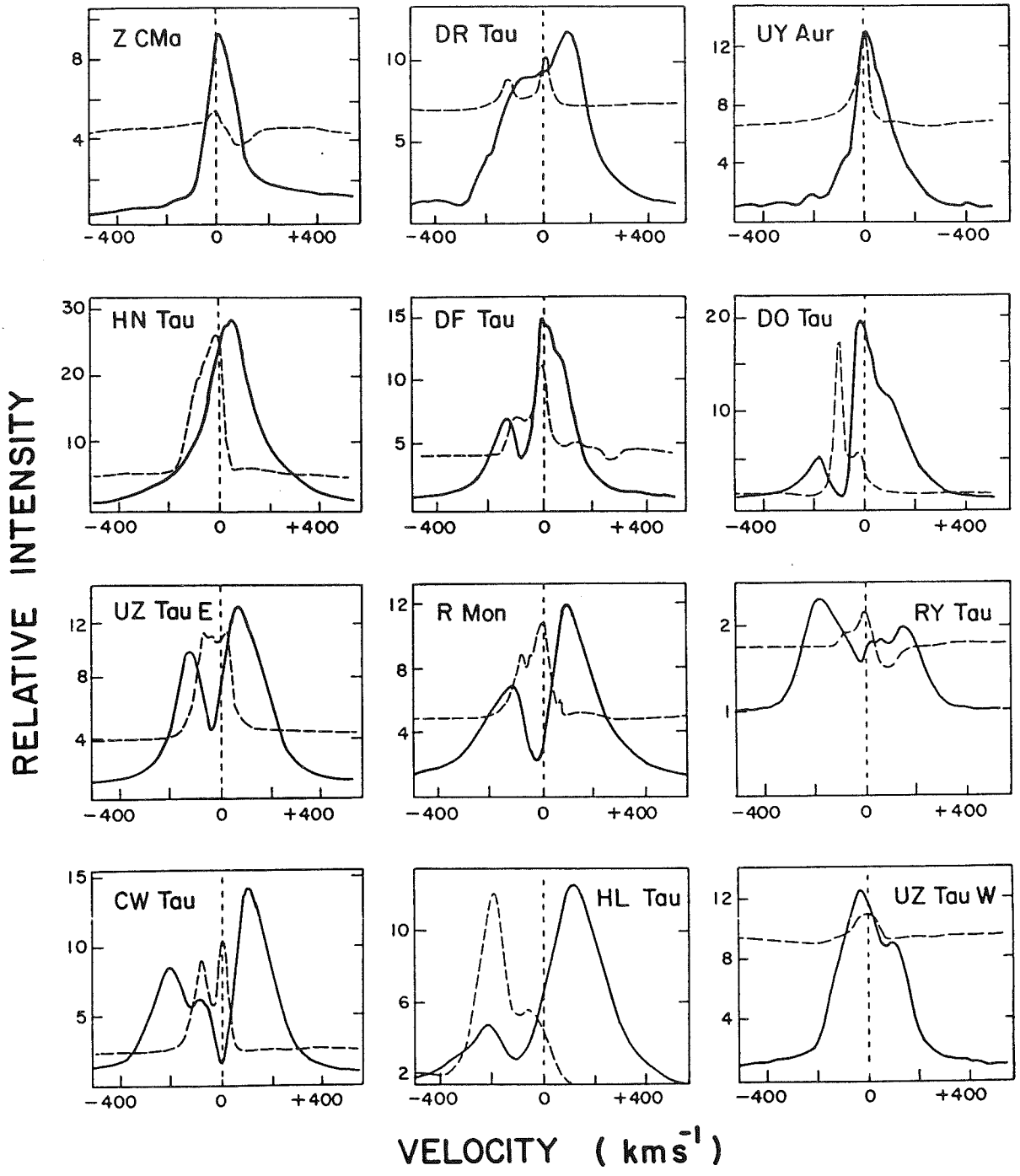

FIG. 4.—The Hα line profiles (*solid lines*) for the program stars are plotted as relative intensity against heliocentric radial velocity. The [O I] lines from Fig. 1 (*dotted lines*) are superposed at identical velocity scales. The vertical lines mark the stellar rest velocity or the velocity of the ambient molecular cloud.

by AJO, who showed that optically thin line emission produced in a constant velocity, spherically symmetric wind cannot be reconciled with the observations through the addition of obscuring material, either from dust embedded within the wind or from dust in a flattened circumstellar disk occulting the receding hemisphere. In both cases, although the original symmetric, flat-topped profile (Beals 1931) does become blue-shifted, the resulting velocity structure has an intensity maximum at the extreme blue edge of the line and then monotonically decreases in intensity to zero or positive velocities, in sharp contrast to the observations.

A likely anisotropic configuration to explore is a bipolar wind, since bipolar wind geometries are common among low luminosity YSOs at earlier evolutionary stages than the optically visible TTS. Two variations on a bipolar wind theme were explored by AJO in an effort to explain the forbidden line velocity structure in TTS. They calculated line profiles resulting from an optically thin, constant velocity wind that in

TABLE 2

RADIAL VELOCITIES OF FORBIDDEN LINES

Star (1)	Line (2)	w_b (km s^{-1}) (3)	v_b (km s^{-1}) (4)	v_c (km s^{-1}) (5)	w_r (km s^{-1}) (6)
CW Tau	[O I] λ6300.23	−143	−67	+9	+64
	[S II] λ6716.4	−108	−62	−4	+31
	[S II] λ6730.8	−127	−57	−4	+45
RY Tau	[O I] λ6300.23	−86	−77	+10	+35
	[S II] λ6716.4	...	...	...	...
	[S II] λ6730.8	...	...	...	...
DF Tau	[O I] λ6300.23	−147	−81	+16	+70
	[S II] λ6716.4	...	...	...	...
	[S II] λ6730.8	...	...	...	...
HL Tau	[O I] λ6300.23	−329	−174	−19	+91
	[S II] λ6716.4	...	−180	0	...
	[S II] λ6730.8	...	−180	−10	...
UZ Tau W	[O I] λ6300.23	−39	...	+9	+78
	[S II] λ6716.4	...	...	...	...
	[S II] λ6730.8	...	...	...	...
UZ Tau E	[O I] λ6300.23	−173	−65, −35	+14	+73
	[S II] λ6716.4	...	...	...	...
	[S II] λ6730.8	−161	−86, −52	−7	+51
HN Tau	[O I] λ6300.23	−152	−61	+11	+81
	[S II] λ6716.4	−176	...	+17	+47
	[S II] λ6730.8	−142	...	+19	+67
DO Tau	[O I] λ6300.23	−136	−74	−01	+84
	[S II] λ6716.4	−101	−76	...	−35
	[S II] λ6730.8	−103	−77	−20:	−08
DR Tau	[O I] λ6300.23	−129	−113	+30	+53
	[S II] λ6716.4	...	...	...	...
	[S II] λ6730.8	...	...	...	...
UY Aur	[O I] λ6300.23	−149	...	+17	+53
	[S II] λ6716.4	...	...	−5	...
	[S II] λ6730.8	−137	...	−2	+37
R Mon	[O I] λ6300.23	−156	−53	+26	+105
	[S II] λ6716.4	−114	...	+25	+98
	[S II] λ6730.8	−130	...	+26	+124
Z CMa	[O I] λ6300.23	...	...	+10	...
	[S II] λ6716.4	...	...	...	...
	[S II] λ6730.8	...	...	−18:	...

Col. (2).—Forbidden line wavelengths are from Osterbrock 1974.

Col. (3).—Heliocentric radial velocities of the extreme blueward wing emission in the forbidden lines.

Col. (4).—Same as col. (3) for velocity of blue emission peaks.

Col. (5).—Same as col. (3) for velocity of central emission peaks.

Col. (6).—Same as col. (3) for velocity of extreme redward wing emission.

TABLE 3

EQUIVALENT WIDTHS (Å)

Star (1)	Hα[a] (2)	Li I[b] λ6707 (3)	[O I][a] λ6300 (4)	[N II][a] λ6584 (5)	[S II][a,c] λ6716 (6)	[S II][a,d] λ6731 (7)	Notes (8)
CW Tau	84	0.27	2.5	<0.04	>0.25	0.61	
					0.19	0.42	blue: $V_1 = -127$, $V_2 = -19$ km s^{-1}
					>0.06*	0.19	red: $V_1 = -19$, $V_2 = +45$ km s^{-1}
RY Tau	10	0.24	0.3	<0.04	*	0.12	
DF Tau	65	0.29	1.6	<0.04	*	<0.04	
HL Tau	46	*	4.5	1.6	1.5	2.4	
UZ Tau W	65	0.53	0.3	<0.04	*	<0.04	
UZ Tau E	82	0.35	3.8	0.22	*	0.34	
HN Tau	158	*	7.0	0.53	0.72	1.40	
DO Tau	90	*	5.3	<0.04	>0.39	0.90	
					0.39	0.83	blue: $V_1 = -103$, $V_2 = -34$ km s^{-1}
					*	0.07	red: $V_1 = -34$, $V_2 = +35$ km s^{-1}
DR Tau	79	0.08	0.5	<0.04	<0.04	<0.04	
UY Aur	47	0.47	1.4	<0.04	*	0.39	
R Mon	72	*	2.3	<0.04	0.49	1.10	
Z CMa	30	(0.16)	0.1	<0.04	<0.04	<0.04	

[a] The equivalent widths are for emission above continuum level.

[b] No photospheric spectrum is seen for HL Tau, HN Tau, or R Mon; a cosmic-ray event mutilated the Li I feature for DO Tau.

[c] An asterisk (*) indicates the presence of Ca I λ6717 absorption.

[d] The [S II] equivalent widths for CW Tau and DO Tau are given first for the entire line profile, and then for the velocity intervals given by $\int_{V_1}^{V_2} dv$.

one case was confined to two opposing bipolar cones (a "filled cone") and in the second was confined to the volume exterior to two bipolar cones (a "hollow cone"), as might occur if the wind in the cones shocks and accelerates material on the cone periphery. In both cases the receding hemisphere of the wind was assumed to be occulted by opaque circumstellar material. The authors concluded that these two scenarios provided a more promising explanation for the forbidden line profiles.

b) A Model of Anisotropic TTS Winds

In this section, we first examine critically how well the constant velocity bipolar wind models proposed by AJO can account for the observed progression of forbidden line profile types. We conclude that a modification of their model provides a more satisfactory explanation of the forbidden lines formed in TTS winds. Following AJO, we also assume that the optically thin forbidden line emission arises in a wind that is characterized by a spatial extent large in comparison to the star, that has achieved terminal velocity, and whose receding material is obscured so that only the approaching hemisphere of the wind is visible. We then introduce a latitude-dependent velocity field as inferred for the wind from R Mon by Jones and Herbig (1982, hereafter JH). These authors interpret the radial velocity progression of upper Balmer shell absorption features seen in reflection along the major axis of the conical nebula as the result of a latitude dependent wind which leaves the polar regions most rapidly and that decreases in speed toward equatorial latitudes. We find that this modification to the AJO wind model accounts successfully for the observed range of forbidden line features, detailed in § II.

Figure 5 sketches the geometric parameters of the wind model. In the stellar frame, the flow is defined by the spherical co-ordinate system r, θ, ϕ. The flow extends radially outward from the star from r_{min} to r_{max}. It is confined either to a cone or shell opening from θ_{min} to θ_{max}. It is symmetric in ϕ about the $\theta = 0$ axis, which is presumed to be coincident with the stellar polar axis. The velocity field is independent of r and is described in normalized units by

$$v(\theta) = v_{max} f(\theta) , \quad (1)$$

where $v_{max} = 1$ is the velocity along the flow axis and $f(\theta) \leq 1$. We assume an isothermal, mass conservative flow over all θ so that the normalized electron density (D_e) at any point in the wind is

$$D_e(r, \theta, \phi) = N_e(r, \theta, \phi)/N_{cr} = D_0(r_{min}/r)^2 v(\theta)^{-1} , \quad (2)$$

where N_{cr}, the critical density of the forbidden line in question, is defined as the density where the downward collisional and radiative rates are equal ($N_{cr} = A_{21}/q_{21}$) and D_0 is D_e at $r = r_{min}, \theta = 0$.

The forbidden line emissivity at any point in the wind, j_{21} (r, θ, ϕ), is given by solving the statistical equilibrium

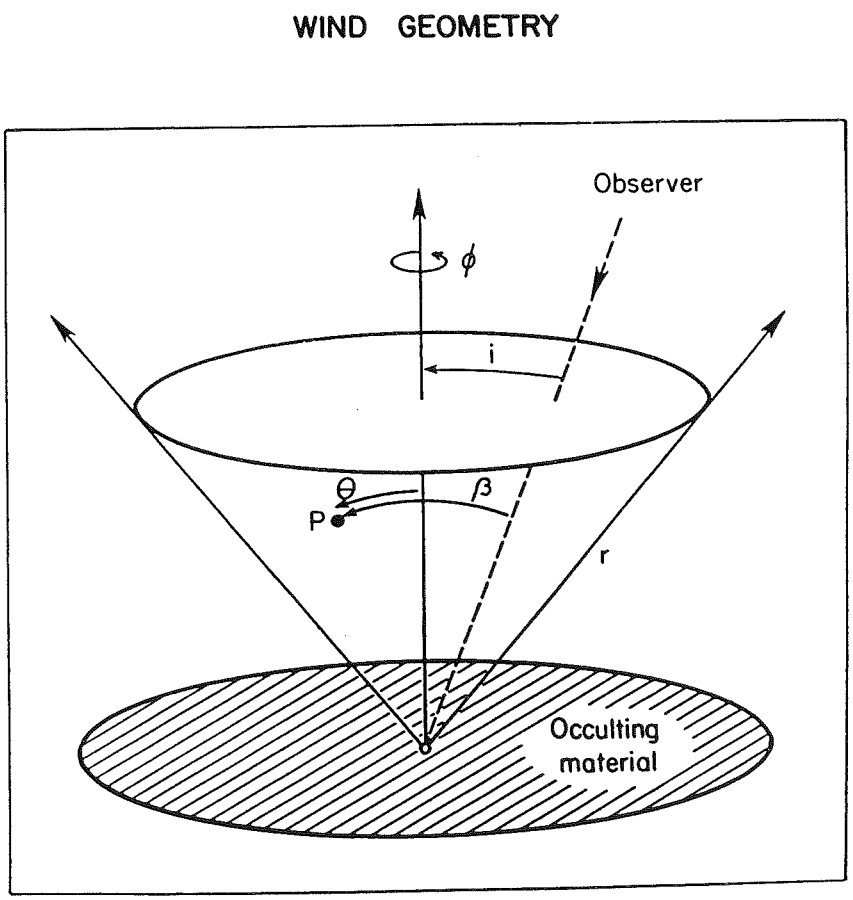

FIG. 5.—The geometric parameters of the latitude-dependent wind model are shown. The wind is azimuthally symmetric in ϕ about the polar ($\theta = 0$) axis. An observer looking from a view angle i with respect to the polar axis sees the radial velocity of gas at a point P as $v_r = v(\theta) \cos \beta$, where $\cos \beta = \cos \theta \cos i + \sin \theta \sin i \cos \phi$. The occulting material in the equatorial plane obscures the receding portion of the wind.

equations in the two level atom approximation, neglecting all stimulated radiative transitions. Under these assumptions, we have

$$N_2/N_1 = (D_e\delta)/(1 + D_e)\,, \tag{3}$$

where δ is the ratio of the collisional rate coefficients $q_{12}/q_{21} = (g_2/g_1)\exp(-h\nu_{21}/kT)$. With $N_1 + N_2 = N_T = \alpha N_e$, the resultant expression for the emissivity per unit volume is

$$j_{21}(r, \theta, \phi) = \alpha q_{12} h\nu_{21} N_{cr}{}^2 D_e{}^2[1 + D_e(\delta + 1)]^{-1} \tag{4}$$

so that

$$j_{21}(r, \theta, \phi) \sim D_e{}^2[1 + D_e(\delta + 1)]^{-1}\,. \tag{5}$$

Since the forbidden lines have low absorption probabilities, the emergent radiation will be optically thin and the total line intensity will be the integral of j_{21} over all volume elements ΔV. The line profile is determined by summing the emission from each volume element ($j_{21} * \Delta V$) in the appropriate radial velocity interval lying between $-v_{max}$ and $+v_{max}$. The radial velocity for each ΔV, as seen by an observer viewing the envelope at an angle i to the flow axis, is

$$v_r(r, \theta, \phi) = -v(\theta)\cos\beta\,, \tag{6}$$

where

$$\cos\beta = \cos\theta\cos i + \sin\theta\sin i\cos\phi\,. \tag{7}$$

Our calculations were carried out on a VAX 11/750 computer. We found that a grid of 5000 θ points and 1000 ϕ points, with 49 evenly distributed velocity bins between $-v_{max}$ and $+v_{max}$ were sufficient to provide a good match to the analytical results of AJO for constant velocity winds.

The shape of the line profile depends solely on the input parameters θ_{min}, θ_{max}, $f(\theta)$, and i. The dependence of the line shape on the starting density and the temperature are found to be negligible for the range of values investigated ($D_0 \leq 5$ and 5000 K $< T <$ 15,000 K). In § IV we will use the observed emission measure and inferred density of the [S II] region to place limits on mass-loss rates from different wind models.

i) *Constant Velocity Winds*

Before describing the line profiles in a latitude-dependent velocity field, it is instructive to examine several examples of constant velocity winds [i.e., $f(\theta) = 1$ and $v(\theta) = v_{max}$]. As an aid in interpreting the emergent line profiles, in Figure 6 we present the surfaces of constant radial velocity for an isotropic constant velocity hemispherical wind ($\theta_{min} = 0°$ and $\theta_{max} = 90°$) as seen from six different view angles: $i = 0°$, 10°, 30°, 45°, 60°, and 80°. In each frame the constant radial velocity surfaces as a function of sin θ and ϕ are displayed, as they would appear in projection from a point looking down the polar axis of the wind. The center of each frame is the flow axis ($\theta = 0°$); the direction to the line of sight vector is marked by + in each frame, which defines the $\beta = 0°$ axis. The angle ϕ is measured

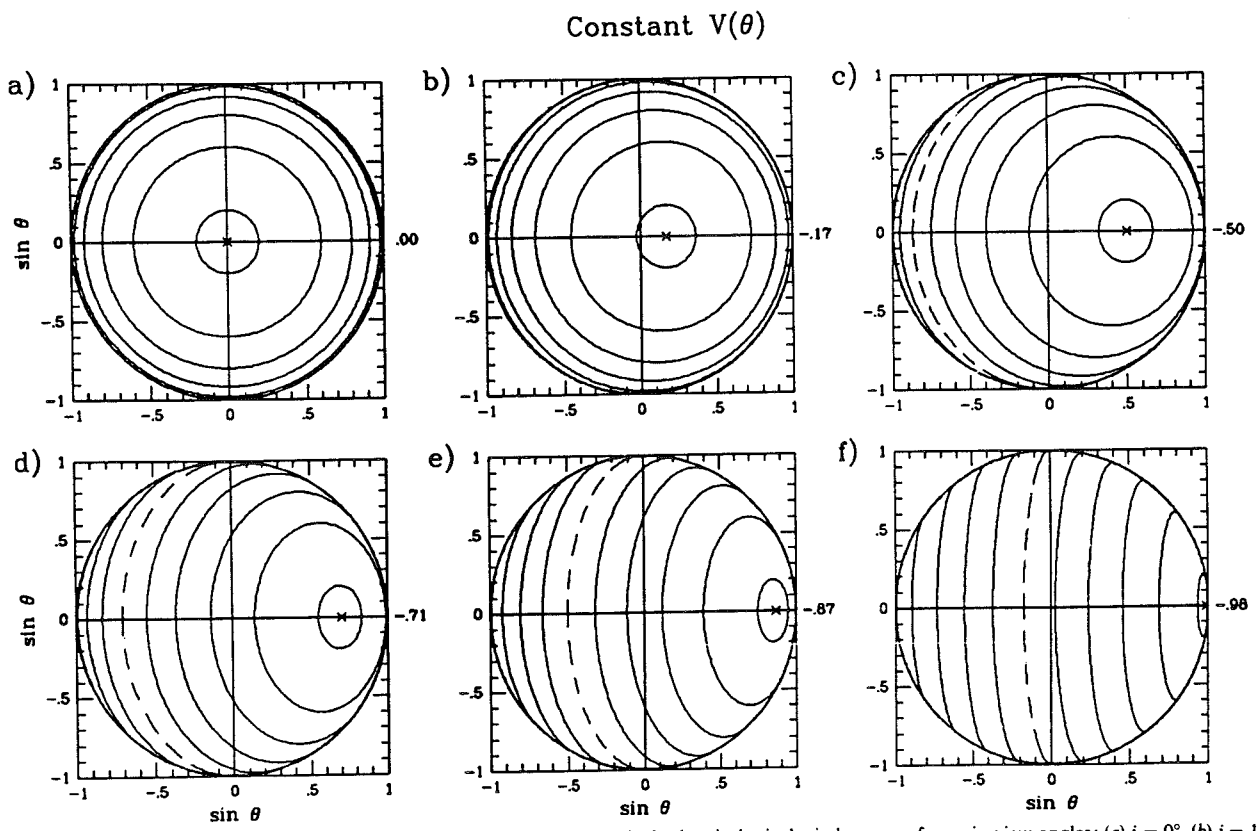

FIG. 6.—The surfaces of constant radial velocity for an isotropic, constant velocity hemispherical wind, as seen from six view angles: (*a*) $i = 0°$, (*b*) $i = 10°$, (*c*) $i = 30°$, (*d*) $i = 45°$, (*e*) $i = 60°$, and (*f*) $i = 80°$. The polar axis ($\theta = 0°$) is at the center of each frame and the azimuthal angle ϕ is measured counterclockwise from the $+x$-axis. Both the x and y axes are sin θ, the projection of the wind opening angle as seen from above. In each frame, the (+) along the $+x$-axis marks the location of the $\beta = 0$ axis (the direction to the observer).

The surfaces of constant radial velocity are ± 0.98, ± 0.8, ± 0.6, ± 0.4, ± 0.2, 0. The zero velocity surface is marked as a dashed line in each frame. Note that the constant radial velocity surfaces are symmetric about the $\beta = 0°$ axis for each view angle. The number in paranetheses to the right of each frame is the radial velocity at $\theta = 90°$, $\phi = 0, \pi$.

counterclockwise and is defined to be 0° in the direction toward the viewer. Note that for a constant velocity wind the surfaces of constant radial velocity (cos β) are symmetric about the $\beta = 0°$ axis.

In Figure 7 we display four possible families of line profiles that can result from the constant velocity wind. The first three cases are those investigated by AJO: (*a*) $\theta_{min} = 0°$, $\theta_{max} = 90°$ (isotropic hemispherical outflow); (*b*) $\theta_{min} = 0°$, $\theta_{max} = 45°$ (filled cone); and (*c*) $\theta_{min} = 45°$, $\theta_{max} = 90°$ (hollow cone). The fourth case is for a thin shell with (*d*) $\theta_{min} = 80°$, $\theta_{max} = 90°$.

The isotropic hemispherical outflow (Fig. 7*a*) was rejected as a viable wind model by AJO since it produces broad single-peaked forbidden line profiles and results in considerable red-shifted emission for view angles >30°. The filled (Fig. 7*b*) and hollow cone (Fig. 7*c*) scenarios were favored by AJO, since they come much closer than the hemispherical wind to accounting for the observed forbidden line velocity structure, although a close inspection of Figure 7 shows that neither model is completely satisfactory in this respect. The simple bipolar flow successfully produces only blueshifted emission for most view angles, but it does not account for the double-peaked velocity structure seen in half of our stars. In contrast, the hollow cone flow can produce a double-peaked velocity structure for at least a narrow range of view angles; however, this is accompanied by considerable emission redward of the systemic velocity. In addition, the relative intensities of the red and blue peaks is such that the bluest peak is always strongest, in contrast to many of the observed profiles. Neither model is successful in producing an extended blueward wing.

The progression from a hollow cone to a thin shell, both with $\theta_{max} = 90°$ (Figs 7*c* and 7*d*) is seen to delineate more sharply the double-peak structure noted by AJO as being most similar in shape to the observed forbidden line profiles. Although the constant velocity thin shell profiles suffer from many of the same inadequacies described above for the hollow cone model, it is useful to examine the origin of the double-peaked structure, since any successful model will need to include some of these features. It is straightforward to show that a constant velocity wind confined to a thin shell of any θ_{max} produces a double-peaked line profile for a view angle $i > 0°$. This results because, although the emergent intensity from each volume element ΔV in the thin shell is identical, the distribution of that energy between $-v_{max}$ and v_{max} will be allocated according to the spread in radial velocity across ΔV. Both the radial velocities and the intensity ratio of the peaks will be affected by this distribution of intensities. These points are addressed separately below:

1. *Radial velocities of the intensity maxima.*—Two intensity

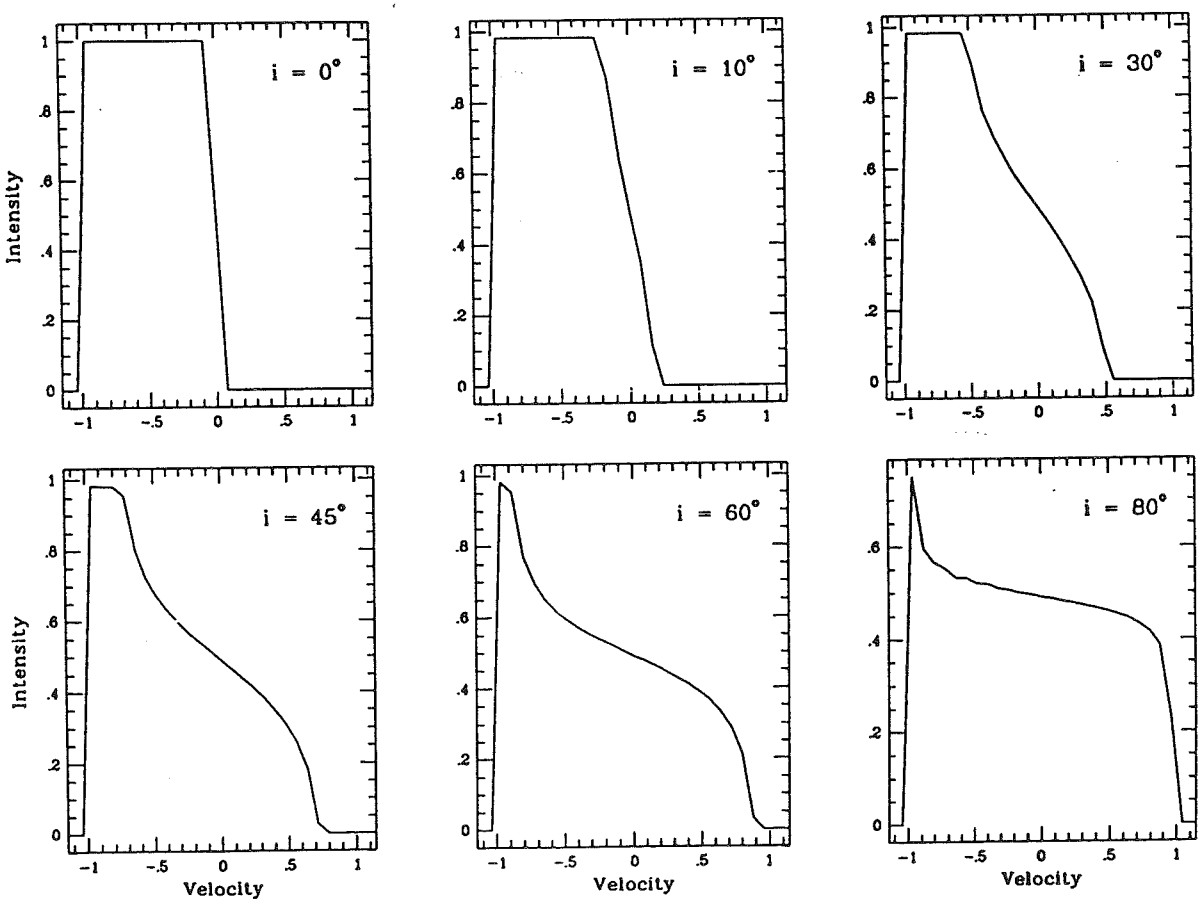

FIG. 7*a*

FIG. 7.—Four families of line profiles for a constant velocity wind. In each case the line profiles are shown for the six view angles: $i = 0°$, 10°, 30°, 45°, 60°, and 80°. All profiles are plotted with the ordinate in units of relative intensity normalized to the peak intensity at $i = 0°$. The abscissa is the radial velocity normalized to the wind speed v_{max}. (*a*) The family of profiles for an isotropic, hemispherical wind, with $\theta_{min} = 0°$ and $\theta_{max} = 90°$. (*b*) The family of profiles for a filled cone, with $\theta_{min} = 0°$ and $\theta_{max} = 45°$. (*c*) The family of profiles for a "hollow cone," with $\theta_{min} = 45°$ and $\theta_{max} = 90°$. (*d*) The family of profiles for a thin shell, with $\theta_{min} = 80°$ and $\theta_{max} = 90°$.

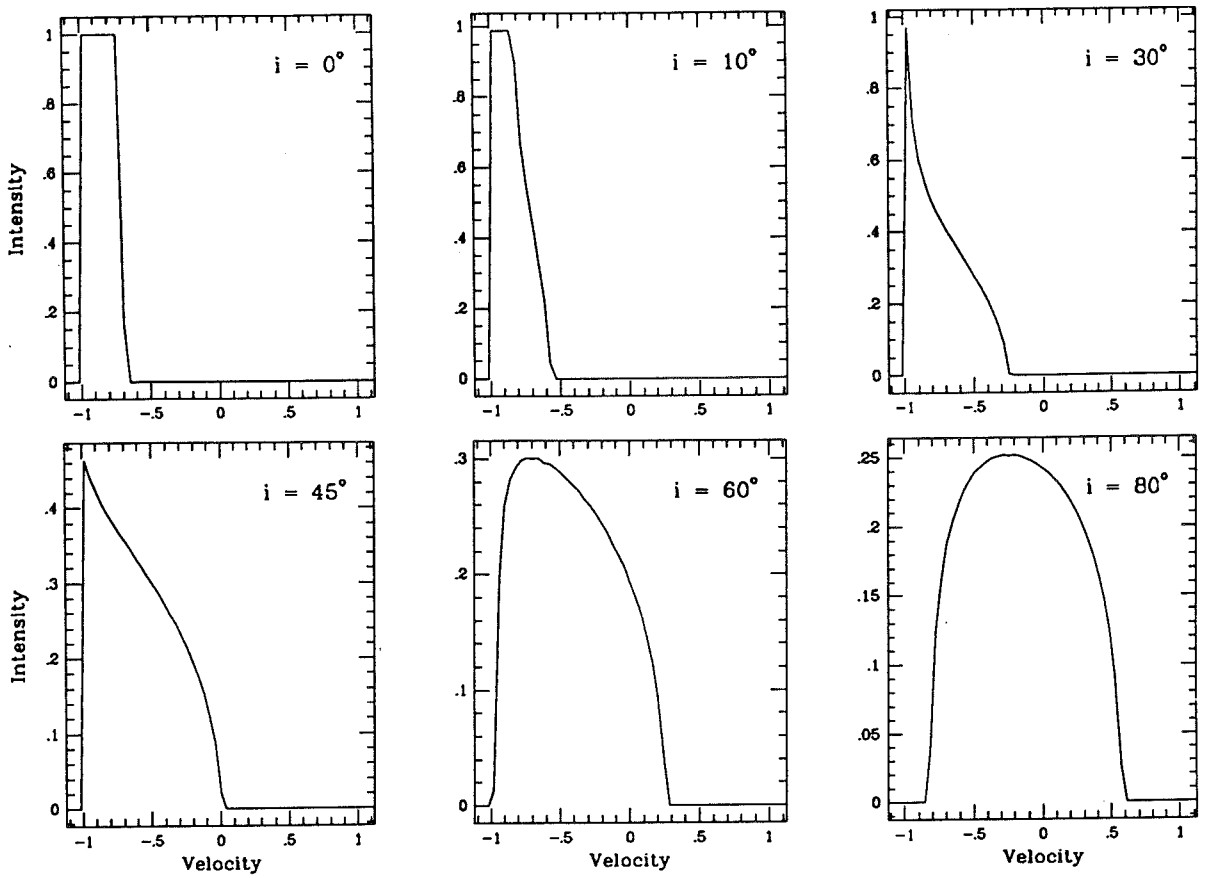
i = 0°
i = 10°
i = 30°
i = 45°
i = 60°
i = 80°
Intensity
Velocity

FIG. 7b

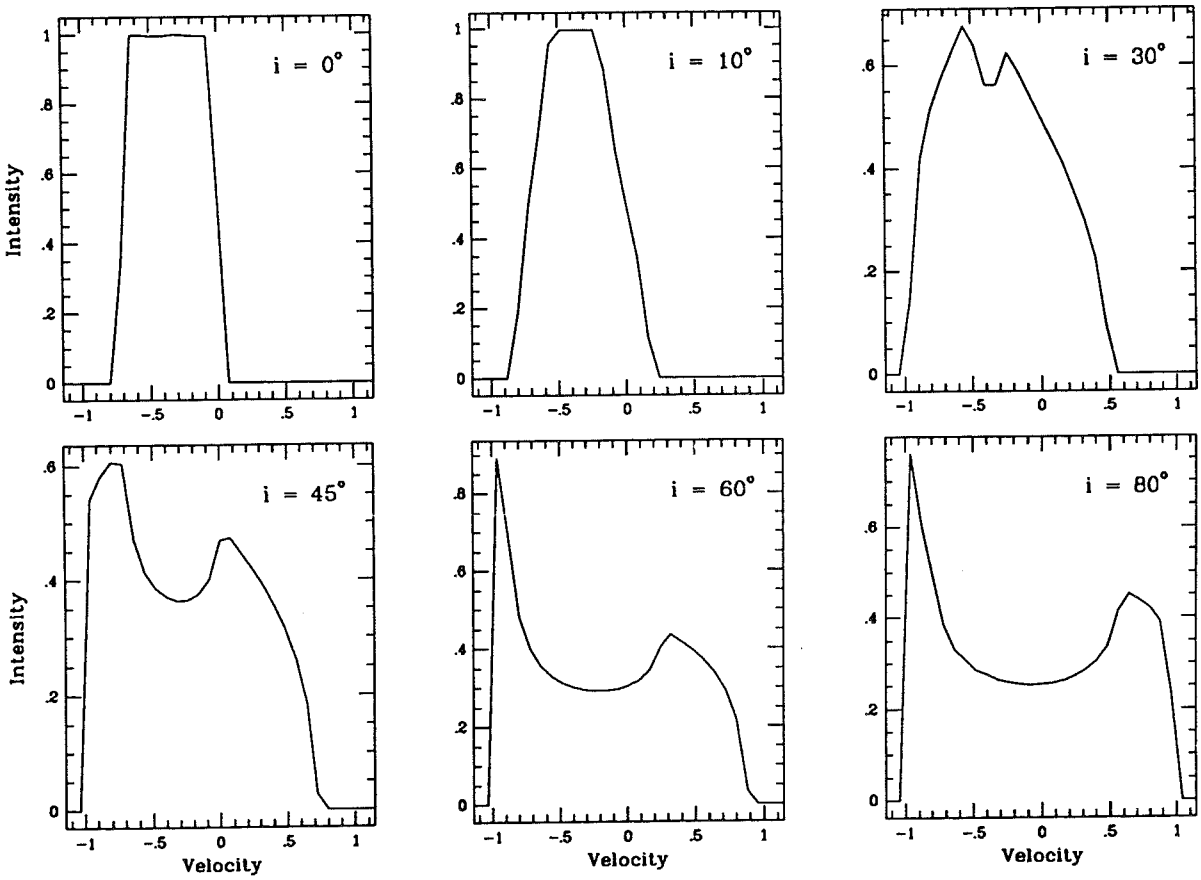
i = 0°
i = 10°
i = 30°
i = 45°
i = 60°
i = 80°
Intensity
Velocity

FIG. 7c

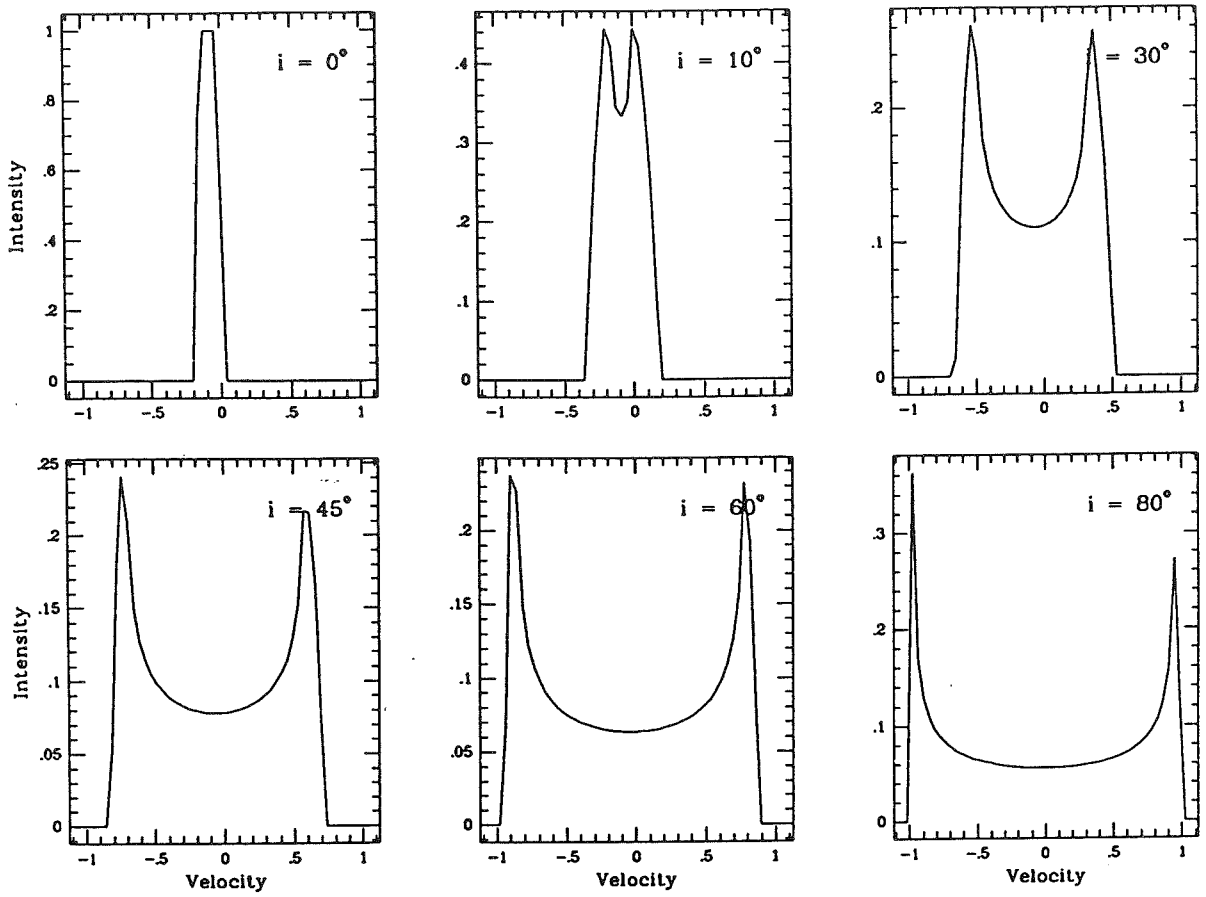

FIG. 7*d*

maxima arise in the constant velocity thin shell because of the behavior of the radial velocity variation in ϕ across each ΔV. Since $dv_r/d\phi \sim \sin \phi$, the dispersion in v_r is smallest at $\phi = 0$ and π, ensuring that the integrated emission from the ΔV at these locations will show the smallest dispersion in radial velocity. This may be seen by inspection of Figure 6. The radial velocities of the two maxima in the line profile for a thin shell of any θ_{max}, with a view angle $i > 0°$ will be:

$$\phi = 0 \text{ (blue peak)}: \quad v_r = \cos \beta = \cos (\theta_{max} - i)$$

$$\phi = \pi \text{ (red peak)}: \quad v_r = \cos \beta = \cos (\theta_{max} + i) .$$

Figure 8 shows the position of the intensity maxima for a set of schematic line profiles for a range of θ_{max} and view angles. Note that some combinations of θ and i give blueward and redward peak velocities similar to those seen in some of the observed forbidden line profiles.

2. *Relative intensities of the maxima.*—The relative intensity of the two peaks in the line profile for $i > 0°$ is determined by the ratio of the radial velocity dispersions in θ across the width of the shell at $\phi = 0$ and π. When, for example,

$$\left.\frac{dv_r}{d\theta}\right|_{\phi=0}, \qquad \left.\frac{dv_r}{d\theta}\right|_{\phi=\pi},$$

the blueward peak will be proportionately stronger than the redward peak, since the energy from the volume element near $\phi = 0$ will be less dispersed in radial velocity across the line profile. It can be seen in Figure 6 that for a thin shell with $\theta_{max} = 90°$, the ratio of the radial velocity dispersions in θ at $\phi = 0$ to $\phi = \pi$ decreases with increasing view angle (until $i = 90°$), accounting for the increasing blue/red intensity ratio with view angle seen in Figures 7*c* and 7*d*.

ii) *Latitude-dependent Wind Velocities*

The partial success of the AJO constant velocity filled and hollow cone models in accounting for the forbidden line profiles in TTS spectra is encouraging, but suggests that modifications to their starting assumptions are in order. We seek a model that will (1) result only in blueshifted line emission and (2) that will be able to reproduce the double-peaked velocity structure that is seen in half of our sample stars. We find that the addition of a latitude dependence to the wind velocity and density not only meets these two criteria, but also successfully reproduces the observed range in forbidden line profile types simply as a result of varying view angles. In addition we find that this model is capable of producing a wide range of relative intensities between the two emission maxima, as observed.

As an initial guess for an $f(\theta)$ law, we adopt a velocity field that decreases linearly with latitude, since it seems to be a reasonable representation of the velocity law inferred by JH for R Mon. For assistance in interpreting the line profiles which follow, we provide in Figure 9 the surfaces of constant radial velocity for a wind with a latitude-dependent velocity that decreases linearly from $f(\theta_{min}) = 1$ to $f(\theta_{max}) = 0.2$, where $\theta_{min} = 0°$, $\theta_{max} = 90°$. (This gives a reasonable match to the inferred velocity law for R Mon for latitudes between 30° and 50°, if the polar velocity is assumed to be 300 km s^{-1}.) Note that the radial velocity surfaces in Figure 9 are simply those in

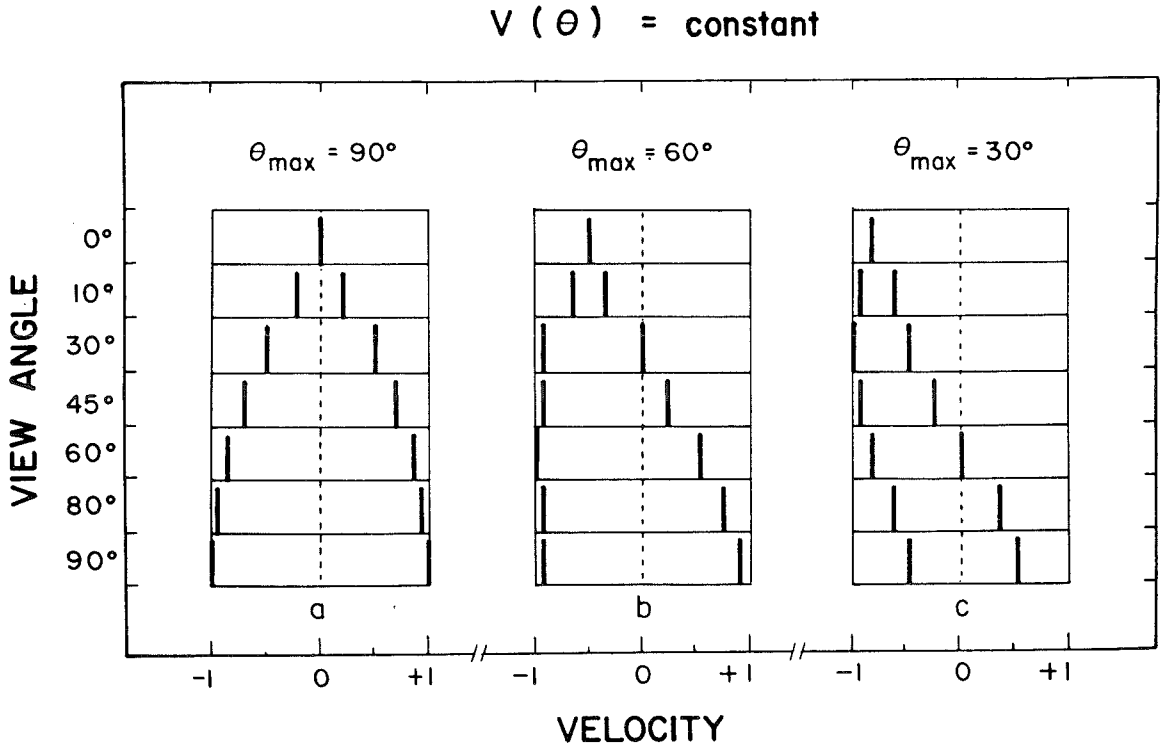

FIG. 8.—Schematic line profiles showing the radial velocities (but not the relative intensities) of the two emission maxima that result from winds with constant velocity confined to very thin shells with (*a*) $\theta_{max} = 90°$, (*b*) $\theta_{max} = 60°$, and (*c*) $\theta_{max} = 30°$ for a range of view angles.

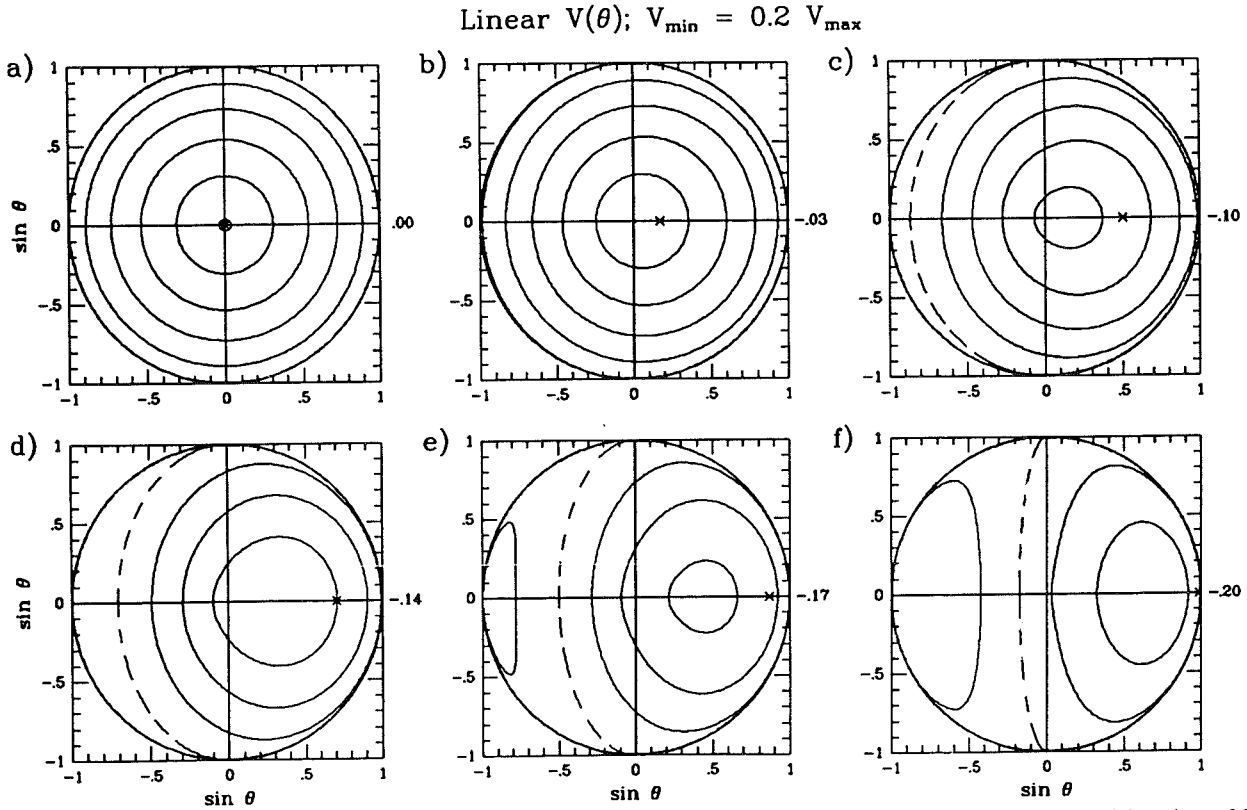

FIG. 9.—The surfaces of constant radial velocity for a latitude-dependent wind characterized by a linear velocity law with the wind speed dropping to $0.2\,v_{max}$ at θ_{max}, with $\theta_{min} = 0°$, $\theta_{max} = 90°$, as seen from six view angles: (*a*) $i = 0°$, (*b*) $i = 10°$, (*c*) $i = 30°$, (*d*) $i = 45°$, (*e*) $i = 60°$, and (*f*) $= 80°$. The axes and orientation are as defined in Fig. 6.

The surfaces of constant radial velocity are ± 0.98, ± 0.8, ± 0.6, ± 0.4, ± 0.2, 0. The zero velocity surface is marked as a dashed line in each frame. Note that the constant radial velocity surfaces are not symmetric about the $\beta = 0$ axis for each view angle. The number to the right of each frame is the radial velocity at $\theta = 90°$, $\phi = 0$.

Figure 7 for the constant velocity wind (cos β) weighted by $v(\theta)$. For example, the radial velocities corresponding to θ_{max} are 0.2 cos β. Also note that the surfaces of constant radial velocity are no longer symmetric about the $\beta = 0°$ axis.

The emergent line profiles for this model are shown in Figure 10*a*. In Figures 10*b* and 10*c*, we display the families of line profiles for two additional latitude-dependent wind models, both of which also have a linear decline in $v(\theta)$ terminating at $f(\theta_{max}) = 0.2$, but which differ in opening angles. In the first case (*b*) $\theta_{max} = 60°$ and in the second (*c*) $\theta_{max} = 30°$.

The effect of the latitude-dependent velocity and density laws on the emergent forbidden line profiles shown in Figure 10 can be described as follows:

1. The general character of the emergent profile as a function of view angle is similar for a wide range of opening angles. At small view angles, a single intensity maximum near zero radial velocity and an extended blue wing result, while at large view angles a double-peaked profile structure is seen, again with an extended blue wing. The variation in the predicted profiles with aspect angle accounts remarkably well for the range of profile types seen in [O I] and [S II] in the TTS observed here.

2. The profiles are strongly affected by the emission near θ_{max}, where the density is rising steeply, such that over half of the fractional contribution to the profile is from the outer 10%–15% of the wind. For this reason, many features of the profiles can be interpreted in the context of the profiles from the constant velocity thin shell examples in Figures 7*d* and 8. Thus, the radial velocities of the emission peaks correspond approximately to the radial velocities at $\theta \approx \theta_{max}$, $\phi = 0, \pi$. Recall from Figure 9 that these will be the radial velocities from the constant velocity thin shells (cos β) weighted by $v(\theta_{max})$.

3. At all but the largest view angles, the contribution to the profiles from the inner region of the wind, where wind velocities (and radial velocities) are high but densities are low, is an extended blue wing.

4. The relative intensities of the double-peaked profiles seen at large view angles is determined by the ratio of

$$\left.\frac{dv_r}{d\theta}\right|_{\phi=0} \quad \text{to} \quad \left.\frac{dv_r}{d\theta}\right|_{\phi=\pi}$$

in the outer few percent of the cone. The latitude dependence in the wind velocity can alter this ratio significantly from the simple constant velocity model, where the blueward peak is always dominant. For example, an examination of Figure 9 for

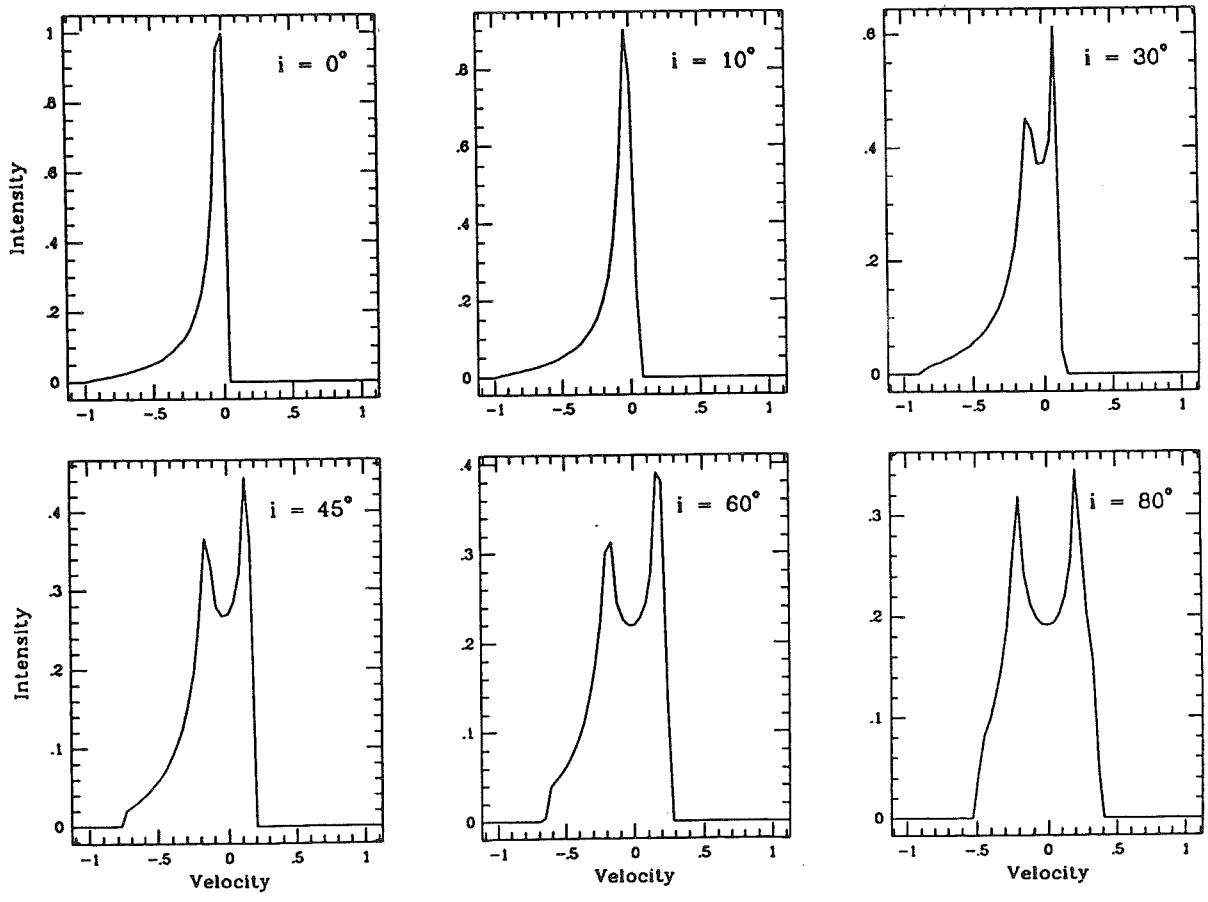

FIG. 10*a*

FIG. 10.—Three families of line profiles for three different models of a latitude-dependent wind. In each case the line profiles are shown for the six view angles: $i = 0°$, 10°, 30°, 45°, 60°, and 80°. All profiles are plotted with the ordinate in units of relative intensity normalized to the peak intensity at $i = 0°$. The abscissa is the radial velocity normalized to the wind speed v_{max} at $\theta = \theta_{min}$.

All three families of profiles are computed for a wind with a linear velocity law decreasing to 0.2 v_{max} at $\theta = \theta_{max}$. The models differ in the opening angle of the wind: (*a*) $\theta_{min} = 0°$ and $\theta_{max} = 90°$, (*b*) $\theta_{min} = 0°$ and $\theta_{max} = 60°$, and (*c*) $\theta_{min} = 0°$ and $\theta_{max} = 30°$.

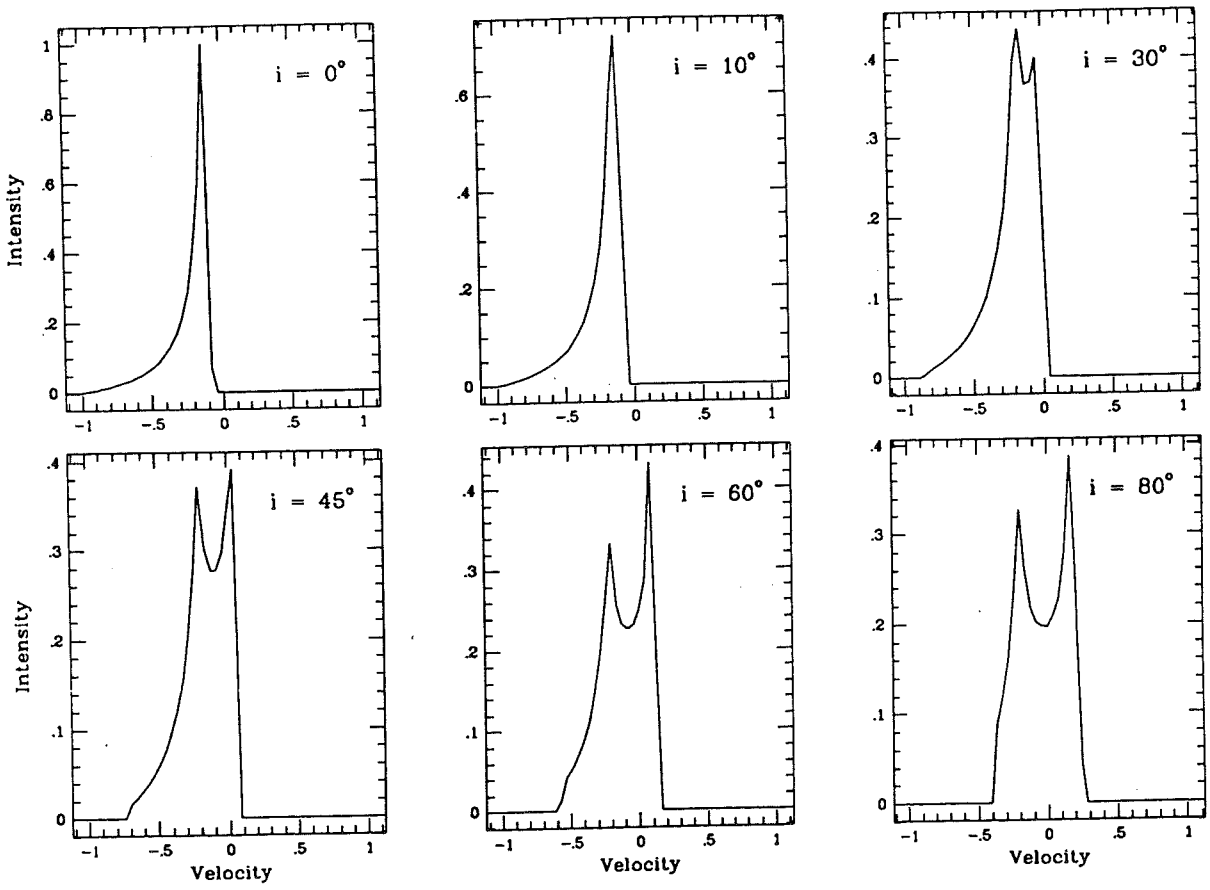

FIG. 10*b*

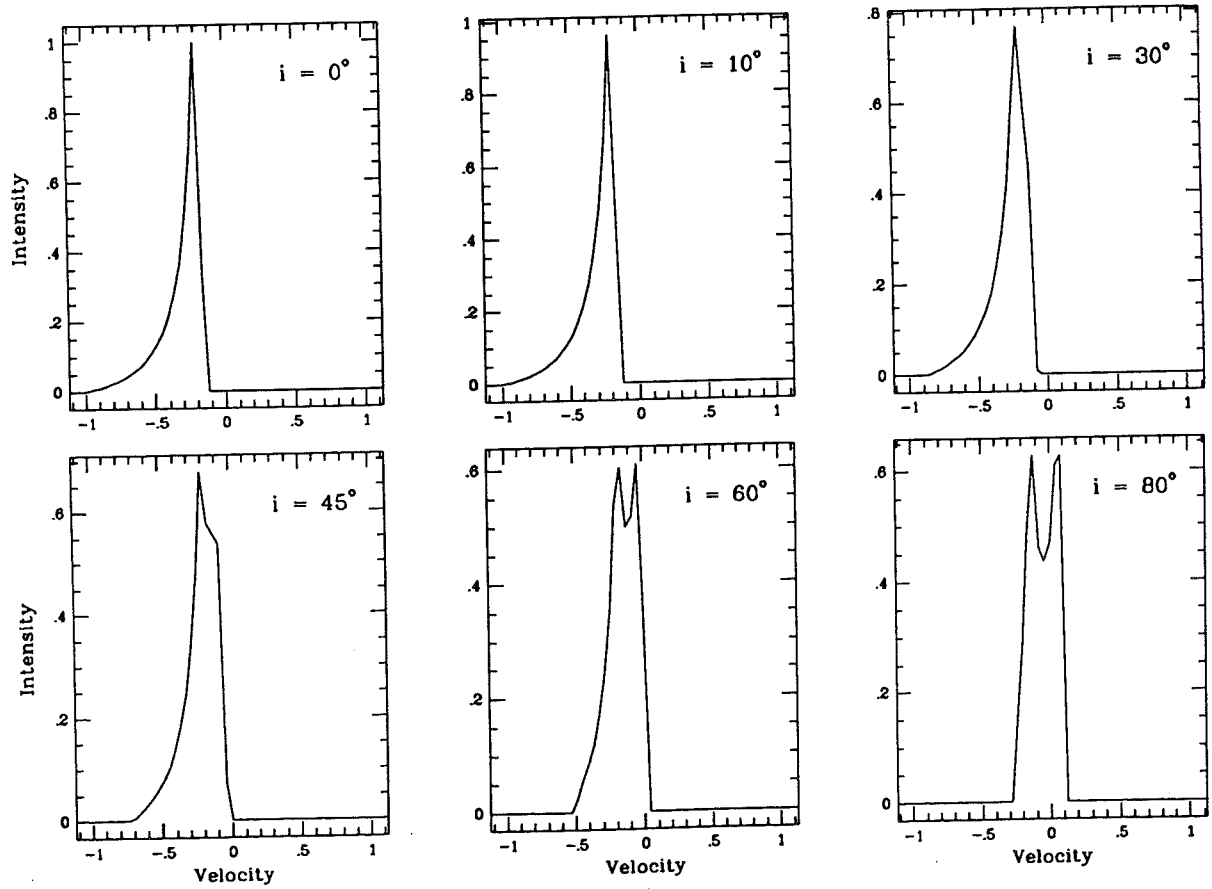

FIG. 10*c*

large view angles shows that near $\theta_{max} = 90°$ the radial velocity dispersion in θ at $\phi = 0$ has become larger than at $\phi = \pi$ (compare with Fig. 6) through the addition of a linearly decreasing $v(\theta)$. Thus a steep enough $v(\theta)$ gradient near θ_{max} will invert what would otherwise be a blue/zero velocity ratio > 1.

iii) *Assessment of Latitude-dependent Wind Models in Accounting for Forbidden Line Profiles*

The observed range of forbidden line profile shapes, from a single peaked maximum near zero velocity accompanied by an extended blue wing to two well separated emission maxima at zero velocity and velocities blueward of ~ 100 km s^{-1}, is readily accounted for by a wind with a latitude-dependent velocity as a consequence of different orientations between the TTS and the line of sight. The flexibility provided by the four independent parameters in our wind model [θ_{min}, θ_{max}, $f(\theta)$, and i] does not allow any stringent limits to be placed on velocity laws or opening angles in the winds of TTS. With the exception of θ_{min}, which must be $\sim 0°$ in order to produce an extended blue wing, we find that there is a wide range of allowed values for these parameters that can reproduce the observed range of forbidden line profile shapes. The effect of each variable on the emergent profiles can be summarized as follows:

$f(\theta)$.—The *slope* of the velocity law is most important in the vicinity of θ_{max}, where it controls the relative intensity of the two emission maxima seen at larger view angles. We find that the shape of the velocity law for $\theta \approx 0°$ has only a minor impact on the predicted profile. As described in the previous section, stronger zero velocity peaks result if the velocity drops sufficiently steeply near θ_{max}; for shallower slopes stronger blueward peaks will result. Since the observed forbidden lines in our sample of TTS have blue to zero velocity intensity ratios ranging from about 3 to 0.5, we infer that a range of velocity laws are found in TTS winds.

A velocity law with a variable slope could result in a difference between forbidden lines characterized by differing critical densities, as is seen in CW Tau for [O I] and [S II], where N_{cr} is $\sim 10^5$ and $\sim 10^4$ cm^{-3}, respectively. The expectation would be that the lines with higher critical densities will have an effective θ_{max} greater than those with lower critical densities, although the magnitude of this effect will be sensitive to the wind parameters and view angle. At large view angles, a $v(\theta)$ with a nonconstant slope could result in a stronger blue/zero velocity emission peak ratio for [S II] than for [O I] if the [S II] is primarily formed in a region with a less steep velocity gradient, as is seen in CW Tau.

The *magnitude* of the normalized wind velocity near θ_{max} affects the line width, which is also sensitive to cos β (see eq. [7]). Our assumption of a constant mass-loss rate with θ for $\theta < \theta_{max}$ limits our calculations to a minimum wind velocity near 0.2 v_{max}. Lower minimum velocities are coupled with such strong density enhancements at θ_{max} that the predicted line profiles are totally insensitive to emission from all other θ.

θ_{max} *and* i.—Winds with opening angles as large as 70° to 90° are not as successful in reproducing the observed forbidden line profiles as are models with smaller opening angles. This results from the symmetry about zero in the radial velocity structure of the line for all view angles (see Fig. 8). Otherwise it is impossible to set more stringent limits on the opening angle of the TTS winds without an independent assessment of i because of their similar effects on the radial velocity (see eq. [7]).

A major shortcoming of our model is that although it is more successful than the constant velocity winds in reproducing the forbidden line profiles, we still have not fully achieved our goal of ensuring that an emission maximum occurs at zero radial velocity for all view angles. For a linear velocity law with a terminal velocity at θ_{max} of 0.2 v_{max} (shown by the family of profiles in Fig. 9), a peak at zero radial velocity results for winds with large opening angles seen at small view angles or for winds with small opening angles seen at large view angles. Additional emission from material with zero radial velocity would still seem to be required in order to ensure sufficient emission at zero velocity from all view angles.

Additional zero velocity emission could be produced by letting the wind velocity decrease to ≈ 0 at θ_{max}, provided we relax our assumption of a constant mass-loss rate with θ, which would otherwise predict a density approaching infinity as $v(\theta)$ approaches zero. Clearly our simple model cannot appropriately handle the velocity and density structure near the "boundary" at θ_{max} that would seem to be required. A decrease to near zero velocity near θ_{max} might be caused by an extrinsic source, such as a wind/cloud interaction along the periphery of a cone, analogous to fluid flow in a pipe. Another possibility is that there is an intrinsic angular dependence of the mass-loss rate and wind momentum as well as the wind velocity, such that they also decrease with increasing polar latitude. We do not attempt to incorporate an angular dependence to the mass loss rate in the model since the addition of another independent variable does not seem justified at present.

IV. THE EFFECT OF A LATITUDE-DEPENDENT WIND ON Hα LINE FORMATION

It is interesting to speculate on the effect of a latitude dependence to the wind velocity on the Hα profile. The symmetry of the broad emission wings (± 500 km s^{-1}) in Hα seen in most TTS shows that this line does not suffer the same occultation that is seen in all the forbidden line profiles. This is not inconsistent with the proposed wind model, since Hα is probably optically thick, the emission will arise much closer to the star than the forbidden lines (tens of stellar radii rather than tens of AU), and it may be a hybrid line, partly formed in the inner wind (Hartmann, Edwards, and Avrett 1982), partly in a chromosphere (Calvet, Basri, and Kuhi 1984), and partly in a warm inner disk, possibly with an active accretion zone (Bertout 1986).

The work of Hartmann, Edwards, and Avrett (1982) on Balmer line formation in TTS winds shows that optically thick lines will have an absorption reversal with a radial velocity characterized by the wind velocity in the region where $\tau \approx 1$. If there is a latitude dependence to the wind velocity, and if we make the simplifying assumption that the radial velocity of the Hα reversal is a measure of the terminal wind speed along the line of sight to the star (cos $\beta = 0$); eq. [7]), then for a given wind model we would predict a clear relationship between the radial velocity of the Hα reversal and the shape of the forbidden line profiles as a function of view angle. In addition there would be a systematic velocity difference between the Hα reversal and the bluest peak in the forbidden line profile with view angle. This velocity difference has been calculated for all of our program stars and has been used to define the sequence of [O I] and Hα line profiles displayed in Figures 1 and 4. These velocity differences are listed in Table 4; they define a progression from -477 km s^{-1} to $+84$ km s^{-1}. (Since Hα can have multiple reversals in some stars, the velocity of the

TABLE 4

VELOCITY DIFFERENCE: Hα REVERSAL – BLUEST [O I] PEAK

Star	Radial Velocity Hα Reversal[a] (km s^{-1})	Radial Velocity [O I] Peak[b] (km s^{-1})	Δv (km s^{-1})
Z CMa	−499	−22	−477
DR Tau	−319	−135	−184
UY Aur	−163	−1	−162
HN Tau[c]	> −150	−82	−70
DF Tau	−85	−93	+8
DO Tau	−86	−94	+8
UZ Tau E	−58	−81	+23
R Mon	−27	−78	+51
RY Tau	−29	−98	+69
CW Tau	−20	−95	+75
HL Tau	−108	−192	+84
UZ Tau W[d]	+67	−7	+74

[a] Radial velocity with respect to the stellar rest velocity (Table 1) for the deepest Hα reversal.

[b] Radial velocity with respect to the stellar rest velocity (Table 1) for the blue peak in [O I].

[c] Technically, there *is* no Hα reversal for HN Tau. The asymmetry of the Hα emission with respect to the stellar velocity suggests that the blue side of the line is being absorbed by material with a large negative velocity.

[d] The Hα reversal for this star is redshifted and the [O I] line has a greater fraction of redshifted emission than any star. Possibly, it is being viewed nearly edge-on, since as $i \rightarrow 90°$, the forbidden lines should become nearly symmetric.

deepest reversal was always selected.) As shown in Figures 1, 4, and 9, we find that the relation between the forbidden line and Hα profiles is as expected from this simple model for most of our sample stars. We discuss this sequence below:

1.—At small view angles, where the observer looks down the polar axis of the wind, the Hα reversal will occur near the maximum wind velocity so the resultant Hα profile might be similar to a classical P Cygni type profile. The corresponding forbidden line would be single peaked with an extended blue wing and centered near zero velocity. The velocity difference between the Hα reversal and the forbidden line peak will be large and negative.

The stars with large negative velocity differences between the Hα reversal and the forbidden emission, expected to be viewed nearer to pole-on, are Z CMa, DR Tau, UY Aur, and HN Tau. Two of the stars may not be good examples of this group, however. The wind of the Herbig Ae/Be star Z CMa is unlike those of the TTS, as evidenced by its extreme P Cygni profile at Hα, and its [O I] line is too weak for its velocity structure to be reliably determined. The star DR Tau is a highly unusual and active T Tauri star (Krautter and Bastien 1980), with an Hα profile riddled with absorption components and the blueward peak in [O I], which should not be present in our simple scheme, is completely separated in velocity from the zero velocity peak making it unique among the stars in our sample.

2.—At larger view angles, the velocity difference will depend upon whether the viewer is looking along a line interior to or exterior to the cone of expanding emitting material. When $i \approx \theta_{max}$ the velocity of the Hα reversal will be equal to the wind velocity at θ_{max}; it will be characterized as a Beals type III P Cygni profile. The forbidden line profile will be double-peaked with the radial velocity of the blueward peak very close to that of the Hα reversal.

The stars eliminate DF Tau and DO Tau have Hα reversals within 8 km s^{-1} of the velocity of the blue forbidden line peaks. If the Hα reversal and [O I] blue peak radial velocities in fact measure the wind velocities near θ_{max} then we can estimate what such velocities might be: a velocity of 80 km s^{-1} would be 0.2 v_{max} if v_{max} = 400 km s^{-1}.

3.—If the view angle $i > \theta_{max}$, one might assume that there would be no Hα reversal. However, the sequence of the velocity difference between the Hα reversal and the bluest forbidden emission peak defined in Table 4 continues into large positive displacements. If there continues to be some velocity of expansion in the Hα formation region that exhibits a decrease with θ for $\theta > \theta_{max}$, then the velocity difference between the Hα reversal and the blue forbidden line peak would be positive, as seen. Admittedly, it is difficult to envision what this implies; it would require that only for $\theta < \theta_{max}$ does the wind have sufficient momentum to push out an extended, high temperature cone. We proceed because a number of stars seem to fall into this category.

The stars with forbidden emission peaks blueward of the Hα reversal are UZ Tau E, R Mon, RY Tau, CW Tau, HL Tau, and UZ Tau W. Independent evidence suggests that two of the stars in this group (R Mon and HL Tau) are in fact viewed nearly edge on (JH; Cohen 1983). The large velocity of the Hα reversal (−107 km s^{-1}) in HL Tau (probably one of the youngest stars in our sample; Cohen 1983) would imply that the wind speed is still very high for $\theta > \theta_{max}$. The other stars in this group show very modest velocities for the Hα reversal. In both CW Tau and HL Tau the velocity of the blue [O I] peak is coincident with a blue emission maximum in Hα. The significance of this is unclear, although the Hα emission arising in the conical wind will not be seen in projection against the star and will exhibit a velocity structure similar to that of the forbidden line. Possibly such a contribution occurs in these two stars.

What is most striking is that when the [O I] profiles are ordered according to the velocity difference between the Hα reversal and the bluest peak in the [O I] profile, the progression of forbidden line profiles follows the sequence predicted by our model for varying the view angle from nearly pole on to nearly edge on. If the opening angles and velocity laws for all TTS winds were roughly the same, the sequence in Table 4 would also be a sequence from small to large viewing angles. We are encouraged by the fact that both R Mon and HL Tau, for which orientations are probably nearly edge on (JH; Cohen 1983), would be inferred to have large viewing angles on the basis of this model.

V. DENSITY, TEMPERATURE, SPATIAL EXTENT, AND MASS-LOSS RATES OF THE FORBIDDEN LINE REGION

a) Constant Velocity, Spherically Symmetric Winds

Independent of our latitude-dependent wind model, we can estimate average densities, sizes and upper limits on the mass-loss rates for TTS winds based on the electron densities inferred from the [S II] λλ6731/6716 ratio and the emission measure for these lines. Table 5 summarizes the results of these estimates for the case of a spherically symmetric, constant velocity wind. The first four columns identify the star, its distance, the A_v from CK or Cohen (1983), and the [S II] λ6731 line intensities, in ergs s^{-1} sr^{-1}. In what follows, all absolute line intensities have been derived by applying the relevant continuum intensities from CK to the equivalent widths measured here to get absolute line fluxes and then correcting for the distances and reddening given in Table 5. Insufficient knowledge of the reddening for DR Tau necessitates its omission from Table 5.

TABLE 5

PROPERTIES OF [S II] EMITTING REGION

Star (1)	d (pc) (2)	A_v (3)	log I_{6731} (ergs s^{-1} sr^{-1}) (4)	[S II]/[O I] (5)	λ6731/λ6716 ($\pm$0.15) (6)	N_e/N_{cr} ($\pm$30%) (7)	R_{cr} (AU) (8)	θ_{cr} (9)	$\dot{M}_{cr}$ ($M_\odot$ yr^{-1}) (10)
CW Tau	160	2.3	27.62	0.3	2.2[b]	2	48	0".3	3×10^{-8}
RY Tau	160	1.9	28.59	0.5	...	...	101	0.6	8×10^{-8}
DF Tau	160	1.9	<28.01	<0.5	...	...	<65	<0.4	$<5 \times 10^{-8}$
HL Tau	160	7	29.78	0.4	1.6	0.2	238	1.5	2×10^{-6}
UZ Tau W	160	0.85	<26.60	<0.25	...	...	<22	<0.1	$<2 \times 10^{-9}$
UZ Tau E	160	1.5	27.35	0.1	...	..	39	0.25	2×10^{-8}
HN Tau	160	0.5	28.02	0.3	1.9	0.4	65	0.5	6×10^{-8}
DO Tau	160	1.35	28.09	0.25	2.1[b]	1.2	69	0.4	6×10^{-8}
UY Aur	160	1.05	27.99	0.4	...	...	64	0.4	2×10^{-8}
R Mon	800	4.2	30.52	0.5	2.1	2	447	0.6	3×10^{-6}
Z CMa	1150	2.8	30.57	0.3	...	...	430	0.4	...

Col. (3).—From Cohen and Kuhi 1979.

Col. (4).—Reddening and distance corrected line intensity with continuum fluxes from Cohen and Kuhi 1979.

Col. (5).—Reddening-corrected line intensity ratio of [λ6731 + λ6716]/[λ6300].

Col. (6).—[S II] intensity ratio; superscript "b" signifies that the ratio is taken over the velocity interval identified as "blue" in Table 3.

Col. (7).—Resultant N_e (Pottasch 1984) expressed relative to the critical density of λ6731, where $N_{cr} = A_{21}/q_{21} = 1.3 \times 10^4$ cm^{-3}.

Col. (8).—Implied radial extent of the [S II] emitting region, assuming (1) $N_e/N_{cr} = 1$; (2) a spherical volume, so that $R_{cr} = (3/4\pi)^{1/3}(\mathrm{EM})^{1/3}N_{cr}^{-2/3}$; and (3) $\mathrm{EM} = 4\pi I_{6731}(h\nu_{12}q_{12}N_1/N_p)^{-1}(1 + N_e/N_{cr})$.

Col. (9).—Projected angular size of [S II] region if $R = R_{cr}$. Nonspherical geometries with a solid angle $< 4\pi$ will have projected sizes scale as $R = R_{cr}(4\pi/\Omega)^{1/3}$.

Col. (10).—The mass-loss rate if $N_e = N_{cr}$, $R = R_{cr}$, $V = w_b$, and $\Omega = 4\pi$. The spectrum of Z CMa does not permit an estimate of W_b. The actual mass-loss rates are probably an order of magnitude smaller than these values.

i) *Electron Density and Temperature*

An average density of the forbidden line emitting regions can be determined from the ratio of the [S II] equivalent widths given in Table 3 and the relation between [S II] line ratios and electron density given by Pottasch (1984). The [S II] ratios for the five stars for which both [S II] lines are measurable, CW Tau, HL Tau, HN Tau, DO Tau, and R Mon, are listed in Table 5, col. (6). (For HL Tau, HN Tau, and R Mon, the Ca I λ6717 line did not interfere with [S II] λ6716 since these stars are heavily veiled and show no photospheric features. For CW Tau and DO Tau, only the bluward [S II] peaks were used to compute the [S II] intensity ratio, since the [S II] λ6716 emission is blended with Ca I λ6717.) The implied densities are close to the critical densities for these lines, defined as the density where the de-excitation collisional and radiative rates are equal. Table 5, col. (7) gives the densities expressed relative to the critical density for the [S II] λ6731 line, 1.3×10^4 cm^{-3}. The upper limits on the equivalent widths for the [S II] λ6716 line for the remaining stars give [S II] ratios consistent with the above five stars.

The inferred densities in the forbidden line emission region are higher than those characteristic of H-H objects, whose average density is about 2000 cm^{-3}, and which range from 100 to 30,000 cm^{-3} (Cantó 1985; Hartmann and Raymond 1984; with application of the Pottasch relation to published intensity ratios). Since [O I] λ6300 has a critical density about 100 times that of the [S II] lines, the ratio of the combined [S II]/[O I] intensity provides an additional diagnostic of the density ranges characterizing TTS spectra as compared to H-H objects. The [S II]/[O I] ratios found for the stars examined here, listed in Table 5, col. (5), have an average value of 0.3 ± 0.1, in contrast to the same ratio in the H-H objects, which is 1.5 ± 0.6 (Dopita 1978; Brugel, Böhm, and Mannery 1981; Dopita, Binette, and Schwartz 1982). The relatively stronger [O I] in the TTS supports the conclusion from the [S II] ratios that the forbidden emission in TTS comes from a region that is denser than the typical H-H object.

The weakness of the [N II] λ6584 feature (whose ionization potential is 6.2 eV greater than S II) argues that the forbidden emission regions around the TTS are more neutral than H-H objects. While the average [N II]/[O I] intensity ratio found in H-H spectra is 0.9 ± 0.5, with a range of values between 0.2 and 1.9, the same ratio in the TTS has a maximum value of 0.07, except for HL Tau, where it is 0.3. Thus the forbidden emission regions around TTS appear to be more neutral and denser than those found in typical H-H objects.

ii) *Spatial Extent*

A characteristic volume (V) of the forbidden emission region can be inferred from the emission measure (EM) and the electron density, where $V = \mathrm{EM}/N_e^2$. (The calculation of the emission measure is described below.) In Table 5, cols. (7) and (8), we tabulate the spatial extents (R_{cr}) that result if the [S II] critical density and a spherical emitting volume are assumed, i.e., if $R_{cr}^3 = 3/4\pi[\mathrm{EM}]N_{cr}^{-2}$. The estimates for R_{cr} range from 20 to 400 AU, but are <100 AU for most of the TTS. The projected angular extents range from 0".1 to 1".5, although most are several tenths of an arcsec. Resolution of such structures, although not feasible with our long slit spectra, could be achieved through speckle techniques or with the Hubble Space Telescope.

The emission measure of the [S II] lines is determined by the [S II] line intensity, by various atomic parameters, the electron density, and the ratio of S II atoms in the ground state to the proton density, N_1/N_p. The exact depencence is given by:

$$\mathrm{EM} = (4\pi I_{21})(h\nu_{21}q_{12}N_1/N_p)^{-1}(1 + N_e q_{21}/A_{21}) .$$

Radiative transition probabilities (A_{21}) are from Mendoza and Zeipen (1982) and collision strengths (q_{ij}) are from Pradhan (1978). The major uncertainty is the [S II] line intensity (I_{21})

derived from our uncalibrated spectra. The application of the continuum fluxes and A_v values from CK to our equivalent widths ignores any continuum variations between the two observing epochs. However, the continuum variations in these stars are usually one to two magnitudes at V (Rydgren *et al.* 1984; Herbst 1986) and since R_{cr} is proportional to $(EM)^{1/3}$, the resultant error in R_{cr} for any individual star is likely to be a factor of a few or less. Our procedure should then at least give a rough estimate of the emission measure and spatial extent characteristic for the group of forbidden line TTS.

For N_1/N_p we adopt the cosmic S/H ratio (1.58×10^{-5}; Allen 1973) since we have no means of estimating the ion concentration of S II/S I; it is unlikely that much S III is present, given the low intensity of [N II]. Approximating N_1/N_p with the S/H ratio then gives lower limits to the emission measures, emitting volumes and spatial extents of the forbidden emission region.

iii) *Mass-Loss Rates*

An upper limit to the mass-loss rate for each star can be estimated by assuming spherically symmetric, constant velocity winds with velocities given by the most extreme blue wing velocity in the forbidden lines (w_b, Table 2) and characterized by the inferred average densities and sizes for the forbidden emission regions. Thus:

$$\dot{M} = 4\pi R_{cr}^2 N_{cr} m_H w_b ,$$

where m_H is the mass of hydrogen. The $\dot{M}$ values listed in Table 5, col. (10) are on the order of $10^{-8}\ M_\odot\ yr^{-1}$ for most of the TTS, although HL Tau and R Mon have mass-loss rates nearly two orders of magnitude higher. These estimates are similar to the mass-loss rates inferred previously for TTS from Hα line profile analysis (Kuhi 1964; Hartmann, Edwards, and Avrett 1982).

b) Consideration of the Latitude-dependent Wind Model

The mass-loss rates given in Table 5 can be revised downward by about an order of magnitude in the context of our latitude-dependent wind models. The characteristic densities inferred from the [S II] line ratio will then be representative of the densest part of the wind near θ_{max}, where the wind velocities are lowest. Thus it is misleading to couple the densest part of the outflow with the highest wind velocities, as in the constant velocity assumption. In addition, if the outflow subtends a solid angle $\Omega < 4\pi$, then the spatial extent will be underestimated, but only by a factor of $(4\pi/\Omega)^{1/3}$, while the expression for the mass loss will be decreased by a factor of $\Omega/4\pi$. For example, if the wind is confined to two opposing 45° cones, the wind speeds near θ_{max} are 20% of v_{max}, and the maximum polar velocity is 300 km s^{-1}, then the $\dot{M}$ values listed in Table 5 will be reduced by about a factor of 10.

VI. CIRCUMSTELLAR DISKS

Thus far in our discussion, we have invoked the presence of an "obscuring screen" to occult the unseen, receding part of the YSO mass outflow mapped by the forbidden lines. It seems most natural to assume that the "screens" are circumstellar disks characterized by polar optical depths $\tau_{6300\,\text{Å}} > 1$ and sizes sufficiently large to obscure the receding outflows. The observations reported here provide no other constraints on the disk characteristics. However, recent studies of one star in our sample, HL Tau, offer important insight into the dimensions, masses, optical depths, and possible evolutionary status of the disks associated with the forbidden line TTS sample discussed here.

In 1984, two groups of observers (Grasdalen *et al.* 1984; Beckwith *et al.* 1984) working contemporaneously obtained high angular resolution observations of HL Tau in the near-infrared (1.6 μm to 3.3 μm). Grasdalen *et al.* report, on the basis of maximum entropy reconstructed images, the presence of a flattened circumstellar structure of long dimension 2″ (320 AU at the distance to HL Tau) and argue from polarimetric measurements that the observed extended structure represents light scattered toward earth by dust in a disk surrounding this YSO. Beckwith *et al.* independently confirm the presence of this flattened structure based on infrared speckle observations of effective spatial resolution approximately 0″.2. The dust mass required to account for the surface brightness of the 2.2 μm scattered light structure is $\sim 10^{-7}\ M_\odot$.

In addition, Beckwith *et al.* (1986) report the detection of CO $J = 1$–0 line emission and 2.7 mm continuum emission from a structure $< 6''$ in size surrounding HL Tau. The gas appears to be bound to the star and to show a signature characteristic of Keplerian motion (Sargent and Beckwith 1987). It seems most plausible that the millimeter line and continuum radiation as well as the scattered light structure observed in the near-infrared are associated with a rotating, circumstellar disk. Attributing the millimeter continuum emission to optically thin thermal radiation from dust at $T \approx 50$ K, the mass of the disk (for an assumed interstellar gas/dust ratio by mass of 100) is $10^{-2} < M/M_\odot < 10^{-1}$. This is far larger than the disk mass derived by Cohen ($< 10^{-4}\ M_\odot$; 1983) from his KAO continuum measurements of HL Tau at 52 μm and 100 μm and *from his assumption that the disk is optically thin at 100 μm.* The disparity in derived masses at millimeter and far-infrared wavelengths can be explained by assuming that the disk surrounding HL Tau is optically thick at 100 μm but optically thin at 2.7 mm (F. Shu, private communication). An optically thick disk with a temperature, $T_d \approx 50$ K (Beckwith *et al.* 1986) must have a projected radiating area equal to that of a circular region 130 AU in radius in order to account for the observed absolute flux at 60 μm. This estimated size lies within a factor of a few of the dimension of the structure observed in the near infrared and *that of the obscuring screen required by the forbidden line observations* (Table 5).

We propose that HL Tau is surrounded by an optically thick ($\tau_v > 1000$) but physically thin disk of radius $\sim$100–200 AU and mass $\sim 10^{-1}$ to $10^{-2}\ M_\odot$; the disk is viewed at an angle of $< 30°$ from equator-on. A disk of this size can provide the obscuring screen required to occult the receding part of the bipolar mass outflow emanating from HL Tau and mapped by the forbidden lines.

In Table 6, we list the disk radii estimated for our sample of TTS based on the assumption that the observed 60 μm emission (*IRAS Point Source Catalog*) arises in an optically thick disk of characteristic temperature 50 K; in all cases, these radii are comparable to or larger than those of the optically thick screens required by the forbidden line observations (see Table 5). We find the assumption that the forbidden line TTS are surrounded by optically thick ($\tau_v > 1000$), physically thin disks to be particularly satisfying in this respect: occultation of the receding part of the flow does not depend on a structure delicately "tuned" to produce $\tau_{6300\,\text{Å}} \approx 1$. Rather, nothing is left to chance and the obscuring screens required by the absence of any redshifted forbidden line components both in our sample

TABLE 6

PREDICTED DISK RADII

Star	F_{60} (Jy)	R_D(AU) (T = 50 K)
CW Tau	3.2	27
RY Tau	18.7	64
DF Tau	1.1	16
HL Tau[a]	76	130
UZ Tau W, E[b]	<2.1	<22
HN Tau	1.3	17
DO Tau	6.1	37
DR Tau	5	33
UY Aur	7.2	40
R Mon	132	855
Z CMa	321	1330

[a] Confused with XZ Tau.
[b] UZ Tau E, W in same beam.

and in that of AJO, are apparently more than robust enough to do the job.

The minimum masses in these disks can be estimated by assuming (*a*) $\tau_{100\,\mu m} = 1$, (*b*) a standard interstellar gas/dust ratio of 100 by mass, and (*c*) $\tau_{100\,\mu m}/\tau_v = 10^{-3}$ (Hildebrand 1983). Under these assumptions,

$$M_d/M_\odot = (\tau_v/1000)(r_d/100\ \mathrm{AU})^2 \times 0.032\ .$$

Hence, for most stars in our sample, the disk masses range from 10^{-2} to $10^{-1}\ M_\odot$.

If our hypothesis regarding the large ($\tau_v > 1000$) polar optical depths of the disks is correct, then the character of the forbidden line profiles should be invariant with wavelength over the range from $\sim$0.6 μm to 10 μm. In particular, forbidden lines observed in the 2 μm and 10 μm windows (where the disk optical depth, by hypothesis, is still large) should exhibit the same blueshifted systemic velocity shown by their optical counterparts. Spectra with a resolution $\lambda/\Delta\lambda > 1000$ which provide accurate velocity determinations should be sufficient to detect any shift in the systemic velocity from that derived from the optical features. Significant shifts redward from the velocities characterizing [O I] and [S II] would indicate that the disk optical depth is much smaller than $\tau_v \approx 1000$. Candidate lines for observation include the [Fe II] lines at 2.05 μm, 2.13 μm, 2.22 μm, and 2.37 μm, [Fe III] lines at 2.15 μm and 2.24 μm, [Ar II] at 6.98 μm, and [Ne II] at 12.78 μm.

Comparison of disk masses estimated from 60 μm and 100 μm observations and from millimeter and submillimeter continuum observations offer, in analogy with HL Tau (Beckwith *et al.* 1986), another diagnostic of the disk optical depth. Structures with M_d (100 μm) $\ll M_d$ (2.7 mm) can be understood if $\tau_{100\,\mu m} > 1$ and $\tau_{2.7\,mm} < 1$. To effect a proper comparison, comparable beam sizes at all wavelengths must be employed. This will require millimeter-interferometric observations (already underway by S. Beckwith and A. Sargent, private communication) combined with "super-resolution" 60 μm and 100 μm observations obtained with the KAO.

It is of interest to note that the oldest stars in our sample as judged by their location in the L, T plane (CK) are CW Tau and HN Tau, which have ages $\sim 3 \times 10^6$ yr. If disks characterized by large optical depths along the polar direction represent precursors to solar systems, then the epoch of planet building or at least of disk clearing takes place at times $> 3 \times 10^6$ yr from the onset of protostellar contraction. From observations of the disks associated with α Lyrae and β Pictoris (Aumann *et al.* 1984; Gillett 1985), we know that the visual optical depth through disks with ages $\sim 10^8$ yr is $\tau_v < 1$. Hence, disk clearing (perhaps driven by planetary formation) must take place between ages of 3×10^6 and 10^8 yr. These time scales are larger by at least two orders of magnitude than theoretical estimates of dust settling times in the primitive solar nebula, after which large planetesimals and planets form very rapidly (Weidenschilling 1984). More stringent constraints on the time scale associated with disk clearing might come from high-resolution spectroscopic observations of the forbidden line profiles in a sample of older, less luminous TTS for which a decrease in polar optical depth might permit observation of redshifted forbidden line emission components. Unfortunately, the absence of strong forbidden line emission in the oldest TTS may in practice vitiate this proposed test.

VII. DISCUSSION AND CONCLUSION

This work allows us to comment on the difference between the forbidden lines found in TTS spectra and those in the spectra of H-H objects. Although both show low excitation metallic emission features of [O I], [S II], and [N II] with line widths on the order of hundreds of km s^{-1} and predominantly negative radial velocities, there appear to be fundamental differences that indicate that the forbidden lines in the TTS spectra arise in stellar winds, while those in the H-H spectra are formed in bow shocks (Schwartz 1983; Raga and Böhm 1986; Hartigan, Raymond, and Hartmann 1987). First, we have shown that the forbidden lines in the TTS spectra are formed in regions of higher density and lower ionization than those in the H-H objects. More to the point, however, are the distinctly different line profile shapes that result from formation in a wind in comparison to those formed in bow shocks. A comparison of our predicted line profile shapes with those computed by Hartigan, Raymond, and Hartmann (1987) shows that the dependence of the line profile shape on aspect angle is strikingly different. In particular, for a face on view ($i \to 0°$) the expected bow shock profile is a double-peaked line, with one blueshifted and one zero velocity peak, while the expected profile from the latitude dependent wind model is a single peaked line near zero velocity with an extended blue wing. For nearly edge on views ($i \to 90°$) the expected bow shock profile becomes broad and symmetric and centered near zero velocity, while the expected profile from the latitude-dependent wind model becomes double-peaked, with one blueshifted and one zero velocity peak. The success of the wind model in accounting for the correspondence between the forbidden line profiles and the velocity of the reversal at Hα leads us to favor the wind model as an explanation of the observed forbidden line profiles in TTS spectra, especially in light of the fact that the predicted view angle from the wind model to HL Tau and R Mon is almost edge-on, as expected. It is of course possible that in some instances unresolved H-H objects may contribute forbidden line emission to TTS spectra, and in fact this may explain the unusual forbidden line structure seen in the spectrum of DR Tau.

If forbidden emission lines can be detected in a larger number of TTS than found in the low-resolution spectroscopic survey of CK, and if these lines can be observed at sufficient spectral resolution ($\Delta\lambda < 1$ Å), they would provide a means of studying the evolution of both TTS winds and circumstellar disks. Major questions regarding the winds are to determine

whether the forbidden line/Hα relation outlined here can be extended to a statistically significant sample of stars and whether the latitude dependence of the velocity, the mass-loss rate, or the wind opening angles evolve with stellar age. The important questions regarding disk evolution are to establish the time scale for disk clearing and to determine how this is related to the process of planet building.

The questions concerning the disk evolution are in principle more straightforward to answer, since they merely require detecting forbidden emission lines over a sufficiently large wavelength range and noting the wavelength dependence of the proportion of blueshifted to redshifted emission. Even in the absence of detectable forbidden emission in the TTS winds, this can be pursued by comparing the disk masses inferred from the far-infrared and from the submillimeter continuum observations of TTS in order to determine when the disks become optically thin at 100 μm. The questions concerning the wind evolution will require a more sophisticated treatment of the wind model than we have presented here, which in turn will require additional observational constraints on the free parameters in the model. Spectroscopic observations of NGC 2261, the conical reflection nebulosity surrounding R Mon, are currently underway that will allow us to measure $v(\theta)$ more precisely, to provide a check on our predicted relationship between Hα and the forbidden line profiles as a function of latitude, and to evaluate whether the mass-loss rate is a function of latitude.

The major conclusions of this work are as follows:

1. The blueshifted forbidden emission lines of [O I] λ6300 and [S II] λλ6731, 6716 in TTS spectra arise in the outer lower density regions of TTS winds. The continuous progression of profile types is best explained by assuming that one is viewing a wind with a latitude dependence from different aspect angles. Such a wind leaves the poles with higher speeds than in the equatorial regions and has a density structure proportional to $r^{-2}v^{-1}$.

2. The radial velocity of the absorption reversal at Hα, although formed closer to the star than the forbidden lines, can also be interpreted in terms of a latitude-dependent velocity. This is shown by the correlation between the velocity difference of the Hα reversal and the bluest forbidden emission peak with the expected forbidden line profile shape as a function of aspect angle.

3. Mass-loss rates from our sample of TTS range from 10^{-7} to 10^{-9} $M_\odot$ yr^{-1}.

4. The absence of redshifted forbidden emission requires that each TTS is surrounded by an opaque circumstellar dust disk of a size sufficient to obscure the receding portion of the winds; such sizes are on the order of tens of AU for most of the stars, but may be as large as several hundred AU in some cases.

5. Independent estimates for the size of the dust disks are made from the 60 μm flux, an assumed dust temperature of 50 K, and an assumed 100 μm optical depth > 1. The inferred disk masses, ranging from 0.01 to 0.1 $M_\odot$, are comparable to the mass thought to characterize protoplanetary systems. Our observations suggest that optically thick dust disks with sizes of approximately 100 AU and with proto–solar system masses surround a number of YSOs of ages up to 3×10^6 yr. If true, estimates of dust settling times in the primitive solar nebula may have to be revised upward by two orders of magnitude.

We wish to acknowledge helpful conversations with L. Hartmann, F. Adams, S. Beckwith, C. Bertout, C. H. Herbig, C. Lada, S. Lizano, J. Raymond, and F. Shu and to extend our thanks to D. Willmarth and C. Pilachowski for their assistance at KPNO and to N. Minutillo and D. M. Chesley for computational assistance in some phases of this work. Two of us, S. E. S. and K. M. S., were supported in this work by grants from NSF and NASA.

REFERENCES

Allen, C. W. 1973, *Astrophysical Quantities* (London: Athlone Press).
Appenzeller, I., Jankovics, I., and Ostreicher, R. 1984, *Astr. Ap.*, **141**, 108 (AJO).
Aumann, H. H., *et al.* 1984, *Ap. J.* (*Letters*), **278**, L23.
Beals, C. S. 1931, *M.N.R.A.S.*, **91**, 966.
Beckwith, S., Sargent, A. I., Scoville, N. Z., Mason, C. R., Zuckerman, B., and Phillip, T. G. 1986, *Ap. J.*, **309**, 755.
Beckwith, S., Zuckerman, B., Skrutskie, M. F., and Dyck, H. M. 1984, *Ap. J.*, **287**, 793.
Bertout, C. 1985, in *Nearby Molecular Clouds*, ed. G. Serra (*Lecture Notes in Physics*), Vol. **237**, p. 161.
———. 1986, in *IAU Symposium 122, Circumstellar Matter*, ed. I. Appenzeller and D. Jordan (Dordrecht: Reidel), in press.
Bieging, J. H., Cohen, M., and Schwartz, P. R. 1984, *Ap. J.*, **282**, 699.
Brugel, E., Böhm, K.-H., and Mannery E. 1981, *Ap. J. Suppl.*, **47**, 117.
Calvet, N., Basri, G., and Kuhi, L. 1984, *Ap. J.*, **227**, 725.
Calvet, N., Cantó, J., and Rodríguez, L. F. 1983, *Ap. J.*, **268**, 739.
Cantó, J. 1981, in *Investigating the Universe*, ed. F. D. Kahn (Dordrecht: Reidel), p. 95.
Cohen, M. 1983, *Ap. J.* (*Letters*), **270**, L69.
Cohen, M., Beiging, J. H., and Schwartz, P. R. 1982, *Ap. J.*, **253**, 707.
Cohen, M., and Kuhi, L. V. 1979, *Ap. J. Suppl.*, **41**, 743 (CK).
Cudworth, K. M., and Herbig, G. H. 1979, *A.J.*, **84**, 548.
DeCampli, W. 1981, *Ap. J.*, **244**, 124.
Dopita, M. 1978, *Ap. J. Suppl.*, **37**, 117.
Dopita, M., Binette, L., and Schwartz, R. D. 1982, *Ap. J.*, **261**, 183.
Edwards, S., and Snell, R. L. 1982, *Ap. J.*, **261**, 151.
Fischer, J., Righini-Cohen, G., and Simon, M. 1980 *Ap. J.* (*Letters*), **238**, L159.
Gillett, F. C. 1985, in *Light in Dark Matter*, ed. F. P. Israel (Dordrecht: Reidel), p. 61.
Grasdalen, G. L., Strom, S. E., Strom, K. M., Capps, R. W., Thompson, D., and Castelaz, M. 1984, *Ap. J.* (*Letters*), **283**, L57.
Hartigan, P., Raymond, J., and Hartmann, L. 1987, *Ap. J.*, in press.
Hartmann, L. W. 1982, *Ap. J. Suppl.*, **48**, 109.
Hartmann, L. W., Edwards, S., and Avrett, E. H. 1982, *Ap. J.*, **261**, 279.
Hartmann, L. W., Hewitt, R., Stahler, S., and Mathieu, R. D. 1986, *Ap. J.*, **309**, 275.
Hartmann, L. W., and Raymond, J. 1984, *Ap. J.*, **276**, 560.
Herbig, G. H. 1962, *Adv. Astr. Ap.*, **1**, 47.
———. 1977, *Ap. J.*, **214**, 747.
Herbst, W. 1986, *Pub. A.S.P.*, **98**, 1088.
Hildebrand, R. H. 1983, *Quart. J.R.A.S.*, **24**, 267.
Jankovics, I., Appenzeller, I., and Krautter, J. 1983, *Pub. A.S.P.*, **95**, 883.
Jones, B. F., and Herbig, G. H. 1982, *A.J.*, **87**, 1223 (JH).
Krautter, J., and Bastien, U. 1980, *Astr. Ap.*, **86**, L6.
Kuan, P. 1975, *Ap. J.*, **202**, 425.
Kuhi, L. V. 1964, *Ap. J.*, **140**, 409.
Lada, C. 1985, *Ann. Rev. Astr. Ap.*, **23**, 267.
Levreault, R. 1985, Ph.D. thesis, University of Texas, Austin.
Mendoza, C., and Zeipen, C. J. 1982, *M.N.R.A.S.*, **198**, 127.
Mundt, R. 1984, *Ap. J.*, **280**, 749.
Mundt, R., and Fried, J. W. 1983, *Ap. J.* (*Letters*), **274**, L83.
Norman, C., and Silk, J. 1980, *Ap. J.*, **238**, 158.
Pottasch, S. 1984, *Planetary Nebulae: A Study in the Late Stages of Stellar Evolution* (Dordrecht: Reidel), p. 51.
Pradhan, A. M. 1978, *M.N.R.A.S.*, **184**, 89P.
Raga, A. C., and Böhm, K. H. 1986, *Ap. J.*, **368**, 829.
Rydgren, A. E., Schmelz, J. T., Zak, D. S., and Vrba, F. J. 1984, *Pub. US Naval Obs.*, **25**, Part I.

Sargent, A., and Beckwith, S. 1987, preprint.
Schneeberger, T. J., Worden, S. P., and Wilkerson, M. S. 1979, *Ap. J. Suppl.*, **41**, 369.
Schwartz, R. C. 1983, *Ann. Rev. Astr. Ap.*, **21**, 209.
Shu, F., Adams, F., and Lizano, S. 1987, *Ap. J.*, in press.
Shull, J. M., and Beckwith, S. 1982, *Ann. Rev. Astr. Ap.*, **20**, 163.
Snell, R. L., Bally, J., Strom, S. E., and Strom, K. M. 1985, *Ap. J.*, **290**, 587.
Strom, K. M., Strom, S. E., Wolff, S. C., Morgan, J., and Wenz, M. 1986, *Ap. J. Suppl.*, **62**, 39.
Ulrich, R., and Knapp, G. R. 1985, preprint.
Weiderschilling, S. 1984, *Icarus*, **60**, 553.

Note added in proof.—A recent study by P. Myers, M. Heyer, R. Snell, and P. Goldsmith (1987, *Ap. J.*, submitted) finds mass-loss rates of $\lesssim 10^{-8}\ M_\odot\ \mathrm{yr}^{-1}$ for a number of low-luminosity embedded YSOs near dense cloud cores. This finding suggests that the winds driving molecular outflows may have $\dot{m}$'s comparable to those of TTS, in contrast to what was stated in the text.

EDWIN R. ANDERSON: KPNO, P.O. Box 26732, Tucson, AZ 85726-6732

SYLVIE CABRIT, K. M. STROM, and S. E. STROM: Five College Astronomy Department, University of Massachusetts, Amherst, MA 01003

SUZAN EDWARDS: Five College Astronomy Department, Smith College, Northampton, MA 01063

INGEBORG HEYER: Institute for Astronomy, 2680 Woodlawn Drive, Honolulu, HI 96822

ANNEXE 8

Forbidden Line Emission and IR Excesses in T Tauri stars: Evidence for Accretion-driven Mass Loss ?

Sylvie Cabrit[1,2], Suzan Edwards[3], Stephen E. Strom[1], Karen M. Strom[1]

[1] *Five College Astronomy Departement,*
University of Massachusetts, Amherst

[2] *Institut d'Astrophysique, Paris*

[3] *Five College Astronomy Departement,*
Smith College, Northampton

to be submitted to *Astronomical Journal*

Preliminary draft

ABSTRACT

We present a statistical study of the [OI], [SII], and [NII] forbidden line emission in T Tauri stars, based on moderate resolution ($\Delta\lambda \sim 1.8$ Å) red spectra (6240 Å to 6760 Å) of 36 objects in Taurus-Auriga with a wide range of Hα emission levels, photospheric luminosities, and IR excesses. We summarize the forbidden line properties of T Tauri stars in terms of line ratios, line fluxes, and centroid velocities, and discuss the processes of line emission compatible with the observations (ionized winds, oblique wind/disk interactions, unresolved jets, or HH objects). We then study the relationship of the forbidden line emission to the properties of the stellar system. The [OI]λ6300 and Hα line fluxes in T Tauri stars are found to be very well correlated with the IR luminosity excess of the object, calculated by subtracting the stellar photospheric contribution from the total spectral energy distribution longward of 0.64 μm. However, no correlation is seen with photospheric luminosity. This result suggests that the forbidden and Hα line strengths are not primarily determined by the internal structure of the star but by the properties of its circumstellar environment. A possible explanation of this result is that the energetic mass-loss in T Tauri stars is powered by accretion of circumstellar disk material onto the stellar surface.

Subject headings: — stars: circumstellar shells — stars: mass loss — stars: pre–main-sequence

I. INTRODUCTION

The presence of energetic stellar winds in T Tauri stars (TTS) has been inferred since the pioneering studies of Herbig (1962) and Kuhi (1964) who noted that blueshifted reversals were commonly found in the strong Hα emission features of TTS spectra. Current estimates of wind mass-loss rates based on analysis of Hα line profiles yield values of 10^{-8} $M_\odot$ yr^{-1} for the most extreme emission TTS (Hartmann, Edwards, and Avrett 1982), implying that the wind kinetic energy can represent up to 1% of the bolometric luminosity (see Edwards and Strom 1988). However, wind mass-loss rates derived from analyses of the Hα line profiles are not accurate, due to the possibly large turbulent contribution to the line broadening (DeCampli 1981, Hartmann 1986), and to uncertainties in the temperature structure of the atmosphere (Crosswell, Hartmann, and Avrett 1987; Natta *et al.* 1988; Alonso-Costa and Kwan 1988).

An alternate approach to studying winds from T Tauri stars is to use the low excitation metallic forbidden lines commonly found in TTS spectra. These optically thin lines offer a direct probe of the geometry, kinematics, and density distribution in the emitting envelope. Low resolution spectra show that 33% of all T Tauri stars possess a [OI]λ6300 line stronger than 0.5 Å (Cohen and Kuhi 1979). Weaker lines of [SII]$\lambda\lambda$6716,6731 and, more rarely, of [NII]$\lambda\lambda$6548,6584 are also observed (Herbig 1962). The line centroid velocity is always blue-shifted with respect to the stellar velocity (Jankovics, Appenzeller, and Krautter 1983), requiring that an *opaque circumstellar disk* be present in order to occult receding material (Appenzeller, Jankovics, and Ostreicher 1984). Optically thick circumstellar disks also seem required to explain the near- and far-infrared excesses of T Tauri stars (*e. g.* Shu, Adams, and Lizano 1987).

Two general classes of models have been proposed to account for the forbidden line emission in T Tauri stars. In the first class of models, the emission arises from the low-density outer parts of an ionized *stellar wind*, at distances $\sim$ 10-100 from the star. Detailed modelling of the forbidden line profiles (Appenzeller, Jankovics, and Ostreicher 1984) shows that spherically symmetric winds cannot reproduce the observed line structure, implying that the winds must be anisotropic. The range of observed forbidden line profile shapes appears best reproduced by a slightly collimated, *latitude-dependent wind* (*i. e.* with a higher velocity and a lower density along the polar axis than toward the equator), seen from different view angles (Edwards *et al.* 1987).

Ionized wind models implicitly assume that high temperatures $\sim 10^4$ K sufficient to collisionally excite the forbidden lines can be maintained at large distances from the star. This assumption was recently challenged by Hartmann and Raymond (1988, hereafter HR), who investigated the temperature structure in an expanding spherical wind with a representative range of wind mass-loss rates and starting temperatures. In all cases, the requisite wind temperatures are obtained only in a high-density region less than a few AU away from the star, and the ratio of [SII]λ6731 to [OI]λ6300 emission is lower than 0.01. This low ratio results from the fact that the critical density of the [SII]λ6731 line ($n_c = 1.3 \times 10^4$ cm^{-3}), at which spontaneous radiative emission and collisional de-excitation of the line are equi-probable, is much lower than that of the [OI]λ6300 line ($n_c = 1.5 \times 10^6$ cm^{-3}), so that dense regions emit preferentially in [OI]λ6300.

To explain the observed strength of the [SII] emission in many T Tauri stars (Edwards *et al.* 1987), a second class of models may need to be invoked, where the forbidden line emission arises not in the wind itself but in *shocks between the wind and circumstellar material.* In this case, however, the forbidden line emission provides only an indirect measure of the wind characteristics. Three kinds of wind/environment interactions might contribute to the forbidden line emission in TTS: (1) low-excitation oblique shocks between the neutral stellar wind and the raised surface of the dense circumstellar disk (HR) ; (2) oblique shocks in unresolved collimated jets, similar to the large-scale optical jets of shock-excited emission that emanate from many embedded outflow sources (Mundt *et al.* 1987); or (3) unresolved Herbig-Haro (HH) objects, which represent a higher excitation manifestation of wind/environment interaction, with shock velocities $\sim$ 200 km s^{-1}. All three options give forbidden line profile shapes that are compatible with high-resolution observations of TTS (HR; Kwan and Tademaru 1988; Hartigan, Raymond, and Hartmann 1987).

It is clearly important to establish which physical process, an ionized wind or a shock (wind/disk interaction, jet, or HH object), is responsible for the forbidden line emission in T Tauri stars, in order to properly interpret forbidden line profiles as probes of TTS winds. Examining the relative and absolute intensities of the forbidden lines in TTS might allow to choose between these options.

Another important issue which we will address here is the respective role of the central star and its circumstellar environment in determining the wind properties: There is

growing evidence that the opaque circumstellar disks inferred from the lack of redshifted forbidden lines (AJO) may represent an active ingredient of the TTS phenomenon, and contribute significantly to the infrared (IR) and ultraviolet (UV) excess of the system through reprocessing of stellar photons and accretion of disk material onto the stellar surface (Adams, Lada, and Shu 1987; Kenyon and Hartmann 1987; Bertout, Basri, Bouvier 1988). Investigating the relation between the forbidden line emission and the photospheric and IR luminosity of the object offers an opportunity to understand the relation between energetic winds, stellar properties, and circumstellar environment in T Tauri stars, and in particular investigate the role of disk accretion in TTS mass-loss.

To address these two issues, we have begun a statistical study of the [OI], [SII], and [NII] forbidden line emission in T Tauri stars, by obtaining moderate resolution ($\Delta\lambda \sim 1.8$ Å) red spectra (6240 Å to 6760 Å) providing higher sensitivity (~ 0.04 Å) and precision in line velocity measurements ($\pm$ 9 km s^{-1}) than the Cohen and Kuhi (1979) database. Follow-up work on selected objects at Echelle resolution is in progress. This contribution presents our results for 36 objects in Taurus-Auriga.

Section II describes our sample, observations, data reduction procedures, and methods for estimating line fluxes and photospheric and IR excess luminosities in our program stars. Sample spectra are shown for stars with differing emission properties. In Section III, we summarize the statistical properties of the forbidden line emission in our sample in terms of relative intensities, line fluxes, and radial velocities. We show that stars with [OI]λ6300 fluxes larger than 10^{-13} erg s^{-1} cm^{-2} tend to have lower [OI]λ6300 centroid velocities and a wider range of [SII]/[OI] ratios than stars with higher forbidden line fluxes. We compare these properties with the results expected for the various processes of forbidden line emission considered above, and discuss the possible origin of the forbidden line emission in TTS.

Section IV investigates the relationship of the Hα and forbidden line emission to other properties of the star/disk system, namely the photospheric luminosity, L_*, and the IR luminosity excess longward of 0.64 μm, L_{IR}, both derived from careful analysis of the observed spectral energy distribution. We find that there exists a very good correlation between the IR luminosity excess and the forbidden lines and Hα fluxes for the TTS stars in our sample, but that there is no dependence of these fluxes on the stellar photospheric luminosity L_*. Since L_* is expected to decline as a function of the stellar age for stars

of a given spectral type, our results suggest that the strength of the Hα and forbidden line emission in a T Tauri star is not determined by the star's internal structure, but by the properties of its *circumstellar environment.* We discuss possible interpretations of this result, in particular the possibility that mass ejection in T Tauri stars is ultimately powered by accretion of disk material onto the star. Section V summarizes our results and suggests future work.

II. DATABASE

a) Sample

Our sample consists of 36 T Tauri stars located in the Taurus-Auriga complex from the catalog of Herbig and Bell (1988), with a range of Hα equivalent widths (from 1.6 Å to 138 Å) representative of this stellar population. In particular, we included eleven objects with reported Hα equivalent widths of less than 5 Å. The spectral types range from G2 to M2, with the large majority between K7 and M0. Four objects (DG Tau, DL Tau, DR Tau, and HL Tau) belong to the class of "continuum + emission" (cont/e) stars, *i. e.* they exhibit an extreme emission spectrum with no apparent photospheric absorption features at moderate resolution, and therefore are of uncertain spectral type (although reliable spectral types for these objects are now becoming available with the advent of high dispersion spectra; Appenzeller [1988]).

For each of the T Tauri stars in this sample, we have made use of published optical, near- and far-infrared photometry (Rydgren *et al.* 1984, Herbig, Vrba, and Rydgren 1986, co-added IRAS database) to determine the spectral energy distribution of the object, and estimate the photospheric contribution L_* to the total luminosity L_{tot}, and the IR excess $L_{IR} = (L_{tot} - L_*)_{IR}$ longward of 0.64 μm (see Section II d). Our estimated photospheric luminosities range from 0.23 $L_\odot$ to 11 $L_\odot$, while our inferred IR excesses range from 0.13 $L_\odot$ to 19 $L_\odot$ (see Table 3).

Our sample thus covers the full range of Hα emission levels, photospheric luminosities, and IR excesses characteristic of the TTS class, which allows us to conduct a statistically significant study of the properties of the forbidden line emission in T Tauri stars and investigate its dependence on the various characteristics of the object.

b) Data Acquisition and Reduction

Our data were obtained in November 1987 with the Cassegrain spectrograph and CCD combination ("Goldcam") mounted on the KPNO 2.1 meter telescope. We used the 1200 line/mm grating (number 36) and an entrance slit width of 200 microns (2.4 arc seconds) to obtain spectra with a dispersion of 0.66 Å/pixel and a wavelength range of 520 Å centered at 6500 Å; the FWHM instrumental resolution is 1.8 Å. For each star, we extracted the stellar spectrum and that of the adjacent night sky. The resulting sky-subtracted intensity/pixel number arrays were transformed to intensity/wavelength vectors by using a dispersion solution established from a He-Ne-Ar source.

From comparison with a grid of dwarf and giant standard stars covering the spectral type range M3 to G0, we classified each of our T Tauri stars for spectral type and compared our results to those of Cohen and Kuhi (1979). Our estimated spectral types do not differ from their values by more than one subclass, with one exception (RY Tau), classified as a K1 by Cohen and Kuhi (1979) and as a G2 by us. 1

Figure 1*a-d* shows examples of spectra for four objects illustrating the range of forbidden line emission strength in TTS. FK Xray2 (Fig. 1*a*) has no apparent forbidden line emission; AA Tau (Fig. 1*b*) has moderate [OI]λ6300 emission, but no other detectable forbidden lines; DK Tau (Fig. 1*c*) has both [OI]λλ6300,6364 and [SII]λλ6716,6731 emission; finally, DG Tau (Fig. 1*d*) has prominent forbidden lines of [OI]λλ6300,6364, [SII]λλ6716,6731, and [NII]λλ6548,6584, together with the strong permitted metallic emission lines characteristic of a cont/e star. The correlation between Hα and forbidden line strength (Cohen and Kuhi 1979) is clearly apparent in this figure.

For each object in our sample, equivalent widths of the forbidden lines, Hα , Ca I λ6450, and LiI λ6707 were measured above a local continuum derived from superposition of the stellar spectrum with that of a relevant dwarf standard, more appropriate than a giant in this wavelength range. This procedure was especially useful around 6300 Å, where late K and M dwarfs show a narrow bump in the continuum which could be mistaken for weak [OI]λ6300 emission in our program stars. Only emission above that level was taken into

1 Holtzmann, Herbst, and Booth (1986) also find a spectral type of G1 to G3 for RY Tau, based on spectra obtained in 1984 and 1985. The photometric data summarized by Herbst (1986) show that RY Tau suddenly increased its brightness in 1984, and is now brighter than in 1979 by about 1 mag at V, consistent with an apparent spectral type change.

account. However, we did not attempt to correct for underlying photospheric absorption at Hα . These corrections are relatively small, $\sim$ 0.7 Å at M0 and 2.7 Å at G5 (Herbig, Vrba, and Rydgren 1986). Col (2) to (7) of Table 1 list our observed equivalent widths of [OI] λ6300, [SII] λ6731, [SII] λ6716, [NII] λ6584, Hα , and Li I λ6707 for the 36 program stars, and col (8) to (10) the observed equivalent width ratios of [SII]λ6716 to [SII]λ6731, [SII]λ6731 to [OI]λ6300, and [NII]λ6584 to [OI]λ6300. Although our typical sensitivity limit (*e. g.* for the [SII] lines) is $\sim$ 0.04 Å, we did not feel confident in confirming any [OI]λ6300 line with EW([OI]) $<$ 0.1 Å, because of the larger uncertainty in the continuum level at that wavelength. The final uncertainties in our measured equivalent widths result mostly from errors on the placement of the continuum level, and are of the order of 20 % for lines stronger than 1 Å and 40% for lines below that level.

c) Extinction corrections and line emission fluxes

While equivalent widths only give a relative measure of the line strength, the total energy flux emitted in the line is an absolute quantity that can be directly compared with observed or predicted fluxes for various processes of line emission. Observed fluxes for Hα and the forbidden lines were calculated for our program stars by adopting a set of published R_c (0.64 μm) magnitudes, summarized in Strom *et al.* (1988). We assumed that the stellar continuum at R_c was similar to its value at the time the photometry was obtained. Since variations at R_c in T Tauri stars are typically $\leq$ 0.5 mag over a few years (Rydgren *et al.* 1984), the uncertainty introduced in our fluxes is probably $\leq$ 0.2 dex (although it could be larger for the cont/e stars, which tend to be more variable).

Our observed line fluxes were then corrected for extinction. We independently estimated A_V values for the stars in our sample and compared our results to those of Cohen and Kuhi (1979) and Herbig, Vrba, and Rydgren (1986). Three estimates of the reddening correction were obtained for each star by fitting the observed $(V - R_c)$, $(R_c - I_c)$, and $(V - I_c)$, to the colors of a main-sequence star of the same spectral type (Bessell 1979). A standard extinction law (Van de Hulst 15; Johnson 1968) was adopted to convert the color corrections into A_V values. The 3 values of A_V were then averaged, and their range (typically $\pm$ 0.2 mag) taken as a measure of the uncertainty in the estimate. Changing the spectral type by half a subclass was found to result in a 0.3 mag difference in A_V.

In all but one case, our A_V value agreed with the reddening correction given by Cohen and Kuhi (1979) and Herbig *et al.* (1986) to within 0.5 mag, and the previously published

value was adopted. Only in the case of DF Tau do we find an A_V very different from the value given by Cohen and Kuhi (0.75 $\pm$ 0.2 here instead of 1.90 $\pm$ 0.6), although we both assume a spectral type of M0.5. Since our value gives a more satisfactory fit to the photometric data that we use, it is adopted hereafter.

For the cont/e stars, we estimated two extreme limits for the extinction correction. A lower limit was obtained using the method described above, assuming a spectral type of K7-M0 for DG Tau, HL Tau, and DL Tau, and of K5 for DR Tau. Since these are the latest types consistent with the strength of the weak absorption lines in high resolution red spectra of these stars (C. Bertout, private communication; Appenzeller 1988), and since the observed V and R_c fluxes are contaminated by the overlying blue continuum emission responsible for their extreme veiling, this approach should underestimate the A_V. A second estimate was obtained by Wenz and Strom (1986, unpublished), by assuming that one is seeing an M0 photosphere at J and H. These latter values (DG Tau: 4.00; HL Tau: 6.40; DL Tau: 2.20; DR Tau: 3.30) are likely to be upper limits to the A_V because the warm circumstellar disk contributes significantly at near-infrared wavelengths in stars with extreme IR excesses (Bertout, Basri, and Bouvier 1988).

Col. (2) to (7) of Table 2 list the R_c magnitudes and A_V values that we adopted for our program stars, and the decimal logarithms of the reddening-corrected fluxes in the forbidden lines and Hα . We estimate the typical uncertainty in A_V to be $\sim$ 0.3 mag, which translates into an additional uncertainty in the fluxes of typically 0.1 dex. For the cont/e stars, only our lower limits to the A_V and the fluxes are given in Table 2(upper limits to the fluxes are obtained using $\log F_{max} = \log F_{min} + 0.33 \times [A_V\,(\max) - A_V\,(\min)]$.).

d) Photospheric luminosities and infrared excesses

We have estimated de-reddened total luminosities L_{tot}, photospheric luminosities L_*, and IR luminosity excesses L_{IR} for all our program stars. These values are listed in col. (4) to (6) of Table 3, while col. (2) and (3) list our adopted spectral types and A_V values (taken from Cohen and Kuhi (1979) or Herbig, Vrba, and Rydgren (1986), except otherwise noted in Table 3).

The procedure used to obtain L_{tot}, L_*, and L_{IR} is qualitatively similar to the method outlined in Strom *et al.* (1988). The total de-reddened luminosity L_{tot} of the object is calculated using published photometric data from 0.33 to 20 μm and IRAS coadded data at

12, 25, 60, and 100 μm (our database is summarized in Strom *et al.* 1988). The photospheric luminosity of the star L_* is estimated by fitting the spectral energy distribution of a standard main-sequence star of the same spectral type (Johnson 1966) to the de-reddened stellar R_c (0.64 μm) magnitude. This filter was selected because it minimizes possible contamination from an accretion disk boundary-layer, which may contribute significantly to the observed flux in the UV and visible range (Bertout, Basri, and Bouvier 1988), and because it is less contaminated than near-infrared measurements by thermal emission from warm circumstellar dust. L_{tot} and L_* are calculated by trapezoidal integration, assuming isotropic emission and a distance of 160 pc to Taurus-Auriga. Both the observed and the standard spectra are extrapolated to infinite wavelengths assuming a Rayleigh-Jeans law $F_\lambda \propto \lambda^{-4}$. The IR luminosity excess L_{IR} is then computed by subtracting the contribution of the standard from the de-reddened spectral energy distribution of the star longward of 0.64 μm.

Uncertainties in the adopted spectral types and A_V values result in typical uncertainties of $\pm$ 0.2 dex and $\pm$ 0.1 dex in our estimated photospheric luminosities and IR excesses. We point out that our procedure underestimates L_{IR} if the slope in the far-infrared is flatter than that of a blackbody, or if the star is heavily veiled at R (in which case we also overestimate L_*). Therefore, our values of L_{IR} should be considered as lower limits, and our values of L_* as upper limits to the true values. For stars with moderate or negligible veiling, our values of L_* are in good agreement with those of Basri and Bertout (1988), obtained by fitting a detailed accretion disk model to the observed spectral energy distribution and Balmer jump. Our values of L_{IR} and L_* for the cont/e stars are more uncertain, since the extinction toward these objects and the contribution of the boundary-layer to their observed R_c flux are poorly known. However, these two effects go in opposite direction, and our values of L_{IR} and L_* in Table 3 for the cont/e stars, calculated using the lower limits to the A_V (see Sec. II c) and assuming no veiling, probably do not differ from the true values by more than $\pm$ 0.2 dex and $\pm$ 0.5 dex respectively.

III. PROPERTIES OF THE FORBIDDEN LINE EMISSION IN T TAURI STARS

a) Observational results

i) Statistics

An [OI]λ6300 line with EW $>$ 0.1 Å is found in 23 of the 36 stars in our sample, which represents a detection rate of 64%. This is consistent with the rate of 41% found by Cohen and Kuhi (1979) for Taurus-Auriga because 12 of our stars show [OI]λ6300 emission below the sensitivity limit of their survey (0.5 Å). Most of the stars with a detectable [OI]λ6300 line are "classical" T Tauri stars with a measured Hα equivalent width larger than 5 Å, but two (HD 283447 and FK Xray 3) have a measured Hα equivalent width smaller than 5 Å.

Our [OI]λ6300 equivalent widths range from 0.1 Å to 18.5 Å, and in general do not differ from the values quoted in Cohen and Kuhi (1979) and Edwards *et al.* (1987) by more than $\sim$ 30% if EW([OI]) $>$ 1 Å and more than 50% otherwise, suggesting that the properties of the [OI] emitting region do not change appreciably over times scales of a few years. Two possible exceptions are DH Tau and DK Tau, for which Cohen and Kuhi report [OI]λ6300 equivalent widths of $<$ 0.5 Å and 0.5 Å respectively, whereas we find 0.9 Å and 1.3 Å.

Among the 23 stars showing detectable [OI]λ6300 emission, 10 stars (*i. e.* 28% of our sample) possess a [SII]λ6731 line with EW $>$ 0.06 Å, and 6 also have a detectable [SII]λ6716 line. The [NII]$\lambda\lambda$6548,6584 lines are detected only in 3 stars (*i. e.* 8 % of our sample), namely DG Tau, HL Tau, and T Tau. These 3 objects have the largest three [SII]λ6731 equivalent widths in our sample, and are also the only ones in our sample to be associated with detectable radio continuum emission (Cohen and Bieging 1986; Brown, Drake, and Mundt 1986), and with known optical jets or HH objects (Mundt 1985; Cohen and Fuller 1985; Bührke, Brugel, and Mundt 1986). [NII] emission thus appears stronger in T Tauri stars with large-scale outflow manifestations.

ii) Density of the [SII] emitting region

The intensity ratio in the [SII]$\lambda\lambda$6716,6731 doublet (see col. (8) of Table 1) can be used to estimate the density of the [SII] emitting region (*e. g.* Czyzak 1986). Four out of the six objects with detectable [SII]λ6716 are either heavily veiled or cont/e stars, in which contamination of the [SII]λ6716 line by nearby CaI λ6717 photospheric absorption is negligible. Their mean [SII] 6716/6731 ratio is 0.50 $\pm$ 0.07, and indicates high electron densities $n_e \sim 10^4$ cm^{-3} close to the critical density of the [SII] lines; a similar result was found by Edwards *et al.* (1987) for a restricted sample of TTS with strong forbidden line emission.

The other two stars where [SII]λ6716 was detected, T Tau and DK Tau, have a [SII] 6716/6731 ratio of 0.29, below the theoretical high-density limit of 0.44. Therefore, it appears that the presence of nearby CaI λ6717 photospheric absorption can significantly reduce the observable [SII]λ6716 emission in unveiled stars. Upper limits on the [SII] 6716/6731 ratio in the remaining four stars with detectable [SII]λ6731 emission are consistent with this effect.

iii) Relationship between the [OI] and [SII] emission in T Tauri stars

Fig. 2 plots the equivalent width of the [OI]λ6300 line versus that of the [SII]λ6731 line for the 23 stars showing detectable [OI]λ6300 emission. The solid squares represent the 10 stars with detectable [SII]λ6731, while the open squares represent the 13 stars with only upper limits to the [SII]λ6731 EW.

In the 10 stars where both lines are detected, the EWs of the two lines clearly appear correlated over 2 orders of magnitude, with a mean [SII]λ6731 to [OI]λ6300 ratio of 0.3, consistent with the value found by Edwards *et al.* (1987) for a restricted sample of TTS with strong forbidden lines. The corresponding mean relationship is plotted as a dashed line in Fig. 2.

However, among the 13 stars without detectable [SII]λ6731, several appear to be incompatible with a [SII]/[OI] ratio of 0.3. Three particularly striking examples are DF Tau, DH Tau and DR Tau, which have significant [OI]λ6300 EWs of 1.4 Å, 0.9 Å, and 0.8 Å, but [SII]/[OI] upper limits of 0.03, 0.04, and 0.07 respectively.

To investigate the *absolute* properties of these low [SII]/[OI] ratio objects, we plot in Fig. 3 the relationship between the [OI] λ6300 and [SII] λ6731 emission in terms of *line fluxes* (see col. (4) and (5) of Table 2), using the same symbols as in Fig. 2. It appears that those stars with unusually low [SII]/[OI] ratios (DF Tau, DH Tau, DR Tau) all have fairly low luminosities in their [OI] line, with an [OI]λ6300 flux lower than $\sim 10^{-13}$ erg s^{-1} cm^{-2}. In contrast, those TTS characterized by a roughly uniform ratio of [SII] to [OI] emission $\sim$ 0.3 have [OI]λ6300 fluxes ranging up to 10^{-11} erg s^{-1} cm^{-2}.

Therefore, T Tauri stars appear to show a larger spread in [SII]λ6731/[OI]λ6300 ratio as their [OI]λ6300 flux decreases, suggesting a wider range of physical conditions in their forbidden line emission regions.

iv) [OI] Centroid Velocities

Col. (8) and (9) of Table 3 list the intensity-weighted velocity centroids of the [OI]λ6300 and Hα lines for the stars in our sample. The line velocities were calculated with respect to the heliocentric stellar velocity, estimated from the average of the LiI λ6707 and CaI λ6450 absorption line velocities and listed in col. (10). We estimate the internal precision of our measurements to be $\sim \pm$ 9 km/s, *i. e.* roughly 10% of our effective resolution.

The [OI]λ6300 centroid velocity appears clearly blueshifted in all but two of the 23 stars where it has been measured, and has radial velocities ranging from + 6 $\pm$ 9 km s^{-1} to -170 $\pm$ 9 km s^{-1}. We find that the four cont/e stars in our sample (HL Tau, DG Tau, DR Tau, and DL Tau), together with the heavily veiled star DO Tau, show the five highest [OI] velocities in our sample (-170, -120, -90, -70, and -75 km s^{-1}). Either this reflects an intrinsically higher wind speed in heavily veiled stars, or it may indicate that we are seeing those stars more pole-on since both the apparent wind speed and the veiling due to accretion from a disk may increase at small view angles (Edwards *et al.* 1987; Bertout, Basri, and Bouvier 1988).

There is a tendency for those TTS with the highest forbidden line luminosities to have larger [OI] radial velocities in comparison to those stars with lower [OI] luminosities. This can be seen in Fig. 4 which compares the distribution of the [OI]λ6300 centroid velocities in T Tauri stars with an [OI]λ6300 flux lower (top panel) or higher (bottom panel) than 10^{-13} erg s^{-1} cm^{-2} . For the purpose of this plot, cont/e stars were assigned an [OI]λ6300 flux equal to the geometric mean of the lower and upper limits derived in section II c). Because most stars where [SII]λ6731 emission was not detected have [OI]λ6300 fluxes lower than 10^{-13} erg s^{-1} cm^{-2}, one finds a similar trend by comparing the [OI] velocities of stars with [SII]λ6731 equivalent widths smaller or larger than 0.06 Å. In particular, the mean and maximum [OI] radial velocities are -66 km s^{-1} and -169 km s^{-1} in the former group, and only -23 km s^{-1} and -89 km s^{-1} in the latter (see col. (8) of Table 3). Since the forbidden lines are optically thin and hence have a total flux that is independent of viewing angle, this trend for higher centroid velocities at higher forbidden line fluxes cannot be due to inclination effects and must reflect a higher expansion velocity in the emitting envelope.

Finally, we observe an anticorrelation between the centroid velocities of the [OI]λ6300 and Hα lines, *i. e.* as the [OI] line becomes more blueshifted, the Hα centroid velocity shifts more to the red, up to + 90 km s^{-1} in HL Tau. Thus, a progression in the mean Hα

centroid velocity is seen, from + 18.4 km s^{-1} in the group of stars where both [OI] and [SII] were detected, to + 3 km s^{-1} in the group where only [OI] was detected, and -12.6 km s^{-1} in the group of stars with no detectable forbidden line emission (see col (9) of Table 3). This anticorrelation is consistent with the trend noted by Edwards *et al.* (1987) on high-resolution spectra that there exists a velocity correspondence between the blueshifted forbidden line emission peak and the absorption reversal in the Hα line profile. The most likely explanation is that the Hα reversal is formed in an *extended expanding envelope* that contributes significantly to the blue-shifted [OI] emission (Edwards *et al.* 1987).

b) Possible origin of the forbidden line emission in TTS

Since the [OI], [SII], and [NII] forbidden lines have different critical densities for collisional de-excitation (1.3×10^6, 1.3×10^4, and 6.5×10^4 cm^{-3}respectively), and correspond to species with different ionization potentials, their relative and absolute line intensities are dependent on the physical conditions in the emission region and can be used to put constraints on the origin of the forbidden line emission in TTS. In this section, we compare the relative and absolute forbidden line intensities in TTS with predictions for various processes of forbidden line emission (wind/disk shocks, non-interacting winds, HH objects, and optical jets) in order to determine which ones are compatible with the observations.

The range of [OI]λ6300 and [SII]λ6731 line fluxes expected for each of the above processes is indicated in Fig. 3. Wind/disk shock models investigated by HR are shown as circular symbols, connected by dashed lines. The three models assume the same disk geometry, and use wind velocities and mass-loss rates of respectively 400 km s^{-1} and 2 $\times 10^{-8}$ $M_\odot$ yr^{-1}; 200 km s^{-1} and 10^{-7} $M_\odot$ yr^{-1}; and 400 km s^{-1} and 2 $\times 10^{-7}$ $M_\odot$ yr^{-1}(in order of increasing [OI]λ6300 flux). The range of forbidden line fluxes predicted by HR for non-interacting spherical winds is shown at the bottom of Fig. 3 as a dashed line. The models assume low X-ray ionisation, a fixed wind velocity of 200 km s^{-1}, and a mass-loss rate increasing from 10^{-8} $M_\odot$ yr^{-1} to 10^{-7} $M_\odot$ yr^{-1}. The point corresponding to 10^{-8} $M_\odot$ yr^{-1} falls out of the limits of the diagram, at coordinates [-14.6,-17]. Finally, the range of forbidden line fluxes expected for HH objects (adopting the dereddened surface brightnesses of Dopita [1978] and assuming a 1" aperture) and for optical jets (Cohen and Jones 1987; assuming a distance of 160 pc) is shown as a shaded area.

To compare the *densities* in their [SII] emitting regions, we plot in Fig. 4 the [SII] 6716/6731 ratio versus the [SII]/[OI] ratio for TTS (solid squares and solid triangles) and

for each process of forbidden line emission. The three wind/disk shock models of HR are shown using the same symbols as in Fig. 3. Non-interacting wind models are not shown since they do not yield significant [SII] emission ([SII]/[OI] $\sim$ 0.003). Herbig-Haro objects from the compilation of Von Hippel, Burnel, and Williams (1988) are plotted as open triangles, and individual emission knots in four well studied optical jets (Cohen and Jones 1987) denoted by open circles.

An additional constraint on the forbidden line emission process in TTS comes from the [NII]/[OI] ratio (see col. (10) of Table 1), which is lower than 0.3 in all T Tauri stars (except from HL Tau and T Tau), and lower than 0.08 in all objects with strong [OI]λ6300 emission (EW([OI]) $\geq$ 0.5 Å).

The following sections discuss the success of each process of forbidden line emission at explaining the properties observed in TTS. We first concentrate on the group of TTS with higher [OI] fluxes ($> 10^{-13}$ erg s^{-1} cm^{-2}), where [SII]/[OI] $\sim$ 0.3. We then turn to the group of T Tauri stars with low [OI]λ6300 fluxes ($\leq 10^{-13}$ erg s^{-1} cm^{-2}), where the [SII]/[OI] ratio ranges from $\sim$ 0.3 to less than 0.03.

i) T Tauri stars with high [OI] fluxes

None of the four processes that we consider can by itself explain the emission properties of this class of objects:

Non-interacting ionized winds, as modelled by HR, cannot reproduce the [SII]/[OI] ratios $\sim$ 0.3 observed in these stars, because the forbidden lines are excited in the dense inner regions of the wind, where the [SII] lines are suppressed relative to [OI] (yielding [SII]/[OI] $\sim$ 0.003). Although the actual temperature structure in the wind might differ from that found by HR in spherical symmetry, it appears unlikely that the [SII] emission in TTS is formed in an ionized non-interacting stellar wind, because the mass-loss rates $\geq 2 \times 10^{-8}$ M$_\odot$ yr^{-1} and envelope sizes $\sim 10 - 100$ AU suggested these high [SII] fluxes (Edwards *et al.* 1987) would predict a level of free-free continuum emission of more than 0.3 mJy at 5GHz (assuming a wind temperature $\sim 10^4$ K and a constant velocity of 200 km s^{-1}) inconsistent with current upper limits for these objects (Bieging, Cohen, and Schwartz 1984).

The wind/disk shock interaction investigated by HR also has difficulties in producing [OI] fluxes $> 10^{-13}$ erg s^{-1} cm^{-2} while keeping [SII]/[OI] $\sim$ 0.3: The three models plotted

in Fig. 3 and 4 show that increasing the wind density at constant wind velocity, or increasing the wind velocity at constant wind density, increases the [OI]λ6300 flux but also *decreases* the [SII]/[OI] ratio, and actually reduces the total [SII] flux in the latter case. To obtain an [OI]λ6300 flux $> 10^{-13}$ erg s^{-1} cm^{-2} and keep [SII]/[OI] $\sim$ 0.3, one would have to increase the wind density and simultaneously decrease the wind velocity; however, this is not compatible with the fact that TTS with [OI] fluxes $> 10^{-13}$ erg s^{-1} cm^{-2} have larger [OI] centroid velocities than TTS with lower [OI] fluxes (see Sec. III c)).

HR have suggested that wind/disk surface instabilities could significantly increase the forbidden line emission efficiency (hence the fluxes) over that predicted by their models, because the wind would be shocked several times and the shocks would be less oblique than in the case of a smooth interaction surface. Detailed hydrodynamic modelling of the wind/disk interaction is required to see whether the efficiency of the wind/disk shock mechanism can be sufficiently increased to actually reproduce the observed fluxes without yielding too high a [SII]/[OI] ratio.

Bright HH objects and jets can produce the [SII]λ6731 fluxes $> 10^{-14}$ erg s^{-1} cm^{-2} observed in this group of stars (see Fig. 3). And although they show on average a higher [SII] 6716/6731 ratio than TTS, indicating a lower density in their [SII] emitting regions (see Fig. 4, and Edwards *et al.* 1987), a significant number of them have [SII] 6716/6731 ratios $\sim$ 0.5-0.6 comparable to the values found in our sample. However, their [SII]/[OI] ratios ($\sim 0.6 - 1.2$) and their [NII]/[OI] ratios ($\sim$ 1.1 in dense HH objects and $\sim$ 0.2-0.6 in jets; Dopita 1978; Cohen and Jones 1987), are two to three times higher than their values in TTS, implying that dense jets or HH objects cannot alone account for the observed forbidden line emission.

A possible explanation for the forbidden line emission in TTS with high [OI]λ6300 fluxes is that, in addition to a dense jet or HH object emitting in [OI], [SII], and [NII], TTS envelopes have an additional component emitting mainly in [OI] (*e. g.* a non-interacting wind with mass-loss rate $\sim 10^{-7} - 10^{-6}$ M$_\odot$ yr^{-1}, or a slow wind from the disk as suggested by Kwan and Tademaru 1988) which reduces the total [SII]/[OI] and [NII]/[OI] ratios. For example, a typical dense jet with [SII] 6716/6731 $\sim$ 0.5, [SII]/[OI] $\sim$ 1.1, [NII]/[OI] $\sim$ 0.2, combined with a non-interacting wind contributing three times as much to the total [OI] flux, would yield line ratios ([SII] 6716/6731 $\sim$ 0.5, [SII]/[OI] $\sim$ 0.3, [NII]/[OI] $\sim$ 0.05) consistent with the values found in typical T Tauri stars. Similarly, the higher [SII]/[OI]

and [NII]/[OI] ratios ($\sim$ 0.4-0.5) observed in HL Tau and T Tau could be explained by a dense HH object with [SII]/[OI] and [NII]/[OI] $\sim$ 1.2, combined with a non-interacting wind contributing twice as much to the total [OI] flux.

Some indication that high forbidden line luminosity T Tauri stars might indeed have a contribution from a jet or HH object-like shock is the fact that the 3 stars in our sample with detectable [NII] emission, namely DG Tau, HL Tau, and T Tau, are also the 3 stars with the strongest [SII]λ6731 EWs, and that stars with higher [SII]λ6731 fluxes tend to fall closer to the locus of HH objects and jets in Fig. 3.

ii) T Tauri stars with low [OI] fluxes

The [OI]λ6300 fluxes of this group of stars appear well reproduced by either wind/disk shock or non-interacting wind models with $\dot{M}_* \sim 2 \times 10^{-8} - 10^{-7}$ $M_\odot$ yr^{-1}and $V_w \sim 200 - 400$ km s^{-1}. Both classes of models predict low [NII]/[OI] ratios consistent with the upper limits that we find for T Tauri stars, because wind/disk interactions involve low-velocity oblique shocks (with [NII]/[OI] $\sim$ 0.01-0.15), while non-interacting winds excite the forbidden lines in a very dense region close to the star, where the [NII] lines are collisionally quenched. However, only the wind/disk shock models appear able to explain the entire range of [SII]λ6731 fluxes and [SII] 6716/6731 ratios observed in this group of TTS. Non-interacting wind models produce very weak [SII]λ6731 emission, with [SII]/[OI] $\sim$ 0.003, and cannot explain the 3 stars in this group with a detectable [SII]λ6731 line, where [SII]/[OI] $\sim$ 0.3.

Finally, the model invoked earlier for stars with high forbidden line fluxes and low [NII]/[OI] ratio, in which the [SII] lines come from an ionised jet while most of the [OI]λ6300 line comes from a denser region, can also apply in these objects, and could reproduce all aspects (line ratios and fluxes) of the observations.

In summary, the strong [SII] (and sometimes [NII]) lines observed in TTS with [OI]λ6300 fluxes greater than 10^{-13} erg s^{-1} cm^{-2} can be explained by moderate or strong shocks in bright jets or HH objects, or possibly by multiple shocks at the wind/disk interface, whereas the weaker [SII] emission found in the other objects could be produced either by less bright jets or HH objects or by more oblique shocks between the wind and a flared circumstellar disk. The observed [SII]/[OI] and [NII]/[OI] line ratios in TTS can be reproduced if most of the [OI]λ6300 emission comes from a dense region (*e. g.* the inner

parts of the stellar wind) or from oblique shocks between the wind and the circumstellar environment.

Higher resolution spectra might allow to choose between these possibilities, since wind/disk shock models predict similar profile shapes in [OI] and [SII] with a single or doubled-peaked structure depending on the inclination angle (HR), while hybrid models with a dense wind and jet(s) or HH object(s) predict several velocity components with differing [SII]/[OI] and [NII]/[OI] ratios.

Two cont/e stars for which high-resolution spectra have become available do show clear evidence for non-uniform forbidden line ratios as a function of velocity, suggestive of a hybrid emission region: In DR Tau, the [OI]λ6300 line profile shows two well-separated peaks, the stronger one centered on the stellar velocity, and the weaker one blue-shifted by $\sim$ 110 km s^{-1}(Edwards *et al.* 1987), but [SII]λ6731 emission is detected only at the velocity of the weaker [OI]λ6300 peak (Appenzeller 1988). In HL Tau, the [OI] and [SII] lines have a similar double-peaked structure, with a blue-to-zero velocity intensity ratio $\sim$ 2-3, but the intensity ratio is clearly higher in the [NII] lines, where the blue-shifted component is much stronger (Edwards *et al.* 1987). A similar study of other T Tauri stars is under way, based on new high-resolution forbidden line spectra.

IV. RELATIONSHIP BETWEEN FORBIDDEN LINE EMISSION AND IR LUMINOSITY EXCESS IN T TAURI STARS

a) Motivation

While observations of blue-shifted forbidden lines have provided additional evidence for the presence of energetic winds in T Tauri stars with $\dot{M}_w > 10^{-9}$ M$_\odot$ yr^{-1}, the nature of the wind driving mechanism remains an issue. Outward propagation of Alfvén waves in the envelope appears the most efficient driving mechanism for low-mass stars (De Campli 1981; Hartmann, Edwards, and Avrett 1982). Mass-loss rates of $\dot{M}_w = 10^{-8}$ M$_\odot$ yr^{-1} can be obtained if 10% of the stellar bolometric luminosity is in the form of Alfvén waves. But the [OI]λ6300 fluxes observed in T Tauri stars suggest even higher values of $\dot{M}_w \sim 10^{-8} - 10^{-6}$ (see Section 3), which seem to require an unreasonable amount of stellar magnetic energy.

An additional problem is the range of wind strengths observed in T Tauri stars, as indicated by their Hα and [OI]λ6300 emission : "weak-emission" T Tauri stars (WTTS,

with $W_\lambda < 5$ Å) have [OI]λ6300 fluxes of less than 10^{-14} erg s^{-1} cm^{-2}, while "classical" T Tauri stars (CTTS, with $W_\lambda > 5$ Å) have [OI]λ6300 fluxes ranging up to 10^{-12} erg s^{-1} cm^{-2}. These differing emission properties do not seem to be due to intrinsic differences in the stellar characteristics: WTTS and CTTS have apparently the same levels of magnetic activity, as indicated by their rotational velocities and X-ray fluxes, and the same internal structure, as indicated by their location in the H-R diagram (Walter *et al.* 1988). It seems that another parameter is governing the wind properties in T Tauri stars.

The only other property distinguishing CTTS from WTTS appears to be the presence of large infrared and ultraviolet excesses, and of a decreased contrast in their photospheric absorption lines ("optical veiling") with respect to standard stars of the same spectral types. These characteristics cannot be understood in terms of a classical stellar-powered chromosphere (Basri and Bertout 1988), and appear best explained in terms of a dusty circumstellar disk accreting onto the central star (Adams, Lada, and Shu 1987; Kenyon and Hartmann 1987; Bertout, Basri, and Bouvier 1988). In this picture, the IR excess arises from warm circumstellar dust heated by viscous dissipation of orbital energy in the disk and by absorption of stellar photons, while the UV excess and optical veiling is due to continuum emission from the hot ($T_{BL} \sim 8000$ K) boundary-layer where keplerian disk material falls onto the slowly rotating stellar surface. The absence of red-shifted forbidden line emission in CTTS is independent evidence for the presence of optically thick circumstellar disks around these stars.

The fact that WTTS do not show the strong IR and UV excesses characteristic of CTTS suggests that they lack optically thick accretion disks, and that the presence of strong Hα and forbidden line emission in T Tauri stars is linked with the presence of such disks. A possible explanation is that the mass ejection in T Tauri stars is in fact powered by accretion of circumstellar material onto the stellar surface (see also Edwards and Strom 1987).

If this is actually the case, then the wind mechanical luminosity should be correlated with the accretion luminosity in TTS, and be independent of the stellar luminosity. The [OI] luminosity is expected to increase with wind mechanical luminosity regardless of the forbidden line emission process, provided that the wind velocity and the geometry and efficiency of the wind/environment interaction are the same in all TTS. On the other hand, the IR excess is expected to increase with accretion luminosity, due to increased

viscous heating of the disk (Lynden-Bell and Pringle 1974; Bertout, Basri, and Bouvier 1988). One would therefore expect to find a correlation between [OI] flux and IR excess in T Tauri stars.

In this section, we offer to test this prediction by investigating in detail the relationship between [OI] luminosity, stellar luminosity, and IR excess in T Tauri stars, using the values of the photospheric luminosities L_* and IR luminosity excesses L_{IR} determined in Sec. II for our program stars.

b) Relationship of L_* and L_{IR} to the [OI]λ6300 fluxes in T Tauri stars

Fig. 6*a* plots the [OI]λ6300 flux as a function of L_* for the 36 stars in our sample, using the same symbols as in Fig.3 for the 23 stars with detectable [OI]λ6300 emission, and starred symbols for the 13 objects without detectable forbidden line emission. We find that the [OI]λ6300 flux does not appear correlated with the stellar photospheric luminosity. In particular, stars where the [OI]λ6300 line is not detectable have the same range of photospheric luminosities ($\sim 0.5 - 2$ L$_\odot$) as stars where the line is detected. This result confirms that the intrinsic properties of the star, as measured by its luminosity, are not the major factor governing the wind properties. On the other hand, Fig. 6*b* shows that *the [OI] flux and the IR luminosity excess are well correlated*, over a range of values spanning more than 2 orders of magnitude. This result shows that [OI]λ6300 emission in T Tauri stars is primarily determined by circumstellar disk properties, and is consistent with the hypothesis that mass-loss in TTS is powered by disk accretion.

The relationship between accretion luminosity and wind mechanical luminosity can be further investigated by removing the contribution of reprocessed stellar light from the total IR excess. For a spatially flat disk, this contribution amounts to 25% of the stellar luminosity (Adams, Lada, and Shu 1987). However, because the disk is optically thick in the infrared, the *observed* IR luminosity L_{IR} can be larger or smaller than the true disk IR luminosity, depending on the inclination of the disk axis to the line of sight, while L_* can be smaller than the true photospheric luminosity, because of occultation of the star by the disk. For a disk seen at random inclination, L_{IR} is equal to the true IR disk luminosity, while L_* is 3/4 of the true photospheric luminosity. The statistical contribution expected for reprocessing of the stellar photons by a spatially flat disk is then $L_{rep} = 1/3\ L_*$, and the statistical IR disk luminosity that can be attributed to accretion is $L_{IR} - L_{rep}$. A

histogram of L_{IR}/L_* for the 36 stars in our sample (Fig. 7) shows that 22 out of the 23 stars with detectable [OI] emission have $L_{IR} > L_{rep}$, while only 6 out of the 13 stars where [OI]λ6300 is not detected do.

The relationship between the [OI]λ6300 flux and $L_{IR} - L_{rep}$ is plotted in Fig. 6*c* using the same symbols as in Fig. 6*a-b*. As could be expected from Fig. 6*a-b*, the correlation remains, with a slope close to 1. If we further assume that the wind velocity and the geometry of the wind/environment interaction surface are the same in all T Tauri stars, Fig. 6*c* implies that (1) the IR accretion luminosity in T Tauri stars, equal to the fraction of the IR excess that does not derive from reprocessing of the stellar photons, varies by about 2 orders of magnitude, (2) the wind mass-loss rate in T Tauri stars, which is roughly proportional to the [OI] flux (see the models of HR in Fig. 3) varies also by about 2 orders of magnitude, (3) the ratio between the two quantities is nearly constant.

We can obtain a rough estimate of the ratio of wind mass-loss rate to disk accretion rate in T Tauri stars by evaluating $\dot{M}_w$ and $\dot{M}_{acc}$ for a star with average properties, like GG Tau ($L_{IR} \sim 1.2$ L$_\odot$, $L_* \sim 1.3$ L$_\odot$, [OI]λ6300 flux $\sim 10^{-13.5}$ erg s^{-1} cm^{-2}, [SII]λ6731 flux $\sim 10^{-14}$ erg s^{-1} cm^{-2}).

The wind mass-loss rate can be estimated independently of any model by assuming that the mass of [OI]λ6300 emitting material $M \sim 1.08 \times 10^{-7}$ M$_\odot$ $\times$ (L([OI])/10^{-4} L$_\odot$) (Kwan and Tademaru 1988) is contained in a spherical volume of constant density $n_e = 10^5$ cm^{-3} and radius R_c, and that $\dot{M}_w = MV_w/R_c$. We find a value of $\dot{M}_w \sim 6 \times 10^{-8}$ M$_\odot$ yr^{-1}, assuming a wind velocity of 200 km s^{-1}typical of forbidden line profile widths (Edwards *et al.* 1987). Note that a similar value $\sim 8 \times 10^{-8}$ M$_\odot$ yr^{-1} would have been found with the method of Edwards *et al.* (1987), where the same assumptions are applied to the [SII]λ6731 emission, assuming an electron density $n_e = n_c = 1.3 \times 10^4$ cm^{-3}.

The mass-accretion rate in GG Tau can be directly derived from $L_{IR} - L_{rep} \sim 0.8$ L$_\odot$ by assuming that this excess represents half of the accretion luminosity $L_{acc} = G\dot{M}_{acc}M_*/R_*$, the other half being emitted at shorter wavelengths in the boundary-layer between the disk and the star (Lynden-Bell and Pringle 1974). If we adopt $R_* \sim 2R_\odot$ and $M_* \sim 0.8M_\odot$ (the values obtained by placing GG Tau on the HR diagram using our estimate of L_*), we find $\dot{M}_{acc} \sim 1.3 \times 10^{-7}$ M$_\odot$ yr^{-1}, close to the value of 1×10^{-7} M$_\odot$ yr^{-1} obtained by Basri and Bertout (1988) for GG Tau from modelling of its spectral energy distribution and Balmer jump.

We thus estimate the ratio of mass-loss to disk accretion rate in GG Tauri to be $\sim$ 0.5, suggesting that the mass-ejection mechanism in T Tauri stars must be very efficient at converting disk gravitational energy into wind kinetic energy. A comparable ratio is found in embedded low-luminosity IR sources driving molecular outflows, where mass-loss rates derived from CO observations are $\sim 10^{-7} - 10^{-6}$ $M_\odot$ yr^{-1} (Edwards and Strom 1988), while accretion rates $\dot{M}_{acc} \sim 10^{-6} - 10^{-5}$ $M_\odot$ yr^{-1} are inferred from modelling of the IR spectral energy distribution of the system (Adams, Lada, and Shu 1987).

However, given the many simplifying assumptions made in their derivation, our values of $\dot{M}_w$ and $\dot{M}_{acc}$ remain order-of-magnitude estimates. As discussed in Sec. III, the [OI]λ6300 flux in T Tauri stars might have a hybrid origin with a contribution from (1) a non-interacting wind, (2) a wind/disk shock interaction, and (3) unresolved jets or HH objects. The models of HR in Fig. 3 of this paper suggest that $\dot{M}_w \sim 5 \times 10^{-8} - 10^{-7}$ $M_\odot$ yr^{-1} in GG Tau, depending on whether the [OI] emission is formed in a non-interacting spherical wind or in an oblique wind/disk interaction with $V_w \sim 200$ km s^{-1}. $\dot{M}_w$ might be lower if a significant fraction of the [OI]λ6300 flux comes from a slower wind component, as suggested by Kwan and Tademaru (1988). Better estimates of the wind mass-loss rate thus require that the forbidden line emission process in T Tauri stars be clearly established. Resolution of this issue awaits high-resolution spectra which will allow a detailed study of the [OI], [SII], and [NII] line ratios in the various velocity components of the forbidden line profiles of T Tauri stars.

Better mass-accretion rates cannot be found at the present time, but the shape of the IR spectral energy distributions of T Tauri stars suggests that there is an additional contribution to the IR excess from an extended "envelope" of cool dust, because they fall less steeply longward of 2 μm than the $\lambda F_\lambda \propto \lambda^{-4/3}$ law expected for spatially flat, steady, viscous accretion disk models (Lynden-Bell and Pringle 1974) or for reprocessing disks (Adams, Lada, and Shu 1987; Kenyon and Hartmann 1987). If we crudely estimate this "envelope" contribution by computing the IR luminosity emitted above the expected $\lambda^{-4/3}$ law, normalized to the observed 2.2μm point, we find that it also correlates with the [OI]λ6300 luminosity and represents an increasing fraction of L_{IR} as the IR excess increases. In particular, all stars in our sample with IR excesses larger than ~ 2 $L_\odot$ (*i. e.* with [OI] fluxes higher than $\sim 10^{-13}$ ergs s^{-1} cm^{-2}) have virtually flat IR spectral energy distributions $\lambda F_\lambda \sim cste$, where the "envelope" contribution dominates the IR excess.

Whether this "envelope" component is heated by reprocessing, non-viscous accretion, direct infall from the surrounding molecular core, or shocks with the stellar wind remains an open question at this time. Final determination of accretion rates in T Tauri stars awaits estimates of their amount of veiling and boundary-layer emission, which are under way (P. Hartigan, private communication).

c) Discussion

An alternative explanation to the correlation between [OI] flux and IR excess in T Tauri stars might be considered, where the increase in IR excess is due to reprocessing of the stellar photons by a disk or circumstellar envelope with an increasing solid angle as seen from the star (the accretion rate remaining fairly constant), while the [OI]λ6300 emission is mostly due to shocks, and reflects a corresponding increase in the interaction surface between the wind and the circumstellar environment (the wind mass-loss rate remaining roughly constant). In this picture, the range of [OI]λ6300 fluxes and IR excesses in T Tauri stars reflects a range of circumstellar geometries rather than a range of wind strengths and accretion levels.

However, one fact indicates that the mass-loss rates and mass-accretion rates are not constant among T Tauri stars: Fig. 8 shows that there exists a correlation between the Hα flux and L_{IR} for the stars in our sample, which disappears once Hα is plotted as a function of L_* (not shown). These results could be expected from Fig. 6 *a-b* since the [OI]λ6300 and Hα fluxes are correlated in T Tauri stars (Cohen and Kuhi 1979). However, the fact that the Hα line in T Tauri stars is 10-100 times stronger than in HH objects (see *e. g.* Dopita 1978), and is not blueshifted with respect to the stellar velocity (Herbig 1977) excludes that the Hα emission is formed in the same circumstellar shock or outer envelope as the forbidden lines. Therefore, the Hα flux must be independent of the *geometry* of the circumstellar environment. Empirical modelling of the Hα line in T Tauri stars (Kuan 1975; Hartmann, Edwards, and Avrett 1982) in fact suggest that most of the Hα emission arises from a heated region within $\sim$ 10 stellar radii. Since the Hα flux appears independent of the stellar photospheric luminosity, its correlation with L_{IR} and [OI] flux can only be understood if Hα is formed in an extended heated atmosphere of the accretion disk boundary-layer or at the base of the wind. The observed range of Hα flux in TTS (about three orders of magnitude) thus requires that a significant range of disk accretion rates and/or wind mass-loss rates be present in T Tauri stars. Hence,

although variations in circumstellar geometry might well be present, the correlation in Fig. 6*b* cannot be attributed to geometrical effects alone, and appears best explained as a correlation between mass-loss rate and mass-accretion rate in T Tauri stars.

V. CONCLUSIONS

The main results of this contribution are the following:

(1) 64 % of the T Tauri stars in our sample show an [OI]λ6300 line stronger than 0.11 Å, and 28 % of our sample show a [SII]λ6731 line stronger than 0.04 Å. The [NII]λ6584 line is detected only in the stars with the highest 3 [SII]λ6731 equivalent widths (these are also the only 3 stars in our sample with associated radio emission and optical jets or HH objects). The [SII] 6716/6731 ratio indicates a density $n_e \geq 10^4$ cm^{-3}in the [SII] emitting region, comparable to that of the densest jets and HH objects observed to date, but the [NII]λ6584/[OI]λ6300 ratio is generally lower than 0.3, which indicates a low shock velocity or low ionisation in the [OI]λ6300 emission region.

(2) T Tauri stars show different behaviors in their [OI] line centroid velocities and [SII]/[OI] ratios depending on their [OI]λ6300 flux: Stars with an [OI]λ6300 flux greater than 10^{-13} ergs s^{-1} cm^{-2} tend to have a large [OI] centroid velocity (~ -80 km s^{-1} on average), and possess detectable [SII]λ6731 emission with [SII]/[OI] $\sim$ 0.3, while stars with an [OI]λ6300 flux lower than 10^{-13} ergs s^{-1} cm^{-2} tend to have a smaller [OI] centroid velocity (~ -23 km s^{-1} on average), and show a larger range of [SII]/[OI] ratios, from $\sim$ 0.3 to less than 0.04. In all stars, the [OI]λ6300 line is blue-shifted, requiring that an opaque circumstellar disk be present.

(3) Processes of forbidden line emission compatible with TTS observations are a) oblique shock interactions between the wind and the raised surface of a flared disk; b) a hybrid model in which dense jets or HH objects produce all the observed [SII] and [NII] emission, while the inner ionised parts of the wind contribute most of the observed [OI] flux; The former model may have difficulties in explaining stars with [OI]λ6300 fluxes higher than 10^{-13} ergs s^{-1} cm^{-2}.

(4) The [OI] and Hα line fluxes are found to be independent of the photospheric luminosity of the object, but correlated with its IR excess luminosity. Most stars where [OI]λ6300 emission is detected have IR luminosity excesses that exceed the statistical contribution expected for reprocessing of the stellar photons by a spatially flat disk. The

most likely explanation of these correlations is that the [OI] flux reflects the wind mass-loss rate while the IR excess reflects the accretion rate through the disk, and that *the energetic mass-ejection in T Tauri stars is powered by accretion of circumstellar disk material onto the stellar surface.* Our data suggest a ratio of mass outflow to disk accretion rate ~ 0.5 if current models of [OI]λ6300 emission and accretion disks in T Tauri stars are adopted.

Several observational tests of this interpretation can be considered:

Quantitative estimates of the veiling in several stars, now under way (P.Hartigan, private communication) will soon provide a more accurate determination of the accretion rate in T Tauri stars, independently of the IR excess. These estimates should correlate with the [OI]λ6300 flux.

On the other hand, high spectral resolution observations ($\Delta\lambda < 1$ Å) of a representative sample of objects will provide better estimates of wind mass-loss rates by establishing whether emission comes from a wind/disk shock or from a hybrid region (dense wind + jet or HH objet). This will require (a) investigating the change in velocity structure of the line profiles with increasing [OI] and [SII] flux, in particular searching for the presence of a distinct higher velocity component in the [OI] line profiles of stars with [OI]λ6300 fluxes greater than 10^{-13} erg s^{-1} cm^{-2} , (b) Studying the [SII]/[OI] and [NII]/[OI] ratios within each velocity component in order to identify the particular emission process responsible for it. HH objects and jets should yield distinctly higher ratios than wind/disk shocks, and non-interacting winds should yield no significant [SII] or [NII] emission. Such a study is presently under way, based on new Echelle spectra of a large sample of T Tauri stars. Better limits on vibrational H_2 emission in T Tauri stars might also set constraints on the shock models compatible with the observations.

Finally, imaging at sub-arcsecond resolution of the [OI] and [SII] emitting regions, and of scattered light from the disk, using the Hubble space telescope or speckle interferometry techniques, will be crucial to (a) determine directly whether the forbidden lines come from elongated jet-like structures, bright HH knots, extended wind envelopes, or shocked disk surfaces, (b) check to which extent changes in forbidden line flux reflect variations in wind mass-loss rate rather than changes in the geometry of the wind/environment interface.

REFERENCES

Adams, F.C., Lada, C.J., and Shu, F.H. 1987, *Ap. J.* , **312**, 788.

Alonso-Costa, J.L., and Kwan, J. 1988, submitted

Appenzeller, I. 1988, preprint

Appenzeller,I., Jankovics,I., and Ostreicher, R. 1984, *Astron. Astrophys* , **141**, 108 (AJO)

Basri, G. and Bertout, C.M. 1988, submitted to *Ap. J.*

Bertout, C., Basri, G., and Bouvier, J. 1988, *Ap. J.* , **330**, 350.

Bieging, J.H., Cohen, M., and Schwartz, P.R. 1984, *Ap. J.* , **282**, 699.

Brown, A., Drake, S.A, and Mundt, R. 1986, in *Cool Stars, Stellar systems, and the Sun*, Eds. M. Zeilik and D.M. Gibson, (Heidelberg: Springer-Verlag) p. 451.

Bührke, T., Brugel, E.W. and Mundt, R. 1986, *Astron. Astrophys* , **163**, 83.

Cohen, M., and Kuhi, L.V. 1979, *Ap. J. Suppl.* , **41**, 743.

Cohen, M., and Fuller, G.A. 1985, *Ap. J.* , **296**, 620.

Cohen, M., and Beiging, J.H. 1986, *A. J.* , **92**, 1396.

Cohen, M., and Jones, B.F. 1987, *Ap. J.* , **321**, 846.

Croswell, K., Hartmann, L., and Avrett, E.H. 1987, *Ap. J.* , **312**, 227.

Czyzak, S., Keyes, C.D., and Aller, L.H. 1986, *Ap. J. Suppl.* , **61**, 159.

DeCampli, W.M. 1981, *Ap. J.* , **244**, 124.

Dopita, M.A. 1978, *Ap. J. Suppl.* , **37**, 117.

Edwards, S., Cabrit, S., Strom, S.E., Heyer, I., Strom, K.M., and Anderson, E. 1986, *Ap. J.* , **321**, 473.

Edwards, S., and Strom, S.E. 1988, in 5^{th} *Cambridge Cool Star Workshop*, Eds. J.L. Linsky, R. Stencel (Berlin: Springer-Verlag) in press

Hartigan, P., Raymond, J., and Hartmann, L. 1987, *Ap. J.* , **316**, 323.

Hartmann, L. 1986, *Fundamentals in Cosmic Physics*, **11**, 279.

Hartmann, L., Edwards, S., and Avrett, A. 1982, *Ap. J.* , **261**, 279.

Hartmann, L., and Raymond, J.C. 1988, *Ap. J.* , submitted (HR)

Herbig, G.H. 1962, *Advances Astron. Astrophys.*, **1**, 47.

Herbig, G.H. 1977, *Ap. J.* , **214**, 747.

Herbig, G.H., and Bell, K.R. 1988, *Lick Observatory Bulletin No. 1111*

Herbig, G.H., Vrba, F.J., and Rydgren, A.E. 1986, *A. J.* , **91**, 575.

Herbst, W. 1986, *Publ. Astron. Soc. Pacific* , **98**, 1088.

Holtzmann, J.A., Herbst, W., and Booth, J. 1986, *A. J.* , **92**, 1387.

Jankovics, I., Appenzeller, I., and Krautter, J. 1983, *Publ. Astron. Soc. Pacific* , **95**, 883.

Johnson, H.L. 1966, *Ann. Rev. Astron. Astrophys.* , **4**, 193.

Johnson, H.L. 1968, in *Stars and Stellar Systems: The Insterstellar Medium*, Eds. B.M. Middlehurst and L.H. Aller, The University of Chicago Press.

Kenyon, S.J., and Hartmann, L. 1987, *Ap. J.* , **323**, 714.

Kuan, P. 1975, *Ap. J.* , **202**, 425.

Kuhi, L.V. 1964, *Ap. J.* , **140**, 1409.

Kwan, J., and Tademaru, E. 1988, *Ap. J.* , **332**, L41.

Lynden-Bell, D., Pringle, J.E. 1974, *Mon. Not. Roy. Astron. Soc.* , **168**, 603.

Mundt, R. 1985 in *Protostars and Planets II*, Eds. D. Black and M. Matthiews, (Tucson: University of Arizona Press) p.414.

Mundt, R., Brugel, E.W., and Bührke, T. 1987, *Ap. J.* , **319**, 275.

Natta, A., Giovanardi, C., Palla, F., and Evans, N.J. 1988, *Ap. J.* in press

Rydgren, A.E., Schmelz, J.T., Zak, D.S., and Vrba, F.J. 1984. *Publ. US Nav. Obs.*, Vol 25, Part 1.

Shu, F.H., Adams, F.C., and Lizano, S. 1987, *Ann. Rev. Astron. Astrophys.* , **25**, 23.

Strom, K.M., Strom, S.E., Edwards, S., Cabrit, S., and Strutskie, M.F. 1989, *A. J.* in press

von Hippel, T., Burnell, S.J., and Williams, P.M., 1988, preprint

Walter F.M., Brown, A., Mathieu, R.D., Myers, P.C., and Vrba, F.J. 1988, *Ap. J.* in press

TABLE 1: LINE EQUIVALENT WIDTHS AND LINE RATIOS

Object	[OI] 6300	[SII] 6731	[SII] 6716	[NII] 6584	Ha	LiI 6707	6716 6731	6731 6300	6584 6300
A. Stars with detectable [OI] and [SII];									
DG Tau	18.50	3.95	1.73	1.41	110.00	0.23	0.44	0.21	0.08
DK Tau	1.30	0.21	0.06	<0.04	27.60	0.50	0.29	0.16	<0.03
DL Tau	0.76	0.16	0.08	<0.04	138.00	0.20	0.50	0.21	<0.05
DO Tau	3.78	0.56	0.32	<0.04	100.90	0.16	0.57	0.15	<0.01
GG Tau	0.30	0.09	<0.04	<0.04	52.00	0.49	<0.44	0.30	<0.13
HD 283447	0.22	0.09	<0.04	<0.04	1.50	0.47	<0.44	0.41	<0.18
HL Tau	4.43	2.52	1.37	1.50	58.00	0.23	0.54	0.57	0.34
LkCa-8	0.34	0.07	<0.04	<0.04	9.00	0.45	<0.57	0.21	<0.12
RY Tau	0.39	0.12	<0.04	<0.04	22.00	0.21	<0.33	0.31	<0.10
T Tau	2.05	0.91	0.29	0.98	59.00	0.40	0.32	0.44	0.48
B. Stars with detected [OI] but no detectable [SII];									
AA Tau	0.38	<0.04	<0.04	<0.04	20.90	0.56	---	<0.11	<0.11
BP Tau	0.19	<0.04	<0.04	<0.04	47.00	0.50	---	<0.21	<0.21
CI Tau	0.29	<0.04	<0.04	<0.04	64.00	0.42	---	<0.14	<0.14
DE Tau	0.32	<0.04	<0.04	<0.04	76.00	0.45	---	<0.13	<0.13
DF Tau	1.38	<0.04	<0.04	<0.04	67.50	0.29	---	<0.03	<0.03
DH Tau	0.95	<0.04	<0.04	<0.04	72.50	0.30	---	<0.04	<0.04
DR Tau	0.83	<0.06	<0.04	<0.04	76.50	0.09	---	<0.07	<0.05
FK Xray3	0.13	<0.04	<0.04	<0.04	4.50	0.55	---	<0.31	<0.31
FM Tau	0.49	<0.04	<0.04	<0.04	113.00	0.19	---	<0.08	<0.08
FX Tau	0.29	<0.04	<0.04	<0.04	13.50	0.57	---	<0.14	<0.14
GH Tau	0.58	<0.04	<0.04	<0.04	14.70	0.57	---	<0.07	<0.07
GK Tau	0.35	<0.06	<0.04	<0.04	30.70	0.45	---	<0.17	<0.11
GM Aur	0.23	<0.04	<0.04	<0.04	70.70	0.40	---	<0.17	<0.17
C. Stars with no detectable [OI] or [SII];									
DI Tau	<0.06	<0.04	<0.04	<0.04	1.20	0.59	----------		
DN Tau	<0.09	<0.04	<0.04	<0.04	15.30	0.59	----------		
DS Tau	<0.11	<0.06	<0.04	<0.04	55.50	0.42	----------		
FK Xray1	<0.06	<0.04	<0.04	<0.04	2.60	0.46	----------		
FK Xray2	<0.06	<0.04	<0.04	<0.04	2.60	0.62	----------		
Haro6-37	<0.06	<0.04	<0.04	<0.04	31.00	0.43	----------		
LkCa3	<0.04	<0.04	<0.04	<0.04	3.60	0.58	----------		
LkCa4	<0.04	<0.04	<0.04	<0.04	5.40	0.56	----------		
LkCa7	<0.04	<0.04	<0.04	<0.04	3.10	0.55	----------		
SU Aur	<0.04	<0.04	<0.04	<0.04	5.00	0.21	----------		
UX Tau a	<0.04	<0.04	<0.04	<0.04	8.00	0.30	----------		
VY Tau	<0.11	<0.05	<0.04	<0.04	3.20	0.52	----------		
V410 Tau	<0.05	<0.04	<0.04	<0.04	2.80	0.46	----------		

TABLE 2: INTRINSIC LINE FLUXES AND CENTROID VELOCITIES

Object	R (mag)	Av (mag)	F[OI]	F[SII]	F[NII]	F(Ha)	V([OI])	V(Ha)	V*
			log F (ergs.s-1.cm-2)					(km.s-1)	
A. stars with detectable [OI] and [SII]									
DG Tau	11.48	0.38	-11.85	-12.52	-12.96	-11.07	-119.1	22.1	18.6
DK Tau	11.50	1.18	-12.74	-13.53	<-14.26	-11.42	-27.2	-25.0	17.7
DL Tau	12.11	0.61	-13.41	-14.09	<-14.69	-11.15	-71.2	20.8	11.2
DO Tau	13.25	1.35	-12.92	-13.75	<-14.90	-11.50	-74.8	42.4	13.4
GG Tau	11.27	0.78	-13.42	-13.94	<-14.30	-11.18	-34.2	-2.7	22.8
HD 283447	9.83	1.36	-12.79	-13.18	<-13.53	-11.95	-5.1	19.2	16.0
HL Tau	13.67	1.28	-13.05	-13.29	-13.52	-11.93	-168.5	90.4	15.7
LkCa-8	12.06	0.25	-13.86	-14.54	<-14.79	-12.43	-33.4	-22.0	11.5
RY Tau	10.03	1.63	-12.53	-13.04	<-13.52	-10.78	-69.6	35.0	15.3
T Tau	9.15	1.44	-11.52	-11.87	-11.84	-10.06	-53.4	3.8	30.5
Mean		1.03	-12.81	-13.38	-13.83	-11.35	-65.7	18.4	17.3
B. stars with [OI] emission, but no detectable [SII];									
AA Tau	12.23	0.93	-13.65	<-14.63	<-14.63	-11.91	-11.6	-5.7	24.0
BP Tau	11.26	0.55	-13.69	<-14.37	<-14.37	-11.30	-17.0	-20.9	21.8
CI Tau	12.19	1.20	-13.66	<-14.52	<-14.52	-11.32	-68.2	-6.9	20.6
DE Tau	11.95	0.20	-13.86	<-14.76	<-14.76	-11.48	-19.4	1.3	3.7
DF Tau	10.96	0.75	-12.64	<-14.18	<-14.18	-10.95	-22.4	2.0	18.6
DH Tau	12.59	1.01	-13.37	<-14.75	<-14.75	-11.49	5.7	4.6	11.9
DR Tau	10.91	0.14	-13.05	<-14.19	<-14.36	-11.08	-89.0	83.5	38.5
FK Xray3	12.19	0.56	-14.22	<-14.74	<-14.74	-12.69	-16.2	-9.5	19.5
FM Tau	13.39	0.90	-14.02	<-15.10	<-15.10	-11.65	3.6	-3.4	12.1
FX Tau	12.74	1.57	-13.76	<-14.62	<-14.62	-12.09	-21.9	-31.6	11.5
GH Tau	11.90	0.53	-13.47	<-14.63	<-14.63	-12.06	-23.0	15.7	14.4
GK Tau	11.66	1.12	-13.40	<-14.16	<-14.34	-11.45	-17.0	0.3	18.0
GM Aur	11.22	0.14	-13.73	<-14.49	<-14.49	-11.24	-1.6	9.9	10.7
Mean		0.74	-13.58	-14.55	-14.58	-11.59	-22.9	3.0	17.3
C. stars with no detectable [OI] or [SII];									
DI Tau	11.80	0.82	<-14.32	<-14.49	<-14.49	-13.02	---	-6.6	12.5
DN Tau	11.53	0.42	<-14.17	<-14.52	<-14.52	-11.94	---	-19.8	16.1
DS Tau	11.73	0.33	<-14.19	<-14.45	<-14.63	-11.49	---	-25.1	20.1
FK Xray1	11.26	0.24	<-14.29	<-14.47	<-14.47	-12.66	---	-10.8	25.9
FK Xray2	11.28	0.25	<-14.30	<-14.47	<-14.47	-12.66	---	-9.7	23.4
LkCa-3	11.01	0.43	<-14.31	<-14.31	<-14.31	-12.35	---	-7.9	20.7
LkCa-4	11.54	0.68	<-14.44	<-14.44	<-14.44	-12.31	---	-1.3	20.5
LkCa-7	11.63	0.62	<-14.49	<-14.49	<-14.49	-12.60	---	-7.7	23.7
Haro 6-37	12.33	1.80	<-14.21	<-14.38	<-14.38	-11.49	---	-16.2	28.5
SU Aur	8.58	0.93	<-13.17	<-13.17	<-13.17	-11.07	---	-3.2	5.9
UX Tau a	10.56	0.20	<-14.20	<-14.20	<-14.20	-11.90	---	-67.6	19.6
VY Tau	12.70	0.85	<-14.40	<-14.75	<-14.84	-12.94	---	-8.5	15.9
V410 Tau	10.21	0.03	<-14.02	<-14.12	<-14.12	-12.27	---	21.1	18.6
Mean		0.58	-14.19	-14.33	-14.35	-12.21	---	-12.6	19.3

TABLE 3: PHOTOSPHERIC LUMINOSITIES AND IR EXCESSES

Object	Spectral Type	Av (mag)	Lbol (Lo)	L* (Lo)	Lir (Lo)	Lir/L*	R* (Ro)	M* (Mo)
A. Stars with detectable [OI] and [SII];								
DG Tau	K7-M0	0.38	8.33	0.82	7.49	9.13	1.93	0.70
DK Tau	K7	1.18	3.44	1.35	2.08	1.54	2.44	0.80
DL Tau	K7-M0	0.61	1.43	0.54	0.89	1.65	1.57	0.70
DO Tau	K7-M0	1.35	2.39	0.32	2.06	6.44	1.22	0.60
GG Tau	K7-M0	0.78	2.58	1.34	1.24	0.93	2.48	0.80
HL Tau	K7-M0	1.28	7.73	0.22	7.51	34.14	0.99	0.60
RY Tau	G2	1.88	18.98	5.09	13.80	2.71	2.28	1.60
T Tau	K1	1.44	29.38	10.37	18.95	1.83	4.16	2.20
HD 283447	K3	1.36	7.64	5.61	2.15	0.38	3.50	1.90
LkCa-8	M0	0.25	0.97	0.49	0.49	1.00	1.53	0.60
Mean		1.05	8.29	2.62	5.67	5.97	2.21	1.05
B. Stars with detected [OI], but no detectable [SII];								
AA Tau	K7-M0	0.93	1.32	0.62	0.66	1.06	1.69	0.60
BP Tau	K7	0.55	1.62	1.02	0.57	0.56	2.13	0.80
CI Tau	K7	1.20	1.64	0.72	0.91	1.26	1.79	0.70
DE Tau	M1	0.20	1.28	0.60	0.68	1.13	1.93	0.45
DF Tau	M0.5	0.75	3.64	2.11	1.46	0.69	3.38	0.50
DH Tau	M0	1.01	0.97	0.54	0.43	0.80	1.61	0.60
DR Tau	K5	0.14	4.05	0.93	3.07	3.30	1.68	1.10
FK Xray3	K7-M0	0.56	0.61	0.48	0.13	0.27	1.49	0.60
FM Tau	M0	0.90	0.57	0.23	0.33	1.43	1.06	0.50
FX Tau	M1	1.57	1.33	0.83	0.50	0.60	2.27	0.45
GH Tau	M2	0.53	1.60	0.96	0.64	0.67	2.70	0.40
GK Tau	K7	1.12	2.25	1.11	1.13	1.02	2.21	0.80
GM Aur	K7-M0	0.14	1.32	0.86	0.46	0.53	1.98	0.70
Mean		0.74	1.71	0.85	0.84	1.03	1.99	0.63
C. Stars with no detectable [OI] or [SII];								
DI Tau	M0	0.82	1.10	0.95	0.16	0.17	2.14	0.40
DN Tau	M0	0.42	1.32	0.90	0.42	0.47	2.08	0.70
DS Tau	K3	0.33	1.21	0.45	0.78	1.73	0.99	1.00
FK Xray1	K7-M0	0.24	1.15	0.88	0.28	0.32	2.02	0.80
FK Xray2	K7-M0	0.25	1.11	0.88	0.24	0.27	2.01	0.80
Haro6-37	K6	1.80	2.58	0.93	1.64	1.76	1.84	1.00
LkCa3	M1	0.43	1.92	1.73	0.21	0.12	3.26	0.40
LkCa4	K7	0.68	1.03	0.87	0.17	0.20	1.96	0.80
LkCa7	K7	0.62	1.00	0.77	0.23	0.30	1.85	0.70
SU Aur	G2	0.93	16.59	11.26	5.14	0.46	3.39	2.00
UX Tau a	K2	0.20	1.89	1.11	0.84	0.76	1.44	1.25
VY Tau	M0	0.85	0.67	0.43	0.24	0.56	1.44	0.60
V410 Tau	K7	0.03	2.13	1.87	0.26	0.14	2.88	0.90
Mean		0.58	2.59	1.77	0.82	0.56	2.10	0.87

FIGURE CAPTIONS

Figure 1*a-d*: Examples of spectra for four objects with increasing forbidden line emission. Fig.1*a*: FK Xray2 (K7-M0); Fig.1*b*: AA Tau (K7-M0); Fig.1*c*: DK Tau (K7); Fig.1*d*: DG Tau (cont/e). The intensity (in arbitrary units) is plotted on a logarithmic scale versus wavelength. The spectra have a resolution of 1.8 Å and a wavelength range of 6240 Å to 6760 Å, that includes the forbidden line doublets of [OI]$\lambda\lambda$6300,6364, [NII]$\lambda\lambda$6548,6584, and [SII]$\lambda\lambda$6716,6731, as well as the Hα line and several prominent photospheric absorptions lines (in particular CaI λ6450, CaI λ6717, and LiI λ6707).

Figure 2: Relationship between the equivalent widths of the [OI]λ6300 and [SII]λ6731 lines for the 23 stars in our sample showing detectable [OI]λ6300 emission. Solid squares are the 10 stars where [SII]λ6731 was detected, while open squares are the 13 stars with only upper limits to the [SII]λ6731 equivalent width. Typical uncertainties on the equivalent widths are shown in the lower right corner. A dashed line shows the mean relationship for the 10 stars where both lines were detected, which corresponds to a [SII]λ6731/[OI]λ6300 ratio of 0.3. Note that several stars have upper limits on the [SII]λ6731 equivalent width that are not compatible with this mean ratio.

Figure 3: Relationship between the [OI] λ6300 and [SII] λ6731 dereddened line fluxes for the 23 T Tauri stars in our sample with detectable [OI]λ6300 emission. As in Fig. 2, solid squares represent stars where [SII] λ6731 was actually detected, while open squares have only upper limits to the [SII]λ6731 flux. For the cont/e stars, a dotted line joins the lower limit (square) and the upper limit (cross) to the fluxes, obtained using respectively a lower and upper limit to the A_V (see text). An arrow shows the vector by which a point would move if the adopted A_V toward the star was increased by 1 mag. Typical uncertainties on the fluxes are shown in the lower right corner. Also plotted are predicted fluxes for three wind/disk shock models (circular symbols connected by a dashed line; HR), for spherical non-interacting wind models (dashed line at the bottom of the figure; HR), and for HH objects and jets (shaded area; from Dopita 1978 and Cohen and Jones 1987). These processes will be discussed in detail in section III.d.

Figure 4: Distribution of the [OI]λ6300 centroid velocities in T Tauri stars with [OI]λ6300 fluxes lower (top panel) or higher (bottom panel) than 10^{-13} erg s^{-1} cm^{-2},

where stars with detectable [SII]λ6731 emission have been hatched, and stars with detectable [NII]λ6584 emission cross-hatched. The group of stars with higher [OI]λ6300 fluxes clearly tends to show higher [OI]λ6300 centroid velocities.

Figure 5: The [SII] 6716/6731 and [SII]λ6731 to [OI]λ6300 line ratios for T Tauri stars and for various processes of forbidden line emission. Solid squares denote stars where both [OI]λ6300 and [SII]λ6731 were detected, but not [NII]λ6584, while solid triangles denote stars where all three lines were detected. Open circles and open triangles show the same line ratios in optical jets (Cohen and Jones 1987), and Herbig-Haro objects (Von Hippel, Burnel, and Williams 1988). As in Figure 3, the three circular symbols connected by dashed lines show predicted ratios for three models of wind/disk shock interactions from HR, with wind velocities and mass-loss rates of respectively 200 km s^{-1} and 10^{-7} $M_\odot$ yr^{-1}, 400 km s^{-1} and 2.10^{-8} $M_\odot$ yr^{-1}, and 400 km s^{-1} and 2.10^{-7} $M_\odot$ yr^{-1}(in order of decreasing [SII]/[OI] ratio). The two horizontal dashed lines mark the asymptotic [SII] 6716/6731 line ratios for $n_e \ll n_c$ and $n_e \gg n_c$, where $n_c = 1.3\ 10^4$ cm^{-3} is the critical density for collisional deexcitation of the [SII]λ6731 line.

Figure 6*a*: Relationship between the [OI]λ6300 flux and the photospheric luminosity L_* for the 36 stars in our sample. Solid squares denote the 10 stars where both [OI]λ6300 and [SII]λ6731 emission was detected, open squares denote the 13 stars where only [OI]λ6300 was detected, and starred symbols denote the 13 objects without detectable forbidden line emission. Typical uncertainties are shown in the lower right corner. The three groups of stars show a similar range of photospheric luminosities despite their differing emission properties.

Figure 6*b*: Same as Fig. 6*a* for the relationship between the [OI]λ6300 flux and the IR luminosity excess L_{IR}. Typical uncertainties are shown in the lower right corner. There is a clear correlation between the two quantities, that was not seen in Fig. 6*a*.

Figure 6*c*: Same as Fig. 6*b*, where the statistical contribution expected for reprocessing by a spatially flat disk $L_{rep} = 1/3\ L_*$ has been removed from the observed IR luminosity excess L_{IR}. Typical uncertainties are shown in the lower right corner.

Figure 7: Histogram of the ratio of the infrared luminosity excess L_{IR} to the photospheric luminosity L_* in T Tauri stars. Stars with detectable [OI]λ6300 emission are hatched, and stars with detectable [SII]λ6731 emission cross-hatched. All stars with

[OI]λ6731 emission have an L_{IR} which exceeds the statistical contribution expected for photon reprocessing by a flat disk $L_{rep} = 1/3\ L_{\star}$.

Figure 8: Same as Fig. 6*b* for the relationship between the Hα flux and the infrared luminosity excess L_{IR}. A correlation is seen, as in Fig. 6*b*.

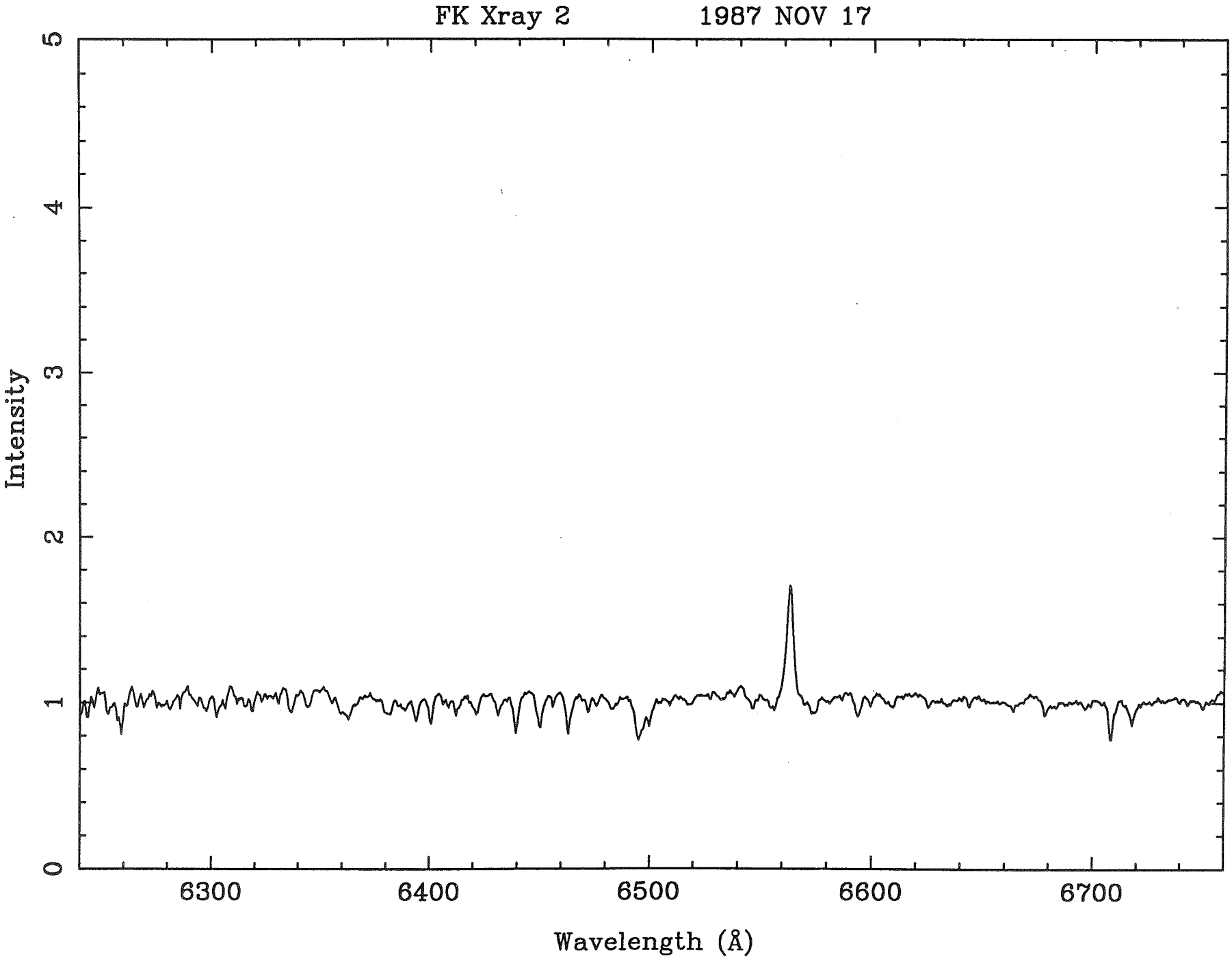
FK Xray 2
1987 NOV 17
Intensity
0
1
2
3
4
5
6300
6400
6500
6600
6700
Wavelength (Å)

Fig.1a

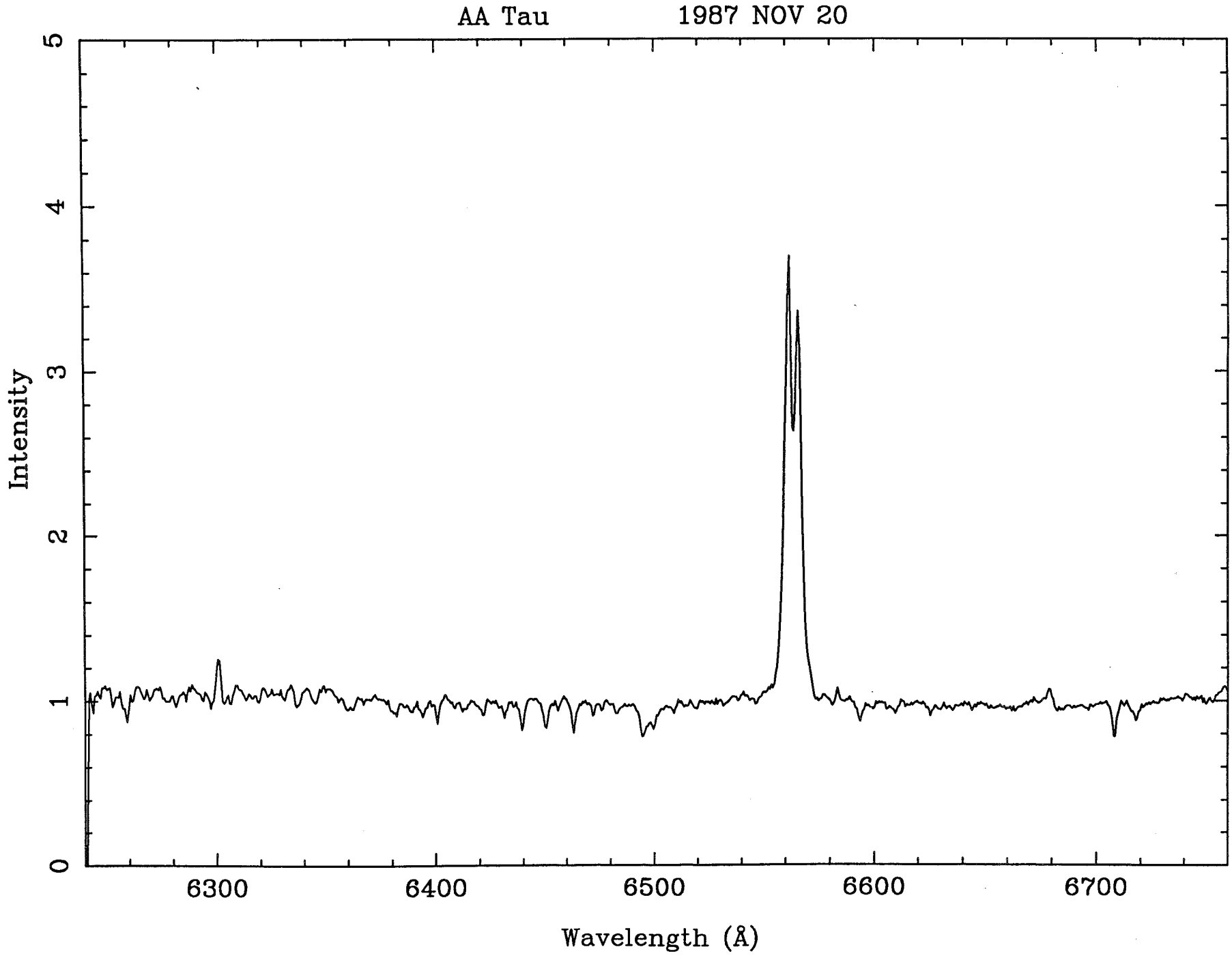
AA Tau
1987 NOV 20
Intensity
0
1
2
3
4
5
6300
6400
6500
6600
6700
Wavelength (Å)

Fig.1b

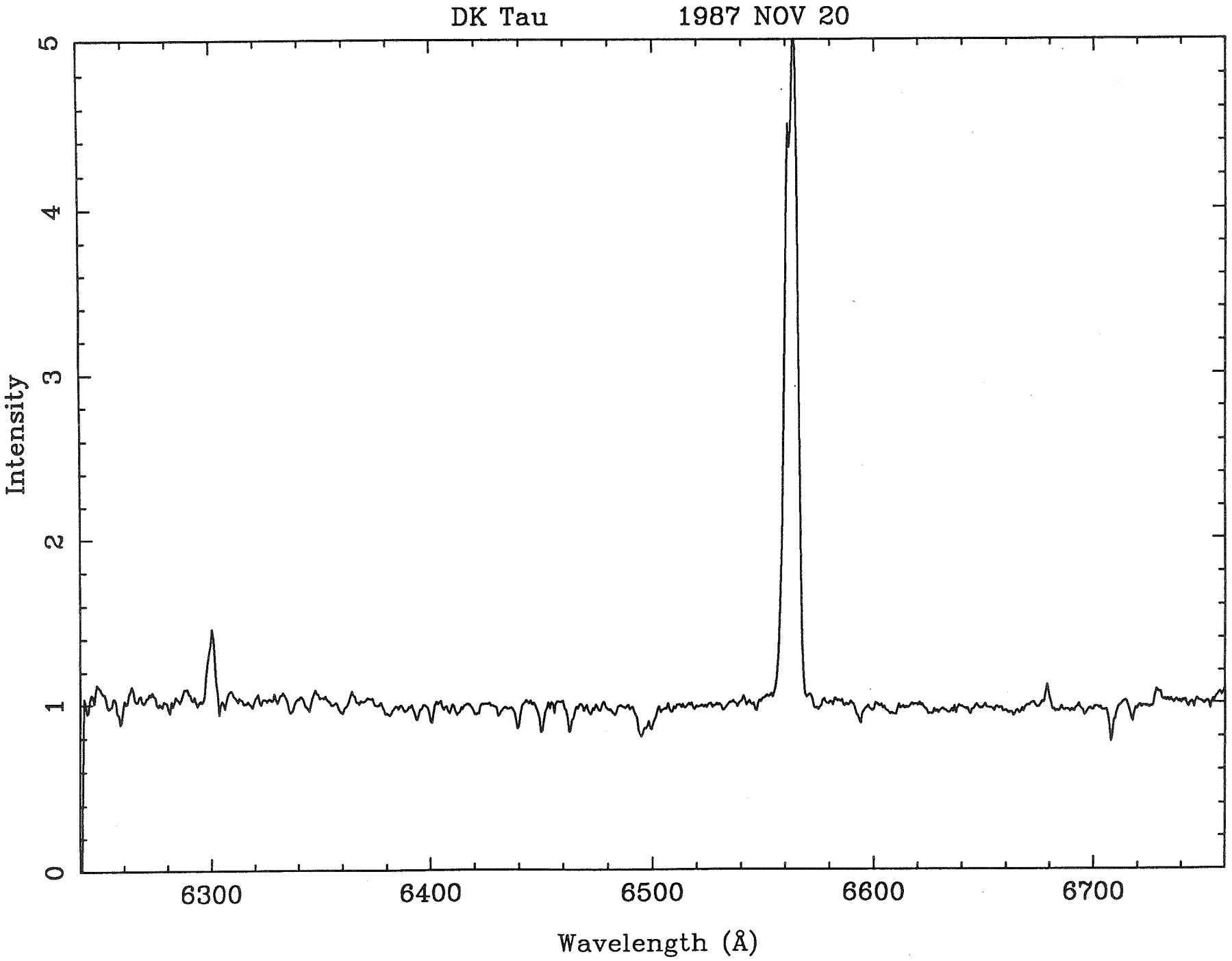
DK Tau
1987 NOV 20
Intensity
0
1
2
3
4
5
6300
6400
6500
6600
6700
Wavelength (Å)

Fig.1c

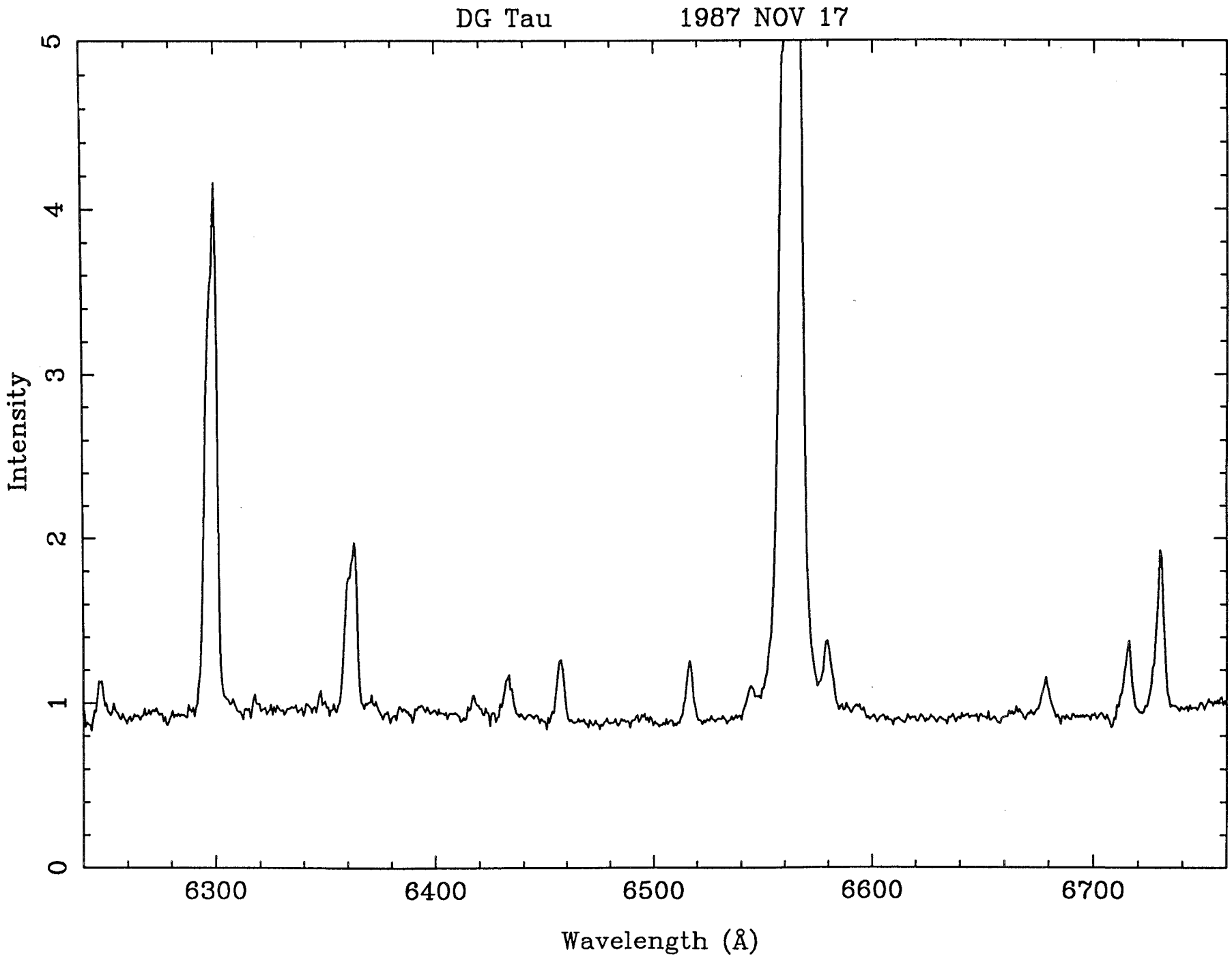
DG Tau
1987 NOV 17
Intensity
0
1
2
3
4
5
6300
6400
6500
6600
6700
Wavelength (Å)

Fig.1d

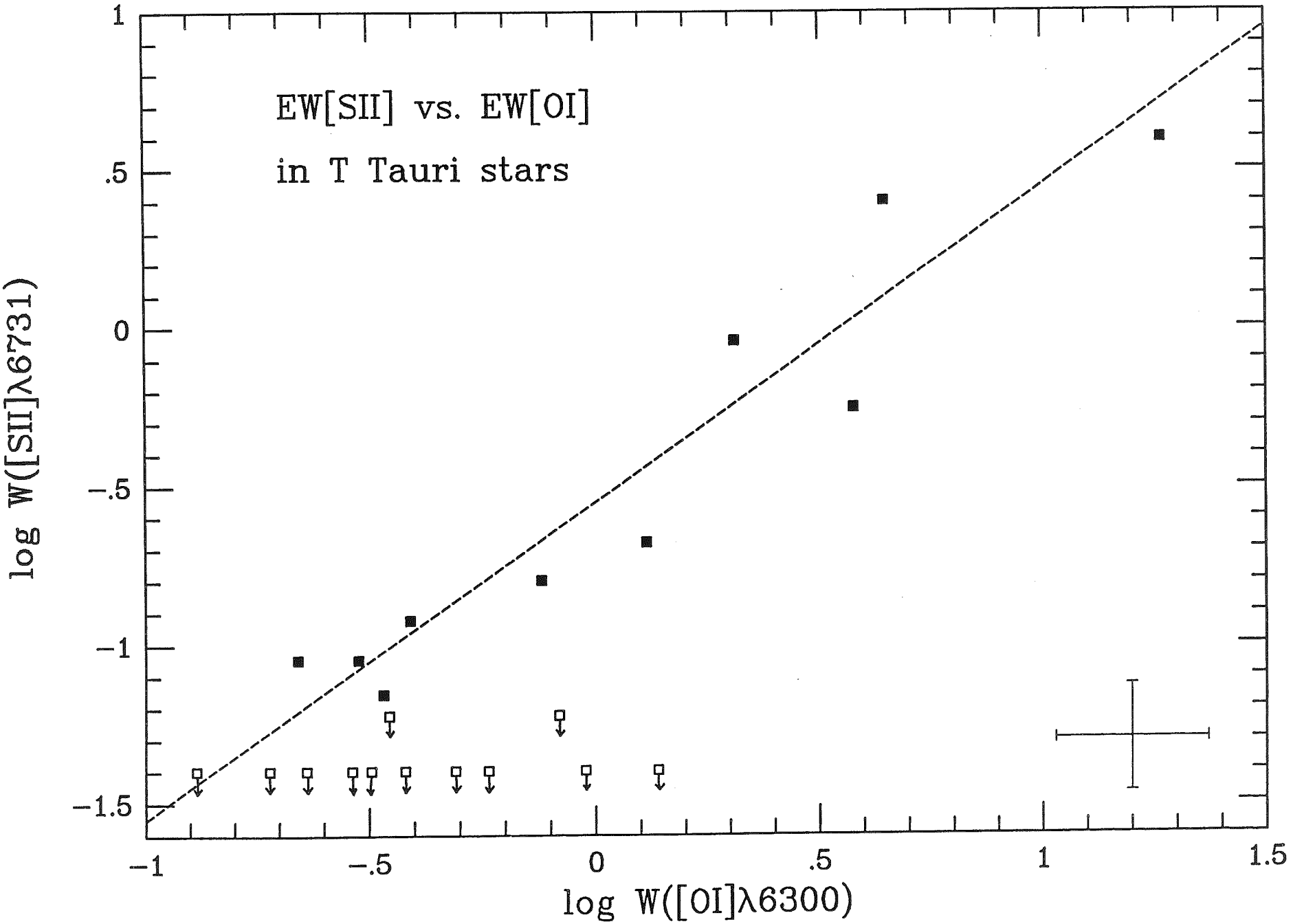
EW[SII] vs. EW[OI]
in T Tauri stars
log W([SII]λ6731)
log W([OI]λ6300)
1
.5
0
-.5
-1
-1.5
-1
-.5
0
.5
1
1.5

Fig.2

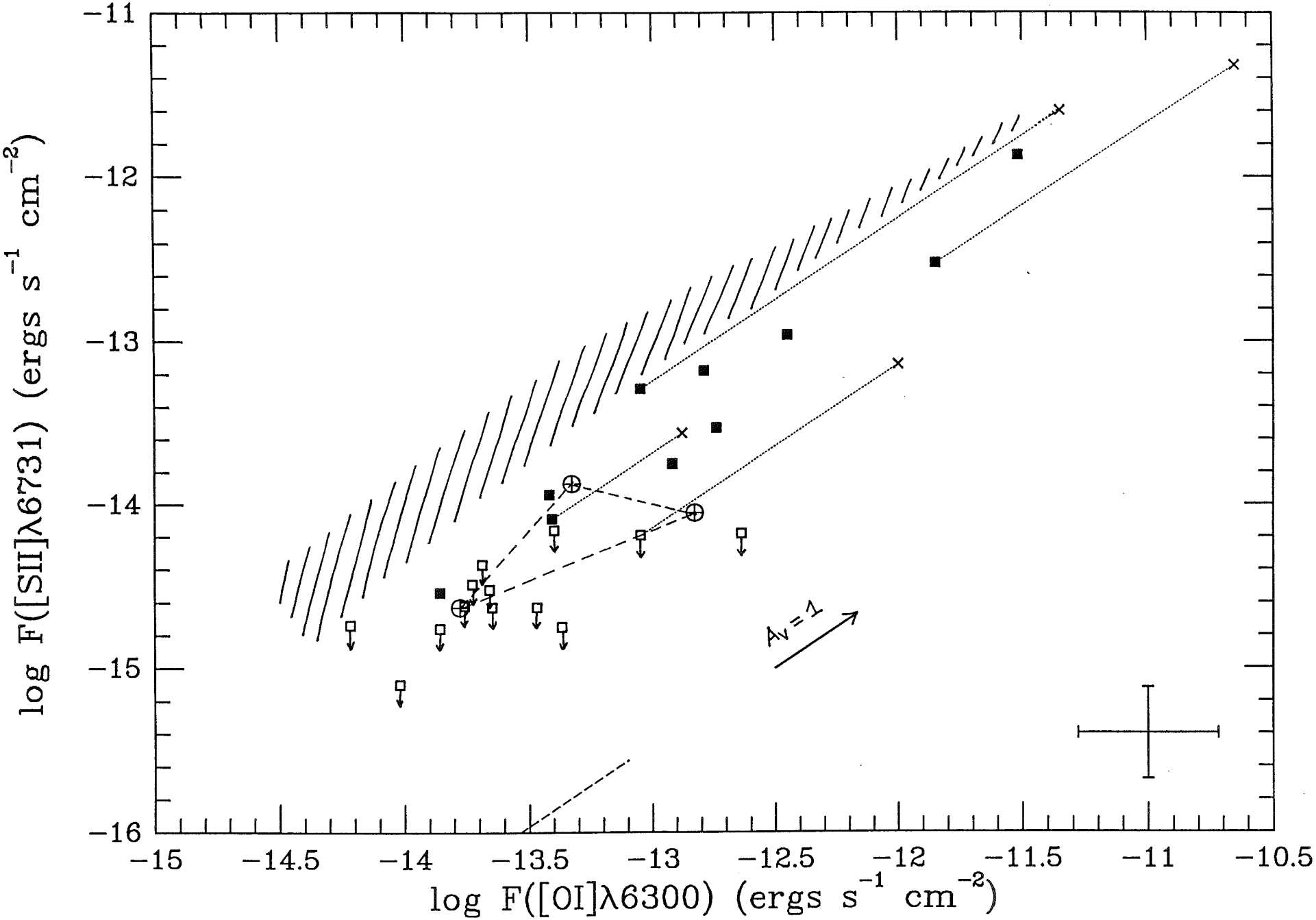
log F([SII]λ6731) (ergs s^{-1} cm^{-2})
log F([OI]λ6300) (ergs s^{-1} cm^{-2})
−11
−12
−13
−14
−15
−16
−15
−14.5
−14
−13.5
−13
−12.5
−12
−11.5
−11
−10.5
$A_V = 1$

Fig.3

Fig.4

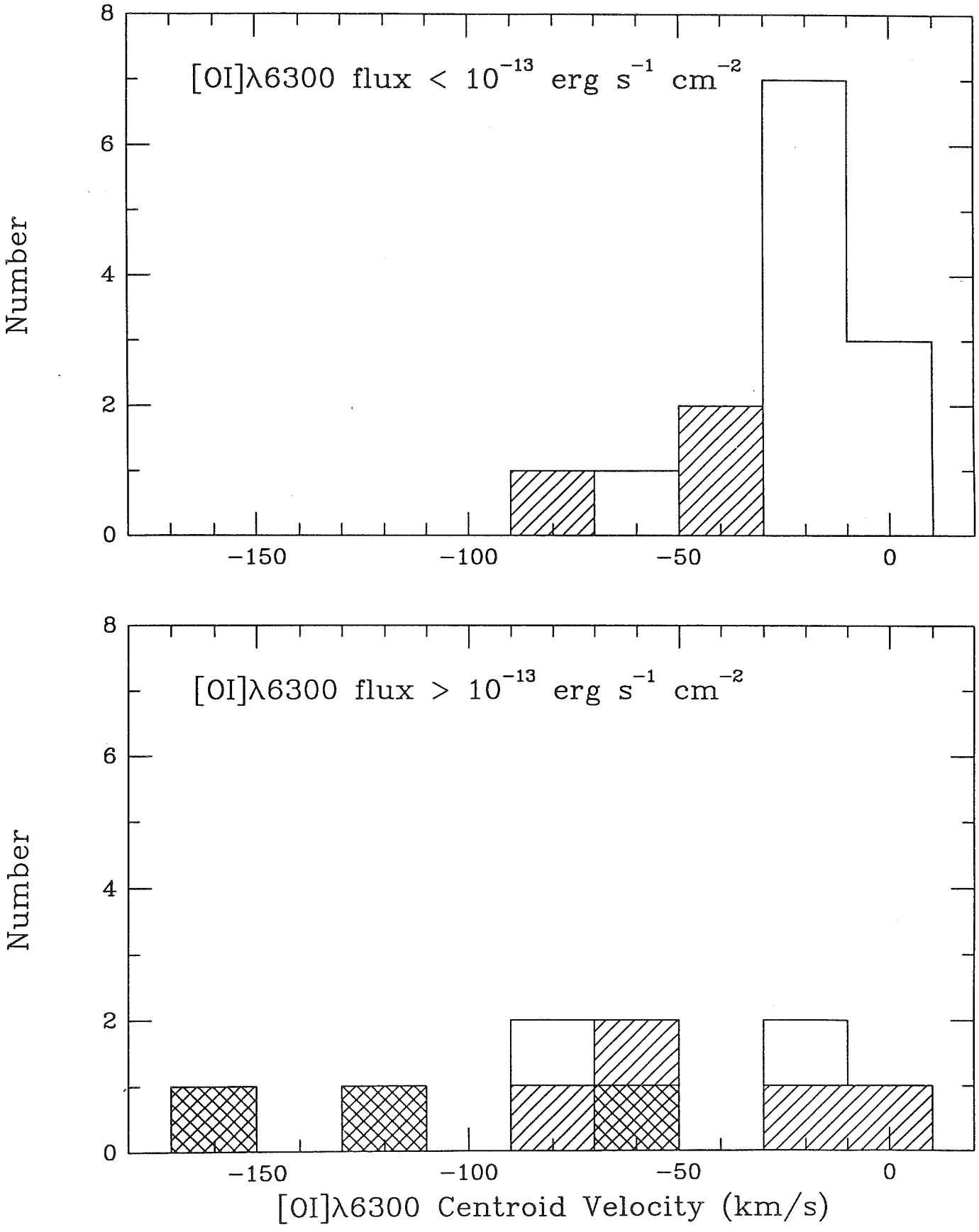
[OI]λ6300 flux < 10^{-13} erg s^{-1} cm^{-2}
[OI]λ6300 flux > 10^{-13} erg s^{-1} cm^{-2}
Number
Number
0
2
4
6
8
−150
−100
−50
0
[OI]λ6300 Centroid Velocity (km/s)

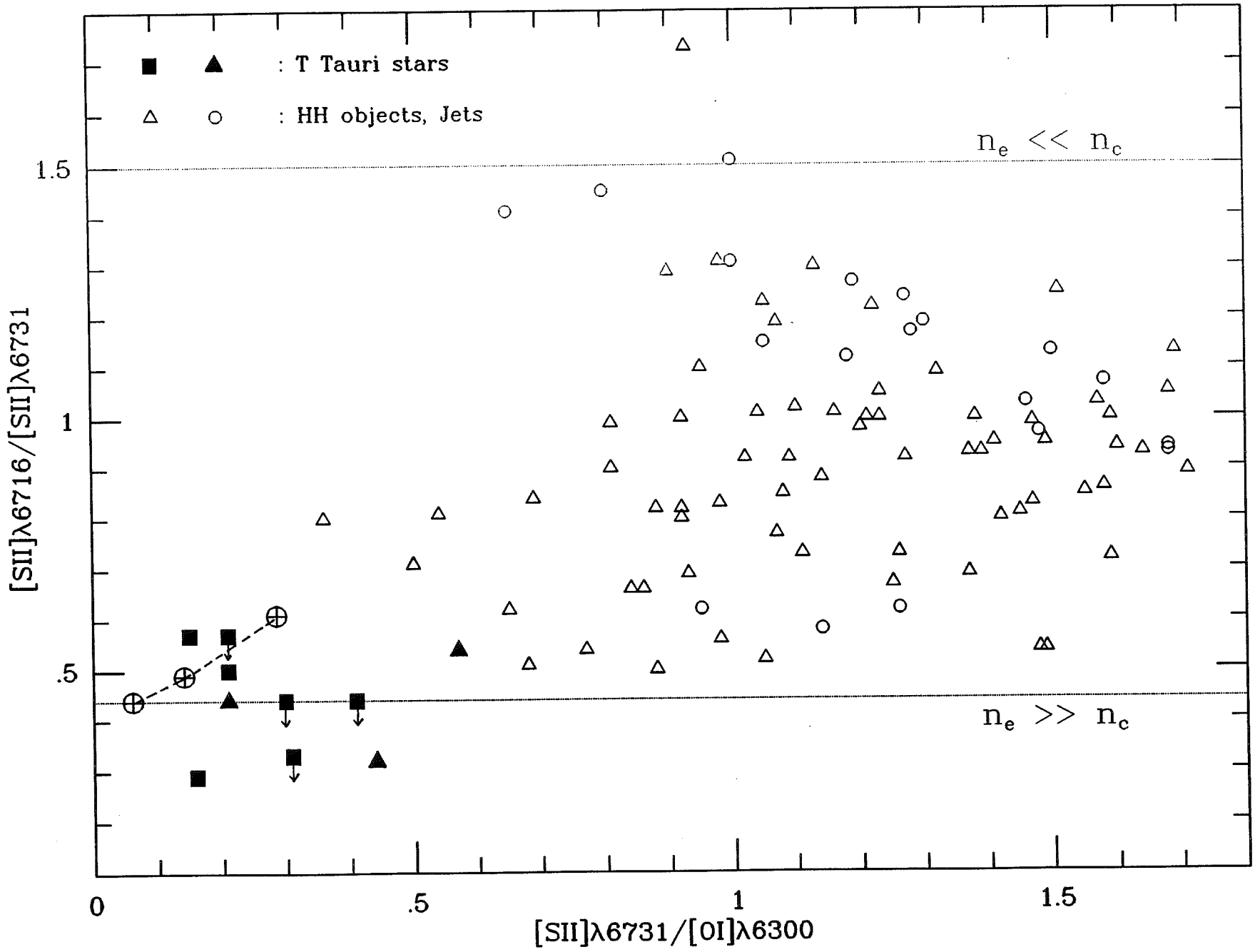
■ ▲ : T Tauri stars
△ ○ : HH objects, Jets
$n_e << n_c$
$n_e >> n_c$
[SII]λ6716/[SII]λ6731
[SII]λ6731/[OI]λ6300
0
.5
1
1.5
.5
1
1.5

Fig.5

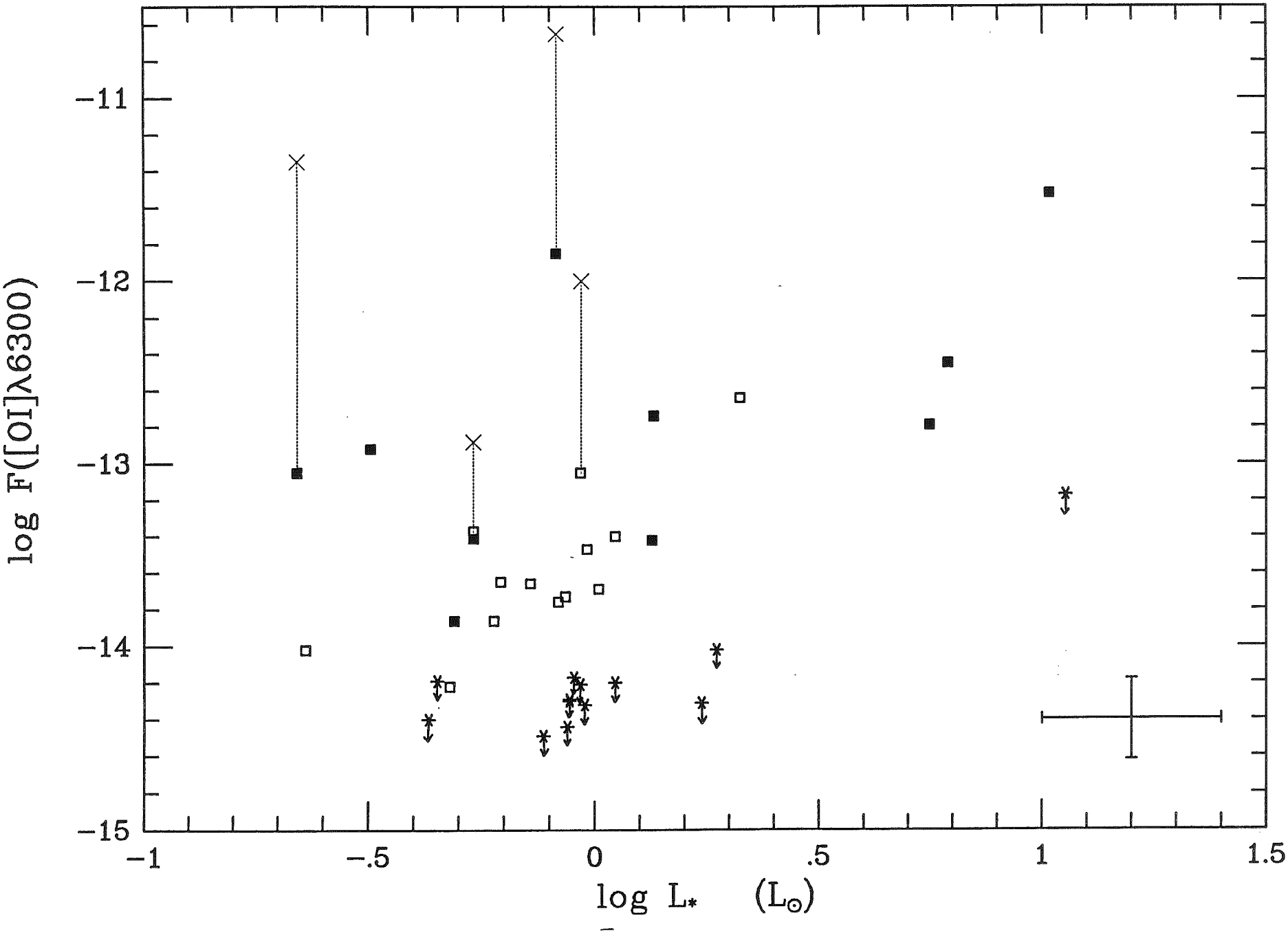

Fig.6a

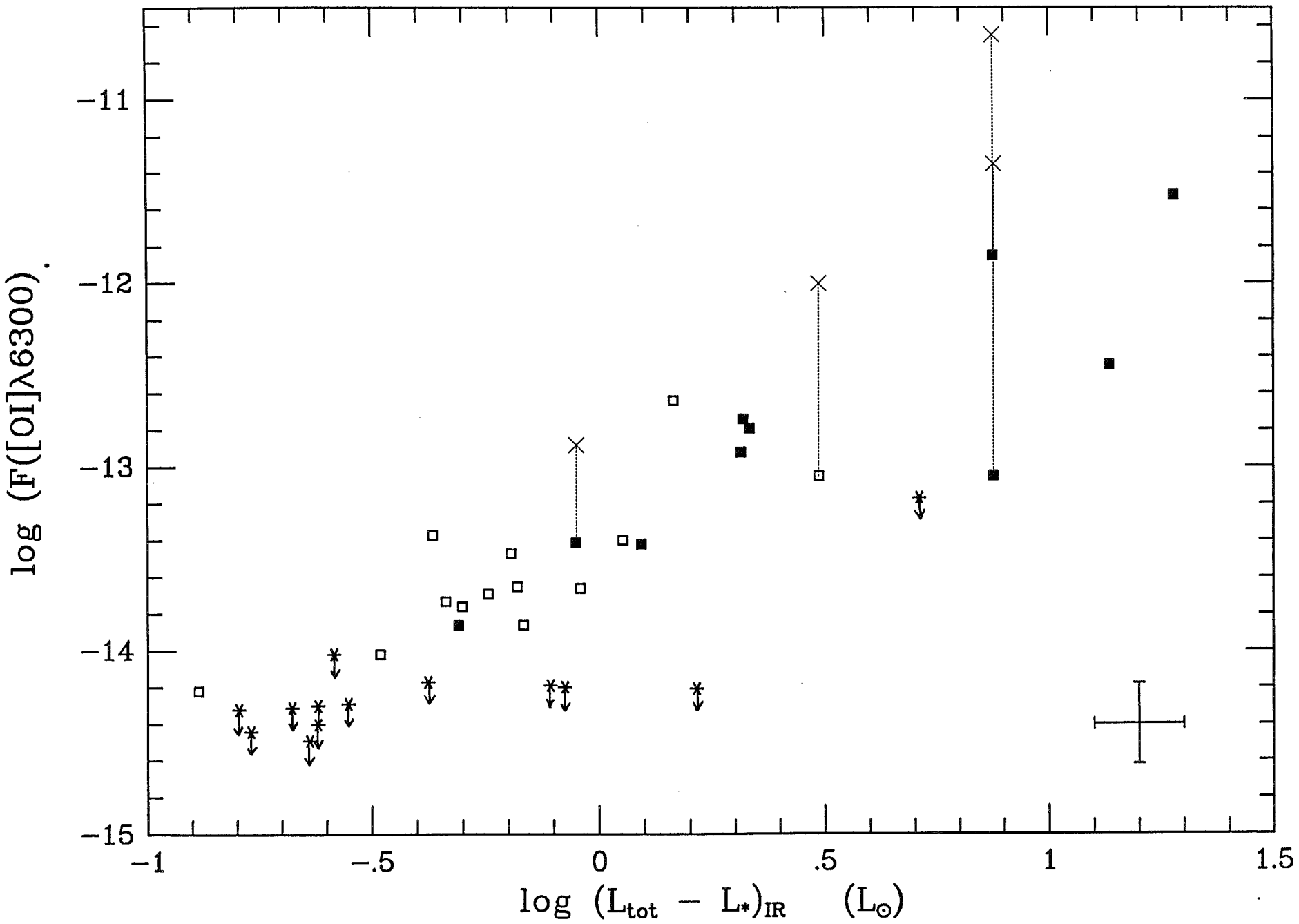

Fig. 6b

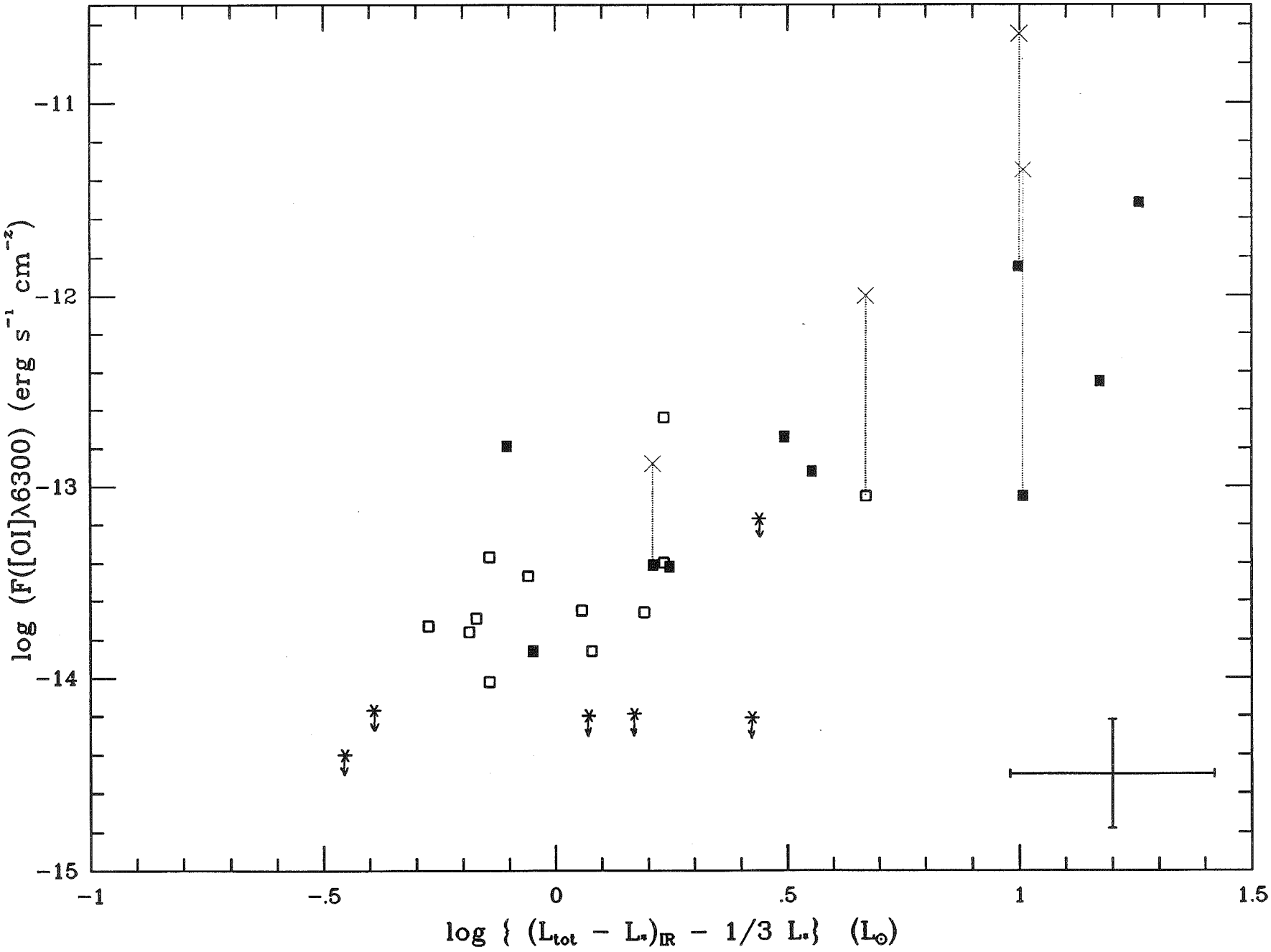
log (F([OI]λ6300) (erg s^{-1} cm^{-2})
−11
−12
−13
−14
−15
−1
−.5
0
.5
1
1.5
log { $(L_{tot} - L_*)_{IR}$ − 1/3 L_*} ($L_\odot$)

Fig.6c

Fig.7

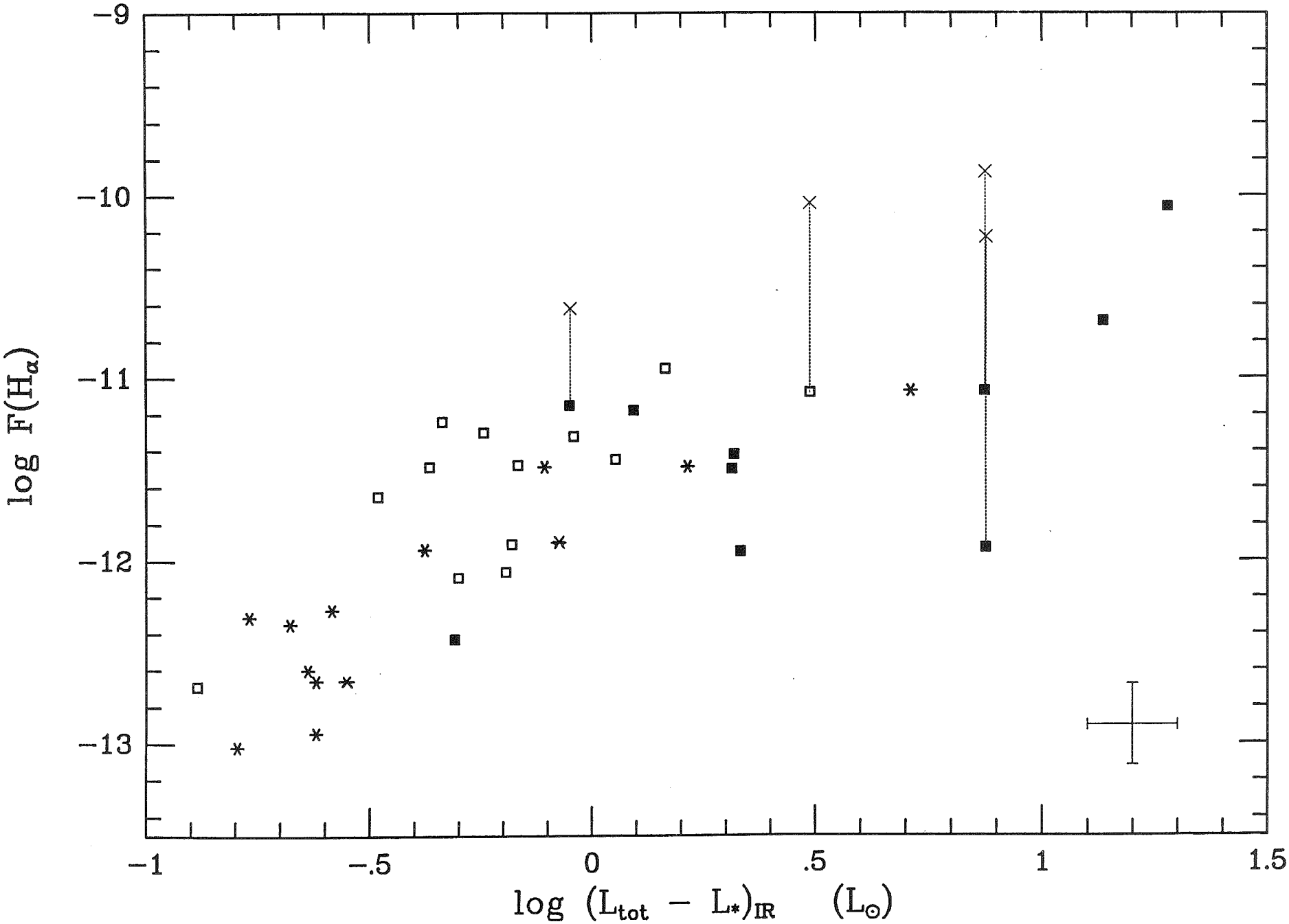

Fig.8

ANNEXE 9

CIRCUMSTELLAR MATERIAL ASSOCIATED WITH SOLAR-TYPE PRE-MAIN SEQUENCE STARS: A POSSIBLE CONSTRAINT ON THE TIMESCALE FOR PLANET-BUILDING

Karen M. Strom
Stephen E. Strom
Suzan Edwards [1]
Sylvie Cabrit [2]
Michael F. Skrutskie

Five College Astronomy Department
University of Massachusetts
Amherst, MA 01003

Paru dans: The Astronomical Journal, 97, 1451

[1] Also at Smith College, Northampton, MA 01063

[2] Now at Institut d'Astrophysique, 98 bis Bd Arago, 75014 Paris, France.

Abstract

This contribution compares the spectral energy distributions characterizing two sets of pre-main sequence stars in Taurus-Auriga: 36 T Tauri stars (TTS) with Hα emission line equivalent widths $W_\lambda(H\alpha) > 10$ Å, and 47 "weak line" T Tauri stars (WTTS) with $W_\lambda(H\alpha) \leq 10$ Å; the latter group includes as a major subset the recently discovered "naked" T Tauri stars. The infrared properties of both classes of objects overlap. Both TTS and WTTS show significant infrared excesses: 84% of the TTS and 36% of the WTTS have observed near-infrared (2.2μ) excesses, $\Delta K \equiv \log \{F_{2.2\mu}(PMS)/ F_{2.2\mu}(standard)\} \geq 0.10$, while 97% and 30% of TTS and WTTS respectively exhibit infrared excesses at $\lambda \geq 10\mu$. Emission from dust embedded in circumstellar disks surrounding WTTS and TTS is the most likely explanation for the observed near- and mid-infrared excesses. The fraction of all pre-main sequence stars (WTTS + TTS) with measurable near-infrared excesses decreases with time; nearly 60% of pre-main sequence stars with ages younger, and only 40% of those older than 3×10^6 yr show $\Delta K \geq 0.10$; only 10% of PMS stars with $t > 10^7$ yr have excesses this large. If this excess near-IR emission arises in the warm, inner regions of circumstellar disks, then the range in timescales for disks to evolve from massive, optically thick to low mass, tenuous structures must be $\sim 3 \times 10^6$ yr to 10^7 yr. At present, this range represents the best available astrophysical constraint on the time available for assembling distributed material in circumstellar disks into planets.

1.Introduction

The population of optically visible, low mass pre-main sequence stars ($M < 1.5\ M_{\odot}$) is sometimes divided into two categories: "classical" T Tauri stars (TTS) and "naked" T Tauri stars (NTTS) (Walter, 1987; Walter et al., 1988, hereafter WBMMV). TTS are objects primarily discovered in the course of objective prism surveys of molecular cloud complexes aimed at locating young stars that show strong Hα emission. As a class the TTS are characterized by:

- strong, broad Hα emission; Hα emission line equivalent widths, $W_\lambda(H\alpha) > 10$Å, and typical line widths exceed 10Å;
- P-Cygni-like structure in Hα as well as Na I D, Ca II and Mg II;
- incipient to strong permitted metallic line emission, and often [O I], [S II] and [Fe II] emission;
- strong Li I absorption with equivalent widths consistent with cosmic and meteoritic abundance (Zappala, 1972);
- excess continuum emission at ultraviolet, optical and infrared wavelengths leading to "spectral veiling", which dilutes the photospheric absorption line spectrum of the star;
- irregular variability with amplitudes ranging from 0.1 mag to 5 mag; in some cases, periodic variations are observed as well (Rydgren et al., 1984a; Vrba et al. 1986; Bouvier, Bertout and Bouchet, 1986; Herbig and Bell, 1988; Vrba et al., 1989);
- ages ranging from $t \sim 2\times10^5$ to $\sim10^7$ yr.

The NTTS are largely discovered in the course of x-ray surveys (Walter and Kuhi, 1981; Feigelson and Kriss, 1981; Feigelson et al. 1987; WBMMV), but in some cases from proper motion surveys in the vicinity of star-forming complexes (Jones and Herbig, 1979), and in others from objective prism searches for stars which exhibit Ca II emission (Herbig, Vrba and Rydgren, 1986, hereinafter HVR). WBMMV suggest that NTTS may constitute as many as 90% of solar-type PMS stars in Taurus-Auriga. As a class, the NTTS show:

- weak, narrow Hα emission; $W_\lambda(H\alpha) < 10$Å and line widths < 10 Å, with no evidence for P-Cygni absorption components;
- no cases of strong permitted metallic line emission; weak or absent forbidden line emission;
- strong Li I absorption;
- no evidence for either significant spectral veiling (at $\lambda > 4000$ Å), or for IR excesses (Walter, 1987);
- regular variability driven by stellar rotation and the consequent periodic appearance of large, long-lived starspots (Rydgren and Vrba, 1983; Rydgren et al., 1984a; Bouvier et al., 1986; Bouvier and Bertout, 1989; Vrba et al., 1989);
- ages ranging from $t \sim 2\times10^5$ to 3×10^7 yr;

Because the TTS and NTTS are intermixed within the same parent molecular cloud complexes, and because their distribution of radial velocities is identical (Hartmann, Soderblom and Stauffer, 1987; WBMMV), they must share a common origin. What then accounts for the

differences in observed characteristics? Are NTTS and WTTS representative of two distinct classes of low mass pre-main sequence (PMS) stars, or is there a continuum of observable properties (infrared excess, spectral veiling, emission line strength) among such stars?

Recent work (see the review by Strom, Strom and Edwards, 1988) suggests that a massive ($M > 0.01\ M_\odot$), optically thick ($\tau_V \sim 1000$) circumstellar disk can in principle account for the excess optical and infrared continuum emission characteristic of TTS:

- accretion through a viscous disk can produce infrared radiation well in excess of that emitted by the typical TTS photosphere; for an accretion rate $M_{acc} \sim 10^{-7}\ M_\odot$/yr, the accretion luminosity is $\sim 1\ L_\odot$ (Lynden-Bell and Pringle, 1974; Hartmann and Kenyon, 1987a,b; Adams, Lada and Shu, 1987, K. Strom et al., 1988);
- accretion can also account for the production of ultraviolet and optical emission at the "boundary layer" between the rapidly rotating inner regions of the accretion disk and the slowly rotating stellar photosphere (Kenyon and Hartmann, 1987; Bertout, Basri and Bouvier, 1988). The luminosity produced in the boundary layer must be comparable to the infrared accretion luminosity;
- when accretion rates drop to values $M_{acc} << 10^{-7}\ M_\odot$/yr, the accretion luminosity becomes small compared to the photospheric luminosity; however reprocessing of stellar photons by dust located in an optically thick circumstellar disk can return up to 0.5 times the stellar luminosity (depending on the disk mass and optical depth, and the viewing geometry) and thus account for significant infrared excesses.

Energetic winds ($L_{wind} > 0.01\ L_*$) with $M_{wind} > 10^{-9}\ M_\odot$/yr and $v \geq 200$ km/s account for the observed P-Cygni structure in the stronger resonance lines, and must contribute significantly to the strong, broad Hα emission in TTS. Forbidden line emission is produced either directly in the wind (Edwards et al, 1987), or in a shock produced at the boundary between the stellar wind and the surface of the disk (Hartmann and Raymond, 1988). The presence of an energetic wind and an active accretion disk appears to be linked (Edwards and Strom, 1988; Cabrit et al., 1989). Emission from an active chromosphere may account for some fraction the ultraviolet excess, and for incipient metallic line emission (Cram, 1979; Calvet, Basri and Kuhi, 1984; Strom, 1983; Finkenzeller and Basri, 1987).

The lack of massive, optically thick disks and their associated energetic winds, seems the most logical explanation for the absence of significant continuum excesses and strong, broad Balmer line emission in NTTS. Are all NTTS born without disks, or do some represent stars which begin their lives as TTS surrounded by massive disks, which then evolve, as a result of a) rapid accretion, b) tidal disruption by a companion star or c) a planet-building episode? What is the characteristic timescale for a PMS star to become "naked"? It is of some considerable importance to answer these questions as a first step toward understanding a) the frequency of disk formation around PMS stars, and b) the timescale for disk evolution, and to learn thereby whether the formation of planetary systems is likely to be frequent or rare, and on what timescale distributed material in disks may be assembled into larger bodies.

In this contribution, we examine a) whether the NTTS represent a distinct class of low mass young stars which lack measurable infrared excesses arising in massive, optically thick disks, and b) the fraction of PMS stars surrounded by such disks as a function of time.

2. Approach and Observational Material

As a first step toward comparing TTS and NTTS properties, it is necessary to agree upon quantitative defining characteristic(s) for members of each class. Because NTTS basically represent that class of low mass PMS stars which were not discovered in surveys for Hα emission line objects but by a variety of other methods, we propose that *to be classified as a NTTS, $W_\lambda(H\alpha) \leq 10$ Å and $L/L_\odot < 30$; all other PMS stars with similar luminosities and larger Hα equivalent widths are classified as TTS.* We note that this definition is similar in spirit to the classification "wt" adopted by Herbig and Bell (1988), with the exception of their choice of 5 Å as the equivalent width which divides a "wt" from a TTS. *Henceforth, we will use the notation WTTS, defined as above, in place of NTTS.*[1] By adopting our definition and the Hα equivalent widths and luminosities reported by Cohen and Kuhi (1979), WBMMV and HVR, we retain as WTTS all objects (39 in number) in the Taurus-Auriga complex classified by WBMMV as NTTS. Of the 132 PMS stars in Taurus-Auriga listed in the Herbig and Bell catalog, an additional 24 stars meet our criteria for inclusion in the WTTS class, thus bringing the total number of WTTS to 63, or 48% of the total *known* PMS population in this star-forming region.

We note that because $W_\lambda(H\alpha)$ is variable (typically at the 20% to 30% level), some "borderline" stars may cross the boundary between the WTTS and TTS classes. Moreover, both because a) the equivalent width of the underlying photospheric Hα absorption line increases from 0.7 Å at M0 to 2.7 Å at G5 (Herbig, Vrba and Rydgren, 1986), and b) for fixed Hα flux, the observed Hα emission line equivalent width will be smaller for stars of higher luminosity, there will be a tendency to classify a larger proportion of earlier-type, more luminous PMS stars as WTTS.

The first goal of our study is to compare the spectral energy distributions of the weak Hα emission stars with TTS in order to examine to what extent the WTTS lack disks as evidenced by measurable IR excesses. We have chosen to examine the WTTS and TTS spectral energy distributions for a sample of PMS stars in the well-studied Taurus-Auriga region. The photometric and spectroscopic properties of the TTS in this region have been catalogued in the extensive surveys by Joy (1945), Herbig and Rao (1972), Rydgren, Strom and Strom (1976), Cohen and Kuhi (1979), Rydgren et al. (1984b), and Herbig and Bell (1988) while the WTTS characteristics have been studied by WBMMV, HVR and Hartmann, Soderblom and Stauffer (1987). *All stars (36 TTS and 47 WTTS) for which optical and near infrared photometry is available from the literature have been included in our discussion.* We list in Table 1 the spectral types and broad band photometry (U (0.35μ) through L (3.5μ) along with their sources, for the WTTS discovered from x-ray searches, proper motion studies, and searches for objects showing Ca II emission but no discernible Hα emission. The photometric measures included in this table represent *mean* values, with the exception of those stars in HRV (denoted by "s" in the "source" column) for which nearly simultaneous optical and near-infrared photometry is available; in these cases, we prefer to adopt an "instantaneous" measure of the spectral energy distribution. In Table 2, we present similar data for the TTS, and for those stars originally classified as TTS, but for

---

1 Note that we include among our WTTS class a few stars classified as "SU" (SU Auriga type) by Herbig and Bell.

which W_λ (Hα) $\leq$ 10 Å, thus making them WTTS by our definition. Again, where nearly simultaneous photometry is available, we list and note (in the "source" column) these instantaneous values. For the convenience of the reader, we also include in Tables 1 and 2, the best available data for stars lacking complete photometric coverage over the range $0.35\mu < \lambda < 3.5\mu$; although listed in these tables, such stars are not included in the discussion which follows.

In Table 3, we list the IRAS[2] fluxes (Jy) or upper limits (italicized entries), along with their estimated 2σ uncertainties derived from examination of one dimensional survey co-adds (ADDSCANS) at the PMS star position listed by Herbig and Bell (1988) for the WTTS; Table 4 presents similar data for the TTS. Where two stars fall within the IRAS beam, we have divided the observed 12μ and 25μ IRAS fluxes in proportion (respectively) to the 10μ and 20μ fluxes measured from the ground (if both are available), and in proportion to the 10μ measurements if 20μ measurements are unavailable; the 60μ and 100μ fluxes have been divided between the two stars in proportion to the longest wavelength ground-based IR measurements available. Strong fluctuations in molecular cloud emission at 60μ and 100μ render many of the listed PMS star fluxes at these wavelengths highly uncertain. Note that we have included for completeness (see Table 5) IRAS fluxes for TTS and WTTS which may not appear in either Tables 1 or 2. No color corrections are applied to the listed fluxes.

In order to derive spectral energy distributions, the observed fluxes must be corrected for interstellar reddening. We assume the (V-R) color to be most representative of the uncontaminated (by spectral veiling) photospheric color, and compute a (V-R) excess from comparison of the observed WTTS and TTS colors and those of *dwarf* standard stars of the same spectral type (Johnson, 1964). A_V is derived by assuming $E(V-R)/A_V = 0.27$ (Johnson, 1968). Reddening-corrected spectral energy distributions are computed by adopting this value of A_V and a standard (van de Hulst 15; Johnson, 1968) interstellar extinction law. We caution that this procedure a) will tend to underestimate reddening for partially veiled TTS, b) does not take into account the possible effects of anomalous extinction or scattering in circumstellar envelopes.

In Figure 1a, we present (for $0.35\mu < \lambda < 12\mu$) the reddening-corrected spectral energy distributions (SEDs) for a sample of TTS chosen to represent the full range of Hα emission strengths characteristic of the class. Figure 1b presents a similar set of SEDs for WTTS. In each case, we also plot the SED for a dwarf[3] standard star of the same spectral type as that adopted for the PMS star; the standard star SEDs have been shifted in order to match the R-band fluxes for the PMS stars.

The results presented in Figure 1 show that:

---

2 The *Infrared Astronomical Satellite* ws developed and operated by the Netherlands Agency for Aerospace Programs (NIVR), the US National Aeronautics and Space Administration (NASA), and the UK Science and Engineering Research Council (SERC).

3 Since the spectral characteristics of the TTS and WTTS are typically closer to those of dwarfs than giants, we choose to effect comparisons of the reddening-corrected spectral energy distributions with those of dwarf standard stars of comparable type (Johnson, 1964); our basic results are not compromised if giant star standards are adopted instead.

- TTS spectral energy distributions exhibit a wide range of infrared characteristics -- from large excesses characterized by broad, slowly declining spectra (Rucinski, 1985; Rydgren and Zak, 1986; Adams, Lada and Shu, 1987; Myers et al., 1987, Bertout, Basri and Bouvier,1988), to small IR excesses which closely follow a Rayleigh-Jeans law for $1\mu < \lambda < 10\mu$;
- WTTS also show a range of IR spectra *whose characteristics overlap those of the TTS* although most show small to modest IR excesses which closely follow a Rayleigh-Jeans law for $1\mu < \lambda < 10\mu$.

For $\lambda \geq 10\mu$, nearly all (35/36) TTS exhibit large excess emission; 14/47 WTTS show detectable mid- to far- infrared excesses (see Tables 3 and 4). *By no means do all WTTS lack IR excesses*. The actual number of PMS stars which have infrared excesses for $\lambda \geq 10\mu$ may be even larger. However, the sensitivity of the IRAS survey is inadquate to measure (or rule out) such excesses for most stars which currently lack mid- and far- IR detections. In Figure 2, we present the SEDs ($0.35\mu < \lambda \leq 100\mu$) for 7 WTTS and FX Tau (a "typical" TTS). While IP Tau, HDE 283447 (≡V773 Tau), and V836 Tau (WK x-ray 3) show spectral energy distributions quite similar to that of FX Tau, the other cases ilustrated are more representative in showing small near-IR-excesses sometimes coupled with relatively large far-IR- excesses.

Until more sensitive mid- and far- infrared measurements are available, we must depend upon near-IR measurements to provide the basis for a statistical comparison of the infrared properties of WTTS and TTS. An appreciation of the distribution of IR excesses among PMS stars of each type can be gleaned from Figure 3, in which we plot histograms depicting the frequency distribution of the parameter $\Delta K \equiv \log \{F_{2.2\mu}\ (PMS)/F_{2.2\mu}\ (standard)\}$. Values of this parameter are listed for each star in Tables 1 and 2, with the exception of heavily-veiled continuum + emission TTS (e.g. HL Tau, DG Tau). The shaded region in Figure 3 provides an indication of the frequency distribution of ΔK for those WTTS originally classified as "naked" (WBMMV). The observational uncertainties in the derived ΔK values (see section 3) are expected to be less than 0.05 dex. Hence, we consider all PMS stars with $\Delta K \geq 0.10$ dex to have significant near-IR excesses. The small number of objects (see Figure 3 and Tables 1 and 2) with computed ΔK values in the range from -0.10 to 0.0 confirms our error and significance estimates.

We conclude from Figure 3 that a) 36% of the WTTS show infrared excesses at K (2.2μ), $\Delta K \geq 0.10$ dex, and b) that while the distribution for the WTTS peaks toward smaller values of ΔK than for the TTS, there is significant overlap in the K distributions for the two classes of low mass PMS stars. *The results presented in figures 1 through 3 suggest that WTTS (and by implication NTTS) and TTS show a continuous range in IR characteristics, and should not on this basis, be considered distinct groups of solar-type PMS stars.*

3. Discussion

3.1 Possible Causes for the Observed Infrared Excesses in WTTS

The results presented in the previous section demonstrate that 36% of WTTS have significant near-IR excesses, $\Delta K \geq 0.10$. We examine below several possible causes for these excesses:

- Combined radiation from a WTTS photosphere and a large cool spot. We computed ΔK assuming that the WTTS SED results from the combined contribution of a spot (T = 2500°K) and a photosphere (T = 4000°K). With the extreme assumption of 50% coverage by the spot,

$\Delta K = 0.07$.

- Excess radiation produced in a "deep" chromosphere. Here, the IR excess is produced in the lower regions of a chromosphere in which the temperature rise begins at $\tau(5000\ \text{Å}) \sim 0.1$ to 0.01 (Calvet, Basri and Kuhi, 1984). In the most extreme model computed by Calvet et al., $\Delta K = 0.05$. However even for this modest predicted IR excess, a corresponding ultraviolet excess, $\Delta U > 1.0$ is calculated -- a result which is inconsistent with observations of WTTS (WBMMV). We should note, however, that chromospheric model parameters have not been optimized to produce maximum IR- and minimum ultraviolet- excesses.

- Non-simultaneity of photometry. WTTS are known to exhibit moderate variations at V (ΔV ~0.1 to 0.7 mag) and smaller variations at longer wavelengths. In most cases, optical and near infrared photometry is not simultaneous, and it is therefore possible that the observed IR excesses owe their origin in part to distortions of WTTS spectral energy distributions wrought by non-simultaneous photometry. The effects of non-simultaneous observations are reduced by adopting mean values of colors and magnitudes. A comparison of the ΔK values computed from mean and simultaneous photometry shows $\Delta K < 0.05$ dex in all cases. Hence, we cannot attribute a significant fraction of the IR excesses in WTTS to non-simultaneity in the observations.

- Errors in the adopted visual extinction and spectral types. As noted in section 2, values of A_V are derived from the adopted spectral types, the observed (V-R) colors and the (V-R) colors for dwarf standard stars of the corresponding spectral type. For a given spectral type, errors in our visual extinction estimates from the combined uncertainties in the photometry and the degree of spectral veiling should not exceed 0.2 mag; the corresponding uncertainty in ΔK is 0.06 dex. The spectral types are almost certainly established to within a subclass. Adopting a spectral type that differs from the nominal published value will change the derived A_V value for a fixed value of (V-R); in combination, the change in type and A_V produces a change of <0.02 dex in ΔK over the range of types included in our sample. Hence, errors in spectral type and visual extinction cannot account for the derived ΔK values for $K > 0.1$ dex.

- Red companion stars. In Figure 4, we present a spectral energy distribution corresponding to the *difference* between that observed for V827 Tau and a standard star of the same type; as before, the R-band flux of the standard star and V827 Tau were matched. The resulting IR excess can be fit by a black body of temperature, T =2430 K and luminosity 0.29 $L_\odot$. The near-IR excesses for a number of WTTS are quite similar to that for V827 Tau and are well fit (over the wavelength range 1.0μ to 3.5μ) by black-bodies with *temperatures* in a relatively narrow range between 2000 to 2500 K; the luminosity excesses fall in the range $0.05 < L/L_\odot < 0.35$. As discussed in section 3.2, the number of stars which show significant near-IR excesses decreases with age; for ages $t > 10^7$ yr, only 10% of PMS stars exhibit observable excesses. Low mass companions (and substellar companions in particular) can account for the properties of the observed near -IR excesses for many WTTS: a) nearly constant temperature, and b) decreasing prevalence with age. Models of the time dependence of the effective temperature of substellar brown dwarfs (Nelson, Rappaport and Joss, 1985; D'Antona and Mazzitelli, 1985; Lunine et al., 1988) predict that brown dwarfs with ages between 10^5 and 10^7 years have effective temperatures between 2000 K and 3000 K with very little dependence on mass ($0.02 < M/M_\odot < 0.08$). Further, for any given mass, the effective temperature remains relatively constant within this age range, while the luminosity decreases

steadily as the brown dwarf radius decreases. Although these properties are compatible with the observed near-IR excesses in many WTTS, the luminosity excesses in most cases exceed the maximum luminosities that the models predict for brown dwarfs ($<0.1\ L_{\odot}$). Furthermore, since 36% of WTTS show such excesses, of which only about 10% survive beyond an age of 10^7 yr (section 3.2), we would predict a substantial population of substellar objects, which surveys of older main-sequence stars have yet to detect (Campbell et al., 1988; Skrutskie, Forrest, and Shure, 1988). Nevertheless, low mass stars or substellar objects could provide the excess luminosity in some WTTS, particularly those still possessing an excess at a relatively late age. The presence or absence of such companions should be established by careful near-IR imaging observations and accurate radial velocity studies of WTTS.

- circumstellar dust. The similarity of the SEDs for WTTS such as V773 Tau (HDE 283447) and IP Tau (LkCa 8) to those of typical TTS, suggests a *dust (and by inference, a disk) origin for the IR excess* in these cases and others (see Figure 2 and Table 3) for which significant mid- and far-IR excesses are observed. For most of the WTTS with significant values of ΔK ($\Delta K \geq 0.10$) but no *as yet detected mid- and far- IR emission*, the relatively high temperatures (T ~2500 K) derived from the near infrared excess radiation forces us to conclude that the emitting dust grains must be small and highly refractory. Moreover, the relative constancy of the temperature (T ~2500 K) of the near IR excesses suggests that the observed radiation must arise from the inner edge of a disk at the point where high temperatures destroy dust ($d < 0.01$ AU for a star of $1\ L_{\odot}$.) The characteristic temperature of the excesses then represents the destruction temperature for the most refractory materials in the circumstellar nebula and is consistent with the highest condensation temperatures predicted for refractory grains in the solar nebula (Lewis, 1972).

Since the luminosity excesses for many WTTS amount to 10% to 20% of the stellar luminosity, such dust must be embedded within a structure which subtends at least 10% to 20% of the solid angle seen from the star (if the flux arises from reprocessed radiation). This argues that *WTTS with relatively large luminosity excesses* must be surrounded by optically thick, massive disks (analogous to those thought to surround TTS), rather than by tenuous disks, generated for example by the collision of planetesimals and subsequent infall owing to Poynting-Robertson drag.

While several of the factors noted above may contribute to producing small ($\Delta K < 0.10$) near-infrared excesses, we believe that emission from circumstellar dust provides the most appealing explantion for the observed excesses in PMS stars with $\Delta K \geq 0.10$. Evidence that dust is located in an optically thick circumstellar *disk* for at least one WTTS is provided by high spectral resolution observations of [O I] emission. Forbidden line emission ([O I] λ 6300 Å, and [S II] λ 6717, 6731 Å) is associated with the outer (r ~ 10 to 100 AU) regions of winds driven by PMS stars. However, in 15 TTS studied to date, only blue-shifted emission is observed, thus requiring the presence of structures -- circumstellar disks -- whose opacity and dimension is sufficient to obscure the receding part of the outflowing gas revealed by the forbidden lines (Edwards et al., 1987; Appenzeller et al., 1984). The [O I] profile measured for the WTTS V 773 Tau from spectra obtained with the Echelle/CCD combination at KPNO, shows a pronouced asymmetry: the blue component is broad and extends to a velocity ~100km/sec blueward of the stellar systemic velocity; no corresponding emission at these velocities is seen in the red-shifted wings of the profile (a detailed discussion of these results will be presented elsewhere; Edwards

et al., 1989 in preparation). We conclude that, as is the case for most TTS, a disk occults the receding portion of the wind traced by [O I]. *Extrapolating the evidence for V773 Tau, we conclude that the 36% of WTTS which have measurable near-IR exceses ($\Delta K \geq 0.10$ dex) are surrounded by circumstellar disks.*

3.2 The Frequency Distribution of IR Excesses Among PMS Stars

We next wish to examine the frequency distribution of IR excesses for all solar-type PMS stars as a function of time. As a first step, we must locate TTS and WTTS in the HR diagram. Effective temperatures for each star listed in Tables 1 and 2 were estimated from the observed spectral type, and the relationship between type and effective temperature adopted by Cohen and Kuhi (1979). We expect the spectral types to be accurate to within one spectral subclass; the corresponding uncertainty in log T_{eff} is approximately ±0.03 dex.

Stellar luminosities, L_*, were computed by demanding that the SED of a luminosity class V star of a spectral type corresponding to that of the PMS star pass through the reddening-corrected SED at R ($\lambda = 0.65\mu$). This procedure assumes a) that the observed infrared excesses derive from accretion or reprocessing in a circumstellar disk (and therefore should not be included in estimating the *stellar* luminosity), and b) that the photospheric luminosity of the star dominates the boundary layer and disk accretion luminosity at R. To the extent that luminosity deriving directly or indirectly from accretion contributes to the observed R-band flux, this luminosity estimate represents an *upper limit* to L_* (see also K. Strom et al., 1988; Cabrit et al., 1989). We list in the final columns of Tables 1 and 2, L_*, along with L_{tot}, the *total* luminosity, calculated by a) integrating the spectral energy distribution from 0.35μ to the longest wavelength for which observed fluxes are available, and b) adding a correction for long wavelength emission according to the precept outlined in Cohen (1973). The uncertainties in log L_* are difficult to estimate; they will reflect a) errors in the adopted interstellar reddening and spectral type, b) the unknown contribution of boundary layer emission to the R-band flux, c) the unknown orientation of the circumstellar disk relative to the line of sight, and d) uncertainties regarding the magnitude and effects of *circumstellar* reddening and scattering. For stars with small luminosity excesses, $\Delta L \equiv (L_{tot} - L_*)/L_* < 0.5$, the uncertainties in L_* should not exceed ±0.1 dex; the corresponding uncertainty in age, log t, for stars on their Hayashi tracks should be ±0.12 dex. For $\Delta L >> 0.5$, the uncertainties in log L_* and log t will be larger, perhaps as great as ±0.3 dex, and ±0.35 dex respectively.

In Figure 5, we present the HR diagram (log L_* versus log T_{eff}) for the WTTS and TTS in Taurus-Auriga. Superposed on the diagrams are the evolutionary tracks and isochrones of VandenBerg et al. (1983) for stars of mass $M \leq 1.0\ M_\odot$, and those published by Cohen and Kuhi (1979) for stars of higher mass. Those objects with *large* infrared excesses, $\Delta K > 0.30$ dex, are plotted as filled circles, whereas those with smaller 2μ excesses are plotted as open circles. In Figure 6, we present a similar plot, but sorted according to Hα equivalent width; WTTS are plotted as open circles, while TTS are plotted as filled circles. Although the uncertainties in the ages of individual stars can be as large as ±0.3 dex, we can draw the following qualitative conclusions from these figures:

- (1) both large and small near-infrared excesses are found among stars younger than 3×10^6 yr;

- (2) the fraction of PMS stars with large near-infrared excesses decreases significantly with increasing age;
- (3) the fraction of PMS stars with $W_\lambda(H\alpha) > 10$ Å decreases significantly with increasing age; 32/55 PMS stars with $t \leq 3x10^6$ yr show W_λ (Hα) > 10 Å, while for $t > 3x10^6$ yr, the fraction is 7/29.

These results suggest an *evolutionary decrease* in both Hα emission strength and infrared excess among solar type PMS stars. Thus, those PMS stars which are initially TTS must eventually lose the strong Hα emission and IR excess characteristic of TTS, and become "post T Tauri stars" (Herbig, 1978).

Points (1) and (2) are illustrated in a slightly different way in Figure 7, in which we plot the frequency distribution of ΔK for stars with ages a) $t \leq 3x10^6$ yr and b) $t > 3x10^6$ yr. The fraction of PMS stars with measurable near-infrared decreases with time; nearly 60% of PMS stars with ages younger than $3x10^6$ yr show $\Delta K \geq 0.10$ dex, while only 40% of older PMS stars show excesses this large. For $\Delta K \geq 0.30$ dex the corresponding percentages are 33% and 15%. Note that only 10% of PMS stars with $t > 10^7$ yr have $\Delta K \geq 0.10$ dex.

If near-IR excesses arise in the warm inner regions of circumstellar disks, then the results presented in Figures 5 and 7 suggest that

- while almost 60% of solar-type PMS with $t \leq 3x10^6$ yr have disks, ~ 40% of such *young* stars must be surrounded by disks with masses too small to detect with certainty from near-infrared observations. These stars could represent objects a) born without disks, or b) objects in which the mass in distributed matter is small, possibly following removal of such material either by rapid accretion, tidal disruption or planet-building.
- Because nearly 60% of solar type PMS stars with ages $t > 3 \times 10^6$ yr lack disks detectable in the near-IR, we conclude that the massive, optically thick disks which initially surround some PMS stars must *evolve*, and become more tenuous.

If *all* solar-type stars form massive (0.01 to 0.1 $M_\odot$) disks, then by $t = 3x10^6$ yr, 40% of PMS stars (the fraction with $\Delta K < 0.10$ dex), are surrounded by remnant disks too tenuous to detect. Because fewer than 10% of PMS stars *older* than 10^7 yr show $\Delta K \geq 0.10$ dex, the disks surrounding all but 10% of PMS stars must have completed their evolution by this time. The majority of disks must therefore have evolutionary timescales in the range $3x10^6$ to 10^7 yr. This range represents the best astrophysical constraint on the likely timescale for planet-building available at present.

It is important to note that the disk frequency statistics inferred from ΔK *exclude* several PMS stars which show small or undetectable near IR excesses, but relatively strong mid- to far- IR excesses (see figure 2); these objects may represent PMS stars surrounded by disks which are optically thin at small radial distances from the star (and therefore produce too little near-IR radiation to be detected), but optically thick at distances r > 1 AU.

4. Conclusions

We have compared the the spectral energy distributions characterizing two sets of pre-main sequence (PMS) stars in Taurus-Auriga: 36 T Tauri stars (TTS) with Hα emission line equivalent

widths $W_\lambda(H\alpha) > 10$ Å, and 47 "weak line" T Tauri stars (WTTS) with $W_\lambda(H\alpha) \leq 10$ Å; the latter group includes 35 stars originally classified as "naked" Tauri stars by Walter (1987). Both WTTS and TTS show significant infrared excesses; 84% of the TTS and 36% of the WTTS have observed 2.2μ fluxes which exceed the expected photospheric fluxes by 0.1 dex. 35/36 TTS and 14/47 WTTS also exhibit infrared excesses at $\lambda \geq 10\mu$. *We conclude that the infrared properties of WTTS and TTS are not distinct, but rather overlap significantly.* In this respect, we differ with Walter et al. (1988) who suggest that most if not all WTTS/NTTS lack infrared excesses.

Emission from dust embedded in circumstellar disks surrounding WTTS and NTTS is the most likely explanation for the near- and mid- infrared excesses observed for these PMS stars. This conclusion is strengthened by observations of [O I] line profiles in a large sample of TTS (Edwards et al., 1987) and in one WTTS discussed here. These profiles show broad, blue-shifted emission which is associated with the approaching component of a stellar wind; the receding component must be obscured by an optically thick circumstellar disk.

The fraction of solar type PMS stars with significant near-infrared excesses ($\Delta K \geq 0.10$ dex) decreases with time. Nearly 60% of PMS stars with ages younger, and only 40% of stars older than 3×10^6 yr show such excesses; just 10% of our sample with $t > 10^7$ years have $\Delta K \geq 0.10$ dex. If excess near-IR emission arises in the warm, inner regions of circumstellar disks, then the timescales for disk evolution, from massive, optically thick disks to low mass, tenuous disks must range from 3×10^6 yr to 10^7 yr. This range represents the best available astrophysical constraint on the likely timescale for planet building.

It is worth noting that the above statistics obtain for all *known* TTS and WTTS in Taurus-Auriga for which adequate photometry is available. However, the areas searched for WTTS and TTS differ, as do the effective sensitivity limits of the surveys. Thus, our conclusions regarding the fraction of solar type PMS stars which may be surrounded by disks could be revised in the light of more complete searches for PMS stars. However, our qualitative conclusions regarding disk evolution and approximate timescales are unlikely to be vitiated.

The small subset of WTTS which show small near-IR excesses, but apparently significant mid- and far- IR excesses merit further scrutiny. Such objects may represent PMS stars in which the *inner disk regions ($r < 0.1$ AU) are relatively devoid of distributed matter*, while the outer disk regions still contain substantial amounts of dust. More sensitive mid-infrared, sub-mm and mm-continuum (e.g. Beckwith et al., 1989) observations of PMS stars with $\Delta K < 0.10$ dex may provide the statistical basis for learning whether this phenomenon is evolutionary and suggestive of different timescales for "clearing" as a function of radial distance from the star.

More sensitive searches for low mass, tenuous disks associated with PMS stars are now possible. With integration times of ~2 hours on a 2- to 3- meter class telescope, it should be possible to improve upon IRAS limits at 12μ by about a factor of 5. For many of the brighter PMS stars in Taurus-Auriga a limiting flux of 0.02 Jy will rule out any excess emission above the Rayleigh-Jeans extrapolation of the stellar photospheric flux. Such observations, combined with mm-continuum surveys currently underway (Beckwith et al., 1989), will provide the basis for a more thorough discussion of the frequency of disk formation around young solar-type PMS stars, and the timescale for disk evolution.

Hα emission also appears to decrease with increasing age. Of 55 PMS stars with $t \leq 3 \times 10^6$ yr, 32 are TTS by our definition, with W_λ (Hα) > 10 Å; only 7/29 with $t > 3 \times 10^6$ yr show

$W_\lambda(H\alpha)$ this large. These statistics, combined with the clear indication of a decrease of IR excess with advancing age, suggest that at least some WTTS must represent the evolutionary descendents of TTS: "post T Tauri stars" (Herbig, 1978; HVR). It would clearly be of considerable value to examine critically other observable characteristics, such as ultraviolet excess, spectral veiling, permitted and forbidden line emission as a next step in defining the evolution of PMS disks, boundary layers, chromospheres and winds.

5. Acknowledgements

This work was supported in part by grants from the National Science Foundation, the NASA Astrophysics Data Program (IRAS), and the NASA Planetary Program. We thank Lee Hartmann and Scott Kenyon for their critical comments.

References

Adams,F., Lada,C.J. and Shu,F. 1987, Ap.J. **312**, 788.

Appenzeller,I., Jankovics,I. and Ostreicher,R. 1984, Astr. Ap. **141**, 108.

Beckwith,S. et al., 1989, Ap.J. (in preparation).

Bertout,C., Basri,G. and Bouvier, J. 1988, Ap.J. **330**, 350.

Bouvier, J., Bertout,C. and Bouchet,P. 1986, Astron. Astrophys. **158**, 149.

Bouvier,J., Bertout,C., Benz,W. and Mayor,M. 1986, Astron. Astrophys. **165**, 110.

Bouvier,J. and Bertout,C. 1988, Astron. Astrophys. (in press).

Cabrit,S., Edwards,S.,Strom,S.E. and Strom,K.M. 1989, A.J.(in preparation)

Calvet,N., Basri,G. and Kuhi,L.V. 1984, Ap.J. **277**, 725.

Campbell,B., Persson,S.E., Strom,S.E., Strom,K.M. and Grasdalen,G.L. 1988, AJ **95**, 1173 .

Campbell,B., Walker, G.A.H. and Yang,S. 1988, Ap.J. (in press).

Cohen, M. 1973, MNRAS, **164**, 395.

Cohen,M. and Kuhi,L.V. 1979, Ap.J. Suppl. **41**, 743.

Cram,L. 1979, Ap.J. **234**, 949.

D'Antona,F. and Mazzitelli,I. 1985, Ap.J. **296**, 502.

Dyck, H.M., Simon,T. and Zuckerman, B. 1982, Ap.J. **270**, L27.

Edwards,S., Cabrit,S., Strom,S.E., Heyer,I., Strom,K.M. and Anderson,E. 1987, Ap.J. **321**,473.

Feigelson,E.D., Jackson,J.M.,Mathieu,R.D.,Myers,P.C. and Walter,F.M. 1987, A.J. **94**,1251.

Feigelson,E.D. and Kriss,G.A. 1981, Ap.J. **248**,L35.

Finzenzeller, U. and Basri,B. 1987, Ap.J. **823**, 823.

Hartmann,L.W. and Kenyon,S.J. 1987a, Ap.J., **312**,243.

Hartmann,L.W. and Kenyon,S.J. 1987b, Ap.J., **322**,393.

Hartmann,L.W., Soderblom,D.R. and Stauffer,J.R. 1987, AJ **93**, 907.

Hartmann,L.W. and Raymond, J. 1988, Ap.J. (submitted).

Herbig,G.H. and Rao,N.K. 1972, Ap.J. **174**, 401.

Herbig,G.H. 1978, in *Problems of Physics and the Evolution of the Universe*, edited by L.V. Mirzoyan (Armenian Academy of Science, Yerevan), p. 171.

Herbig, G.H., Vrba,F.J. and Rydgren, A.E. 1986, A.J. **91**,575.(HVR)

Herbig, G.H. and Bell,K.R. 1988, Lick Observatory Bulletin No.1111.

Johnson, H.L. 1964, Ann. Rev. Astron. Astrophys. **4**, 193.

Johnson, H.L. 1968, in *Stars and Stellar Systems: The Interstellar Medium* ed. by B.M. Middlehurst and L.H. Aller, The University of Chicago Press.

Jones,B.F. and Herbig,G.H. 1979, A.J. **84**, 1872.

Joy,A. 1945, Ap.J. **102**, 168.

Kenyon,S.J. and Hartmann,L.W. 1987, Ap.J. **323**, 714.

Lewis, J.S. 1972, Earth Planet. Sci. Lett. **15**, 286.

Lunine,J.I., Hubbard,W.B., Burrows,A.S., Wang, Y.-P., and Garlow,K. 1988, Ap.J. (submitted).

Lynden-Bell,D. and Pringle,J. 1974, MNRAS, **168**, 603.

Myers,P., Fuller,G.A., Mathieu,R.D., Beichman,C.A., Benson,P.J., Schild,R.E. and Emerson,J.P. 1987, Ap.J. **319**, 340.

Nelson,L.A., Rappaport,S. and Joss,P.C. 1985, Nature, **316**, 42.

Rucinski, S. 1985, A.J. **90**, 2321.

Rydgren,A.E., Strom,S.E. and Strom,K.M. 1976, Ap.J. Suppl. **30**, 307.

Rydgren,A.E. and Vrba,F.J. 1983, Ap.J. **267**,191.

Rydgren,A.E., Zak,D.S., Vrba,F.J., Chugainov,P.F. and Zajtseva,G.U. 1984a, A.J. **89**, 1015.

Rydgren,A.E., Schmelz,J.T., Zak,D.S. and Vrba,F.J. 1984b, Pub. U.S.N.O. XXV, Part I.

Rydgren,A.E. and Zak,D.S. 1986, Pub. A.S.P. **99**, 141.

Skrutskie,M.F., Forrest,W.J. and Shure,M.A. 1986, in *Proceedings of the Workshop on the Astrophysics of Brown Dwarfs* ed. M. Kafatos (Cambridge: Cambridge Univ. Press).

Strom,S.E. 1983, Rev. Mexicana Astr. Ap. **7**, 201.

Strom,K.M., Strom,S.E., Kenyon,S.J. and Hartmann,L.W. 1988, A.J. **95**, 534.

Strom,S.E., Strom,K.M. and Edwards,S. 1988 in *NATO Advanced Study Institute: Galactic and Extragalactic Star Formation* ed. by R. Pudritz and M. Fich (Dordrecht: Kluwer Academic Publishing).

VandenBerg, D.A., Hartwick,F.A., Dawson,P. and Alexander,D.R. 1983, Ap.J. **266**, 747.

Vrba,F.J., Rydgren,A.E., Chugainov,P.F., Shakovskaya,N.I. and Zak,D.S. 1986, Ap.J. **306**, 199.

Vrba,F.J., Rydgren,A.E., Chugainov,P.F., Shakovskaya,N.I. and Weaver,W.B. 1989, Ap.J. (in press).

Walter,F.M. 1987, Pub. A.S.P. **99**, 31.

Walter,F.M., Brown,A., Mathieu,R.D., Myers,P.C. and Vrba,F.J. 1988, A.J., **96**, 297.

Walter,F.M. and Kuhi,L.V. 1981, Ap.J. **250**,254.

Zappala, R.R. 1972, Ap.J. **172**, 57.

Figure Captions

Figure 1a: A plot of the reddening-corrected spectral energy distributions ($0.35\mu < \lambda \leq 12\mu$) for a sample of T Tauri stars (open circles) chosen to represent the full range of Hα emission strengths characteristic of the class. Also included for each star is the spectral energy distribution of a dwarf standard star (filled triangles) of a spectral type corresponding to that of the TTS. The flux of the TTS and the standard star have been forced to agree at R (0.65μ).

Figure 1b: Same as Figure 1a except for WTTS (pre-main sequence stars with Hα emission equivalent widths, $W_\lambda(H\alpha) \leq 10$ Å).

Figure 2: A plot of the reddening-corrected spectral energy distribution ($0.35\mu < \lambda \leq 100\mu$) for 7 WTTS and the T Tauri star, FX Tau; the observed points for the WTTS and FX Tau are plotted as open circles. Also plotted are the spectral energy distributions of dwarf standard stars (filled triangles) of spectral types corresponding to those of the WTTS, and that of FX Tau. The fluxes of the WTTS and FX Tau and those of the standard stars have been forced to agree at R (0.65μ). Note the similarity of the spectral energy distributions for FX Tau and the WTTS HDE 283447 (≡V 773 Tau), IP Tau, and V 836 Tau. Note as well the small *near*-infrared excess and relatively large mid- to far- infrared excess for the remaining WTTS. The case of SAO 76411A in particular, suggests an IR excess which may have its origin in a circumstellar disk in which the optical depth of emitting material in the inner disk is small, while that in the outer disk is large.

Figure 3: The frequency distribution of the quantity $\Delta K \equiv \log\{F_{2.2\mu}(PMS)/F_{2.2\mu}(standard)\}$, the 2.2μ infrared excess, for WTTS (top) and TTS (bottom). The shaded region in the top panel represents the domain occupied by WTTS originally classified as "naked" TTS (Walter et al., 1988). Note that a) 36% of the WTTS show excesses, $\Delta K \geq 0.10$ dex, and b) that while the distribution for the WTTS peaks toward smaller values of ΔK, there is significant overlap in the two distributions. It does not appear as if WTTS (which are dominated in number by "naked" TTS; Walter, 1987) lack infrared excesses.

Figure 4: A plot of the *difference* between the reddening-corrected spectral energy distribution for V827 Tau and that of a standard star of the same spectral type. The infrared excess of V827 Tau appears tolerably well fit by a black body of T ~2430 K. The luminosity of this excess component is $\sim 0.29 L_\odot$. The near-IR excesses of a significant number of WTTS appear quite similar to that of V827 Tau.

Figure 5: An HR diagram for all 83 PMS stars in Taurus-Auriga for which adequate optical and infrared photometry is available. Plotted in this diagram are effective temperatures derived from the absorption line spectral types and *photospheric* luminosities computed as described in the text. Stars with $\Delta K \geq 0.30$ dex are plotted as filled circles, while those with smaller IR excesses are indicated with open circles. Superposed are the PMS tracks computed by Vanden Berg for stars with $M \leq 1.0\ M_\odot$, and those published by Cohen and Kuhi (1979) for higher mass stars; the isochrones for the lower mass stars correspond (upper right to lower left) to 0.1,0.3,1.0,3.0,10.0 $\times 10^6$ yr. The 3×10^6 yr isochrone plotted by Cohen and Kuhi (1979) for higher mass stars is also shown.

Figure 6: Same as Figure 5 except that filled circles represent PMS stars with $W_\lambda(H\alpha) > 10$ Å, while open circles represent stars with smaller Hα equivalent widths.

Figure 7: The frequency distribution of the near-infrared excess, ΔK (see text) for stars with ages $t > 3x10^6$ yr and $t \leq 3x10^6$ yr. Note that a) nearly 60% of young PMS stars have measurable ($\Delta K > 0.10$) near-infrared excesses, and b) that the fraction of PMS stars with such excesses decreases for ages $t >> 3x10^6$ yr. If near-IR excesses derive from emitting dust embedded in massive, optically thick circumstellar disks surrounding PMS stars, then the fraction of stars surrounded by such disks must decrease with time.

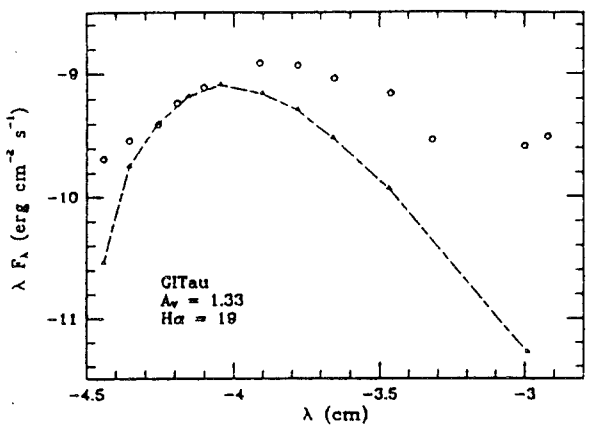
GITau
A_V = 1.33
Hα = 19
λ F_λ (erg cm^{-2} s^{-1})
λ (cm)

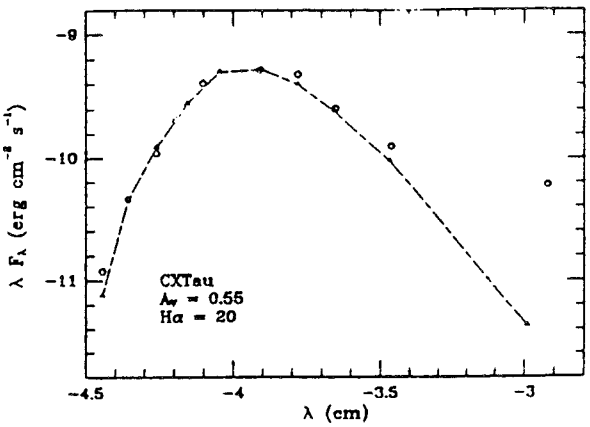
CXTau
A_V = 0.55
Hα = 20
λ F_λ (erg cm^{-2} s^{-1})
λ (cm)

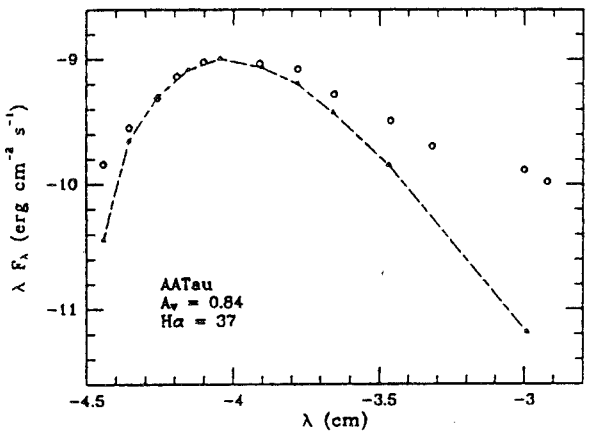
AATau
A_V = 0.84
Hα = 37
λ F_λ (erg cm^{-2} s^{-1})
λ (cm)

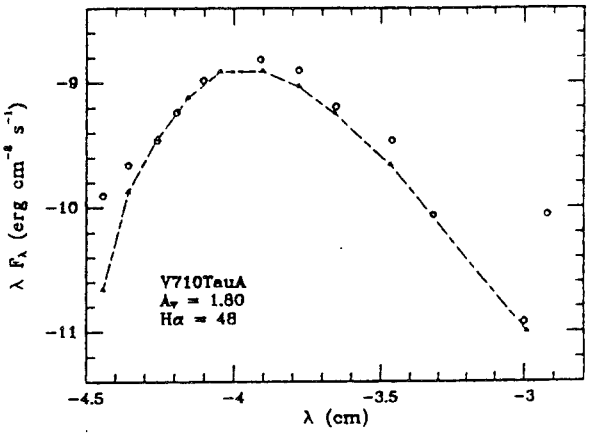
V710TauA
A_V = 1.80
Hα = 48
λ F_λ (erg cm^{-2} s^{-1})
λ (cm)

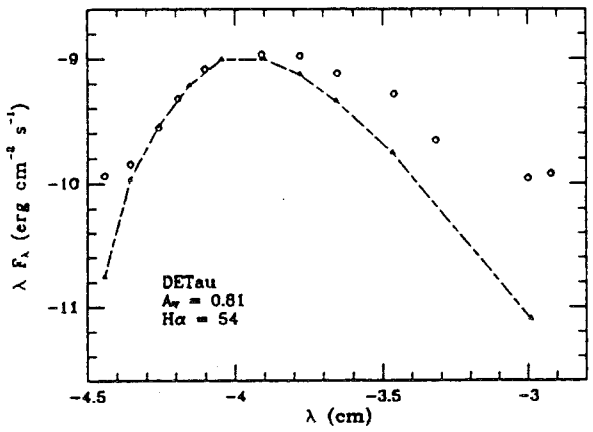
DETau
A_V = 0.81
Hα = 54
λ F_λ (erg cm^{-2} s^{-1})
λ (cm)

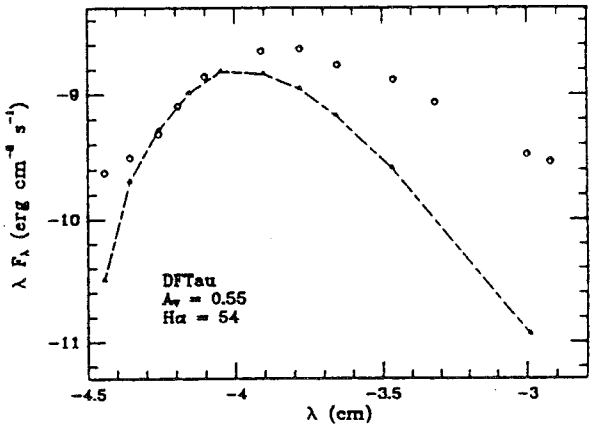
DFTau
A_V = 0.55
Hα = 54
λ F_λ (erg cm^{-2} s^{-1})
λ (cm)

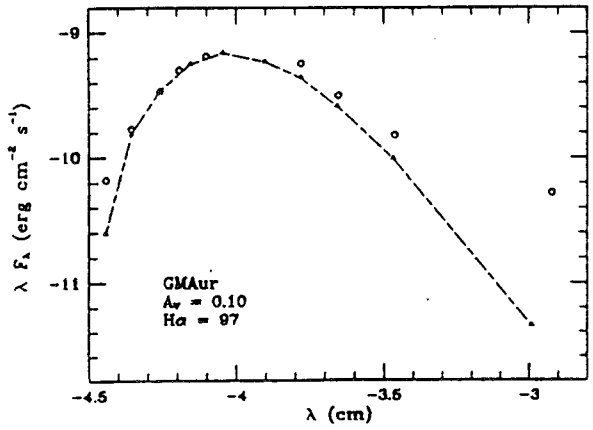
GMAur
A_V = 0.10
Hα = 97
λ F_λ (erg cm^{-2} s^{-1})
λ (cm)

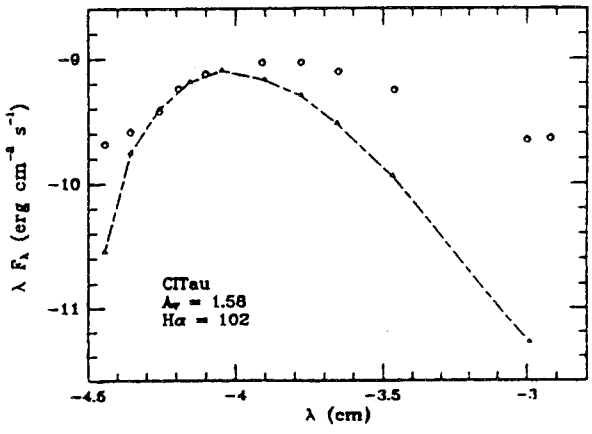
CITau
A_V = 1.58
Hα = 102
λ F_λ (erg cm^{-2} s^{-1})
λ (cm)

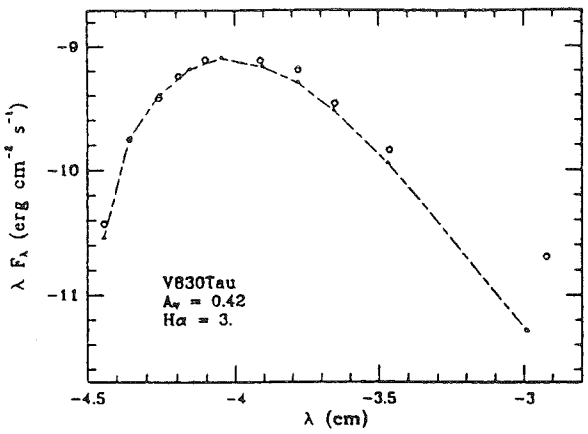
V830Tau
A_V = 0.42
Hα = 3.
λ (cm)
λ F_λ (erg cm^{-2} s^{-1})

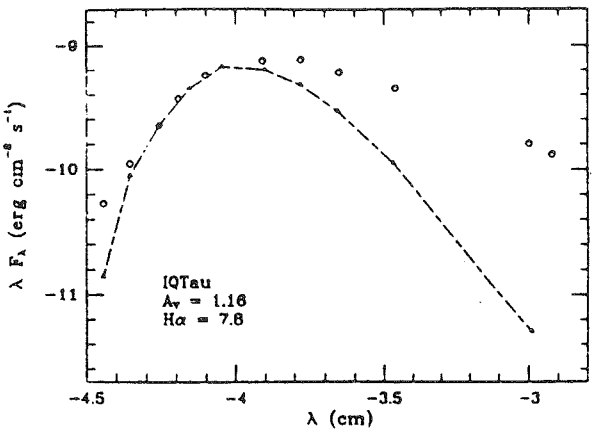
IQTau
A_V = 1.16
Hα = 7.8
λ (cm)
λ F_λ (erg cm^{-2} s^{-1})

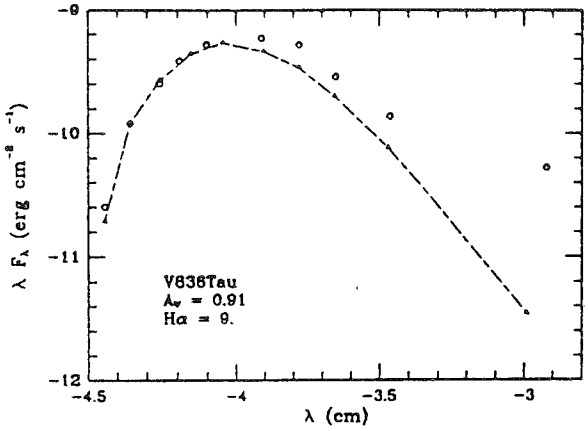
V836Tau
A_V = 0.91
Hα = 9.
λ (cm)
λ F_λ (erg cm^{-2} s^{-1})

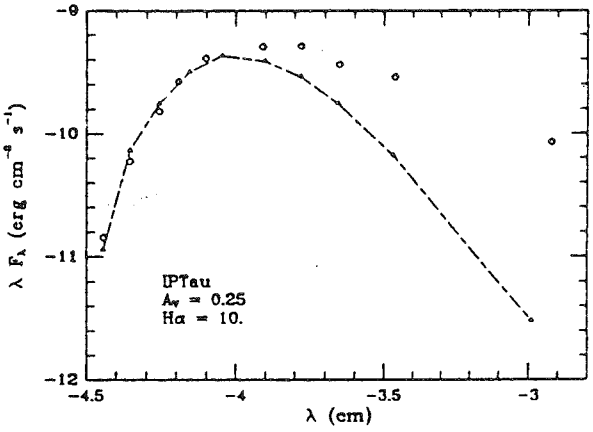
IPTau
A_V = 0.25
Hα = 10.
λ (cm)
λ F_λ (erg cm^{-2} s^{-1})

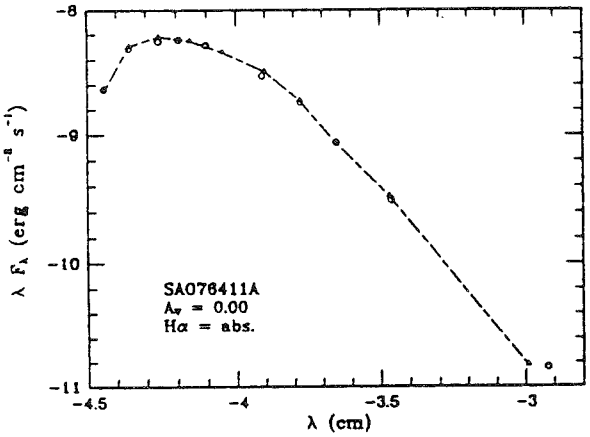
SA076411A
A_V = 0.00
Hα = abs.
λ (cm)
λ F_λ (erg cm^{-2} s^{-1})

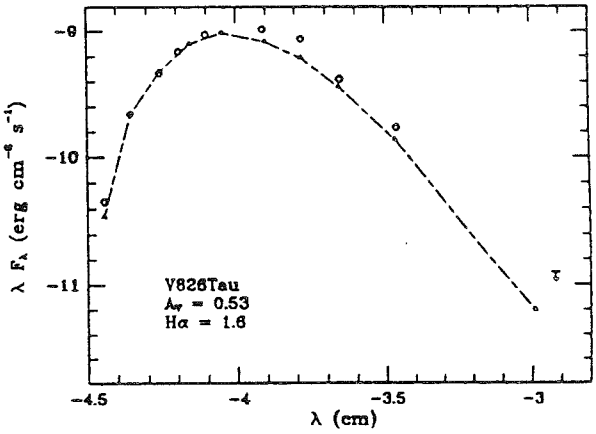
V826Tau
A_V = 0.53
Hα = 1.6
λ (cm)
λ F_λ (erg cm^{-2} s^{-1})

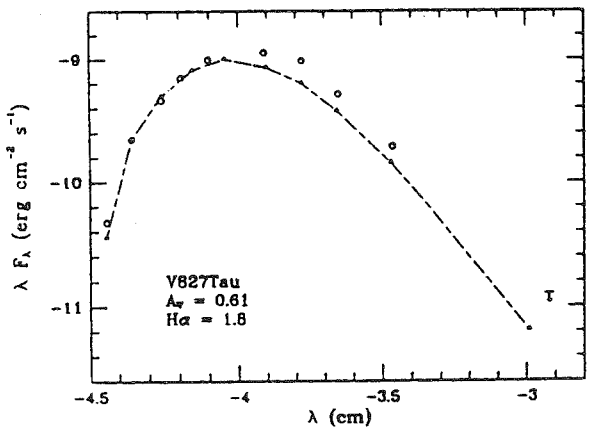
V827Tau
A_V = 0.61
Hα = 1.8
λ (cm)
λ F_λ (erg cm^{-2} s^{-1})

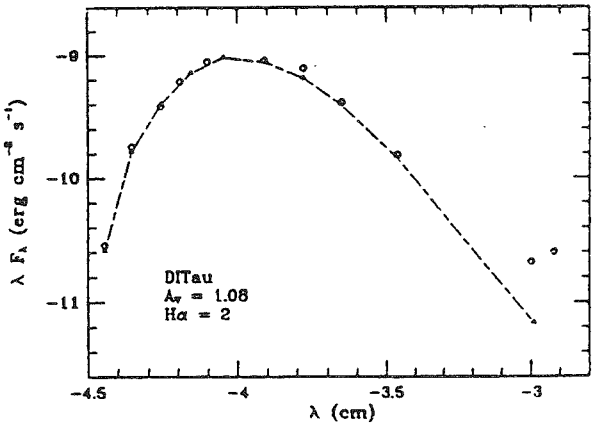
DITau
A_V = 1.08
Hα = 2
λ (cm)
λ F_λ (erg cm^{-2} s^{-1})

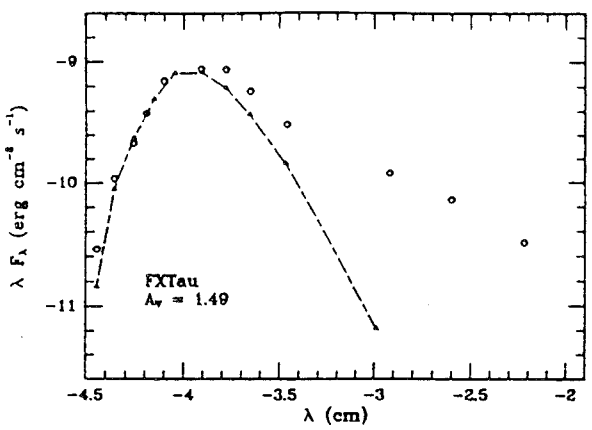
FXTau
A_V = 1.49
λ $F_λ$ (erg cm^{-2} s^{-1})
λ (cm)

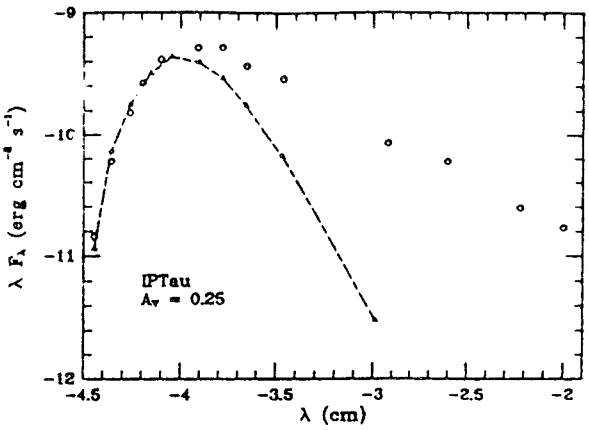
IPTau
A_V = 0.25
λ $F_λ$ (erg cm^{-2} s^{-1})
λ (cm)

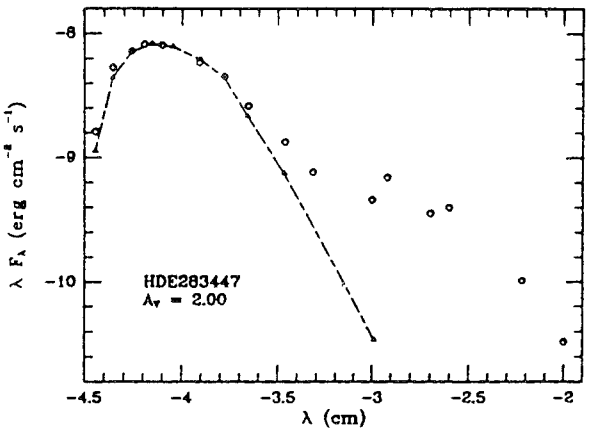
HDE283447
A_V = 2.00
λ $F_λ$ (erg cm^{-2} s^{-1})
λ (cm)

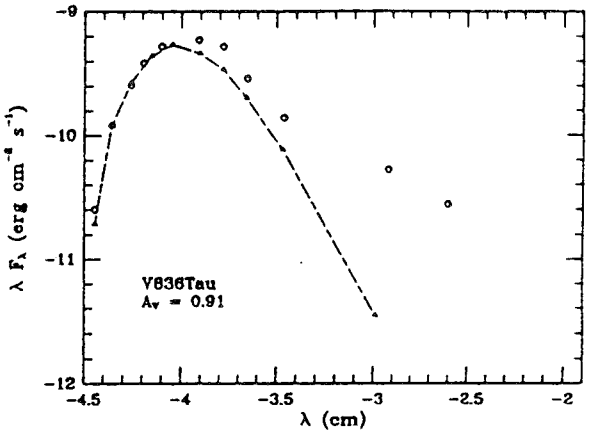
V836Tau
A_V = 0.91
λ $F_λ$ (erg cm^{-2} s^{-1})
λ (cm)

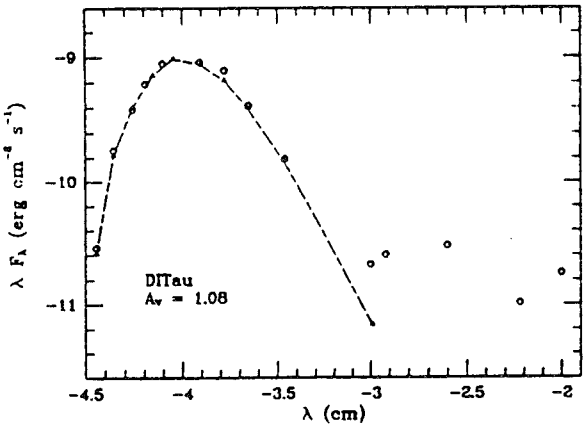
DITau
A_V = 1.08
λ $F_λ$ (erg cm^{-2} s^{-1})
λ (cm)

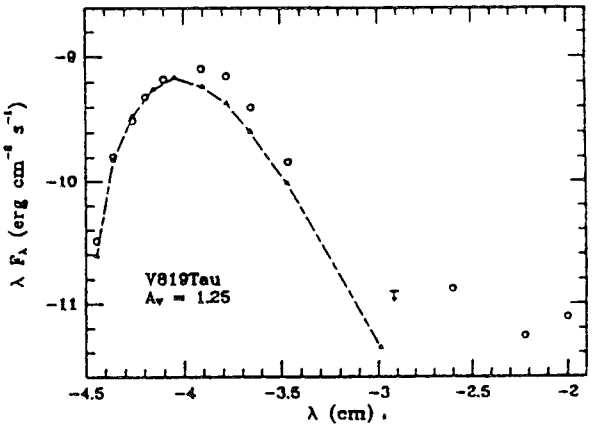
V819Tau
A_V = 1.25
λ $F_λ$ (erg cm^{-2} s^{-1})
λ (cm)

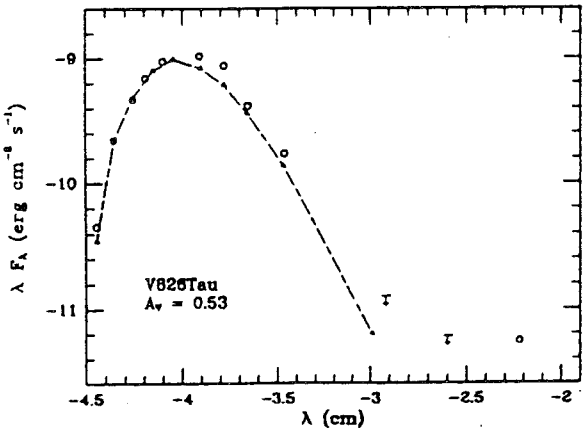
V826Tau
A_V = 0.53
λ $F_λ$ (erg cm^{-2} s^{-1})
λ (cm)

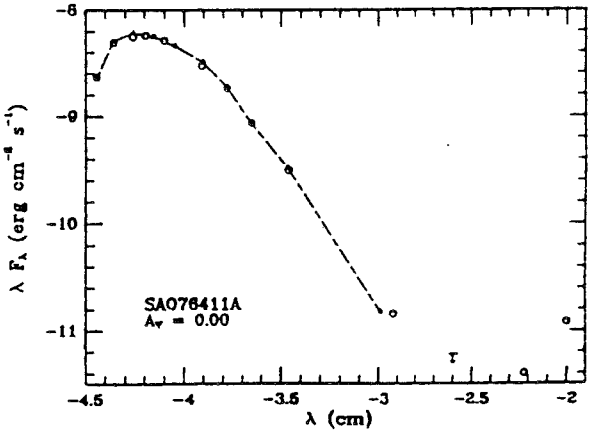
SA076411A
A_V = 0.00
λ $F_λ$ (erg cm^{-2} s^{-1})
λ (cm)

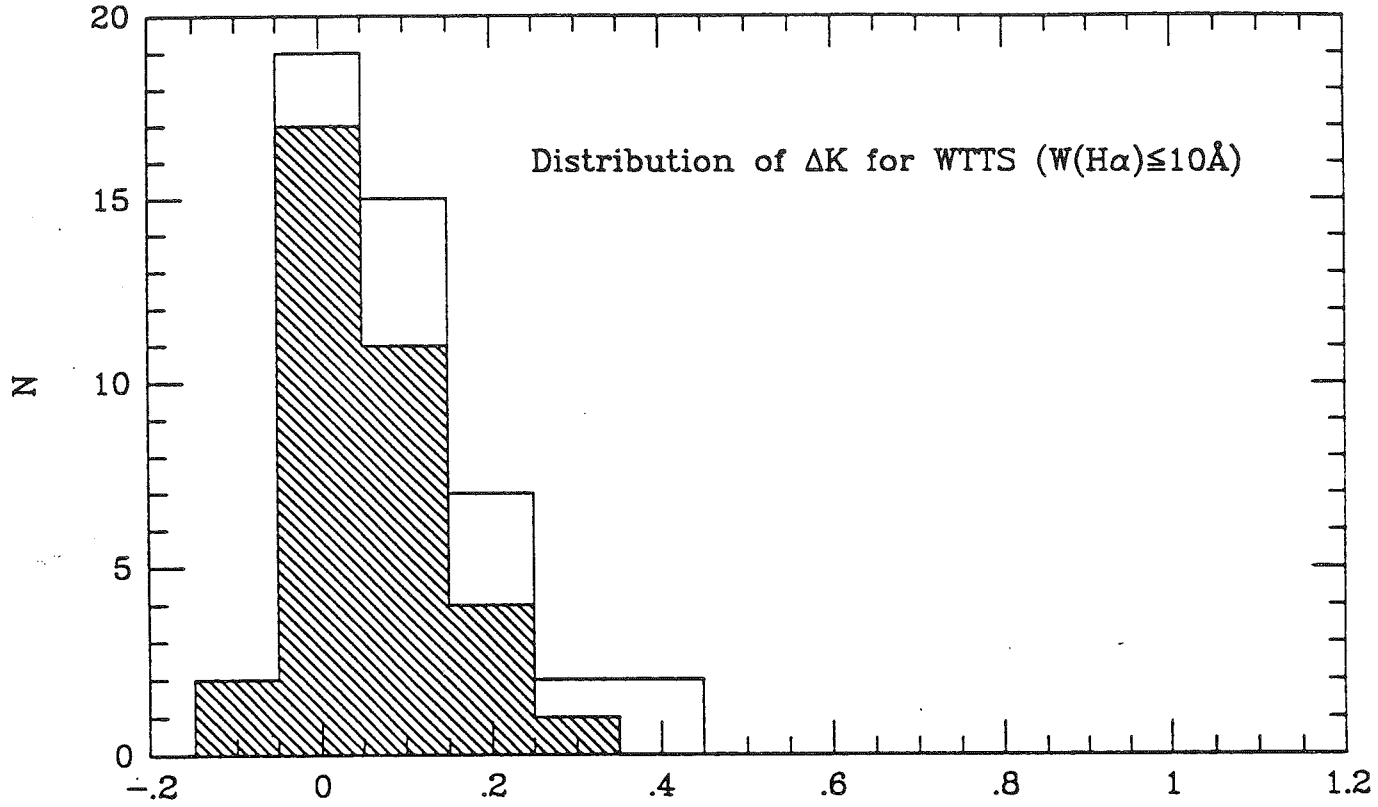
Distribution of ΔK for WTTS (W(Hα)≤10Å)
N
20
15
10
5
0
−.2
0
.2
.4
.6
.8
1
1.2

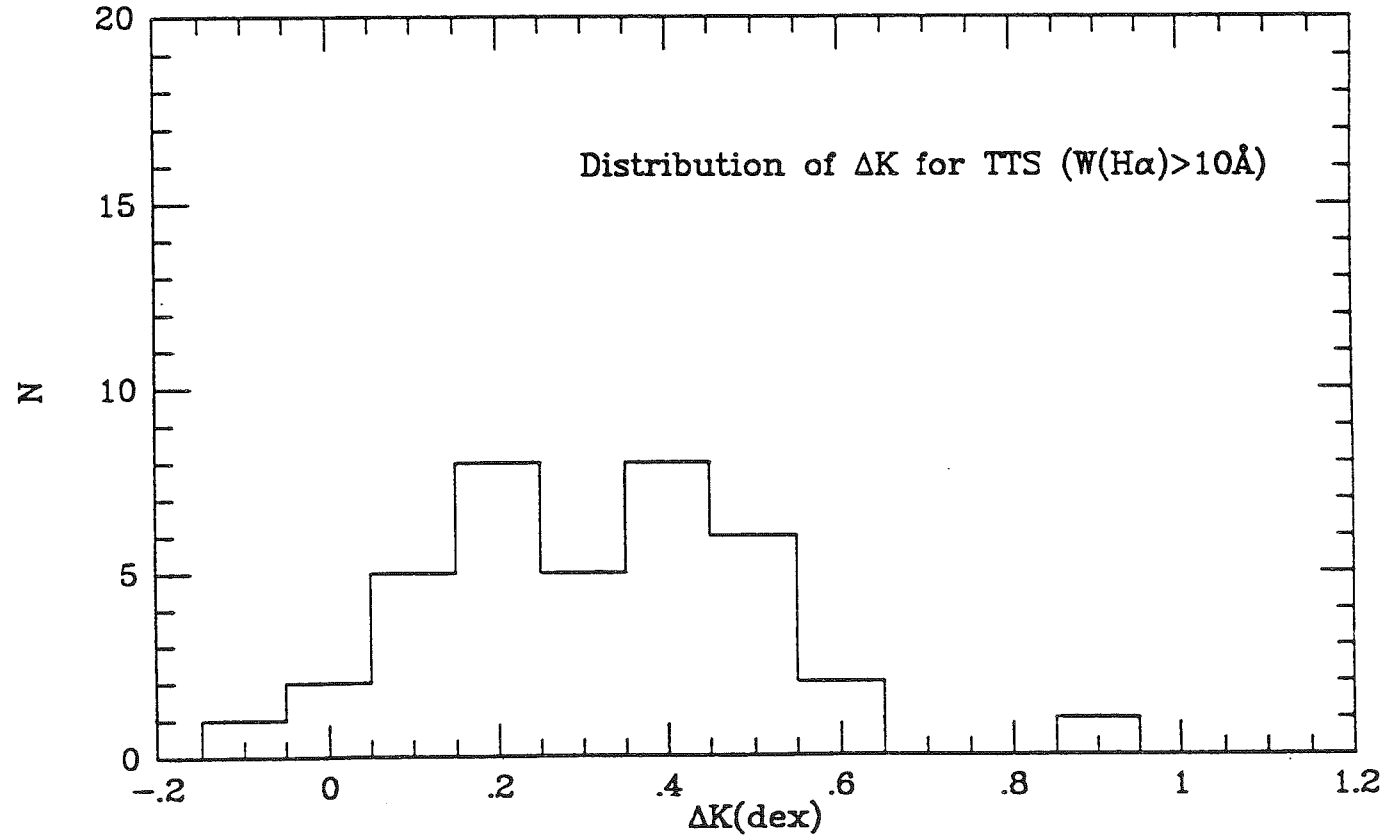
Distribution of ΔK for TTS (W(Hα)>10Å)
N
20
15
10
5
0
−.2
0
.2
.4
.6
.8
1
1.2
ΔK(dex)

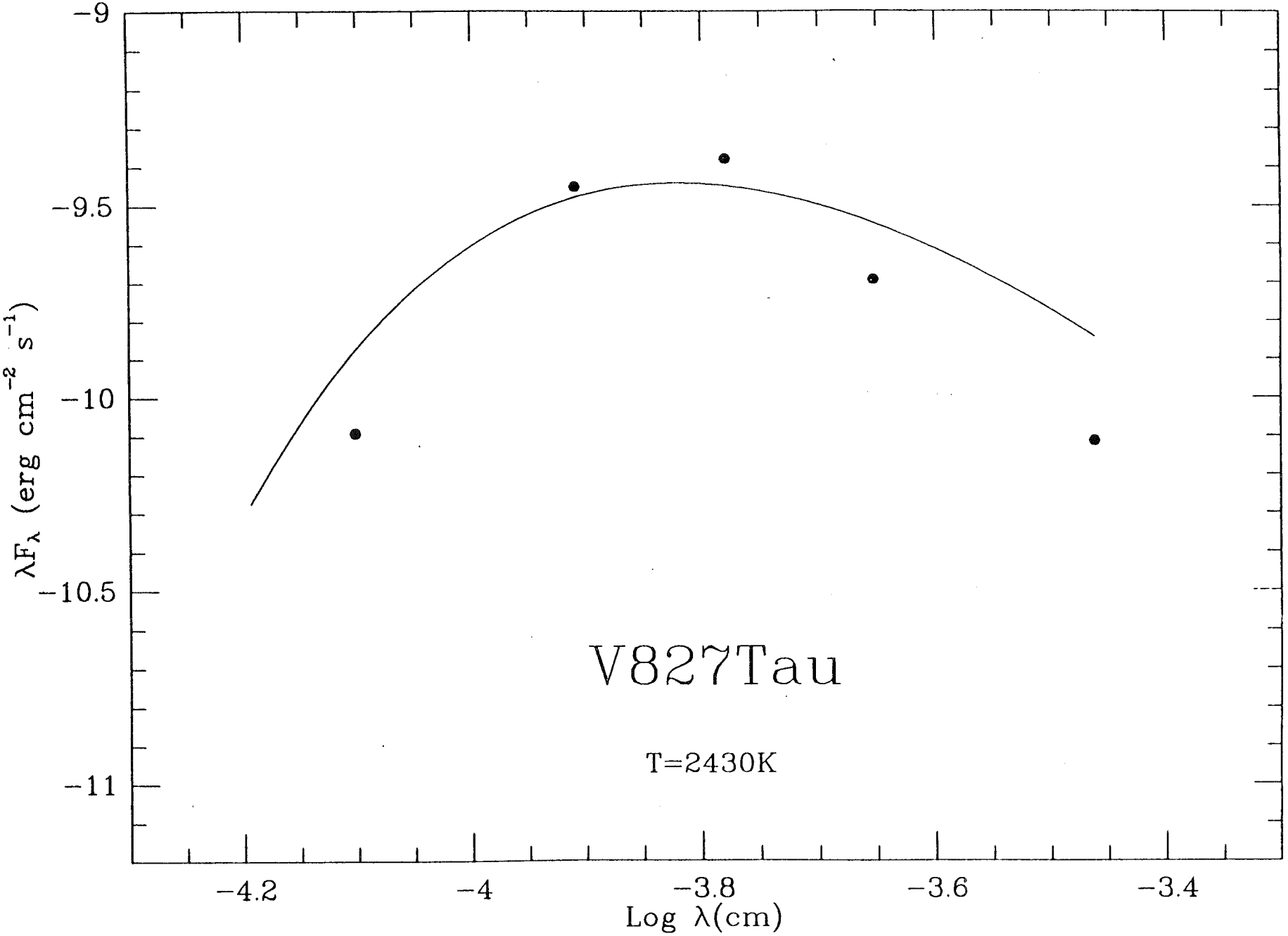
−9
−9.5
−10
−10.5
−11
λF_λ (erg cm^{-2} s^{-1})
−4.2
−4
−3.8
−3.6
−3.4
Log λ(cm)
V827Tau
T=2430K

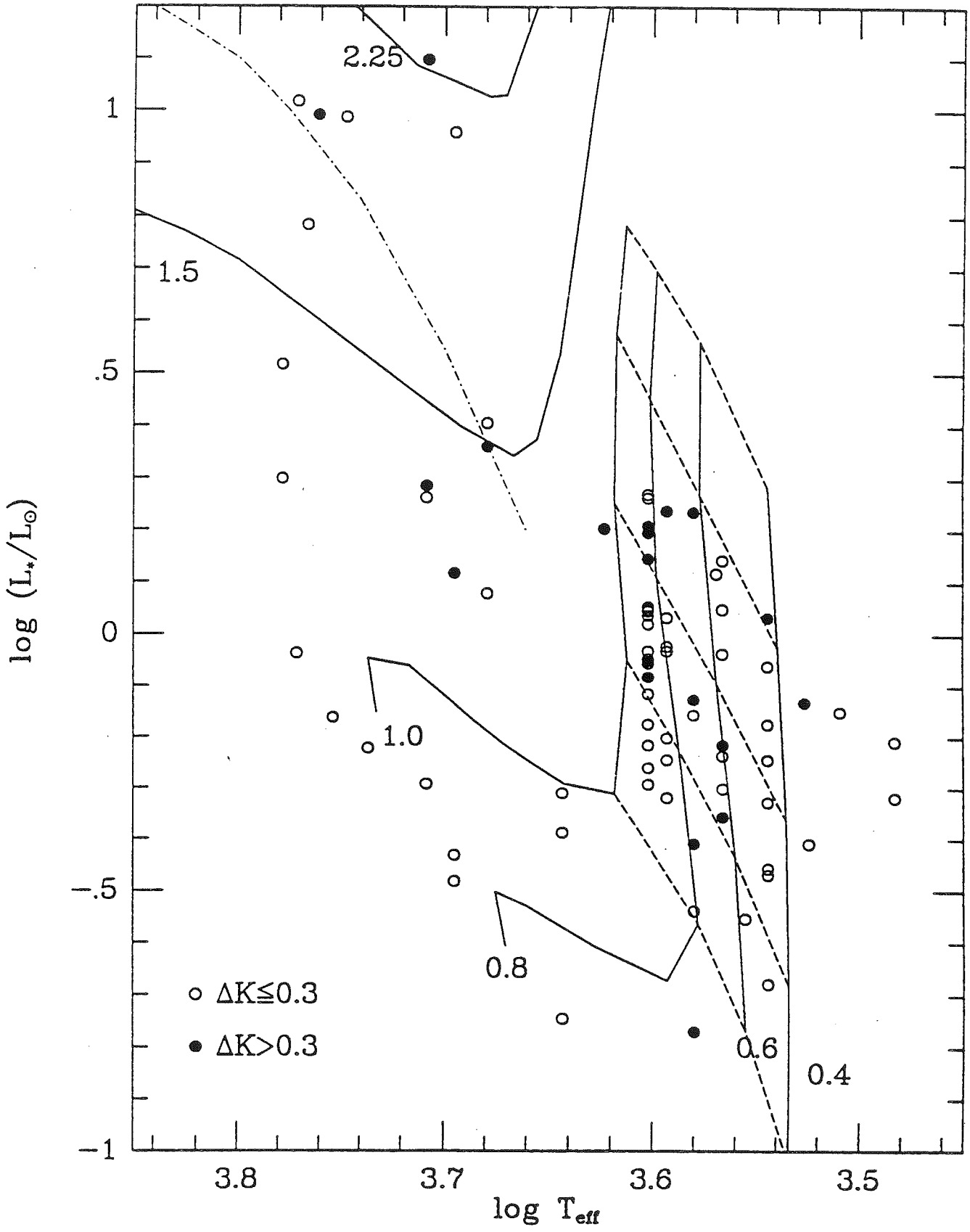
2.25
1.5
1.0
0.8
0.6
0.4
1
.5
0
−.5
−1
3.8
3.7
3.6
3.5
log T_eff
log (L*/L⊙)
ΔK≦0.3
ΔK>0.3

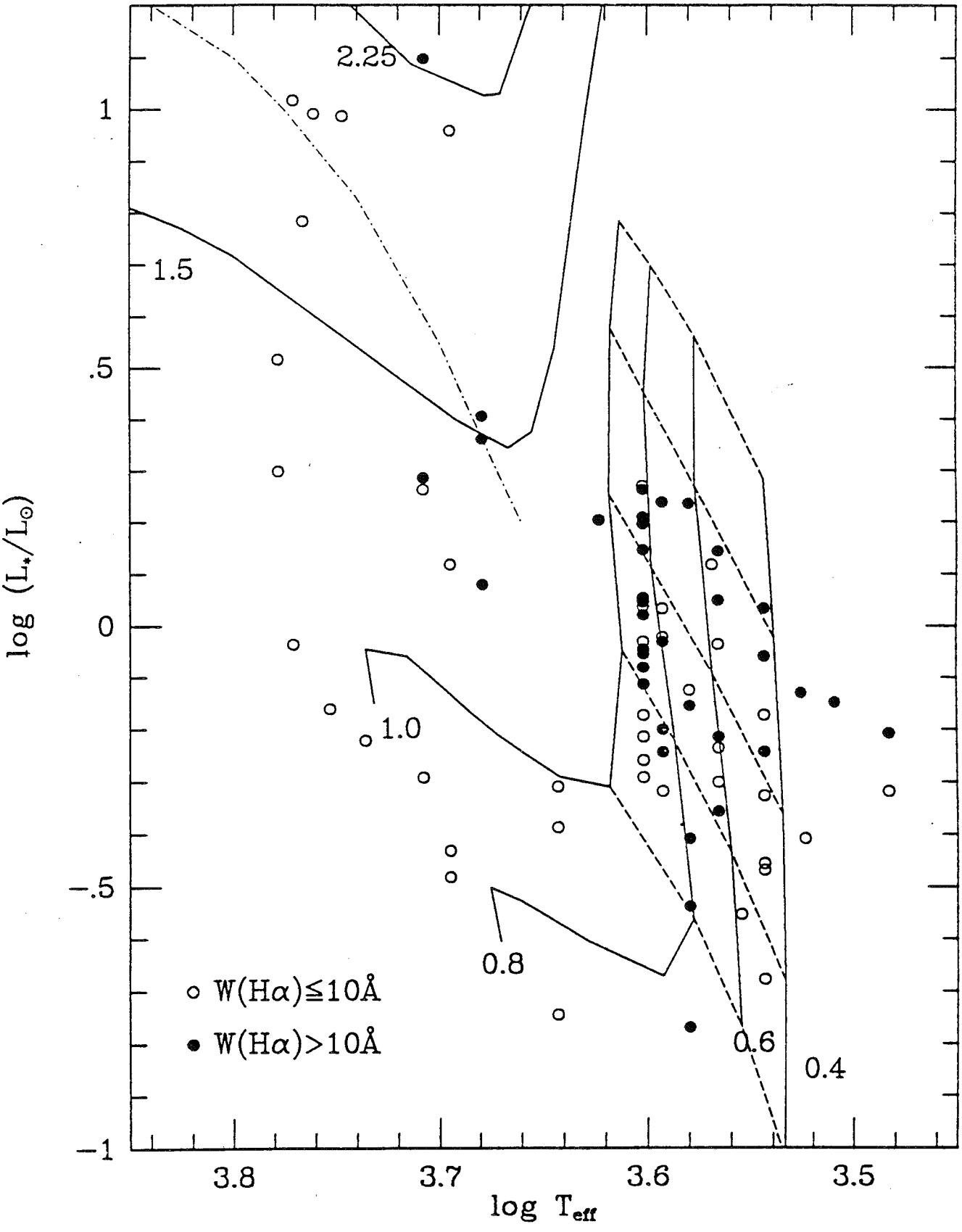
2.25
1.5
1.0
0.8
0.6
0.4
W(Hα)≦10Å
W(Hα)>10Å
log (L*/L⊙)
log Teff
1
.5
0
−.5
−1
3.8
3.7
3.6
3.5

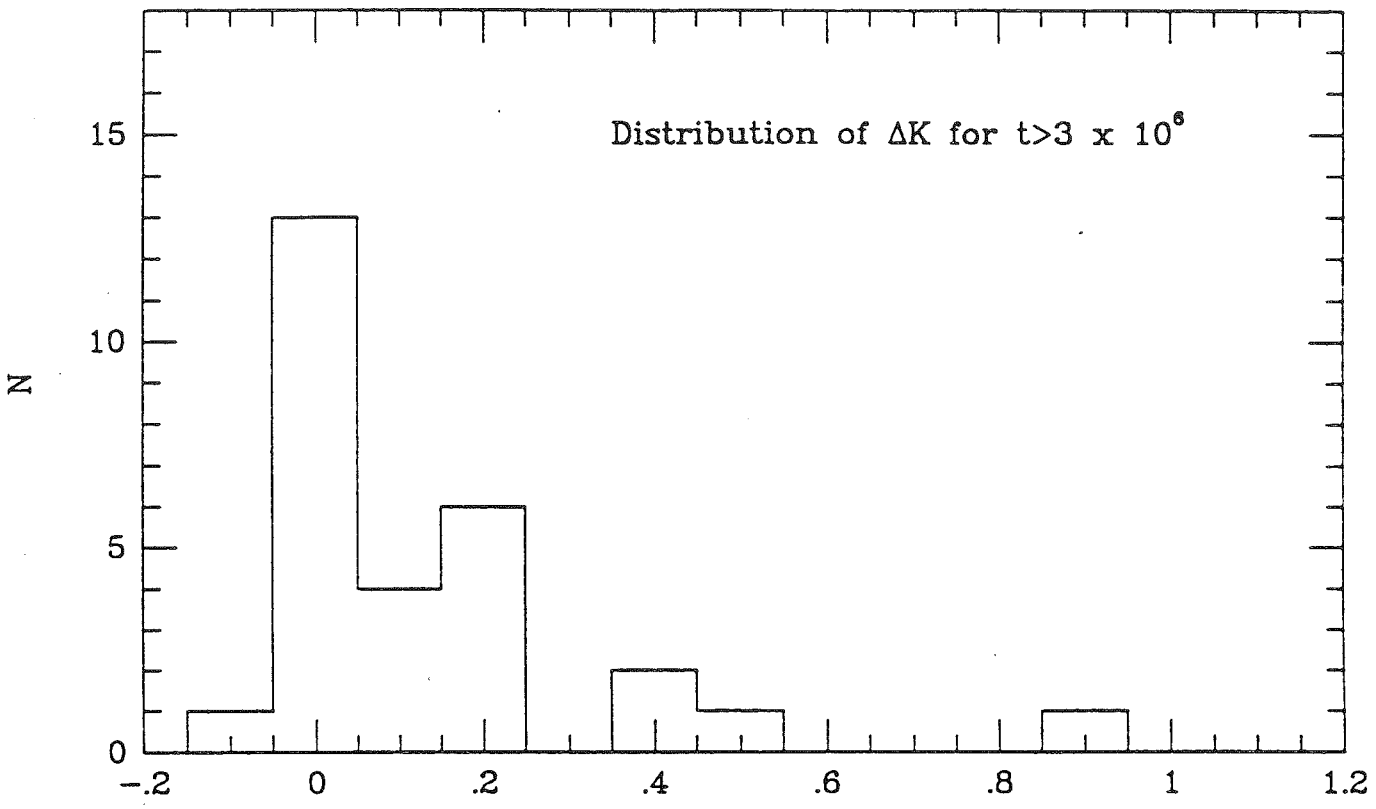
Distribution of ΔK for t>3 x 10^6
N
15
10
5
0
−.2
0
.2
.4
.6
.8
1
1.2

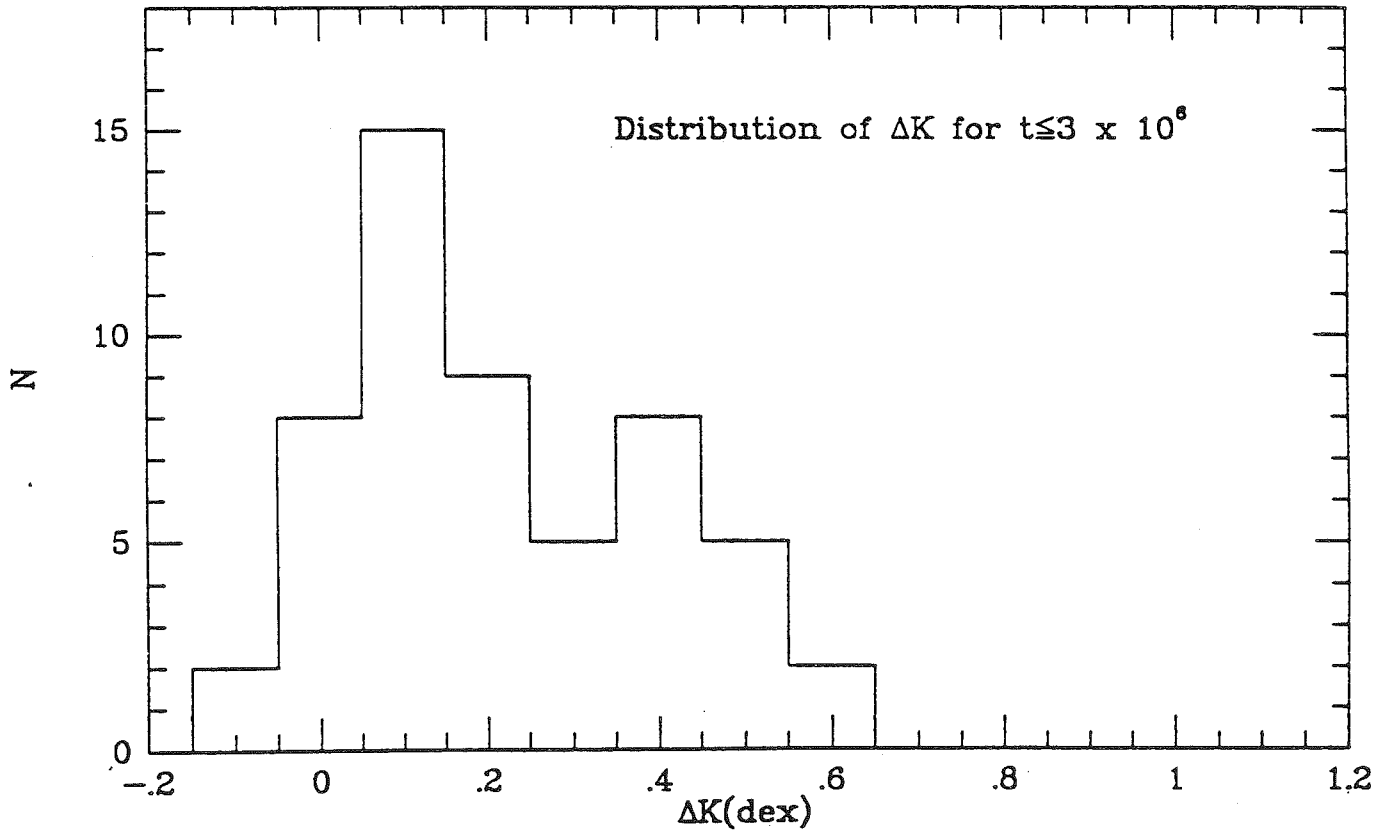
Distribution of ΔK for t≤3 x 10^6
N
15
10
5
0
−.2
0
.2
.4
.6
.8
1
1.2
ΔK(dex)

Table 1

Photometric and Spectroscopic Data for WTTS

HBC	Name	U	B	V	R_C	I_C	J	H	K	L	Source	SpT	W(Hα)	Source	A_V	ΔK	L_*	L_{tot}
347	032641+2420	13.38	12.95	12.05	11.52	11.01	10.36	9.86	9.72	9.57	9	K1	0.2	9	0.30	0.03	0.50	0.53
351	034903+2431	14.22	13.38	12.25	11.55	10.84	9.95	9.31	9.15	8.99	9	K5	1.6	9	0.04	0.14	0.49	0.59
352	035120+3154SW	12.99	12.71	11.85	11.34	10.82	10.18	9.81	9.65		9	G0	0.8a	9	0.91	0.01	0.88	0.92
353	035120+3154NE	13.61	13.25	12.31	11.75	11.18	10.49	10.04	9.94		9	G5	1.0a	9	1.03	-0.01	0.67	0.69
354	035135+2528NW	15.64	14.90	13.79	13.10	12.47					9	K3		9	0.61			
355	035135+2528SE	14.01	13.59	12.67	12.13	11.60	10.56	10.02	9.93		9	K2	0.3a	9	0.15	0.18	0.27	0.37
	SAO 76411A	9.55	9.44	8.85	8.51	8.19	7.85	7.57	7.51	7.45	9	G1	1.0a	9	0.00	0.00	6.03	5.95
356	040012+2545S												0.9	9				
357	040012+2545N	14.63	13.96	12.91	12.28	11.67	10.88	10.31	10.17		9	K2	1.8	9	0.61	0.01	0.33	1.07
358	040047+2603W	16.83	15.99	14.52	13.40	11.85	10.32	9.67	9.40	9.14	9	M2	7.8	9	0.68	0.06	0.33	0.39
359	040047+2603E	16.46	15.57	14.17	13.09	11.74	10.45	9.78	9.55	9.42	9	M2	2.4	9	0.42	-0.02	0.34	0.34
	SAO 76428	10.01	10.00	9.47	9.17	8.87	8.44	8.18	8.12	8.06	9	F8	1.3a	9	0.00	0.04	3.26	3.37
360	040142+2150SW	17.28	16.54	14.97	13.72	12.24					9	M3	7.6	9	1.10			
361	041042+2150NE	18.19	16.61	15.09	13.92	12.41					9	M3	5.7	9	0.61			
362	040234+2143	16.92	16.04	14.67	13.60	12.30	10.96	10.30	10.05		9	M2	4.0	9	0.38	0.00	0.20	0.24
365	LkCa 1	16.26	15.22	13.73	12.52	11.07	9.65	8.91	8.66	8.53	5s	M4V	4.0	5	0.08	-0.08	0.77	0.64
366	Anon 1		15.38:	13.52:							4	M0V	3.0	5				
368	LkCa 3	14.89	13.61	12.10	11.01	9.78	8.47	7.76	7.53	7.32	5s	M1V	2.5	5,3	0.87	-0.05	2.56	2.48
370	LkCa 4	15.16	13.96	12.49	11.54	10.56	9.28	8.57	8.35	8.17	5s	K7:V	5.0	5	0.95	0.07	1.11	1.23
371	LkCa 5	16.43	15.06	13.56	12.51	11.33	10.05	9.34	9.12	8.87	5s	M2V	4.0	5	0.23	0.01	0.46	0.49
372	041529+1652	15.13	14.37	13.26	12.60	11.99	11.15	10.63	10.49		9	K5	4.0	9	0.00	0.04	0.18	0.21
374	Hubble 4	15.61:	14.41:	12.73:			8.52	7.61	7.26	7.40	4,2	K7	3.0	4,5,1				
376	041559+1716	14.29	13.41	12.28	11.59	10.92	9.94	9.33	9.19	9.08	9	K7	0.7	9	0.00	0.15	0.45	0.56
378	V819 Tau	16.12	14.81	13.24	12.24	11.16	9.59	8.77	8.50	8.29	9	K7V	1.7	7,9	1.25	0.19	0.75	1.03
379	LkCa 7	15.11	13.94	12.55	11.63	10.58	9.26	8.56	8.33	8.28	5s	K7V	4.0	5,9	0.76	0.14	0.93	1.15
380	HDE 283572	10.19	9.87	9.04	8.34	7.83	7.46	7.04	6.93	6.85	9	G5IV	abs	9	0.57	-0.05	10.81	9.88
382	LkCa 21											M3,4	6.0	5				
385	IP Tau	15.43	14.50	13.04	12.06	11.09	9.83	8.97	8.44	7.54	5s	M0:V	10	5	0.25	0.31	0.48	1.00
388	042417+1744	11.44	11.13	10.34	9.88	9.45	8.90	8.49	8.40	8.24	9	K1	0.5a	9	0.00	0.00	1.81	1.90
392	042835+1700	14.74	13.71	12.53	11.81	11.15	10.30	9.68	9.57	9.53	9	K5	0.2	9	0.15	0.05	0.40	0.44
397	L1551-51	14.30	13.29	12.06	11.31	10.61	9.56	8.93	8.77	8.60	9	K7	0.5	9	0.00	0.09	0.65	0.78
398	HK Tau/G2			13.7:				8.50	8.05	7.85	1	M0.5	1.2	1				
399	V827 Tau	14.70	13.58	12.18	11.29	10.34	9.05	8.33	8.13	7.97	9	K7	1.8	7,9	0.61	0.14	1.11	1.40
400	V826 Tau	14.63	13.51	12.11	11.23	10.35	9.13	8.43	8.32	8.09	9	K7	1.6	7,9	0.53	0.06	1.07	2.20:
403	L1551-55	16.06	14.72	13.22	12.28	11.37	10.29	9.55	9.35	9.18	9	K7	0.7	9	0.91	-0.03	0.54	0.54
405	V830 Tau	14.67	13.58	12.21	11.35	10.50	9.42	8.72	8.54	8.28	9	K7	3.0	7,9	0.42	0.07	0.89	1.05

407	043124+1824	14.18	13.70	12.67	12.04	11.43	10.60	10.09	9.98		9	G8	0.3a	9	1.22	-0.01	0.59	0.63
408	Wa Tau/1	11.91	11.33	10.37	9.80	9.27	8.52	7.99	7.85	7.76	8	K0IV	0.5	8	0.57	0.07	2.94	3.05
	043220+1815	12.12	11.77	10.95	10.46	9.98	9.40	9.10	8.96		9	F8	1.3a	9	0.91	-0.04	2.01	1.99
409	FF Tau	17.41	15.73	13.67							7	K7,M0V	1.4	5				
411	Tau/3			17.3:							1	M1	4.6	1				
412	043230+1746	16.67	15.68	14.12	12.92	11.55	10.06	9.33	9.10	8.95	9	M2	9.0	9	1.18	-0.10	0.65	0.58
414	HP Tau/G3			14.8:				8.42	7.90	7.97	1	K7	2.0	1				
415	HP Tau/G2	13.38	12.46	11.07	10.21	9.36		7.38	7.19	6.84	10	G0:nIII	4.5	1	2.80	0.01	10.40	10.78
417	LkCa 14			13:							5	M0:V	0.9	5				
419	LkCa 15	14.20	13.41	12.09	11.31	10.57					5	K5:V	12.7	5,3				
420	IW Tau	15.23	14.04	12.51	11.52	10.51	9.29	8.55	8.33	8.19	5s	K7V	4.0	5	1.22	-0.03	1.37	1.41
421	Tau/4			14.9:							1	M1.5	1.8	1				
422	LkHα 332/G2			14.7:				8.60	8.13	7.50	1	K7	3.1	1				
423	LkHα 332/G1			15.1:				7.31	6.10	5.51	1	M1	3.7	1				
426	LkCa 19	12.48	11.87	10.85	10.25	9.68					9	K0V	0.5v	5,9				
427	045251+3016	13.97	12.88	11.60	10.81	10.05	9.21	8.46	8.27	8.07	9	K7	0.7	9	0.00	0.06	1.09	1.26
429	V836 Tau	15.84	14.66	13.13	12.19	11.21	9.84	9.05	8.75	8.33	9	K7V	9.0v	7,9	0.91	0.16	0.60	0.85

References

1. Cohen, M. and Kuhi,L.V. 1979,Ap.J.Suppl., 41, 743.

2. Elias,J.T. 1978, Ap.J., 224, 857.

3. Hartmann,L.W., Soderblom,D.R., and Stauffer,J.R. 1987, A.J.,93, 907.

4. Herbig,G.H. 1977, Ap.J.,214, 747.

5. Herbig,G.H., Vrba, F.J., and Rydgren,A.E. 1986, A.J., 91, 575.

6. Hojaev,A.S., 1986, Astrophys. 24, 39 [24,65].

7. Mundt,R., Walter,F.M., Feigelson,E.D., Finkenzellar,U., Herbig,G.H., and Odell,A.P., 1983, Ap.J. 269, 229.

8. Walter,F.M. 1986, Ap.J. 306, 573.

9. Walter,F.M., Brown,A., Mathieu,R.D., Myers,P.C., and Vrba,F.J., 1988, A.J. 96, 297.

10. Vrba,F.J., Rydgren,A.E., Chugainov,P.F., Shakovskaya,N.I., and Weaver,W.B. 1989,Ap.J. (in press).

Table 2

Basic Data for TTS and for WTTS Formerly Classified as TTS

HBC	Name	U	B	V	R_C	I_C	J	H	K	L	Source	SpT	W(Hα)	Source	A_V	ΔK	L_*	L_{tot}
									TTS									
23	FM Tau	14.56	15.01	14.30	13.50	12.40	10.32	9.39	8.71	7.93	9	M0	71	3				
24	FN Tau	17.48	16.64	14.95			9.54	8.65	8.22	7.49	7,9	M5	25	3				
25	CW Tau	13.74	13.59	12.36	11.42	10.60	9.00	7.87	6.86	5.62	9s	K3	135	3	2.16	0.52	2.3	4.4
26	FP Tau	16.21	15.46	13.91	12.78	11.39	9.96	9.15	8.84	8.49	9s	M5.5	39	2,3	0.00	-0.06	0.6	0.6
27	CX Tau	16.09	15.24	13.67	12.57	11.27	9.88	9.09	8.83	8.46	9s	M2	20	2,3	0.55	0.03	0.6	0.7
28	CY Tau	14.11	14.53	13.35	12.38	11.20	9.76	8.90	8.42	7.81	9s	M1	70	3	0.14	0.32	0.4	0.9
30	DD Tau	14.57	15.03	14.11	13.09	11.55	9.56	8.62	7.97	6.88	6,9	M1	182	3	1.36	0.40	0.6	2.4
32	BP Tau	13.82	13.62	12.36	11.43	10.53	9.17	8.40	8.01	7.53	6s	K7	40	3	0.84	0.19	1.1	1.6
33	DE Tau	14.03	14.31	12.95	11.87	10.66	9.15	8.26	7.71	6.93	6s	M1	54	3	0.81	0.22	1.1	1.6
34	RY Tau	12.27	11.86	10.92	10.28	9.63	8.00	6.78	5.74	4.47	6s	K1	21	3	0.55	0.94	1.9	14.0
35	T Tau	11.69	11.07	9.89	9.11	8.45	7.15	6.18	5.40	4.16	6s	K1	38	3	1.67	0.42	12.5	35.5
36	DF Tau	12.85	13.17	12.08	11.08	9.94	8.32	7.40	6.81	5.89	9s	M0.5	54	3	0.55	0.41	1.7	3.4
37	DG Tau	12.85	13.09	12.17	11.33	10.48	8.96	7.81	6.73	5.03	9	C	113	3				
38	DH Tau	15.33	15.32	13.92	12.80	11.53	9.80	8.88	8.33	7.65	8s	M0	53	3	1.52	0.29	0.6	1.1
45	DK Tau	14.05	13.77	12.45	11.47	10.48	8.88	7.82	7.03	5.97	9s	K7	19	3	1.40	0.43	1.6	4.2
46	ZZ Tau	16.05	15.76	14.28	13.04	11.29	9.52	8.78	8.54	8.36	9	M4	16	3,2	0.65	0.05	0.7	0.8
48	HK Tau	18.32	17.48	15.75	14.29	12.73	10.33	9.08	8.37	7.63	6,9	M0.5	29	3	3.38	0.28	0.7	1.5
49	HL Tau	16.16	15.92	14.55	13.47	12.36	10.21	8.67	7.10	5.34	9s	C	65	3				
50	XZ Tau	16.31	16.37	14.94	13.59	11.81	9.34	8.16	7.17	5.85	9s	M3	274	3	1.71	0.62	0.7	4.1
51	V710 TauA	15.53	15.20	13.65	12.46	10.99	9.02	8.21	8.00	7.34	9,7s	M1	48	3	1.80	0.06	1.4	1.7
52	UZ TauE	13.67	14.06	13.08	11.97	10.60	8.45	7.60	7.02	6.40	1,3	M1	82	2,3	0.61	0.50	1.1	12.0
54	GG Tau	13.81	13.75	12.35	11.36	10.38	8.79	7.85	7.25	6.39	6s	K7	55	5,3	1.21	0.36	1.6	3.0
55	GH Tau	15.06	14.48	12.95	11.90	10.61	9.30	8.38	7.86	7.05	9	M2	15	3	0.25	0.23	0.9	1.4
56	GI Tau	14.23	14.27	13.09	12.08	11.05	9.16	8.22	7.55	6.60	8s	K7	19	3	1.33	0.49	0.9	2.0
57	GK Tau	14.02	13.64	12.37	11.45	10.53	9.00	8.01	7.32	6.42	8s	K7	16	5,3	0.78	0.49	1.1	2.2
58	DL Tau	13.96	14.19	13.05	12.11	11.15	9.69	8.77	8.12	7.11	6s	C	105	3				
59	IS Tau		16.28	14.29		11.54	9.52	8.51	7.97	7.19	8	K2	12	3				
60	HN Tau	14.76	15.07	14.23	13.34	12.60	10.87	9.60	8.36	6.83	6	C	139	2,3				
61	CI Tau	14.62	14.72	13.37	12.32	11.22	9.50	8.50	7.76	6.83	6s	K7	102v	3,2	1.58	0.42	0.9	1.9
62	DM Tau	14.99	15.14	13.99	12.99	11.85	10.41	9.70	9.45	9.18	6s	M0.5	140	3	0.55	0.13	0.3	0.5
63	AA Tau	13.82	13.62	12.36	11.43	10.53	9.33	8.53	8.13	7.42	6s	K7	37	3	0.84	0.15	1.1	1.6
64	HO Tau	15.63	15.98	14.84	13.81	12.51		10.31	9.52	8.94	9,3	M0.5	115	3	0.73	0.35	0.2	0.3
65	DN Tau	14.46	13.72	12.33	11.40	10.44	9.16	8.37	8.03	7.51	6s	M0	12	3	0.35	0.21	0.9	1.4
66	HP Tau	15.73	14.83	13.16	12.07	11.00	9.34	8.24	7.47	6.52	9s	K3	35	3	3.08	0.26	2.6	5.0
67	DO Tau	15.59	15.70	14.30	13.11	11.79	9.64	8.44	7.49	6.24	6s	K7	109	2,3	2.44	0.58	0.8	2.9

69	V955 Tau	17.69	16.51	14.74	13.32	11.96		8.42	7.73	6.93	9,3	K7	12.7	2,3	3.85	0.20	1.8	3.0
70	DP Tau	15.48	15.65	14.31	13.20	12.05	10.32	9.18	8.36	7.09	9s	M0.5	86	3	1.22	0.46	0.4	1.3
71	GO Tau	16.58	16.35	14.89	13.62	12.30	10.73	9.83	9.39	8.67	9	M0	81	3	2.44	-0.05	0.6	0.7
72	DQ Tau	16.06	15.14	13.55	12.41	11.25	9.56	8.63	8.08	7.17	9s	K7	113	2,3	2.13	0.18	1.1	1.8
73	Haro 6-37	15.37	14.98	13.42	12.28	11.09	9.14	7.99	7.23	6.27	9s	K6	26	3	2.44	0.44	1.6	3.2
74	DR Tau	11.64	12.23	11.57	10.91	10.25	8.54	7.46	6.45	5.15	9	C	87	3				
75	DS Tau	12.68	12.78	11.90	11.16	10.46	9.33	8.59	8.16	7.49	9s	K3	59	3	0.93	0.23	1.2	1.8
76	UY Aur	13.68	13.61	12.37	11.39	10.46	8.91	7.85	7.05	5.87	9s	K7	73	3	1.14	0.48	1.4	4.6
77	GM Aur	13.55	13.22	12.03	11.22	10.50		8.82	8.59	8.22	9,3	K7	97	2,3	0.10	0.09	0.8	1.3
80	RW Aur	11.47	11.84	11.09	10.42	9.68	8.54	7.62	6.87	5.79	9	C	84	3				
									WTTS									
367	V773 Tau	13.12	12.02	10.65	9.80	8.94	7.63	6.83	6.48	5.86	8s	K2	1.5	3	2.04	0.10	9.1	10.3
29	V410 Tau	13.04	12.10	10.92	10.18	9.48	8.33	7.73	7.54	7.41	8s	K7	2.1	2	0.00	0.13	1.9	2.4
31	CZ Tau	18.07	16.91	15.33	14.13	12.38	10.52	9.76	9.33	8.35	6,9	M1.5	3.5	3	1.36	0.19	0.3	1.0
39	DI Tau	15.96	14.46	12.86	11.81	10.74	9.41	8.63	8.40	8.20	8s	M0	2	3	1.08	0.01	1.1	1.2
41	IQ Tau	15.43	15.08	13.53	12.43	11.27	9.64	8.64	8.00	7.06	9s	M0.5	7.8	3	1.16	0.32	0.8	1.5
42	UX TauB	16.32	15.12	13.67	12.63	11.29			8.77	8.73	6,7	M1	4	3	0.57	0.14	0.5	0.6
43	UX TauA	13.19	12.42	11.32	10.66	9.99			7.58	6.98	6,4	K2	3.9	3	0.47	0.44	1.3	2.4
44	FX Tau	16.62	15.54	13.90	12.71	11.25	9.55	8.57	8.06	7.46	9s	M1	9.6	3	1.49	0.19	0.9	1.4
47	V927 Tau	17.00	16.15	14.61	13.38	11.51		8.97	8.66	8.55	9,3	M5.5	4.7	3	0.00	0.08	0.5	0.5
68	VY Tau	16.50	15.26	13.75	12.71	11.53	9.85	9.10	8.79	8.32	9s	M0	4.9	3	1.02	0.21	0.5	0.8
79	SU Aur	10.27	9.87	9.03	8.51	8.02	7.03	6.46	5.95	5.21	10s	G2III	4v	3	0.64	0.41	9.8	16.0

References

1. Bastian,U. and Mundt,R. 1979, Ap.J.Suppl., **36**, 57.

2. Cabrit,S., Edwards,S., Strom,S.E. and Strom,K.M. 1989, AJ (in preparation).

3. Cohen, M. and Kuhi,L.V. 1979,Ap.J.Suppl., **41**, 743.

4. Grasdalen, unpublished, reported in Rydgren et.al. 1984b.

5. Herbig,G.H. 1977, Ap.J.,**214**, 747.

6. Rydgren,A.E., Schmeltz,J.T., and Vrba, F.J. 1982, Ap.J. **256**, 168.

7. Rydgren,A.E., Strom,S.E., and Strom,K.M. 1976, Ap.J.Suppl.**30**, 307.

8. Rydgren,A.E. and Vrba,F.J. 1981, A.J., **86**, 725.

9. Rydgren,A.E. and Vrba,F.J. 1983, A.J., **88**, 1017.

10. Warner,J.W., Hubbard,R.P., and Gallagher,J.S. 1978, A.J., **83**, 1614.

Table 3

IRAS Fluxes for the WTTS

HBC	Name	12μ	25μ	60μ	100μ
347	032641+2420	*0.08*	*0.07*	*0.12*	*0.35*
351	034903+2431	*0.09*	*0.05*	*0.13*	*
352+353	035120+3154	*0.05*	*0.04*	*0.12*	*0.2*
354+355	035135+2528	*0.07*	*0.04*	*0.04*	*
	SAO 76411	0.06H	*0.03*	0.08E	0.39D
356+357	040012+2545	*0.04*	*0.04*	0.16G	
358+359	040047+2603	*0.04*	*0.04*	*0.06*	
	SAO 76428	*0.04*	*0.04*	*0.08*	
360+361	040142+2150	*	*	*0.10*	
362	040234+2143	*0.08*	*0.04*	*0.08*	
365	LkCa 1	*0.05*	*0.07*	*0.17*	
366	Anon 1	*0.09*	*0.05*	*0.12*	*
368	LkCa 3	*0.05*	*0.05*	*0.10*	
370	LkCa 4	*0.10*	*0.04*	*0.11*	
371	LkCa 5	*0.06*	*0.04*	*0.12*	
372	041529+1652	*0.07*	*0.05*	*0.18*	
374	Hubble 4	*	*	*	*
376	041559+1716	*0.08*	*0.05*	*0.12*	*0.7*
378	V819 Tau	*0.10*	0.11F	0.11F	0.26H
379	LkCa 7	*0.06*	*0.04*	*0.11*	*0.2*
380	HDE 283572	0.11F	*0.19*	*	*
382	LkCa 21	0.77F	0.91F	*	*
385	IP Tau	0.34B	0.51A	0.49C	0.57H
388	042417+1744	0.13H	*0.04*	*0.08*	
392	042835+1700	*0.05*	*0.04*	*0.09*	
397	L1551-51	*0.07*	*0.05*	*0.15*	
398	HK Tau/G2	*0.09*	*0.17*	*0.20*	
399	V827 Tau	*0.05*	*0.08*	*0.14*	
400	V826 Tau	*0.07*	*0.08*	.11H	
403	L1551-55	*0.07*	*0.04*	*0.11*	
405	V830 Tau	0.08H	*0.09*	*0.10*	0.34G
407	043124+1824	*0.07*	*0.04*	*0.12*	
408	Wa Tau/1	*0.05*	*0.03*	*0.10*	*1.4*
	043220+1815	*0.05*	*0.06*	*0.14*	
409	FF Tau	*0.07*	*0.03*	*0.12*	*4.2*
411	Tau/3	0.45A	0.37B	0.12G	
412	043230+1746	*0.07*	*0.03*	*0.12*	*0.2*
414	HP Tau/G3	*	*	*	*
415	HP Tau/G2	*	*	*	*
417	LkCa 14	*0.05*	*0.02*	*	*
419	LkCa 15	0.27B	0.39A	1.58A	2.64D
420	IW Tau	*0.09*	*0.05*	*0.16*	
421	Tau/4	*0.09*	1.04B	1.50B	*
422	LkHα 332/G2	*	*	*	*
423	LkHα 332/G1	*	*	*	*
426	LkCa 19	*0.08*	*0.07*	*0.18*	
427	045251+3016	0.11G	0.30E	0.08F	*
429	V836 Tau	0.21B	0.23B	*	*

Notes

The error codes for the measurement of the IRAS fluxes are as follows:A,5%; B,10%; C,15%; D,20%; E,25%; F,30%; G,50%; H,100%.

Individual Objects

351. The observed "hump" at 100μ, while centered on the optical position, is broader than the 100 μ beam profile.

354,355. The source profile is broader at 60 and 100μ than the IRAS beam profiles.

360,361. A strong source to the north prevents measurement at 12μ and 25μ.

366. This object lies in the wings of a nearby, bright source.

374. This object lies in the wings of a very strong source (Elias 1); consequently, it is not possible to list meaningful upper limits.

380. A bright source dominates the plot scale at 60 and 100μ making accurate measurement impossible.

382. This object lies in the wings of the RY Tau profile at 60μ and 100μ.

414,415. The intensities for these objects cannot be separated from that of HP Tau.

417. At 60μ and 100μ, the IRAS flux is dominated by a strong source to the north.

421. At 100μ the intensity peak is displaced from the object position.

422,423. The intensities for these objects cannot be separated from that of V955 Tau (LkH 332).

427. A strong source to the north limits our ability to measure the IRAS fluxes.

429. The background fluctuates strongly at 60 and 100μ.

Table 4

IRAS Fluxes for TTS and WTTS Formerly Classified as TTS

HBC	Name	12μ	25μ	60μ	100μ	notes
			TTS			
23	FM Tau	0.67H	0.91F			*
24	FN Tau	0.62B	1.57B	1.74B	0.7H	
25	CW Tau	2.61B	4.14D	3.56F		
26	FP Tau	0.16G	0.27D	0.34F		
27	CX Tau	0.24F	0.40F	0.34G		
28	CY Tau	0.27D	0.25E	0.15G		
30	DD Tau	0.23B	3.64B	5.9G		*
32	BP Tau	0.56B	0.64B	0.41B	1.08F	
33	DE Tau	0.48B	0.80B	1.21B		
34	RY Tau	19.47A	29.79A	20.48A	15.91F	
35	T Tau	16.48A	49.56A	111.74A	121.85A	
36	DF Tau	1.16B	1.28D	0.65D		
37	DG Tau	10.64B	23.59B	41.59B	53.13B	*
38	DH Tau	0.17B	0.40B	0.33D	0.98F	*
45	DK Tau	2.24A	2.64A	1.64D	3.67D	
46	ZZ Tau	0.16F	0.12G			*
48	HK Tau	0.31C	1.03B	2.76B	6.6F	
49	HL Tau	7.84A	29.08A	70.5A	74.5A	*
50	XZ Tau	3.36A	6.82A	16.5A	17.5A	*
51	V710 TauA	0.35D	0.49D	0.53F		*
52	UZ TauE	1.51B	1.91B	2.41B	1.26G	*
54	GG Tau	1.37B	1.90B	3.35B	6.03B	
55	GH Tau	0.69B	1.03B	1.16B		*
56	GI Tau	1.23A	1.67A	0.96A		*
57	GK Tau	1.23A	1.67A	0.96A		*
58	DL Tau	1.06B	1.51B	1.50B	3.0G	
59	IS Tau	0.32D	0.31D	0.20F		
60	HN Tau	1.59A	2.02A	1.43D		
61	CI Tau	0.92B	1.38B	2.41B	2.32D	
62	DM Tau	*0.09*	0.37E	0.85E		
63	AA Tau	0.42C	0.62C	1.28D	3.36F	
64	HO Tau	*0.11*	0.23F	0.17G		*
65	DN Tau	0.38B	0.69D	0.82B		
66	HP Tau	2.41A	4.26A	8.33C	21.86E	*
67	DO Tau	2.04A	4.26A	6.91A	7.95F	*
69	V955 Tau	0.73A	0.82C	1.74B	11.0D	*
70	DP Tau	0.81B	1.32B	0.92D	1.9H	
71	GO Tau	0.18F	0.20G	0.38F		
72	DQ Tau	0.74D	1.25D	1.04D		
73	Haro 6-37	1.20C	1.20B	0.79C		
74	DR Tau	3.57A	4.80A	5.76A	6.2G	
75	DS Tau	0.34A	0.38A	0.37B		
76	UY Aur	3.85A	7.30A	7.89A	6.8F	
77	GM Aur	0.21E	1.18C	3.16C	3.93G	
80	RW Aur	2.60A	4.04A	3.34A	1.70D	

WTTS

367	V773 Tau	2.80B	3.40B	2.0F	1.1H	
29	V410 Tau	0.9G	*.17*			
31	CZ Tau	0.96G	2.4H			*
39	DI Tau	0.10B	0.24B	0.20D	0.60F	*
41	IQ Tau	0.52A	0.76B	0.83З		
42+43	UX TauA&B	0.30D	1.81B	3.90B	5.51F	*
44	FX Tau	0.49B	0.61C	0.65E		
47	V927 Tau	*0.04*	*0.04*	*0.10*		
68	VY Tau	0.11G	0.26D	0.43F		
79	SU Aur	4.27B	14.30A	17.16E	43.61B	*

Notes

23. FM Tau. This star is located near V773 Tau, a much stronger source, making flux measurements difficult, particularly at the longer wavelengths.

30,31. DD and CZ Tau. While the contributions from these stars could be measured separately on the ADDSCAN traces, their intensity-position profiles did overlap.

37. DG Tau. DG Tau b lies within the point source profile for this star.

38,39. DH and DI Tau. The measured IRAS flux has been divided between the two stars in proportion to their ground based 10μ fluxes. The error codes refer to the accuracy of the combined measurement.

42,43. UX Tau A and B. The listed measurement refers to both components. Since A is much brighter than B in the near infrared, the total IRAS flux has been assigned to A for the purposes of computing L_{tot}.

46. ZZ Tau. At 60μ and 100μ a strong source to the south, listed in Table 5, makes measurement of the contribution from ZZ Tau impossible.

49,50. HL and XZ Tau. The flux has been divided between the two stars in proportion to their ground based 10 and 20μ fluxes. The error codes refer to the accuracy of the *combined* flux measurement.

51. V710 TauA. This measurement refers to both components of the double. The total flux has been assigned to A in computing L_{tot}.

52. UZ TauE. Both components of the double lie within the IRAS beam. The total flux has been assigned to UZ Tau E in computing L_{tot}.

55. GH Tau. V807 Tau lies within the IRAS beam for this star. The total IRAS flux has been assigned to GH Tau.

56,57. GI and GK Tau. The IRAS flux has been divided equally between these two stars since their 10μ fluxes (observed from the ground are nearly equal.

64. HO Tau The peak is displaced from the stellar position at longer wavelengths.

66. HP Tau. HBC 414 and 415 lie within the IRAS beam for this star. The total flux has been assigned to HP Tau in the absence of ground-based measurements for HBC 414 and 415.

67. DO Tau. HV Tau lies within the IRAS beam for this star. The total flux has been assigned to DO Tau.

69. V955 Tau. HBC 422 and 423 lie within the IRAS beam for this star. The total flux has been assigned to V955 Tau in the absence of ground-based measurements for HBC 422 and 423.

79. SU Aur. AB Aur is nearby but does not significantly influence the measurements.

Table 5

IRAS Fluxes for Additional Stars

HBC	Name	12μ	25μ	60μ	100μ	notes
369	FO Tau	0.49B	0.71D	0.66F		
373	V892 Tau	37.10A	107.6A	88.9B	233.D	*
377	FQ Tau	*0.11*	*0.09*	*0.20*		
	FR Tau	0.16G	0.08H	0.11H		
	T Tau NW	1.74A	2.09A	1.40D		*
383	FS Tau	1.61A	4.47A	7.60A	12.7D	*
	FU Tau	0.14G	0.22H	*0.16*	1.7H	
	GT Tau	*0.09*	*0.07*			
384	FT Tau	0.42D	0.63D	0.91G	1.7G	
386	FV Tau	1.93B	3.39B	3.56F		*
	HH31D	0.23D	1.53A	4.78A	11.8B	*
389	Haro 6-10	16.65A	43.1A	66.6A	55.5A	*
	FW Tau	0.11H	*0.12*	*0.07*		
	ZZ Tau/FIR	0.72B	1.9B	3.8B	5.3F	*
396	Haro 6-13	1.20A	4.50A	7.82A	11.8B	
	HI Tau	*0.04*	*0.08*	*0.08*		
401,402	FY,FZ Tau	1.51B	1.76B	1.11D	*1.34*	*
	SVS 1849	*0.07*	*0.06*	*0.15*		
	IT Tau	0.27F	0.48D	0.38F		
	HQ Tau	1.70B	2.29B	1.50F		
	FG Tau	*0.06*	*0.05*	0.22G		
	HDE 283579	*0.09*	0.26G	0.78F		
	FI Tau	*0.06*	*0.09*	*0.20*		
	HT Tau	0.10G	0.13H	*0.16*		
	GN Tau	0.59B	0.76D	0.80F		
	Haro 6-32	*0.38*	*0.17*			*
	S9557	*0.11*	*0.07*	*0.20*		
	HD29647	0.74	1.06	10.84	17.87	*
	Haro 6-33	0.73B	1.70A	3.08B		*
	SVS 1099	*0.05*	0.13F	*0.09*		
	Haro 6-36	0.10G	*0.17*	*0.10*		
	Haro 6-39	0.14H	0.36F	0.50D		

Notes

373. V892 Tau. At 60μ, another source appears to the north; at 100μ, the source is far broader than the point source function.

T Tau NW. This star was discovered on a coadd of the IRAS field surrounding T Tau. A moderate resolution (~10Å) optical spectrum shows this object to be an M1 IV type star with Hα and the NaI D lines in emission; W(Hα) = 27 Å. Measurements made at KPNO on 23 October, 1986 (UT) give: K = 7.94, (J-K) = 2.15, and (H-K) = 0.73. Its position is α = 04:18:47.3; δ = 19:27:10. At 60μ, a source ~ 4′ south appears; at 100μ, this is the dominant source.

383. FS Tau. Haro 6-5b lies within the IRAS beam for these measurements.

386. FV Tau. This star lies very near to DG Tau, and itself has a companion. The measurements are probably affected by the strong contribution from DG Tau.

HH31D. This source is extended at 60μ and 100μ.

389. Haro 6-10. There are low level wings of extended emission associated with this source.

ZZ Tau/FIR. This source lies ~ 45" S of ZZ Tau, and is probably the source of the outflow reported by Heyer, M., Snell,R.L., Goldsmith,P.F. and Myers, P.C. 1987, Ap.J. 321, 370.

401,402. FY and FZ Tau. The individual contributions from these stars cannot be separated.

Haro 6-32. No measurements are possible at 60μ and 100μ due to the proximity of a much stronger source.

HD29647. This late B star, the object of many interstellar line studies, has been presumed to lie behind the Taurus molecular clouds. The IRAS data shows that it is clearly associated with the clouds since it heats nearby material; substantial extended nebulosity surrounds the star in all bands. The stellar fluxes reported here are taken from the co-adds.

Haro 6-33. This star lies within the extended emission surrounding HD29647, making measurement difficult at $\lambda \leq 60\mu$, and impossible at 100μ. Measurements made at KPNO on 24 October, 1986 (UT) give: K = 9.62, (J-K) = 2.82, and (H-K) = 1.14.